Thesis presented to the Instituto Tecnológico de Aeronáutica, in partial fulfillment of the requirements for the degree of Doctor of Science in the Graduate Program of Physics, Field of Astrophysics.

Khashayar Kianfar

MULTIWAVELENGTH STUDIES OF AGN FEEDING & FEEDBACK MECHANISMS IN THE NEARBY UNIVERSE

Thesis approved in its final version by signatories below:

Franciole da Cunha Marinho

Prof. Dr. Franciole da Cunha Marinho

Advisor

Prof. Dr. Paola Andreani

Co-advisor

Campo Montenegro
São José dos Campos, SP - Brazil
2025

Cataloging-in Publication Data
Documentation and Information Division

Kianfar, Khashayar
Multiwavelength studies of AGN feeding & feedback mechanisms in the nearby Universe / Khashayar Kianfar.
São José dos Campos, 2025.
299f.

Thesis of Doctor of Science – Course of Physics. Area of Astrophysics – Instituto Tecnológico de Aeronáutica, 2025. Advisor: Prof. Dr. Franciole da Cunha Marinho. Co-advisor: Prof. Dr. Paola Andreani.

1. Galaxias. 2. Dinâmica dos gases. 3. Física. I. Instituto Tecnológico de Aeronáutica. II. Title.

BIBLIOGRAPHIC REFERENCE

KIANFAR, Khashayar. **Multiwavelength studies of AGN feeding & feedback mechanisms in the nearby Universe**. 2025. 299f. Thesis of Doctor of Science – Instituto Tecnológico de Aeronáutica, São José dos Campos.

CESSION OF RIGHTS

AUTHOR'S NAME: Khashayar Kianfar
PUBLICATION TITLE: Multiwavelength studies of AGN feeding & feedback mechanisms in the nearby Universe.
PUBLICATION KIND/YEAR: Thesis / 2025

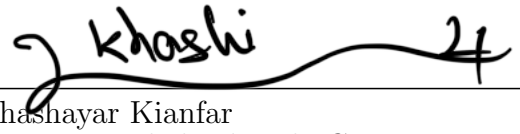

Khashayar Kianfar
Praça Marechal Eduardo Gomes, 50 - Vila das Acacias
12228-900 – São José dos Campos–SP

MULTIWAVELENGTH STUDIES OF AGN FEEDING & FEEDBACK MECHANISMS IN THE NEARBY UNIVERSE

Khashayar Kianfar

Thesis Committee Composition:

Prof. Dr.	Brett Vern Carlson	Chair of committee	-	ITA
Prof. Dr.	Franciole da Cunha Marinho	Advisor	-	ITA
Prof. Dr.	Paola Andreani	Co-advisor	-	ESO
Prof[a]. Dr[a].	Thaisa Storchi Bergmann	External Referee	-	UFRGS
Prof. Dr.	Rodolfo Valentim da Costa Lima	External Referee	-	UNIFESP
Prof. Dr.	Tobias Frederico	Internal Referee	-	ITA

ITA

To my beloved parents,
To Behnaz
and my guiding star, Paola,
For Manuel, whose legacy lives on in every step of this journey,

You are the heartbeats of my path, the light that led me forward, and the love that inspired my soul.

With deepest gratitude and love,
Khashi

Acknowledgments

To my parents, whose unwavering love and support have been the guiding light throughout my journey. Behnaz, my love, you are the reason I am here, and your presence has been the source of inspiration and strength that propels me forward. I extend heartfelt gratitude to Prof. Manuel Malheiro, my beloved advisor, who saw potential in me and nurtured my growth as a researcher. His guidance, dedication, and belief in my abilities have been instrumental in shaping my academic path. This thesis stands as a tribute to Prof. Malheiro, whose influence remains deeply embedded in my work. I am honored to be his last student, and I carry forward his legacy with immense respect and admiration.

I also extend sincere thanks to Prof. Franciole da Cunha Marinho, who has graciously taken on the role of my official advisor. His support and guidance during this final phase have been invaluable, helping me bring this work to completion.

My deepest appreciation goes to Dr. Paola Andreani, who has been a true guiding light in my life and career. As a mentor, she has not only shaped my path in becoming an astronomer but also supported my pursuit of realizing childhood dreams. Paola, thank you for your unwavering encouragement, insight, and faith in me throughout my journey. Your influence has been profound and transformative.

I am deeply grateful to my thesis committee members: Prof. Dr. Thaisa Storchi Bergmann, Dr. Rodolfo Valentim da Costa Lima, Prof. Tobias Frederico, and Prof. Brett Vern Carlson. At numares AG, I have found a supportive professional family whose encouragement has been instrumental in balancing my career and academic pursuits. I extend special thanks to my colleagues Johannes, Tobias, Marouane, Michele, and Kerstin, whose camaraderie and teamwork have provided invaluable support. am grateful to my colleagues and collaborators, including J.A. Fernández-Ontiveros, F. Combes, L. Spinoglio, E. Hatziminaoglou, C. Ricci, A. Bewketu-Belete, M. Imanishi, M. Pereira-Santaella, and R. Slater, for their invaluable contributions and assistance during our research on the TWIST sample. To my dear friends Kamyar and Flavia, thank you for your friendship and support throughout this journey. Sergio and Carla, you have been remarkable friends and mentors, offering guidance, wisdom, and encouragement. To Mehdi

and Kayhan, your friendships have been a source of joy and strength, and you have been like big brothers to me throughout this journey. To Parisa and Ali, along with the rest of my family, your love and encouragement have been a constant source of motivation. I am grateful for your unwavering belief in my abilities. I also extend my heartfelt thanks to my friends at ESO and ITA, whose camaraderie and support have enriched my life. To my previous teachers and advisors, including Prof. Habib Mazharmousavi and Dr. Abbasi, your wisdom and guidance have left an indelible mark on my academic journey. I am grateful for the knowledge and skills you imparted to me.

This dedication is a reflection of the collective love, support, and inspiration I have received from my cherished family, friends, colleagues, and mentors. With immense gratitude, I dedicate my work to all of you, honoring the memory of Prof. Malheiro and celebrating the support of all who have shaped this journey.

"Into this Universe, and Why not knowing
Nor Whence, like Water willy-nilly flowing;
And out of it, as Wind along the Waste,
I know not Whither, willy-nilly blowing."
— Omar Khayyam
Translated by Edward Fitzgerald

Resumo

Esta tese investiga o papel dos núcleos ativos de galáxias (AGN) na dinâmica do gás molecular e na formação estelar em suas galáxias hospedeiras, com foco na amostra TWIST de galáxias próximas ao AGN. Usando dados de alta resolução de CO(2-1) obtidos pelo Atacama Large Millimeter/submillimeter Array (ALMA) e observações em múltiplos comprimentos de onda, analisamos a interação entre AGNs e o meio interestelar (ISM), examinando como a atividade do AGN impulsiona fluxos de gás, tanto de entrada quanto de saída, que moldam a evolução das galáxias.

Nosso estudo inicia-se com uma análise detalhada de NGC 4593, uma galáxia Seyfert 1 com um barra proeminente e núcleo ativo. Utilizamos observações de CO(2-1) do ALMA junto com modelagem cinemática por meio das ferramentas 3D-Barolo e discFit para avaliar a distribuição e a dinâmica do gás. A modelagem revelou uma estrutura complexa, incluindo uma zona molecular central (CMZ) análoga, com um movimento rotacional intenso e características não circulares significativas alinhadas com o potencial da barra. Detectamos um fluxo molecular ao longo do eixo menor da galáxia, estendendo-se a aproximadamente 220 pc do núcleo e compreendendo cerca de 10% do fluxo total de CO(2-1) da galáxia. A massa total de gás molecular é estimada em $1 - 5 \times 10^8\, M_\odot$, e a massa do buraco negro supermassivo (SMBH) foi calculada como $\log\left(M_{\rm BH}/M_\odot\right) = 6.89 \pm 0.04$. A modelagem da distribuição espectral de energia (SED) com CIGALE revelou uma fração de AGN de 0,88 e uma taxa de formação estelar moderada de 0,42 $M_\odot\,\mathrm{ano}^{-1}$, indicando formação estelar em andamento, apesar da forte influência do AGN.

Com base nesse arcabouço, aplicamos a mesma metodologia a 20 galáxias adicionais da amostra TWIST. Para cada galáxia, derivamos a cinemática e a morfologia do gás molecular utilizando o 3D-Barolo e realizamos o ajuste da distribuição espectral de energia com o CIGALE, a fim de determinar as taxas de formação estelar, as luminosidades dos AGN, as frações de AGN, as massas estelares, as massas de gás molecular e as massas dos buracos negros. Nossa análise identificou assinaturas claras de fluxos de entrada ou de saída de gás em várias galáxias, permitindo-nos calcular as taxas de massa dos escoamentos para aproximadamente 20 das 41 galáxias estudadas.

Abstract

This thesis investigates the role of AGN in influencing the molecular gas dynamics and star formation within their host galaxies, focusing on the TWIST sample of nearby AGN host galaxies. Using high-resolution CO(2-1) data from the ALMA and multi-wavelength observations, we analyze the interaction between AGNs and the interstellar medium (ISM), examining how AGN activity drives gas inflows and outflows that shape galaxy evolution.

Our study begins with a detailed analysis of NGC 4593, a Seyfert 1 galaxy with a prominent bar and active nucleus. We used ALMA CO(2-1) observations alongside 3D-Barolo and discFit kinematic modeling to assess gas distribution and dynamics. The modeling reveals a complex structure, including a central molecular zone (CMZ)-like ring with strong rotational motion and significant non-circular features aligned with the bar potential. We detect a molecular outflow along the galaxy's minor axis, extending approximately 220 pc from the nucleus and comprising about 10% of the galaxy's total CO(2-1) flux. The estimated total molecular gas mass is $1 - 5 \times 10^8\,M_\odot$, and the supermassive black hole (SMBH) mass is calculated to be $\log(M_{\rm BH}/M_\odot) = 6.89 \pm 0.04$. Spectral energy distribution (SED) modeling with CIGALE reveals an AGN fraction of 0.88 and a moderate star formation rate of 0.42 $M_\odot\,{\rm yr}^{-1}$.

Building on this framework, we applied the same methodology to 20 additional galaxies within the TWIST sample. For each galaxy, we derived the kinematics and morphology of the molecular gas using 3D-Barolo and performed spectral energy distribution fitting with CIGALE to determine star formation rates, AGN luminosities, AGN fractions, stellar masses, molecular gas masses, and black hole masses. Our analysis identified clear signatures of either gas inflows or outflows in several galaxies, enabling us to calculate outflow mass rates for roughly 20 of the 41 galaxies studied.

List of Figures

FIGURE 2.1 – Galaxy with AGN jet. 30
FIGURE 2.2 – Region of quasar J0529-4351. 30
FIGURE 2.3 – Star field surrounding quasar 3C 273. 31
FIGURE 2.4 – Sketch of AGN unification model. 34

FIGURE 3.1 – Image grid of TWIST sample galaxies. 49
FIGURE 3.2 – Luminosity Function for Seyfert 1 and Seyfert 2 Galaxies 50
FIGURE 3.3 – 12 µm flux and luminosity distributions. 57

FIGURE 4.1 – The ALMA Array on the Chajnantor Plateau. 59
FIGURE 4.2 – Comparison of CO(2-1) emission masking. 65

FIGURE 5.1 – Multi-wavelength observations of NGC 4593. 69
FIGURE 5.2 – CO(2-1) moment maps from the ALMA Band 6 data cube of NGC 4593, created using CASA. 72
FIGURE 5.3 – Channel maps for CO(2-1) emission in NGC 4593. 74
FIGURE 5.4 – Detailed intensity, velocity, and dispersion maps for the CO(2-1) emission in NGC 4593, developed using 3D-Barolo. 76
FIGURE 5.5 – Position-velocity (p-v) diagrams of the CO(2-1) emission in NGC 4593 77
FIGURE 5.6 – CO(2-1) observed velocity field and corresponding residuals derived from discFit modelling for NGC 4593. 81
FIGURE 5.7 – Comparison between the spiral arm widths and disc scale height as a function of radius in NGC 4593. 82
FIGURE 5.8 – Kinematic and structural parameters of NGC 4593 as a function of radius. 84

FIGURE 5.9 – Analysis of molecular gas dynamics in NGC 4593. 88

FIGURE 5.10 –SED of NGC 4593 derived using CIGALE. 96

FIGURE 5.11 –Relationship between IR luminosity ($L_{\rm IR}$) and CO(2-1) luminosity ($L_{\rm CO(2-1)}$) within a 3 kpc aperture for the TWIST sample 100

FIGURE 5.12 –SFR vs. M_* relation for AGN host galaxies. 107

FIGURE 5.13 –Heatmap of Parameters for the TWIST Sample 109

FIGURE 5.14 –Mass Outflow Rate vs. AGN Bolometric for the TWIST sample. . . 112

FIGURE 5.15 –Depletion Time vs. Stellar Mass for the Sample 114

FIGURE 5.16 –AGN Bolometric Luminosity vs. SFR for the Sample 115

FIGURE B.1 – Moment maps for MCG-05-11-06. 152

FIGURE B.2 – Moment maps for NGC 1320. 153

FIGURE B.3 – Moment maps for NGC 1566. 154

FIGURE B.4 – Moment maps for NGC 2992. 155

FIGURE B.5 – Moment maps for NGC 1125. 156

FIGURE B.6 – Moment maps for IC 5063. 156

FIGURE B.7 – Moment maps for IC 5169. 157

FIGURE B.8 – Moment maps for MCG-06-30-15. 158

FIGURE B.9 – Moment maps for Mrk1333. 159

FIGURE B.10 –Moment maps for NGC 424. 160

FIGURE B.11 –Moment maps for NGC 613. 161

FIGURE B.12 –Moment maps for NGC 4941. 161

FIGURE B.13 –Moment maps for NGC 6890. 162

FIGURE B.14 –Moment maps for NGC 7496. 162

FIGURE B.15 –Moment maps for NGC 3976. 163

FIGURE B.16 –Moment maps for NGC 4412. 164

FIGURE B.17 –Moment maps for NGC 4593. 165

FIGURE B.18 –Moment maps for NGC 4968. 166

FIGURE B.19 –Moment maps for NGC 5506. 167

FIGURE B.20 –Moment maps for NGC 5861. 168

FIGURE B.21 –Moment maps for TOL 1238. 169

FIGURE C.1 –Intensity, velocity, and dispersion maps for IC 5169. 171
FIGURE C.2 –Intensity, velocity, and dispersion maps for IC 5063. 172
FIGURE C.3 –Intensity, velocity, and dispersion maps for IC 3639. 173
FIGURE C.4 –Intensity, velocity, and dispersion maps for Mrk 1333. 174
FIGURE C.5 –Intensity, velocity, and dispersion maps for MCG-5-11-06. 175
FIGURE C.6 –Intensity, velocity, and dispersion maps for MCG-6-30-15. 176
FIGURE C.7 –Intensity, velocity, and dispersion maps for NGC 424. 177
FIGURE C.8 –Intensity, velocity, and dispersion maps for NGC 613. 178
FIGURE C.9 –Intensity, velocity, and dispersion maps for NGC 1125. 179
FIGURE C.10 –Intensity, velocity, and dispersion maps for NGC 1320. 180
FIGURE C.11 –Intensity, velocity, and dispersion maps for NGC 1566. 181
FIGURE C.12 –Intensity, velocity, and dispersion maps for NGC 2992. 182
FIGURE C.13 –Intensity, velocity, and dispersion maps for NGC 4845. 183
FIGURE C.14 –Intensity, velocity, and dispersion maps for NGC 4941. 184
FIGURE C.15 –Intensity, velocity, and dispersion maps for NGC 5506. 185
FIGURE C.16 –Intensity, velocity, and dispersion maps for NGC 5861. 186
FIGURE C.17 –Intensity, velocity, and dispersion maps for NGC 6890. 187
FIGURE C.18 –Intensity, velocity, and dispersion maps for NGC 7172. 188
FIGURE C.19 –Intensity, velocity, and dispersion maps for NGC 7496. 189

FIGURE D.1 –Position-Velocity diagram for IC 5169. 190
FIGURE D.2 –Position-Velocity diagram for IC 5063. 191
FIGURE D.3 –Position-Velocity diagram for MCG-5-11-06. 192
FIGURE D.4 –Position-Velocity diagram for MCG-6-30-15. 193
FIGURE D.5 –Position-Velocity diagram for Mrk 1333. 194
FIGURE D.6 –Position-Velocity diagram for IC 3639. 195
FIGURE D.7 –Position-Velocity diagram for NGC 424. 196
FIGURE D.8 –Position-Velocity diagram for NGC 613. 197
FIGURE D.9 –Position-Velocity diagram for NGC 1125. 198

FIGURE D.10 –Position-Velocity diagram for NGC 1320. 199
FIGURE D.11 –Position-Velocity diagram for NGC 1566. 200
FIGURE D.12 –Position-Velocity diagram for NGC 2992. 201
FIGURE D.13 –Position-Velocity diagram for NGC 4845. 202
FIGURE D.14 –Position-Velocity diagram for NGC 4941. 203
FIGURE D.15 –Position-Velocity diagram for NGC 5506. 204
FIGURE D.16 –Position-Velocity diagram for NGC 5861. 205
FIGURE D.17 –Position-Velocity diagram for NGC 6890. 206
FIGURE D.18 –Position-Velocity diagram for NGC 7496. 207
FIGURE D.19 –Position-Velocity diagram for NGC 7172. 208

FIGURE E.1 – Best-fit parameters for the galaxy IC5169 209
FIGURE E.2 – Best-fit parameters for the galaxy MCG-6-30-15 210
FIGURE E.3 – Best-fit parameters for the galaxy MCG-5-11-06 211
FIGURE E.4 – Best-fit parameters for the galaxy ngc1566 212
FIGURE E.5 – Best-fit parameters for the galaxy IC5063 213
FIGURE E.6 – Best-fit parameters for the galaxy ngc613 214
FIGURE E.7 – Best-fit parameters for the galaxy ngc1125 215
FIGURE E.8 – Best-fit parameters for the galaxy ngc1320 216
FIGURE E.9 – Best-fit parameters for the galaxy ngc2992 217
FIGURE E.10 –Best-fit parameters for the galaxy ngc4845 218
FIGURE E.11 –Best-fit parameters for the galaxy ngc4941 219
FIGURE E.12 –Best-fit parameters for the galaxy ngc5506 220
FIGURE E.13 –Best-fit parameters for the galaxy IC3639 221
FIGURE E.14 –Best-fit parameters for the galaxy ngc5861 222
FIGURE E.15 –Best-fit parameters for the galaxy ngc6890 223
FIGURE E.16 –Best-fit parameters for the galaxy ngc6890 224
FIGURE E.17 –Best-fit parameters for the galaxy ngc424 225
FIGURE E.18 –Best-fit parameters for the galaxy NGC7172 226
FIGURE E.19 –Best-fit parameters for the galaxy Mrk1333 227

FIGURE F.1 – Line emission profile of the IC 5169. 228
FIGURE F.2 – Line emission profile of the NGC 424. 229
FIGURE F.3 – Line emission profile of the ngc 1320. 230
FIGURE F.4 – Line emission profile of the ngc 613. 231
FIGURE F.5 – Line emission profile of the ngc 2992. 232
FIGURE F.6 – Line emission profile of the ngc 5861. 233
FIGURE F.7 – Line emission profile of the ngc 4845. 234
FIGURE F.8 – Line emission profile of the ngc 4941. 235
FIGURE F.9 – Line emission profile of the ngc 1566. 236
FIGURE F.10 –Line emission profile of the ngc 7496. 237
FIGURE F.11 –Line emission profile of the ngc 6890. 238
FIGURE F.12 –Line emission profile of the ngc 5506. 239
FIGURE F.13 –Line emission profile of the Mrk1333. 240
FIGURE F.14 –Line emission profile of the MCG-6-30-15. 241

FIGURE G.1 –scatter BHAR avg part 1 242
FIGURE G.2 –scatter BHAR avg part 2 243
FIGURE G.3 –scatter BH mass log part 1 244
FIGURE G.4 –scatter BH mass log part 2 245
FIGURE G.5 –scatter F 12 part 1 246
FIGURE G.6 –scatter F 12 part 2 247
FIGURE G.7 –scatter F CO21 part 1 248
FIGURE G.8 –scatter F CO21 part 2 249
FIGURE G.9 –scatter L bol part 1 250
FIGURE G.10 –scatter L bol part 2 251
FIGURE G.11 –scatter Log Dynamical Mass BAROLO part 1 252
FIGURE G.12 –scatter Log Dynamical Mass BAROLO part 2 253
FIGURE G.13 –scatter Log L IR part 1 254
FIGURE G.14 –scatter Log L IR part 2 255
FIGURE G.15 –scatter Log MH2 3kpc part 1 256

FIGURE G.16 –scatter Log MH2 3kpc part 2 257
FIGURE G.17 –scatter M H2 Barolo avg part 1 258
FIGURE G.18 –scatter M H2 Barolo avg part 2 259
FIGURE G.19 –scatter Max Velocity BAROLO part 1 260
FIGURE G.20 –scatter Max Velocity BAROLO part 2 261
FIGURE G.21 –scatter Mean Dispersion BAROLO part 1 262
FIGURE G.22 –scatter Mean Dispersion BAROLO part 2 263
FIGURE G.23 –scatter Mean Inclination BAROLO part 1 264
FIGURE G.24 –scatter Mean Inclination BAROLO part 2 265
FIGURE G.25 –scatter Peak Surface Density BAROLO part 1 266
FIGURE G.26 –scatter Peak Surface Density BAROLO part 2 267
FIGURE G.27 –scatter Radius Max Velocity BAROLO part 1 268
FIGURE G.28 –scatter Radius Max Velocity BAROLO part 2 269
FIGURE G.29 –scatter SFR part 1 270
FIGURE G.30 –scatter SFR part 2 271
FIGURE G.31 –scatter agn.fracAGN CIGALE part 1 272
FIGURE G.32 –scatter agn.fracAGN CIGALE part 2 273
FIGURE G.33 –scatter agn.luminosity CIGALE part 1 274
FIGURE G.34 –scatter agn.luminosity CIGALE part 2 275
FIGURE G.35 –scatter log L OIV part 1 276
FIGURE G.36 –scatter log L OIV part 2 277
FIGURE G.37 –scatter log M star part 1 278
FIGURE G.38 –scatter log M star part 2 279
FIGURE G.39 –scatter outflow rate central part 1 280
FIGURE G.40 –scatter outflow rate central part 2 281
FIGURE G.41 –scatter sfh.sfr10Myrs CIGALE part 1 282
FIGURE G.42 –scatter sfh.sfr10Myrs CIGALE part 2 283
FIGURE G.43 –scatter stellar.lum CIGALE part 1 284
FIGURE G.44 –scatter stellar.lum CIGALE part 2 285

FIGURE G.45 –scatter stellar.m star CIGALE part 1 286
FIGURE G.46 –scatter stellar.m star CIGALE part 2 287

FIGURE H.1 –SED for NGC 424. 288
FIGURE H.2 –SED for IC3639. 289
FIGURE H.3 –SED for IC5063. 289
FIGURE H.4 –SED for NGC 1068. 290
FIGURE H.5 –SED for NGC 1320. 290
FIGURE H.6 –SED for NGC 1386. 291
FIGURE H.7 –SED for NGC 1566. 291
FIGURE H.8 –SED for NGC 1566. 292
FIGURE H.9 –SED for NGC 4941. 292
FIGURE H.10 –SED for NGC 4968. 293
FIGURE H.11 –SED for NGC 5506. 293
FIGURE H.12 –SED for NGC 6890. 294
FIGURE H.13 –SED for NGC 7314. 294
FIGURE H.14 –SED for NGC 7582. 295
FIGURE H.15 –SED for M-06-30-15. 295
FIGURE H.16 –SED for M-05-11-06. 296
FIGURE H.17 –SED for IC5169. 296
FIGURE H.18 –SED for NGC1125. 297
FIGURE H.19 –SED for MRK1333. 297
FIGURE H.20 –SED for NGC613. 298
FIGURE H.21 –SED for NGC7496. 298
FIGURE H.22 –SED for NGC5861. 299
FIGURE H.23 –SED for NGC4845. 299
FIGURE H.24 –SED for NGC7172. 300
FIGURE H.25 –SED for NGC1052. 300

List of Tables

TABLE 3.1 – Observed properties of the local AGN TWIST sample. 51

TABLE 5.1 – Photometry data for NGC 4593 70

TABLE 5.2 – ALMA Observations of NGC 4593 70

TABLE 5.3 – CIGALE-derived parameters for NGC 4593 97

TABLE 5.4 – ALMA CO(2-1) mosaic observations compared to APEX observations and molecular mass estimates 101

TABLE A.1 – Photometry data for sample galaxies (Table 1) 143

TABLE A.2 – Photometry data for sample galaxies (Table 2) 144

TABLE A.3 – Photometry data for sample galaxies 144

TABLE A.4 – Black hole accretion rate of the local AGN TWIST sample. 145

TABLE A.5 – 3D-Barolo and TWIST results for the galaxies in the sample. 146

TABLE A.6 – CIGALE-derived parameters for galaxies (Part 1) 147

TABLE A.7 – CIGALE-derived parameters for galaxies (Part 2) 148

TABLE A.8 – CIGALE-derived parameters for galaxies (Part 3) 149

TABLE A.9 – CIGALE-derived parameters for galaxies (Part 4) 150

TABLE A.10 – CIGALE-derived parameters for galaxies (Part 5) 151

List of Abbreviations and Acronyms

AGN	Active Galactic Nuclei
SMBH	Supermassive Black Hole
ISM	Interstellar Medium
SFR	Star Formation Rate
UV	Ultraviolet
IR	Infrared
SNR	Supernova Remnant
ALMA	Atacama Large Millimeter/submillimeter Array
TWIST	Twelve Micron Sample WInd Statistics
MUSE	Multi Unit Spectroscopic Explorer
CCA	Chaotic Cold Accretion
CGM	Circumgalactic Medium
CASA	Common Astronomy Software Applications
CO SLED	CO Spectral Line Energy Distribution
NIR	Near-Infrared
MIR	Mid-Infrared
FIR	Far-Infrared
BHAR	Black Hole Accretion Rate
NED	NASA/IPAC Extragalactic Database
PAH	Polycyclic Aromatic Hydrocarbon
LINERS	Low-Ionization Nuclear Emission-line Regions
SED	Spectral Energy Distribution
HST	Hubble Space Telescope
STIS	Space Telescope Imaging Spectrograph
GALEX	Galaxy Evolution Explorer
IRAS	Infrared Astronomical Satellite

List of Symbols

c	Speed of light
G	Gravitational constant
h	Planck's constant
$\hbar$	Reduced Planck's constant ($h/2\pi$)
$M_{\rm BH}$	Mass of a black hole
$M_\odot$	Solar mass
$R_\odot$	Solar radius
$L_\odot$	Solar luminosity
ρ	Density
v	Velocity
E	Energy
P	Power
F	Force
T	Temperature
λ	Wavelength
ν	Frequency
z	Redshift
H_0	Hubble constant
t	Time
r	Radial distance
ϕ	Azimuthal angle
α	Right ascension
δ	Declination
Σ	Surface brightness

Contents

1 Introduction 24

1.1 Aim 24

1.2 Research Objectives 25

1.3 Motivation 25

1.4 Work Organization 26

2 Feeding & Feedback processes in AGNs 28

2.1 Active Galactic Nuclei - AGN 28

2.1.1 What is an AGN? 28

2.1.2 AGN Classification and Discovery: A Window into Cosmic Activity . 30

2.1.3 Open Questions in AGN Research: Unveiling the Unknowns 31

2.1.4 Types of Active Galactic Nuclei 33

2.2 Galaxy Evolution and Star Formation 35

2.2.1 Star Formation and Star Formation Rates (SFR) 35

2.3 Feeding & Feedback 36

2.3.1 Quasar Mode 36

2.3.2 Kinetic or Radio Mode 36

2.3.3 Feeding & Feedback: Positive and Negative Processes 37

2.4 Obscured AGN 38

2.5 Outflows in AGN: Types and Significance 39

2.6 Cold Molecular Outflows 40

2.6.1 Primary Driving Mechanisms of Cool Outflows in Galaxies 40

2.6.2 Impact of Powerful Quasars on Neutral-Atomic Gas Kinematics . . . 41

2.6.3 Factors Determining the Fate of Cool Outflowing Material 42
2.6.4 Numerical Challenges in Modeling Radiation Coupling to Cool Gas . 42
2.7 Multiwavelength Studies of AGN Feeding & Feedback 43
2.8 CO - Observation of the Molecular Gas 43
2.9 How to Detect Molecular Outflows? 44

3 The TWIST Sample 47
3.1 Sample Overview 47
3.2 Ancillary Data 48
3.2.1 UV Observations 48
3.2.2 Optical Observations 50
3.2.3 NIR Observations 50
3.2.4 MIR Observations 51
3.2.5 FIR Observations 52
3.2.6 mm Observations 52
3.2.7 Radio Observations 52
3.2.8 X-ray Observations 52
3.2.9 SED Fitting and Analysis 53
3.3 ALMA Observations and Data Processing 53
3.4 Characterisation of the TWIST Sample 54
3.5 First Results and Implications 56

4 Data processing 58
4.1 ALMA, Interferometry, and Imaging 58
4.1.1 The ALMA 58
4.1.2 Physics of Radio Astronomy and Interferometry 59
4.1.3 Imaging with ALMA 61
4.1.4 Applications to TWIST Observations 61
4.2 Continuum and Continuum Subtraction 62
4.2.1 What is Continuum Emission? 62
4.2.2 Why is Continuum Subtraction Necessary? 63

4.2.3 Data Calibration and Post-Processing . . . 63
4.2.4 Data Cube Computations . . . 63
4.2.5 Overview and Need for Extended Emission Estimation . . . 64
4.2.6 Masking Process for CO(2-1) Emission Regions . . . 64

5 Results . . . 66
5.1 Case Study: NGC 4593 . . . 67
5.1.1 ALMA Observations and Data Reduction . . . 68
5.1.2 Molecular Gas Properties of NGC 4593 . . . 71
5.1.3 3D-Barolo Model of NGC 4593 . . . 75
5.1.4 DiskFit Modelling on NGC 4593 . . . 79
5.1.5 Gas Kinematics in NGC 4593 . . . 81
5.1.6 Estimating Molecular Gas Mass . . . 83
5.1.7 Estimation of SMBH Mass in NGC 4593 . . . 86
5.1.8 Evidence of Non-Circular Motion and Molecular Inflow or Outflows . 89
5.1.9 Central Molecular Zone (CMZ) Ring . . . 91
5.1.10 The SED . . . 93
5.1.11 Challenges in Kinematic Modelling . . . 95
5.2 Statistical Results of the TWIST Sample . . . 98
5.2.1 3D-Barolo Kinematic Modeling Results . . . 101
5.2.2 SED Analysis of the TWIST Sample . . . 105
5.2.3 Exploratory Data Analysis . . . 106
5.2.4 Outflow mass rate vs other parameters . . . 111

6 Conclusion . . . 116

Bibliography . . . 118

Appendix A – TWIST sample Photometry . . . 142

Appendix B – TWIST sample Results . . . 152

Appendix C – TWIST sample Results 3D-Barolo Results (Maps) . . . 170

Appendix D – TWIST sample Results - PV diagrams . . . 190

Appendix E – TWIST Fit Parameter results 209

Appendix F – TWIST sample Result - Line Profile Emission 228

Appendix G – TWIST Exploratory Data Analysis 242

Appendix H – SED 288

1 Introduction

1.1 Aim

The primary objective of this research is to investigate the impact of active galactic nuclei (AGN) on the evolution of their host galaxies, with a specific emphasis on the nearby Universe. Active galactic nuclei are regions surrounding supermassive black holes (SMBHs) where accretion of matter results in the release of substantial energy. This energy can influence star formation and alter the interstellar medium (ISM) in a manner that shapes the galaxy's development (FABIAN, 2012; HECKMAN; BEST, 2014). Understanding the mechanisms by which AGN affect their host galaxies is crucial, particularly in the context of gas dynamics, both inflows and outflows, and how these processes relate to the broader evolution of SMBHs and galaxies.

In this context, AGN feedback—a term that broadly encompasses the various ways energy and momentum from AGN activity impact the surrounding environment—plays a pivotal role. This feedback can lead to the suppression of star formation by ejecting gas from the central regions of galaxies through powerful outflows, thereby transitioning galaxies from star-forming phases to more quiescent states (SILK; REES, 1998; CROTON *et al.*, 2006; HOPKINS *et al.*, 2006). However, the inflow of gas toward the SMBH can also provide the fuel necessary to power AGN activity and may even trigger star formation in the galactic center. Thus, the interplay between AGN fueling and feedback remains a critical aspect of galaxy evolution, necessitating a detailed investigation.

This research will leverage data from the Twelve-micron WInd STatistics (TWIST) sample, employing a combination of data analysis techniques and astrophysical modeling. Through this comprehensive approach, the aim is to elucidate how AGN activity influences the growth and transformation of galaxies in the local Universe.

1.2 Research Objectives

We study cold molecular gas to reveal and better understand AGN mechanisms and their interactions with host galaxies. By tracing the motion and distribution of this gas, we can investigate how AGN feeding and feedback processes influence galaxy evolution. Using high-resolution CO(2–1) data from the TWIST sample—which includes 41 AGN host galaxies observed with the ALMA—we aim to uncover whether the gas is being drawn inward to fuel the supermassive black hole (SMBH) or expelled outward through AGN-driven feedback. This analysis provides a better understanding of the role of AGN activity in shaping their host galaxies (RUSH *et al.*, 1993).

In addition to ALMA data, we'll bring in observations from across the electromagnetic spectrum, including high-energy gamma rays and X-rays, as well as optical and radio wavelengths. This multi-wavelength approach helps us look at different physical processes happening at various scales within these galaxies. By combining data from multiple wavelengths, we aim to create a more complete picture of how AGNs impact their environments.

The key objectives of this study are:

- To detect and model the motion of gas inflows and outflows using tools like DiskFit and 3D-Barolo (SELLWOOD; SPEKKENS, 2015).
- To measure the physical properties of the molecular gas, such as its mass, velocity, and energy, to see how AGNs affect star formation and the structure of the galaxy.
- Explore the relationship between SMBH mass and stellar velocity dispersion (the $M_{\mathrm{BH}} - \sigma$ relation), and understand how AGN feedback influences this connection (KORMENDY; HO, 2013).
- Investigate what happens to the molecular gas that gets expelled by AGN-driven outflows, whether it leaves the galaxy completely or transforms into other types of gas, such as atomic or ionized gas.
- To use advanced data science techniques, including machine learning and statistical modeling, to improve our models of how AGNs feed and influence their galaxies.

1.3 Motivation

The motivation for this research stems from the fact that, to date, there is no clear understanding of the physics behind the mechanisms of AGN (RICHARDS; HALL, 2004; BECKMANN; SHRADER, 2013; CZERNY; YOU, 2016). Although many ideas, models, and

simulations have been proposed, our limited access to high-quality data has hindered our ability to fully grasp these processes (LAHA *et al.*, 2021; SUN *et al.*, 2020; HARRISON; ALMEIDA, 2024). One of the main challenges is understanding how AGN feeding, which drives black hole growth and can even support star formation, balances with AGN feedback, which often suppresses these same processes (STORCHI-BERGMANN; SCHNORR-MÜLLER, 2019a; HARRISON, 2017; BOOTH; SCHAYE, 2013). With advancements in observational capabilities, such as the high-resolution cold molecular gas tracing provided by ALMA, we hope to uncover new insights and shed light on this enduring mystery. Despite the gaps in our knowledge, current observations and studies leave no doubt that AGN activity is a key player in galaxy evolution.

A major reason for pursuing this study is the availability of high-resolution data from the ALMA. The TWIST sample, which includes 41 nearby AGN host galaxies, gives us a unique chance to look at molecular gas in incredible detail. ALMA's ability to capture high-resolution images of inflows and outflows makes it possible to study these processes on scales that we couldn't reach before, especially in the nearby Universe.

What makes this research even more exciting is the ability to combine data from across the electromagnetic spectrum, from high-energy X-rays to optical, infrared, and radio waves. Each wavelength shows a different part of the galaxy's story, like different instruments in an orchestra coming together to form a complete symphony. To fully understand how AGNs influence their galaxies, we can't just rely on one type of observation. We need the full range of wavelengths to see the whole picture of how AGNs impact their surroundings.

In this study, we focus on understanding AGN feeding and feedback mechanisms by examining the kinematics and morphology of cold gas. Additionally, we develop detailed SED models to derive key physical properties such as molecular outflow rates, SFR, stellar mass, AGN luminosity, BH mass, and H_2 mass. By analyzing these parameters, we aim to better understand how AGNs influence galaxy growth and evolution.

1.4 Work Organization

This research is organized into six chapters, each building on the previous one to explore how AGN feeding and feedback influence the evolution of galaxies.

Chapter 1 introduces the research by outlining the main objectives, motivation, and background. It also provides a thorough review of existing literature on AGN feeding and feedback processes, giving context to the work.

Chapter 2 covers the fundamental concepts of AGNs, focusing on their different types

and the main mechanisms of feeding and feedback. This chapter also discusses the observational methods used to study AGNs, particularly through multi-wavelength observations.

Chapter 3 focuses on the TWIST sample, which includes 41 nearby AGN host galaxies. It explains why these galaxies were selected, how the data were collected, and their significance for studying AGN-related processes.

Chapter 4 details the data analysis and data science techniques applied in the research, with a particular focus on ALMA observations and multi-wavelength data. It explains the data cleaning, processing, and analysis steps, utilizing various astrophysical models to study galaxy dynamics.

Chapter 5 presents the results of the research, including findings on AGN-driven outflows, gas inflows, and their effects on galaxy structure and star formation. This chapter also examines the statistical relationships between AGN activity and galaxy morphology.

Chapter 6 summarizes the research findings and discusses their broader impact on our understanding of galaxy evolution. It also highlights potential directions for future research.

2 Feeding & Feedback processes in AGNs

In Chapter 2, we focus on the different types of AGNs, especially those found in the nearby universe. We also explain the main observational methods, particularly the use of multi-wavelength data from radio to X-ray. The chapter then explores the processes of feeding and feedback, discussing how they influence the evolution of host galaxies.

2.1 Active Galactic Nuclei - AGN

2.1.1 What is an AGN?

At the center of most galaxies lies a SMBH, a gravitational powerhouse with a mass ranging from millions to billions times that of the Sun ($M_{\odot}$). These SMBHs dominate their galactic centers, consuming gas, dust, and stellar material from their surroundings. When an SMBH actively accretes material, it forms an accretion disk, where the gas spirals inward and heats up due to friction. This process of accretion generates intense radiation, giving rise to what is known as an AGN, which can outshine the galaxy itself (KORMENDY; RICHSTONE, 1995; MAGORRIAN *et al.*, 1998).

The energy output of AGNs spans the entire electromagnetic spectrum, from radio waves to gamma rays. The mechanism behind this immense luminosity is the conversion of gravitational potential energy into thermal energy and radiation as the gas moves closer to the black hole. This phenomenon makes AGNs some of the most luminous objects in the universe (LYNDEN-BELL, 1969; SHAKURA; SUNYAEV, 1973).

2.1.1.1 Accretion and Energy Generation: How a Black Hole Feeds

Accretion is the process by which a black hole draws in matter. AGN play a central role in the evolution of galaxies by regulating star formation and shaping galactic structure. The immense energy generated by the accretion of matter onto supermassive black holes

fuels these powerful engines, driving feedback mechanisms that influence the surrounding interstellar medium. Feedback from Active Galactic Nuclei, primarily in the form of winds and jets, can expel or heat gas, thereby suppressing star formation and limiting the overall growth of the galaxy (SILK; REES, 1998; FABIAN, 2012). As material spirals toward the SMBH, it loses angular momentum, heats up, and emits radiation. The efficiency of this process is around 10%, meaning a significant portion of the mass-energy of the infalling material is converted into radiation (THORNE, 1974). The luminosity of the AGN, which is directly tied to the accretion rate, is expressed as:

$$L = \eta \dot{M} c^2 \tag{2.1}$$

where L is the luminosity, $\eta \approx 0.1$ is the efficiency, $\dot{M}$ is the mass accretion rate, and c is the speed of light. As material falls closer to the SMBH, gravitational potential energy is converted into heat and radiation, powering the AGN.

2.1.1.2 Eddington Luminosity and Feedback Mechanisms

A black hole cannot accrete material indefinitely. As accretion increases, so does the outward radiation pressure, which eventually counteracts the gravitational pull. This balance, known as the Eddington limit, determines the maximum luminosity a black hole can achieve before radiation halts further accretion (EDDINGTON, 1988; BEGELMAN; MEIER, 1982):

$$L_{\text{Edd}} = \frac{4\pi G M m_p c}{\sigma_T} \tag{2.2}$$

where L_{Edd} is the Eddington luminosity, M is the black hole's mass, m_p is the proton mass, and σ_T is the Thomson scattering cross-section for electrons.

If the SMBH attempts to exceed this limit, powerful winds and relativistic jets are produced, expelling excess matter. These jets, made of charged particles moving at near-light speeds, can extend thousands of light-years and significantly influence the host galaxy by heating or expelling gas, thus suppressing star formation (BLANDFORD; ZNAJEK, 1977; KING, 2003). Such feedback mechanisms are essential in regulating galaxy growth by removing the gas that would otherwise fuel star formation.

2.1.1.3 AGN Luminosity: Outshining Entire Galaxies

AGN luminosity can surpass the combined output of billions of stars, making AGNs among the most luminous objects in the universe. This bolometric luminosity is a direct result of the accretion process, where the intense radiation emitted by the accretion disk

FIGURE 2.1 – An artificial image of a galaxy with an AGN jet at its centre. Image credit: *NASA*.

outshines the galaxy. The most extreme AGNs, such as quasars, can be detected across vast cosmic distances due to their extraordinary brightness (HOPKINS *et al.*, 2005).

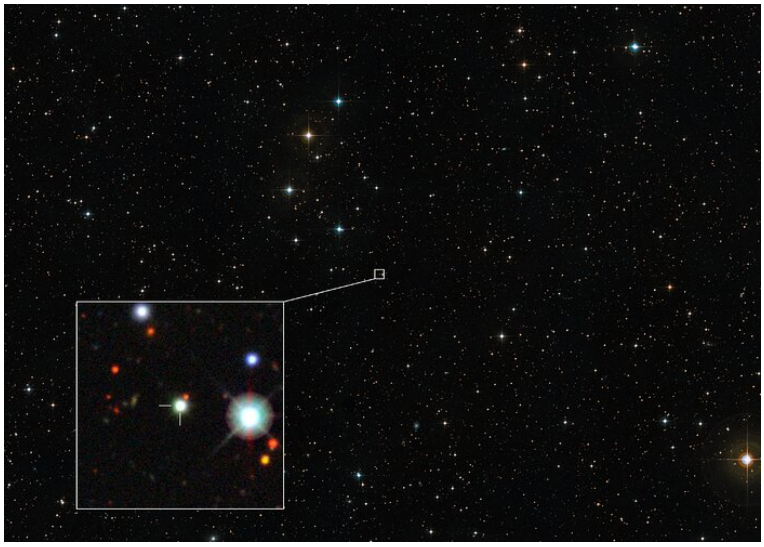

FIGURE 2.2 – The region of the sky where quasar J0529-4351, the most luminous object ever observed in the universe, is located. The quasar was identified using ESO's Very Large Telescope (VLT) (WOLF *et al.*, 2024). Image credit: *ESO / DSS2*.

2.1.2 AGN Classification and Discovery: A Window into Cosmic Activity

The discovery of AGNs in the 1960s revolutionised the understanding of galaxies. Previously, galaxies were thought to derive their light output solely from stars. However, the identification of highly luminous, distant objects like quasars and Seyfert galaxies, powered by SMBHs, revealed that many galaxies have dynamic, active cores (SCHMIDT, 1963; HAZARD *et al.*, 2013). AGNs were initially discovered through their strong radio emissions, with 3C 273 being one of the first quasars identified.

FIGURE 2.3 – The star field surrounding the exceptionally bright quasar 3C 273. Without the guiding arrow, the quasar would likely go unnoticed amidst the stars. Image credit: SDSS / Aladin.

2.1.2.1 AGN Influence on Galaxy Evolution: Feedback and Regulation

The immense energy produced by the accretion of matter onto SMBHs fuels winds and relativistic jets capable of expelling or heating gas in the ISM, thereby suppressing star formation and regulating the galaxy's overall growth (SILK; REES, 1998; FABIAN, 2012; MATTEO *et al.*, 2005). This feedback is thought to drive the transition of massive galaxies from star-forming to quiescent states.

The relationship between the mass of a supermassive black hole ($M_{\rm BH}$) and the stellar velocity dispersion (σ) of its host galaxy, known as the $M_{\rm BH} - \sigma$ relation, suggests a tight coupling between black hole growth and bulge formation (KORMENDY; HO, 2013). Expressed as a power-law $M_{\rm BH} \propto \sigma^{\alpha}$, where α typically ranges between 3 and 6, this relation is observed in both inactive galaxies and, with proper corrections, active galaxies (MATTEO *et al.*, 2008; CARRARO *et al.*, 2020). For AGNs, discrepancies in this relation have been attributed to challenges such as sample selection bias, AGN contamination, and rotational contributions to velocity dispersion, but work using the LLAMA sample has shown that, after corrections, AGNs align well with the $M_{\rm BH} - \sigma$ relation of inactive galaxies, reinforcing the co-evolutionary link between SMBHs and their host galaxies (CAGLAR *et al.*, 2020).

2.1.3 Open Questions in AGN Research: Unveiling the Unknowns

Despite substantial advances, several key questions in AGN research remain unresolved, particularly concerning the precise mechanisms that govern the inflow of gas onto SMBHs and how this accretion triggers feedback processes. Known drivers, such as gravitational torques from galactic structures and complex accretion disk dynamics, are not yet fully understood in their entirety (HOPKINS *et al.*, 2006; HOPKINS *et al.*, 2012; ALEXANDER;

HICKOX, 2012; SPRINGEL *et al.*, 2005).

AGN feedback emerges through a combination of powerful relativistic jets, energy-rich winds, and radiation pressure, each playing distinct roles in regulating the ISM. The feedback can be broadly categorized into two modes: radiative and kinetic. The radiative mode, which is dominant when the AGN is in a high-accretion state near the Eddington limit, generates intense radiation and winds that can eject or heat gas, quenching star formation in the host galaxy (FABIAN, 2012; CIELO *et al.*, 2018). Conversely, the kinetic mode operates primarily through collimated jets, which transfer mechanical energy into the surrounding hot gas, inflating cavities and creating shock waves that prevent cooling flows in galaxy clusters (MCNAMARA; NULSEN, 2012; MORGANTI, 2017; GASPARI *et al.*, 2011).

An important feature of AGN feedback is the multi-phase nature of outflows. These outflows consist of hot ionized gas, warm ionized and neutral gas, and cold molecular components, each interacting with the galactic environment differently. For instance, recent observations have shown that cold molecular gas can condense from the hot halo through processes driven by thermal instabilities, forming structures that rain down onto the SMBH and fuel further AGN activity (WADA *et al.*, 2016; GASPARI *et al.*, 2018; OLIVARES *et al.*, 2022). This intricate cycle, known as chaotic cold accretion (CCA), creates a feedback loop in which cooling, turbulence, and accretion are closely linked, driving AGN variability and galactic regulation (GASPARI, 2015).

The spin of the black hole is a critical parameter influencing the energy output of AGN feedback. High-spin SMBHs can tap into the rotational energy of the black hole to power relativistic jets, resulting in more efficient and energetic feedback (BLANDFORD; ZNAJEK, 1977; MCKINNEY *et al.*, 2012). The spin can also affect the collimation and orientation of jets, impacting how feedback energy is distributed throughout the galaxy. In cases of low-spin black holes, the feedback may be less energetic and more isotropic, leading to different evolutionary outcomes for the host galaxy. The connection between black hole spin, jet power, and feedback mechanisms remains an area of active research, with simulations and theoretical models striving to capture these complex dynamics (ISHIBASHI, 2020).

While AGN feedback is a dominant force in galaxy evolution, it is not the sole driver of galactic change. Stellar feedback from supernovae and stellar winds, as well as large-scale gravitational interactions, contribute to the overall dynamics of galaxies. In massive galaxy clusters, the hot intracluster medium (ICM) is shaped not only by AGN-driven turbulence but also by mergers and large-scale structure formation, adding complexity to the feedback landscape (VAZZA *et al.*, 2017; VAZZA *et al.*, 2011; GASPARI *et al.*, 2018). These processes can further stir the hot gas, enhancing thermal instabilities and aiding in the formation of cold molecular clouds that participate in CCA.

Despite advancements in high-resolution simulations, such as those for adaptive hydrodynamics (FRYXELL *et al.*, 2000), significant challenges remain in connecting these models to observations. Simulations provide physical information into the microphysics of AGN feedback, but real observations, constrained by limited spatial and temporal resolution, cannot always validate these models directly (CRAIN; VOORT, 2023; HARRISON *et al.*, 2018). Instruments like ALMA and the Multi Unit Spectroscopic Explorer (MUSE) have started to offer a more detailed look at the multi-phase gas interactions, yet much of the inner workings of AGN feedback remain obscured (GASPARI *et al.*, 2020). Thus, ongoing efforts are required to bridge the gap between theoretical predictions and empirical data, refining our understanding of how AGN activity regulates galaxy evolution over cosmic timescales (SCHOLTZ *et al.*, 2018).

2.1.3.1 The Unified Model of Active Galactic Nuclei: A Matter of Perspective

The unified model of Active Galactic Nuclei, introduced in the 1990s, proposes that the various observed types of AGNs are fundamentally the same objects viewed from different angles. According to this model, a thick torus of dust and gas surrounds the supermassive black hole and its accretion disk, obscuring the inner regions when viewed edge-on. This orientation-dependent view explains why some AGNs, such as Seyfert 1 galaxies, exhibit both broad and narrow emission lines, as the broad-line region is visible, while others, like Seyfert 2 galaxies, show only narrow lines due to the torus blocking the central regions (URRY; PADOVANI, 1995).

Blazars, another type of AGN, are observed when the relativistic jets are pointed almost directly at Earth. In this case, the intense radiation from the jets dominates, making blazars some of the brightest sources in the universe. Figure 2.4 illustrates this model, showing how the visibility of the central regions, jets, and emission lines depends on the observer's angle relative to the torus and jet axis.

2.1.4 Types of Active Galactic Nuclei

AGNs are categorized based on their observational properties, which depend on factors like orientation, the nature of the accreting material, and the presence of relativistic jets. The primary AGN types include Seyfert galaxies, quasars, and radio galaxies (PADOVANI *et al.*, 2017), and their classification is summarized in the AGN unification model (Figure 2.4).

Seyfert galaxies, first described by Carl Seyfert in 1943, are AGNs with bright nuclei and strong emission lines, categorized into Seyfert 1 (S1) and Seyfert 2 (S2) types (SEYFERT *et al.*, 1979). Seyfert 1 galaxies display both broad and narrow emission lines, reflecting a direct view of the central region and the high-speed gas near the supermas-

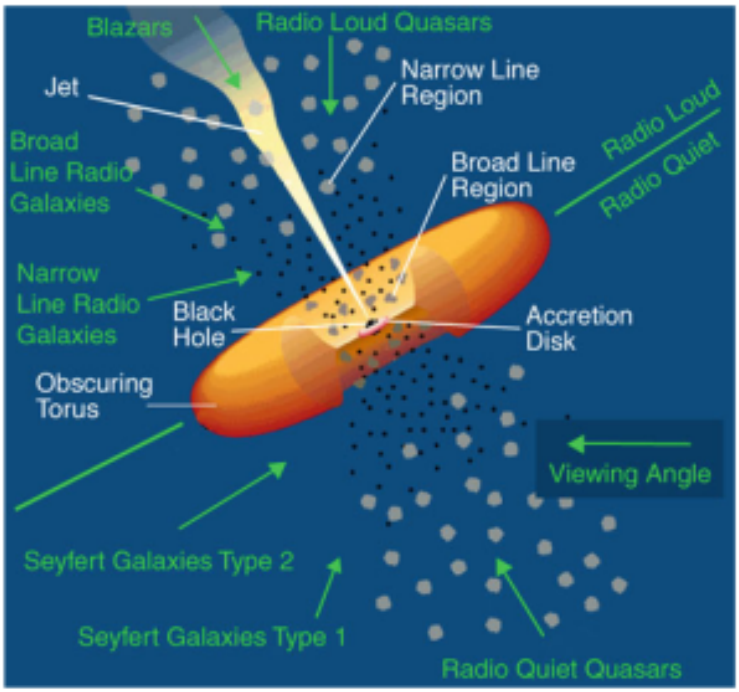

FIGURE 2.4 – Sketch of the AGN unification model, where the appearance of an AGN depends on the observer's line of sight. A thick, dusty torus obscures the central engine when viewed edge-on, resulting in a narrow-line Seyfert 2 classification. When the AGN is viewed closer to the jet axis, the broad-line region becomes visible, leading to a Seyfert 1 classification. If the AGN is observed directly along the jet axis, it appears as a blazar. Credit: NASA.

sive black hole. Seyfert 2 galaxies, on the other hand, exhibit only narrow lines because the broad-line region is obscured by a dusty torus (SCHMITT, 1998). The terms **Type 1** and **Type 2** are often used interchangeably with S1 and S2 to describe Seyfert galaxies. According to the unified model, this difference arises due to orientation: when the line of sight to the nucleus is blocked by the torus, the AGN appears as a Seyfert 2; when the central engine is unobstructed, it appears as a Seyfert 1 (AUDIBERT *et al.*, 2017). Recent studies using advanced techniques, such as infrared and millimeter interferometry, have revealed that the torus is clumpy and dynamic, with outflows and winds influencing its structure (HÖNIG; KISHIMOTO, 2017; JAFFE *et al.*, 2004; LÓPEZ-GONZAGA *et al.*, 2014).

Quasars are extremely luminous AGNs, similar in many ways to Seyfert 1 galaxies but much more powerful. They are typically observed at high redshifts, where they dominate the light of their host galaxies. Quasars exhibit both broad and narrow emission lines, and their immense luminosity is attributed to high accretion rates onto their central black holes. They are essential for studying the early universe and the formation of massive galaxies (OSTERBROCK; FERLAND, 2006).

Radio galaxies are AGNs with powerful jets that emit strongly at radio wavelengths. These jets, which can extend hundreds of thousands of light-years, reveal how AGNs transfer energy to their surroundings. AGNs are categorized as radio-loud or radio-quiet

depending on the strength of their radio emissions, though the origin of this dichotomy is still debated (MILEY; BREUCK, 2008). The study of radio galaxies is crucial for understanding AGN feedback mechanisms, as these jets are key drivers of gas removal and heating in their host galaxies.

Blazars are AGNs observed along the jet axis. This orientation causes their emission to be relativistically boosted, making them extremely bright and variable. Another important subtype is low-ionization nuclear emission-line regions (LINERs), which have lower ionization levels in their emission lines. LINERs may represent a weaker form of AGN activity or a transition between AGNs and normal galaxies.

In this work, we focus on AGNs in the nearby universe because they allow us to study the detailed structure and dynamics of these systems. The proximity of these galaxies provides the resolution needed to investigate their kinematics, morphology, and multi-phase gas components, which are essential for understanding AGN feeding and feedback processes. Furthermore, the nearby universe offers a diverse sample of AGN types, including rare subtypes such as hidden Seyfert 1 galaxies and LINERs, enabling a comprehensive exploration of AGN diversity.

The AGN unification model (Figure 2.4) provides a framework for understanding these types. However, discoveries such as changing-look AGNs and the role of non-thermal pressure components suggest that this model must account for evolving and dynamic AGN structures (OSTERBROCK; FERLAND, 2006; YANG *et al.*, 2018; NODA; DONE, 2018).

2.2 Galaxy Evolution and Star Formation

Galaxies are the fundamental building blocks of the Universe, composed primarily of stars, gas, dust, and dark matter (PEI *et al.*, 1999). Their formation and evolution are driven by complex processes that include gravitational collapse, large-scale structure formation through hierarchical merging, gas accretion, chemical enrichment, and the cycling of gas into and out of the interstellar medium (ISM) (SCOVILLE *et al.*, 2017). Over cosmic time, galaxies exhibit diverse morphologies (e.g., spiral, elliptical, irregular) and span a wide range of masses and luminosities. Understanding the interplay among these components is central to unraveling the life cycles of galaxies (WHITE; REES, 1978; BLUMENTHAL *et al.*, 1984).

2.2.1 Star Formation and Star Formation Rates (SFR)

A critical aspect of galaxy evolution is how efficiently a galaxy converts gas into stars (SAINTONGE *et al.*, 2012; TACCONI *et al.*, 2020). The **SFR** measures the amount of stellar

mass produced per unit time (typically expressed in solar masses per year, $M_\odot\,yr^{-1}$) (LADA *et al.*, 2010). Observationally, SFRs can be inferred from various diagnostics such as Hα line emission, ultraviolet continuum emission, infrared luminosities from dust re-radiation, and even radio emission (JR, 1998; CALZETTI *et al.*, 2007; JR; EVANS, 2012).

The star formation process is influenced by both internal and external factors (MCKEE; OSTRIKER, 2007). Internally, the thermal and turbulent support of gas, feedback from previous generations of stars (e.g., supernovae), and the presence of a central AGN can regulate star formation (OSTRIKER; SHETTY, 2011). Externally, processes like galaxy mergers and gas accretion from the intergalactic medium can trigger (or suppress) star formation (DRESSLER *et al.*, 1984; COMBES, 2005). Over cosmic time, the star formation history of the Universe shows a broad peak around redshift $z \sim 2$, after which the global SFR density declines to the present day (HEAVENS *et al.*, 2004; MADAU; DICKINSON, 2014).

2.3 Feeding & Feedback

AGN feedback refers to the process by which energy released by an AGN interacts with its host galaxy. The two primary modes of AGN feedback are the quasar mode and the kinetic or radio mode, each having distinct mechanisms and effects on the host galaxy.

2.3.1 Quasar Mode

Also known as the radiative mode, the quasar mode is associated with high accretion rates onto the SMBH at the galaxy's center (WEINBERGER *et al.*, 2016). This mode is characterized by the emission of radiation across the electromagnetic spectrum, particularly in the optical and ultraviolet wavelengths. The energy output in quasar mode can ionize and heat the ISM, driving powerful outflows that suppress star formation by expelling gas from the galaxy. Such outflows are critical in transitioning galaxies from active, star-forming phases to quiescent states (Cano-Díaz, M. *et al.*, 2012; CHEUNG *et al.*, 2016).

The luminosity of an AGN in this mode can be expressed by the well-known Eddington luminosity formula (2.2), which sets the upper limit on the AGN's energy output before radiation pressure halts further accretion (SIKORA *et al.*, 2006).

2.3.2 Kinetic or Radio Mode

The kinetic or radio mode is typically associated with lower accretion rates, where energy is primarily released in the form of relativistic jets. These jets, composed of

high-velocity plasma, interact with the ISM, heating the gas and preventing further star formation. This mode is linked with galaxies in the red or quiescent phase, where star formation has already been suppressed, and the galaxy's evolution is largely passive (YUAN; NARAYAN, 2014; DUBOIS *et al.*, 2011).

Jets in the kinetic mode are observed primarily in the radio part of the spectrum. The energy they carry can create buoyant bubbles in the galaxy's halo, disrupting the cooling of gas and inhibiting its condensation, which is necessary for star formation on larger scales. The power of these jets depends on the velocity, density and cross-sectional area of the jet. This process has a profound effect on the long-term evolution of galaxies, especially in massive elliptical galaxies (CATTANEO *et al.*, 2009; MANGALAM; WIITA, 2009).

2.3.3 Feeding & Feedback: Positive and Negative Processes

The growth and evolution of SMBHs and their host galaxies are tightly interconnected through two complementary processes: feeding and feedback (MCNAMARA; NULSEN, 2007; GITTI *et al.*, 2012; GASPARI *et al.*, 2020; SCHAWINSKI *et al.*, 2007).

Feeding refers to the accretion of matter onto the SMBH, which fuels the AGN. This process is driven by various mechanisms, such as stellar winds, cooling flows from hot gas, and interactions like galaxy mergers. As the gas spirals inward under the black hole's intense gravitational pull, it forms an accretion disk. The gravitational potential energy of the infalling material is converted into radiation, resulting in the immense luminosity that characterizes AGNs (STORCHI-BERGMANN; SCHNORR-MÜLLER, 2019b).

Feedback, on the other hand, involves the transfer of energy and momentum from the AGN back into the surrounding galactic environment. This energy release can occur in different forms, including radiation pressure, powerful winds, and relativistic jets. AGN-driven outflows can heat or expel gas from the galaxy, inhibiting star formation and regulating the growth of the host galaxy (WAGNER *et al.*, 2012). This regulatory role is believed to be a key factor behind observed correlations like the $M_{\mathrm{BH}} - \sigma$ relation, which links the mass of the SMBH to the velocity dispersion of stars in the galaxy's bulge (CATTANEO *et al.*, 2009; CRENSHAW *et al.*, 2003).

However, AGN feedback is not always negative. Under certain conditions, AGNs can act as catalysts for star formation. By compressing the interstellar medium (ISM) and inducing gas clouds to collapse, AGN-triggered star formation may occur, providing a more nuanced view of how AGNs influence galaxy evolution. Although this positive feedback mechanism is still under investigation, it highlights the dual role of AGNs in both quenching and promoting star formation (COMBES, 2017).

2.4 Obscured AGN

An obscured AGN is an AGN where the emission from the accretion disk surrounding a SMBH is hidden by intervening material, such as dust and gas (HICKOX; ALEXANDER, 2018). This obscuring material absorbs and scatters a substantial portion of the AGN's light, making it difficult to observe directly, particularly at ultraviolet (UV), optical, and soft X-ray wavelengths. Dust, composed of carbonaceous and silicate grains, is effective at blocking UV to infrared (IR) light, whereas gas absorption dominates at X-ray energies (ALMEIDA; RICCI, 2017). The degree of obscuration depends on the wavelength, the amount of obscuring material, and the optical depth, which measures the fraction of light absorbed along the line of sight. Traditionally, obscured AGN are identified by the absence of broad emission lines from the broad-line region (BLR) in optical spectra, indicating heavy dust obscuration. This level of obscuration corresponds to an extinction of 5–10 magnitudes in the V-band and a gas column density of $N_H > 10^{22}$ cm^{-2} in X-rays (MERLONI *et al.*, 2013). While the BLR near the accretion disk is obscured, the narrow-line region (NLR), which is farther out and influenced by the host galaxy's gravitational potential, is often still visible (BUCHNER *et al.*, 2015).

Identifying obscured AGN is challenging because the obscuring material significantly reduces AGN emission, and the host galaxy's light, such as starlight and emission from star-forming regions, can dilute the AGN signature (BARROWS *et al.*, 2021; POULIASIS *et al.*, 2020). This makes it difficult to distinguish the AGN from normal galactic processes, especially at wavelengths where the host galaxy dominates. The effectiveness of UV-optical observations in identifying unobscured AGN lies in the brightness of the accretion disk at these wavelengths. As a result, alternative strategies are required to detect obscured AGN, and a multiwavelength approach becomes essential (LAMASSA *et al.*, 2010; HICKOX; ALEXANDER, 2018).

AGN obscuration occurs across three main regimes: the nuclear torus, circumnuclear starbursts, and galaxy-scale material. The nuclear torus, a clumpy structure of dust and gas near the SMBH, obscures the accretion disk and BLR along certain lines of sight. The clumpiness allows some mid-IR emission to escape, explaining why obscured AGN can have mid-IR SEDs similar to those of unobscured AGN. Circumnuclear starbursts, located tens to hundreds of parsecs from the SMBH, are triggered by gas inflows that also fuel SMBH accretion. These starbursts contribute to UV and optical obscuration, adding complexity to the AGN environment. On larger scales, obscuration can occur throughout the galaxy, especially during mergers. Mergers funnel gas and dust toward the galaxy's center, increasing column densities and often leading to Compton-thick conditions. Obscured quasars, which exhibit stronger far-IR emission than their unobscured counterparts, are linked to these galaxy-wide star formation processes (ALMEIDA; RICCI,

2017; DORODNITSYN *et al.*, 2011; BUCHNER; BAUER, 2016; RICCI *et al.*, 2017a; RICCI *et al.*, 2021).

2.5 Outflows in AGN: Types and Significance

An outflow is a large-scale ejection of gas from the central regions of a galaxy, typically launched under the influence of powerful processes associated with an AGN (CRENSHAW *et al.*, 2003; ZUBOVAS; KING, 2012). These processes can include radiation pressure exerted by the accretion disk, magnetically driven winds, or interactions with relativistic jets (CAO, 2014; OHSUGA; MINESHIGE, 2011).

Outflows are a fundamental manifestation of AGN feedback, acting as conduits through which energy and momentum flow from the central engine into the surrounding galaxy (LAHA *et al.*, 2021; WAGNER *et al.*, 2013). These large-scale ejections of gas can arise from multiple physical processes, including radiation pressure from the accretion disk, magnetically launched winds, and interactions with relativistic jets. Although stellar feedback (e.g., supernova-driven winds) can also drive material out of galaxies, AGN-driven outflows typically exhibit higher velocities, can carry a significant fraction of the galactic gas reservoir, and often have a more dramatic impact on the evolution of their host galaxies (HOPKINS *et al.*, 2011; ISHIBASHI; FABIAN, 2015a).

Ionized outflows are frequently identified by broad, blueshifted emission or absorption lines in optical, ultraviolet, and X-ray spectra (CRENSHAW *et al.*, 2003; PINTO *et al.*, 2016). These lines attest to gas that has been heated and ionized close to the AGN, accelerating outward at thousands of kilometers per second. High-ionization tracers (e.g., OIII, CIV, or Fe lines in X-rays) are particularly useful for probing the most energetic regions near the black hole (CAPPI, 2006). Ionized outflows directly modulate the accretion process by evacuating gas that might otherwise feed the black hole; they can also alter star formation in the host galaxy by heating or expelling the interstellar medium (ISM) (CARNIANI *et al.*, 2016).

Neutral atomic outflows, identified through lines such as Na, I, D or H, I (21-cm), provide a complementary view of gas that has not been fully ionized (CONCAS *et al.*, 2019). Because it retains some fraction of dust and cooler, denser material, a neutral gas can trace feedback processes at slightly larger distances from the black hole (PERNA *et al.*, 2015; MORGANTI *et al.*, 2005). Atomic outflows also demonstrate how multiphase outflow components can coexist, with ionized gas potentially enveloping cooler, neutral regions that are partly shielded from intense AGN radiation (EVERETT *et al.*, 2002; BARON *et al.*, 2020; FLUETSCH *et al.*, 2021). Their detection often relies on absorption line spectroscopy, where foreground neutral gas imprints blueshifted features on the galaxy's continuum

light (NEELEMAN *et al.*, 2017; BORTHAKUR *et al.*, 2010).

Molecular outflows, often detected via the millimeter and infrared lines of molecules such as CO or OH, can carry a substantial fraction of the outflowing mass (STURM *et al.*, 2011; VEILLEUX *et al.*, 2020). Because molecular gas is closely connected to star formation, the expulsion or redistribution of this phase can significantly influence a galaxy's ability to form new stars (GENZEL *et al.*, 2010; SCHINNERER; LEROY, 2024). Further details on the nature, drivers, and implications of molecular outflows are discussed in the section 2.6.

Outflows rarely occur in a single, homogeneous phase. Instead, they often emerge as complex, multiphase structures in which highly ionized, warm neutral, and cold molecular gas coexist (GASPARI *et al.*, 2018; OLIVARES *et al.*, 2022; MACCAGNI *et al.*, 2021). The relative importance of each phase depends on factors such as the luminosity of the AGN, the nuclear geometry, and the density and temperature of the surrounding environment(GASPARI *et al.*, 2012).

Gaseous outflows commonly exhibit a well defined temperature ranges, extending from hot, highly ionised plasma with temperatures on the order of 10^6–10^8 K (TOMBESI *et al.*, 2013) through warm ionised gas at 10^3–10^6 K (MINGOZZI *et al.*, 2019; DAVIES *et al.*, 2020), neutral atomic gas at $\sim 10^2$–10^3 K (ROBERTS-BORSANI; SAINTONGE, 2019), and even colder molecular gas below $\sim 10^2$ K (FLUETSCH *et al.*, 2021; VEILLEUX *et al.*, 2020).

2.6 Cold Molecular Outflows

Cold molecular outflows are a key component of AGN feedback (HERRERA-CAMUS *et al.*, 2019; FIORE *et al.*, 2017; VEILLEUX *et al.*, 2020). These outflows, consisting primarily of cold molecular gas with temperatures below 10^4 K, neutral atomic material, and dust, are observed in a wide range of galactic environments, both near and far. They are driven by the energy released from stellar processes and the accretion of gas onto SMBHs at the centers of galaxies. Observations have shown that these outflows can reach velocities from several hundred to thousands of kilometers per second and extend over kiloparsec scales. The outflows are often detected through molecular lines such as CO and OH, using instruments like ALMA, which provide quantities such the mass, velocity, and distribution of the expelled gas (CICONE *et al.*, 2014).

2.6.1 Primary Driving Mechanisms of Cool Outflows in Galaxies

Cool outflows in galaxies are primarily driven by energy and momentum injected into the interstellar medium (ISM) from both stellar processes and AGN. These outflows play

a crucial role in regulating star formation and influencing the distribution of metals within and beyond galaxies (FLUETSCH *et al.*, 2019).

Stellar-driven outflows are fueled by the energy and momentum injected by massive stars through mechanisms like stellar winds and supernova explosions (HAYWARD; HOPKINS, 2015). Stellar winds from massive stars create over-pressured regions that can drive large-scale outflows, often observed as galactic winds. Supernovae further enhance this effect by releasing a substantial amount of energy and momentum into the surrounding ISM, pushing the gas outward (MURRAY *et al.*, 2010; HOPKINS *et al.*, 2011). In starburst galaxies experiencing intense star formation, radiation pressure from massive stars also plays a significant role. Photons emitted by these stars exert force on dust grains in the ISM, transferring momentum and accelerating the gas (NATH; SILK, 2009). However, the efficiency of radiation pressure in driving cool outflows is a topic of debate (ISHIBASHI; FABIAN, 2015b; MURRAY *et al.*, 2010).

AGN-driven processes are often more powerful than stellar processes, especially in galaxies hosting luminous quasars (HARRISON, 2013). AGN-driven winds, powered by the accretion of matter onto SMBHs, can reach velocities of 0.01–0.1 times the speed of light, significantly impacting the surrounding ISM. These fast nuclear winds interact with the ISM to create a hot, expanding bubble that accelerates pre-existing molecular clouds or promotes the in-situ formation of cool gas through cooling and condensation (KING; POUNDS, 2015; TOMBESI *et al.*, 2015).

Direct radiation pressure from AGNs can also drive cool outflows by exerting force on dust grains in the ISM. The intense radiation field of an AGN can accelerate the gas, but the efficiency of this mechanism is debated. Cloud disruption and the optical depth of the dusty gas can limit its effectiveness. Radio jets from AGNs can also drive outflows by interacting with the ISM, creating shocks and cavities that push and accelerate the gas. However, the overall contribution of radio jets to the population of cool outflows is thought to be less significant compared to AGN winds and radiation pressure, except in specific cases where jet activity dominates.

2.6.2 Impact of Powerful Quasars on Neutral-Atomic Gas Kinematics

Powerful quasars can greatly influence the kinematics of neutral-atomic gas in galaxies, often driving outflows with velocities, momentum, and energy far exceeding those generated by stellar processes (NESVADBA *et al.*, 2016; BISCHETTI *et al.*, 2019). However, the intense radiation from quasars can ionize and destroy neutral gas unless it is shielded by dust or embedded within the outflow itself (HAMANN *et al.*, 2013). **Na I** outflows, observed in dusty starburst and active galaxies, are examples where dust provides such shielding, protecting the gas from ionization (CHEN *et al.*, 2010; RUPKE *et al.*, 2005).

2.6.3 Factors Determining the Fate of Cool Outflowing Material

The fate of cool outflowing material depends on several factors, including its velocity relative to the escape velocity, phase transitions, and the potential for star formation (ZUBOVAS; KING, 2014; MARTIN, 2006). Outflows must exceed the local escape velocity to escape the galaxy's gravitational pull, but drag forces can reduce this likelihood. Phase transitions between cold molecular, cool neutral-atomic, and warm or hot ionized phases add complexity, as interactions with the surrounding medium and heating or cooling processes can alter the outflow's state (HECKMAN *et al.*, 2015).

In some cases, cool gas may condense and form stars if it becomes gravitationally unstable. However, only a small fraction of outflowing material, often less than 20%, is observed to escape. Observational challenges, such as decreasing density and brightness at larger distances, make it difficult to detect escaping clouds (SCANNAPIECO, 2013; SCANNAPIECO, 2017). The multi-phase nature of outflows also complicates predictions, as molecular clouds may dissolve into warmer phases or survive and cool further, depending on competing processes like gravitational instabilities and thermal instabilities (FERRARA; SCANNAPIECO, 2016; SCHNEIDER *et al.*, 2018).

2.6.4 Numerical Challenges in Modeling Radiation Coupling to Cool Gas

Modeling the interaction between radiation and cool gas in galactic outflows is computationally intensive due to the need to resolve scales from the photon mean free path to galactic dimensions. Accurately representing radiative transfer, especially in optically thick regimes, requires sophisticated methods to capture frequency diffusion and instabilities (SCHNEIDER *et al.*, 2020; NOVAK *et al.*, 2012). Current simulations struggle with these challenges, and advancements in numerical methods are needed to improve the accuracy of models.

Several questions remain unanswered, including the conditions under which cool gas can escape a galaxy, the efficiency of energy coupling between various mechanisms, and the factors determining cloud survival or destruction. Addressing these questions requires multi-wavelength observations and advanced simulations that can accurately model the complex physics of outflows. (BOLATTO *et al.*, 2019; VEILLEUX *et al.*, 2020; THOMPSON; HECKMAN, 2024).

2.7 Multiwavelength Studies of AGN Feeding & Feedback

Multiwavelength observations are essential for studying the complex feeding and feedback processes in AGNs. These processes occur on different scales, often described as micro, meso, and macro scales, each of which requires observations across a range of wavelengths for a comprehensive understanding (GASPARI *et al.*, 2020).

At the micro scale (from the event horizon of the SMBH to a few parsecs), multiwavelength observations can reveal the geometry of the accretion and ejection flows close to the SMBH. This scale is crucial for understanding how matter is funneled onto the SMBH, the role of magnetic fields in driving jets, and the partitioning of kinetic energy into various outflows (GIUSTINI; PROGA, 2019; DOELEMAN *et al.*, 2008).

At the meso scale (from a few parsecs to several kiloparsecs), multiwavelength observations allow us to study the kinetic energy and momentum rates required to drive AGN feedback. Observations in radio, optical, and X-ray wavelengths can trace the interaction between the chaotic inflows of cold gas, known as "chaotic cold accretion" (CCA), and the molecular torus and accretion disk. This scale is particularly important for understanding how outflows interact with the surrounding gas and the long-term evolution of filamentary structures, which can extend up to 100 kpc from the galaxy center (MCKINLEY *et al.*, 2021; COSTA *et al.*, 2014).

At the macro scale (from kiloparsecs to megaparsecs), multiwavelength studies help us understand how AGN feedback affects the circumgalactic medium (CGM) and the broader intergalactic environment. X-ray and ultraviolet observations can reveal how AGN-driven outflows heat the CGM, suppressing cooling flows that would otherwise fuel new star formation. These large-scale feedback processes are critical for regulating galaxy growth over cosmic timescales. Additionally, phenomena such as galaxy mergers and ram-pressure stripping, where galaxies lose gas as they move through hot intergalactic medium, are essential in shaping the evolution of AGN feedback at macro scales (GASPARI *et al.*, 2020).

Multiwavelength observations across these scales provide a comprehensive view of AGN feeding and feedback, highlighting how AGNs influence the formation and evolution of galaxies over the Hubble time (TOMBESI, 2019).

2.8 CO - Observation of the Molecular Gas

Carbon monoxide (CO) is a fundamental tracer of cold molecular gas in galaxies, which is crucial for studying dense regions where star formation occurs. Although molecular hydrogen (H_2) is the most abundant molecule in the universe, it is extremely challenging

to observe directly because H_2 lacks a dipole moment and does not emit strong rotational or vibrational transitions under typical cold interstellar conditions. Instead, CO, which is well-mixed with the cold H_2 gas, is widely used as a reliable tracer. CO emits strong rotational transitions in the radio and millimeter/submillimeter wavelengths, making it easier to detect with radio telescopes and particularly valuable for studying the cold molecular gas in galaxies and AGN environments (BOLATTO *et al.*, 2013).

The excitation of CO transitions depends on the gas temperature and density, providing a clear view into the physical conditions of molecular gas in galaxies. Constructing the CO Spectral Line Energy Distribution (CO SLED) by measuring the intensities of different CO transitions allows astronomers to infer whether the gas is heated by various mechanisms. These excitation processes include far-ultraviolet (FUV) photons from massive stars, X-ray photons from AGN, collisions, turbulence, or energetic particles such as cosmic rays (PAPADOPOULOS *et al.*, 2010; KAMENETZKY *et al.*, 2018). By comparing the CO SLEDs of AGN host galaxies to non-AGN galaxies with similar properties, we can determine the impact of AGN activity on the molecular gas and star formation efficiency.

The ALMA is instrumental in these studies, offering high sensitivity and resolution to explore the kinematics and morphology of molecular gas. Bu observations of CO in AGN host galaxies with ALMA, we can investigate both the inflow of gas feeding the supermassive black hole and the outflows driven by AGN feedback. These AGN-driven outflows can have significant consequences, such as altering the star formation rate, structure, and overall evolution of the host galaxy. Observing cold molecular outflows through CO emission is crucial to understanding the feedback mechanisms that influence the galaxy (WEISS *et al.*, 2005; HUSEMANN *et al.*, 2017).

By analyzing the relative intensities of CO transitions, one can also determine if the AGN is heating the molecular gas. When an AGN heats its surroundings, it increases the energy of the gas molecules, making higher-energy CO transitions more easily excited and resulting in stronger emission. Modeling CO emission across multiple transitions thus provides a way to quantify the AGN's impact on the molecular gas and understand the broader role of AGN-driven feedback (ANDREANI *et al.*, 2018; PEREIRA-SANTAELLA *et al.*, 2013; WERF, 2010; FLUETSCH *et al.*, 2019).

2.9 How to Detect Molecular Outflows?

Detecting molecular outflows and investigating the processes of AGN feeding and feedback require a comprehensive approach. This involves utilizing high-resolution data and employing advanced modeling techniques to interpret the complex gas dynamics within galaxies. Both feeding and feedback are multifaceted phenomena, encompassing not only

outflows but also gas inflows, turbulence, and heating mechanisms .

The first step is to obtain CO emission data from galaxies using the ALMA. CO is a critical tracer of cold molecular gas, and ALMA's high sensitivity and resolution make it ideal for capturing detailed information on the kinematics and distribution of molecular gas in galaxies. Once the data is collected, the following steps are applied:

- **Map the CO Emissions**: The CO emission data is processed to create detailed maps of the molecular gas distribution. Tools like the CASA (Common Astronomy Software Applications) package are used to visualize the spatial structure of CO emissions, which helps in identifying potential molecular outflows and other dynamical features in the galaxy.

- **Analyze for Outflow Signatures**: The CO emission maps are then examined for signs of outflows. AGN-driven outflows often manifest as high-velocity, bipolar structures, with distinct redshifted and blueshifted regions indicating gas moving toward and away from the observer. These features are key indicators of AGN feedback processes at work. To further analyze the kinematics of the galaxy, the 3D Barolo software is used to model the rotation curves based on the CO data cubes.[1] This method reconstructs the 3D structure of the galaxy's rotating disk and provides description of the overall gas dynamics. Deviations from the rotational model can point to AGN-driven outflows or other perturbations like supernova-driven winds and shock fronts.

- **Correlate with MUSE Data**: MUSE data is used to study the ionized gas in the galaxy, offering complementary information into the gas dynamics. By comparing MUSE data with CO emission maps, relationships between ionized and molecular gas can be explored, providing a clearer picture of how AGN activity influences the surrounding gas.

- **Estimate Mass and Energy of the Outflow**: The velocity information from the CO emission maps is used to estimate the mass and energy of the outflow. By analyzing the Doppler shifts of the CO lines, the outflow's kinetic energy and mass can be quantified, revealing the impact of AGN activity on the host galaxy's gas reservoir.

- **Compare Outflow Parameters to the SMBH**: The mass and energy of the outflow are compared to the properties of the galaxy's central SMBH. This comparison helps determine the relative contribution of AGN-driven feedback versus other processes, such as stellar winds or supernovae, in powering the outflow.

[1] A data cube is a multi-dimensional data structure that contains spatial and spectral information, typically represented as two spatial dimensions (e.g., right ascension and declination) and one spectral dimension (e.g., velocity or wavelength).

- **Refine with High-Resolution Data**: While this methodology provides a comprehensive approach to studying molecular gas dynamics and AGN feedback, higher-resolution ALMA observations may be necessary to explore the innermost regions of galaxies. Such data can shed light on the dusty torus around the AGN, the role of molecular tracers, and the influence of bars in triggering star formation or shocks.

3 The TWIST Sample

Chapter 3 focuses on the Twelve-micron WInd STatistics (TWIST) sample, which serves as the experimental foundation for this study. We present the characteristics of the 41 AGN host galaxies in the TWIST sample, selected from the 12-micron sample (RUSH *et al.*, 1993). This chapter provides an in-depth discussion of why these galaxies were chosen, the criteria used for their selection, and their relevance for studying AGN feeding and feedback mechanisms. We also outline the types of data collected, including CO(2–1) molecular gas observations using the Atacama Large Millimeter/submillimeter Array (ALMA) and other complementary datasets, which allow for a multi-wavelength view of the galaxies. This chapter lays the groundwork for the subsequent data analysis.

3.1 Sample Overview

The TWIST project focuses on understanding how AGN influence galaxy evolution through feedback and feeding processes. By studying a representative sample of nearby AGN, selected from the extended IRAS 12 μm galaxy sample, TWIST aims to investigate how molecular gas both fuels SMBHs and drives outflows that regulate star formation. The project uses high-resolution observations from ALMA to provide a detailed statistical analysis of these mechanisms.

The galaxies in this project come from the extended 12 μm galaxy sample (RUSH *et al.*, 1993), which includes 893 sources with fluxes greater than 0.22 Jy, located at galactic latitudes above 25°, and observed by the Infrared Astronomical Satellite (IRAS) (NEUGEBAUER *et al.*, 1984). These galaxies have confirmed spectroscopic redshifts, and the sample is complete down to 0.3 Jy. Unlike optical or ultraviolet selections, the 12 μm flux represents about one-fifth of the bolometric flux in Seyfert galaxies, making it an effective method for including both obscured and unobscured AGN without bias.

Out of the 145 AGN in the extended 12 μm sample, we selected 22 Seyfert galaxies for ALMA observation. These galaxies lie within a distance range of 10 to 30 Mpc and have declinations greater than 10°, ensuring optimal observation conditions and reducing issues like shadowing and scheduling conflicts. Additionally, we included 19 AGN from

the same sample with similar ALMA archival data, bringing the total number of galaxies in our study to 41. Most of the galaxies in our sample are spiral galaxies, with only a few being elliptical. Figure 3.1 presents an image grid of all the galaxies in our selected dataset, offering a visual overview of the sample galaxies used in this study.

The final sample consists of 14 type 1 AGN (34%), including Seyfert 1 and hidden broad-line region (S1h) galaxies, 20 Seyfert 2 galaxies (49%), and 7 low-ionization nuclear emission-line regions (LINERs) (17%). Compared to the broader 12 μm sample, where type 1 AGN make up 37%, type 2 AGN 43%, and LINERs 20%, our sample has a slight over-representation of Seyfert 2 galaxies.

With 41 galaxies, our sample is large enough to enable statistical analysis of the prevalence of inflows and outflows in both type 1 and type 2 AGN, especially around the knee of the AGN luminosity function. The AGN luminosity function, which describes the number density of AGNs as a function of luminosity, is critical for understanding how AGN activity evolves. The transition point, or "knee," at $L \sim 10^{44}$ erg/s (see Figure 3.2), represents the luminosity at which the AGN population shifts from being dominated by abundant, lower-luminosity AGNs to rarer, higher-luminosity AGNs. Figure 3.2 illustrates this function, with the knee marked as a key feature that highlights this transition.

Table. 3.1 provides details on key characteristics of each galaxy in the sample, such as their luminosity, redshift, and 12 μm flux density, which are critical for our statistical analyses.

3.2 Ancillary Data

To enhance our understanding of the properties of the selected active galaxies in the TWIST sample, we collected a broad range of multi-wavelength observations. This comprehensive approach allows us to investigate the AGN feeding and feedback mechanisms in greater depth. By leveraging data across different wavelengths, we can accurately characterize dust and gas properties, star formation rates (SFRs), AGN contributions, and various physical parameters within each galaxy. Our TWIST sample benefits from an excellent suite of ancillary data, including observations spanning from the X-rays to the radio regime, detailed below. A summary of all photometric data used in the spectral energy distribution (SED) fitting for our sample is provided in Table A.1 in Appendix A.

3.2.1 UV Observations

UV data play a crucial role in tracing the unobscured star formation within the AGN host galaxies. Observations from the Galaxy Evolution Explorer (GALEX) provide mea-

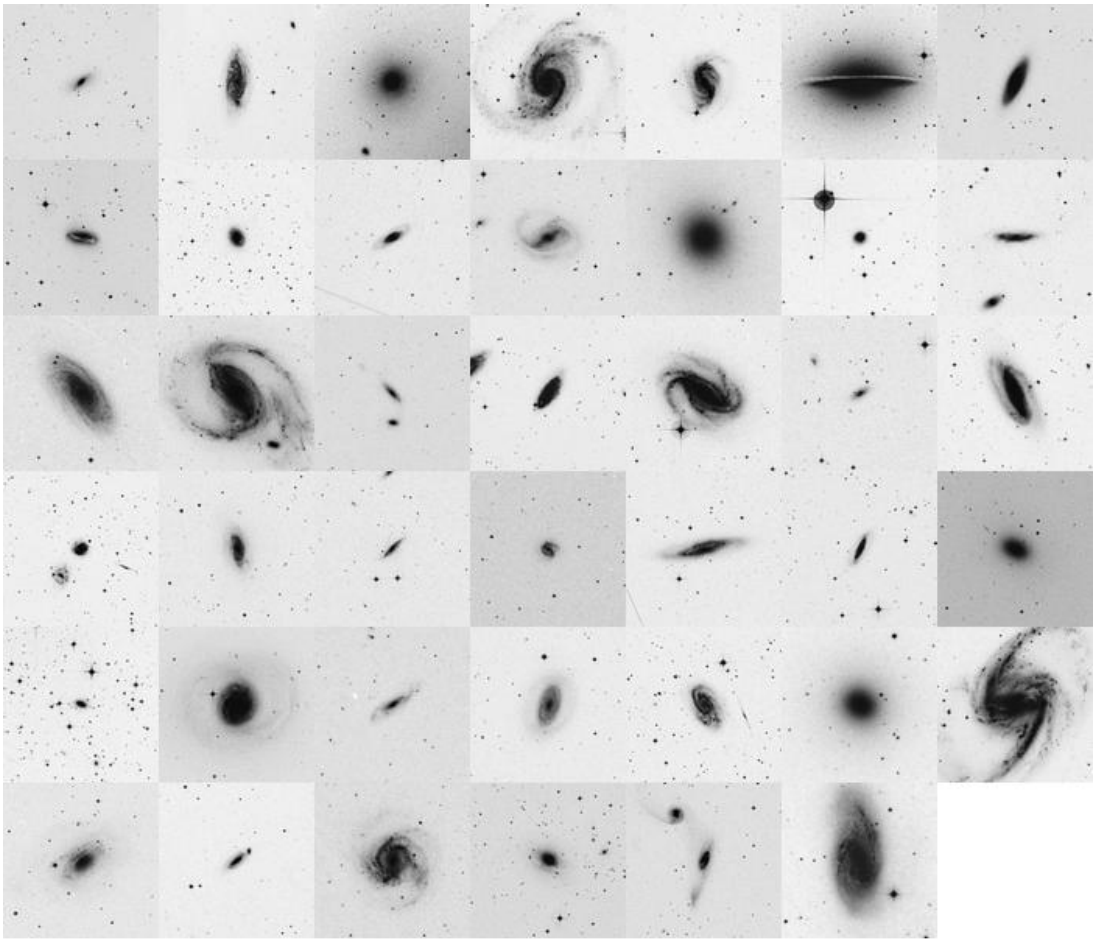

FIGURE 3.1 – Image grid of the TWIST sample galaxies, highlighting the visual diversity within the selected dataset. Each panel shows one galaxy from the TWIST sample, illustrating a range of morphological types and AGN classifications (Seyfert 1, Seyfert 1h, Seyfert 2, and LINER). North is at the top and east is to the left. The panels consist of images from the Sloan Digital Sky Survey (SDSS) and the Digitized Sky Survey (DSS), each with a cutout aperture of approximately 102 arcseconds.

surements in both the far-ultraviolet (FUV, ∼1528 Å) and near-ultraviolet (NUV, ∼2310 Å), capturing emission from young, massive stars and serving as a key indicator of recent star formation activity. These UV data, however, are sensitive to dust extinction, offering another point of view into the dust distribution within the galaxy's central regions. This information complements IR data by providing a clearer view of less obscured stellar populations, aiding in our understanding of the star formation history and distribution of young stellar clusters around the AGN (RUSH *et al.*, 1993).

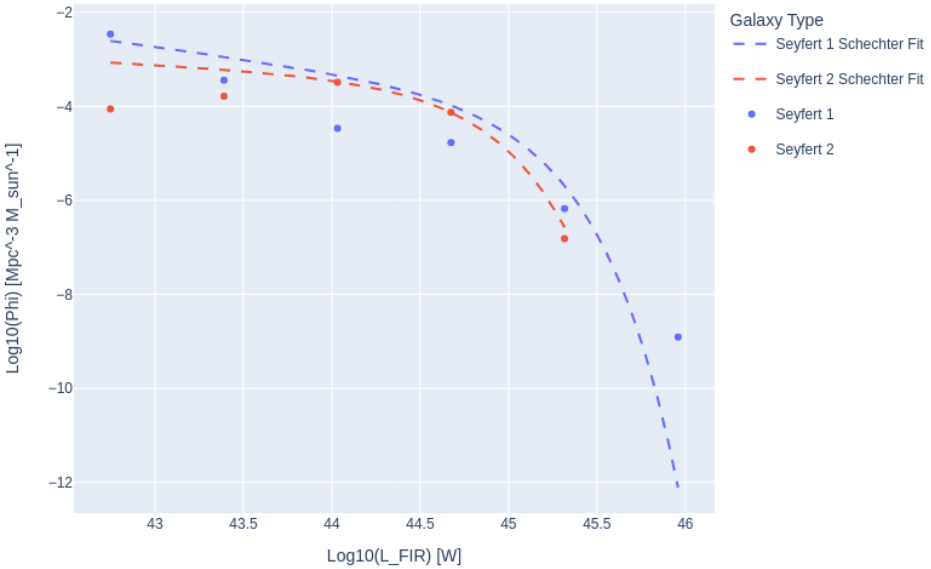

FIGURE 3.2 – Luminosity function for Seyfert 1 and Seyfert 2 galaxies in the extended 12 μm galaxy sample (RUSH *et al.*, 1993). The plot shows the logarithm of the far-infrared luminosity versus the logarithm of the space density (ϕ) of galaxies. A distinct knee is observed in the luminosity function: Seyfert 1 galaxies exhibit a knee at approximately $L \sim 10^{45}$ erg/s, while Seyfert 2 galaxies display a knee at lower luminosities. Blue points and a dashed blue line represent the distribution and fit for Seyfert 1 galaxies, whereas red points and a dashed red line correspond to Seyfert 2 galaxies.

3.2.2 Optical Observations

Optical data provide essential information about the stellar populations, galaxy morphology, and structural features. Johnson photometry in the U, B, and V bands has been used to establish a baseline for stellar population measurements. High-resolution optical imaging data from the Hubble Space Telescope (HST), Space Telescope Imaging Spectrograph (STIS) in UV, near-infrared (NIR), and optical bands have also been incorporated. These data are invaluable for analyzing central bulge properties, dust lanes, and asymmetries that might signal galaxy interactions or mergers, which could influence AGN feeding mechanisms (HUNT; MALKAN, 1999; RUSH *et al.*, 1996).

3.2.3 NIR Observations

The near-infrared (NIR) range, encompassing wavelengths from 1 to 2.5 μm, is particularly effective for probing older stellar populations and tracing the bulk of the galaxy's stellar mass. We use data from the 2 Micron All-Sky Survey (2MASS) in the J, H, and K_s bands and additional higher-resolution NIR observations from ESO's Very Large Telescope (VLT). NIR observations are useful because they suffer less from dust extinction

TABLE 3.1 – Observed properties of the local AGN TWIST sample.

Name	RA	Dec	$IRAS_{12\mu m}Flux$	Redshift (z)	D_L (Mpc)	AGN Type	$log(M_\star)[M_\odot]$	L_{bol}
(1)	(2)	(3)	(4)	(5)	(6)	(7)	(8)	(9)
NGC 424	01:11:27.63	-38:05:00.5	1.1	0.011764	48.8	S1h	10.24	44.368
NGC 613	01:34:18.17	-29:25:06.1	2.35	0.00494	20.4	S2	11.02	42.3
NGC 1052	02:41:04.8	-08:15:20.8	0.22	0.005037	20.8	LIN	10.59	42.6
NGC 1068	02:42:40.71	-00:00:47.8	40.6	0.00424	15.6	S1h	10.91	44.421
NGC 1097	02:46:19.05	-30:16:29.6	2.88	0.001461	18.5	LIN	11.33	42.279
NGC 1125	02:51:40.27	-16:39:03.7	0.32	0.010931	45.3	S2	10.20	43.602
NGC 1320	03:24:48.70	-03:02:32.2	0.33	0.008883	36.7	S2	10.19	43.802
NGC 1365	03:33:36.37	-36:08:25.4	4.42	0.005457	22.5	S1	11.01	43.741
NGC 1386	03:36:46.18	-35:59:57.9	0.52	0.002895	11.9	S1h	10.01	43.509
ESO 420-G13	04:13:49.69	-32:00:25.1	0.95	0.011908	49.4	S2	10.18	44.1
NGC 1566	04:20:00.4	-54:56:16.1	1.95	0.005017	20.7	S1	10.66	42.717
NGC 2992	09:45:42.05	-14:19:35.0	0.51	0.00771	31.9	S1	10.16	
NGC 3169	10:14:15.05	+03:27:57.9	1.2	0.00413	17.0	LIN	10.29	
NGC 3627	11:20:14.96	+12:59:29.5	4.17	0.002425	10.0	LIN	10.27	
NGC 3976	11:55:57.29	+06:44:58.0	0.24	0.008329	34.4	S2	10.27	
NGC 4303	12:21:54.90	+04:28:25.1	3.43	0.005224	21.5	S2	10.68	
NGC 4374	12:25:03.74	+12:53:13.1	0.24	0.003392	14.0	S2	10.59	
NGC 4412	12:26:36.08	+03:5752.9	0.22	0.007652	31.6	S2	9.673	
NGC 4418	12:26:54.62	-00:52:39.4	1.00	0.007268	30.0	S2	9.775	
NGC 4486	12:30:49.42	+12:23:28.0	0.22	0.004293	17.6	LIN	10.92	
NGC 4501	12:31:59.16	+14:25:13.4	2.29	0.007609	31.4	S2	11.75	42.824
NGC 4593	12:39.39.43	-05:20:39.3	0.47	0.009	39.0	S1	10.60	44.163
NGC 4594	12:39:59.43	-11:37:23.0	0.74	0.003416	14.1	LIN	11.63	42.145
IC 3639	12:40:52.85	-36:45:21.1	0.66	0.010924	45.3	S1h	10.08	44.172
Mrk 1333	12:42:25.26	-06:58:16.6	0.29	0.009433	39.0	S2	10.19	
NGC 4845	12:58:01.19	01:34:33.0	0.47	0.00411	16.9	S2	10.03	
NGC 4941	13:04:13.1	-05:33:05.8	0.39	0.003696	15.2	S2	10.13	42.825
NGC 4968	13:07:05.98	-23:40:37.3	0.62	0.009863	40.8	S2	10.10	44.196
M-06-30-15	13:35:53.71	34:17:43.9	0.33	0.007749	32.0	S1	9.604	43.97
NGC 5506	14:14:14.89	-03:12:27.3	0.25	0.006181	25.2	S1h	10.77	44.144
NGC 5806	15:00:00.40	+01:53:28.70	0.44	0.004533	18.7	S2	9.856	
NGC 5861	15:09:16.09	-11:19:18.0	0.75	0.006174	25.5	S2	10.40	
NGC 6890	20:18:18:10	-44:18:24.2	0.36	0.008069	33.4	S2	10.34	43.565
IC 5063	20:52:02.34	-57:04:07.6	1.15	0.011348	47.0	S1h	10.59	44.328
NGC 7172	22:02:01.89	-31:52:10.8	0.43	0.008683	35.9	S2	10.72	43.984
NGC 7213	22:09:16.31	-47:09:59.8	0.65	0.005839	24.1	LIN	11.28	43.72
IC 5169	22:10:09.98	-36:05:19.0	0.26	0.010374	43.0	S2	10.19	
NGC 7314	22:35:46.19	-26:03:01.7	0.55	0.004763	19.6	S1h	9.943	43.404
NGC 7496	23:09:47.29	-43:25:40.6	0.62	0.0055	22.7	S2	10.01	42.691
NGC 7582	23:18:23.5	-42:22.14.0	2.31	0.005254	21.7	S1h	10.87	43.825
NGC 7590	23:18:54.81	-42:14:20.6	0.69	0.05255	21.7	S2	10.11	42748

Notes: (1) Object name; (2,3) 2MASS coordinates (NASA/IPAC Extragalactic Database (NED)[a]); (4) IRAS 12 μm flux in Jy; (5) Redshift (z); (6) Luminosity distance in Mpc; (7) AGN type: Seyfert 1 (S1), hidden broad-line region (S1h), Seyfert 2 (S2), and LINER (LIN); (8) Logarithm of stellar mass ($M_\star$) (SCHOMBERT *et al.*, 2019). (9) Bolometric Luminosity (L_{bol} [log ($erg\,s^{-}1$)]) (SPINOGLIO *et al.*, 2024)

[a] `https://ned.ipac.caltech.edu/`

compared to optical light, enabling clearer analysis of the central regions where AGN activity is prominent. These data help in assessing the mass distribution and understanding the gravitational potential that governs AGN-driven inflows and outflows (JARRETT *et al.*, 2003; SKRUTSKIE *et al.*, 2006).

3.2.4 MIR Observations

Mid-infrared (MIR) observations are crucial for isolating the dusty torus surrounding the AGN and differentiating between AGN-heated and star formation-related dust. Spectral data from the *Spitzer* Infrared Spectrograph (IRS) provide high-resolution measurements in the 5–20 μm range, crucial for distinguishing AGN emission from star formation. Additionally, photometric data from the Wide-field Infrared Survey Explorer (WISE) at 3.4, 4.6, 12, and 22 μm further characterize the warm and hot dust components. For select galaxies, supplementary MIR observations from the *Spitzer* IRAC and MIPS in-

struments provide additional data points for accurate modeling of SEDs (CUTRI *et al.*, 2012; TOMMASIN *et al.*, 2010).

3.2.5 FIR Observations

Far-infrared (FIR) observations, obtained from the *Herschel* PACS instrument at 70, 100, and 160 μm, are used in detecting cold dust emission, which is directly associated with active star-forming regions. IRAS data at 12, 25, 60, and 100 μm provide complementary coverage, enhancing our capability to model the dust emission and derive total infrared luminosities (TIRs). These FIR data are needed for understanding how AGN activity affects star-forming regions through feedback mechanisms (SPINOGLIO *et al.*, 1995; PEREIRA-SANTAELLA *et al.*, 2014).

3.2.6 mm Observations

Our millimeter observations focus on the CO(2–1) molecular line to trace the distribution and dynamics of cold molecular gas. We simultaneously observe the CS(5–4) line, a high-density gas tracer, and millimeter continuum bands to estimate dust masses. The separate measurements of gas mass (via CO) and dust mass (via continuum) enable us to determine the gas-to-dust ratio, a key parameter for understanding the interstellar medium (ISM) conditions around the AGN (COMBES *et al.*, 2014; COMBES *et al.*, 2013).

3.2.7 Radio Observations

Radio data are used for analyzing synchrotron emission from AGN jets and nuclear regions, which influence AGN feedback processes. Observations from the Very Large Array (VLA) at 1.4 GHz and 8.4 GHz are used to map the radio emission from AGN jets and lobes. This information is used for understanding how jets impact the ISM, drive outflows, and regulate star formation. Radio emission provides a complementary view to optical and IR data, offering insights into the distribution of energetic processes within the galaxy (RUSH *et al.*, 1996; THEAN *et al.*, 2000).

3.2.8 X-ray Observations

X-ray data from *XMM-Newton* and *Swift* satellites provide measurements from the high-energy environments surrounding AGNs. Due to the penetrating nature of X-rays, these observations allow us to correct for absorption effects and derive intrinsic AGN luminosities, even in obscured cases. X-ray measurements are then used for estimating

bolometric luminosities and black hole accretion rates (BHARs), which are fundamental for understanding AGN activity and its influence on galaxy evolution (BRIGHTMAN; NANDRA, 2011; RUSH; MALKAN, 1995).

3.2.9 SED Fitting and Analysis

Our multi-wavelength SED fitting process integrates data from UV to radio, enabling the derivation of key parameters like dust mass, SFRs, and Eddington ratios. By disentangling AGN emission from stellar processes, we can accurately model AGN-host galaxy interactions. The derived parameters are used to correlate gas dynamics with AGN activity, thus elucidating how AGNs regulate or promote star formation through feedback (CIESLA *et al.*, 2015; SALOMÉ *et al.*, 2023).

3.3 ALMA Observations and Data Processing

The TWIST project utilised ALMA to obtain high-resolution observations of the CO(2-1) emission line at 230.5 GHz, the CS(5-4) line at 245 GHz, and 1.2 mm continuum data for 22 galaxies. The CO(2-1) line is particularly useful for tracing cold molecular gas, which is typically concentrated in the central regions of galaxies and serves as a key indicator of kinematic and morphological properties. Observations focused on the central 3x3 kpc^2 region of each galaxy, achieving a spatial resolution of 30-50 pc. This high spatial resolution is essential for resolving fine structures in the molecular gas, such as inflows, outflows, and turbulent regions, as well as for detecting molecular outflows with masses as low as 10^2 $M_\odot$.

For the TWIST sample, CO(2-1) observations provide information on the kinematic behavior and distribution of molecular gas in AGN host galaxies. By mapping the velocity field, which represents the spatial distribution of line-of-sight velocities across the galaxy, we can visualize how the gas moves relative to the galaxy's center. In disk galaxies, this typically manifests as a velocity gradient, where gas on one side of the galaxy approaches the observer while gas on the opposite side recedes. This organized rotational pattern reveals the galaxy's overall kinematic structure and allows us to identify deviations in velocity that may be driven by external influences, such as nearby galaxies or AGN activity.

In addition to velocity fields, velocity dispersion provides insight into the spread of velocities within a specific region of gas, often indicating the presence of turbulence. High velocity dispersion in the central areas of a galaxy, for instance, can signal dynamic processes such as AGN-driven outflows or intense star formation, both of which introduce

kinetic energy into the surrounding gas. For CO(2-1) data, increased velocity dispersion near the AGN or along prominent structures, like spiral arms, suggests that these regions may be undergoing disturbances due to non-gravitational forces. This measure of velocity spread allows us to assess where gas is relatively calm and where it is energetically stirred, providing key information on regions of active feedback or turbulent mixing.

Non-circular motions, which represent deviations from the standard rotation of the gas disk, are also necessary for understanding how AGN influence their host galaxies. In the context of CO(2-1) observations, non-circular motions appear as irregularities in the velocity field or abrupt changes in velocity dispersion. These motions are often associated with inflows or outflows of gas, as well as with structures such as bars or tidal interactions, and suggest that the gas is experiencing forces beyond simple rotational dynamics. For example, inflows of gas toward the center or outflows driven by AGN feedback exhibit distinctive non-circular motion patterns, helping to locate and characterize areas where AGN activity is affecting the galaxy's molecular gas structure.

To extend our study, we also integrated archival ALMA data for 19 additional galaxies with comparable spatial and spectral resolution, ensuring uniformity across the sample. Data were calibrated and processed using the CASA software package (BEAN *et al.*, 2022), following ALMA's standard calibration pipeline. Imaging was performed using a Briggs weighting scheme to balance sensitivity and resolution. The final data cubes were cleaned and reconstructed, enabling detailed extraction of the kinematic properties (See 4.1.4).

3.4 Characterisation of the TWIST Sample

The TWIST sample enables a detailed examination of key properties within AGN host galaxies, including stellar mass, star formation rate (SFR), and black hole accretion rate (BHAR). Stellar masses were estimated using the mass-to-light ratio and the observed J and V magnitudes, as reported in the NASA/IPAC Extragalactic Database (NED). SFRs were determined based on the luminosity of the Polycyclic Aromatic Hydrocarbon (PAH) feature at 11.3 μm, following the calibration method of (WU *et al.*, 2009).

The distribution of 12 μm flux and infrared luminosity for the TWIST sample is shown in Figure 3.3, comparing Seyfert 1 AGN (hatched blue with "+"), Seyfert 2 AGN (hatched red with "x"), and LINERs (hatched green with "."). This figure provides estimates into the variation in flux and luminosity across AGN types. For instance, Seyfert 1 galaxies generally exhibit higher infrared luminosities compared to Seyfert 2 galaxies, consistent with Seyfert 1 AGNs being less obscured and having more direct emission from the active nucleus. LINERs, on the other hand, display a wider spread in both flux and luminosity, which may reflect diverse accretion rates and lower-luminosity AGN activity. Understand-

ing these distinctions is essential for examining how AGN type correlates with host galaxy properties, which is further discussed in Chapter 4 in the context of kinematic analysis.

Two independent estimates of the BHAR were derived to account for uncertainties, particularly in obscured AGN. The lower estimate is based on X-ray bolometric corrections following the method of (LUSSO *et al.*, 2012), yielding an average BHAR of $0.05\,M_{\odot}$/yr, while the higher estimate is derived from mid-infrared luminosities (SPINOGLIO *et al.*, 1995), with an average BHAR closer to $0.2\,M_{\odot}$/yr. This range, potentially spanning an order of magnitude, illustrates the challenges in accurately quantifying accretion processes due to inherent variability and the influence of obscuration on bolometric corrections. The broad BHAR distribution reflects the diversity of accretion rates among the TWIST sample and emphasizes the need for multi-wavelength data to improve accuracy in measuring AGN accretion.

To distinguish AGN activity from star formation within each galaxy, we employed the ratio of [OIV] to [NeII] emission as a diagnostic tool. This ratio serves as an indicator of the dominant energy source, with higher values suggesting AGN dominance over star formation. By quantifying this ratio, we can more accurately assess how AGN processes influence the interstellar medium (ISM) and star-forming regions, enabling a refined separation of AGN-driven and star formation-driven emissions across the TWIST sample.

Inflow processes, which transfer molecular gas from the galactic disc to the nuclear region, play a major role in feeding both star formation and black hole accretion. High-resolution CO(2-1) observations reveal evidence of molecular inflows in several TWIST galaxies, with galaxies such as NGC 1097 and NGC 1566 exhibiting clear spiral structures that channel gas toward the central supermassive black hole (SMBH). For instance, NGC 1097 shows well-defined molecular streams with an inflow rate of approximately 0.2 $M_{\odot}$/year (FATHI *et al.*, 2013). These observations are essential for identifying and characterising the mechanisms by which gas reaches the nuclear region, fueling both AGN activity and central star formation.

Conversely, AGN feedback manifests as energy injection into the surrounding ISM, often observed as molecular outflows that expel gas from the galaxy's central region. This process can quench star formation by reducing the gas available for new star formation episodes. In several TWIST galaxies, including NGC 613, powerful AGN-driven molecular outflows have been detected. For instance, NGC 613 exhibits an outflow with a mass of approximately 2×10^6 $M_{\odot}$ and a mass outflow rate of 27 $M_{\odot}$/year (AUDIBERT *et al.*, 2019b). Such high outflow rates, which surpass the SFRs in these galaxies, suggest that these outflows are primarily AGN-driven rather than starburst-driven. This feedback is particularly significant for understanding how AGN influence their host galaxies' long-term evolution by regulating gas dynamics and star formation.

This analysis of the TWIST sample's key properties, including stellar mass, SFR, BHAR, and gas kinematics, provides a foundation for investigating AGN-host interactions and the impact of AGN activity on galactic environments. Further discussions on the kinematic properties and AGN feedback mechanisms are presented in chapters 4 and 5.

3.5 First Results and Implications

Preliminary analysis of the TWIST sample has already provided significant insights into the prevalence and characteristics of inflows and outflows in nearby AGN. The high-resolution CO(2-1) maps reveal extended molecular gas structures in all galaxies, with outflows detected in five objects and compact CS(5-4) emission in several others (Kianfar, K. *et al.*, 2024; FERNÁNDEZ-ONTIVEROS *et al.*, 2020; BELETE *et al.*, 2021). Continuum emission at 1.2 mm was also detected in all galaxies, either as point-like sources at the nucleus or as extended emission associated with dust in the galaxy's disc.

Further analysis of the TWIST sample will focus on quantifying the energy injected by the AGN into the ISM, measuring the outflow masses and rates, and deriving the gravitational torques that drive inflows. This will allow for a more complete understanding of how AGN influence their host galaxies and contribute to galaxy evolution.

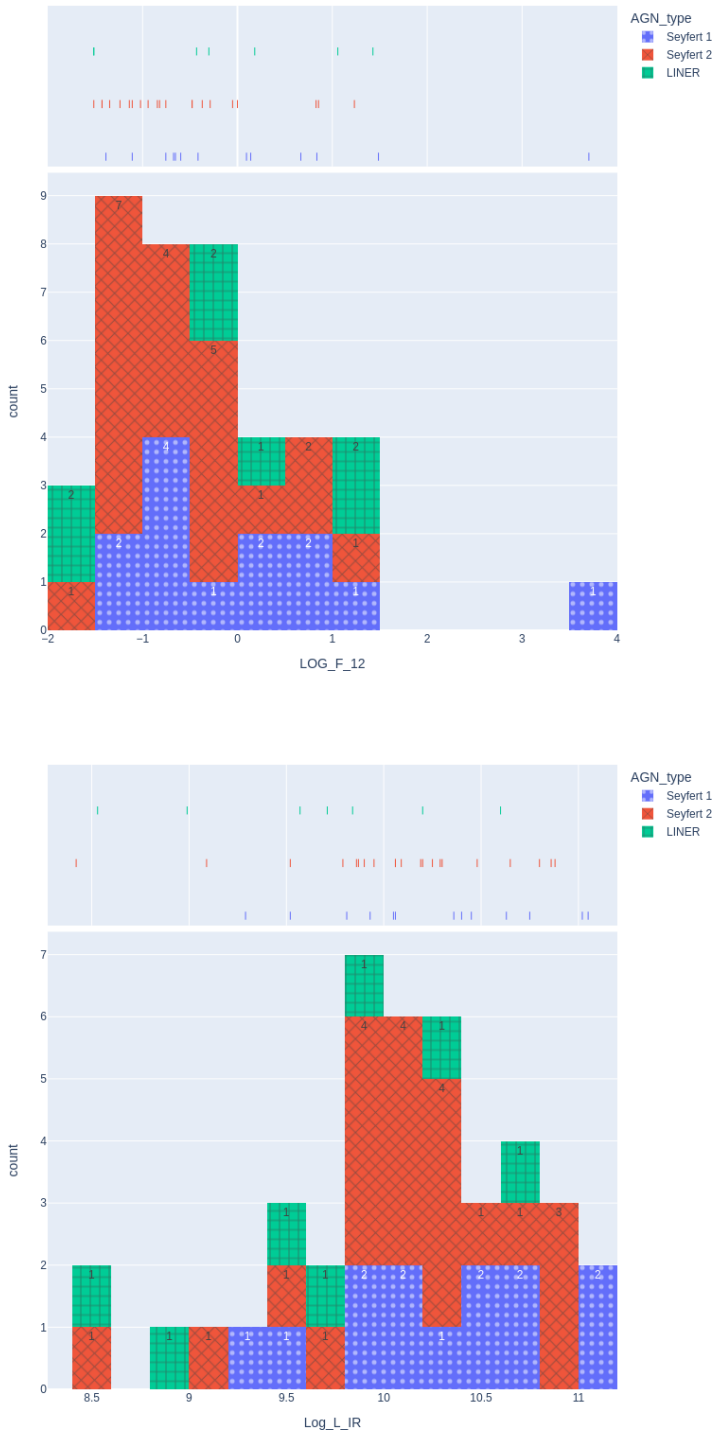

FIGURE 3.3 – 12 µm flux (top) and luminosity (bottom) distributions of the parent extended 12 µm sample (empty histogram), together with the Seyfert 1 AGN (hatched blue with "+"), Seyfert 2 AGN (hatched red with "x"), and the LINERs (hatched green with "."). The lower panel shows the logarithm of the IR (2–1000 µm) luminosity, $L_{\rm IR}$, in units of solar luminosity ($L_{\odot}$), computed from the IRAS flux densities following (SANDERS; MIRABEL, 1996).

4 Data processing

Chapter 4 details the Data Analysis and Data Science processing, where we begin by discussing the astrophysical datasets collected from various observatories, with a particular focus on ALMA observations. This chapter covers the entire data pipeline, starting with data cleaning and pre-processing. Then it moves into the processes of kinematic analysis, focusing on the galaxy rotation curves, gas flows, and molecular gas dynamics within AGN host galaxies.

Advanced Python-based tools, such as NumPy, SciPy, and Astropy, are used to perform precise and detailed analyses of these datasets. By integrating multiple observational wavelengths, the morphology and kinematics of molecular gas and its interactions with the AGN are analysed. Statistical techniques and data science methodologies are applied to ensure a robust, comprehensive understanding of the data.

4.1 ALMA, Interferometry, and Imaging

4.1.1 The ALMA

ALMA is a state-of-the-art observatory located in the Atacama Desert in Chile, at an elevation of 5,000 meters. It consists of 66 high-precision antennas, including fifty-four 12m antennas and twelve 7m antennas. These antennas operate at millimeter and submillimeter wavelengths, covering a frequency range of 30 GHz to 950 GHz across ten observing bands. ALMA is a collaboration between Europe, North America, East Asia, and Chile, designed to provide unparalleled sensitivity and resolution for studying cold gas and dust in the Universe.

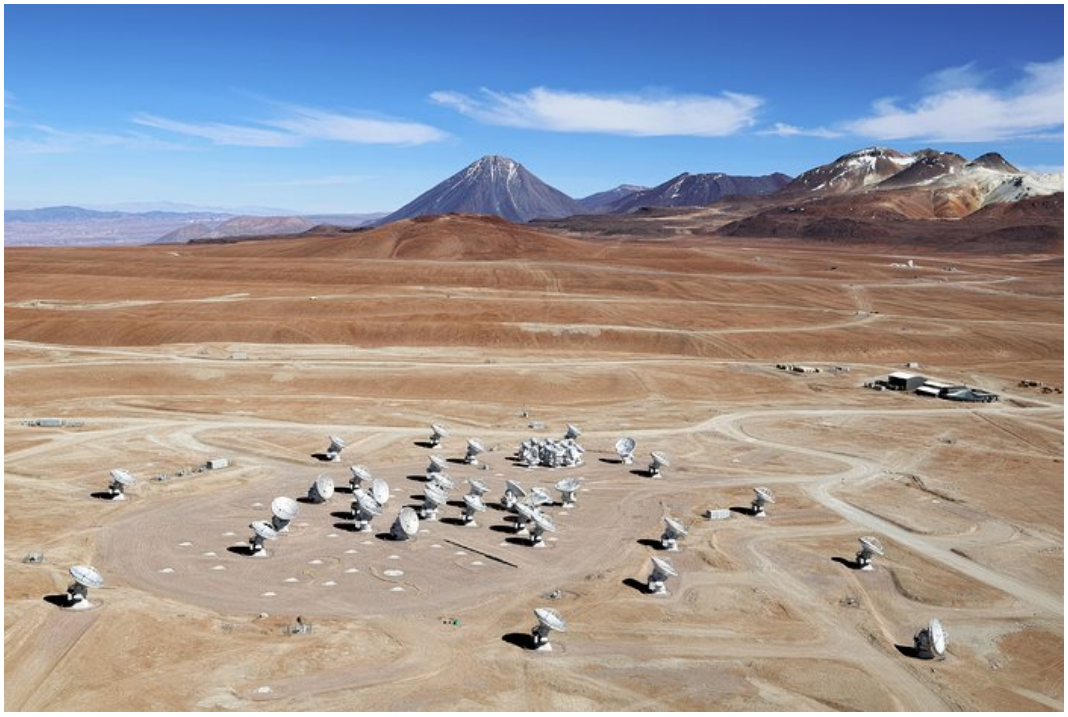

FIGURE 4.1 – An aerial view of the Chajnantor Plateau, situated at an altitude of 5000 meters in the Chilean Andes, where the antennas of the ALMA are located. The array comprises fifty-four 12-metre antennas and twelve 7-metre antennas, which form the ALMA Compact Array (ACA). In the background, prominent peaks such as Cerro Chajnantor, Cerro Toco, and Juriques are visible. This image was captured in December 2012, a few months before ALMA's official inauguration. Credit: Clem & Adri Bacri-Normier (wingsforscience.com)/ESO.

4.1.2 Physics of Radio Astronomy and Interferometry

4.1.2.1 Angular Resolution and Interferometry Principles

In radio astronomy, the angular resolution (θ) of a telescope determines its ability to distinguish fine spatial details. For a single-dish telescope, the resolution depends on the observing wavelength (λ_{obs}) and the dish diameter (D):

$$\theta \propto \frac{\lambda_{\text{obs}}}{D}. \tag{4.1}$$

For millimeter and submillimeter wavelengths, achieving sub-arcsecond resolution with a single dish would require impractically large apertures. ALMA overcomes this limitation by employing interferometry, where signals from multiple antennas are combined to simulate a much larger aperture. In an interferometer, the angular resolution is determined by the longest baseline (B_{max}), the maximum separation between any two antennas:

$$\theta \propto \frac{\lambda_{\text{obs}}}{B_{\text{max}}}. \tag{4.2}$$

This approach allows ALMA to achieve angular resolutions as fine as 0.01 arcseconds

in its most extended configurations, which is comparable to the resolving power of the Hubble Space Telescope at optical wavelengths.

4.1.2.2 The UV Plane and Aperture Synthesis

The signals from each pair of antennas (a baseline) measure a Fourier component of the sky's brightness distribution, known as a visibility. These visibilities sample the UV plane, a representation of spatial frequencies in the observed field. The distribution of baselines in the array, along with Earth's rotation during observations, determines the coverage of the UV plane. A well-sampled UV plane is crucial for reconstructing high-fidelity images of the sky.

The incomplete sampling of the UV plane leads to artifacts in the image, known as sidelobes, which are introduced by the interferometer's point spread function (PSF). Imaging techniques such as CLEAN ((HÖGBOM, 1974)) are used to deconvolve the dirty image, removing the effects of the PSF and reconstructing a cleaner, more accurate representation of the sky brightness.

4.1.2.3 Configurations and Missing Flux

ALMA's 12m array can be arranged in ten different configurations (C-1 to C-10), each with a distinct range of angular resolutions and maximum recoverable scales (MRS).

- Compact configurations (e.g., C-1, C-2): Shorter baselines provide sensitivity to large angular scales, making them suitable for observing extended structures.
- Extended configurations (e.g., C-9, C-10): Longer baselines offer higher resolution, ideal for resolving compact features.

However, the 12m array is limited by its shortest baselines, which set a lower bound on the angular scale of emission that can be detected. This results in the "missing flux" problem, where large-scale, diffuse emission is filtered out. To address this, ALMA employs:

- **The 7m Array:** Shorter baselines complement the 12m array, recovering some of the missing large-scale emission.
- **Total Power (TP) Array:** Single-dish measurements provide total flux, capturing all angular scales.
- **Multi-Configuration Observations:** Combining data from compact and extended configurations improves UV-plane coverage, enhancing image fidelity.

4.1.3 Imaging with ALMA

The image processing with ALMA consists of several steps:

1. **Calibration:** Corrects for instrumental and atmospheric effects using calibrator sources.
2. **Fourier Transformation:** Converts calibrated visibilities into a ”dirty image,” representing the sky convolved with the array’s PSF.
3. **Deconvolution:** Removes PSF artifacts using algorithms like CLEAN to produce a ”clean” image.
4. **Data Combination:** Integrates data from different configurations or arrays to recover a wide range of spatial scales.

The weighting scheme chosen during imaging affects the trade-off between resolution and sensitivity:

- **Natural Weighting:** Maximizes sensitivity by prioritizing short baselines, suitable for faint, extended sources.
- **Uniform Weighting:** Enhances resolution by weighting all baselines equally, at the cost of sensitivity.
- **Briggs Weighting:** Provides a balance between sensitivity and resolution by adjusting a robustness parameter.

4.1.4 Applications to TWIST Observations

For the TWIST project, the 12m array was used in extended configurations to achieve the high spatial resolution required to resolve gas dynamics in AGN-hosting galaxies. Archival 7m array data were incorporated to address missing flux issues, enabling a more complete analysis of molecular gas inflows, outflows, and feedback mechanisms. This combined approach ensured robust UV-plane coverage and minimized artifacts in the reconstructed images.

4.2 Continuum and Continuum Subtraction

4.2.1 What is Continuum Emission?

In astronomical observations, continuum emission refers to radiation that spans a broad range of wavelengths or frequencies, rather than being confined to specific spectral lines. In ALMA's millimeter and submillimeter wavelength range, continuum emission typically arises from various physical processes, including thermal dust emission, synchrotron radiation, and free-free emission. Each of these sources provides information of interest from different components of the galaxy.

Thermal dust emission, which dominates in the far-infrared to millimeter range, provides information about the total dust content within a galaxy. This emission traces cold dust heated by the interstellar radiation field and is often correlated with star formation regions, as dust tends to accumulate around active star-forming areas, re-radiating absorbed stellar energy at longer wavelengths. Therefore, the strength and spatial distribution of thermal dust continuum emission can serve as an indirect indicator of star formation activity.

Synchrotron radiation, generated by relativistic electrons spiraling around magnetic fields, is a common source of continuum emission in active galactic nuclei (AGN). This type of emission is particularly useful for identifying and studying relativistic jets emitted from AGNs, as synchrotron radiation is highly polarized and spans a wide range of frequencies. It provides estimates of the magnetic field strength and structure within the jet, as well as the overall energetic environment around the AGN.

Free-free emission, or Bremsstrahlung, arises from interactions between electrons and ions in ionized gas, typically near star-forming regions or AGNs. This emission can be used to estimate the ionized gas content and is often associated with HII regions, providing further information about star formation rates and ionization sources within the galaxy.

For CO(2-1) observations, the focus is on capturing spectral line emission from molecular gas, which is often superimposed on this continuum background. Accurately isolating the CO(2-1) line requires subtracting the continuum emission, which is done by fitting the continuum in channels without line emission and then removing it from the dataset. This ensures that the analysis of the molecular gas dynamics is free from continuum interference.

4.2.2 Why is Continuum Subtraction Necessary?

The presence of continuum emission can obscure the spectral features of the CO(2-1) line, making it difficult to accurately determine the properties of the molecular gas. Continuum subtraction is the process of separating the broad continuum emission from the narrow spectral line emission. This is achieved by fitting the continuum in frequency channels where no line emission is present, and then subtracting this fit from the entire dataset.

4.2.3 Data Calibration and Post-Processing

The data for the TWIST project were calibrated and processed using the CASA package, adhering to standard ALMA Observatory procedures. For the Cycle 5 observations targeting the TWIST sample, pipeline version 5.4.0 was utilized for both calibration and imaging. Archival data from earlier cycles, used for supplementary analysis, were initially calibrated with CASA version 4.7.0 and subsequently reprocessed in CASA 5.4.0 to ensure uniformity across the dataset. Imaging for the TWIST galaxies was executed using Briggs weighting with a robust parameter of 0.5 to balance sensitivity and resolution, optimizing the recovery of the molecular gas structures critical to the study.

4.2.4 Data Cube Computations

From the CO(2-1) data cubes, it calculated three key moment maps: the integrated intensity, the velocity field, and the velocity dispersion map. Each of these provides distinct measurements of the characteristics of the molecular gas in the TWIST sample galaxies. For instance, the integrated intensity map, also known as the moment 0 map, represents the total CO(2-1) emission at each position and reveals the molecular gas distribution and column density across the galaxy. This is particularly useful for identifying regions with dense molecular gas, often associated with star formation and central activity.

To ensure the data quality, channels with a signal-to-noise ratio above five times the median absolute deviation were selectively included, reducing the impact of noise on the computed moment maps.

The calibration and processing of the data followed the standard protocols using CASA package, as per ALMA guidelines described in Section 4.1.3. Observations from cycles 5 and 6 were calibrated with CASA pipeline version 5.4.0, while earlier archival data was initially processed with CASA version 4.7.0, and later standardized to version 5.4.0 for consistency. The imaging post-processing across all galaxies was uniformly executed in CASA version 5.4.0, utilizing customized scripts tailored to enhance the consistency and

quality of the dataset.

4.2.5 Overview and Need for Extended Emission Estimation

The ALMA observations targeted the CO(2-1) transition line, which is centered at a rest frequency of 230.5 GHz and serves as a crucial tracer of molecular gas mass in galaxies. This line is sensitive to gas at intermediate excitation temperatures, making it especially valuable for studying the dense, star-forming regions around AGN. However, a potential limitation in interferometric observations is the "missing flux" problem, where extended emission on larger spatial scales can go undetected due to the lack of short baselines in the interferometer array. This missing extended emission can skew the analysis by underrepresenting the total molecular gas content, particularly in the more diffuse and extended regions of the galaxy.

To ensure data accuracy, it is essential to evaluate the extent of missing flux and, where necessary, supplement the interferometric data with single-dish observations. This complementary approach helps capture the full spatial distribution of the CO emission, especially critical for accurately assessing both the molecular gas mass and its dynamics. In this study, such considerations allow for a more reliable interpretation of the CO(2-1) data, thereby ensuring that key processes, such as AGN-driven outflows and galaxy-wide gas dynamics, are comprehensively represented.

4.2.6 Masking Process for CO(2-1) Emission Regions

After completing the spectral resampling, it was applied a masking procedure to highlight the CO(2-1) emission regions with significant signal. Masking is a crucial step in this context, as it helps to suppress noise and ensure that the moment maps reflect the true physical properties of the molecular gas distribution.

The masking process began by setting an initial threshold at twice the root mean square (rms) of the noise level, effectively filtering out all pixels below $2 \times$ rms, which were deemed insignificant. This threshold selection was based on established practices that balance the need to capture low-level emission while avoiding spurious noise peaks (FERNÁNDEZ-ONTIVEROS *et al.*, 2020). However, this automatic mask alone did not fully capture the intricate structures within the emission regions, especially those involving faint features like inflows and outflows.

To enhance the accuracy of the emission region definition, the initial threshold mask was manually refined by visually inspecting individual channels of the data cube. This manual refinement enabled us to adjust areas where the automated mask either overestimated or underestimated emission extents. Through these adjustments, faint emission

features that were initially missed were recovered by the automated thresholding while excluding areas dominated by noise. This manual refinement proved essential for the accurate study of weak emission features critical to understanding AGN feeding and feedback processes.

To illustrate the improvements achieved through this procedure, Figure 4.2 presents a comparison between the initial threshold mask and the refined mask for a representative channel. The comparison shows how manual adjustments allow for more detailed capture of faint emission regions, which automated thresholding alone would overlook.

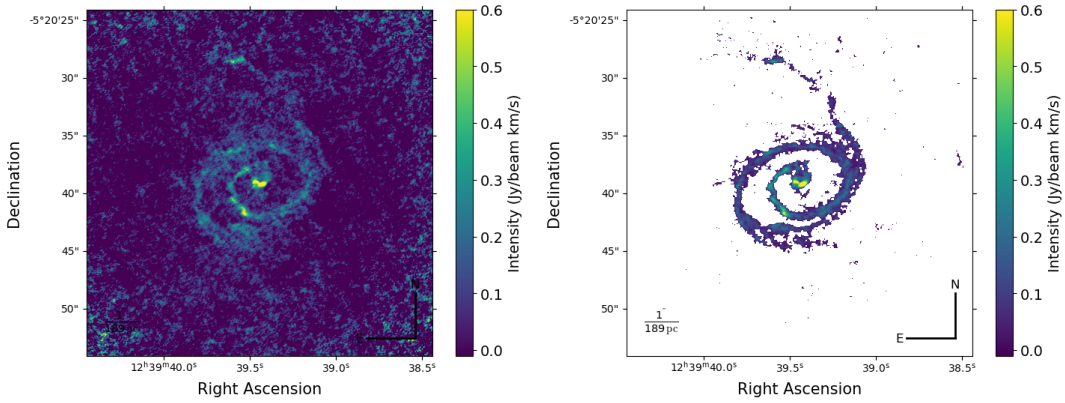

FIGURE 4.2 – Comparison of CO(2-1) emission masking before (left) and after (right) manual refinement for a representative channel. The refined mask better isolates faint emission features, particularly inflows and outflows, enhancing the overall quality of the data for subsequent analysis.

The combination of masking, spectral resampling, and primary beam correction procedures enabled us to produce high-quality CO(2-1) data cubes, accurately representing the molecular gas dynamics within our sample galaxies. This level of refinement is essential for precisely identifying inflows feeding the central black hole, as well as outflows responsible for regulating star formation by expelling gas from the galaxy. The final moment maps derived from these enhanced data cubes provide a robust basis for studying AGN-driven gas dynamics and feedback processes in our sample.

5 Results

This chapter presents the results obtained from our investigation of the molecular gas dynamics and broader physical properties of the TWIST sample of AGN host galaxies. Leveraging high-resolution ALMA CO(2–1) observations, it examines the role of molecular gas in fueling SMBHs and its relationship with star formation and feedback processes. The analysis integrates multi-wavelength datasets, providing a comprehensive view of the interaction between AGN activity and the ISM.

The methodology was initially developed and validated using NGC 4593 as a case study. This galaxy, characterized by complex kinematics and a rich observational data set, served as a benchmark for refining data reduction, kinematic modeling, and physical property derivation techniques. Through this process, it established robust frameworks for estimating key quantities, such as the SMBH mass ($M_{\rm BH}$), molecular gas mass ($M_{\rm H_2}$), and SFR.

Extending the refined methodology to the entire TWIST sample, we conducted a systematic analysis of molecular gas inflows and outflows, as well as AGN-driven feedback mechanisms. The results, supported by SED modeling, reveal trends in infrared luminosity ($L_{\rm IR}$), AGN luminosity, and dust properties, providing information on the interaction between AGN activity and galactic evolution. Statistical comparisons with existing literature further contextualize these findings, highlighting both commonalities and distinct behaviors among different AGN subtypes.

The remainder of this chapter is structured as follows. Section 5.1 details the findings for NGC 4593, including its kinematic properties and SED-derived characteristics, as published in (Kianfar, K. *et al.*, 2024). Section 5.2 extends the analysis to the full TWIST sample, emphasizing statistical trends and macroscopic kinematics of the cold molecular gas of the galaxy. Detailed individual galaxy results are provided in Appendix A.

5.1 Case Study: NGC 4593

NGC 4593 is a face-on spiral galaxy in the southern sky, located at approximately $D \approx 39 \pm 4$ Mpc (MARINOVA; JOGEE, 2007), with coordinates $\alpha = 12^h\,39^m\,39.4^s$ and $\delta = -5^\circ\,20'\,39''$. Morphologically classified as (R)SB(rs)b (VAUCOULEURS *et al.*, 1991), NGC 4593 presents a well-defined barred spiral structure with prominent nuclear, inner, and outer rings. The central bar in this galaxy likely plays a key role in channeling gas towards the nucleus, driving inflows that influence the dynamics of the central region. This characteristic bar and ring structure suggests an efficient mechanism for transferring angular momentum outward, enabling material to flow inward—a process often linked to supermassive black hole (SMBH) feeding in barred spiral galaxies.

Multi-wavelength imaging of NGC 4593 provides a comprehensive view of its structure. Figure 5.1 displays the galaxy in different bands, highlighting both large-scale and central features. The left panel shows a background merged image from the *Hubble* Space Telescope (HST) Wide Field Planetary Camera 2 (WFPC2) using the F606W and F547 M filters. The zoomed region (Figure. 5.1, top) highlights the inner galaxy with the AGN at its center. In the middle panel, one see a closer view of the HST image with contours from the ALMA CO (J=2-1) emission line moment-0 map, illustrating the molecular gas distribution in NGC 4593. The contours reveal the intensity of CO emission, emphasizing regions with significant molecular gas presence at levels of $Contours = [0.25, 0.35, 0.4, 0.5, 1, 2, 4, 6]$. The right panel provides a wider view from the Digitized Sky Survey (DSS) for a broader perspective of NGC 4593's position within its environment.

A key component of our analysis involves constructing the SED of NGC 4593 to better understand the galaxy's star formation and AGN characteristics. This approach utilizes photometry data across multiple wavelengths, enabling us to capture the combined emissions from stellar populations, interstellar dust, and the AGN. Table 5.1 presents the photometry data were employed for this purpose, spanning a wide range of bands from X-ray to mid-infrared wavelengths. These data, including observations and error bars, were used as input for the Code Investigating GALaxy Emission (CIGALE; (BOQUIEN *et al.*, 2019)), which decomposes the SED into its stellar, dust, and AGN components. CIGALE's flexibility in model fitting is particularly valuable for NGC 4593, as it accommodates complex star formation histories and the AGN's contribution to the overall energy output.

The inner regions of NGC 4593 display a nuclear dust ring, which channels gas inward along radial dust lanes aligned with the bar structure. Such dust features are associated with gas inflows toward the central nucleus, supported by morphological studies on gas dynamics (WU *et al.*, 2021; HUNT *et al.*, 2008; LAINE, 2001). These inflows are instrumental

in understanding active galactic nucleus (AGN) feeding mechanisms, as they contribute to the material reservoir around the SMBH.

NGC 4593 is classified as a Seyfert 1 galaxy, with strong, broad emission lines associated with high-velocity gas close to the black hole. The galaxy has been extensively studied across multiple wavelengths, displaying polarized continuum emission and variability in X-ray, UV, and radio bands. Observations have detected time lags between various energy bands, such as delays between far-ultraviolet (FUV) and near-ultraviolet (NUV) emissions, as well as between soft ($0.3 - 0.5\,\mathrm{keV}$) and hard ($4.0 - 10.0\,\mathrm{keV}$) X-ray bands. These delays offer clarity into the physical conditions and distances within the AGN's central engine (SRIRAM *et al.*, 2009; KUMARI *et al.*, 2023; KAMMOUN *et al.*, 2021). The presence of these time lags suggests a stratified structure in the AGN accretion disk, where different regions respond variably to changes in the central energy source.

The density profile within NGC 4593's circumnuclear medium follows a power-law distribution, indicating a smooth and continuous gas environment around the SMBH (WANG *et al.*, 2022). This density structure is important for accurately modeling gas dynamics and understanding the physical environment around the black hole, as it impacts the efficiency of AGN-driven feedback and SMBH feeding processes.

In summary, NGC 4593's morphological features and dynamic central region make it an ideal candidate for in-depth study, both as an individual case and as a reference for the methodologies applied across the TWIST sample. The information gained from NGC 4593 have formed the foundation of our analysis approach, including methods for exploring molecular gas dynamics, estimating molecular gas mass ($M_{\mathrm{H_2}}$) and star formation rates (SFR), and interpreting AGN variability across multiple wavelengths.

5.1.1 ALMA Observations and Data Reduction

The ALMA observations of NGC 4593 were conducted on January 4, 2018, during Cycle 5 (Project ID: 2017.1.00236.S, PI: Matthew A. Malkan) with a spectral configuration centered on the CO(2-1) transition in Band 6 at a rest frequency of 230.5380 GHz. The synthesized beam size achieved was $0.029'' \times 0.027''$, with an rms sensitivity of 0.36 mJy/beam over 0.9767 GHz, distributed across 1920 channels and totaling 1.875 GHz in bandwidth. Detailed observational parameters are provided in Table 5.2.

Data calibration and imaging were conducted with the Common Astronomy Software Applications (**CASA**) software (BEAN *et al.*, 2022). The calibration employed pipeline version 5.1.1-5, while image reconstruction was performed using **Hogbom** deconvolution and **Briggs** weighting with a robustness factor of 2.0. This process resulted in a beam size of $12.8'' \times 6.5''$ at a position angle of $-59.3°$, which corresponds to 438×345 pc^2 at

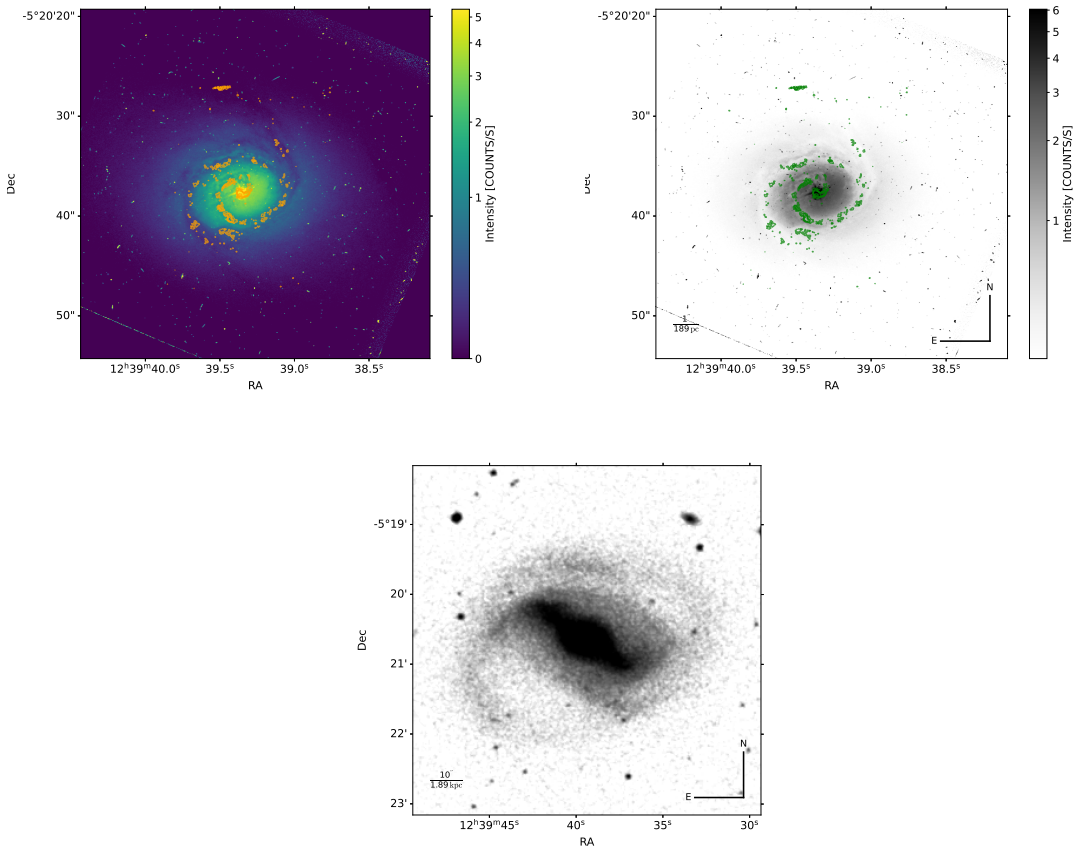

FIGURE 5.1 – Multi-wavelength observations of NGC 4593. Left: Background merged image from *Hubble* Space Telescope (HST) observations, combining data from the Wide Field Planetary Camera 2 (WFPC2) using the F606W and F547 M filters. Right: Zoomed region of the HST image with contours from the ALMA CO (J=2-1) emission line moment-0 map, illustrating the distribution and intensity of CO emission with contour levels of $Contours = [0.25, 0.35, 0.4, 0.5, 1, 2, 4, 6]$. Bottom: Digitized Sky Survey (DSS) image of the galaxy (Image credit: DSS, STScI).

TABLE 5.1 – Photometry data for NGC 4593

Observed band	Flux	Significance	Systematic Error (%)	Ref.
Swift (2–10 keV)	3.16×10^{-11} erg cm^{-2} s^{-1}	No uncertainty reported	10%	(1)
Swift (14–195 keV)	3.4×10^{-10} erg cm^{-2} s^{-1}	90% confidence	10%	(1)
GALEX (FUV)	3.60 ± 0.05 mJy	1σ	5%	(2)
GALEX (NUV)	5.91 ± 0.03 mJy	1σ	5%	(2)
2MASS (J)	415.00 ± 7.71 mJy	1σ	2%	(3)
2MASS (H)	494.00 ± 10.20 mJy	1σ	2%	(3)
2MASS (Ks)	427.00 ± 12.40 mJy	1σ	2%	(4)
IRAC (3.6 μm)	125.00 ± 8.03 mJy	1σ	5%	(5)
IRAC (4.5 μm)	134.00 ± 21.00 mJy	1σ	5%	(5)
IRAC (5.8 μm)	163.00 ± 23.95 mJy	1σ	5%	(5)
IRAC (8.0 μm)	229.00 ± 33.16 mJy	1σ	5%	(6)
IRAS (12 μm)	299.00 ± 73.00 mJy	Uncertainty, confidence not specified	10%	(7)
Spitzer MIPS (24 μm)	633.00 ± 89.00 mJy	No uncertainty reported	10%	(5)
ALMA (Band 6)	8.13 ± 0.22 mJy	1σ	10%	(8)
ALMA (Band 3)	8.42 ± 0.06 mJy	1σ	10%	(8)

Notes: This table presents the photometry data for NGC 4593 across a range of observed bands, including X-ray, UV, near-infrared, and mid-infrared wavelengths. Flux values are given in units of mJy, except for the *Swift* X-ray data, which are expressed in erg cm^{-2} s^{-1}. The uncertainties listed in the flux column correspond to the statistical errors of the measurements. We scale the mid-IR observations of Spitzer using the 12um flux ratio between the Spitzer data and the Optical data. The 2MASS data at 2.2um have also been scaled to take out the galactic emission. The significance column denotes the confidence level associated with the data, while the systematic error indicates the potential percentage uncertainty due to instrumental calibration or observational conditions.
References: (1) (RICCI *et al.*, 2017b); (2) (BOUQUIN *et al.*, 2018); (3) (MCALARY *et al.*, 1983); (4) (JARRETT *et al.*, 2003); (5) (SKRUTSKIE *et al.*, 2006); (6) (CUTRI *et al.*, 2012); (7) (TOMMASIN *et al.*, 2010); (8) Obtained in this work based on ALMA observation project IDs: 2017.1.00236.S and 2018.1.00576.S.

TABLE 5.2 – ALMA Observations of NGC 4593

Parameter	Value
Band	6 (mosaic)
Emission	CO(2–1)
Frequency (GHz)	228.628
BMAJ (arcsec)	0.232
BMIN (arcsec)	0.183
BPA (°)	−59.3
RMS (Jy beam^{-1} km s^{-1})	7×10^{-4}
V_{sys} (km s^{-1})	2491
Velocity width (km s^{-1})	310
Velocity range (km s^{-1})	1990
Velocity resolution (km s^{-1})	2.4

Notes: Details of ALMA Band 6 (mosaic) observations for NGC 4593, collected under Project ID: 2017.1.00236.S. Parameters include the ALMA Band, target emission line, central frequency, synthesized beam major and minor axes (BMAJ, BMIN), beam position angle (BPA), and noise level (RMS). V_{sys} denotes the systemic velocity, with the velocity width indicating the observed line width. The velocity range specifies data cube coverage relative to V_{sys}, and velocity resolution indicates the spectral resolution.

a distance of 39 Mpc. The field of view (FOV) covered a diameter of 27″ (5.1 kpc), with the largest recoverable angular scale reaching 2.6″, approximately 490 pc.

The spectral sensitivity for the CO(2-1) data reached 0.1 mJy/beam for the continuum and an rms noise of 0.7 mJy/beam for spectral line data at 10 km/s resolution. Initial imaging was performed at a native velocity resolution of 2.4 km/s, as noted in Table 5.2, with data later resampled to a coarser 10 km/s resolution to optimize the signal-to-noise ratio for kinematic analysis while preserving essential emission features.

In addition to the CO(2-1) observations, an expanded multi-wavelength dataset was utilized to analyze the SED of NGC 4593. The SED was constructed using photometry from various bands, including U, B, V from Johnson (MCALARY *et al.*, 1983), FUV, NUV from GALEX (BOUQUIN *et al.*, 2018), and mid-IR constraints from *Spitzer*-IRS (TOMMASIN *et al.*, 2010). Further contributions include near-infrared data from 2MASS in J and H bands (JARRETT *et al.*, 2003; SKRUTSKIE *et al.*, 2006), mid-IR data from WISE (CUTRI *et al.*, 2012), and UV, NIR, and optical imaging from HST/STIS (MALKAN *et al.*, 1998; CACKETT *et al.*, 2018). These data provide robust parameters for dust content, star formation rates (SFRs), and AGN Eddington ratios, facilitating an in-depth investigation of AGN-driven feedback and gas dynamics within the galaxy.

For further analysis, we incorporated additional ALMA Band 3 continuum data from Project Code 2018.1.00576.S, observed at frequencies of 89.509 to 105.494 GHz, achieving an angular resolution of 0.25″. The Band 3 data's continuum sensitivity was 0.0259 mJy/beam over a 5-minute integration period.

This combined approach, encompassing CO(2-1) data and multi-wavelength observations, enabled a comprehensive examination of NGC 4593's gas dynamics and star-forming properties in relation to AGN feedback mechanisms (CIESLA *et al.*, 2015; ATLEE *et al.*, 2011; KAROUZOS *et al.*, 2014; SALOMÉ *et al.*, 2023).

5.1.2 Molecular Gas Properties of NGC 4593

In our analysis of the molecular gas within NGC 4593, were utilised high-resolution CO(2-1) observations acquired from ALMA Band 6, allowing a detailed examination of the distribution, velocity field, and kinematics of the cold molecular gas. Figure 5.2 presents the moment maps derived from these data, providing a better view into the structure and motion of the molecular gas in this Seyfert galaxy.

The moment-0 map in Figure 5.2 represents the integrated intensity across the line profile, effectively tracing the spatial distribution of molecular gas within NGC 4593. This map reveals a significant concentration of molecular gas in the nuclear regions of the galaxy, with intensity values spanning up to 6.0 Jy/beam $\cdot$ km/s. The gas is primarily concentrated in a central circumnuclear region, suggesting active processes, such as gas inflows, likely fueled by the prominent galactic bar. The observed flux of CO(2-1) emis-

sion is calculated to be approximately 100 Jy km/s, indicating a substantial reservoir of molecular gas concentrated near the galaxy's central regions. The moment-1 map, also

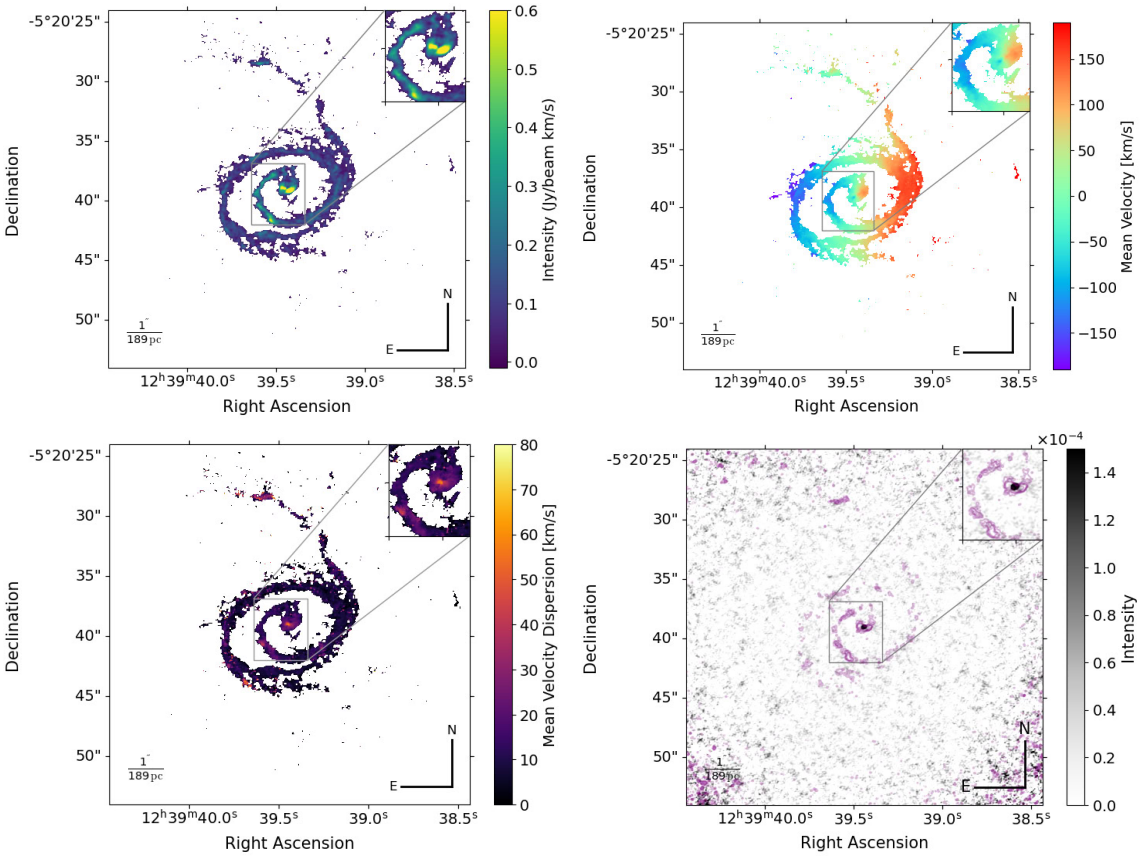

FIGURE 5.2 – Top Left: Integrated intensity (moment-0 map) showing the spatial distribution of the line flux, with a total calculated flux of approximately 100 Jy km/s. The colour bar represents the intensity scale in Jy km/s per beam units. Top Right: Intensity-weighted velocity (moment-1 map) with scale bar units in km/s, tracing gas velocities and kinematics within the galaxy. Bottom Left: Intensity-weighted velocity dispersion (moment-2 map) with scale bar units in km/s. Bottom Right: ALMA Band 6 continuum image (background) displaying the dust distribution, overlaid with CO(2-1) emission moment-0 map contours from ALMA observation Project ID: 2017.1.00236.S.

displayed in Figure 5.2, shows the intensity-weighted velocity field, which provides a detailed look at the kinematic patterns of molecular gas, in units of km/s. This map reflects the overall rotation of the molecular gas within NGC 4593, revealing a systematic velocity gradient across the galaxy's central region, aligned with the orientation of the bar. The symmetry and gradient observed in the velocity field imply that the majority of the molecular gas is dynamically stable, exhibiting rotation-dominated motion around the central nucleus. This motion aligns with theoretical expectations for barred spiral galaxies where the bar structure facilitates gas inflow towards the central regions, possibly contributing to the AGN activity observed in NGC 4593.

Additionally, the moment-2 map, representing the intensity-weighted velocity dispersion of the molecular gas, is shown in the lower left panel of Figure 5.2. The velocity dispersion provides information on the non-circular motions and local turbulence within

the gas. High dispersion values in certain regions of the map suggest areas where the gas may be experiencing additional forces, potentially associated with AGN-driven outflows or other dynamic interactions within the nucleus. The dispersion values show distinct peaks around the nucleus, suggesting enhanced turbulence or velocity mixing in these regions, likely induced by the active galactic nucleus (AGN) or by the gravitational influence of the bar, which drives gas into the central area, where it interacts dynamically.

A unique feature observed in NGC 4593 is the presence of an asymmetric one-arm spiral structure in the CO distribution, evident from the moment-0 map in Figure 5.2. This distinctive morphology corresponds to a logarithmic $m = 1$ mode, a pattern typically characterised by a single dominant spiral arm, rather than a symmetric two-armed spiral structure. The presence of an $m = 1$ mode is unusual in the nuclear regions of barred galaxies (SHAW *et al.*, 1995; PHOOKUN *et al.*, 1993; ANN; THAKUR, 2005; THAKUR *et al.*, 2009), and its appearance in NGC 4593 suggests a significant departure from axisymmetric equilibrium. This mode could potentially result from internal instabilities within the galactic disc or from external tidal interactions. The asymmetry implies that the gas dynamics in NGC 4593 are complex, potentially shaped by gravitational torques from the bar or by tidal interactions with nearby structures or galaxies.

To complement the molecular gas distribution, the bottom right panel of Figure 5.2 displays the continuum emission observed in Band 6, which traces the dust content within the galaxy. Overlaid on this continuum map are contours of the moment-0 map of CO(2-1) emission, offering a direct comparison between the dust and molecular gas distributions. The continuum emission aligns closely with the CO emission, reinforcing the association between molecular gas and dust in the galaxy's inner regions. This alignment indicates that molecular gas is likely the primary phase of the ISM in NGC 4593, facilitating star formation in these dust-rich regions.

Figure 5.3 shows channel maps of CO(2-1) emission in NGC 4593, which were generated to examine the spatial distribution and velocity components of molecular gas at various frequency channels. The channel maps reveal the velocity-resolved structure of the CO emission, spanning from -230 km/s to $+156$ km/s relative to the systemic velocity of the galaxy, estimated to be approximately 12.56 km/s. This velocity range was selected to capture the full width of the CO(2-1) line, encompassing both the approaching and receding gas components. Each channel is incremented by 10 km/s, providing a fine-grained view of the molecular gas kinematics across the disc of NGC 4593.

The channel maps show distinct structures in the CO emission, with spatially coherent regions that reflect the organised rotation of the gas. Notably, the maps highlight the nuclear concentration of molecular gas and trace the motion of gas in the arms and bar. The top row of the channel maps displays selected channels at negative velocities (blue-shifted relative to $v_{\rm sys}$), which trace the gas moving toward the observer. In contrast, the

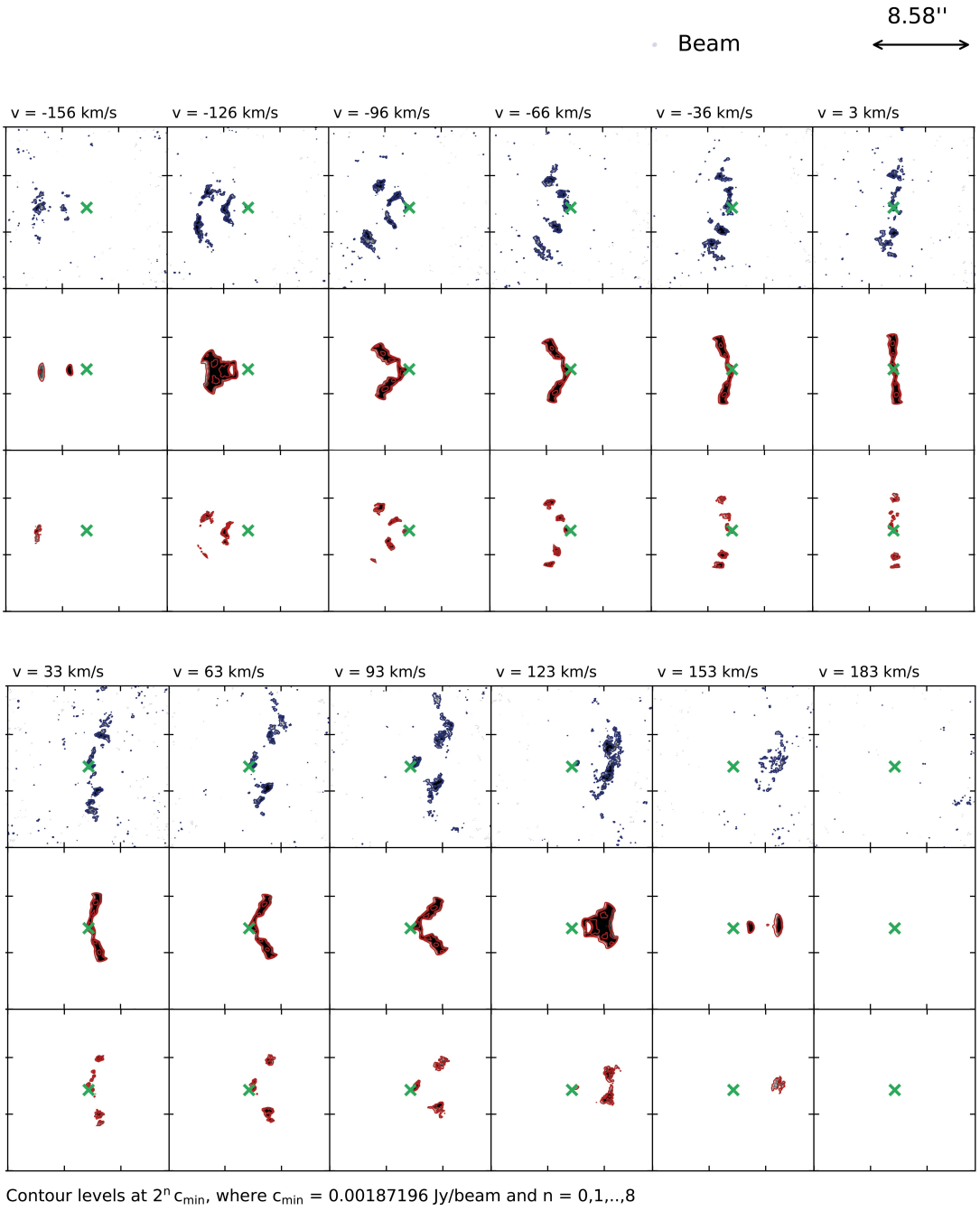

FIGURE 5.3 – CO(2-1) channel maps from the ALMA Band 6 data cube, generated using 3D-Barolo modelling, provide details into the morphology and gas kinematics of NGC 4593. The channel maps display velocities ranging from −230 km/s (top left) to +156 km/s (bottom right), relative to the galaxy's systemic velocity ($v_{\rm sys}$). This $v_{\rm sys}$ is estimated as the central velocity in the global line profile, valued at 12.56 km/s. The velocities presented signify deviations from this systemic velocity. Maps are shown in increments of 10 km/s, and each square box covers an area of 8.58″. The top row displays selected channels in blue, while the middle and bottom rows depict maps normalised using the azimuthal and local normalisation methods, respectively, highlighting distinct patterns in the emission's spatial distribution and intensity. A green cross in each panel marks the disc's centre, and solid red lines represent the RMS noise level ($\sigma_{\rm rms}$) of 0.7 mJy.

positive velocities in the middle and bottom rows (red-shifted) depict gas moving away from the observer, providing a comprehensive view of the molecular gas kinematics.

5.1.3 3D-Barolo Model of NGC 4593

To analyze the kinematics of NGC 4593's molecular gas, were employed the 3D-Barolo software (TEODORO; FRATERNALI, 2015), which performs a three-dimensional tilted-ring analysis of emission line data cubes. This approach models the galaxy by decomposing it into concentric rings, each defined by parameters such as rotation velocity, inclination, and position angle. Using these tilted rings, 3D-Barolo reconstructs the velocity field, allowing for a precise extraction of the galaxy's rotation curve and the distribution of gas column density.

The tilted-ring model assumes the galaxy is comprised of a thin, co-planar gas disk dominated by rotation, where each ring can possess independent values of inclination, position angle, and rotational velocity. This framework is effective for examining galaxy kinematics, as it can account for non-axisymmetric features, such as bars or spiral arms, while still retrieving accurate rotation velocities even in cases where the gas deviates from pure circular motion. The basic principles involve estimating the circular velocity and inclination angle of each ring, which are then adjusted iteratively until the modeled and observed kinematic data match closely.

3D-Barolo constructs an artificial disc model based on the observational input cube by simulating each ring's spatial and velocity distributions according to the galaxy's known parameters, such as systemic velocity, position angle, and inclination. The software populates each ring with gas clouds distributed according to a Gaussian profile, allowing for the reproduction of both rotation and velocity dispersion. This artificial model is then convolved with the observed beam, ensuring that the model replicates the resolution constraints of the actual observations and addresses issues such as beam smearing, which broadens the observed velocity field and reduces the apparent peak velocities.

For NGC 4593, were used two types of gas column density normalisations available in 3D-Barolo: **LOCAL** and **AZIM**. The **LOCAL** normalisation performs a pixel-by-pixel adjustment, effectively highlighting non-axisymmetric structures and preventing local irregularities, such as clumps or voids, from skewing the overall fit. This method is particularly advantageous in galaxies with complex morphologies or irregular gas distributions, as it provides a detailed view of local kinematic features. On the other hand, the **AZIM** normalisation uses azimuthally averaged flux for each ring as the normalisation factor, yielding a broader, global perspective on the galaxy's rotation. This normalisation approach is ideal for understanding large-scale kinematic structures, such as symmetric rotation curves or averaged velocity dispersion profiles.

Using the CO(2-1) data cube at a spectral resolution of 10 km/s as input, 3D-Barolo generated models based on the moment-0 maps (see Fig. 5.2) for the galaxy center and systemic velocity (V_{SYS}). As shown in Fig. 5.4, the models reveal a structured velocity

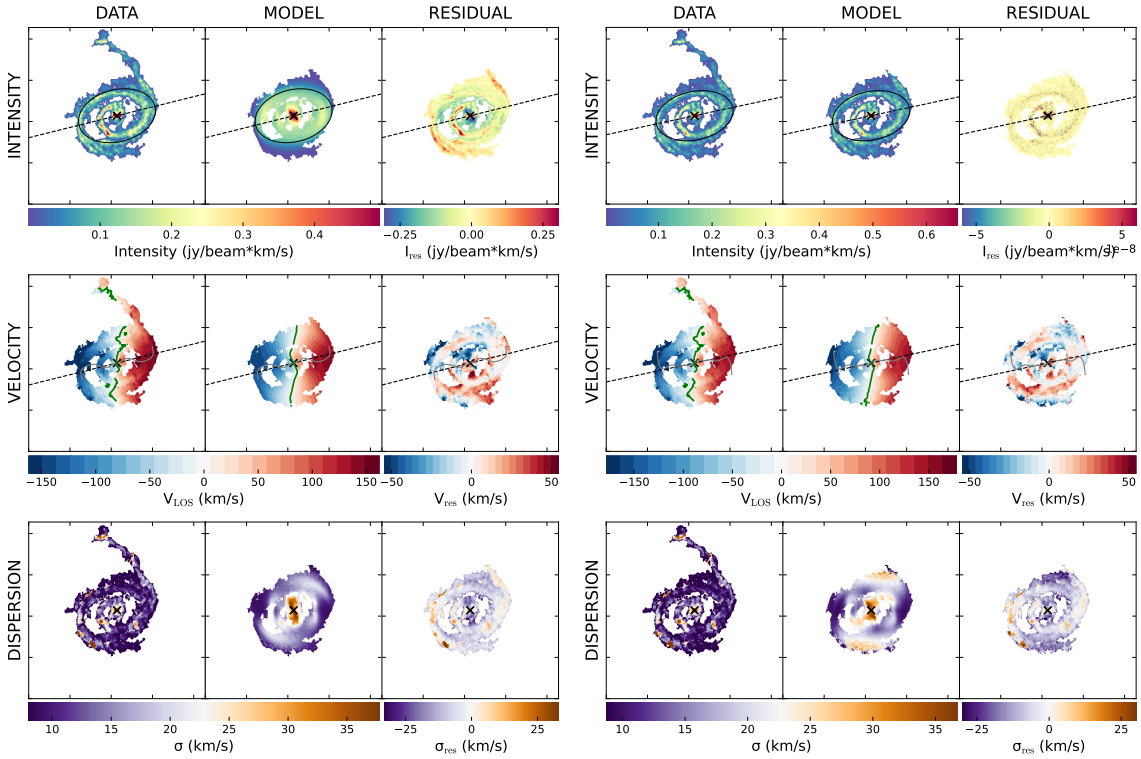

FIGURE 5.4 – The figure is divided into two panels: the left panel shows the azimuthal normalised model, while the right shows the local normalised model. Each panel consists of a 3x3 grid of images (rows: intensity, velocity, dispersion; columns: data, model, residuals). The top row presents the CO(2-1) intensity maps across the field of view, with the colour bar representing the intensity scale in $\mathrm{Jy\,km\,s^{-1}}$ per beam units. The middle row shows the velocity maps, depicting gas velocities across the field of view in km/s. The bottom row displays the velocity dispersion of the CO(2-1) line across the field of view, also denoted in km/s. The left column in each panel shows the data, the middle column displays the model, and the right column provides the residuals.

field with residuals up to ± 50 km/s, consistent across both azimuthal and local normalisation methods. The velocity dispersion maps exhibit variations up to 50 km/s, reflecting complex, ordered gas dynamics. The velocity field spans from -150 to 150 km/s for both the data and model, while residuals show a range of -50 to 50 km/s. Dispersion values range from 10 to 35 km/s, and intensity values from 0.002 to 0.016 Jy km/s.

The position-velocity $(p - v)$ diagrams along the major and minor axes, shown in Fig. 5.5, reveal significant kinematic patterns. In the major axis diagram (top panel), observed rotation velocities align closely with the best-fit model, confirming a consistent rotation curve. Along the minor axis (bottom panel), deviations from the rotational model, particularly in a region highlighted by a green circle, suggest possible inflows or outflows. These discrepancies, found 1.5″ to 2″ from the galaxy center, may indicate non-circular motions or feedback processes such as AGN-driven outflows or gravitational interactions, contributing to complex gas kinematics.

In the minor axis position-velocity $(p - v)$ diagram, the model highlights intriguing non-rotational gas motions, particularly evident approximately 1.5″ south of the AGN

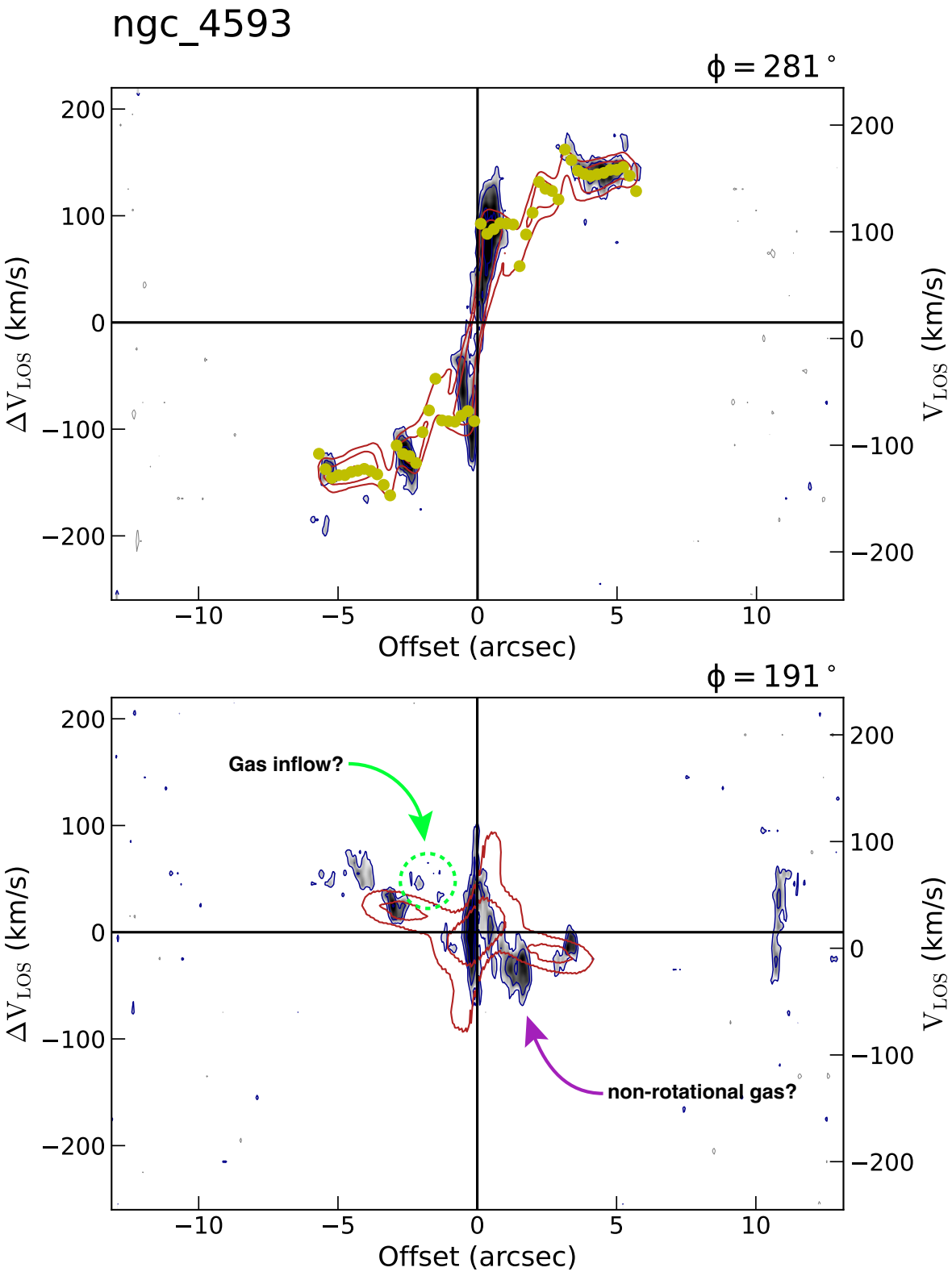

FIGURE 5.5 – Position-velocity (p-v) diagrams of the CO(2-1) emission in NGC 4593 extracted from the data and 3D-BAROLO model along the major (top panel) and minor (bottom panel) axes. Blue solid contours illustrate the p-v diagram derived from the data cube, while red solid contours depict the p-v diagram from the model cube. Contour levels for both data and model are set at $[1, 2, 4, 8, 16, 32, 64] \times l$, with $l = 0.0012$. In the top panel, yellow solid dots represent the rotation velocity of each ring from the best-fit disc model. The dashed light green circle in the bottom panel highlights a region where a potential gas inflow or outflow is located. These p-v diagrams reveal the spatial and kinematic structure of CO(2-1) emission in NGC 4593.

center, where redshifted gas motion deviates from a pure rotation profile. The dashed green circle in Fig. 5.5 marks an area roughly 2″ from the center where gas shows signs of inflow or outflow. This region, where model and data contours differ, points to the existence of vertical or radial gas motions—possibly linked to mechanisms such as AGN feedback, inflows driven by gravitational torques, or interactions with adjacent galactic structures. Further out, between 4″ and 6″, an underestimation of molecular gas by the model suggests an area where outflows or other non-rotational dynamics may be at play, potentially signaling cold molecular outflows.

The results indicate a structured and orderly rotation in the inner regions, with deviations along the minor axis that may signal outflows or other non-circular gas motions influenced by AGN activity or gravitational perturbations. This detailed modeling approach provides information not only into the rotational dynamics but also into the physical processes shaping the molecular gas in the galaxy's central regions, enhancing our understanding of AGN-host galaxy interactions and the mechanisms fueling the central supermassive black hole.

Note: The Physics of the 3D-Barolo Modeling Technique

To accurately model the kinematics of NGC 4593 and other galaxies in TWIST sample, were applied 3D-Barolo, which uses a 3D tilted-ring model to interpret emission line data cubes (teodoro; fraternali, 2015). This approach dissects the galaxy into concentric rings, each with distinct parameters such as rotation speed, inclination, and position angle. By constructing the galaxy in this way, 3D-Barolo offers a more complete view of the velocity structure than traditional two-dimensional methods, especially when dealing with observational effects like beam smearing, which can distort velocity measurements.

Each ring in the tilted-ring model is considered a flat, thin disk, dominated by rotation. This setup enables the extraction of precise rotation curves, while still capturing non-circular features such as bars or spiral arms. For each ring, the rotational velocity, $v_{\rm rot}$, is derived using:

$$v_{\rm obs}(R,\theta) = v_{\rm sys} + v_{\rm rot}(R)\sin(i)\cos(\theta) \tag{5.1}$$

where $v_{\rm obs}(R,\theta)$ is the observed line-of-sight velocity at radius R and azimuthal angle θ, $v_{\rm sys}$ represents the systemic velocity of the galaxy, i is the inclination angle, and θ denotes the azimuthal angle within the galaxy's plane. This approach simplifies the interpretation of the galaxy's rotation-dominated structure, and deviations from this model can point to dynamic phenomena, such as gas inflows or outflows, or structural variations due to a

central bar.

3D-Barolo constructs an artificial data cube by populating each ring with gas clouds that follow a Gaussian distribution in velocity, reflecting both intrinsic velocity dispersion σ and the telescope's resolution. The Gaussian profile describing the velocity distribution is given by

$$f(v) = \frac{1}{\sqrt{2\pi\sigma^2}} \exp\left(-\frac{(v - v_{\rm rot})^2}{2\sigma^2}\right) \tag{5.2}$$

where σ represents the gas's velocity dispersion in Km/s within each ring. This profile captures velocity variations within the ring due to turbulence and thermal effects, providing an accurate reconstruction of gas dynamics.

To align the model with observed data resolution, 3D-Barolo convolves the simulated data with the telescope's beam profile. This step maintains the model's fidelity to real observations and mitigates artificial broadening, which could reduce observed velocity gradients and obscure the rotating gas's dynamics.

The 3D-Barolo model offers two normalization options for gas column density: **LOCAL**, which adjusts the column density on a pixel-by-pixel basis, and **AZIM**, which applies azimuthally averaged flux for each ring. The **LOCAL** normalization is particularly effective for capturing detailed, non-axisymmetric structures, making it suitable for areas with pronounced density variations or irregular gas distributions. Alternatively, the **AZIM** normalization provides a smooth, global perspective of the gas distribution, useful for analyzing symmetric rotation curves or large-scale velocity dispersion profiles.

Together, these techniques allow 3D-Barolo to model complex galaxy kinematics accurately, facilitating detailed analyses of rotation curves, gas inflows and outflows, and other key features within galaxy disks.

5.1.4 DiskFit Modelling on NGC 4593

To complement and cross-verify our kinematic analysis obtained from the 3D-Barolo model, were also employed the discFit software (spekkens; sellwood, 2007). discFit is particularly useful for modelling a galaxy's two-dimensional kinematic structure and allows for decomposition into various components such as disc, bulge, and bar structures, when present. By using discFit with the same initial conditions applied in the 3D-Barolo model, we aimed to verify the consistency of our results and probe any structural complexities within NGC 4593's kinematic patterns.

In discFit, we used the galaxy's velocity moment map as an input, generating an idealised model of the velocity field that includes rotation, inclination, and position an-

gle as parameters for each component. Unlike the 3D-BAROLO model, which operates in three dimensions and incorporates vertical disc height (via the Z_0 parameter), DISCFIT remains in two dimensions, simplifying the model by assuming the galaxy as a thin disc. This difference between 3D-BAROLO's three-dimensional framework and DISCFIT's two-dimensional approach is particularly notable in areas with strong non-axisymmetric features, such as bars and spiral arms, as well as along the galaxy's outer edge, where vertical height may play a more significant role.

In Fig. 5.6, the left panel shows the observed velocity field of NGC 4593's CO(2-1) emission. The middle panel presents model, and the right panel representing the residuals, derived by subtracting the DISCFIT model from the observed data, with contours representing the residuals at $5\sigma_{rms}$ intervals. In the lower panel of Fig. 5.6, we compare the rotation curves derived from both 3D-BAROLO and DISCFIT, examining the results with and without the inclusion of radial velocity components. Notable deviations appear, especially in the central region and along the prominent eastern spiral arm. The DISCFIT model aligns well with the overall rotational pattern but does not fully capture the non-circular motions seen in the 3D-BAROLO model, particularly near the nucleus where non-axisymmetric features are most pronounced.

This discrepancy likely stems from the dimensional difference between the models: 3D-BAROLO's consideration of disc scale-height allows it to account for slight deviations in gas distribution above and below the plane, particularly within the innermost regions. In the case of DISCFIT, however, the assumption of a thin, two-dimensional disc restricts its flexibility in representing such vertical features. As seen in Fig. 5.6, DISCFIT does not respond as strongly to the data "bumps"—local increases in velocity—that 3D-BAROLO accommodates by adjusting the radial velocity component. This difference suggests that 3D-BAROLO may overfit to certain axisymmetric features, especially where radial velocity components are significant, while DISCFIT offers a more stable fit across the disc.

In Fig. 5.7, we compare the spiral arm widths of NGC 4593, measured from the CO(2-1) molecular gas data, with the disc scale height derived from 3D-BAROLO. Within the inner disc region (up to about 5.5″), the spiral arms exhibit widths ranging from 1.0″ to 1.3″. Beyond this radius, within the single-arm region, the widths increase slightly, between 1.35″ and 1.45″. Though NGC 4593's face-on orientation complicates direct measurements of flaring (increased height at greater radii), the relationship between the spiral arm width and scale height suggests mild flaring, comparable to that observed in other galaxies (PATRA, 2020).

Our analysis shows that while DISCFIT is adept at capturing the general rotation and axisymmetric features in NGC 4593, it lacks the three-dimensional flexibility needed to model vertical deviations or non-axisymmetric features. Conversely, 3D-BAROLO's three-dimensional approach provides more detailed morphological findings but may overfit

in areas of strong non-circular motion, highlighting the complementary strengths and limitations of each method in studying molecular gas kinematics.

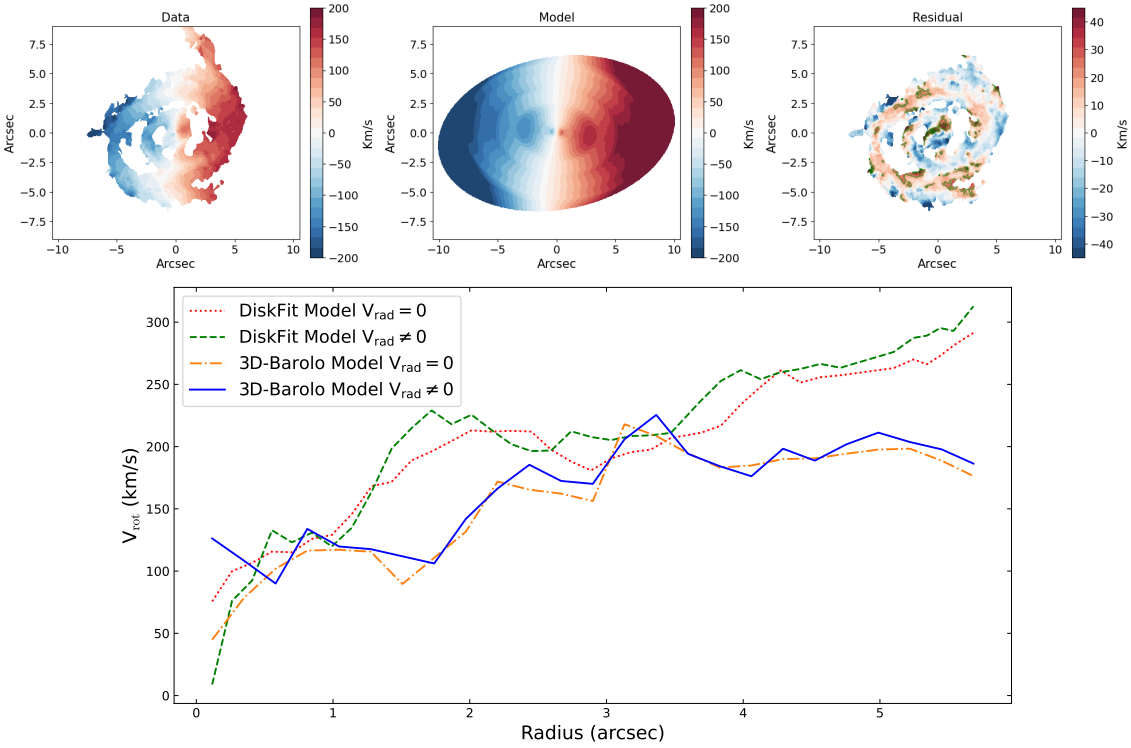

FIGURE 5.6 – CO(2-1) observed velocity field and corresponding residuals derived from DISCFIT modelling for NGC 4593. The left panel showcases the observed velocity field of the CO(2-1) emission, with the scale bar units given in km/s. The right panel shows the residuals produced by subtracting the DISCFIT model from the observed data, with green contours representing levels of $5\sigma_{rms}$. The bottom panel compares the rotation curve velocities (V_{rot}) obtained from both 3D-BAROLO and DISCFIT models, considering cases with and without radial velocity (V_{rad}).

5.1.5 Gas Kinematics in NGC 4593

Our kinematic analysis of NGC 4593, illustrated in Fig. 5.8, leverages a detailed 3D-BAROLO analysis applied to the ALMA Band 6 data. This analysis provides details into six key parameters: $V_{\rm rot}$ (rotation velocity), $\sigma_{\rm gas}$ (gas velocity dispersion), $v_{\rm rad}$ (radial velocity), ϕ (azimuthal angle), i (inclination angle), and Σ (surface gas density). Each parameter, mapped as a function of galactocentric radius, contributes uniquely to our understanding of the galaxy's dynamic structure and gas distribution.

The rotation velocity $V_{\rm rot}$ provides the primary measurement of ordered motion within the disk and serves as an indicator of the mass distribution. Higher rotation velocities in the inner regions typically correspond to higher central mass concentrations, often linked to the presence of a supermassive black hole or a dense stellar bulge. In NGC 4593, the observed $V_{\rm rot}$ supports a rotationally supported disk structure, central to modeling the gravitational potential of the galaxy.

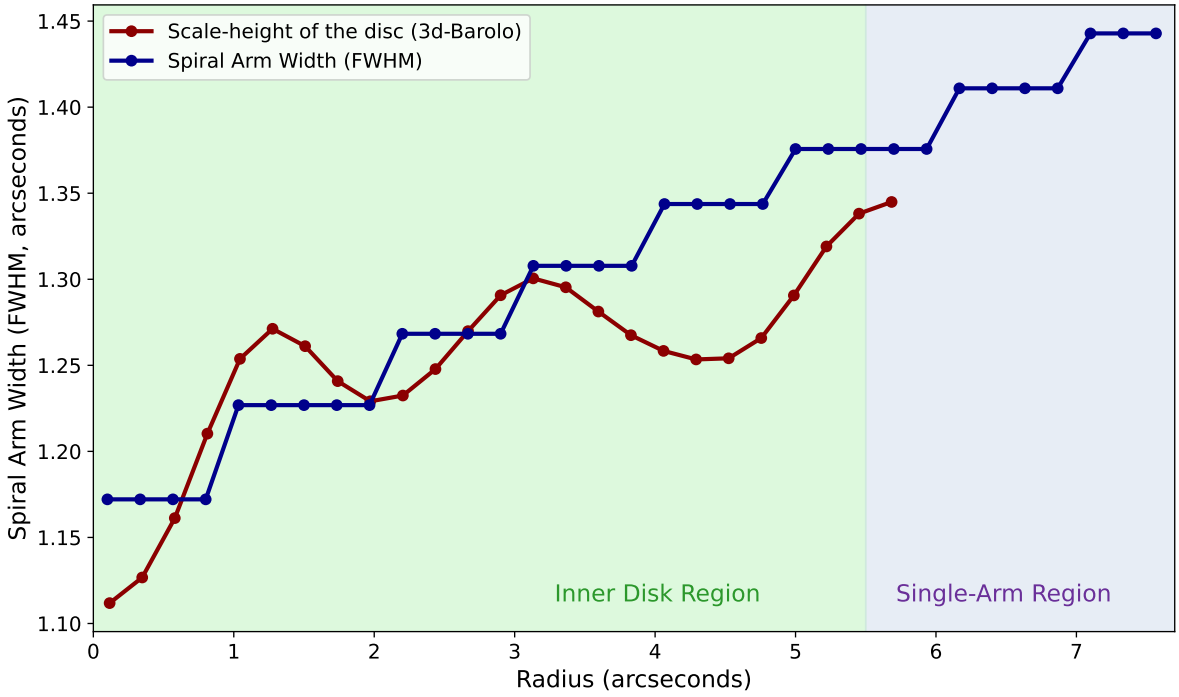

FIGURE 5.7 – Comparison between the spiral arm widths and disc scale height as a function of radius in NGC 4593. The blue line represents the spiral arm widths, estimated from the observational data of CO(2-1) molecular gas. The red line shows the disc scale height, derived from 3D-Barolo modelling.

The gas velocity dispersion $\sigma_{\rm gas}$ represents the random motions of the gas and is essential for understanding turbulent processes within the disk. Elevated $\sigma_{\rm gas}$ values may signal regions of increased turbulence due to feedback from active galactic nuclei (AGN) or star formation, which could affect gas stability and star formation rates. In our analysis, the observed $\sigma_{\rm gas}$ values across the radius highlight spatially varying dynamical states in NGC 4593's gas distribution.

Radial velocity $v_{\rm rad}$ is particularly relevant in barred spiral galaxies like NGC 4593, where it can reveal gas flows directed toward or away from the galactic center. Non-zero $v_{\rm rad}$ values may indicate inflows fueling central activity or outflows driven by feedback mechanisms. In NGC 4593, we note variations in $v_{\rm rad}$ that suggest complex gas flows, potentially shaped by the galaxy's bar structure and central activity.

The azimuthal angle ϕ and inclination angle i define the orientation of the galactic disk. The average inclination of 47.4° and position angle (PA) of 276° in NGC 4593 align the major axis approximately along an East-West (E-W) direction, placing the near side to the north and the far side to the south. This orientation was corroborated by examining the dust lane morphology in Hubble Space Telescope (HST) images (see Fig. 5.1) and was further supported by extended MUSE observations (Brok *et al.*, 2020). The position and inclination angles provide a baseline for interpreting the kinematic model and comparing it with observed asymmetries in gas motion.

Surface gas density Σ measures the distribution of molecular gas, a crucial parameter for understanding both gas dynamics and star formation potential. Regions with higher Σ are often associated with higher star formation rates, driven by the availability of molecular gas as fuel for star formation. Mapping Σ across the galaxy, therefore, reveals new information into the underlying potential for star formation in different regions and allows us to evaluate gas depletion trends over time.

The kinematic model, based on an axisymmetric assumption within 3D-Barolo, serves as an idealized framework to interpret NGC 4593's gas motions. However, the residual maps (see Figs. 5.4, 5.6) reveal deviations from purely rotational motion, highlighting non-axisymmetric components. Redshifted residuals in these maps should not necessarily be interpreted as receding gas but may also indicate regions where the gas velocity is less blueshifted than predicted by the symmetric model. These residuals likely arise from unmodeled radial gas flows, bar-driven motions, or other dynamic effects not captured by 3D-Barolo's symmetric assumption.

Barred galaxies, such as NGC 4593, often exhibit complex gas dynamics due to the bar's influence on the gas distribution. Studies of similar systems, such as NGC 2110, have shown that bar potentials can drive significant radial gas flows, create non-axisymmetric velocity fields, and influence molecular outflows (Schnorr-Müller *et al.*, 2014). In NGC 4593, the presence of redshifted and blueshifted residuals suggests that the bar likely drives gas toward the central regions, potentially fueling AGN activity or contributing to the observed molecular asymmetries.

The analysis of these parameters, therefore, not only illustrates the structure and dynamics of NGC 4593 but also highlights the role of bars in shaping the kinematics of barred spiral galaxies. Our findings imply that the bar-induced instabilities in NGC 4593 contribute to its observed kinematic asymmetries and may influence both star formation and AGN feedback, delivers understanding into the interaction between the galactic bar and the molecular gas reservoir.

5.1.6 Estimating Molecular Gas Mass

To quantify the molecular gas mass $M(H_2)$ in NGC 4593, we calculated the CO(2–1) line luminosity, $L'_{\mathrm{CO(2-1)}}$, based on the method outlined by (Solomon; Bout, 2005). This calculation is essential because $M(H_2)$ uncovers details into the amount of cold gas available for star formation and AGN fueling within the galaxy, both of which are important in understanding the overall gas dynamics and evolutionary state of NGC 4593.

The CO(2-1) line luminosity is calculated using the following equation:

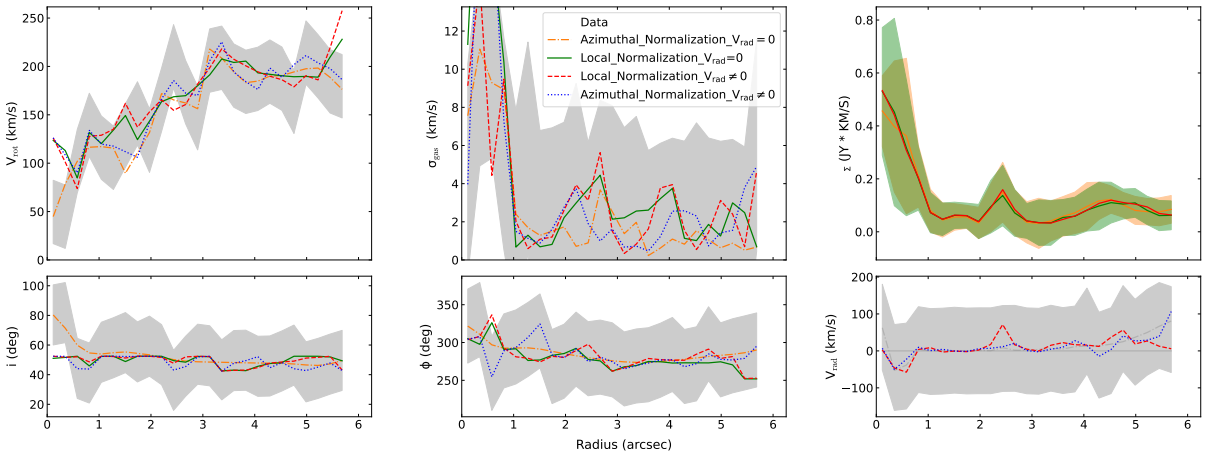

FIGURE 5.8 – Kinematic and structural parameters of NGC 4593 as a function of radius. Top row, from left to right: **Rotation Velocity** ($V_{\rm rot}$), **Velocity Dispersion** ($\sigma_{\rm gas}$), and **Surface Density** (Σ). Bottom row, from left to right: **Inclination Angle** (i) showing the variation of inclination with radius, **Position Angle** (ϕ) illustrating the fluctuation of position angle with radius, and **Radial Velocity** ($V_{\rm rad}$) displaying the radial velocity (km/s) versus radius, marked in grey. In each subplot, the observational data are represented by grey points with error bars. The fitted azimuthal normalisation with $V_{\rm rad} = 0$ is depicted by an orange line with a dash-dot pattern, while the local normalisation series with $V_{\rm rad} = 0$ is shown as a solid green line. The local normalisation with $V_{\rm rad} \neq 0$ is represented by a dashed red line, and the azimuthal normalisation with $V_{\rm rad} \neq 0$ is indicated by a dotted blue line.

$$L'_{\rm CO(2-1)} = 3.25 \times 10^7 \, S_{\rm CO}\Delta v \, \nu_{\rm obs}^{-2} \, D_L^2 \, (1+z)^{-3}, \tag{5.3}$$

where $S_{\rm CO}\Delta v$ is the integrated CO(2-1) flux, $\nu_{\rm obs}$ is the observed frequency of the CO(2-1) transition (230 GHz), D_L is the luminosity distance to NGC 4593 (39 Mpc), and z is the galaxy's redshift (0.009). The term $S_{\rm CO}\Delta v$ represents the total flux density from the CO(2-1) line, which reflects the amount of CO emission across the observed region and serves as a tracer of molecular hydrogen (H_2).

From the ALMA CO(2-1) moment-0 map (Fig. 5.2), we measured a flux density of 146.3 ± 1.1 Jy km s^{-1} for a circular region with a radius of 12″. Substituting these values, we obtained:

$$L'_{\rm CO(2-1)} \approx 1.40 \pm 0.10 \times 10^8 \text{ K km s}^{-1} \text{ pc}^2. \tag{5.4}$$

The CO(2-1) line luminosity is then converted to the CO(1-0) transition, $L'_{\rm CO(1-0)}$, by applying a standard conversion ratio. The CO(1-0) transition is often used as the primary reference for molecular gas mass calculations since it directly traces H_2 across varying environments. Based on typical ratios observed in galaxies with moderate to high star formation rates, including (ultra) luminous infrared galaxies ((U)LIRGs), we used a conversion factor of $L'_{\rm CO(2-1)}/L'_{\rm CO(1-0)} \approx 5.0$ (KAMENETZKY *et al.*, 2016). This yielded:

$$L'_{\mathrm{CO}(1-0)} \approx (0.28 \pm 0.02) \times 10^8 \text{ K km s}^{-1} \text{ pc}^2. \tag{5.5}$$

To estimate the molecular gas mass M_{H_2} from $L'_{\mathrm{CO}(1-0)}$, we employed a CO-to-H_2 conversion factor α_{CO}. This conversion factor varies with environmental conditions and metallicity in the ISM, and values between $0.8\,M_\odot\,(\text{K km s}^{-1}\,\text{pc}^2)^{-1}$ and $3.2\,M_\odot\,(\text{K km s}^{-1}\,\text{pc}^2)^{-1}$ are commonly used for environments ranging from AGN-influenced regions to normal galactic disks (BOLATTO *et al.*, 2013). For NGC 4593, which contains both star-forming regions and AGN activity, we adopted this range to estimate:

$$M_{H_2} = \alpha_{\mathrm{CO}}\, L'_{\mathrm{CO}(1-0)} \approx (0.22 - 0.90) \times 10^8\, M_\odot. \tag{5.6}$$

This range represents the plausible bounds of M_{H_2} given the varying ISM conditions in the galaxy. The mass of molecular gas is particularly significant in assessing the potential for star formation and in quantifying the cold gas available for accretion by the AGN.

One potential source of uncertainty in our mass estimate is the interferometric filtering of extended CO emissions. Interferometers such as ALMA are sensitive primarily to compact structures, potentially missing more diffuse CO(2-1) emission that extends beyond the instrument's spatial sensitivity scale. This effect could lead to an underestimation of the true CO(2-1) flux and, consequently, of the total molecular gas mass in NGC 4593. Should significant CO(2-1) emission extend beyond the ALMA resolution, the actual molecular gas mass could exceed our current estimates.

Furthermore, the choice of the CO-to-H_2 conversion factor α_{CO} introduces additional uncertainty. In environments with high radiation fields or turbulence, such as those found near AGNs, the effective value of α_{CO} can be lower than in quiescent regions, affecting mass estimates. Studies comparing various galactic environments suggest that α_{CO} may vary by a factor of up to four (BOLATTO *et al.*, 2013), making it important to consider this range when interpreting the estimated $M(H_2)$.

In summary, the molecular gas mass in NGC 4593, estimated within a range of $0.22 - 0.90 \times 10^8\, M_\odot$, provides a basis for understanding the cold gas reservoir in the galaxy. This mass estimate not only reflects the current state of the galaxy's ISM but also offers input for further analysis of star formation and AGN fueling mechanisms. Additional observations with improved sensitivity to extended emission could help refine this estimate and provide a more comprehensive understanding of the molecular gas content in NGC 4593.

5.1.7 Estimation of SMBH Mass in NGC 4593

To estimate the mass of the supermassive black hole (SMBH) $M_{\rm BH}$ in NGC 4593, we adopted the methodology of (SMITH *et al.*, 2021), which correlates the SMBH mass with the rotational dynamics of the host galaxy using molecular gas kinematics. This approach is particularly advantageous for SMBH mass estimation in galaxies where direct dynamical methods, such as stellar or gas dynamical modeling, are limited by resolution constraints or a lack of clear kinematic tracers. The relationship between SMBH mass and host galaxy rotation is expressed as follows:

$$\log\left(\frac{M_{\rm BH}}{M_\odot}\right) = (7.5 \pm 0.1) + (8.5 \pm 0.9)\left[\log\left(\frac{W_{50}}{\sin i}\,\mathrm{km\ s^{-1}}\right) - 2.7\right], \tag{5.7}$$

where $M_{\rm BH}$ represents the SMBH mass, W_{50} is the full width at half-maximum (FWHM) of a double-peaked CO(2-1) emission line profile, and i denotes the inclination angle of the CO disc. This empirical relationship, derived from observations of a sample of galaxies with well-constrained SMBH masses, has a scatter of 0.6 dex, which is comparable to other SMBH mass estimation techniques, such as bulge stellar velocity dispersion correlations (with an intrinsic scatter of ~ 0.5 dex). By correlating SMBH mass to observable galaxy rotation parameters, this method provides a robust framework for estimating $M_{\rm BH}$ using ALMA observations of molecular gas.

To determine W_{50}, we measured the width of the CO(2-1) emission line profile at half-maximum using the procedure described by (TILEY *et al.*, 2016). Specifically, we applied a Gaussian double-peak profile fit to the CO(2-1) line emission across the field of view (FOV) obtained from the 3D-BAROLO modeling. This double-peak profile approach, illustrated in Fig. 5.9, accurately characterizes the observed integrated CO(2-1) emission profile, which often displays double-peaked features in galaxies with prominent rotation. The line width at half-maximum, W_{50}, is derived as:

$$W_{50} = 2(w + \sigma\sqrt{2\ln 2}), \tag{5.8}$$

where w is the velocity half-width at half-maximum (HWHM), and σ represents the velocity width of the Gaussian peaks. This formulation accounts for the shape and spread of each peak, ensuring an accurate representation of W_{50} across the double-peak profile. From this analysis, we measured $W_{50} \approx 314 \pm 10\,\mathrm{km/s}$. Additionally, the inclination angle of the CO disc, derived from 3D-BAROLO kinematic modeling, was found to be $i \approx 47.7^\circ \pm 1.1^\circ$ (Fig. 5.8), consistent with the galaxy's orientation inferred from both molecular and stellar kinematic analyses.

Substituting these values into the SMBH mass equation, we obtained an estimated

SMBH mass:

$$\log\left(\frac{M_{\rm BH}}{M_\odot}\right) = 6.89 \pm 0.04. \tag{5.9}$$

This mass estimate aligns closely with results from alternative SMBH mass measurement techniques. For instance, the WISDOM project, which uses CO kinematics to estimate SMBH masses in galaxies, reported a value of $\log\left(\frac{M_{\rm BH}}{M_\odot}\right) = 6.86$ for NGC 4593 (TILEY *et al.*, 2016). Additionally, the mass estimated through reverberation mapping by (DENNEY *et al.*, 2006) yielded an SMBH mass of $\log\left(\frac{M_{\rm BH}}{M_\odot}\right) = 6.99$. The consistency across these methods reinforces the reliability of our estimation approach and supports the use of molecular gas kinematics as a viable proxy for SMBH mass, particularly in cases where traditional methods may be limited.

Figure 5.9 provides a comparative analysis of molecular gas dynamics in NGC 4593. The top panel highlights regions with potential non-circular motion, indicated by a red circle (region a) around areas with velocity anomalies potentially linked to cold molecular gas outflows. These deviations are visible on the mean velocity map in the background and suggest dynamic processes possibly driven by AGN feedback or bar-driven instabilities. The dashed circle in the center (region b) encompasses a central molecular zone (CMZ)-like ring, which contains a significant concentration of molecular gas and may act as a reservoir for AGN fueling.

The bottom panel in Fig. 5.9 compares the CO(2-1) ALMA observations (green line) with the 3D-BAROLO model fit (blue line) for NGC 4593, displaying the average flux as a function of velocity. Residuals (orange line) reveal minor discrepancies between the model and observed flux, with potential contributions from outflowing gas indicated in red around region (a). These comparisons highlight the dynamic interactions within NGC 4593's molecular gas, as well as the role of the SMBH and potential outflows in influencing the kinematic structure.

Overall, our results indicate that the SMBH in NGC 4593 has an estimated mass of $M_{\rm BH} \sim 6.89 \pm 0.04 \log M_\odot$, a value that aligns with both kinematic and reverberation mapping approaches. This analysis underscores the potential of molecular gas kinematics as a complementary tool for SMBH mass estimation, providing a means to assess SMBH properties in diverse galactic environments.

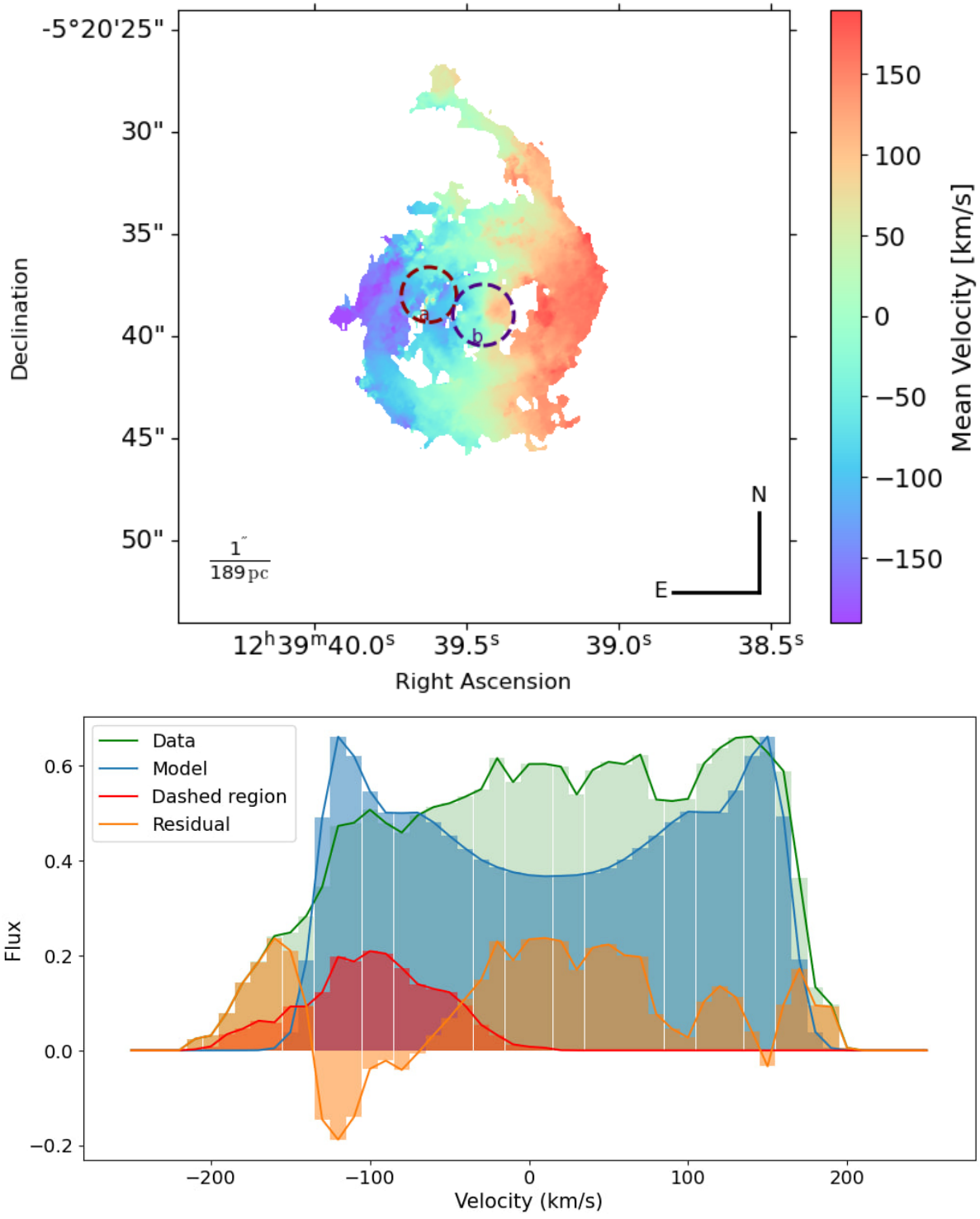

FIGURE 5.9 – Analysis of molecular gas dynamics in NGC 4593. Top: Red-circled region (a) indicates potential non-circular motion due to the outflow of cold molecular gas, visible on the mean velocity map (background). The central dashed circle (region b) highlights the CMZ-like ring, which contains significant molecular gas. Bottom: Comparison between the CO(2-1) ALMA observations (green) and the 3D-Barolo model (blue) for NGC 4593. The plot shows the average flux as a function of velocity, with residuals (orange) and possible outflowing gas from region (a) highlighted in red.

5.1.8 Evidence of Non-Circular Motion and Molecular Inflow or Outflows

Our kinematic analysis using 3D-Barolo on NGC 4593 reveals complex gas dynamics that indicate significant departures from purely circular motion. The CO gas distribution displays a prominent one-arm spiral structure, suggesting the presence of an $m = 1$ density wave or perturbation within the galaxy's nuclear regions. This type of one-armed spiral pattern is rare in barred galaxies and hints at a strong, non-axisymmetric component in the gravitational potential, which deviates from the assumptions of an axisymmetric velocity field typically applied in 3D-Barolo modeling. This structure implies that while circular motion dominates in certain regions, non-circular motions are also present and may significantly impact the molecular gas kinematics near the nucleus.

The differences in kinematic fit between the northern and southern regions of NGC 4593 highlight the model's limitations in fully capturing the complexity of the observed molecular gas distribution and motion. Such discrepancies are consistent with previous studies, such as those by (BARBOSA *et al.*, 2006), which noted deviations from axisymmetric models in the ionized gas kinematics of barred galaxies. These deviations provide further evidence that non-circular motions are influenced by bar-driven effects and that additional dynamical components may be necessary to accurately represent the galaxy's inner kinematics.

Within the bar region of NGC 4593, an inner CO ring structure emerges, which clarifies complexities into the interplay between the bar dynamics and molecular gas distribution. This ring's kinematic position angle (PA) of approximately $-59.3°$ contrasts sharply with the morphological PA of 46°, suggesting that the ring structure is elliptical and that both stellar and gas orbits are elongated. This misalignment between the kinematic and morphological PAs likely results from non-circular motions driven by the gravitational influence of the bar, which causes gas to accumulate along radial dust lanes and form elliptical orbits. Such a configuration is often seen in barred galaxies, where bars channel gas inward and accumulate material within nuclear rings, providing a mechanism for fueling AGN activity and shaping the circumnuclear environment.

The AGN at the center of NGC 4593 plays an important role in shaping the galaxy's nuclear structure. As demonstrated by (GADOTTI, 2008), the AGN exerts a strong influence over both the light profile and the kinematic properties of the central region. The central bar and potential AGN-driven feedback create conditions that influence the nuclear gas flow, potentially driving non-circular motions and creating regions of enhanced molecular gas density. The apparent misalignment and poor fit within the nuclear region in our model may therefore reflect the limits of the 3D-Barolo assumptions, as axisymmetry does not fully capture the complex orbital dynamics likely influenced by the bar

and AGN feedback processes.

The central region of NGC 4593 is also characterized by the presence of a pseudobulge, which has been identified through Ks-band surface photometry as a non-classical bulge structure (KORMENDY *et al.*, 2006). The formation of pseudobulges is often linked to secular evolutionary processes in galaxies with prominent bars, where bar-driven gas inflows gradually build up the central mass. The misalignment between the bar and bulge in NGC 4593, coupled with its pseudobulge, suggests that the galaxy has likely experienced complex evolutionary processes, deviating from the standard pathway dominated by slow, bar-induced gas inflows alone. In this case, the nuclear dust ring and associated radial dust lanes act as channels for gas inflow, supporting potential central starburst activity that contributes to the pseudobulge's development.

Further findings into the non-circular motions in NGC 4593 arise from the residuals observed in 3D-BAROLO velocity dispersion maps. These residuals, illustrated in Fig. 5.9, highlight regions of excess velocity dispersion unaccounted for by the model. Such excesses suggest additional kinematic components, potentially arising from turbulence or unresolved molecular inflows or outflows. In the CO(2-1) mean velocity map (Fig. 5.9), the dashed red circle, marked as region (a), highlights an area located about $2''$ to $3''$ northeast of the galactic center where non-circular motion is evident. This region, likely linked to inflows or outflows of cold molecular gas, contributes approximately 10% of the galaxy's total flux, with about half of this flux evident in the residuals. Consequently, around 5% of the total flux can be attributed to non-circular motions, indicating significant gas activity. The estimated gas mass in this region is approximately $(0.5 - 2.5) \times 10^7\ M_\odot$.

While some of these residuals could theoretically be associated with extraplanar gas, such as that seen several kiloparsecs above the disks of other spiral galaxies (FRATERNALI *et al.*, 2002; LI *et al.*, 2021), this possibility is less likely for NGC 4593. Due to the galaxy's low inclination, distinguishing in-plane non-circular motions from extraplanar outflows remains challenging. However, the velocities of these residuals are relatively small and align more with in-plane dynamics rather than significant extraplanar outflows, which would typically show velocities considerably higher than those of in-plane motions (MARASCO *et al.*, 2019). Extraplanar gas in other systems, such as the Milky Way, generally consists of low-density atomic hydrogen and accounts for only a small fraction of the total mass (typically under 15%) (SÖDING *et al.*, 2024). Furthermore, the global SFR in NGC 4593 does not indicate conditions that would drive strong star-formation-driven outflows, nor is the galaxy located in a particularly crowded environment that would suggest gas stripping or strong tidal interactions (KORMENDY *et al.*, 2006).

Consequently, while extraplanar gas cannot be entirely ruled out, it is unlikely to significantly impact the observed kinematics in NGC 4593. Instead, the residual gas flux likely represents an inflow or outflow of molecular gas. Further support for this inter-

pretation comes from the bump in rotation velocity, radial velocity, surface density, and velocity dispersion at the same radius observed in the 3D-Barolo results (Fig. 5.8). This region shows a noticeable rise and fall in rotation velocity, indicating localized perturbations in the velocity field. Similarly, deviations in the radial velocity profile from the expected symmetry suggest inflow or outflow dynamics, as does the excess surface density, which suggests gas accumulation. The increase in velocity dispersion in this region further underscores the disturbed state of the molecular gas.

The combination of these characteristics—rotation velocity anomalies, radial velocity deviations, elevated surface density, and excess velocity dispersion—provides compelling evidence of non-circular motion and molecular inflows or outflows in NGC 4593. These observations highlight the limitations of the axisymmetric assumptions in the 3D-Barolo models and underscore the importance of non-axisymmetric bar potentials in shaping the galaxy's gas dynamics. The findings here contribute to a deeper understanding of how bar-driven processes and AGN feedback collectively shape the molecular gas structure and kinematics in barred spiral galaxies.

5.1.9 Central Molecular Zone (CMZ) Ring

The central molecular zone (CMZ) is a dense, gas-rich region typically located within the innermost few hundred parsecs of galaxies, often characterized by elevated star formation rates and significant dynamic activity. The CMZ's structure and molecular gas concentration are influenced by the gravitational effects of the galactic bar, and potentially by AGN activity, making it a key site for studying central gas dynamics and galactic evolution (Morris *et al.*, 1983; Bally *et al.*, 1987). Due to its high molecular gas density and proximity to the nucleus, the CMZ serves as a central engine, driving various dynamic processes that can impact both star formation and black hole activity.

In barred galaxies, bar-induced gravitational torques create inflows of molecular gas toward the galaxy's central regions. These inflows funnel material into the CMZ, forming high-density molecular rings that concentrate gas and dust in a compact region. The gravitational influence of the bar generates shocks and streaming motions along the bar's length, channeling molecular gas inward and enhancing gas density in the CMZ. This increased density has significant implications: it can fuel enhanced star formation rates (SFRs), provide a reservoir for AGN activity, and drive turbulent flows within the CMZ. The interaction between inflowing gas and the central black hole (BH) may trigger episodic accretion events, fueling AGN activity and contributing to AGN-driven feedback that regulates the growth and activity of the BH (Sormani; Barnes, 2019; Hatchfield *et al.*, 2021; Tress *et al.*, 2024).

Our analysis of NGC 4593 suggests the presence of a CMZ-like ring in the innermost

regions of the galaxy, as illustrated in Fig. 5.9. The bar structure of NGC 4593, extending approximately 35″ in length (MULCHAEY; REGAN, 1997), aligns in a configuration that channels molecular gas into the CMZ-like ring via gravitational torques. This configuration produces shock fronts along the bar, guiding gas into elliptical orbits within the CMZ, consistent with bar-driven inflow mechanisms observed in other barred spiral galaxies (ATHANASSOULA, 1992). These inward gas flows not only supply material to the CMZ but also contribute to a dynamically complex environment in which gas density, velocity dispersion, and molecular gas inflow patterns interact.

The CMZ-like ring in NGC 4593, with its high molecular gas concentration, is positioned to play a pivotal role in the galaxy's evolution. The dense molecular gas within this ring can significantly impact SFRs, enhance AGN activity, and influence the broader dynamical state of the galaxy. Previous studies, such as (ARMILLOTTA *et al.*, 2020) and (TORII *et al.*, 2013), have highlighted how CMZ rings can act as stabilizing or destabilizing forces in galactic evolution, depending on the inflow dynamics and AGN feedback. The CMZ in NGC 4593 may thus serve as a region for sustaining AGN-driven feedback loops or promoting star formation within the central kiloparsec.

Quantitative estimates indicate that this CMZ-like ring, located within a radius of approximately 2″, contains roughly 20% of the total molecular gas mass in NGC 4593, translating to a mass range of approximately $0.2 - 1.0 \times 10^8\,M_\odot$. This concentration suggests that a substantial fraction of the galaxy's molecular gas is localized in this compact region, supporting high gas densities that exceed the average values for the broader galaxy. The surface density of molecular gas in the CMZ-like ring is estimated to range from $\Sigma \sim 0.26 - 0.34\,\mathrm{Jy\,km/s}$, in contrast to the average molecular gas surface density across the entire galaxy, which is about $\Sigma \sim 0.10 - 0.14\,\mathrm{Jy\,km/s}$. Therefore, the surface density within the CMZ-like ring is approximately 2.5 times higher than the galaxy-wide average, underscoring the enhanced molecular gas concentration and its potential to support elevated star formation rates.

The velocity structure within the CMZ-like ring reveals strong rotational motion, along with indications of non-circular streaming inflow, likely driven by the bar's gravitational influence. By analyzing the residual velocity field from our 3D-BAROLO model, we observe significant residuals concentrated in the central regions of the galaxy. These residuals indicate a velocity profile consistent with inflow or outflow patterns that are oriented perpendicular to the primary velocity map of NGC 4593. Notably, the majority of these central residuals are positive, suggesting an inflow of molecular gas toward the nucleus.

This inflow pattern, aligned with the bar structure, supports the hypothesis of bar-driven accretion into the CMZ and possibly toward the central black hole. Such inward flows could sustain the AGN and provide a source of gas that may periodically accrete onto the SMBH, triggering episodes of AGN feedback that can influence the surrounding

gas environment. These findings contribute to the broader understanding of how central molecular zones function as pivotal regions for both star formation and black hole accretion, and highlight the role of non-circular inflow patterns in concentrating molecular gas in the CMZ of NGC 4593.

5.1.10 The SED

The SED of a galaxy is a useful tool for characterizing its components, allowing us to disentangle contributions from stars, dust, and AGN activity. By analyzing the SED of NGC 4593, we can better understand the galaxy's physical properties, star formation history, and the influence of its active galactic nucleus (AGN). To model the SED, we employed the Code Investigating GALaxy Emission (CIGALE; (BOQUIEN *et al.*, 2019; YANG *et al.*, 2020; YANG *et al.*, 2022)), a versatile software designed to fit observed photometric data with model templates that account for stellar, AGN, and dust emission. CIGALE's flexibility allowed us to customize model parameters to reflect NGC 4593's specific characteristics.

Table 5.1 summarizes the photometric data used as input for CIGALE, including wavelength coverage, fluxes, and associated uncertainties. To capture the star formation history (SFH), we adopted a "delayed" model, which assumes a gradual rise in the SFR followed by an exponential decline. This model also includes an optional recent burst component to simulate periods of heightened star formation, which may be linked to galaxy interactions or internal dynamical processes. This SFH is particularly suitable for galaxies like NGC 4593, which exhibit complex star formation patterns influenced by bar-driven gas inflows and AGN activity.

For the Stellar Population Synthesis (SPS), we used a Single Stellar Population (SSP) model based on (BRUZUAL; CHARLOT, 2003) with a Chabrier Initial Mass Function (IMF). This model assumes a metallicity of 0.02 and a minimum separation age of 10 Myr, which provides a realistic estimate of the stellar populations' age distribution within NGC 4593. Dust attenuation, an important factor for accurately modeling UV and optical emissions, was applied using the attenuation modules from (CALZETTI *et al.*, 2000) and (LEITHERER *et al.*, 2002). These modules account for the extinction effects of interstellar dust and the complex distribution of dust in star-forming regions. The dust emission model is based on (DALE *et al.*, 2014), incorporating various infrared (IR) templates to represent the re-emission of absorbed light at IR wavelengths.

For the AGN component, CIGALE supports a two-phase torus model (STALEVSKI *et al.*, 2016) that accounts for the AGN's dusty environment and its multi-wavelength emission. This model links the X-ray and UV/optical emissions using the $\alpha_{\rm ox}$–$L_{\nu,2500}$ relation (JUST *et al.*, 2007), with a maximum deviation $|\Delta\alpha_{\rm ox}|_{\rm max} = 0.2$ to account for

intrinsic scatter in this relationship. We assumed a face-on type-1 AGN for NGC 4593, aligning with findings from (MOUNTRICHAS *et al.*, 2021) and (CIESLA *et al.*, 2015), who analyzed similar AGNs using CIGALE. This face-on inclination is consistent with our 3D-BAROLO results, which indicate a low inclination angle for the galaxy. While certain parameters, such as the AGN's inclination angle and position angle (PA), were derived directly from our kinematic analysis, other parameters were allowed greater flexibility to ensure a robust fit to the observed photometry.

The resulting SED fit, shown in Fig. 5.10, represents the best-fitting model based on the initial parameter conditions and photometric data. The model includes specific AGN torus parameters: an outer-to-inner radius ratio ($R_{\rm out}/R_{\rm in}$) of 20, with values ranging between 10 and 30, and a half-opening angle consistent with a type-1 AGN viewing perspective. This configuration reflects the torus structure's geometry, assuming that the inner edge of the torus aligns closely with the central accretion disc. The dust density gradient in the torus was set to 1.0 for both polar angle and radial direction, which provides a realistic estimate of the dust distribution and its impact on observed IR emission.

The SED model parameters include the power-law index δ, set to -0.36 to adjust the optical slope of the AGN disc, and an edge-on optical depth of 4.37 ± 0.93 at $9.7\,\mu$m. These parameters are indicative of a prominent dusty torus structure around the AGN, in alignment with the line of sight to the bright accretion disc and central engine, confirming the type-1 classification of NGC 4593. The AGN fraction, defined as the AGN luminosity divided by the total IR luminosity, was determined to be 0.876 ± 0.052, underscoring the AGN's significant influence on the galaxy's overall spectrum. Detailed results from the CIGALE fitting procedure are provided in Table 5.3.

NGC 4593, as a late-type barred spiral (SB) galaxy hosting a type-1 AGN, exhibits a bolometric luminosity of $\log(L_{\rm bol}) = 44.163$, placing it in the high-luminosity AGN category. The AGN's contribution to the galaxy's spectrum is dominant, with a disc luminosity of $1.26 \times 10^{36}\,$erg/s and an intrinsic 2-10 keV X-ray luminosity of $L_{\nu,2\,\rm keV} = 1.11 \times 10^{18}\,$erg/s. These values support the presence of a powerful central black hole, with an estimated mass of $\log\left(\frac{M_{\rm BH}}{M_\odot}\right) = 6.86$.

Despite the AGN's high luminosity, the galaxy's SFR remains moderate. CIGALE's analysis yielded an SFR of $0.43\,M_\odot\,{\rm yr}^{-1}$ and a stellar mass of $\log({\rm M_*/M_\odot}) = 10.646$. Alternative SFR estimates from PAH11.25μm and [CII]158μm lines provided values of $0.36\,M_\odot$/year and $0.19\,M_\odot$/year, respectively. The total FIR luminosity-based SFR was higher at $1.2\,M_\odot$/year, derived from the FIR luminosity of $\log({\rm L_{FIR}}) = 43.43$ (JR, 1998; SPINOGLIO *et al.*, 1995). The specific star formation rate (sSFR) of $4.4\times10^{-11}\,{\rm yr}^{-1}$ suggests notable star formation relative to the stellar mass, potentially influenced by AGN-driven feedback mechanisms.

NGC 4593 lies on the threshold between high- and low-luminosity AGNs, with $\log_{10}(L_{\rm AGN}) \approx 44$. High-luminosity AGNs typically show a positive correlation between SFR and AGN luminosity, while low-luminosity AGNs may exhibit a weakly negative or negligible correlation (ROSARIO *et al.*, 2013). However, studies such as those by (PITCHFORD *et al.*, 2016) and (HATZIMINAOGLOU *et al.*, 2018) indicate that this correlation is complex, as some FIR-bright AGNs display signs of mergers or companion interactions, factors which can influence both SFR and AGN luminosity independently.

Our analysis places NGC 4593 within the high-luminosity AGN regime. The AGN fraction relative to the IR luminosity is 0.87, and its bolometric luminosity of over 10^{44} erg/s highlights the dominance of AGN emission in its SED. While this dominance emphasizes the AGN's significant contribution to IR emission, it does not imply a straightforward link between AGN luminosity and star formation rates. This finding suggests that although AGN activity substantially influences the IR spectrum, it may not directly drive star formation within the galaxy.

According to (ZHUANG; HO, 2023), AGNs and their host galaxies evolve along distinct trajectories on the black hole mass (M_{BH}) versus stellar mass (M_*) plane. Galaxies positioned above the M_{BH}–M_* relation tend to grow by increasing stellar mass more rapidly than black hole mass, while galaxies on the relation evolve proportionally in both parameters. NGC 4593 aligns with this "horizontal growth path," indicating that radiative-mode AGN feedback is insufficient to fully suppress star formation, while kinetic-mode feedback may also be insufficient for significant long-term quenching. The high AGN fraction and steady stellar mass growth suggest that AGN feedback does not strongly constrain star formation, allowing the galaxy to maintain moderate star formation rates despite significant AGN influence.

5.1.11 Challenges in Kinematic Modelling

Our kinematic analysis of NGC 4593 reveals several challenges in accurately modeling its gas dynamics, primarily due to the clear presence of an $m = 1$ asymmetry, or lopsided feature, within the molecular gas distribution. This asymmetry indicates a deviation from the axisymmetric structure assumed by the 3D-BAROLO modeling tool, which is optimized for galaxies with relatively symmetric, circular motions. The presence of an $m = 1$ mode suggests that variations between the northern and southern regions of the galaxy introduce complex dynamics that the model cannot adequately fit. These asymmetries may reflect underlying structural irregularities or interactions that disrupt the circular flow, resulting in non-axisymmetric motions.

A further complication arises from the close alignment between the bar's position angle (PA) and the kinematic PA, which obscures the true inclination and potentially

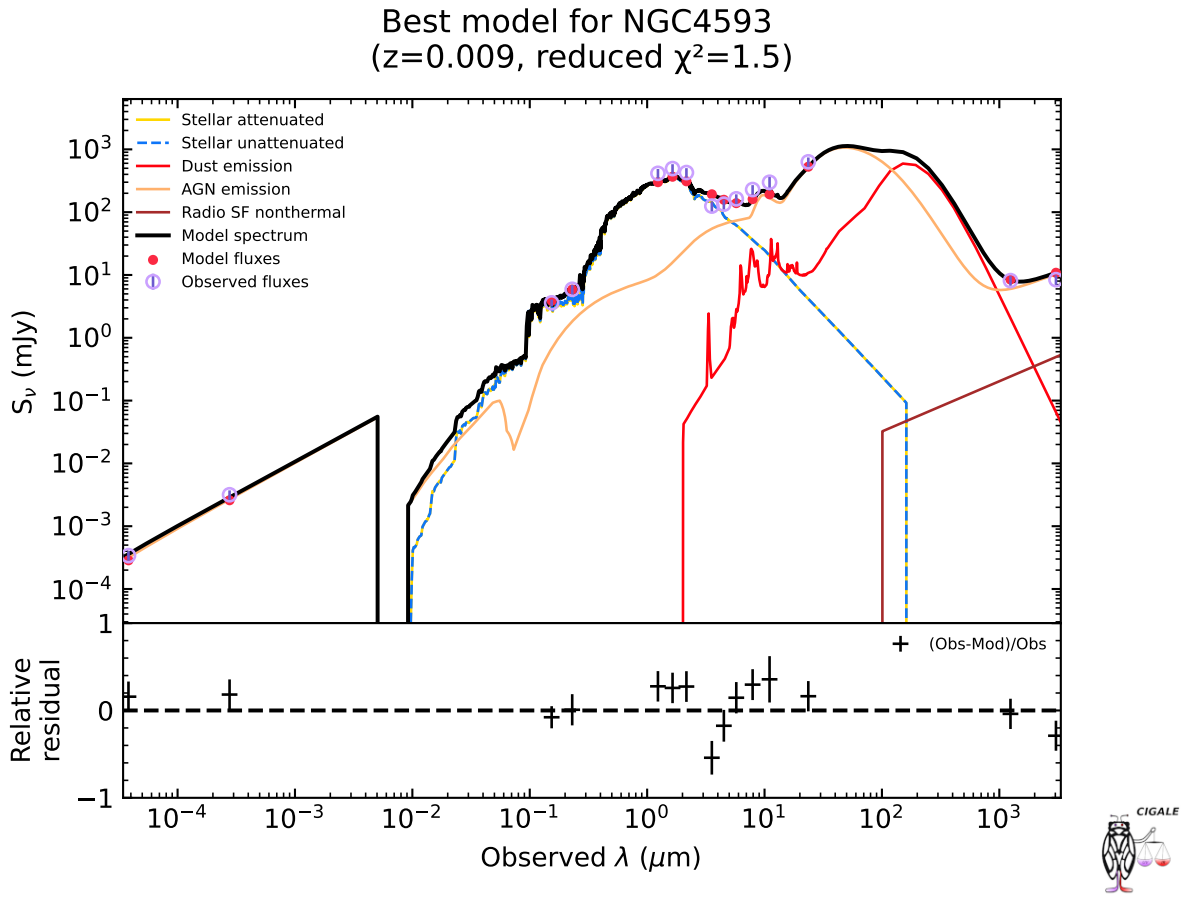

FIGURE 5.10 – SED of NGC 4593 derived using CIGALE. The plot shows the observed SED, indicated by red points, compared to the best-fit model represented by the solid black line. The constituent components of the model are illustrated as follows: dust emission (red line), AGN emission (orange line), and stellar emission, both attenuated (yellow dashed line) and unattenuated (blue dashed line). The vertical axis denotes the flux density S_ν in mJy, while the horizontal axis represents the wavelength λ in μm. This SED plot provides a comprehensive view of the various emission components contributing to the observed radiation from NGC 4593.

TABLE 5.3 – CIGALE-derived parameters for NGC 4593

Parameter	Value
$L_{\mathrm{IR,AGN}}/L_{\mathrm{IR,total}}$	0.876 ± 0.052
$\log(L_{\mathrm{AGN,torus}}\,[\mathrm{erg\,s^{-1}}])$	36.193 ± 0.049
$\log(L_{\mathrm{AGN,disc}}\,[\mathrm{erg\,s^{-1}}])$	36.096 ± 0.116
$\log(L_{\mathrm{AGN,total\,dust}}\,[\mathrm{erg\,s^{-1}}])$	36.510 ± 0.050
$\log(L_{\mathrm{AGN,6\,\mu m}}\,[\mathrm{erg\,s^{-1}}])$	35.784 ± 0.048
$\log(L_{\mathrm{AGN,accretion\,power}}\,[\mathrm{erg\,s^{-1}}])$	36.492 ± 0.047
$\log(L_{\mathrm{AGN,polar\,dust}}\,[\mathrm{erg\,s^{-1}}])$	36.224 ± 0.057
$\log(L_{\mathrm{AGN}}\,[\mathrm{erg\,s^{-1}}])$	36.651 ± 0.048
$\log(L_{\mathrm{stellar}}\,[\mathrm{erg\,s^{-1}}])$	37.402 ± 0.035
$\log(M_*/M_\odot)$	10.633 ± 0.039
$\log(M_{\mathrm{stellar\,gas}}\,[M_\odot])$	10.535 ± 0.041
$\log(\mathrm{SFR}_{\mathrm{integrated}}\,[M_\odot\,\mathrm{yr^{-1}}])$	10.888 ± 0.039
$\log(\mathrm{SFR}_{\mathrm{current}}\,[M_\odot\,\mathrm{yr^{-1}}])$	-0.367 ± 0.045
$\log(\mathrm{SFR}_{100\,\mathrm{Myr}}\,[M_\odot\,\mathrm{yr^{-1}}])$	-0.329 ± 0.042
$\log(\mathrm{SFR}_{10\,\mathrm{Myr}}\,[M_\odot\,\mathrm{yr^{-1}}])$	-0.364 ± 0.045

Notes: CIGALE-derived parameters for NGC 4593, including luminosity components of the stellar population, active galactic nucleus (AGN), accretion disc, and dust structures (polar, torus, and total). SFRs reflect the current and past 10 and 100 million-year averages. These values are estimated based on CIGALE fitting results.

introduces systematic biases. In the presence of the outer ring, which often deviates from a perfectly circular structure, the assumptions of circular orbits in 3D-Barolo may produce inaccurate inclination estimates. This misalignment affects the velocity field by failing to account for the gradual shifts in PA that are typical of elliptical orbits within barred structures. The assumption of isotropic circular motion in 3D-Barolo fails to capture the subtle velocity gradients expected in such orbits, limiting the model's ability to reproduce the observed velocity patterns. Consequently, the model's predicted radial velocities cannot reflect the actual elongated gas motions, particularly within the outer ring, as it assumes uniform circular rotation rather than the elliptical orbit shapes often associated with bar-driven flows.

An additional limitation is the reliance on the CO(2-1) line as the primary tracer of molecular gas content in NGC 4593. The CO(2-1) line is effective in tracing dense molecular gas, but it does not capture the entirety of the molecular mass. Regions with lower-density molecular gas or extended diffuse emission may be underrepresented in our data, leading to a potential underestimation of the total molecular gas mass in the galaxy. Interferometric observations, such as those conducted by ALMA, tend to filter out extended emissions, particularly those with low surface brightness on larger spatial scales. This filtering effect leads to missing flux, further suggesting that our molecular

gas mass estimates may be lower than the actual values.

The impact of missing flux is particularly evident in regions with pronounced non-circular motions, such as those influenced by the bar or spiral arms. In these areas, the distribution of molecular gas is more dispersed and less concentrated in high-density regions, leading to an underrepresentation of extended gas in the observed data. Consequently, the 3D-Barolo model's assumption of axisymmetry is unable to fully capture the spatial extent of the molecular gas distribution, omitting significant features such as the single-arm spiral pattern observed in NGC 4593. This limitation emphasizes the need for a more comprehensive modeling approach that can account for the non-axisymmetric, bar-driven gas flows that are integral to the kinematics of barred galaxies.

To overcome these limitations in future studies, employing a kinematic model that incorporates non-axisymmetric potentials could provide a more accurate representation of NGC 4593's complex gas dynamics. Methods such as bisymmetric or triaxial models can accommodate the influence of bar-driven perturbations, allowing for elongated and elliptical orbits in the analysis. Additionally, using complementary data, such as multiple CO transitions (e.g., CO(1-0) or CO(3-2)) and alternative molecular tracers, may provide a more complete picture of the molecular gas distribution. These approaches would help to capture both the dense and diffuse molecular gas components, providing a more reliable total gas mass estimate and improving the accuracy of kinematic models.

In summary, while 3D-Barolo is a robust tool for axisymmetric galaxies with circular rotation, its limitations in modeling barred galaxies with complex gas dynamics, such as NGC 4593, highlight the need for more flexible modeling approaches. The lopsided $m = 1$ feature, proximity of bar and kinematic PAs, and the influence of extended gas structures complicate the kinematic picture of NGC 4593, suggesting that a model incorporating non-axisymmetric potentials and accounting for missing flux would more accurately reflect the observed dynamics in this galaxy.

5.2 Statistical Results of the TWIST Sample

In this section, we present statistical findings from the TWIST sample, focusing on molecular gas content, black hole mass estimates, and relationships between CO and IR luminosity. This analysis applies the detailed methodology established for NGC 4593 to the broader sample, revealing trends and distinctive characteristics across various AGN types and galaxy morphologies. A complete set of CO(2-1) emission moment maps for each galaxy in the TWIST sample is provided in Appendix A.

For each galaxy in the TWIST sample, we derive the molecular hydrogen mass ($M_{\mathrm{H_2}}$) and CO(2-1) luminosities from ALMA observations, measured within both 100 pc and

3 kpc apertures. These values are summarized in Table 5.4. By comparing measurements across different apertures and instruments, this table provides a detailed view of the molecular gas distribution in nuclear and extended regions.

Molecular hydrogen masses ($M_{\mathrm{H_2}}$) were estimated using the calibration

$$M_{\mathrm{H_2}} = \alpha_{CO}\, M_{\odot}/L'_{\mathrm{CO}}\,(\mathrm{K\ km\ s^{-1}\ pc^2}) \tag{5.10}$$

from (SOLOMON; SAGE, 1988), and the conversion factor α_{CO} ranging from $0.8\,M_{\odot}$ to $3.2\,M_{\odot}$ ((BOLATTO *et al.*, 2013)). Applying this factor to ALMA data provides a consistent estimation of the molecular gas mass within nuclear (100 pc) and extended (3 kpc) regions, allowing us to assess how the gas distribution varies with AGN activity in the sample (Table 5.4).

To examine the relationships between CO luminosity, IR luminosity, and molecular gas mass, Figure 5.11 presents a series of diagnostic plots. In Figure 5.11(a), we plot total IR luminosity as a function of CO(2-1) luminosity within a 3 kpc ALMA aperture, with symbols representing galaxy morphological types based on Hubble classifications (Table 5.4). Figure 5.11(b) shows IR luminosity against molecular hydrogen mass, with color coding based on AGN activity type. Both plots feature dashed lines representing best-fit linear relationships derived from least-squares fitting:

$$\log(L_{\mathrm{IR}}/L_{\odot}) = 0.55 \times \log(L_{\mathrm{CO}}/(\mathrm{K\ km\ s^{-1}\ pc^2})) + 5.81 \tag{5.11}$$

and

$$\log(L_{\mathrm{IR}}/L_{\odot}) = 0.55 \times \log(M_{\mathrm{H_2}}/M_{\odot}) + 5.44. \tag{5.12}$$

Additionally, the trend line from (KAMENETZKY *et al.*, 2016) for FIR luminosity as a function of CO(2-1) luminosity is included for reference:

$$\log(L_{\mathrm{FIR}}) = 0.66 \times \log(L_{\mathrm{CO(2\text{-}1)}}) + 4.9. \tag{5.13}$$

This reference relationship is shown in purple in Figure 5.11(a). Our AGN-hosting sample shows a higher $L_{\mathrm{IR}}/L'_{\mathrm{CO}}$ ratio than typical star-forming galaxies, suggesting that AGN activity contributes additional energy, elevating the IR luminosity beyond levels attributable solely to star formation. This observation aligns with findings in NGC 4593, where the AGN's impact on IR luminosity is reflected in elevated $L_{\mathrm{IR}}/L_{\mathrm{CO}}$ ratios. These results underscore the role of AGN-driven processes in shaping molecular gas dynamics across the TWIST sample.

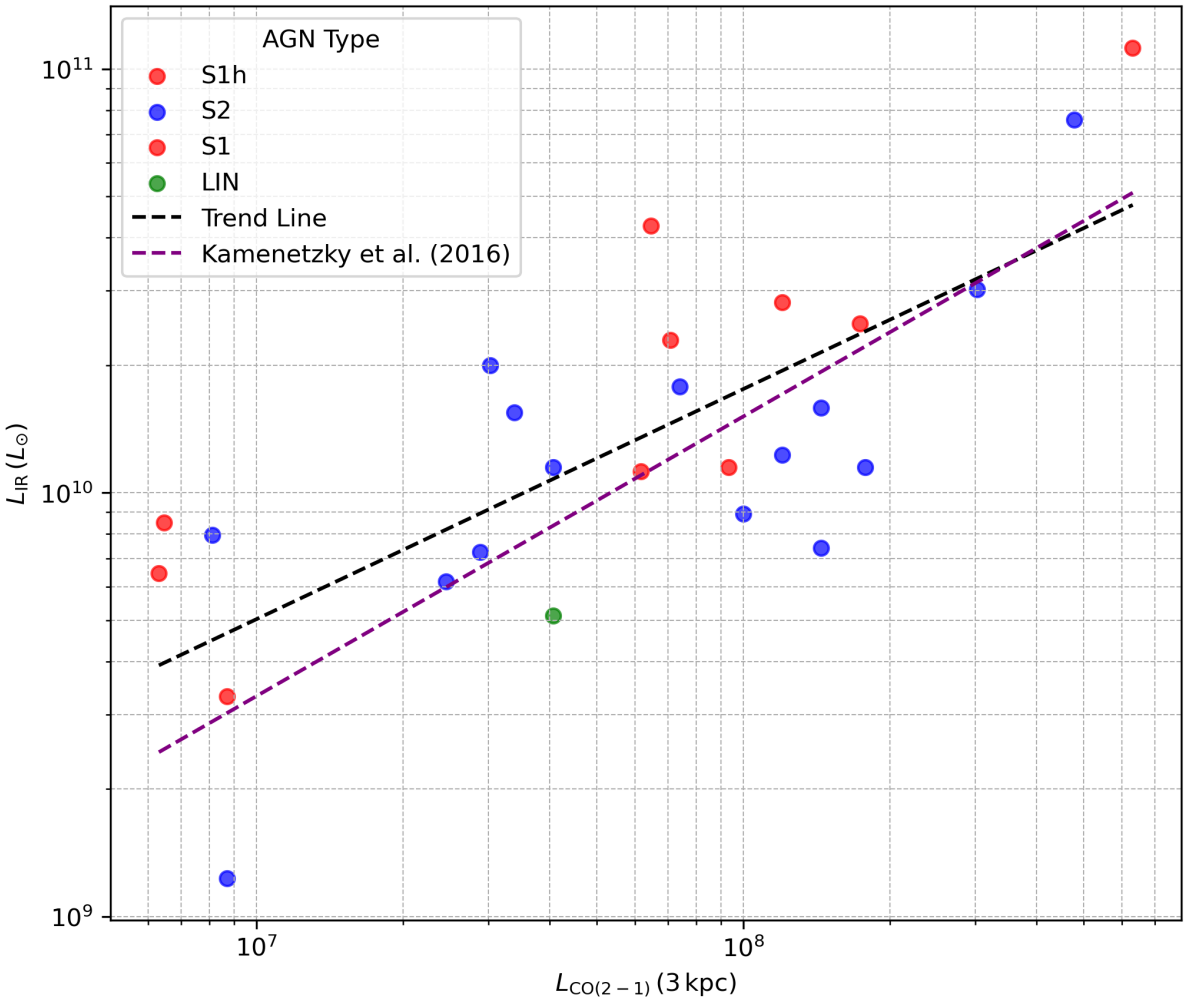

FIGURE 5.11 – Relationship between IR luminosity ($L_{\rm IR}$) and CO(2-1) luminosity ($L_{\rm CO(2-1)}$) within a 3 kpc aperture for the TWIST sample, color-coded by AGN activity type. The black dashed line indicates the best-fit relation for the sample, while the purple dashed line shows the relation from (KAMENETZKY *et al.*, 2016), with shaded bands denoting uncertainties. These results highlight the influence of AGN activity on IR luminosity, showing an elevated $L_{\rm IR}/L_{\rm CO}$ ratio in AGN-host galaxies compared to star-forming galaxies.

TABLE 5.4 – ALMA CO(2-1) mosaic observations compared to APEX observations and molecular mass estimates

NAME	$\log L_{CO(2-1),100\,pc}$ [K km s^{-1} pc^2]	$\log L_{CO(2-1),3\,kpc}$ [K km s^{-1} pc^2]	$\log L_{CO(2-1),APEX}$ [K km s^{-1} pc^2]	$\log M_{H_2,100\,pc}$ [$M_\odot$]	$\log M_{H_2,3\,kpc}$ [$M_\odot$]	$\log M_{H_2,APEX}$ [$M_\odot$]
NGC0424	6.32	6.81	7.09	6.98	7.48	8.35
NGC613	7.05	8.48	-	7.71	9.14	-
NGC1052	-	-	-	-	-	-
NGC1068	-	-	-	-	-	-
NGC1097	-	-	-	-	-	-
NGC1125	6.67	7.53	7.99	7.33	8.19	8.66
NGC1320	6.34	7.39	7.91	7.01	8.05	8.57
NGC1365	5.98	8.80	-	6.64	9.46	-
NGC1386	-	-	-	-	-	-
ESO420-G13	7.12	8.68	-	7.78	9.34	-
NGC1566	6.54	8.08	-	7.23	8.74	-
NGC2992	5.40	8.24	8.48	6.06	8.90	9.14
NGC3169	-	-	-	-	-	-
NGC3627	-	-	-	-	-	-
NGC3976	5.25	6.91	-	5.92	7.57	-
NGC4303	-	-	-	-	-	-
NGC4374	-	-	-	-	-	-
NGC4412	6.91	7.46	-	7.58	8.13	-
NGC4418	-	-	-	-	-	-
NGC4486	-	-	-	-	-	-
NGC4501	-	-	-	-	-	-
NGC4593	6.37	7.97	-	7.04	8.63	-
NGC4594	-	-	-	-	-	-
IC3639	7.18	7.81	8.55	7.85	8.47	9.21
Mrk1333	6.80	8.25	-	7.47	8.91	-
NGC4845	6.48	8.16	-	7.15	8.82	-
NGC4941	5.73	6.94	-	6.39	7.60	-
NGC4968	6.16	8.00	-	6.82	8.60	-
M-06-30-15	5.94	6.94	-	6.62	7.60	-
NGC5506	6.60	7.79	8.00	7.26	8.45	8.66
NGC5806	-	-	-	-	-	-
NGC5861	7.15	7.87	-	7.82	8.53	-
NGC6890	6.75	7.61	8.38	7.41	8.27	9.05
IC5063	6.03	7.85	8.18	6.69	8.51	8.84
NGC7172	-	-	-	-	-	-
NGC7213	4.51	7.61	8.09	5.18	8.27	8.75
IC5169	6.90	8.16	-	7.57	8.82	-
NGC7314	6.03	6.80	-	6.69	7.46	-
NGC7496	7.20	8.08	8.21	7.86	8.74	8.87
NGC7582	-	-	-	-	-	-
NGC7590	5.39	7.48	-	6.06	8.14	-

Notes: This table presents from the left to right. for each galaxy of the sample: NAME, CO(2-1) luminosity in 100pc, 3kpc and single dish APEX. H_2 mass in 100pc, 3kpc and single dish APEX

5.2.1 3D-Barolo Kinematic Modeling Results

To analyze the molecular gas dynamics across the TWIST sample, we applied 3D-Barolo kinematic modeling to the CO(2-1) data for each galaxy. This modeling allowed us to extract key parameters, including rotation velocity, velocity dispersion, and inclination, for the cold molecular gas in the central regions. The 3D-Barolo results provide information into the velocity structure and reveal deviations from circular rotation in some cases, indicating potential non-circular motions influenced by bars, interactions, or AGN-driven processes.

Our 3D-Barolo modeling yielded moment maps for each galaxy, displaying the observed CO velocity fields, the modeled kinematic structures (representing idealized rotating disks), and the residuals (the difference between observed velocity fields and the idealized disk model). These maps are provided in Appendix A and Table A.5, where each galaxy's velocity field, intensity distribution, and residual maps are detailed. For many galaxies in the sample, the residual maps show deviations from the idealized disk model predictions, often highlighting regions with enhanced velocity dispersion or irreg-

ular velocity structures. These residuals can indicate localized non-circular motions that potentially correspond to outflows or inflows in the molecular gas.

5.2.1.1 AGN Host Galaxies with Observed Outflows

For several AGN host galaxies within the TWIST sample, strong non-circular motions detected in the residuals suggest the presence of molecular gas outflows. **ESO 420-G13**, for example, exhibits a prominent molecular gas outflow along its minor axis, extending 340–600 pc from the nucleus. The molecular gas mass in this galaxy is estimated at $13.07 \pm 0.02 \times 10^8\, M_\odot$ when using a LIRG/ULIRG $\alpha_{\rm CO}$ factor, and $1.45 \pm 0.04 \times 10^7\, M_\odot$ with a Milky Way $\alpha_{\rm CO}$ factor. This outflow, likely AGN-driven, has a mass of approximately $8 \times 10^6\, M_\odot$ and a projected velocity of 160 km/s, suggesting an outflow rate of $14\, M_\odot$/yr. Radiation pressure, star formation, and supernovae appear insufficient to drive such an outflow, indicating AGN jet activity as the likely mechanism (FERNÁNDEZ-ONTIVEROS *et al.*, 2020).

While applying 3D-BAROLO modeling across the TWIST sample, it became evident that not all galaxies could be successfully analyzed. Limitations in observational data, such as low signal-to-noise ratios, incomplete coverage, or archival data resolution, constrained modeling for some objects. Additionally, the 3D-BAROLO framework introduces biases in cases of complex velocity fields or low inclinations, further complicating the analysis. As a result, we focus here on a subset of galaxies for which robust kinematic models and meaningful residuals could be derived, enabling detailed investigations into molecular gas dynamics and AGN-driven processes.

NGC 2992 ((Figure B.4)) shows pronounced AGN-driven feedback with a Seyfert type that varies between Seyfert 1.9 and Seyfert 2, attributed to a fluctuating ionizing continuum. X-ray data highlight intense AGN activity with a broad Fe Kα line around $\sim 5 - 7$ keV (SHU *et al.*, 2010). A blueshifted outflow, with a mass rate of $\sim 2\, M_\odot\, {\rm yr}^{-1}$ and kinematic power of $\sim 2 \times 10^{40}$ erg s^{-1}, extends from the nucleus, reshaping the ISM (GUOLO-PEREIRA *et al.*, 2021). Observations by (ZANCHETTIN *et al.*, 2023) reveal a multiphase structure in the outflow, with an ultrafast component reaching $0.4c$ and a kpc-scale ionized wind, driven primarily by AGN feedback.

Regarding our results, it is worth noting that (ZANCHETTIN *et al.*, 2023) also utilized the same ALMA dataset in their study but processed it using a different data cube and analysis approach. While they measured an integrated $S_{\rm CO}$ flux density of 132.54 ± 0.03 Jy km s^{-1}, our reanalysis, which involved refined masking and re-building of the ALMA image, yielded a significantly higher flux density of 230 Jy km s^{-1}. This discrepancy is likely due to differences in the applied masking techniques and assumptions during data reduction. Additionally, the full-width at half-maximum (FWHM) velocity

range in our work was determined to be $-240.17\,\mathrm{km\ s^{-1}}$ to $250.17\,\mathrm{km\ s^{-1}}$, corresponding to a total width of $490.34\,\mathrm{km\ s^{-1}}$, which is slightly broader than the $470 \pm 10\,\mathrm{km\ s^{-1}}$ reported in their study.

For the molecular outflow regions, we estimate the molecular gas mass using a conversion factor of $\alpha_{\mathrm{CO}} = 3.82\,M_{\odot}\,(\mathrm{K\ km\ s^{-1}\,pc^2})^{-1}$, to be $4.34 \times 10^7\,M_{\odot}$, closely aligning with their result of $4.1 \times 10^7\,M_{\odot}$ derived from the same observation, but diverging slightly from $4.3 \times 10^7\,M_{\odot}$ obtained from an alternative observation. For the total molecular outflow mass across the two regions, our analysis yields $1.03 \times 10^7\,M_{\odot}$ and $5.99 \times 10^6\,M_{\odot}$, higher than their reported values. These results confirm the presence of molecular outflows at both edges of the galaxy, as identified through 3D-Barolo modeling. The residual maps derived from 3D-Barolo support this conclusion, highlighting non-circular motions consistent with AGN-driven feedback in NGC 2992 (see Appendix C.12 for detailed residual maps and kinematic analysis).

In **NGC 1566** (Figure B.3), a molecular outflow has been identified with an outflow rate of approximately $5.6\,M_{\odot}\,\mathrm{yr^{-1}}$, driven by AGN activity as observed through CO (J=2-1) ALMA data and Gemini-GMOS IFU observations of ionized gas kinematics (Slater *et al.*, 2019). This outflow decelerates from a velocity of $180\,\mathrm{km\ s^{-1}}$ near the nucleus to a near stop at approximately 72 pc. The outflow encompasses both ionized and molecular gas, where the ionized component exhibits a more spherical morphology compared to the disk-aligned molecular outflow. Additionally, streaming inflows have been observed along nuclear spiral arms at about $50\,\mathrm{km\ s^{-1}}$, indicating gas inflow that may contribute to feeding the central AGN.

NGC 5506 (Figure B.19) is an optically obscured Narrow-Line Seyfert 1 (NLSy1) galaxy, notable for hosting both a type 1 AGN and a nuclear water vapor megamaser, suggesting complex AGN-driven feedback (Nagar *et al.*, 2002). X-ray data show flux and spectral variability, with absorption by a column density of $3 \times 10^{22}\,\mathrm{cm^{-2}}$, and a soft excess requiring both photo-ionized and collisionally ionized models (Sun *et al.*, 2018; Soldi *et al.*, 2011). The high black hole spin (0.93 ± 0.04) and strong outflow features indicate that a powerful AGN jet likely drives feedback processes, impacting the surrounding ISM. In the Seyfert galaxy **NGC 5506**, recent observations using ALMA and MEGARA have uncovered a multiphase outflow driven by AGN activity, affecting both molecular and ionized gas phases. The cold molecular gas, traced by CO(3-2), forms a rotating disc within the central 1.2 kpc, but also displays non-circular motions associated with an outflow. This outflow has a molecular mass outflow rate of approximately $8\,M_{\odot}\,\mathrm{yr^{-1}}$ and extends up to 350 pc from the AGN. Ionized gas, indicated by [OIII] emission with velocities up to 1000 km/s, confirms the AGN-driven origin of the outflow and underscores the feedback's impact on the surrounding gas dynamics. With a bolometric luminosity of $\sim 10^{44}\,\mathrm{erg\ s^{-1}}$, these findings highlight the AGN's role in influencing the interstellar

medium on kiloparsec scales ((ESPOSITO *et al.*, 2024)).

NGC 613 (Figure B.11) shows a significant molecular outflow in its nuclear region, likely AGN-driven, as observed in ALMA Cycles 3 and 4 data (AUDIBERT *et al.*, 2019a). A 2-arm trailing nuclear spiral within $r \lesssim 100$ pc channels gas inward, while broad CO(3-2) wings reveal an outflow with velocities up to $\pm 300\,\mathrm{km\ s^{-1}}$, carrying an estimated $2 \times 10^6\,M_\odot$ at a rate of $27\,M_\odot\,\mathrm{yr}^{-1}$. The high kinetic power, at about 20% of the AGN luminosity, suggests an earlier stronger AGN phase may have boosted this outflow. Thus, NGC 613 exemplifies dynamic AGN feedback, where inflows and outflows self-regulate central gas accretion.

In **NGC 4593**, we estimate the molecular gas outflow rate ($\dot{M}_{\mathrm{out}}$) to be between 1.32 and $8.82\,M_\odot\,\mathrm{yr}^{-1}$. This outflow, located approximately $2''$ or 340 pc from the nucleus, contains a molecular gas mass between 0.5 and $2.5 \times 10^7\,M_\odot$ and has an outflow velocity ranging from 90 to 120 km/s (Kianfar, K. *et al.*, 2024). The AGN-driven outflow in NGC 4593 demonstrates significant feedback effects, expelling molecular gas at a substantial rate and likely impacting the star-forming material available in the central regions of the galaxy.

NGC 4968 also shows non-circular motions in the central 1 kpc region, with residual velocities reaching up to 115 km/s. A bisymmetric model best fits the observed kinematics, suggesting that the residuals stem from a bar structure in the nuclear region. This galaxy's molecular gas mass is estimated to range between $3 - 12 \times 10^7\,M_\odot$, based on a CO-to-$H_2$ conversion factor spanning 0.8 to 3.2 (BELETE *et al.*, 2021).

Based on the findings in (SORMANI *et al.*, 2023) regarding **NGC 1097**, this barred spiral galaxy exhibits a significant bar-driven inflow rate that sustains its nuclear ring and influences its star formation activity. The estimated mass inflow rate toward the nuclear ring is approximately $\dot{M}_{\mathrm{inflow}} = 3.0 \pm 2.1\,M_\odot\,\mathrm{yr}^{-1}$. This inflow primarily supports a nuclear SFR of about $1.8 - 2\,M_\odot\,\mathrm{yr}^{-1}$, suggesting that the inflow rate provides the necessary material for ongoing star formation within the nuclear ring.

In **NGC 1365**, the molecular gas outflow rate ($\dot{M}_{\mathrm{out}}$) is calculated to be approximately $35^{+16}_{-8}\,M_\odot\,\mathrm{yr}^{-1}$, with a molecular gas outflow mass ($M_{\mathrm{Mol,\ outflow}}$) of $1.37 \times 10^8\,M_\odot$. The outflow radius ($R_{\mathrm{out}}$) is estimated at about 598 pc, with an outflow velocity (V_{out}) of $73^{+35}_{-17}\,\mathrm{km\,s^{-1}}$ (GAO *et al.*, 2021). This AGN-driven outflow further exerts a momentum flux rate ($\dot{P}_{\mathrm{out}} \approx 2.1 \times 10^{34}\,\mathrm{g\ cm\ s^{-2}}$), which is a significant feedback mechanism impacting the galaxy's interstellar medium.

5.2.1.2 AGN Host Galaxies without Observed Outflows

In contrast, some AGN host galaxies in the TWIST sample display little evidence of molecular gas outflows in their kinematic structures. For these galaxies, 3D-Barolo residuals indicate primarily circular motions or mild streaming motions aligned with bar structures, without the high-velocity residuals typically associated with AGN-driven outflows. These galaxies may still exhibit AGN feedback, but it appears to be insufficient to drive large-scale molecular gas outflows observable in the CO(2-1) emission.

For instance, **NGC 4845** displays mostly circular motions in its molecular gas kinematics, with only minor non-circular motions observed in the residual maps. A bisymmetric model best fits this galaxy, suggesting a bar-driven mechanism for the observed kinematics. The estimated molecular gas mass in NGC 4845 ranges between $9 - 36 \times 10^7\,M_\odot$ (Belete *et al.*, 2021).

For **MCG-06-30-15**, the kinematics are also dominated by circular motions in the central 1 kpc region, with only minimal residuals observed. The molecular gas mass is estimated between $1 - 4 \times 10^7\,M_\odot$ (Belete *et al.*, 2021). Neither NGC 4845 nor MCG-06-30-15 shows significant outflow components, with gas dynamics being consistent with circular or bar-driven motions, suggesting quiescent gas dynamics without observable AGN-driven feedback.

Overall, 3D-Barolo modeling across the TWIST sample reveals a range of kinematic behaviors, from clear AGN-driven outflows to bar-driven inflows and relatively quiescent gas dynamics. These findings emphasize the diversity of AGN-hosting galaxies, illustrating how varying AGN and bar dynamics influence the molecular gas distribution and kinematics. Appendix A includes the complete collection of residual and moment maps, which provide a basis for comparing the molecular gas dynamics and AGN feedback mechanisms across the TWIST sample.

5.2.2 SED Analysis of the TWIST Sample

To gain comprehensive details into the star formation activity, dust properties, and AGN contributions in the TWIST sample, we performed SED analysis for each galaxy. As with NGC 4593, we utilized the Code Investigating GALaxy Emission (CIGALE; (Boquien *et al.*, 2019)) to model the SEDs based on multi-wavelength photometry data. These data span a broad spectral range, enabling us to effectively disentangle emissions from stellar populations, interstellar dust, and AGN activity in each galaxy.

The photometry data used for the SED fitting are summarized in Tables A.1–A.3 in Appendix A, where detailed measurements across UV, optical, and IR bands are provided for each galaxy. These photometric measurements serve as inputs for CIGALE, allowing

us to maintain consistency in the modeling process across the sample. In this analysis, we applied the same SED modeling approach established for NGC 4593, using a delayed star formation history (SFH) with optional recent bursts, as well as modules for stellar population synthesis, dust attenuation, and AGN emission, as outlined in the previous section about NGC 4593's SED.

The resulting SED plots for a subset of the galaxies in our are available in Appendix A, providing a visual representation of the best-fitting model components, including stellar emission, dust re-emission, and AGN contribution. The reason that we could not get all of the sample was that we did not have all photometry data for all galaxies for our purpose. These plots offer a detailed view of how each component contributes to the overall emission spectrum of each galaxy, facilitating comparisons within the TWIST sample.

Figure 5.12 illustrates the relationship between the SFR and stellar mass (M_*) for AGN host galaxies within the sample, analyzed according to their Hubble classifications and AGN types. This figure serves as a comparative benchmark, showing how TWIST sample galaxies align with the $z = 0$ main sequence of star formation (Elbaz et al. 2011), and thus explains thoroughly the distinctiveness of star formation and AGN activity in different morphological and AGN classes.

For quantitative parameters, Tables A.6–A.10 in Appendix A summarizes the derived physical quantities for each galaxy, including total IR luminosity ($L_{\rm IR}$), AGN luminosity, AGN fraction, stellar mass (M_*), SFR, and dust parameters. By examining these quantities, we gain an understanding of how star formation and AGN activities vary across the sample and how these factors correlate with molecular gas dynamics and galaxy morphology.

5.2.3 Exploratory Data Analysis

To lay the foundation for this study, we performed an exploratory data analysis (EDA) to evaluate and consolidate the available datasets. This step was crucial in understanding the structure, quality, and limitations of the data before delving into detailed modeling and analysis. The data for this project were gathered from multiple sources, including archival data from the NASA/IPAC Extragalactic Database (NED) and observational data obtained through the ALMA. Additionally, during this study, new physical parameters were derived through modeling techniques such as 3D-Barolo for kinematic analysis and SED fitting using CIGALE. These newly derived parameters were integrated with existing data to provide a comprehensive view of the TWIST sample.

Before creating any pair plots, we performed a comprehensive feature engineering step to address strong inter-correlations among numerous parameters. Specifically, we applied

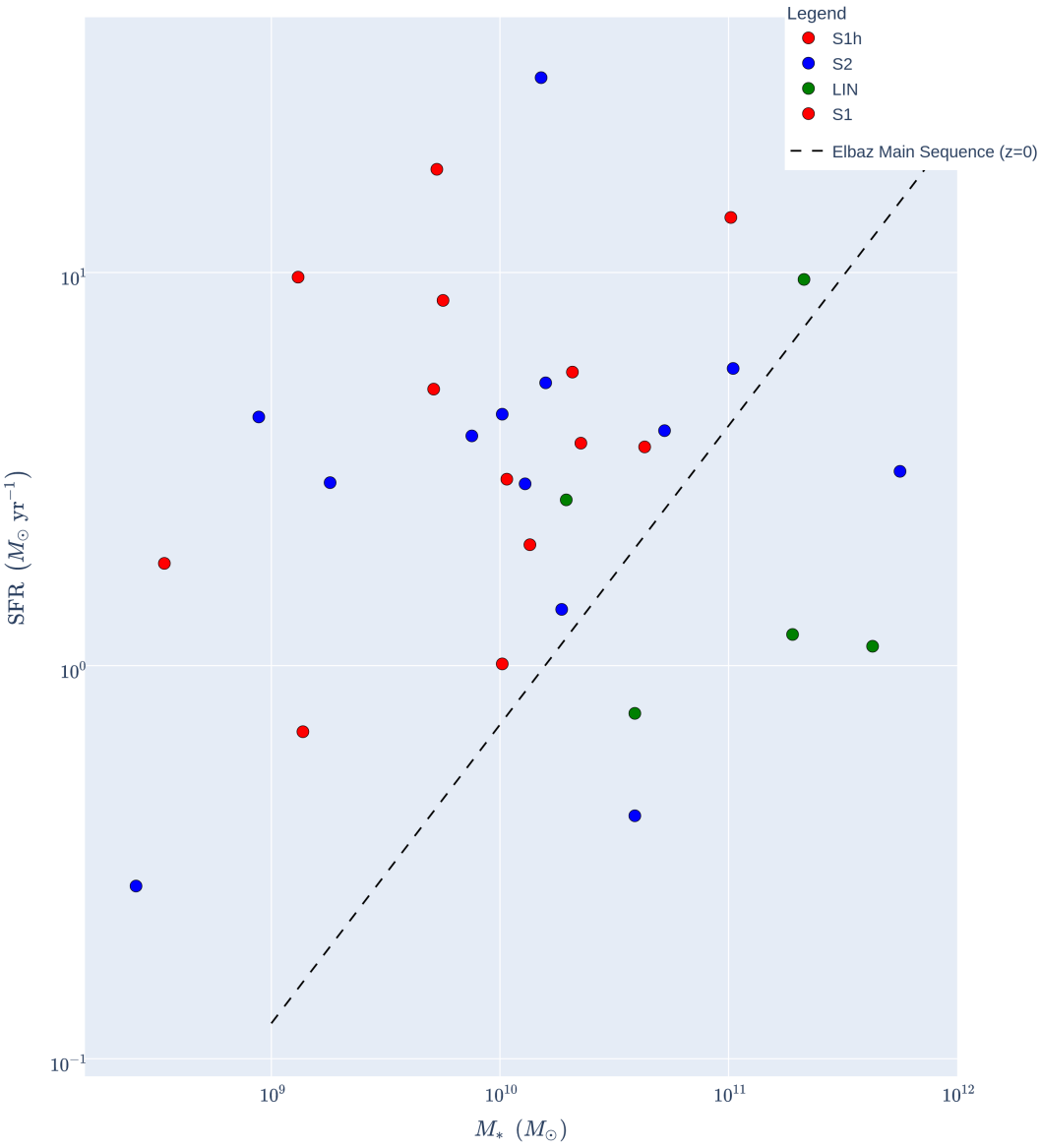

FIGURE 5.12 – The figure shows the relationship between the SFR and stellar mass (M_*) for a sample of AGN host galaxies, color-coded by AGN type. The dashed black line denotes the main-sequence relation at $z = 0$ from the (ELBAZ *et al.*, 2011) study, representing the typical SFR-M_* relation for star-forming galaxies. For galaxies where we performed SED fitting using CIGALE, the SFR and M_* values are updated with our results, while values for other galaxies are adopted from (MORDINI *et al.*, 2021) (SFR) and (SCHOMBERT *et al.*, 2019) (M_*). This figure highlights how AGN host galaxies populate the SFR-M_* plane relative to the main sequence, showcasing a variety of AGN activity levels.

the Pearson correlation coefficient to generate a heatmap of all numerical variables, as illustrated in Figure 5.13. Creating a heatmap at this stage serves a practical purpose: with numerous variables in the dataset, it can be difficult to spot strong correlations and potential redundancy simply by inspecting raw numbers. The visual layout of a heatmap makes it easier to identify pairs (or clusters) of features that convey overlapping information, which in turn helps refine our hypotheses and streamline further analysis. By focusing on the variables that exhibit significant correlations, we can avoid excessive complexity in our models and reduce potential multicollinearity issues. This targeted approach not only enhances interpretability but also lays a more robust groundwork for subsequent modeling efforts. Through this analysis, we discovered multiple instances of overlapping or redundant information, leading us to reduce the dimensionality of our dataset for improved interpretability. For example, certain outflow mass parameters showed particularly strong correlations with star-formation rates, emphasizing the importance of minimizing multicollinearity in subsequent modeling. By focusing on the most salient variables, we were able to streamline the data and set the stage for more nuanced explorations in the later sections of this thesis.

At the outset of the project, we followed the traditional data analysis pipeline: data gathering, cleaning, aggregation, modeling, and visualization. This approach ensured that the dataset was prepared systematically, addressing issues such as missing values, inconsistent measurements, and potential biases. The EDA stage was particularly instrumental in identifying patterns, correlations, and anomalies within the data, as well as highlighting areas where additional observations or corrections might be necessary.

Despite our efforts, several challenges arose due to incomplete data. For example, the lack of sufficient photometric data points for some galaxies prevented the complete SED fitting for the entire sample using CIGALE. Similarly, due to limited coverage and resolution constraints, 3D-Barolo kinematic modeling could not be performed for all galaxies in the TWIST sample. Another issue encountered was missing flux in the ALMA data, a common challenge when working with interferometric observations. This flux loss, inherent to observations with large arrays such as ALMA, can impact the accuracy of derived molecular gas masses and outflow rates. These limitations underscore the need for additional observations to improve the completeness and reliability of the dataset.

In this appendix (Figure G), we present the results of the EDA in detail, including the distribution of key parameters, correlations among variables, and potential outliers or anomalies within the sample. Figure 5.13 provides a heatmap visualization of the correlations between key parameters, offering clarity into the overall structure of the dataset. Such visualizations help to identify regions where data is sparse, highlighting areas that require further observations or modeling efforts. Moreover, they enable the detection of possible anomalies and outliers that may warrant closer investigation.

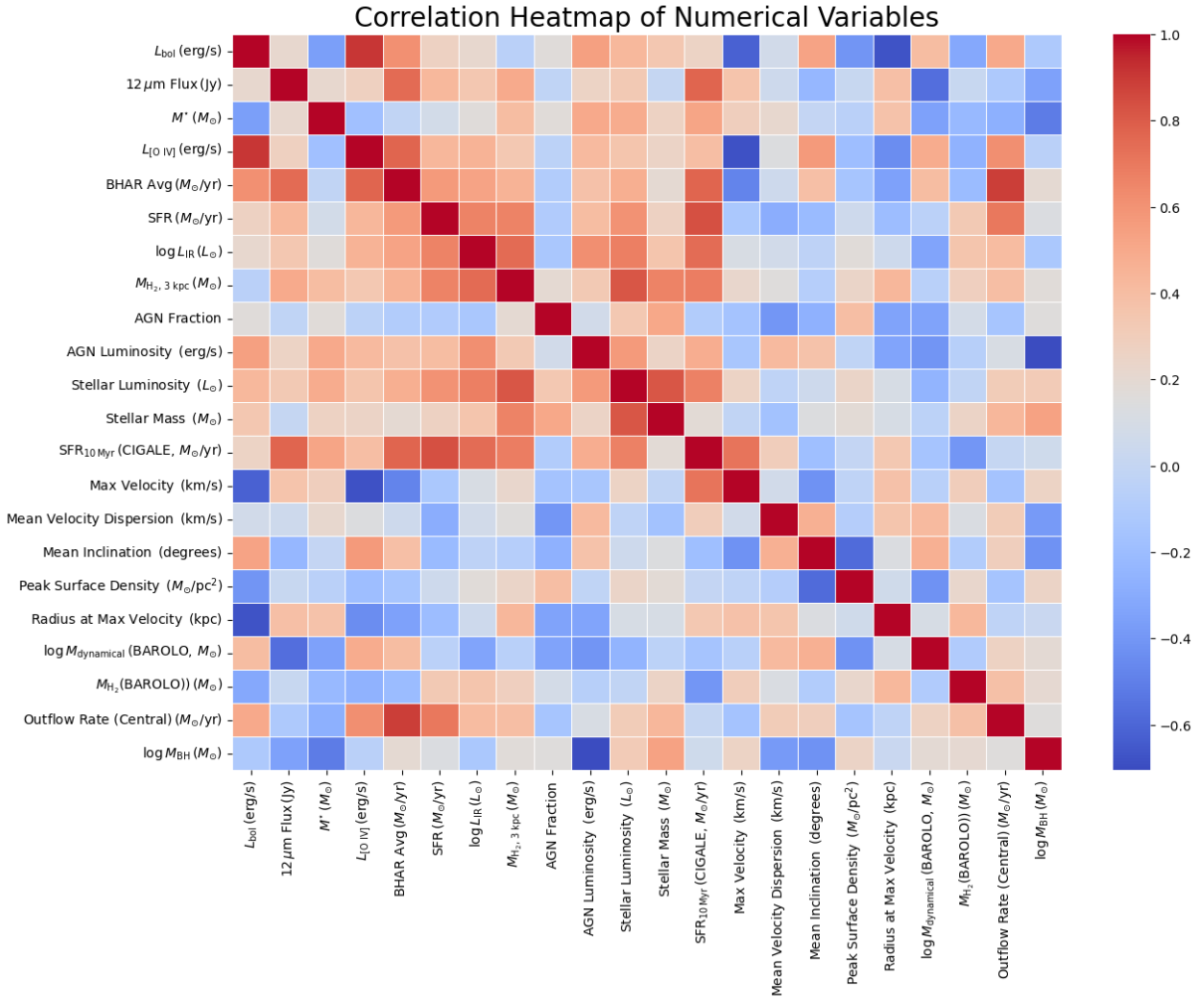

FIGURE 5.13 – Heatmap illustrating the Pearson correlation coefficients among key parameters in the TWIST sample. Lighter shades denote strong positive correlations (values closer to +1), while darker shades represent strong negative correlations (values closer to -1). This visualization not only reveals potential redundancies or overlaps in information among parameters but also highlights regions of sparse data or anomalies. Identifying these correlations early on helps streamline subsequent modeling by reducing multicollinearity and focusing on the most salient features.

While this analysis brings new information into the dataset, it is important to emphasize that this is not a complete data analysis. The identified gaps in photometric coverage and ALMA observations leave room for further work. Nevertheless, the EDA represents an essential step in understanding the TWIST sample holistically, guiding the subsequent steps in data modeling and interpretation.

In summary, the EDA highlights the strengths and limitations of the dataset, providing a clear pathway for refining the data and addressing gaps in future work. The appendix serves as a detailed repository of this initial analysis, offering transparency and a foundation for the subsequent investigations discussed in this thesis.

5.2.3.1 Outflow mass rate calculation

The calculation of mass outflow rates ($\dot{M}_{\rm out}$) provides a quantitative measure of the impact AGN-driven winds can have on their host galaxies by regulating star formation and redistributing the ISM. Following the approach of (MAIOLINO *et al.*, 2012), we define:

$$\dot{M}_{\rm out} = \frac{v_{\rm out}\, M_{\rm gas}}{R_{\rm out}}, \tag{5.14}$$

where $v_{\rm out}$ is the outflow velocity, $M_{\rm gas}$ is the mass of the outflowing gas, and $R_{\rm out}$ is the maximum radial extent of the outflow. This formula assumes a steady-state flow with a roughly uniform gas density across the outflow.

5.2.3.1.1 Extracting $v_{\rm out}$ and $R_{\rm out}$. A common strategy to identify outflow kinematics from an ALMA CO data cube is to compare two different fits to the galaxy's line-of-sight velocity field (SABATINI *et al.*, 2018; SLATER *et al.*, 2019). In the first fit, we assume *pure rotation*, described by ((KRAJNOVIC *et al.*, 2006)):

$$v_{\rm los}(R,\theta) \;=\; v_{\rm sys} \;+\; v_{\rm rot}(R)\,\sin(i)\,\cos(\theta), \tag{5.15}$$

where $v_{\rm sys}$ is the systemic velocity, $v_{\rm rot}(R)$ is the rotation curve as a function of radius R, i is the inclination of the disk, and θ is the azimuthal angle in the plane of the disk. Subtracting this rotation-only model from the observed data cube yields a *residual* velocity field that can highlight non-circular motions, including possible inflows or outflows.

Next, we include a *radial* velocity component:

$$v_{\rm los}(R,\theta) \;=\; v_{\rm sys} \;+\; v_{\rm rot}(R)\,\sin(i)\,\cos(\theta) \;+\; v_{\rm rad}(R)\,\sin(i)\,\sin(\theta). \tag{5.16}$$

Here, $v_{\rm rad}(R) > 0$ indicates radial expansion (outflow) in the disk plane, whereas $v_{\rm rad}(R) < 0$ corresponds to inflow. If introducing $v_{\rm rad}(R) \neq 0$ substantially improves the fit, we

interpret that as direct evidence of outflowing (or inflowing) gas.

Under this scheme, the local outflow velocity at radius R can be defined as

$$v_{\rm out}(R) = v_{\rm rad}(R) \quad \text{for } v_{\rm rad}(R) > 0.$$

Here, "local" indicates that the outflow velocity is determined at each individual radial position within the galaxy. In other words, at every radius R, if the radial velocity $v_{\rm rad}(R)$ is positive (i.e., the gas is moving outward), then this value is taken as the local outflow velocity $v_{\rm out}(R)$; regions where $v_{\rm rad}(R)$ is zero or negative (implying no outflow or inflow) are excluded from this measurement. A single characteristic outflow velocity is then taken as either the maximum or a flux-weighted mean of $v_{\rm out}(R)$ across the region with detected outflow signatures. Likewise, the outflow radius is given by:

$$R_{\rm out} \equiv \text{ the largest radius for which } v_{\rm rad}(R) > 0. \tag{5.17}$$

We adopt this approach—implemented via 3D-Barolo (see 5.2.1 —to measure $v_{\rm out}$ and $R_{\rm out}$ for each galaxy in our TWIST sample. Comparing the residual velocity fields and channel maps between these two fits (*pure rotation* vs. *rotation + radial*) helps us robustly identify the presence of outflowing gas.

5.2.3.1.2 Important Points in $v_{\rm rot}(R)$ and $v_{\rm rad}(R)$. When modeling a galaxy using a tilted-ring approach, it is not uncommon to see critical abrupt transitions or discontinuities in the derived rotation curve, $v_{\rm rot}(R)$, or radial velocity curve, $v_{\rm rad}(R)$. These can arise if the gas kinematics are altered by bars, rings, or warps in the disk, producing abrupt changes in the best-fit parameters between consecutive rings. Non-axisymmetric structures such as bars may drive inflows (negative $v_{\rm rad}$) at certain radii and outflows (positive $v_{\rm rad}$) elsewhere, causing a sign change in $v_{\rm rad}(R)$. In some AGN host galaxies, inflow can dominate in the central region, while an outflow becomes significant at larger radii. Inclination or position-angle changes can also manifest as discontinuities if the disk is warped. In practice, inspecting residual maps, channel maps, and moment maps helps confirm whether these "critical points" reflect genuine physical features or simply modeling artifacts.

5.2.4 Outflow mass rate vs other parameters

To examine how AGN power correlates with the strength of the outflow, we plot the mass outflow rate, $\dot{M}_{\rm out}$, as a function of AGN luminosity, $L_{\rm AGN}$, in Figure 5.14. Our findings suggest that more luminous AGNs tend to drive higher outflow rates, in agreement with scenarios in which powerful AGN episodes can eject or heat the central

gas, reducing the fuel supply for star formation. This feedback can thus contribute to regulating both star formation and black hole growth over cosmic time.

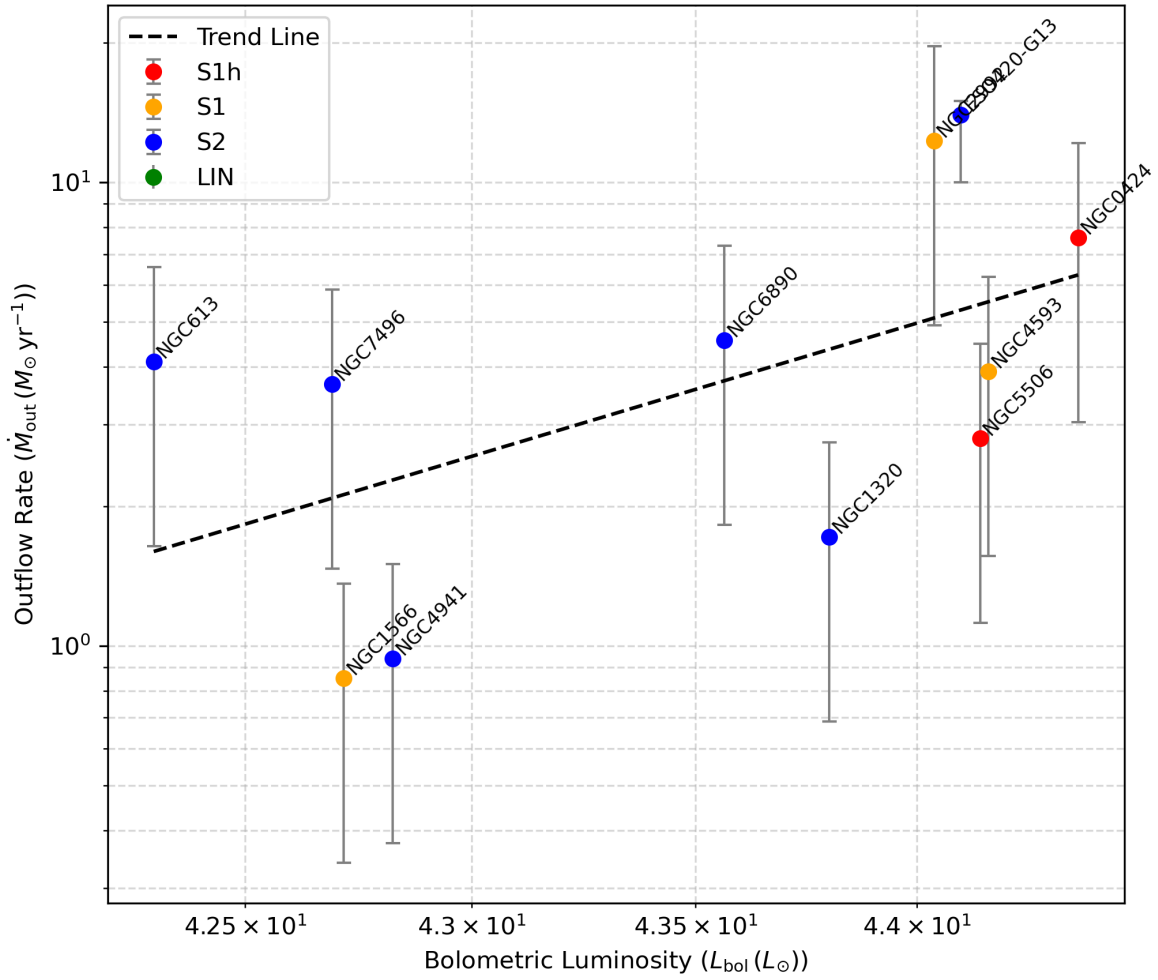

FIGURE 5.14 – Mass outflow rate ($\dot{M}_{\rm out}$) as a function of AGN luminosity ($L_{\rm bol}$) for the TWIST sample (see Table. 3.1) . Each data point represents a galaxy, with colors indicating AGN types. The dashed line shows the best-fit trend, suggesting that galaxies with more luminous AGNs tend to have higher outflow rates, indicative of stronger feedback processes.

Expanding on this analysis (see Appendix G), explores the outflow mass rate as a function of a broad set of parameters. In addition to bolometric luminosity, distance, star formation rate, stellar mass, and the mean velocity dispersion derived from BAROLO, the analysis now incorporates parameters obtained from CIGALE (namely, the active galactic nucleus fraction, active galactic nucleus accretion power, and active galactic nucleus luminosity) as well as the average black hole accretion rate. The results indicate that the outflow mass rate increases with increasing [O IV] luminosity and molecular gas mass. Regarding the average black hole accretion rate, the outflow mass rate rises when the logarithm of the black hole mass is around 6, remains approximately constant until a logarithm of 7, and then decreases. In terms of star formation rate, the outflow mass rate is nearly independent and constant for galaxies with low star formation rates (with log-

arithmic star formation rates below –0.2) and begins to increase for galaxies with higher star formation rates (approaching a logarithmic value of 0). These results stand in contrast to previous predictions by (STORCHI-BERGMANN; SCHNORR-MÜLLER, 2019b), who estimated the ratio of inflow rate to black hole accretion rate to be between 0.1 and 10; in our analysis, the ratio of outflow mass rate to black hole accretion rate is considerably higher, averaging between about 3 and 500.

Cap5 Additionally, the position of a galaxy relative to the star formation main sequence provides further context for understanding the impact of AGN-driven outflows. Galaxies with high $\dot{M}_{\rm out}$ that fall below the main sequence are likely experiencing suppressed star formation due to AGN feedback, while those closer to the main sequence typically show lower outflow rates, indicating less disruptive feedback. This raises questions about whether AGN activity alone is sufficient to move galaxies off the main sequence or whether other processes, such as mergers or environmental interactions, also contribute.

A case study of NGC 4593 further illustrates the effects of AGN-driven outflows. In this galaxy, the molecular gas outflow rate ($\dot{M}_{\rm out}$) is estimated to be between 1.32 and 8.82 $M_\odot\,{\rm yr}^{-1}$, with an outflow velocity of 90 to 120 km/s (Kianfar, K. *et al.*, 2024). Located approximately 2″ (or 340 pc) from the nucleus, this outflow expels a molecular gas mass of 0.5 to 2.5 $\times\,10^7\,M_\odot$. Such feedback processes reduce the availability of cold gas in the central regions, potentially quenching star formation and reshaping the ISM.

The implications of these findings extend beyond the host galaxies. By driving gas and metals into the intergalactic medium (IGM), AGN outflows contribute to the chemical enrichment of their surroundings, influencing the formation of nearby galaxies. More luminous AGNs, which produce stronger outflows, are likely to have a more significant role in shaping the composition of the IGM.

While these trends are compelling, the relatively small size of the TWIST sample imposes limitations on the robustness of these results. Incomplete data, such as missing CIGALE or BAROLO parameters, further restrict the analysis. Expanding the dataset with additional observations will help validate these findings and reduce potential biases.

We also analyzed the molecular gas depletion time ($\tau_{\rm dep} = M_{\rm gas}/{\rm SFR}$) as a function of stellar mass (M_*) for the sample, as shown in Figure 5.15. The results indicate that galaxies with higher stellar masses exhibit longer depletion times. This suggests that more massive galaxies retain molecular gas for extended periods, allowing sustained star formation over longer timescales. For galaxies hosting luminous AGNs, AGN feedback may act to reduce the available molecular gas, thus affecting their overall star formation efficiency and depletion times.

The relationship between AGN bolometric luminosity ($L_{\rm bol}$) and SFR for the sample is shown in Figure 5.16. A positive correlation is observed, where galaxies with higher $L_{\rm bol}$

tend to exhibit higher SFRs. This suggests that AGN activity may coexist with ongoing star formation, particularly in galaxies where AGN-driven outflows are less disruptive or occur outside of active star-forming regions. However, for galaxies below the star formation main sequence, this relationship weakens, likely due to stronger AGN feedback suppressing star formation. These observations underline the dual role of AGNs in both facilitating and regulating star formation within their host galaxies.

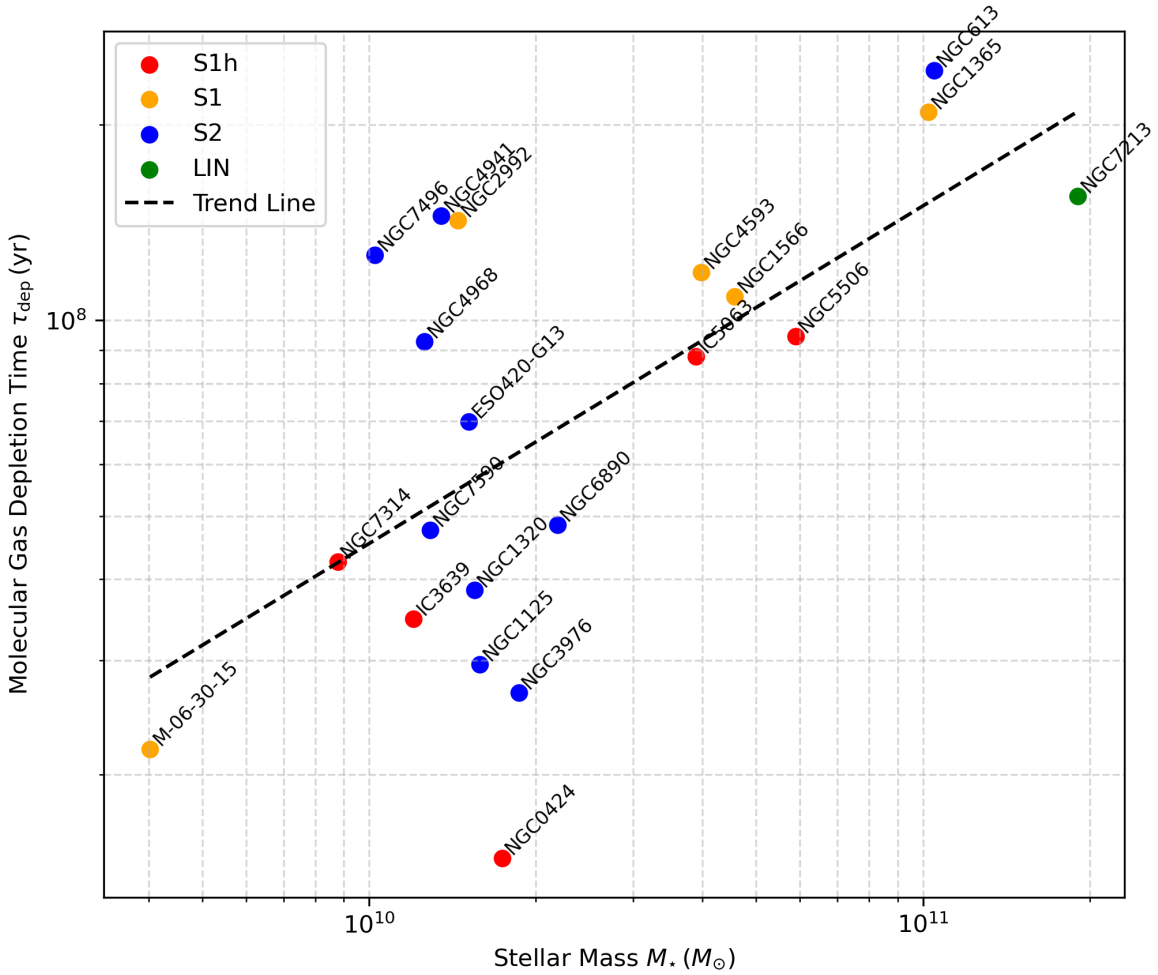

FIGURE 5.15 – Molecular gas depletion time, $\tau_{\rm dep} = \frac{M_{\rm H_2}}{\rm SFR}$, as a function of stellar mass $M_\star$ for the sample. Here, $M_{\rm H_2}$ is defined as the total molecular gas mass derived from ALMA CO observations (Table 5.4) using a standard CO-to-H_2 conversion factor (see Section 5.1 for details). Each point represents a galaxy, color-coded by AGN type, and the dashed line indicates the best-fit trend. The trend suggests that galaxies with higher stellar masses tend to exhibit longer depletion times, implying that more massive galaxies may sustain larger reservoirs of molecular gas for extended star formation activity.

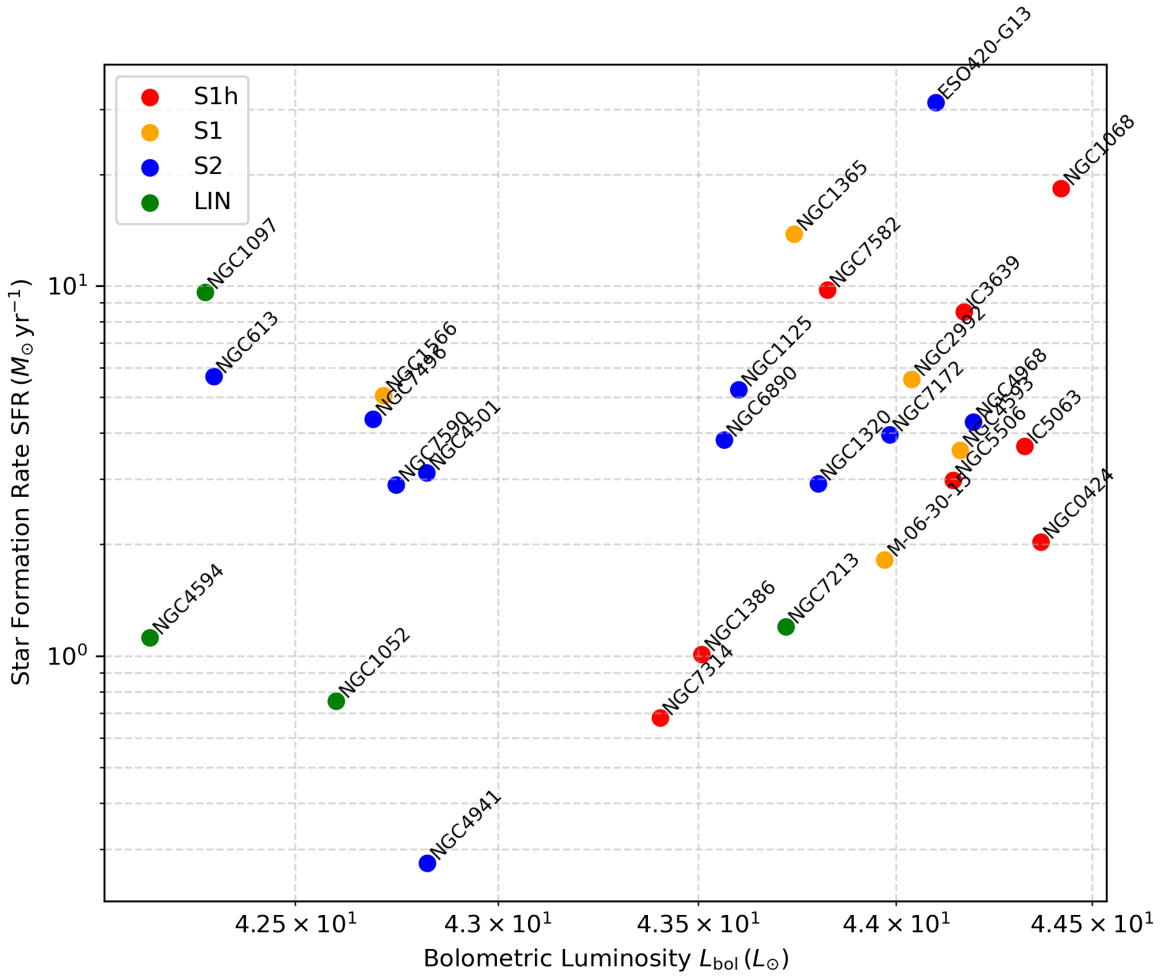

FIGURE 5.16 – AGN bolometric luminosity L_{bol} plotted against SFR for the sample galaxies. Each point represents a galaxy, color-coded by AGN type.

6 Conclusion

In this study, we investigated the molecular gas dynamics and AGN feedback processes in the TWIST sample, focusing initially on the Seyfert 1 AGN galaxy NGC 4593 as a detailed case study. NGC 4593 was selected as the starting point for this analysis because it offers comprehensive data, including ALMA CO(2-1) observations, multi-wavelength photometry, and archival measurements, enabling a full exploration of kinematics, morphology, and spectral properties. By applying and refining methodologies on this well-studied galaxy, we developed a robust framework to analyze the broader TWIST sample systematically.

For NGC 4593, we used ALMA CO(2-1) data to examine the molecular gas dynamics, employing 3D-Barolo and discFit to model the kinematics and morphological features of the molecular gas. Our kinematic analysis revealed a distinct one-arm structure in the molecular gas distribution, consistent with an $m = 1$ density wave or perturbation. While the gas exhibits predominantly regular rotational motion, non-circular velocities were detected in the northeast region of the galaxy, approximately $2''$ to $3''$ (~ 220 pc) from the center, indicating the presence of a molecular gas outflow. This outflow region contains an estimated $(0.5 - 2.5) \times 10^7\, M_\odot$, approximately 10% of the total flux of the galaxy. These findings are consistent with previous observations of kinematic perturbations in the ionized gas (BARBOSA *et al.*, 2006).

Using SED fitting performed with CIGALE, we characterized the galaxy's SFR and AGN contribution. The SED revealed a strong AGN component, with the AGN fraction contributing 0.87 to the IR luminosity, highlighting the substantial role of AGN activity in shaping the galaxy's spectrum. Despite the high AGN luminosity ($L_{\rm bol} > 10^{44}$ erg/s), the SFR in NGC,4593 remains moderate, suggesting a possible suppression of star formation by AGN feedback. The molecular gas mass of the galaxy, estimated to be $1.0 \sim 5.0 \times 10^8\, M_\odot$, further supports the hypothesis that AGN feedback influences gas availability in the central regions.

With the methodologies tested and validated on NGC 4593, we extended our analysis to the full TWIST sample. For each galaxy, we performed kinematic modeling using 3D-Barolo and carried out spectral energy distribution fitting with CIGALE to derive

key physical parameters such as molecular gas mass, star formation rate, AGN contribution, rotation curves, and non-circular motions. Although some galaxies had incomplete datasets (e.g., photometric gaps or missing ALMA flux), we were able to robustly determine these parameters for a significant fraction of the sample.

A major outcome of our study is the estimation of outflow mass rates for 20 galaxies (detailed in Chapter 5.2.3.1). These outflows, identified through residual maps and velocity dispersion profiles, underscore the role of AGN feedback in redistributing or removing gas from the central regions. In our analysis, galaxies with pronounced AGN signatures typically exhibit prominent outflows, with mass outflow rates increasing in tandem with AGN bolometric luminosity.

Overall, the TWIST sample reveals a diverse range of molecular gas dynamics—from AGN-driven outflows to bar-induced inflows—which highlights the complex interplay between AGN feedback, star formation, and gas kinematics. These results illustrate that, while AGN feedback can suppress star formation in some cases, it may coexist with or even promote star formation in others, depending on the local conditions and energy distribution.

Bibliography

ALEXANDER, D. M.; HICKOX, R. C. What drives the growth of black holes? **New Astronomy Reviews**, Elsevier, v. 56, n. 4, p. 93–121, 2012.

ALMEIDA, C. R.; RICCI, C. Nuclear obscuration in active galactic nuclei. **Nature Astronomy**, v. 1, p. 679 – 689, 2017. Available at: https://api.semanticscholar.org/CorpusID:53607914.

ANDREANI, P.; RETANA-MONTENEGRO, E.; ZHANG, Z.-Y.; PAPADOPOULOS, P.; YANG, C.; VEGETTI, S. Extreme conditions in the molecular gas of lensed star-forming galaxies at z˜ 3. **Astronomy & Astrophysics**, EDP Sciences, v. 615, p. A142, 2018.

ANN, H.; THAKUR, P. Formation of nuclear spirals in barred galaxies. **The Astrophysical Journal**, IOP Publishing, v. 620, n. 1, p. 197, 2005.

ARMILLOTTA, L.; KRUMHOLZ, M. R.; TEODORO, E. M. D. The life cycle of the central molecular zone–ii. distribution of atomic and molecular gas tracers. **Monthly Notices of the Royal Astronomical Society**, Oxford University Press, v. 493, n. 4, p. 5273–5289, 2020.

ATHANASSOULA, E. Bars within bars and the fueling of active galactic nuclei. **Monthly Notices of the Royal Astronomical Society**, v. 259, p. 345–364, 1992.

ATLEE, D. W.; MARTINI, P.; ASSEF, R. J.; KELSON, D. D.; MULCHAEY, J. S. A multi-wavelength study of low-redshift clusters of galaxies. i. comparison of x-ray and mid-infrared selected active galactic nuclei. **The Astrophysical Journal**, IOP Publishing, v. 729, n. 1, p. 22, 2011.

AUDIBERT, A.; COMBES, F.; GARCÍA-BURILLO, S.; DASYRA, K. Feeding and feedback in nuclei of galaxies. **Proceedings of the International Astronomical Union**, Cambridge University Press, v. 15, n. S359, p. 307–311, 2019.

AUDIBERT, A.; COMBES, F.; GARCíA-BURILLO, S.; AL. et. Alma captures feeding and feddback from the active galactic nucleus in ngc 613*. **Astronomy and Astrophysics**, v. 632, p. A33, 2019.

AUDIBERT, A.; RIFFEL, R.; SALES, D. A.; PASTORIZA, M. G.; RUSCHEL-DUTRA, D. Probing the active galactic nucleus unified model torus properties in seyfert galaxies. **Monthly Notices of the Royal Astronomical Society**, Oxford University Press, v. 464, n. 2, p. 2139–2173, 2017.

BALLY, J.; STARK, A. A.; WILSON, R. W.; HENKEL, C. Galactic center molecular clouds. i-spatial and spatial-velocity maps. **Astrophysical Journal Supplement Series (ISSN 0067-0049), vol. 65, Sept. 1987, p. 13-82.**, v. 65, p. 13–82, 1987.

BARBOSA, F. K. B.; STORCHI-BERGMANN, T.; FERNANDES, R. C.; WINGE, C.; SCHMITT, H. Gemini/gmos integral field unit stellar kinematics of the nuclear region of six nearby active galaxies. **Monthly Notices of the Royal Astronomical Society**, Blackwell Publishing Ltd Oxford, UK, v. 371, n. 1, p. 170–184, 2006.

BARON, D.; NETZER, H.; DAVIES, R. I.; PROCHASKA, J. X. Multiphase outflows in post-starburst e+ a galaxies-ii. a direct connection between the neutral and ionized outflow phases. **Monthly Notices of the Royal Astronomical Society**, Oxford University Press, v. 494, n. 4, p. 5396–5420, 2020.

BARROWS, R. S.; COMERFORD, J. M.; STERN, D. K.; ASSEF, R. J. A catalog of host galaxies for wise-selected agn: Connecting host properties with nuclear activity and identifying contaminants. **The Astrophysical Journal**, v. 922, 2021. Available at: https://api.semanticscholar.org/CorpusID:235755180.

BEAN, B.; BHATNAGAR, S.; CASTRO, S.; MEYER, J. D.; EMONTS, B.; GARCIA, E.; GARWOOD, R.; GOLAP, K.; VILLALBA, J. G.; HARRIS, P. *et al.* Casa, common astronomy software applications for radio astronomy. **Publications of the Astronomical Society of the Pacific**, IOP Publishing, v. 134, n. 1041, p. 114501, 2022.

BECKMANN, V.; SHRADER, C. R. The agn phenomenon: open issues. **arXiv preprint arXiv:1302.1397**, 2013.

BEGELMAN, M. C.; MEIER, D. L. Thick accretion disks-self-similar, supercritical models. **Astrophysical Journal, Part 1, vol. 253, Feb. 15, 1982, p. 873-896. Research supported by the Science Research Council of England**, v. 253, p. 873–896, 1982.

BELETE, A. B.; ANDREANI, P.; FERNÁNDEZ-ONTIVEROS, J.; HATZIMINAOGLOU, E.; COMBES, F.; SIRRESSI, M.; SLATER, R.; RICCI, C.; DASYRA, K.; CICONE, C. *et al.* Molecular gas kinematics in the nuclear region of nearby seyfert galaxies with alma. **Astronomy & Astrophysics**, EDP Sciences, v. 654, p. A24, 2021.

BISCHETTI, M.; MAIOLINO, R.; CARNIANI, S.; FIORE, F.; PICONCELLI, E.; FLUETSCH, A. Widespread qso-driven outflows in the early universe. **Astronomy & Astrophysics**, EDP Sciences, v. 630, p. A59, 2019.

BLANDFORD, R. D.; ZNAJEK, R. L. Electromagnetic extraction of energy from kerr black holes. **Monthly Notices of the Royal Astronomical Society**, Oxford University Press Oxford, UK, v. 179, n. 3, p. 433–456, 1977.

BLUMENTHAL, G. R.; FABER, S.; PRIMACK, J. R.; REES, M. J. Formation of galaxies and large-scale structure with cold dark matter. **Nature**, Nature Publishing Group UK London, v. 311, n. 5986, p. 517–525, 1984.

BOLATTO, A. D.; ARMUS, L.; VEILLEUX, S.; LEROY, A. K.; WALTER, F.; MUSHOTZKY, R.; SANDSTROM, K. M.; MARTINI, P.; SCHNEIDER, E. E.; WONG, T.; DECARLI, R.; CASEY, C. M.; RIECHERS, D. A.; MEIER, D. S.; NARAYANA, D.

Astro2020 science white paper: Cold gas outflows, feedback, and the shaping of galaxies. **arXiv: Astrophysics of Galaxies**, 2019. Available at: https://api.semanticscholar.org/CorpusID:102491723.

BOLATTO, A. D.; WOLFIRE, M.; LEROY, A. K. The co-to-h2 conversion factor. **Annual Review of Astronomy and Astrophysics**, Annual Reviews, v. 51, p. 207–268, 2013.

BOOTH, C.; SCHAYE, J. The interaction between feedback from active galactic nuclei and supernovae. **Scientific Reports**, Nature Publishing Group UK London, v. 3, n. 1, p. 1738, 2013.

BOQUIEN, M.; BURGARELLA, D.; ROEHLLY, Y.; BUAT, V.; CIESLA, L.; CORRE, D.; INOUE, A.; SALAS, H. Cigale: a python code investigating galaxy emission. **Astronomy & Astrophysics**, EDP Sciences, v. 622, p. A103, 2019.

BORTHAKUR, S.; TRIPP, T. M.; YUN, M. S.; MOMJIAN, E.; MEIRING, J. D.; BOWEN, D. V.; YORK, D. G. Using 21 cm absorption in small impact parameter galaxy–quasar pairs to probe low-redshift damped and sub-damped lyα systems. **The Astrophysical Journal**, IOP Publishing, v. 713, n. 1, p. 131, 2010.

BOUQUIN, A. Y.; PAZ, A. G. de; MUÑOZ-MATEOS, J. C.; BOISSIER, S.; SETH, K.; ZARITSKY, D.; PELETIER, R. F.; KNAPEN, J. H.; GALLEGO, J. The galex/s4g surface brightness and color profiles catalog. i. surface photometry and color gradients of galaxies. **The Astrophysical Journal Supplement Series**, IOP Publishing, v. 234, n. 2, p. 18, 2018.

BRIGHTMAN, M.; NANDRA, K. An xmm–newton spectral survey of 12 μm selected galaxies–i. x-ray data. **Monthly Notices of the Royal Astronomical Society**, The Royal Astronomical Society, v. 413, n. 2, p. 1206–1235, 2011.

BROK, M. den; CAROLLO, C. M.; ERROZ-FERRER, S.; FAGIOLI, M.; BRINCHMANN, J.; EMSELLEM, E.; KRAJNOVIĆ, D.; MARINO, R. A.; ONODERA, M.; TACCHELLA, S. *et al.* The muse atlas of discs (mad): Ionized gas kinematic maps and an application to diffuse ionized gas. **Monthly Notices of the Royal Astronomical Society**, Oxford University Press, v. 491, n. 3, p. 4089–4107, 2020.

BRUZUAL, G.; CHARLOT, S. Stellar population synthesis at the resolution of 2003. **Monthly Notices of the Royal Astronomical Society**, Blackwell Science Ltd Oxford, UK, v. 344, n. 4, p. 1000–1028, 2003.

BUCHNER, J.; BAUER, F. E. Galaxy gas as obscurer – ii. separating the galaxy-scale and nuclear obscurers of active galactic nuclei. **Monthly Notices of the Royal Astronomical Society**, v. 465, p. 4348–4362, 2016. Available at: https://api.semanticscholar.org/CorpusID:119227238.

BUCHNER, J.; GEORGAKAKIS, A.; NANDRA, K.; BRIGHTMAN, M.; MENZEL, M. L.; LIU, Z.; HSU, L.-T.; SALVATO, M.; RANGEL, C.; AIRD, J.; MERLONI, A.; ROSS, N. P. Obscuration-dependent evolution of active galactic nuclei. **The Astrophysical Journal**, v. 802, 2015. Available at: https://api.semanticscholar.org/CorpusID:28195363.

CACKETT, E. M.; CHIANG, C.-Y.; MCHARDY, I.; EDELSON, R.; GOAD, M. R.; HORNE, K.; KORISTA, K. T. Accretion disk reverberation with hubble space telescope observations of ngc 4593: evidence for diffuse continuum lags. **The Astrophysical Journal**, IOP Publishing, v. 857, n. 1, p. 53, 2018.

CAGLAR, T.; BURTSCHER, L.; BRANDL, B.; BRINCHMANN, J.; DAVIES, R. I.; HICKS, E. K.; KOSS, M.; LIN, M.-Y.; MACIEJEWSKI, W.; MÜLLER-SÁNCHEZ, F. *et al.* Llama: The mbh–*sigma* relation of the most luminous local agns. **Astronomy & Astrophysics**, EDP Sciences, v. 634, p. A114, 2020.

CALZETTI, D.; ARMUS, L.; BOHLIN, R. C.; KINNEY, A. L.; KOORNNEEF, J.; STORCHI-BERGMANN, T. The dust content and opacity of actively star-forming galaxies. **The Astrophysical Journal**, IOP Publishing, v. 533, n. 2, p. 682, 2000.

CALZETTI, D.; KENNICUTT, R.; ENGELBRACHT, C.; LEITHERER, C.; DRAINE, B.; KEWLEY, L.; MOUSTAKAS, J.; SOSEY, M.; DALE, D.; GORDON, K. *et al.* The calibration of mid-infrared star formation rate indicators. **The Astrophysical Journal**, IOP Publishing, v. 666, n. 2, p. 870, 2007.

Cano-Díaz, M.; Maiolino, R.; Marconi, A.; Netzer, H.; Shemmer, O.; Cresci, G. Observational evidence of quasar feedback quenching star formation at high redshift. **A&A**, v. 537, p. L8, 2012. Available at: https://doi.org/10.1051/0004-6361/201118358.

CAO, X. The outflows accelerated by the magnetic fields and radiation force of accretion disks. **The Astrophysical Journal**, IOP Publishing, v. 783, n. 1, p. 51, 2014.

CAPPI, M. Relativistic blue-and red-shifted absorption lines in agns. **Astronomische Nachrichten: Astronomical Notes**, Wiley Online Library, v. 327, n. 10, p. 1012–1019, 2006.

CARNIANI, S.; MARCONI, A.; MAIOLINO, R.; BALMAVERDE, B.; BRUSA, M.; CANO-DÍAZ, M.; CICONE, C.; COMASTRI, A.; CRESCI, G.; FIORE, F. *et al.* Fast outflows and star formation quenching in quasar host galaxies. **Astronomy & Astrophysics**, EDP Sciences, v. 591, p. A28, 2016.

CARRARO, R.; RODIGHIERO, G.; CASSATA, P.; BRUSA, M.; SHANKAR, F.; BARONCHELLI, I.; DADDI, E.; DELVECCHIO, I.; FRANCESCHINI, A.; GRIFFITHS, R. *et al.* Coevolution of black hole accretion and star formation in galaxies up to z= 3.5. **Astronomy & Astrophysics**, EDP Sciences, v. 642, p. A65, 2020.

CATTANEO, A.; FABER, S.; BINNEY, J.; DEKEL, A.; KORMENDY, J.; MUSHOTZKY, R.; BABUL, A.; BEST, P.; BRÜGGEN, M.; FABIAN, A. *et al.* The role of black holes in galaxy formation and evolution. **Nature**, Nature Publishing Group, v. 460, n. 7252, p. 213–219, 2009.

CHEN, Y.-M.; TREMONTI, C. A.; HECKMAN, T. M.; KAUFFMANN, G.; WEINER, B. J.; BRINCHMANN, J.; WANG, J. Absorption-line probes of the prevalence and properties of outflows in present-day star-forming galaxies. **The Astronomical Journal**, v. 140, p. 445 – 461, 2010. Available at: https://api.semanticscholar.org/CorpusID:119187489.

CHEUNG, E.; BUNDY, K.; CAPPELLARI, M.; PEIRANI, S.; RUJOPAKARN, W.; WESTFALL, K.; YAN, R.; BERSHADY, M.; GREENE, J. E.; HECKMAN, T. M. *et al.* Suppressing star formation in quiescent galaxies with supermassive black hole winds. **Nature**, Nature Publishing Group UK London, v. 533, n. 7604, p. 504–508, 2016.

CICONE, C.; MAIOLINO, R.; STURM, E.; GRACIÁ-CARPIO, J.; FERUGLIO, C.; NERI, R.; AALTO, S.; DAVIES, R.; FIORE, F.; FISCHER, J. *et al.* Massive molecular outflows and evidence for agn feedback from co observations. **Astronomy & Astrophysics**, EDP Sciences, v. 562, p. A21, 2014.

CIELO, S.; BIERI, R.; VOLONTERI, M.; WAGNER, A. Y.; DUBOIS, Y. Agn feedback compared: jets versus radiation. **Monthly Notices of the Royal Astronomical Society**, Oxford University Press, v. 477, n. 1, p. 1336–1355, 2018.

CIESLA, L.; CHARMANDARIS, V.; GEORGAKAKIS, A.; BERNHARD, E.; MITCHELL, P.; BUAT, V.; ELBAZ, D.; LEFLOC'H, E.; LACEY, C.; MAGDIS, G. *et al.* Constraining the properties of agn host galaxies with spectral energy distribution modelling. **Astronomy & Astrophysics**, EDP Sciences, v. 576, p. A10, 2015.

COMBES, F. Dynamical triggering of starbursts. *In*: AMERICAN INSTITUTE OF PHYSICS. **AIP Conference Proceedings**. **Proceedings** [...]. [*S.l.: s.n.*], 2005. v. 783, n. 1, p. 43–49.

COMBES, F. Agn feedback and its quenching efficiency. **Frontiers in Astronomy and Space Sciences**, Frontiers Media SA, v. 4, p. 10, 2017.

COMBES, F.; GARCÍA-BURILLO, S.; CASASOLA, V.; HUNT, L.; KRIPS, M.; BAKER, A.; BOONE, F.; ECKART, A.; MARQUEZ, I.; NERI, R. *et al.* Alma observations of feeding and feedback in nearby seyfert galaxies: an agn-driven outflow in ngc 1433. **Astronomy & Astrophysics**, EDP Sciences, v. 558, p. A124, 2013.

COMBES, F.; GARCÍA-BURILLO, S.; CASASOLA, V.; HUNT, L.; KRIPS, M.; BAKER, A.; BOONE, F.; ECKART, A.; MARQUEZ, I.; NERI, R. *et al.* Alma reveals the feeding of the seyfert 1 nucleus in ngc 1566. **Astronomy & Astrophysics**, EDP Sciences, v. 565, p. A97, 2014.

CONCAS, A.; POPESSO, P.; BRUSA, M.; MAINIERI, V.; THOMAS, D. Two-face (s): ionized and neutral gas winds in the local universe. **Astronomy & Astrophysics**, EDP Sciences, v. 622, p. A188, 2019.

COSTA, T.; SIJACKI, D.; HAEHNELT, M. G. Feedback from active galactic nuclei: energy- versus momentum-driving. **Monthly Notices of the Royal Astronomical Society**, v. 444, p. 2355–2376, 2014. Available at: https://api.semanticscholar.org/CorpusID:56071385.

CRAIN, R. A.; VOORT, F. van de. Hydrodynamical simulations of the galaxy population: enduring successes and outstanding challenges. **Annual Review of Astronomy and Astrophysics**, Annual Reviews, v. 61, n. 1, p. 473–515, 2023.

CRENSHAW, D. M.; KRAEMER, S. B.; GEORGE, I. M. Mass loss from the nuclei of active galaxies. **Annual Review of Astronomy and Astrophysics**, Annual Reviews 4139 El Camino Way, PO Box 10139, Palo Alto, CA 94303-0139, USA, v. 41, n. 1, p. 117–167, 2003.

CROTON, D. J.; SPRINGEL, V.; WHITE, S. D.; LUCIA, G. D.; FRENK, C. S.; GAO, L.; JENKINS, A.; KAUFFMANN, G.; NAVARRO, J.; YOSHIDA, N. The many lives of active galactic nuclei: cooling flows, black holes and the luminosities and colours of galaxies. **Monthly Notices of the Royal Astronomical Society**, Blackwell Science Ltd Oxford, UK, v. 365, n. 1, p. 11–28, 2006.

CUTRI, R. *et al.* Explanatory supplement to the wise all-sky data release products. **Explanatory Supplement to the WISE All-Sky Data Release Products**, p. 1, 2012.

CZERNY, B.; YOU, B. Accretion in active galactic nuclei and disk-jet coupling. **Astronomische Nachrichten**, Wiley Online Library, v. 337, n. 1-2, p. 73–81, 2016.

DALE, D. A.; HELOU, G.; MAGDIS, G. E.; ARMUS, L.; DÍAZ-SANTOS, T.; SHI, Y. A two-parameter model for the infrared/submillimeter/radio spectral energy distributions of galaxies and active galactic nuclei. **The Astrophysical Journal**, IOP Publishing, v. 784, n. 1, p. 83, 2014.

DAVIES, R. *et al.* Ionized outflows in local luminous agn: what are the real densities and outflow rates? **Monthly Notices of the Royal Astronomical Society**, Oxford University Press, v. 498, n. 3, p. 4150–4177, 2020.

DENNEY, K. D.; BENTZ, M. C.; PETERSON, B. M.; POGGE, R. W.; CACKETT, E. M.; DIETRICH, M.; FOGEL, J. K.; GHOSH, H.; HORNE, K. D.; KUEHN, C. *et al.* The mass of the black hole in the seyfert 1 galaxy ngc 4593 from reverberation mapping. **The Astrophysical Journal**, IOP Publishing, v. 653, n. 1, p. 152, 2006.

DOELEMAN, S. S. *et al.* Event-horizon-scale structure in the supermassive black hole candidate at the galactic centre. **Nature**, v. 455, p. 78–80, 2008. Available at: https://api.semanticscholar.org/CorpusID:4424735.

DORODNITSYN, A. V. *et al.* Agn obscuration through dusty, infrared-dominated flows. ii. multidimensional, radiation-hydrodynamics modeling. **The Astrophysical Journal**, v. 747, 2011. Available at: https://api.semanticscholar.org/CorpusID:119237979.

DRESSLER *et al.* The evolution of galaxies in clusters. *In*: SPRINGER. **Clusters and Groups of Galaxies**. **Proceedings** [...]. [*S.l.: s.n.*], 1984. p. 117–132.

DUBOIS, Y.; DEVRIENDT, J.; SLYZ, A. D.; TEYSSIER, R. Self-regulated growth of supermassive black holes by a dual jet-heating active galactic nucleus feedback mechanism: methods, tests and implications for cosmological simulations. **Monthly Notices of the Royal Astronomical Society**, v. 420, p. 2662–2683, 2011. Available at: https://api.semanticscholar.org/CorpusID:119179840.

EDDINGTON, A. S. **The internal constitution of the stars**. [*S.l.*]: Cambridge University Press, 1988.

ELBAZ *et al.* Goods–herschel: an infrared main sequence for star-forming galaxies. **Astronomy & Astrophysics**, EDP Sciences, v. 533, p. A119, 2011.

ESPOSITO, F.; ALONSO-HERRERO, A.; GARCÍA-BURILLO, S.; CASASOLA, V.; COMBES, F.; DALLACASA, D.; DAVIES, R.; GARCÍA-BERNETE, I.; GARCÍA-LORENZO, B.; MUÑOZ, L. H. *et al.* Agn feedback in the local universe:

Multiphase outflow of the seyfert galaxy ngc 5506. **Astronomy & Astrophysics**, EDP Sciences, v. 686, p. A46, 2024.

EVERETT, J.; KÖNIGL, A.; ARAV, N. Observational evidence for a multiphase outflow in quasar first j1044+ 3656. **The Astrophysical Journal**, IOP Publishing, v. 569, n. 2, p. 671, 2002.

FABIAN, A. C. Observational evidence of active galactic nuclei feedback. **Annual Review of Astronomy and Astrophysics**, Annual Reviews, v. 50, p. 455–489, 2012.

FATHI *et al.* Alma follows streaming of dense gas down to 40 pc from the supermassive black hole in ngc 1097. **The Astrophysical Journal Letters**, IOP Publishing, v. 770, n. 2, p. L27, 2013.

FERNÁNDEZ-ONTIVEROS, J.; DASYRA, K.; HATZIMINAOGLOU, E.; MALKAN, M.; PEREIRA-SANTAELLA, M.; PAPACHRISTOU, M.; SPINOGLIO, L.; COMBES, F.; AALTO, S.; NAGAR, N. *et al.* A co molecular gas wind 340 pc away from the seyfert 2 nucleus in eso 420-g13 probes an elusive radio jet. **Astronomy & Astrophysics**, EDP Sciences, v. 633, p. A127, 2020.

FERRARA, A.; SCANNAPIECO, E. On the formation of molecular clumps in qso outflows. **The Astrophysical Journal**, v. 833, 2016. Available at: https://api.semanticscholar.org/CorpusID:118514175.

FIORE, F.; FERUGLIO, C.; SHANKAR, F.; BISCHETTI, M.; BONGIORNO, A.; BRUSA, M.; CARNIANI, S.; CICONE, C.; DURAS, F.; LAMASTRA, A. *et al.* Agn wind scaling relations and the co-evolution of black holes and galaxies. **Astronomy & Astrophysics**, EDP Sciences, v. 601, p. A143, 2017.

FLUETSCH, A.; MAIOLINO, R.; CARNIANI, S.; MARCONI, A.; CICONE, C.; BOURNE, M.; COSTA, T.; FABIAN, A.; ISHIBASHI, W.; VENTURI, G. Cold molecular outflows in the local universe and their feedback effect on galaxies. **Monthly Notices of the Royal Astronomical Society**, Oxford University Press, v. 483, n. 4, p. 4586–4614, 2019.

FLUETSCH, A.; MAIOLINO, R.; CARNIANI, S.; ARRIBAS, S.; BELFIORE, F.; BELLOCCHI, E.; CAZZOLI, S.; CICONE, C.; CRESCI, G.; FABIAN, A. C. *et al.* Properties of the multiphase outflows in local (ultra) luminous infrared galaxies. **Monthly Notices of the Royal Astronomical Society**, Oxford University Press, v. 505, n. 4, p. 5753–5783, 2021.

FRATERNALI, F.; MOORSEL, G. van; SANCISI, R.; OOSTERLOO, T. Deep hi survey of the spiral galaxy ngc 2403. **The Astronomical Journal**, IOP Publishing, v. 123, n. 6, p. 3124, 2002.

FRYXELL, B.; OLSON, K.; RICKER, P.; TIMMES, F. X.; ZINGALE, M.; LAMB, D.; MACNEICE, P.; ROSNER, R.; TRURAN, J.; TUFO, H. Flash: An adaptive mesh hydrodynamics code for modeling astrophysical thermonuclear flashes. **The Astrophysical Journal Supplement Series**, IOP Publishing, v. 131, n. 1, p. 273, 2000.

GADOTTI, D. A. Image decomposition of barred galaxies and agn hosts. **Monthly Notices of the Royal Astronomical Society**, Blackwell Publishing Ltd Oxford, UK, v. 384, n. 1, p. 420–439, 2008.

GAO, Y.; EGUSA, F.; LIU, G.; KOHNO, K.; BAO, M.; MOROKUMA-MATSUI, K.; KONG, X.; CHEN, X. The nuclear region of ngc 1365: Star formation, negative feedback, and outflow structure. **The Astrophysical Journal**, IOP Publishing, v. 913, n. 2, p. 139, 2021.

GASPARI, M. The self-regulated agn feedback loop: the role of chaotic cold accretion. **Proceedings of the International Astronomical Union**, Cambridge University Press, v. 11, n. S319, p. 17–20, 2015.

GASPARI, M.; MCDONALD, M.; HAMER, S.; BRIGHENTI, F.; TEMI, P.; GENDRON-MARSOLAIS, M.; HLAVACEK-LARRONDO, J.; EDGE, A. C.; WERNER, N.; TOZZI, P. *et al.* Shaken snow globes: kinematic tracers of the multiphase condensation cascade in massive galaxies, groups, and clusters. **The Astrophysical Journal**, IOP Publishing, v. 854, n. 2, p. 167, 2018.

GASPARI, M.; MELIOLI, C.; BRIGHENTI, F.; D'ERCOLE, A. The dance of heating and cooling in galaxy clusters: three-dimensional simulations of self-regulated active galactic nuclei outflows. **Monthly Notices of the Royal Astronomical Society**, Blackwell Publishing Ltd Oxford, UK, v. 411, n. 1, p. 349–372, 2011.

GASPARI, M.; RUSZKOWSKI, M.; SHARMA, P. Cause and effect of feedback: multiphase gas in cluster cores heated by agn jets. **The Astrophysical Journal**, IOP Publishing, v. 746, n. 1, p. 94, 2012.

GASPARI, M.; TOMBESI, F.; CAPPI, M. Linking macro-, meso-and microscales in multiphase agn feeding and feedback. **Nature Astronomy**, Nature Publishing Group, v. 4, n. 1, p. 10–13, 2020.

GENZEL, R.; TACCONI, L.; GRACIA-CARPIO, J.; STERNBERG, A.; COOPER, M.; SHAPIRO, K.; BOLATTO, A.; BOUCHÉ, N.; BOURNAUD, F.; BURKERT, A. *et al.* A study of the gas–star formation relation over cosmic time. **Monthly notices of the royal astronomical Society**, Blackwell Publishing Ltd Oxford, UK, v. 407, n. 4, p. 2091–2108, 2010.

GITTI, M.; BRIGHENTI, F.; MCNAMARA, B. R. Evidence for agn feedback in galaxy clusters and groups. **Advances in Astronomy**, Hindawi, v. 2012, 2012.

GIUSTINI, M.; PROGA, D. A global view of the inner accretion and ejection flow around super massive black holes. **Astronomy & Astrophysics**, 2019. Available at: https://api.semanticscholar.org/CorpusID:118716878.

GUOLO-PEREIRA, M.; RUSCHEL-DUTRA, D.; STORCHI-BERGMANN, T.; SCHNORR-MÜLLER, A.; FERNANDES, R. C.; COUTO, G.; DAMETTO, N.; HERNANDEZ-JIMENEZ, J. A. Exploring the agn-merger connection in arp 245 i: Nuclear star formation and gas outflow in ngc 2992. **Monthly Notices of the Royal Astronomical Society**, Oxford University Press, v. 502, n. 3, p. 3618–3637, 2021.

HAMANN, F.; CHARTAS, G.; MCGRAW, S. M.; HIDALGO, P. R.; SHIELDS, J. C.; CAPELLUPO, D. M.; CHARLTON, J. C.; ERACLEOUS, M. Extreme-velocity quasar outflows and the role of x-ray shielding. **Monthly Notices of the Royal Astronomical Society**, v. 435, p. 133–148, 2013. Available at: https://api.semanticscholar.org/CorpusID:26853047.

HARRISON, C. The impact of agn on their host galaxies. **Proceedings of the International Astronomical Union**, Cambridge University Press, v. 9, n. S304, p. 284–290, 2013.

HARRISON, C. Impact of supermassive black hole growth on star formation. **Nature Astronomy**, Nature Publishing Group UK London, v. 1, n. 7, p. 0165, 2017.

HARRISON, C.; COSTA, T.; TADHUNTER, C.; FLÜTSCH, A.; KAKKAD, D.; PERNA, M.; VIETRI, G. Agn outflows and feedback twenty years on. **Nature Astronomy**, Nature Publishing Group UK London, v. 2, n. 3, p. 198–205, 2018.

HARRISON, C. M.; ALMEIDA, C. R. Observational tests of active galactic nuclei feedback: An overview of approaches and interpretation. **Galaxies**, MDPI, v. 12, n. 2, p. 17, 2024.

HATCHFIELD, H. P.; SORMANI, M. C.; TRESS, R. G.; BATTERSBY, C.; SMITH, R. J.; GLOVER, S. C.; KLESSEN, R. S. Dynamically driven inflow onto the galactic center and its effect upon molecular clouds. **The Astrophysical Journal**, IOP Publishing, v. 922, n. 1, p. 79, 2021.

HATZIMINAOGLOU, E.; FARRAH, D.; HUMPHREYS, E.; MANRIQUE, A.; PÉREZ-FOURNON, I.; PITCHFORD, L.; SALVADOR-SOLÉ, E.; WANG, L. On the multiplicity of alma compact array counterparts of far-infrared bright quasars. **Monthly Notices of the Royal Astronomical Society**, Oxford University Press, v. 480, n. 4, p. 4974–4990, 2018.

HAYWARD, C. C.; HOPKINS, P. F. How stellar feedback simultaneously regulates star formation and drives outflows. **Monthly Notices of the Royal Astronomical Society**, v. 465, p. 1682–1698, 2015. Available at: https://api.semanticscholar.org/CorpusID:33220684.

HAZARD, C.; MACKEY, M.; SHIMMINS, A.; SCHMIDT, M.; GREENSTEIN, J. L.; MATTHEWS, T. A.; OKE, J. B. 120. the discovery of quasars. *In*: **A Source Book in Astronomy and Astrophysics, 1900–1975**. [*S.l.*]: Harvard University Press, 2013. p. 803–810.

HEAVENS, A.; PANTER, B.; JIMENEZ, R.; DUNLOP, J. The star-formation history of the universe from the stellar populations of nearby galaxies. **Nature**, Nature Publishing Group UK London, v. 428, n. 6983, p. 625–627, 2004.

HECKMAN, T. M.; ALEXANDROFF, R.; BORTHAKUR, S.; OVERZIER, R. A.; LEITHERER, C. The systematic properties of the warm phase of starburst-driven galactic winds. **The Astrophysical Journal**, v. 809, 2015. Available at: https://api.semanticscholar.org/CorpusID:118444565.

HECKMAN, T. M.; BEST, P. N. The coevolution of galaxies and supermassive black holes: insights from surveys of the contemporary universe. **Annual Review of Astronomy and Astrophysics**, Annual Reviews, v. 52, n. 1, p. 589–660, 2014.

HERRERA-CAMUS, R. *et al.* Agn feedback in a galaxy merger: multi-phase, galaxy-scale outflows with a fast molecular gas blob 6 kpc away from iras f08572+3915. **Astronomy & Astrophysics**, 2019. Available at: https://api.semanticscholar.org/CorpusID:208076407.

HICKOX, R. C.; ALEXANDER, D. M. Obscured active galactic nuclei. **Annual Review of Astronomy and Astrophysics**, Annual Reviews, v. 56, p. 625–671, 2018.

HÖGBOM, J. Aperture synthesis with a non-regular distribution of interferometer baselines. **Astronomy and Astrophysics Supplement, Vol. 15, p. 417**, v. 15, p. 417, 1974.

HÖNIG, S. F.; KISHIMOTO, M. Dusty winds in active galactic nuclei: reconciling observations with models. **The Astrophysical Journal Letters**, IOP Publishing, v. 838, n. 2, p. L20, 2017.

HOPKINS, P. F.; HAYWARD, C. C.; NARAYANAN, D.; HERNQUIST, L. The origins of active galactic nuclei obscuration: the 'torus' as a dynamical, unstable driver of accretion. **Monthly Notices of the Royal Astronomical Society**, The Royal Astronomical Society, v. 420, n. 1, p. 320–339, 2012.

HOPKINS, P. F.; HERNQUIST, L.; COX, T. J.; MATTEO, T. D.; MARTINI, P.; ROBERTSON, B.; SPRINGEL, V. Black holes in galaxy mergers: evolution of quasars. **The Astrophysical Journal**, IOP Publishing, v. 630, n. 2, p. 705, 2005.

HOPKINS, P. F.; HERNQUIST, L.; COX, T. J.; MATTEO, T. D.; ROBERTSON, B.; SPRINGEL, V. A unified, merger-driven model of the origin of starbursts, quasars, the cosmic x-ray background, supermassive black holes, and galaxy spheroids. **The Astrophysical Journal Supplement Series**, IOP Publishing, v. 163, n. 1, p. 1, 2006.

HOPKINS, P. F.; QUATAERT, E.; MURRAY, N. Stellar feedback in galaxies and the origin of galaxy-scale winds. **Monthly Notices of the Royal Astronomical Society**, v. 421, p. 3522–3537, 2011. Available at: https://api.semanticscholar.org/CorpusID:55334702.

HUNT, L.; MALKAN, M. Morphology of the 12 micron seyfert galaxies. i. hubble types, axial ratios, bars, and rings. **The Astrophysical Journal**, IOP Publishing, v. 516, n. 2, p. 660, 1999.

HUNT, L. K.; COMBES, F.; GARCÍA-BURILLO, S.; SCHINNERER, E.; KRIPS, M.; BAKER, A. J.; BOONE, F.; ECKART, A.; LÉON, S.; NERI, R. *et al.* Molecular gas in nuclei of galaxies (nuga)-ix. the decoupled bars and gas inflow in ngc 2782. **Astronomy & Astrophysics**, EDP Sciences, v. 482, n. 1, p. 133–150, 2008.

HUSEMANN, B.; DAVIS, T.; JAHNKE, K.; DANNERBAUER, H.; URRUTIA, T.; HODGE, J. Integral field spectroscopy of nearby quasi-stellar objects–ii. molecular gas content and conditions for star formation. **Monthly Notices of the Royal Astronomical Society**, Oxford University Press, v. 470, n. 2, p. 1570–1586, 2017.

ISHIBASHI, W. Agn anisotropic radiative feedback set by black hole spin. **Monthly Notices of the Royal Astronomical Society**, Oxford University Press, v. 495, n. 2, p. 2515–2523, 2020.

ISHIBASHI, W.; FABIAN, A. C. Agn feedback: galactic-scale outflows driven by radiation pressure on dust. **Monthly Notices of the Royal Astronomical Society**, Oxford University Press, v. 451, n. 1, p. 93–102, 2015.

ISHIBASHI, W.; FABIAN, A. C. Agn feedback: galactic-scale outflows driven by radiation pressure on dust. **Monthly Notices of the Royal Astronomical Society**, v. 451, p. 93–102, 2015. Available at: https://api.semanticscholar.org/CorpusID:119275048.

JAFFE, W.; MEISENHEIMER, K.; RÖTTGERING, H.; LEINERT, C.; RICHICHI, A.; CHESNEAU, O.; FRAIX-BURNET, D.; GLAZENBORG-KLUTTIG, A.; GRANATO, G.-L.; GRASER, U. *et al.* The central dusty torus in the active nucleus of ngc 1068. **Nature**, Nature Publishing Group UK London, v. 429, n. 6987, p. 47–49, 2004.

JARRETT, T.; CHESTER, T.; CUTRI, R.; SCHNEIDER, S.; HUCHRA, J. The 2mass large galaxy atlas. **The Astronomical Journal**, IOP Publishing, v. 125, n. 2, p. 525, 2003.

JR, R. C. K. The global schmidt law in star-forming galaxies. **The astrophysical journal**, IOP Publishing, v. 498, n. 2, p. 541, 1998.

JR, R. C. K.; EVANS, N. J. Star formation in the milky way and nearby galaxies. **Annual Review of Astronomy and Astrophysics**, Annual Reviews, v. 50, n. 1, p. 531–608, 2012.

JUST, D. W.; BRANDT, W.; SHEMMER, O.; STEFFEN, A.; SCHNEIDER, D.; CHARTAS, G.; GARMIRE, G. The x-ray properties of the most luminous quasars from the sloan digital sky survey. **The Astrophysical Journal**, IOP Publishing, v. 665, n. 2, p. 1004, 2007.

KAMENETZKY, J.; PRIVON, G.; NARAYANAN, D. Recovering the physical properties of molecular gas in galaxies from co sled modeling. **The Astrophysical Journal**, IOP Publishing, v. 859, n. 1, p. 9, 2018.

KAMENETZKY, J.; RANGWALA, N.; GLENN, J.; MALONEY, P.; CONLEY, A. Relations with co rotational ladders of galaxies across the herschel spire archive. **The Astrophysical Journal**, IOP Publishing, v. 829, n. 2, p. 93, 2016.

KAMMOUN, E.; PAPADAKIS, I.; DOVČIAK, M. Modelling the uv/optical continuum time-lags in agn. **Monthly Notices of the Royal Astronomical Society**, Oxford University Press, v. 503, n. 3, p. 4163–4171, 2021.

KAROUZOS *et al.* A tale of two feedbacks: star formation in the host galaxies of radio agns. **The Astrophysical Journal**, IOP Publishing, v. 784, n. 2, p. 137, 2014.

Kianfar, K.; Andreani, P.; Fernández-Ontiveros, J. A.; Combes, F.; Spinoglio, L.; Hatziminaoglou, E.; Ricci, C.; Bewketu-Belete, A.; Imanishi, M.; Pereira-Santaella, M.; Slater, R.; Malheiro, M. Agn feeding along a one-armed spiral in ngc 4593 - a study using alma co(2–1) observations. **A&A**, v. 691, p. A118, 2024. Available at: https://doi.org/10.1051/0004-6361/202451185.

KING, A. Black holes, galaxy formation, and the mbh-σ relation. **The Astrophysical Journal**, IOP Publishing, v. 596, n. 1, p. L27, 2003.

KING, A. R.; POUNDS, K. A. Powerful outflows and feedback from active galactic nuclei. **arXiv: Astrophysics of Galaxies**, 2015. Available at: https://api.semanticscholar.org/CorpusID:118494522.

KORMENDY, J.; CORNELL, M. E.; BLOCK, D. L.; KNAPEN, J. H.; ALLARD, E. L. Pseudobulges in the disk galaxies ngc 7690 and ngc 4593. **The Astrophysical Journal**, IOP Publishing, v. 642, n. 2, p. 765, 2006.

KORMENDY, J.; HO, L. C. Coevolution (or not) of supermassive black holes and host galaxies. **Annual Review of Astronomy and Astrophysics**, Annual Reviews, v. 51, n. 1, p. 511–653, 2013.

KORMENDY, J.; RICHSTONE, D. Inward bound—the search for supermassive black holes in galactic nuclei. **Annual Review of Astronomy and Astrophysics, Volume 33, 1995, pp. 581.**, v. 33, p. 581, 1995.

KRAJNOVIC, D.; CAPPELLARI, M.; ZEEUW, P. T. D.; COPIN, Y. Kinemetry: a generalization of photometry to the higher moments of the line-of-sight velocity distribution. **Monthly Notices of the Royal Astronomical Society**, The Royal Astronomical Society, v. 366, n. 3, p. 787–802, 2006.

KUMARI, K.; DEWANGAN, G.; PAPADAKIS, I.; BEARD, M. W.; MCHARDY, I.; SINGH, K.; BHATTACHARYA, D.; BHATTACHARYYA, S.; CHANDRA, S. Contrasting x-ray/uv time-lags in seyfert 1 galaxies ngc 4593 and ngc 7469 using astrosat observations. **Monthly Notices of the Royal Astronomical Society**, Oxford University Press, v. 521, n. 3, p. 4109–4121, 2023.

LADA, C. J.; LOMBARDI, M.; ALVES, J. F. On the star formation rates in molecular clouds. **The Astrophysical Journal**, IOP Publishing, v. 724, n. 1, p. 687, 2010.

LAHA, S.; REYNOLDS, C. S.; REEVES, J.; KRISS, G.; GUAINAZZI, M.; SMITH, R.; VEILLEUX, S.; PROGA, D. Ionized outflows from active galactic nuclei as the essential elements of feedback. **Nature Astronomy**, Nature Publishing Group UK London, v. 5, n. 1, p. 13–24, 2021.

LAINE, S. Ngc 7479: A case study. **Astrophysics and Space Science**, Springer, v. 276, p. 667–674, 2001.

LAMASSA, S. M.; HECKMAN, T. M.; PTAK, A. F.; MARTINS, L. P.; WILD, V.; SONNENTRUCKER, P. Indicators of intrinsic active galactic nucleus luminosity: A multi-wavelength approach. **The Astrophysical Journal**, v. 720, p. 786 – 810, 2010. Available at: https://api.semanticscholar.org/CorpusID:118679543.

LEITHERER, C.; CALZETTI, D.; MARTINS, L. P. Ultraviolet spectra of star-forming galaxies with time-dependent dust obscuration. **The Astrophysical Journal**, IOP Publishing, v. 574, n. 1, p. 114, 2002.

LI, A.; MARASCO, A.; FRATERNALI, F.; TRAGER, S.; VERHEIJEN, M. A. A kinematic analysis of ionized extraplanar gas in the spiral galaxies ngc 3982 and ngc 4152. **Monthly Notices of the Royal Astronomical Society**, Oxford University Press, v. 504, n. 2, p. 3013–3028, 2021.

LÓPEZ-GONZAGA, N.; JAFFE, W.; BURTSCHER, L.; TRISTRAM, K.; MEISENHEIMER, K. Revealing the large nuclear dust structures in ngc 1068 with midi/vlti. **Astronomy & Astrophysics**, EDP Sciences, v. 565, p. A71, 2014.

LUSSO, E.; COMASTRI, A.; SIMMONS, B.; MIGNOLI, M.; ZAMORANI, G.; VIGNALI, C.; BRUSA, M.; SHANKAR, F.; LUTZ, D.; TRUMP, J. *et al.* Bolometric luminosities and eddington ratios of x-ray selected active galactic nuclei in the xmm-cosmos survey. **Monthly Notices of the Royal Astronomical Society**, Blackwell Science Ltd Oxford, UK, v. 425, n. 1, p. 623–640, 2012.

LYNDEN-BELL, D. Galactic nuclei as collapsed old quasars. **Nature**, v. 223, n. 5207, 1969.

MACCAGNI *et al.* Agn feeding and feedback in fornax a-kinematical analysis of the multi-phase ism. **Astronomy & Astrophysics**, EDP Sciences, v. 656, p. A45, 2021.

MADAU, P.; DICKINSON, M. Cosmic star-formation history. **Annual Review of Astronomy and Astrophysics**, Annual Reviews, v. 52, n. 1, p. 415–486, 2014.

MAGORRIAN *et al.* The demography of massive dark objects in galaxy centers. **The Astronomical Journal**, IOP Publishing, v. 115, n. 6, p. 2285, 1998.

MAIOLINO, R.; GALLERANI, S.; NERI, R.; CICONE, C.; FERRARA, A.; GENZEL, R.; LUTZ, D.; STURM, E.; TACCONI, L.; WALTER, F. *et al.* Evidence of strong quasar feedback in the early universe. **Monthly Notices of the Royal Astronomical Society: Letters**, The Royal Astronomical Society, v. 425, n. 1, p. L66–L70, 2012.

MALKAN, M. A.; GORJIAN, V.; TAM, R. A hubble space telescope* imaging survey of nearby active galactic nuclei. **The Astrophysical Journal Supplement Series**, IOP Publishing, v. 117, n. 1, p. 25, 1998.

MANGALAM, A.; WIITA, P. J. The changing interstellar medium of massive elliptical galaxies and cosmic evolution of radio galaxies and quasars. **Monthly Notices of the Royal Astronomical Society**, Blackwell Publishing Ltd Oxford, UK, v. 397, n. 4, p. 2216–2224, 2009.

MARASCO, A.; FRATERNALI, F.; HEALD, G.; BLOK, W. de; OOSTERLOO, T.; KAMPHUIS, P.; JÓZSA, G.; VARGAS, C.; WINKEL, B.; WALTERBOS, R. *et al.* Halogas: the properties of extraplanar hi in disc galaxies. **Astronomy & Astrophysics**, EDP Sciences, v. 631, p. A50, 2019.

MARINOVA, I.; JOGEE, S. Characterizing bars at z˜ 0 in the optical and nir: Implications for the evolution of barred disks with redshift. **The Astrophysical Journal**, IOP Publishing, v. 659, n. 2, p. 1176, 2007.

MARTIN, C. L. Mapping large-scale gaseous outflows in ultraluminous infrared galaxies with keck ii esi spectra: Spatial extent of the outflow. **The Astrophysical Journal**, v. 647, p. 222 – 243, 2006. Available at: https://api.semanticscholar.org/CorpusID:119338312.

MATTEO, T. D.; COLBERG, J.; SPRINGEL, V.; HERNQUIST, L.; SIJACKI, D. Direct cosmological simulations of the growth of black holes and galaxies. **The Astrophysical Journal**, IOP Publishing, v. 676, n. 1, p. 33, 2008.

MATTEO, T. D.; SPRINGEL, V.; HERNQUIST, L. Energy input from quasars regulates the growth and activity of black holes and their host galaxies. **nature**, Nature Publishing Group UK London, v. 433, n. 7026, p. 604–607, 2005.

MCALARY, C. W.; MCLAREN, R.; MCGONEGAL, R.; MAZA, J. A near-infrared and optical study of x-ray selected seyfert galaxies. i-observations. **The Astrophysical Journal Supplement Series**, v. 52, p. 341–362, 1983.

MCKEE, C. F.; OSTRIKER, E. C. Theory of star formation. **Annu. Rev. Astron. Astrophys.**, Annual Reviews, v. 45, n. 1, p. 565–687, 2007.

MCKINLEY, B. *et al.* Multi-scale feedback and feeding in the closest radio galaxy centaurus a. **Nature Astronomy**, v. 6, p. 109–120, 2021. Available at: https://api.semanticscholar.org/CorpusID:242757213.

MCKINNEY, J. C.; TCHEKHOVSKOY, A.; BLANDFORD, R. D. General relativistic magnetohydrodynamic simulations of magnetically choked accretion flows around black holes. **Monthly Notices of the Royal Astronomical Society**, Blackwell Publishing Ltd Oxford, UK, v. 423, n. 4, p. 3083–3117, 2012.

MCNAMARA, B.; NULSEN, P. Heating hot atmospheres with active galactic nuclei. **Annu. Rev. Astron. Astrophys.**, Annual Reviews, v. 45, p. 117–175, 2007.

MCNAMARA, B.; NULSEN, P. Mechanical feedback from active galactic nuclei in galaxies, groups and clusters. **New Journal of Physics**, IOP Publishing, v. 14, n. 5, p. 055023, 2012.

MERLONI, A. *et al.* The incidence of obscuration in active galactic nuclei. **Monthly Notices of the Royal Astronomical Society**, v. 437, p. 3550–3567, 2013. Available at: https://api.semanticscholar.org/CorpusID:55396130.

MILEY, G. K.; BREUCK, C. de. Distant radio galaxies and their environments. **The Astronomy and Astrophysics Review**, v. 15, p. 67–144, 2008.

MINGOZZI, M.; CRESCI, G.; VENTURI, G.; MARCONI, A.; MANNUCCI, F.; PERNA, M.; BELFIORE, F.; CARNIANI, S.; BALMAVERDE, B.; BRUSA, M. *et al.* The magnum survey: different gas properties in the outflowing and disc components in nearby active galaxies with muse. **Astronomy & Astrophysics**, EDP Sciences, v. 622, p. A146, 2019.

MORDINI, S.; SPINOGLIO, L.; FERNÁNDEZ-ONTIVEROS, J. A. Calibration of mid-to far-infrared spectral lines in galaxies. **Astronomy & Astrophysics**, EDP Sciences, v. 653, p. A36, 2021.

MORGANTI, R. The many routes to agn feedback. **Frontiers in Astronomy and Space Sciences**, Frontiers, v. 4, p. 42, 2017.

MORGANTI, R.; TADHUNTER, C. N.; OOSTERLOO, T. A. Fast neutral outflows in powerful radio galaxies: a major source of feedback in massive galaxies. **Astronomy & Astrophysics**, EDP Sciences, v. 444, n. 1, p. L9–L13, 2005.

MORRIS, M.; POLISH, N.; ZUCKERMAN, B.; KAIFU, N. The temperature of molecular gas in the galactic center region. **Astronomical Journal (ISSN 0004-6256), vol. 88, Aug. 1983, p. 1228-1235.**, v. 88, p. 1228–1235, 1983.

MOUNTRICHAS, G.; BUAT, V.; GEORGANTOPOULOS, I.; YANG, G.; MASOURA, V.; BOQUIEN, M.; BURGARELLA, D. Galaxy properties of type 1 and 2 x-ray selected agn and a comparison among different classification criteria. **Astronomy & Astrophysics**, EDP Sciences, v. 653, p. A70, 2021.

MULCHAEY, J. S.; REGAN, M. W. A survey for bars in seyfert galaxies. **Astrophysical Journal Letters**, v. 482, p. L135, 1997.

MURRAY, N.; M'ENARD, B.; THOMPSON, T. A. Radiation pressure from massive star clusters as a launching mechanism for super-galactic winds. **The Astrophysical Journal**, v. 735, 2010. Available at: https://api.semanticscholar.org/CorpusID:119238458.

NAGAR, N. M.; OLIVA, E.; MARCONI, A.; MAIOLINO, R. Ngc 5506 unmasked as a narrow line seyfert 1:-a direct view of the broad line region using near-ir spectroscopy. **Astronomy & Astrophysics**, EDP Sciences, v. 391, n. 2, p. L21–L24, 2002.

NATH, B. B.; SILK, J. I. Starburst-driven galactic outflows. **Monthly Notices of the Royal Astronomical Society: Letters**, v. 396, 2009. Available at: https://api.semanticscholar.org/CorpusID:17891405.

NEELEMAN, M.; KANEKAR, N.; PROCHASKA, J. X.; RAFELSKI, M.; CARILLI, C. L.; WOLFE, A. M. [c ii] 158-μm emission from the host galaxies of damped lyman-alpha systems. **Science**, American Association for the Advancement of Science, v. 355, n. 6331, p. 1285–1288, 2017.

NESVADBA, N. P. H.; DROUART, G.; BREUCK, C. de; BEST, P. N.; SEYMOUR, N.; VERNET, J. Gas kinematics in powerful radio galaxies at z 2: Energy supply from star formation, agn, and radio jets. **Astronomy and Astrophysics**, v. 600, 2016. Available at: https://api.semanticscholar.org/CorpusID:62810380.

NEUGEBAUER, G.; HABING, H.; DUINEN, R. V.; AUMANN, H.; BAUD, B.; BEICHMAN, C.; BEINTEMA, D.; BOGGESS, N.; CLEGG, P.; JONG, T. D. *et al.* The infrared astronomical satellite (iras) mission. **Astrophysical Journal, Part 2-Letters to the Editor (ISSN 0004-637X), vol. 278, March 1, 1984, p. L1-L6. Research supported by the Science and Engineering Research Council and NASA.**, v. 278, p. L1–L6, 1984.

NODA, H.; DONE, C. Explaining changing-look agn with state transition triggered by rapid mass accretion rate drop. **Monthly Notices of the Royal Astronomical Society**, v. 480, n. 3, p. 3898–3906, 08 2018. ISSN 0035-8711. Available at: https://doi.org/10.1093/mnras/sty2032.

NOVAK, G. S.; OSTRIKER, J. P.; CIOTTI, L. Radiative transfer and radiative driving of outflows in active galactic nuclei and starbursts. **Monthly Notices of the Royal Astronomical Society**, v. 427, p. 2734–2756, 2012. Available at: https://api.semanticscholar.org/CorpusID:118458376.

OHSUGA, K.; MINESHIGE, S. Global structure of three distinct accretion flows and outflows around black holes from two-dimensional radiation-magnetohydrodynamic simulations. **The Astrophysical Journal**, IOP Publishing, v. 736, n. 1, p. 2, 2011.

OLIVARES, V.; SALOMÉ, P.; HAMER, S.; COMBES, F.; GASPARI, M.; KOLOKYTHAS, K.; O'SULLIVAN, E.; BECKMANN, R.; BABUL, A.; POLLES, F. *et al.* Gas condensation in brightest group galaxies unveiled with muse-morphology and kinematics of the ionized gas. **Astronomy & Astrophysics**, EDP Sciences, v. 666, p. A94, 2022.

OSTERBROCK, D. E.; FERLAND, G. J. **Astrophysics Of Gas Nebulae and Active Galactic Nuclei**. [*S.l.*]: University science books, 2006.

OSTRIKER, E. C.; SHETTY, R. Maximally star-forming galactic disks. i. starburst regulation via feedback-driven turbulence. **The Astrophysical Journal**, IOP Publishing, v. 731, n. 1, p. 41, 2011.

PADOVANI, P. *et al.* Active galactic nuclei: what's in a name? **The Astronomy and Astrophysics Review**, Springer, v. 25, p. 1–91, 2017.

PAPADOPOULOS, P. P.; WERF, P. Van der; ISAAK, K.; XILOURIS, E. M. Co spectral line energy distributions of infrared-luminous galaxies and active galactic nuclei. **The Astrophysical Journal**, IOP Publishing, v. 715, n. 2, p. 775, 2010.

PATRA, N. N. Theoretical modelling of two-component molecular discs in spiral galaxies. **Astronomy & Astrophysics**, EDP Sciences, v. 638, p. A66, 2020.

PEI, Y. C.; FALL, S. M.; HAUSER, M. G. Cosmic histories of stars, gas, heavy elements, and dust in galaxies. **The Astrophysical Journal**, IOP Publishing, v. 522, n. 2, p. 604, 1999.

PEREIRA-SANTAELLA, M. *et al.* Herschel/spire submillimeter spectra of local active galaxies. **The Astrophysical Journal**, IOP Publishing, v. 768, n. 1, p. 55, 2013.

PEREIRA-SANTAELLA, M.; SPINOGLIO, L.; WERF, P. P. van der; LÓPEZ, J. P. Warm molecular gas temperature distribution in six local infrared bright seyfert galaxies. **Astronomy & Astrophysics**, EDP Sciences, v. 566, p. A49, 2014.

PERNA, M. *et al.* Galaxy-wide outflows in z˜ 1.5 luminous obscured quasars revealed through near-ir slit-resolved spectroscopy. **Astronomy & Astrophysics**, EDP Sciences, v. 574, p. A82, 2015.

PHOOKUN, B.; VOGEL, S. N.; MUNDY, L. G. Ngc 4254: a spiral galaxy with an m= 1 mode and infalling gas. **Astrophysical Journal v. 418, p. 113**, v. 418, p. 113, 1993.

PINTO, C.; MIDDLETON, M. J.; FABIAN, A. C. Resolved atomic lines reveal outflows in two ultraluminous x-ray sources. **Nature**, Nature Publishing Group UK London, v. 533, n. 7601, p. 64–67, 2016.

PITCHFORD, L.; HATZIMINAOGLOU, E.; FELTRE, A.; FARRAH, D.; CLARKE, C.; HARRIS, K.; HURLEY, P.; OLIVER, S.; PAGE, M.; WANG, L. Extreme star formation events in quasar hosts over 0.5< z< 4. **Monthly Notices of the Royal Astronomical Society**, The Royal Astronomical Society, v. 462, n. 4, p. 4067–4077, 2016.

POULIASIS, E.; MOUNTRICHAS, G.; GEORGANTOPOULOS, I.; RUIZ, A.; YANG, M.; BONANOS, A. Z. An obscured agn population hidden in the vipers galaxies:

identification through spectral energy distribution decomposition. **Monthly Notices of the Royal Astronomical Society**, v. 495, p. 1853–1873, 2020. Available at: https://api.semanticscholar.org/CorpusID:218502453.

RICCI, C.; PRIVON, G. C.; PFEIFLE, R. W.; ARMUS, L.; IWASAWA, K.; TORRES-ALBÀ, N.; SATYAPAL, S.; BAUER, F. E.; TREISTER, E.; HO, L. C.; AALTO, S.; ARÉVALO, P.; BARCOS-MUÑOZ, L.; CHARMANDARIS, V.; DÍAZ-SANTOS, T.; EVANS, A. S.; GAO, T.; INAMI, H.; KOSS, M. J.; LANSBURY, G. B.; LINDEN, S. T.; MEDLING, A. M.; SANDERS, D. B.; SONG, Y.; STERN, D. K.; U, V.; UEDA, Y.; YAMADA, S. A hard x-ray view of luminous and ultra-luminous infrared galaxies in goals – i. agn obscuration along the merger sequence. **Monthly Notices of the Royal Astronomical Society**, 2021. Available at: https://api.semanticscholar.org/CorpusID:236318320.

RICCI, C.; RICCI, C.; BAUER, F. E.; TREISTER, E.; SCHAWINSKI, K.; PRIVON, G. C.; BLECHA, L.; ARÉVALO, P.; ARMUS, L.; HARRISON, F.; HO, L. C.; IWASAWA, K.; SANDERS, D. B.; STERN, D. K. Growing supermassive black holes in the late stages of galaxy mergers are heavily obscured. **Monthly Notices of the Royal Astronomical Society**, v. 468, p. 1273–1299, 2017. Available at: https://api.semanticscholar.org/CorpusID:119327207.

RICCI, C.; TRAKHTENBROT, B.; KOSS, M. J.; UEDA, Y.; VECCHIO, I. D.; TREISTER, E.; SCHAWINSKI, K.; PALTANI, S.; OH, K.; LAMPERTI, I. *et al.* Bat agn spectroscopic survey. v. x-ray properties of the swift/bat 70-month agn catalog. **The Astrophysical Journal Supplement Series**, IOP Publishing, v. 233, n. 2, p. 17, 2017.

RICHARDS, G. T.; HALL, P. B. Agn physics with the sloan digital sky survey. *In*: **AGN Physics with the Sloan Digital Sky Survey**. **Proceedings** [...]. [*S.l.: s.n.*], 2004. v. 311.

ROBERTS-BORSANI, G.; SAINTONGE, A. The prevalence and properties of cold gas inflows and outflows around galaxies in the local universe. **Monthly Notices of the Royal Astronomical Society**, Oxford University Press, v. 482, n. 3, p. 4111–4145, 2019.

ROSARIO, D. *et al.* The mean star formation rate of x-ray selected active galaxies and its evolution from z 2.5: Results from pep-herschel. **Astronomy & Astrophysics**, v. 560, p. A72, 2013.

RUPKE, D. S.; VEILLEUX, S.; SANDERS, D. Outflows in infrared-luminous starbursts at z< 0.5. i. sample, na i d spectra, and profile fitting. **The Astrophysical Journal Supplement Series**, IOP Publishing, v. 160, n. 1, p. 87, 2005.

RUSH, B.; MALKAN, M. A. The soft-x-ray spectral shape of x-ray-weak seyferts. **arXiv preprint astro-ph/9507110**, 1995.

RUSH, B.; MALKAN, M. A.; EDELSON, R. A. The radio properties of seyfert galaxies in the 12 micron and cfa samples. **The Astrophysical Journal**, IOP Publishing, v. 473, n. 1, p. 130, 1996.

RUSH, B.; MALKAN, M. A.; SPINOGLIO, L. The extended 12 micron galaxy sample. **The Astrophysical Journal Supplement Series**, v. 89, n. 1, p. 1, 1993.

SABATINI, G.; GRUPPIONI, C.; MASSARDI, M.; GIANNETTI, A.; BURKUTEAN, S.; CIMATTI, A.; POZZI, F.; TALIA, M. Unveiling the inner morphology and gas kinematics of ngc 5135 with alma. **Monthly Notices of the Royal Astronomical Society**, Oxford University Press, v. 476, n. 4, p. 5417–5431, 2018.

SAINTONGE, A. *et al.* The impact of interactions, bars, bulges, and active galactic nuclei on star formation efficiency in local massive galaxies. **The Astrophysical Journal**, IOP Publishing, v. 758, n. 2, p. 73, 2012.

SALOMÉ, Q.; KRONGOLD, Y.; LONGINOTTI, A. L.; BISCHETTI, M.; GARCÍA-BURILLO, S.; VEGA, O.; SÁNCHEZ-PORTAL, M.; FERUGLIO, C.; JIMÉNEZ-DONAIRE, M. J.; ZANCHETTIN, M. V. Star formation efficiency and agn feedback in narrow-line seyfert 1 galaxies with fast x-ray nuclear winds. **Monthly Notices of the Royal Astronomical Society**, Oxford University Press, v. 524, n. 2, p. 3130–3145, 2023.

SANDERS, D.; MIRABEL, I. Luminous infrared galaxies. **Annual Review of Astronomy and Astrophysics**, Palo Alto, Calif., USA: Annual Reviews, c1963-, v. 34, n. 1, p. 749–792, 1996.

SCANNAPIECO, E. Understanding galaxy outflows as the product of unstable turbulent support. **The Astrophysical Journal Letters**, v. 763, 2013. Available at: https://api.semanticscholar.org/CorpusID:118390953.

SCANNAPIECO, E. The production of cold gas within galaxy outflows. **The Astrophysical Journal**, v. 837, 2017. Available at: https://api.semanticscholar.org/CorpusID:119358046.

SCHAWINSKI, K.; THOMAS, D.; SARZI, M.; MARASTON, C.; KAVIRAJ, S.; JOO, S.-J.; YI, S. K.; SILK, J. Observational evidence for agn feedback in early-type galaxies. **Monthly Notices of the Royal Astronomical Society**, Blackwell Publishing Ltd Oxford, UK, v. 382, n. 4, p. 1415–1431, 2007.

SCHINNERER, E.; LEROY, A. K. Molecular gas and the star-formation process on cloud scales in nearby galaxies. **Annual Review of Astronomy and Astrophysics**, Annual Reviews, v. 62, p. 369–436, 2024.

SCHMIDT, M. **3C 273: A Star-Like Object with Large Red-Shift., 197 (4872): 1040**. [*S.l.*]: March, 1963.

SCHMITT, H. R. The difference between the narrow-line regions of seyfert 1 and seyfert 2 galaxies. **The Astrophysical Journal**, IOP Publishing, v. 506, n. 2, p. 647, 1998.

SCHNEIDER, E. E.; OSTRIKER, E. C.; ROBERTSON, B. E.; THOMPSON, T. A. The physical nature of starburst-driven galactic outflows. **The Astrophysical Journal**, v. 895, 2020. Available at: https://api.semanticscholar.org/CorpusID:211296542.

SCHNEIDER, E. E.; ROBERTSON, B. E.; THOMPSON, T. A. Production of cool gas in thermally driven outflows. **The Astrophysical Journal**, v. 862, 2018. Available at: https://api.semanticscholar.org/CorpusID:119390955.

SCHNORR-MÜLLER, A.; STORCHI-BERGMANN, T.; NAGAR, N. M.; ROBINSON, A.; LENA, D.; RIFFEL, R. A.; COUTO, G. S. Feeding and feedback in the inner kiloparsec of the active galaxy ngc 2110. **Monthly Notices of the Royal Astronomical Society**, Oxford University Press, v. 437, n. 2, p. 1708–1724, 2014.

SCHOLTZ, J. *et al.* Identifying the subtle signatures of feedback from distant agn using alma observations and the eagle hydrodynamical simulations. **Monthly Notices of the Royal Astronomical Society**, Oxford University Press, v. 475, n. 1, p. 1288–1305, 2018.

SCHOMBERT, J.; MCGAUGH, S.; LELLI, F. The mass-to-light ratios and the star formation histories of disc galaxies. **Monthly Notices of the Royal Astronomical Society**, Oxford University Press, v. 483, n. 2, p. 1496–1512, 2019.

SCOVILLE, N. *et al.* Evolution of interstellar medium, star formation, and accretion at high redshift. **The Astrophysical Journal**, IOP Publishing, v. 837, n. 2, p. 150, 2017.

SELLWOOD, J.; SPEKKENS, K. Diskfit: a code to fit simple non-axisymmetric galaxy models either to photometric images or to kinematic maps. **arXiv preprint arXiv:1509.07120**, 2015.

SEYFERT, C.; LANG, K.; GINGERICH, O. e. K. R. Nuclear emission in spiral nebulae. *In*: **A Source Book in Astronomy and Astrophysics, 1900–1975**. [*S.l.*]: Harvard University Press, 1979. p. 738–743.

SHAKURA, N. I.; SUNYAEV, R. A. Black holes in binary systems. observational appearance. **Astronomy and Astrophysics, Vol. 24, p. 337-355**, v. 24, p. 337–355, 1973.

SHAW, M.; AXON, D.; PROBST, R.; GATLEY, I. Nuclear bars and blue nuclei within barred spiral galaxies. **Monthly Notices of the Royal Astronomical Society**, The Royal Astronomical Society, v. 274, n. 2, p. 369–387, 1995.

SHU, X.; YAQOOB, T.; MURPHY, K.; BRAITO, V.; WANG, J.; ZHENG, W. Ngc 2992 in an x-ray high state observed by xmm-newton: Response of the relativistic fe kα line to the continuum. **The Astrophysical Journal**, IOP Publishing, v. 713, n. 2, p. 1256, 2010.

SIKORA, M.; STAWARZ Łukasz; LASOTA, J. Radio loudness of active galactic nuclei: Observational facts and theoretical implications. **The Astrophysical Journal**, v. 658, p. 815 – 828, 2006. Available at: https://api.semanticscholar.org/CorpusID:10154491.

SILK, J.; REES, M. J. Quasars and galaxy formation. **arXiv preprint astro-ph/9801013**, 1998.

SKRUTSKIE, M. *et al.* The two micron all sky survey (2mass). **The Astronomical Journal**, IOP Publishing, v. 131, n. 2, p. 1163, 2006.

SLATER, R. *et al.* Outflows in the inner kiloparsec of ngc 1566 as revealed by molecular (alma) and ionized gas (gemini-gmos/ifu) kinematics. **Astronomy & Astrophysics**, EDP Sciences, v. 621, p. A83, 2019.

SMITH, M. D.; BUREAU, M.; DAVIS, T. A.; CAPPELLARI, M.; LIU, L.; ONISHI, K.; IGUCHI, S.; NORTH, E. V.; SARZI, M. Wisdom project–vi. exploring the relation

between supermassive black hole mass and galaxy rotation with molecular gas. **Monthly Notices of the Royal Astronomical Society**, Oxford University Press, v. 500, n. 2, p. 1933–1952, 2021.

SÖDING, L.; EDENHOFER, G.; ENSSLIN, T. A.; FRANK, P.; KISSMANN, R.; PHAN, V. H. M.; RAMÍREZ, A.; ZHANDINEJAD, H.; MERTSCH, P. Spatially coherent 3d distributions of hi and co in the milky way. **arXiv preprint arXiv:2407.02859**, 2024.

SOLDI, S.; BECKMANN, V.; GEHRELS, N.; JONG, S. D.; LUBINSKI, P. High-energy emission from ngc 5506, the brightest hard x-ray narrow line seyfert 1 galaxy. **arXiv preprint arXiv:1105.5993**, 2011.

SOLOMON, P.; BOUT, P. V. Molecular gas at high redshift. **Annu. Rev. Astron. Astrophys.**, Annual Reviews, v. 43, p. 677–725, 2005.

SOLOMON, P.; SAGE, L. Star-formation rates, molecular clouds, and the origin of the far-infrared luminosity of isolated and interacting galaxies. **Astrophysical Journal, Part 1 (ISSN 0004-637X), vol. 334, Nov. 15, 1988, p. 613-625. NASA-supported research.**, v. 334, p. 613–625, 1988.

SORMANI, M. C.; BARNES, A. T. Mass inflow rate into the central molecular zone: observational determination and evidence of episodic accretion. **Monthly Notices of the Royal Astronomical Society**, Oxford University Press, v. 484, n. 1, p. 1213–1219, 2019.

SORMANI, M. C. *et al.* Fuelling the nuclear ring of ngc 1097. **Monthly Notices of the Royal Astronomical Society**, Oxford University Press, v. 523, n. 2, p. 2918–2927, 2023.

SPEKKENS, K.; SELLWOOD, J. Modeling noncircular motions in disk galaxies: Application to ngc 2976. **The Astrophysical Journal**, IOP Publishing, v. 664, n. 1, p. 204, 2007.

SPINOGLIO, L.; FERNÁNDEZ-ONTIVEROS, J. A.; MALKAN, M. A. The spectral energy distributions and bolometric luminosities of local agn: Study of the complete 12 μm agn sample. **The Astrophysical Journal**, IOP Publishing, v. 964, n. 2, p. 117, 2024.

SPINOGLIO, L.; MALKAN, M. A.; RUSH, B.; CARRASCO, L.; RECILLAS-CRUZ, E. Multiwavelength energy distributions and bolometric luminosities of the 12–micron galaxy sample. **arXiv preprint astro-ph/9506139**, 1995.

SPRINGEL, V.; MATTEO, T. D.; HERNQUIST, L. Modelling feedback from stars and black holes in galaxy mergers. **Monthly Notices of the Royal Astronomical Society**, Blackwell Science Ltd Oxford, UK, v. 361, n. 3, p. 776–794, 2005.

SRIRAM, K.; AGRAWAL, V.; RAO, A. Energy-dependent time lags in the seyfert 1 galaxy ngc 4593. **The Astrophysical Journal**, IOP Publishing, v. 700, n. 2, p. 1042, 2009.

STALEVSKI, M.; RICCI, C.; UEDA, Y.; LIRA, P.; FRITZ, J.; BAES, M. The dust covering factor in active galactic nuclei. **Monthly Notices of the Royal Astronomical Society**, Oxford University Press, v. 458, n. 3, p. 2288–2302, 2016.

STORCHI-BERGMANN, T.; SCHNORR-MÜLLER, A. Observational constraints on the feeding of supermassive black holes. **Nature Astronomy**, Nature Publishing Group UK London, v. 3, n. 1, p. 48–61, 2019.

STORCHI-BERGMANN, T.; SCHNORR-MÜLLER, A. Observational constraints on the feeding of supermassive black holes. **Nature Astronomy**, v. 3, p. 48–61, 2019. Available at: https://api.semanticscholar.org/CorpusID:102352645.

STURM, E. *et al.* Massive molecular outflows and negative feedback in ulirgs observed by herschel-pacs. **The Astrophysical Journal Letters**, IOP Publishing, v. 733, n. 1, p. L16, 2011.

SUN, M.; XUE, Y.; BRANDT, W.; GU, W.-M.; TRUMP, J. R.; CAI, Z.; HE, Z.; LIN, D.-b.; LIU, T.; WANG, J. Corona-heated accretion-disk reprocessing: a physical model to decipher the melody of agn uv/optical twinkling. **The Astrophysical Journal**, IOP Publishing, v. 891, n. 2, p. 178, 2020.

SUN, S.; GUAINAZZI, M.; NI, Q.; WANG, J.; QIAN, C.; SHI, F.; WANG, Y.; BAMBI, C. Multi-epoch analysis of the x-ray spectrum of the active galactic nucleus in ngc 5506. **Monthly Notices of the Royal Astronomical Society**, Oxford University Press, v. 478, n. 2, p. 1900–1910, 2018.

TACCONI, L. J.; GENZEL, R.; STERNBERG, A. The evolution of the star-forming interstellar medium across cosmic time. **Annual Review of Astronomy and Astrophysics**, Annual Reviews, v. 58, n. 1, p. 157–203, 2020.

TEODORO, E. D.; FRATERNALI, F. 3d barolo: a new 3d algorithm to derive rotation curves of galaxies. **Monthly Notices of the Royal Astronomical Society**, Oxford University Press, v. 451, n. 3, p. 3021–3033, 2015.

THAKUR, P.; ANN, H.; JIANG, G. Effect of central mass concentration on the formation of nuclear spirals in barred galaxies. **The Astrophysical Journal**, IOP Publishing, v. 693, n. 1, p. 586, 2009.

THEAN, A.; PEDLAR, A.; KUKULA, M. J.; BAUM, S. A.; O'DEA, C. P. High-resolution radio observations of seyfert galaxies in the extended 12-μ m sample—i. the observations. **Monthly Notices of the Royal Astronomical Society**, Blackwell Science Ltd Oxford, UK, v. 314, n. 3, p. 573–588, 2000.

THOMPSON, T. A.; HECKMAN, T. M. Theory and observation of winds from star-forming galaxies. **Annual Review of Astronomy and Astrophysics**, v. 62, p. 529–591, 2024. Available at: https://api.semanticscholar.org/CorpusID:270440330.

THORNE, K. S. Disk-accretion onto a black hole. ii. evolution of the hole. **Astrophysical Journal, Vol. 191, pp. 507-520 (1974)**, v. 191, p. 507–520, 1974.

TILEY, A. L.; BUREAU, M.; SAINTONGE, A.; TOPAL, S.; DAVIS, T. A.; TORII, K. The tully–fisher relation of cold gass galaxies. **Monthly Notices of the Royal Astronomical Society**, Oxford University Press, v. 461, n. 4, p. 3494–3515, 2016.

TOMBESI, F. Tracing agn feedback, from the smbh horizon up to cluster scales. **Proceedings of the International Astronomical Union**, v. 15, p. 218 – 222, 2019. Available at: https://api.semanticscholar.org/CorpusID:233340289.

TOMBESI, F.; CAPPI, M.; REEVES, J.; NEMMEN, R. S.; BRAITO, V.; GASPARI, M.; REYNOLDS, C. S. Unification of x-ray winds in seyfert galaxies: from ultra-fast outflows to warm absorbers. **Monthly Notices of the Royal Astronomical Society**, Oxford University Press, v. 430, n. 2, p. 1102–1117, 2013.

TOMBESI, F.; MELÉNDEZ, M.; VEILLEUX, S.; REEVES, J.; GONZÁLEZ-ALFONSO, E.; REYNOLDS, C. Wind from the black-hole accretion disk driving a molecular outflow in an active galaxy. **Nature**, Nature Publishing Group UK London, v. 519, n. 7544, p. 436–438, 2015.

TOMMASIN, S.; SPINOGLIO, L.; MALKAN, M. A.; FAZIO, G. Spitzer-irs high-resolution spectroscopy of the 12 μm seyfert galaxies. ii. results for the complete data set. **The Astrophysical Journal**, IOP Publishing, v. 709, n. 2, p. 1257, 2010.

TORII, K.; ENOKIYA, R.; FUKUI, Y.; YAMAMOTO, H.; KAWAMURA, A.; MIZUNO, N.; ONISHI, T.; OGAWA, H. Detailed distributions of the co j=(2- 1)/j=(1-0) intensity ratios toward a large area of the central molecular zone. **Proceedings of the International Astronomical Union**, Cambridge University Press, v. 9, n. S303, p. 106–108, 2013.

TRESS, R. *et al.* Magnetic field morphology and evolution in the central molecular zone and its effect on gas dynamics. **arXiv preprint arXiv:2403.13048**, 2024.

URRY, C. M.; PADOVANI, P. Unified schemes for radio-loud active galactic nuclei. **Publications of the Astronomical Society of the Pacific**, v. 107, p. 803 – 803, 1995.

VAUCOULEURS, G. de; VAUCOULEURS, A. de; CORWIN, J.; BUTA, R.; PATUREL, G.; FOUQUÉ, P. **Third reference catalogue of bright galaxies**. [*S.l.*]: Springer, 1991.

VAZZA, F.; BRUNETTI, G.; GHELLER, C.; BRUNINO, R.; BRÜGGEN, M. Massive and refined-ii. the statistical properties of turbulent motions in massive galaxy clusters with high spatial resolution. **Astronomy & Astrophysics**, EDP Sciences, v. 529, p. A17, 2011.

VAZZA, F.; JONES, T. W.; BRÜGGEN, M.; BRUNETTI, G.; GHELLER, C.; PORTER, D.; RYU, D. Turbulence and vorticity in galaxy clusters generated by structure formation. **Monthly Notices of the Royal Astronomical Society**, Oxford University Press, v. 464, n. 1, p. 210–230, 2017.

VEILLEUX, S.; MAIOLINO, R.; BOLATTO, A. D.; AALTO, S. Cool outflows in galaxies and their implications. **The Astronomy and Astrophysics Review**, Springer, v. 28, p. 1–173, 2020.

WADA, K.; SCHARTMANN, M.; MEIJERINK, R. Multi-phase nature of a radiation-driven fountain with nuclear starburst in a low-mass active galactic nucleus. **The Astrophysical Journal Letters**, IOP Publishing, v. 828, n. 2, p. L19, 2016.

WAGNER, A.; UMEMURA, M.; BICKNELL, G. Ultrafast outflows: galaxy-scale active galactic nucleus feedback. **The Astrophysical Journal Letters**, IOP Publishing, v. 763, n. 1, p. L18, 2013.

WAGNER, A. Y.; UMEMURA, M.; BICKNELL, G. V. Ultrafast outflows: Galaxy-scale active galactic nucleus feedback. **The Astrophysical Journal Letters**, v. 763, 2012. Available at: https://api.semanticscholar.org/CorpusID:55230203.

WANG, Y.; HE, Z.; MAO, J.; KAASTRA, J.; XUE, Y.; MEHDIPOUR, M. Density profile of the ambient circumnuclear medium in seyfert 1 galaxies. **The Astrophysical Journal**, IOP Publishing, v. 928, n. 1, p. 7, 2022.

WEINBERGER, R.; SPRINGEL, V.; HERNQUIST, L.; PILLEPICH, A.; MARINACCI, F.; PAKMOR, R.; NELSON, D.; GENEL, S.; VOGELSBERGER, M.; NAIMAN, J.; TORREY, P. Simulating galaxy formation with black hole driven thermal and kinetic feedback. **Monthly Notices of the Royal Astronomical Society**, v. 465, n. 3, p. 3291–3308, 11 2016. ISSN 0035-8711. Available at: https://doi.org/10.1093/mnras/stw2944.

WEISS, A.; DOWNES, D.; WALTER, F.; HENKEL, C. Multiple co lines in smm j16359+ 6612–further evidence for a merger. **Astronomy & Astrophysics**, EDP Sciences, v. 440, n. 2, p. L45–L49, 2005.

WERF, P. P. o. van der. Black hole accretion and star formation as drivers of gas excitation and chemistry in markarian 231. **Astronomy & Astrophysics**, EDP Sciences, v. 518, p. L42, 2010.

WHITE, S. D.; REES, M. J. Core condensation in heavy halos: a two-stage theory for galaxy formation and clustering. **Monthly Notices of the Royal Astronomical Society**, Oxford University Press Oxford, UK, v. 183, n. 3, p. 341–358, 1978.

WOLF, C.; LAI, S.; ONKEN, C. A.; AMRUTHA, N.; BIAN, F.; HON, W. J.; TISSERAND, P.; WEBSTER, R. L. The accretion of a solar mass per day by a 17-billion solar mass black hole. **Nature Astronomy**, Nature Publishing Group UK London, v. 8, n. 4, p. 520–529, 2024.

WU, Y.; CHARMANDARIS, V.; HUANG, J.; SPINOGLIO, L.; TOMMASIN, S. Spitzer/irs 5–35 μm low-resolution spectroscopy of the 12 μm seyfert sample. **The Astrophysical Journal**, IOP Publishing, v. 701, n. 1, p. 658, 2009.

WU, Y.-T.; TREJO, A.; ESPADA, D.; MIYAMOTO, Y. Morphological and kinematical analysis of the double-barred galaxy ngc 3504 using alma co (2–1) data. **Monthly Notices of the Royal Astronomical Society**, Oxford University Press, v. 504, n. 3, p. 3111–3127, 2021.

YANG, G.; BOQUIEN, M.; BUAT, V.; BURGARELLA, D.; CIESLA, L.; DURAS, F.; STALEVSKI, M.; BRANDT, W.; PAPOVICH, C. X-cigale: Fitting agn/galaxy seds from x-ray to infrared. **Monthly Notices of the Royal Astronomical Society**, Oxford University Press, v. 491, n. 1, p. 740–757, 2020.

YANG, G. *et al.* Fitting agn/galaxy x-ray-to-radio seds with cigale and improvement of the code. **The Astrophysical Journal**, IOP Publishing, v. 927, n. 2, p. 192, 2022.

YANG, Q.; WU, X.-B.; FAN, X.; JIANG, L.; MCGREER, I.; SHANGGUAN, J.; YAO, S.; WANG, B.; JOSHI, R.; GREEN, R.; WANG, F.; FENG, X.; FU, Y.; YANG, J.; LIU, Y. Discovery of 21 new changing-look agns in the northern sky. **The Astrophysical**

Journal, The American Astronomical Society, v. 862, n. 2, p. 109, jul 2018. Available at: https://dx.doi.org/10.3847/1538-4357/aaca3a.

YUAN, F.; NARAYAN, R. Hot accretion flows around black holes. **Annual Review of Astronomy and Astrophysics**, v. 52, p. 529–588, 2014. Available at: https://api.semanticscholar.org/CorpusID:21704624.

ZANCHETTIN, M. V. *et al.* Ngc 2992: Interplay between the multiphase disc, wind, and radio bubbles. **Astronomy & Astrophysics**, EDP Sciences, v. 679, p. A88, 2023.

ZHUANG, M.-Y.; HO, L. C. Evolutionary paths of active galactic nuclei and their host galaxies. **The Astrophysical Journal**, v. 945, n. 2, p. 154, 2023.

ZUBOVAS, K.; KING, A. Clearing out a galaxy. **The Astrophysical Journal Letters**, IOP Publishing, v. 745, n. 2, p. L34, 2012.

ZUBOVAS, K.; KING, A. R. Galaxy-wide outflows: cold gas and star formation at high speeds. **Monthly Notices of the Royal Astronomical Society**, v. 439, p. 400–406, 2014. Available at: https://api.semanticscholar.org/CorpusID:55816989.

Appendix A - TWIST sample Photometry

TABLE A.1 – Photometry data for sample galaxies (Table 1)

id	xray boxcar 2to10keV	xray 14 195filter	FUV	NUV
NGC1386	-	-	0.0432 ± 4.32	1.63
ESO420-G13	-	-	-	-
NGC4845	-	-	0.36 ± 36.0	1.42 ± 142.0
IC5063	0.00283	0.000268 ± 0.0268	0.0441 ± 4.41	0.118 ± 11.8
NGC1365	0.00213	0.000251 ± 0.0251	46.1 ± 4610.0	64.3 ± 6430.0
NGC4412	-	-	2.99 ± 299.0	4.45 ± 445.0
NGC6890	-	-	0.0337 ± 3.37	0.0864 ± 8.64
NGC7314	0.00288	0.000227 ± 0.0227	0.0178 ± 1.78	0.0401 ± 4.01
NGC4594	-	-	23.3 ± 2330.0	34.0 ± 3400.0
IC3639	-	-	-	-
IC5169	-	-	0.0133 ± 1.33	0.0443 ± 4.43
NGC4941	0.000345	8e-05 ± 0.00797	2.91 ± 291.0	4.7 ± 470.0
NGC4501	-	-	12.5 ± 1250.0	25.4 ± 2540.0
NGC1097	-	-	33.1 ± 3310.0	49.7 ± 4970.0
NGC3627	-	-	31.6 ± 3160.0	58.6 ± 5860.0
NGC7213	0.000834	0.000154 ± 0.0154	-	-
NGC4486	-	-	4.55 ± 455.0	8.64 ± 864.0
NGC0424	0.013	8.5e-05 ± 0.0085	0.0716 ± 7.16	0.117 ± 11.7
NGC1052	0.000517	0.000124 ± 0.0124	0.661 ± 66.1	1.21
NGC4303	-	-	45.7 ± 4570.0	61.4 ± 6140.0
M-06-30-15	0.00287	0.000235 ± 0.0235	0.0293 ± 2.93	0.0759 ± 7.59
Mrk1333	-	-	0.0271 ± 2.71	0.0533 ± 5.33
NGC3169	-	-	6.25 ± 625.0	11.2 ± 1120.0
NGC7590	-	-	7.8 ± 780.0	11.4 ± 1140.0
NGC7496	-	-	0.739 ± 73.9	1.0 ± 100.0
NGC613	-	-	15.1 ± 1510.0	24.7 ± 2470.0
NGC1566	0.005	7.7e-05 ± 0.00772	55.2 ± 5520.0	67.3 ± 6730.0
NGC5806	-	-	1.69 ± 169.0	4.61 ± 461.0
NGC7582	0.035	0.000325 ± 0.0325	2.94 ± 294.0	6.79 ± 679.0
NGC4968	-	-	0.0107 ± 1.07	0.0236 ± 2.36
NGC1125	-	-	-	-
NGC4374	-	-	2.09 ± 209.0	2.73
NGC7172	0.00235	0.000632 ± 0.0632	-	-
NGC1320	-	-	0.0601 ± 6.01	0.0832 ± 8.32
NGC4418	-	-	-	-
NGC4593	0.00246	0.000349 ± 0.0349	1.48 ± 148.0	1.9 ± 190.0
NGC1068	0.0185	0.00015 ± 0.015	23.0 ± 2300.0	43.9 ± 4390.0
NGC5861	-	-	7.52 ± 752.0	11.4 ± 1140.0
NGC2992	0.000524	0.000129 ± 0.0129	1.45 ± 145.0	1.63 ± 163.0
NGC3976	-	-	4.02 ± 402.0	5.7 ± 570.0
NGC5506	0.00797	0.000946 ± 0.0946	0.0474 ± 4.74	0.107 ± 10.7

Notes: This table presents selected photometric properties for sample galaxies. Values marked '-' indicate unavailable data.

TABLE A.2 – Photometry data for sample galaxies (Table 2)

id	2mass J	2mass H	2mass Ks	spitzer irac ch1
NGC1386	108.0 ± 10800.0	137.0 ± 13700.0	121.0 ± 12100.0	201.0 ± 20100.0
ESO420-G13	49.7 ± 4970.0	42.6 ± 4260.0	61.4 ± 6140.0	-
NGC4845	477.0 ± 47700.0	64.3 ± 6430.0	472.0 ± 47200.0	258.0 ± 25800.0
IC5063	57.7 ± 5770.0	42.3 ± 4230.0	66.1 ± 6610.0	85.6 ± 8560.0
NGC1365	152.0 ± 15200.0	119.0 ± 11900.0	1640.0 ± 164000.0	1200.0 ± 120000.0
NGC4412	15.0 ± 1500.0	8.66 ± 866.0	15.6 ± 1560.0	50.3 ± 5030.0
NGC6890	42.8 ± 4280.0	28.3 ± 2830.0	47.2 ± 4720.0	44.5 ± 4450.0
NGC7314	23.9 ± 2390.0	13.4 ± 1340.0	345.0 ± 34500.0	29.7 ± 2970.0
NGC4594	623.0 ± 62300.0	410.0 ± 41000.0	652.0 ± 65200.0	3810.0 ± 381000.0
IC3639	41.4 ± 4140.0	33.2 ± 3320.0	46.3 ± 4630.0	50.7 ± 5070.0
IC5169	28.0 ± 2800.0	14.3 ± 1430.0	36.7 ± 3670.0	-
NGC4941	57.3 ± 5730.0	46.5 ± 4650.0	334.0 ± 33400.0	180.0 ± 18000.0
NGC4501	2080.0 ± 208000.0	2430.0 ± 243000.0	162.0 ± 16200.0	1070.0 ± 107000.0
NGC1097	195.0 ± 19500.0	2110.0 ± 211000.0	1860.0 ± 186000.0	1200.0 ± 120000.0
NGC3627	2940NGC0424.0 ± 294000.0	3410.0 ± 341000.0	2780.0 ± 278000.0	1740.0 ± 174000.0
NGC7213	197.0 ± 19700.0	245.0 ± 24500.0	211.0 ± 21100.0	174.0 ± 17400.0
NGC4486	227.0 ± 22700.0	284.0 ± 28400.0	2900.0 ± 290000.0	1390.0 ± 139000.0
NGC0424	33.3 ± 3330.0	39.5 ± 3950.0	88.0 ± 8800.0	207.0 ± 20700.0
NGC1052	180.0 ± 18000.0	134.0 ± 13400.0	190.0 ± 19000.0	338.0 ± 33800.0
NGC4303	116.0 ± 11600.0	92.4 ± 9240.0	125.0 ± 12500.0	44.5 ± 4450.0
M-06-30-15	48.8 ± 4880.0	46.7 ± 4670.0	76.5 ± 7650.0	107.0 ± 10700.0
Mrk1333	45.0 ± 4500.0	40.3 ± 4030.0	56.8 ± 5680.0	70.4 ± 7040.0
NGC3169	714.0 ± 71400.0	147.0 ± 14700.0	738.0 ± 73800.0	420.0 ± 42000.0
NGC7590	61.8 ± 6180.0	42.1 ± 4210.0	63.3 ± 6330.0	160.0 ± 16000.0
NGC7496	27.3 ± 2730.0	20.3 ± 2030.0	29.5 ± 2950.0	126.0
NGC613	112.0 ± 11200.0	75.4 ± 7540.0	890.0 ± 89000.0	567.0 ± 56700.0
NGC1566	125.0 ± 12500.0	87.2 ± 8720.0	137.0 ± 13700.0	661.0
NGC5806	54.7 ± 5470.0	40.9 ± 4090.0	59.3 ± 5930.0	154.0 ± 15400.0
NGC7582	104.0 ± 10400.0	794.0 ± 79400.0	722.0 ± 72200.0	458.0 ± 45800.0
NGC4968	79.9 ± 7990.0	27.3 ± 2730.0	37.8 ± 3780.0	38.4 ± 3840.0
NGC1125	-	-	-	26.8 ± 2680.0
NGC4374	316.0 ± 31600.0	390.0 ± 39000.0	319.0 ± 31900.0	1160.0 ± 116000.0
NGC7172	248.0 ± 24800.0	54.8 ± 5480.0	295.0 ± 29500.0	176.0 ± 17600.0
NGC1320	45.7 ± 4570.0	-	55.0 ± 5500.0	64.4 ± 6440.0
NGC4418	24.8 ± 2480.0	20.1 ± 2010.0	26.3 ± 2630.0	10.9 ± 1090.0
NGC4593	415.0 ± 41500.0	66.2 ± 6620.0	357.0 ± 35700.0	220.0 ± 22000.0
NGC1068	511.0 ± 51100.0	734.0 ± 73400.0	1060.0 ± 106000.0	3800.0
NGC5861	18.3 ± 1830.0	9.62 ± 962.0	21.0 ± 2100.0	145.0 ± 14500.0
NGC2992	186.0 ± 18600.0	245.0 ± 24500.0	218.0 ± 21800.0	116.0 ± 11600.0
NGC3976	18.3 ± 1830.0	67.7 ± 6770.0	20.0 ± 2000.0	123.0 ± 12300.0
NGC5506	191.0 ± 19100.0	77.3 ± 7730.0	319.0 ± 31900.0	189.0 ± 18900.0

Notes: This table presents selected photometric properties for sample galaxies. Values marked '-' indicate unavailable data.

TABLE A.3 – Photometry data for sample galaxies

id	spitzer irac ch2	spitzer irac ch3	spitzer irac ch4	IRAS1
NGC1386	98.8 ± 9880.0	157.0 ± 15700.0	383.0 ± 38300.0	493.0 ± 49300.0
ESO420-G13	-	-	-	525.0 ± 52500.0
NGC4845	-	-	-	404.0 ± 40400.0
IC5063	124.0 ± 12400.0	219.0 ± 21900.0	564.0 ± 56400.0	1070.0 ± 107000.0
NGC1365	327.0 ± 32700.0	604.0 ± 60400.0	3210.0 ± 321000.0	3370.0 ± 337000.0
NGC4412	2.69 ± 269.0	9.05 ± 905.0	25.3 ± 2530.0	230.0 ± 23000.0
NGC6890	37.2 ± 3720.0	52.6 ± 5260.0	63.1 ± 6310.0	342.0 ± 34200.0
NGC7314	27.7 ± 2770.0	32.6 ± 3260.0	43.8 ± 4380.0	268.0 ± 26800.0
NGC4594	111.0 ± 11100.0	2180.0 ± 218000.0	49.4 ± 4940.0	740.0 ± 74000.0
IC3639	50.4 ± 5040.0	89.7 ± 8970.0	416.0 ± 41600.0	643.0 ± 64300.0
IC5169	-	-	-	198.0 ± 19800.0
NGC4941	26.5 ± 2650.0	28.4 ± 2840.0	40.1 ± 4010.0	184.0 ± 18400.0
NGC4501	64.6 ± 6460.0	49.3 ± 4930.0	2140.0 ± 214000.0	1020.0 ± 102000.0
NGC1097	388.0 ± 38800.0	906.0 ± 90600.0	4290.0 ± 429000.0	1990.0 ± 199000.0
NGC3627	1320.0 ± 132000.0	2200.0 ± 220000.0	7500.0 ± 750000.0	4170.0 ± 417000.0
NGC7213	138.0 ± 13800.0	137.0 ± 13700.0	172.0 ± 17200.0	606.0 ± 60600.0
NGC4486	375.0	302.0	22.3 ± 2230.0	231.0 ± 23100.0
NGC0424	301.0 ± 30100.0	414.0 ± 41400.0	671.0 ± 67100.0	1100.0 ± 110000.0
NGC1052	207.0 ± 20700.0	163.0 ± 16300.0	136.0 ± 13600.0	203.0 ± 20300.0
NGC4303	28.4 ± 2840.0	55.6 ± 5560.0	141.0 ± 14100.0	1060.0 ± 106000.0
M-06-30-15	128.0 ± 12800.0	157.0 ± 15700.0	239.0 ± 23900.0	380.0 ± 38000.0
Mrk1333	-	-	-	297.0 ± 29700.0
NGC3169	272.0 ± 27200.0	360.0 ± 36000.0	79.2 ± 7920.0	1220.0 ± 122000.0
NGC7590	27.2 ± 2720.0	33.2 ± 3320.0	182.0 ± 18200.0	564.0 ± 56400.0
NGC7496	21.0 ± 2100.0	47.5 ± 4750.0	272.0 ± 27200.0	347.0 ± 34700.0
NGC613	-	-	-	997.0 ± 99700.0
NGC1566	480.0 ± 48000.0	910.0 ± 91000.0	2110.0 ± 211000.0	831.0 ± 83100.0
NGC5806	-	-	-	197.0 ± 19700.0
NGC7582	285.0 ± 28500.0	516.0 ± 51600.0	2070.0 ± 207000.0	1620.0 ± 162000.0
NGC4968	43.5 ± 4350.0	71.2 ± 7120.0	212.0 ± 21200.0	391.0 ± 39100.0
NGC1125	24.4 ± 2440.0	47.9 ± 4790.0	160.0 ± 16000.0	174.0 ± 17400.0
NGC4374	463.0 ± 46300.0	285.0 ± 28500.0	25.6 ± 2560.0	165.0 ± 16500.0
NGC7172	127.0 ± 12700.0	190.0 ± 19000.0	328.0 ± 32800.0	437.0 ± 43700.0
NGC1320	73.5 ± 7350.0	117.0 ± 11700.0	265.0 ± 26500.0	330.0 ± 33000.0
NGC4418	21.4 ± 2140.0	-	-	935.0 ± 93500.0
NGC4593	134.0 ± 13400.0	163.0 ± 16300.0	290.0 ± 29000.0	344.0 ± 34400.0
NGC1068	5100.0	13000.0	23000.0	36100.0 ± 3610000.0
NGC5861	-	-	-	522.0 ± 52200.0
NGC2992	106.0 ± 10600.0	145.0 ± 14500.0	251.0 ± 25100.0	630.0 ± 63000.0
NGC3976	-	-	-	199.0 ± 19900.0
NGC5506	568.0 ± 56800.0	732.0 ± 73200.0	1100.0 ± 110000.0	1280.0 ± 128000.0

Notes: This table presents selected photometric properties for sample galaxies. Values marked '-' indicate unavailable data.

TABLE A.4 – Black hole accretion rate of the local AGN TWIST sample.

NAME	BHAR1	BHAR2
NGC0424	0.0164-0.0592	0.0342-0.0971
NGC613	0.00091-0.00920	0.000187-0.000558
NGC1052	0.00021-0.00354	0.000155-0.000463
NGC1068	0.1455-0.2419	0.2206-0.6156
NGC1097	0.00044-0.00580	-
NGC1125	0.0224-0.0724	0.00863-0.0248
NGC1320	0.00971-0.04230	0.0122-0.0351
NGC1365	0.0521-0.1248	0.00804-0.0232
NGC1386	0.0038-0.0233	0.00393-0.0114
ESO420-G13	0.0342-0.0952	0.02479-0.07063
NGC1566	0.000618-0.00717	0.000283-0.000840
NGC2992	0.0368-0.0998	0.0194-0.0555
NGC3169	9.62e-05-0.00216	-
NGC3627	4.26e-05-0.00128	1.76e-05-5.38e-05
NGC3976	0.000196-0.003419	-
NGC4303	-	-
NGC4374	2.46e-05-0.00090	-
NGC4412	-	-
NGC4418	-	-
NGC4486	0.000169-0.00311	-
NGC4501	0.001005-0.00981	-
NGC4593	0.0122-0.0490	0.00337-0.00978
NGC4594	0.000106-0.00210	-
IC3639	0.0114-0.0470	0.0198-0.0565
Mrk1333	-	-
NGC4845	-	-
NGC4941	0.00189-0.01473	0.00144-0.00421
NGC4968	0.01497-0.05589	0.0258-0.0730
M-06-30-15	0.00692-0.0340	0.00409-0.01186
NGC5506	0.0434-0.0110	0.01013-0.02909
NGC5806	-	-
NGC5861	-	-
NGC6890	0.00282-0.01905	0.00518-0.0150
IC5063	0.0712-0.1526	0.06194-0.1749
NGC7172	0.0156-0.0575	0.0111-0.0318
NGC7213	0.00033-0.00478	-
IC5169	-	-
NGC7314	0.00673-0.0334	0.00530-0.0153
NGC7496	-	-
NGC7582	0.0341-0.0950	0.01573-0.0450
NGC7590	0.000625-0.00722	-

Notes: This table presents from the left to right. for each galaxy of the sample: NAME, black hole accretion rate (BHAR1) derived from the flux of the [OIV] line and the calibration given by (MORDINI *et al.*, 2021), blach hole accretion rate (BHAR2) derived from the flux of the [NeV] line and the calibration given by (MORDINI *et al.*, 2021),

TABLE A.5 – 3D-Barolo and TWIST results for the galaxies in the sample.

NAME	$\sigma\,[km/s]$	$log(M_{dynamical})\,[M_\odot]$	$log(M_{BH})\,[M_\odot]$	$\dot{M}_{outflow}\,[M_\odot]$	$M_{H2}\,[M_\odot]$
NGC0424	9.588	9.789	4.130	1.726	7.047
NGC613	6.589	11.415	6.507	8.995	8.459
NGC1125	2.178	9.740	4.175	0.152	7.447
NGC1320	3.650	10.775	5.836	0.413	7.591
ESO420-G13	7.181	9.246	6.751	6.075	8.732
NGC1566	9.118	11.556	4.594	2.218	8.114
NGC2992	11.932	11.216	7.501	3.754	8.232
NGC4593	2.564	10.521	6.903	1.253	8.100
IC3639	2.622	10.920	6.907	12.755	8.108
Mrk1333	14.027	11.041	6.104	19.184	8.260
NGC4845	6.573	10.954	5.011	0.125	8.167
NGC4941	4.872	11.115	8.676	0.367	7.012
M-06-30-15	4.481	9.632	5.028	-	7.112
NGC5506	13.487	10.781	6.481	1.307	7.861
NGC5861	7.552	9.092	5.412	1.821	7.800
NGC6890	2.363	11.023	6.225	1.685	7.946
IC5063	19.794	11.276	7.086	1.553	7.947
NGC7172	26.944	10.702	7.595	1.210	8.285
IC5169	7.919	10.667	6.375	2.464	8.196
NGC7496	5.544	11.263	7.310	3.339	8.126

Notes: This table is presented from left to right. Galaxy name, velocity mean dispersion, logarithm of dynamical mass, logarithm of BH mass, outflow mass rate, molecular gas mass

TABLE A.6 – CIGALE-derived parameters for galaxies (Part 1)

Name	$L_{\mathrm{IR,AGN}}/L_{\mathrm{IR,total}}$	$\log(L_{\mathrm{AGN,torus}}\,[\mathrm{erg\,s^{-1}}])$	$\log(L_{\mathrm{AGN,disc}}\,[\mathrm{erg\,s^{-1}}])$
IC5063	0.1202	35.8540	37.1089
NGC7314	0.0998	34.1150	35.6604
IC3639	0.0850	35.5297	36.6462
NGC0424	0.2057	35.5505	37.4431
NGC7582	0.0761	35.6273	36.8466
NGC1068	0.2014	36.6152	36.9346
NGC5506	0.1984	35.2630	37.0365
NGC6890	0.1599	35.2538	36.0273
NGC4941	0.1897	34.7224	34.5942
NGC4968	0.2795	36.4780	35.5457
NGC7172	0.2982	36.5299	35.6206
NGC4593	0.8763	36.1938	36.0961
ESO420-G13	0.0010	33.8151	33.4596
NGC1052	0.0033	36.1389	35.9340
M-06-30-15	0.1849	35.4070	36.5410
NGC1566	0.1777	36.2999	37.1342
NGC2992	0.0755	35.4006	36.0864
NGC1125	0.1312	36.0444	35.2234
IC5169	0.0010	33.7656	32.7489
NGC1320	0.1557	35.5508	36.3708
NGC7496	0.1013	35.5328	34.9390
NGC5861	0.2948	35.2520	36.1378
NGC4845	0.1257	35.3542	35.2005
NGC613	0.0602	35.3843	36.1899
Mrk1333	0.0548	35.4637	36.0222

TABLE A.7 – CIGALE-derived parameters for galaxies (Part 2)

Name	$\log(L_{\mathrm{AGN,total\,dust}}\,[\mathrm{erg\,s^{-1}}])$	$\log(L_{\mathrm{AGN,6\,\mu m}}\,[\mathrm{erg\,s^{-1}}])$	$\log(L_{\mathrm{AGN,acc\,pow}}\,[\mathrm{erg\,s^{-1}}])$
IC5063	35.8540	36.4460	36.7097
NGC7314	34.1150	34.9777	35.2612
IC3639	35.5297	35.9982	36.2470
NGC0424	35.5505	36.7481	37.0439
NGC7582	35.6273	36.1873	36.4474
NGC1068	36.6152	36.5261	36.5355
NGC5506	35.2630	36.3446	36.6374
NGC6890	35.2538	35.5023	36.8650
NGC4941	34.7224	34.4398	35.4870
NGC4968	36.4780	36.0228	36.7764
NGC7172	36.5299	36.2068	36.6926
NGC4593	36.5102	35.7847	36.4924
ESO420-G13	33.8151	33.5276	34.5076
NGC1052	36.1389	35.8957	36.8863
M-06-30-15	35.4070	35.8947	36.1419
NGC1566	36.2999	36.5775	36.7350
NGC2992	35.4006	35.5230	35.6872
NGC1125	36.0444	35.6198	36.3678
IC5169	33.7656	33.3697	33.9824
NGC1320	35.5508	35.8190	37.2091
NGC7496	35.5328	35.1309	36.0388
NGC5861	35.2520	35.5770	37.0269
NGC4845	35.3542	35.1531	36.1610
NGC613	35.3843	35.6429	37.0199
Mrk1333	35.4637	35.5518	36.8888

TABLE A.8 – CIGALE-derived parameters for galaxies (Part 3)

Name	$\log(L_{\rm AGN}\,[{\rm erg\,s^{-1}}])$	$\log(L_{\rm stellar}\,[{\rm erg\,s^{-1}}])$	$\log(M_*/M_\odot)$
IC5063	37.1324	37.0464	9.7599
NGC7314	35.6726	35.5828	8.7996
IC3639	36.6782	36.9230	9.7512
NGC0424	37.4486	36.5057	9.4187
NGC7582	36.8720	36.9935	9.9271
NGC1068	37.1047	37.3301	9.7110
NGC5506	37.0438	36.3592	9.4295
NGC6890	36.0949	36.5948	9.6356
NGC4941	34.9640	35.9516	9.2913
NGC4968	36.5260	37.0719	9.6083
NGC7172	36.5804	37.1489	9.9147
NGC4593	36.6518	37.4025	10.6469
ESO420-G13	33.9738	37.1420	10.1853
NGC1052	36.3495	40.1415	13.1674
M-06-30-15	36.5718	36.4571	9.6923
NGC1566	37.1936	37.0976	9.6588
NGC2992	36.1678	37.1510	10.3993
NGC1125	36.1055	37.0251	9.4955
IC5169	33.8055	36.8835	9.5464
NGC1320	36.4320	36.7966	9.8455
NGC7496	35.6314	36.5796	8.9109
NGC5861	36.1909	36.2985	8.6236
NGC4845	35.5852	36.4365	9.3290
NGC613	36.2531	36.9800	9.3110
Mrk1333	36.1282	36.9413	10.0625

TABLE A.9 – CIGALE-derived parameters for galaxies (Part 4)

Name	$\log(M_{\text{stellar gas}}\,[M_\odot])$	$\log(\text{SFR}_{\text{integrated}}\,[M_\odot\,\text{yr}^{-1}])$	$\log(\text{SFR}_{\text{current}}\,[M_\odot\,\text{yr}^{-1}])$
IC5063	9.6545	10.0114	1.5830
NGC7314	8.7462	9.0747	0.0286
IC3639	9.6577	10.0080	1.0838
NGC0424	9.3375	9.6810	0.3917
NGC7582	9.8474	10.1901	1.1907
NGC1068	9.5239	9.9285	3.4872
NGC5506	9.3653	9.6996	0.2326
NGC6890	9.5753	9.9075	0.3728
NGC4941	9.2461	9.5704	0.0434
NGC4968	9.4565	9.8400	1.8048
NGC7172	9.8042	10.1640	1.8642
NGC4593	10.5490	10.9017	0.4290
ESO420-G13	10.1049	10.4480	1.2877
NGC1052	13.0372	13.4082	776.6334
M-06-30-15	9.6414	9.9686	0.2134
NGC1566	9.5174	9.8949	1.9039
NGC2992	10.3469	10.6749	0.9369
NGC1125	9.3296	9.7214	1.6733
IC5169	9.4105	9.7848	0.9941
NGC1320	9.7817	10.1158	0.5555
NGC7496	8.7136	9.1244	0.6179
NGC5861	8.4275	8.8376	0.3193
NGC4845	9.2353	9.5857	0.3384
NGC613	9.1138	9.5245	1.5518
Mrk1333	9.9936	10.3304	0.7641

TABLE A.10 – CIGALE-derived parameters for galaxies (Part 5)

Name	$\log(\mathrm{SFR}_{100\,\mathrm{Myr}}\,[M_\odot\,\mathrm{yr}^{-1}])$	$\log(\mathrm{SFR}_{10\,\mathrm{Myr}}\,[M_\odot\,\mathrm{yr}^{-1}])$
IC5063	1.5921	1.5839
NGC7314	0.0291	0.0287
IC3639	1.0952	1.0848
NGC0424	0.3959	0.3921
NGC7582	1.2051	1.1920
NGC1068	3.4904	3.4875
NGC5506	0.2357	0.2329
NGC6890	0.3782	0.3733
NGC4941	0.0444	0.0435
NGC4968	1.8163	1.8059
NGC7172	1.8893	1.8664
NGC4593	0.4689	0.4325
ESO420-G13	1.3166	1.2903
NGC1052	844.0440	782.4715
M-06-30-15	0.2167	0.2137
NGC1566	1.9144	1.9049
NGC2992	0.9552	0.9385
NGC1125	1.6797	1.6739
IC5169	1.0179	0.9963
NGC1320	0.5658	0.5564
NGC7496	0.6178	0.6179
NGC5861	0.3193	0.3193
NGC4845	0.3434	0.3388
NGC613	1.5516	1.5518
Mrk1333	0.7784	0.7654

Appendix B - TWIST sample Results

Moment maps for TWIST sample

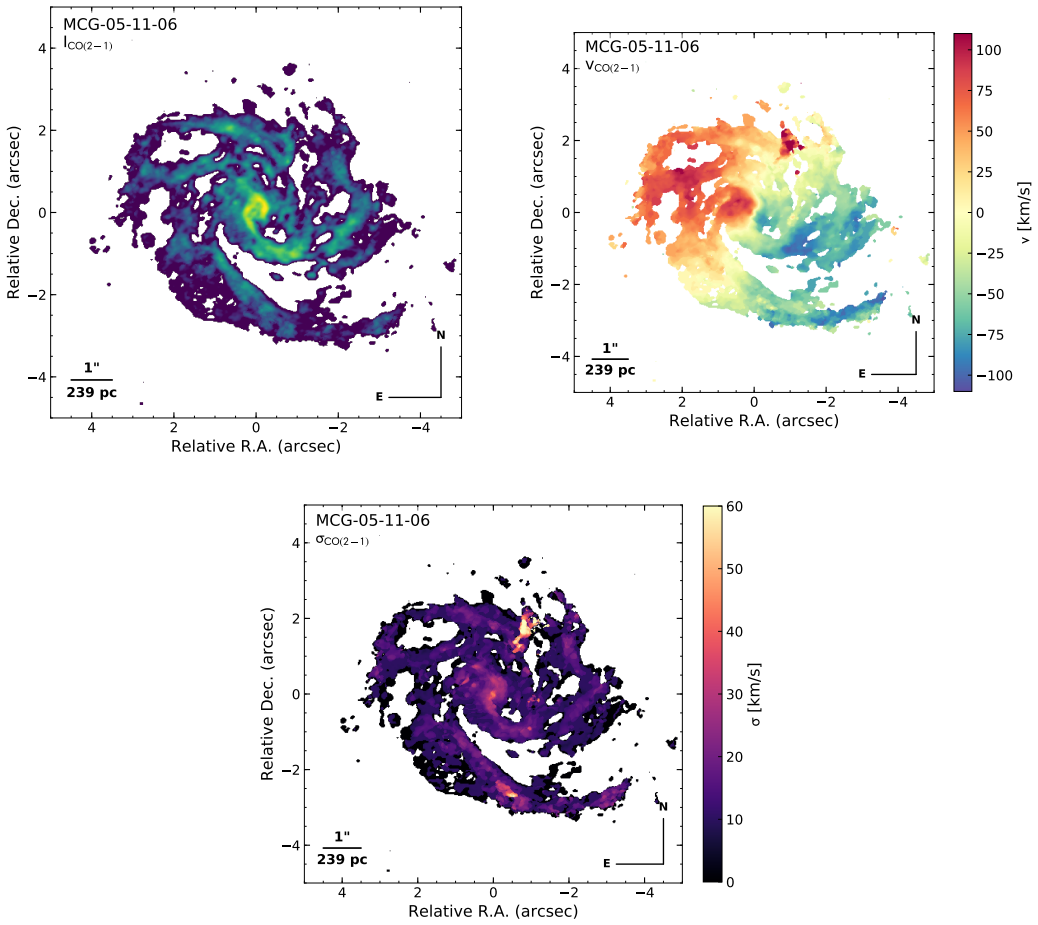

FIGURE B.1 – Moment 0 (left), Moment 1 (center), and Moment 2 (right) maps of the $CO(2-1)$ emission line for the Seyfert 2 galaxy MCG-05-11-06. The Moment 0 map shows the integrated intensity, the Moment 1 map shows the velocity field, and the Moment 2 map displays the velocity dispersion.

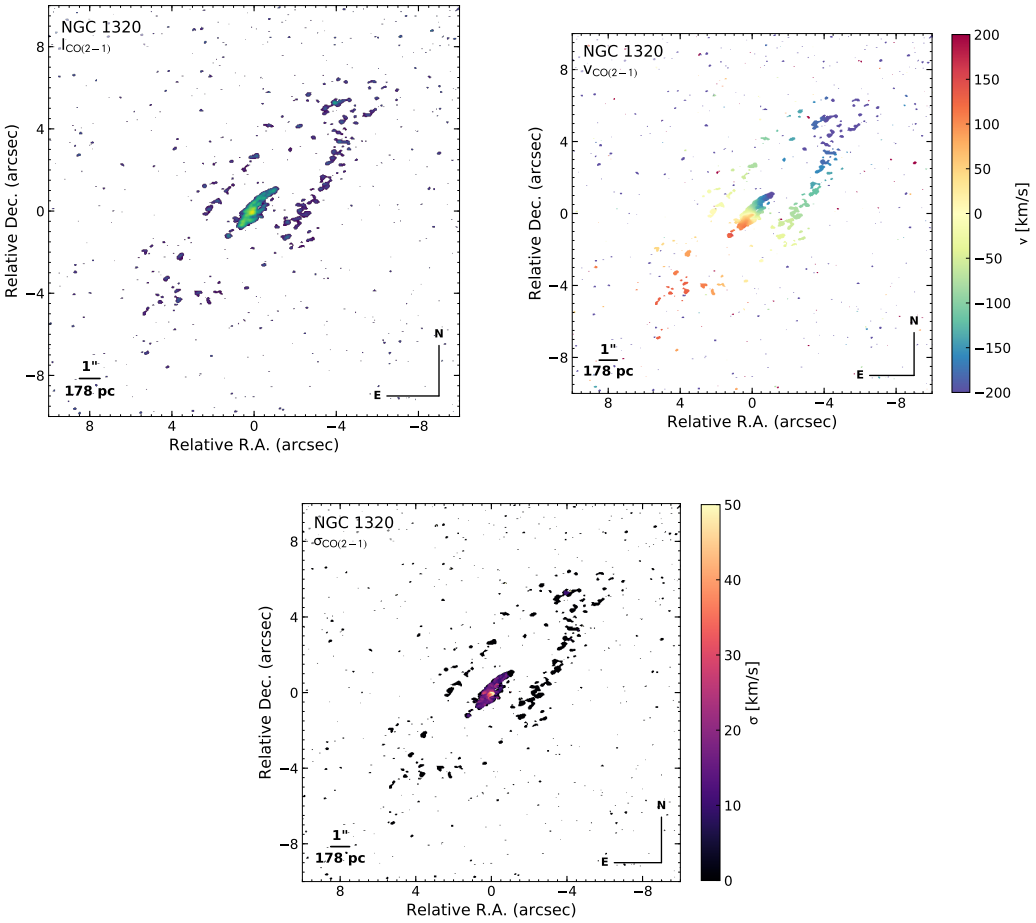

FIGURE B.2 – Moment 0 (left), Moment 1 (center), and Moment 2 (right) maps of the $CO(2-1)$ emission line for the galaxy NGC 1320. The Moment 0 map shows the integrated intensity, the Moment 1 map shows the velocity field, and the Moment 2 map displays the velocity dispersion.

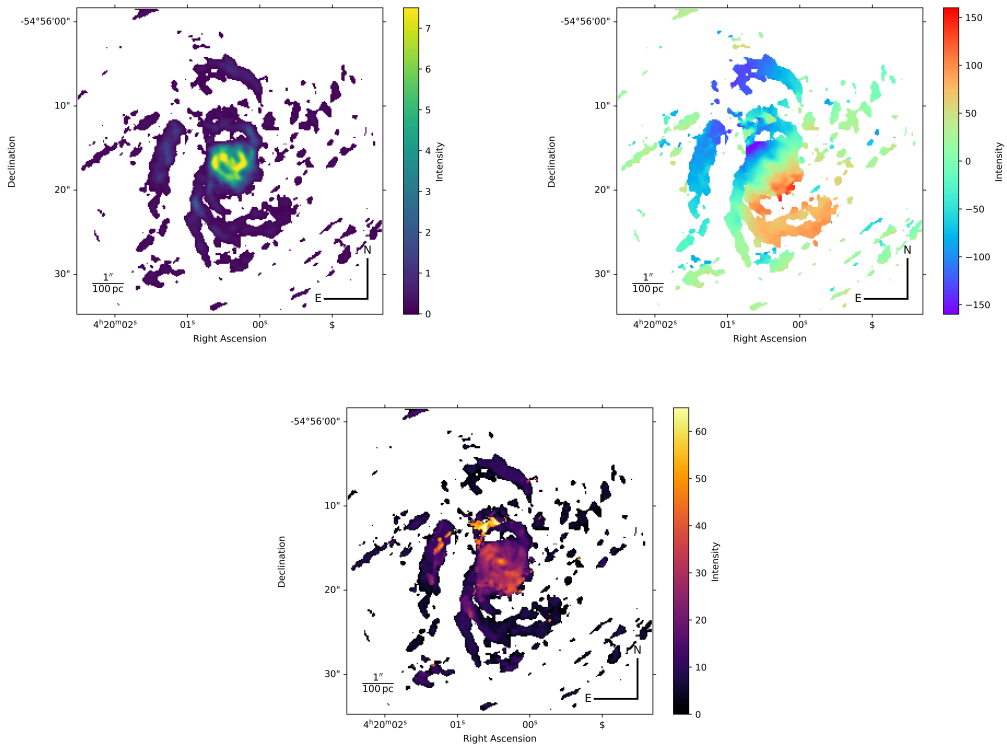

FIGURE B.3 – Moment 0 (left), Moment 1 (center), and Moment 2 (right) maps of the $CO(2-1)$ emission line for the galaxy NGC 1566. The Moment 0 map shows the integrated intensity, the Moment 1 map shows the velocity field, and the Moment 2 map displays the velocity dispersion.

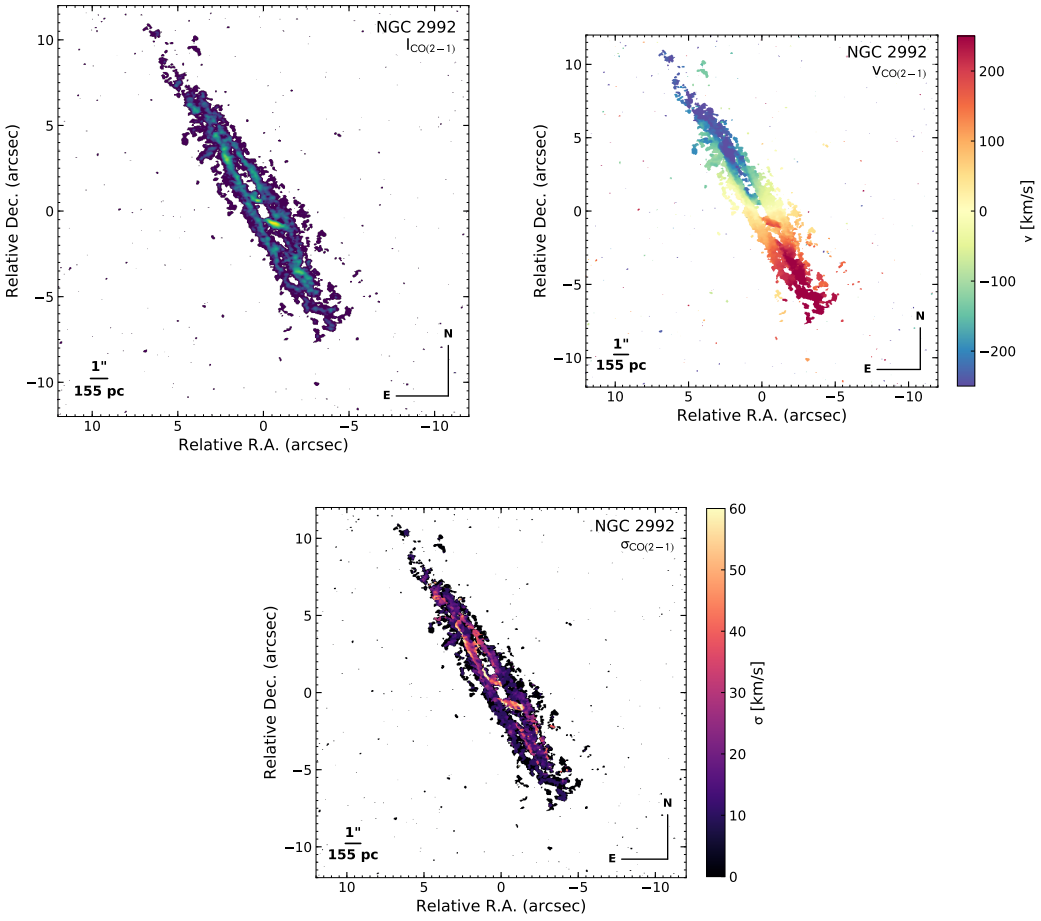

FIGURE B.4 – Moment 0 (left), Moment 1 (center), and Moment 2 (right) maps of the $CO(2-1)$ emission line for the galaxy NGC 2992. The Moment 0 map shows the integrated intensity, the Moment 1 map shows the velocity field, and the Moment 2 map displays the velocity dispersion.

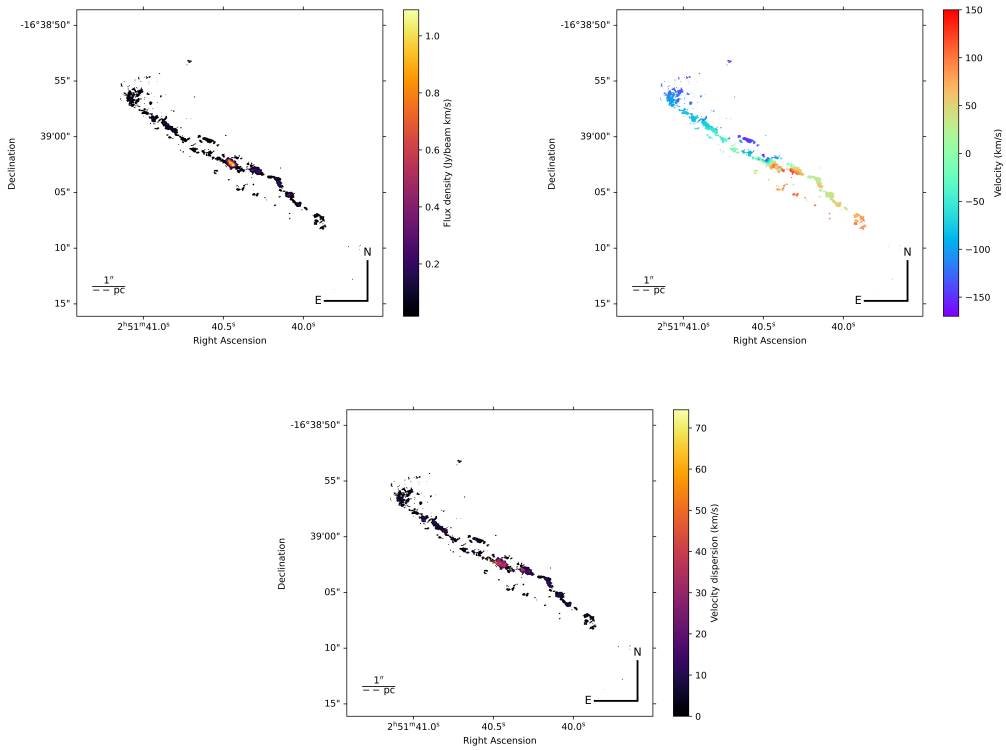

FIGURE B.5 – Moment 0 (left), Moment 1 (center), and Moment 2 (right) maps of the $CO(2-1)$ emission line for the galaxy NGC 1125. The Moment 0 map shows the integrated intensity, the Moment 1 map shows the velocity field, and the Moment 2 map displays the velocity dispersion.

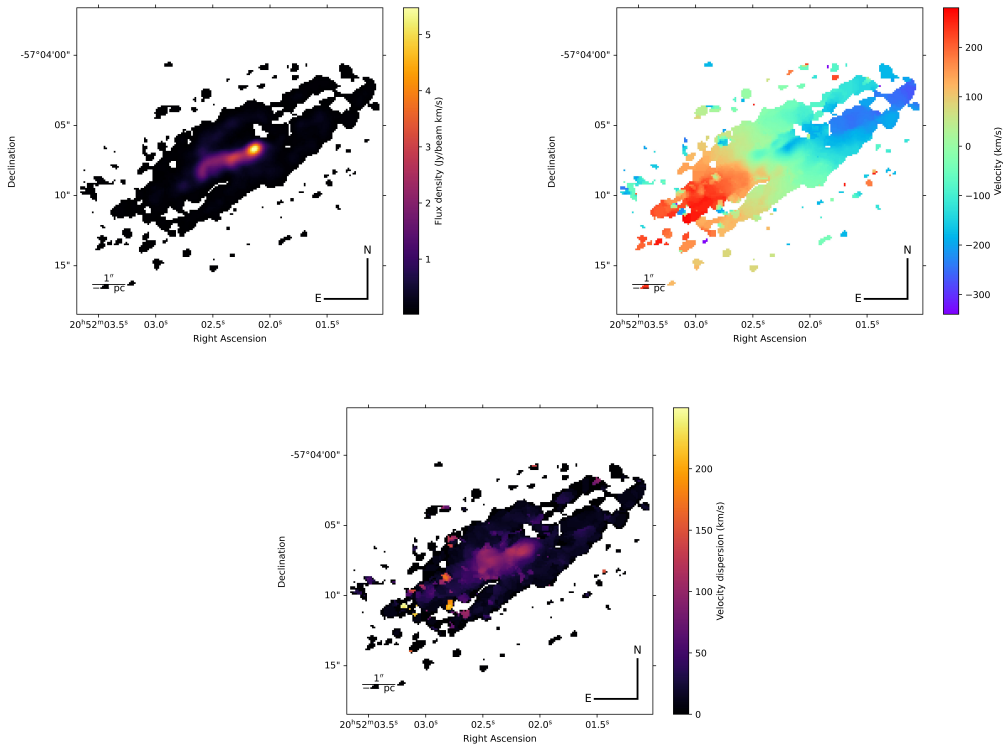

FIGURE B.6 – Moment 0 (left), Moment 1 (center), and Moment 2 (right) maps of the $CO(2-1)$ emission line for the galaxy IC 5063. The Moment 0 map shows the integrated intensity, the Moment 1 map shows the velocity field, and the Moment 2 map displays the velocity dispersion.

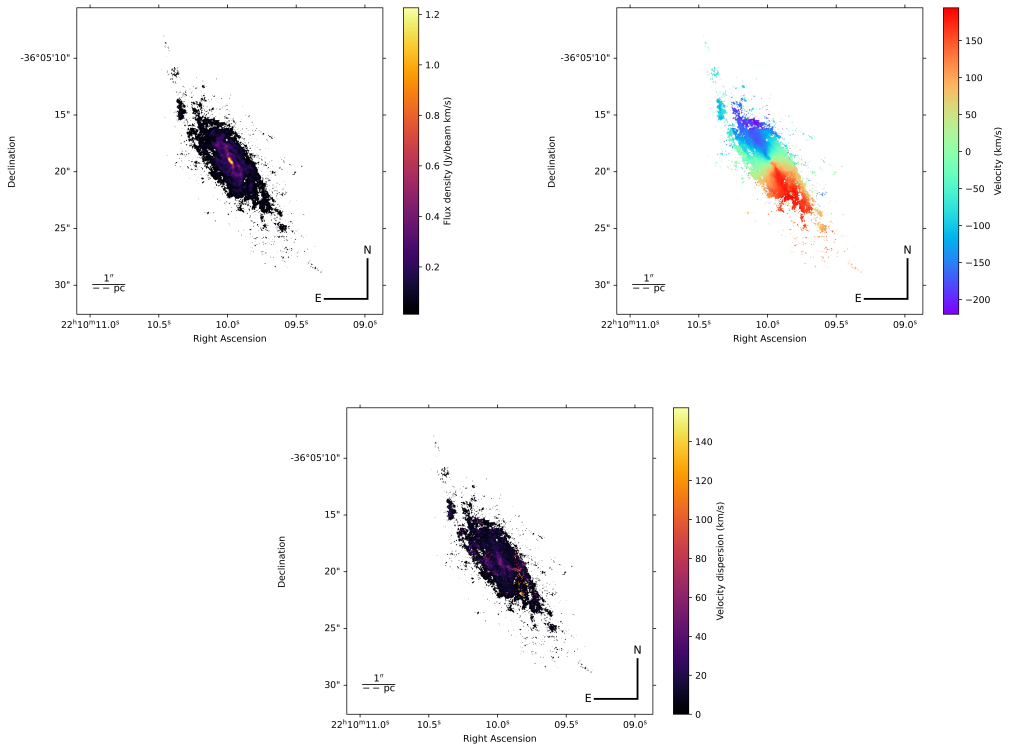

FIGURE B.7 – Moment 0 (left), Moment 1 (center), and Moment 2 (right) maps of the $CO(2-1)$ emission line for the galaxy IC 5169. The Moment 0 map shows the integrated intensity, the Moment 1 map shows the velocity field, and the Moment 2 map displays the velocity dispersion.

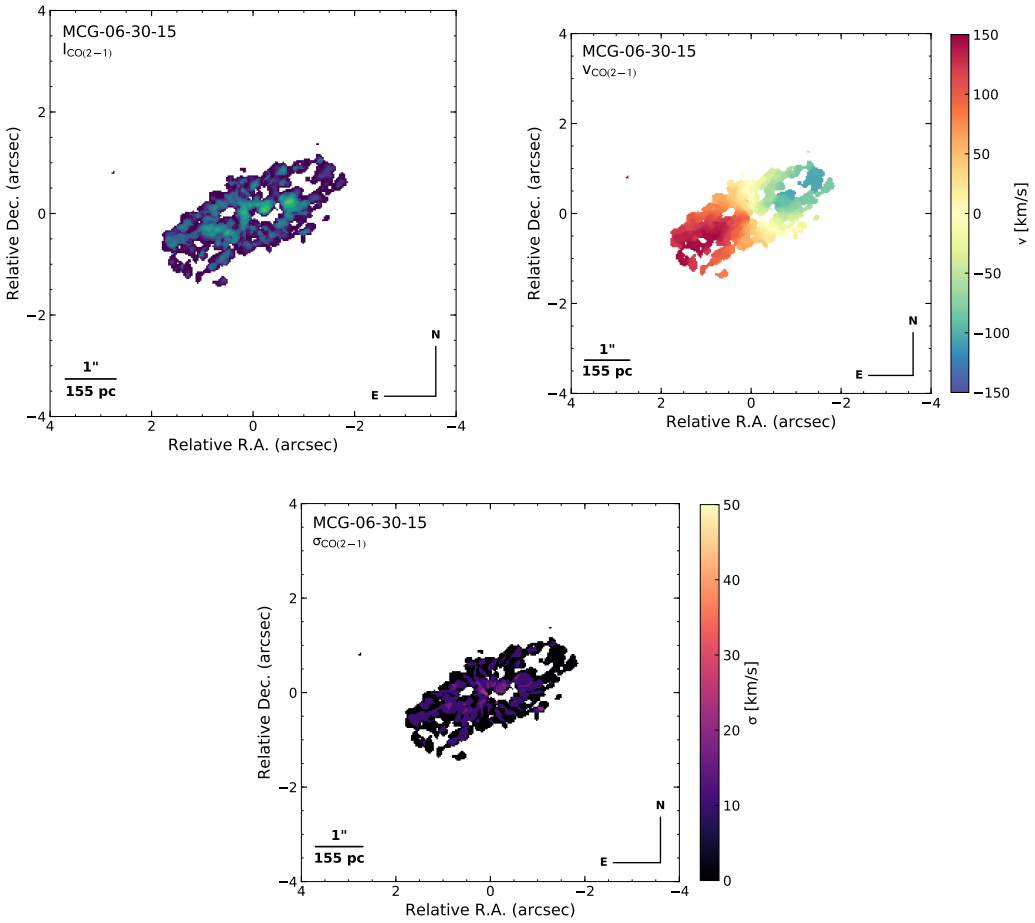

FIGURE B.8 – Moment 0 (left), Moment 1 (center), and Moment 2 (right) maps of the $CO(2-1)$ emission line for the galaxy MCG-06-30-15. The Moment 0 map shows the integrated intensity, the Moment 1 map shows the velocity field, and the Moment 2 map displays the velocity dispersion.

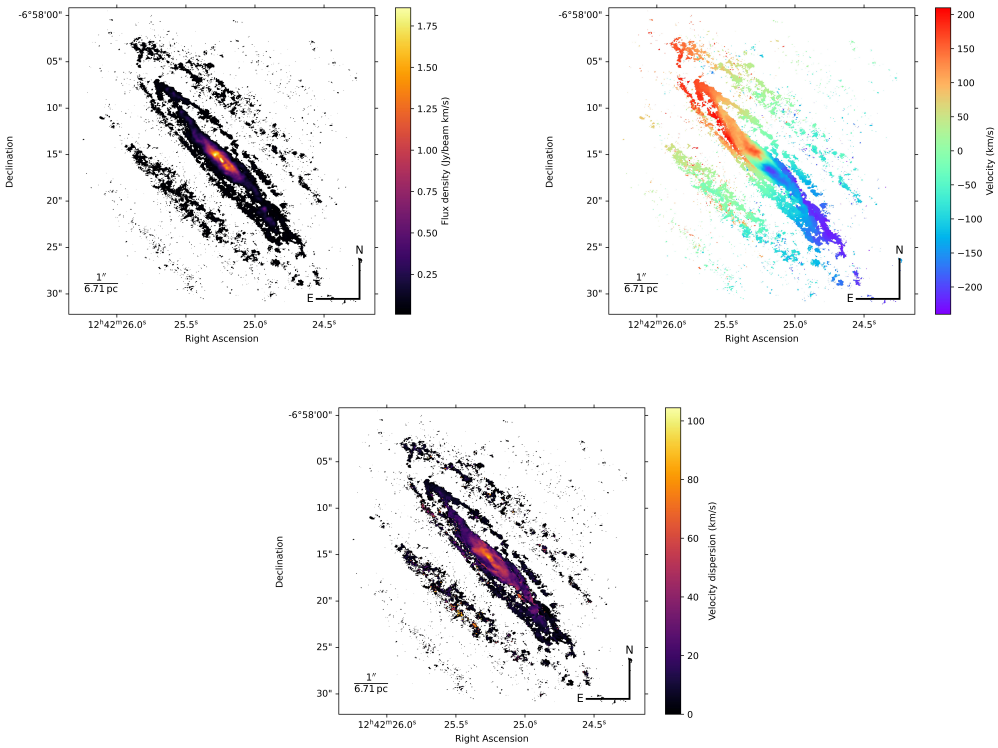

FIGURE B.9 – Moment 0 (left), Moment 1 (center), and Moment 2 (right) maps of the $CO(2-1)$ emission line for the galaxy Mrk1333. The Moment 0 map shows the integrated intensity, the Moment 1 map shows the velocity field, and the Moment 2 map displays the velocity dispersion.

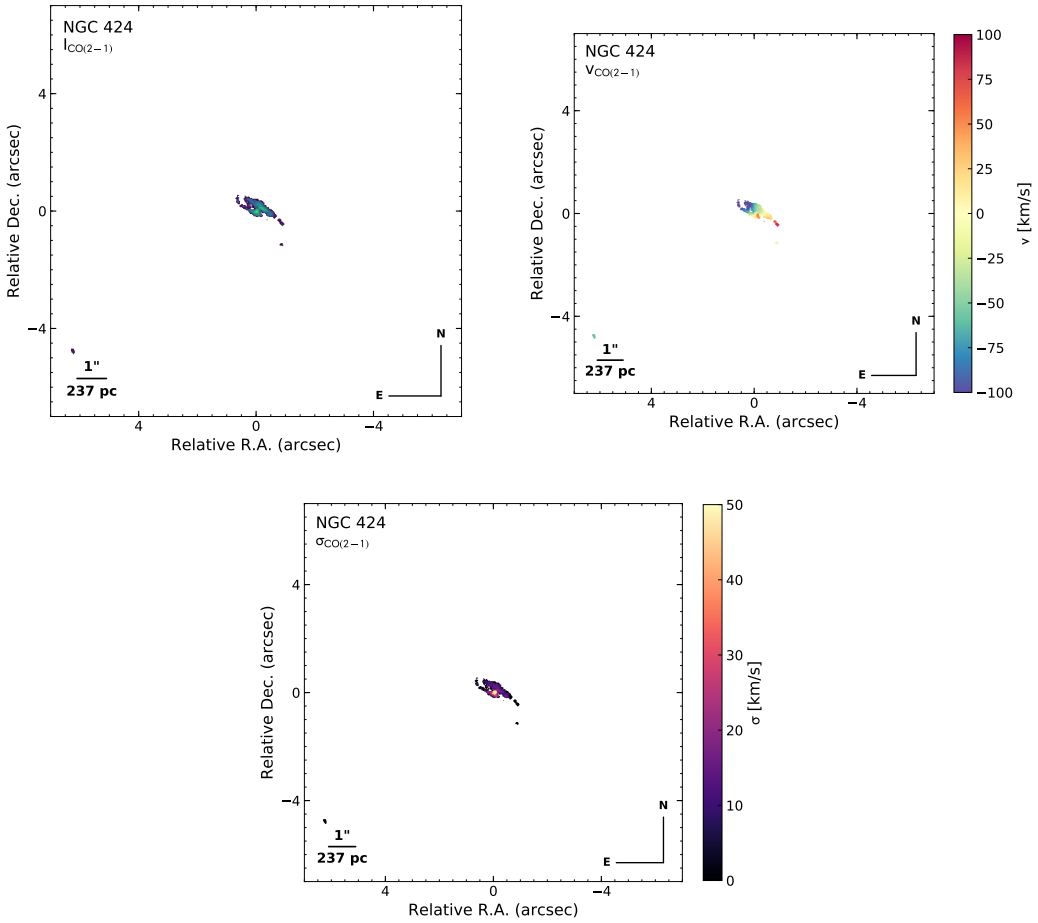

FIGURE B.10 – Moment 0 (left), Moment 1 (center), and Moment 2 (right) maps of the $CO(2-1)$ emission line for the galaxy NGC 424. The Moment 0 map shows the integrated intensity, the Moment 1 map shows the velocity field, and the Moment 2 map displays the velocity dispersion.

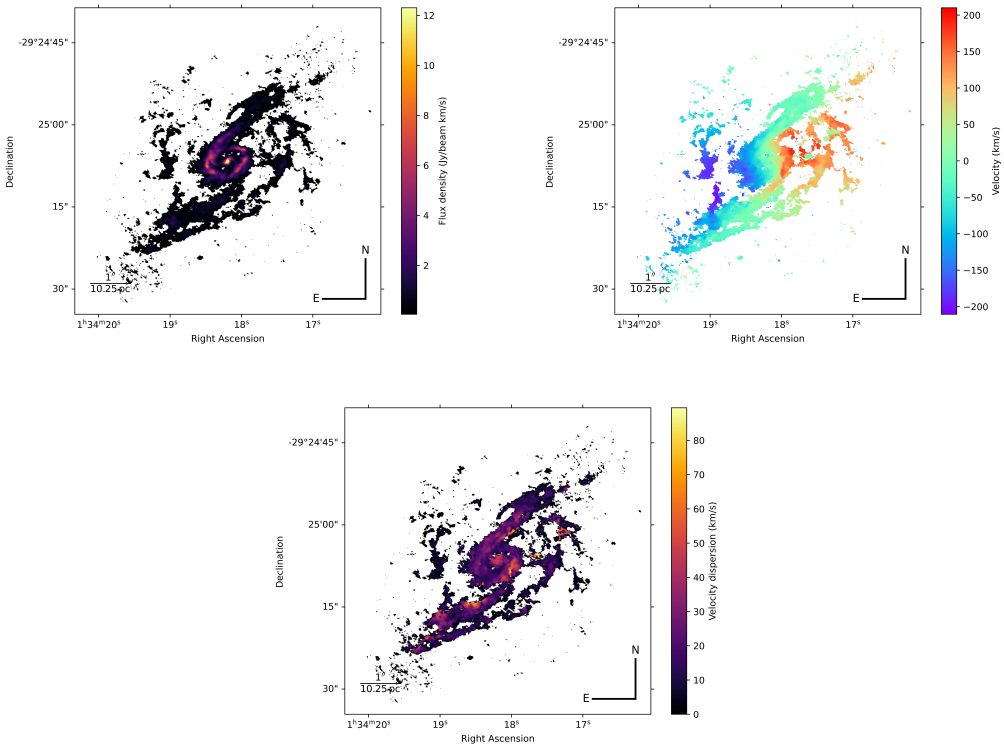

FIGURE B.11 – Moment 0 (left), Moment 1 (center), and Moment 2 (right) maps of the $CO(2-1)$ emission line for the galaxy NGC 613. The Moment 0 map shows the integrated intensity, the Moment 1 map shows the velocity field, and the Moment 2 map displays the velocity dispersion.

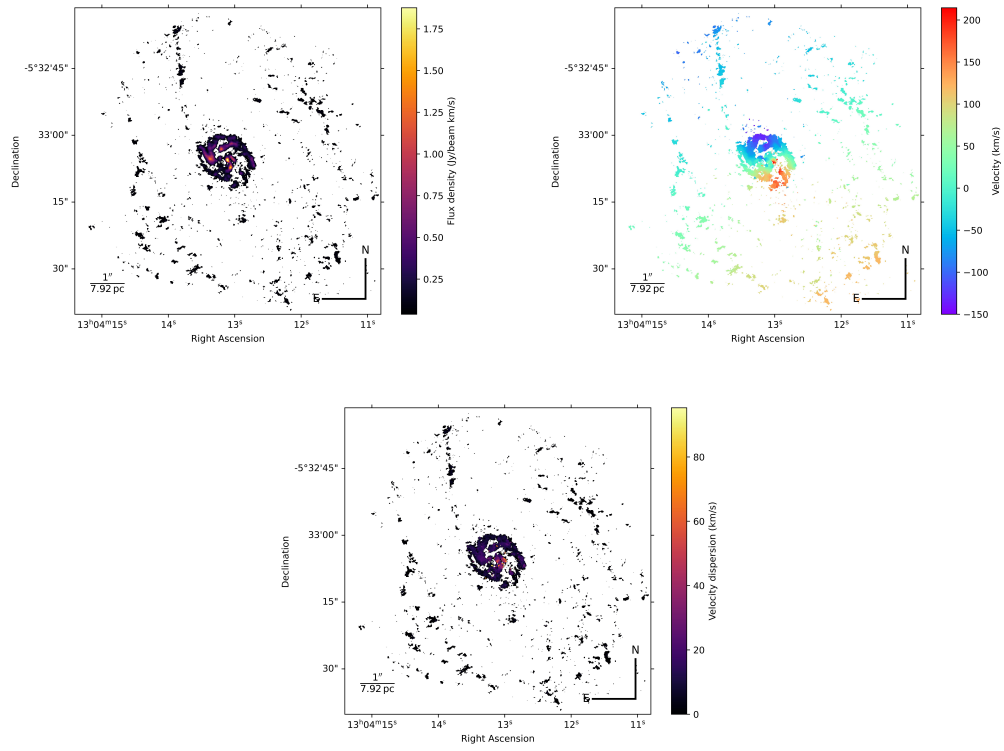

FIGURE B.12 – Moment 0 (left), Moment 1 (center), and Moment 2 (right) maps of the $CO(2-1)$ emission line for the galaxy NGC 4941. The Moment 0 map shows the integrated intensity, the Moment 1 map shows the velocity field, and the Moment 2 map displays the velocity dispersion.

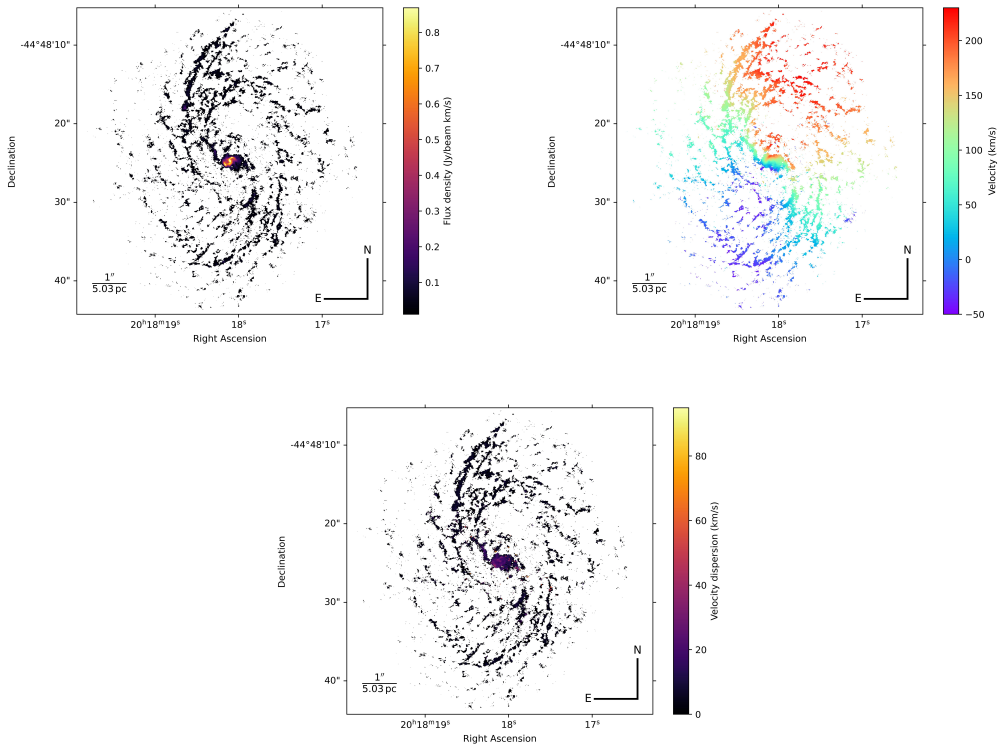

FIGURE B.13 – Moment 0 (left), Moment 1 (center), and Moment 2 (right) maps of the $CO(2-1)$ emission line for the galaxy NGC 6890. The Moment 0 map shows the integrated intensity, the Moment 1 map shows the velocity field, and the Moment 2 map displays the velocity dispersion.

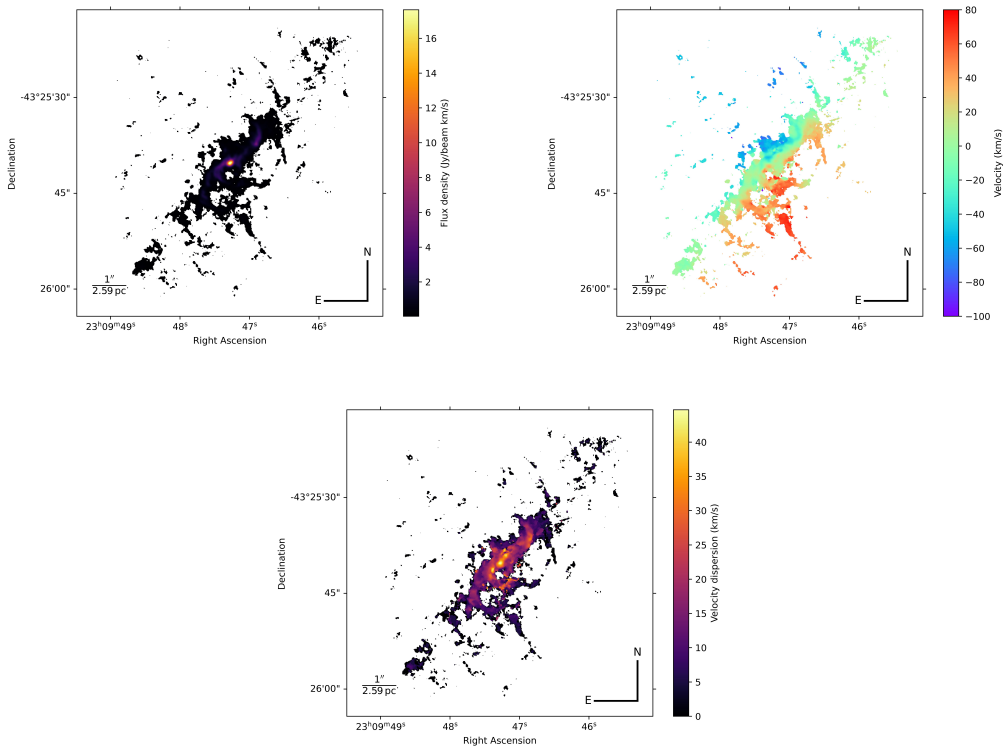

FIGURE B.14 – Moment 0 (left), Moment 1 (center), and Moment 2 (right) maps of the $CO(2-1)$ emission line for the galaxy NGC 7496. The Moment 0 map shows the integrated intensity, the Moment 1 map shows the velocity field, and the Moment 2 map displays the velocity dispersion.

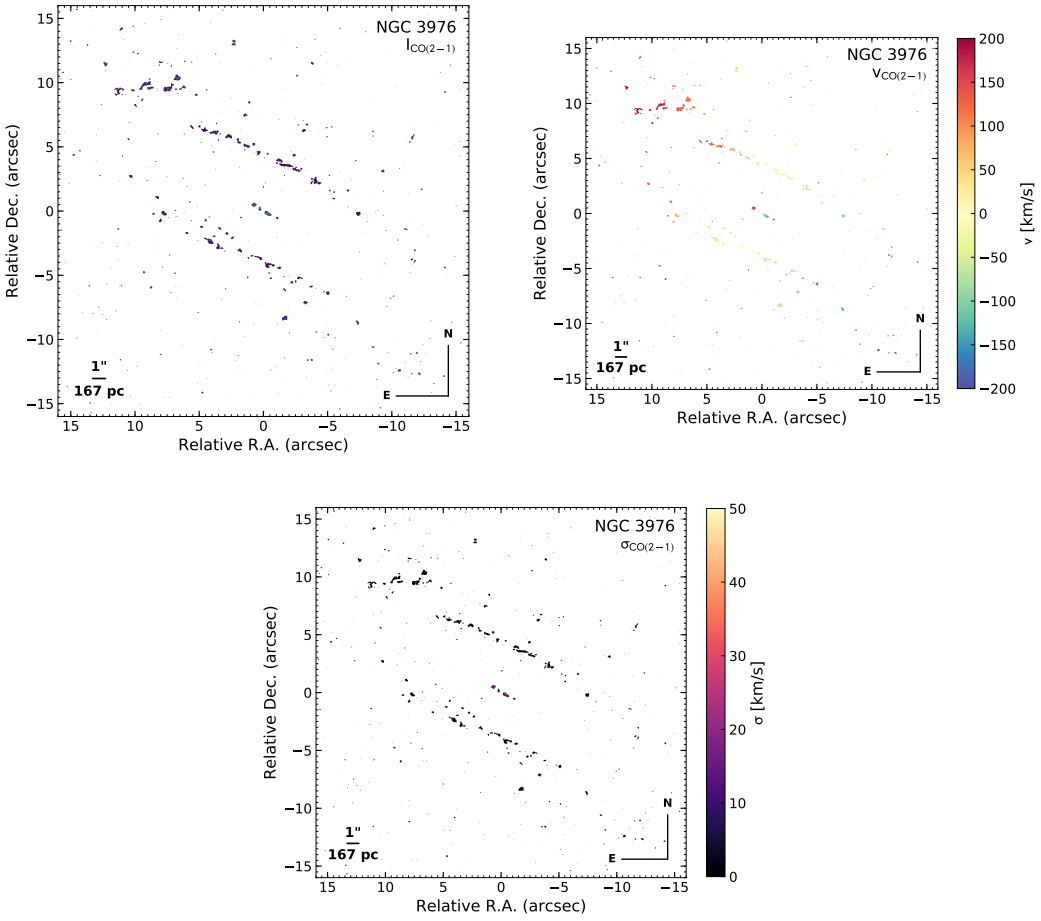

FIGURE B.15 – Moment 0 (left), Moment 1 (center), and Moment 2 (right) maps of the $CO(2-1)$ emission line for the galaxy NGC 3976. The Moment 0 map shows the integrated intensity, the Moment 1 map shows the velocity field, and the Moment 2 map displays the velocity dispersion.

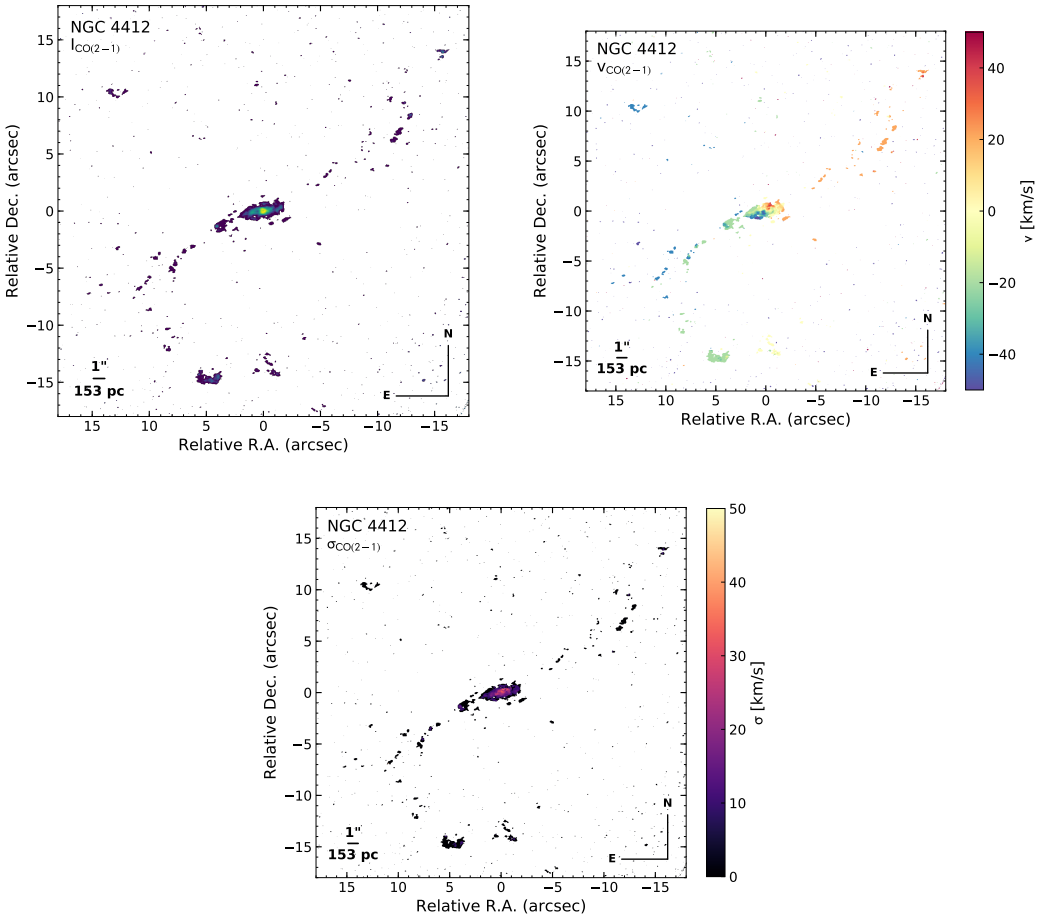

FIGURE B.16 – Moment 0 (left), Moment 1 (center), and Moment 2 (right) maps of the $CO(2-1)$ emission line for the galaxy NGC 4412. The Moment 0 map shows the integrated intensity, the Moment 1 map shows the velocity field, and the Moment 2 map displays the velocity dispersion.

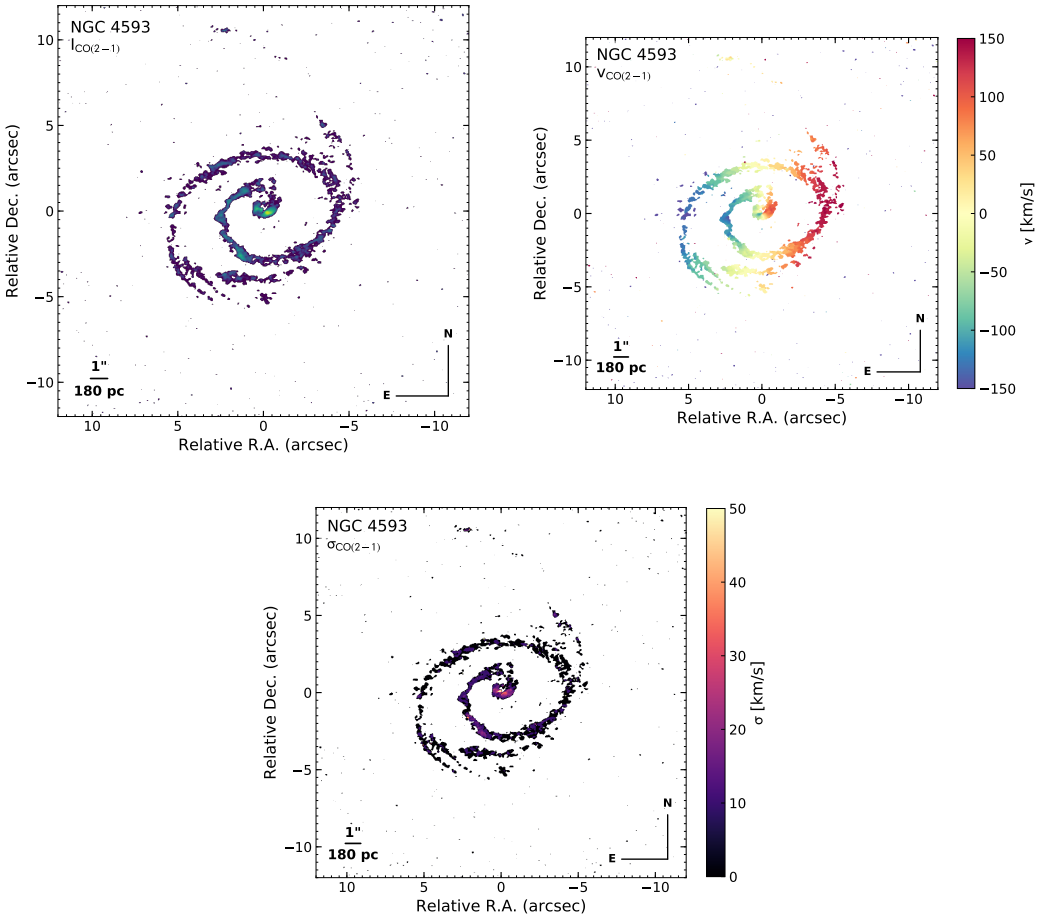

FIGURE B.17 – Moment 0 (left), Moment 1 (center), and Moment 2 (right) maps of the $CO(2-1)$ emission line for the galaxy NGC 4593. The Moment 0 map shows the integrated intensity, the Moment 1 map shows the velocity field, and the Moment 2 map displays the velocity dispersion.

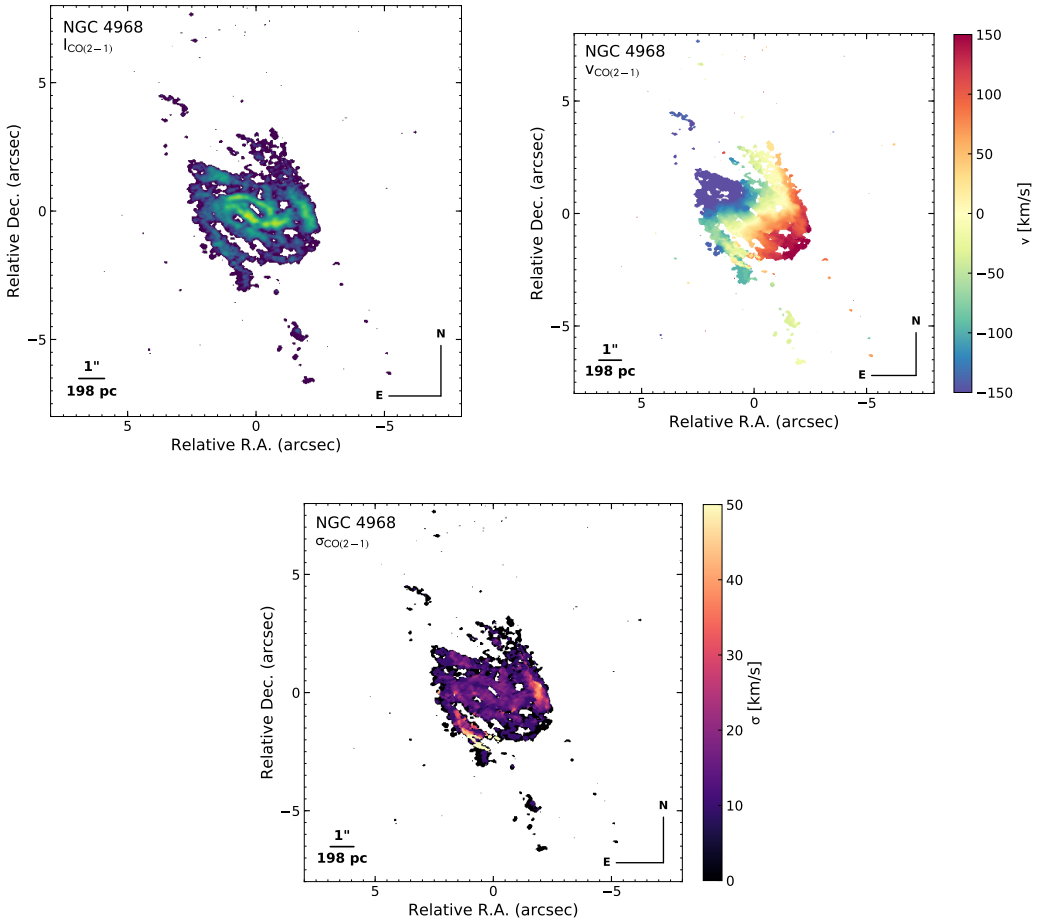

FIGURE B.18 – Moment 0 (left), Moment 1 (center), and Moment 2 (right) maps of the $CO(2-1)$ emission line for the galaxy NGC 4968. The Moment 0 map shows the integrated intensity, the Moment 1 map shows the velocity field, and the Moment 2 map displays the velocity dispersion.

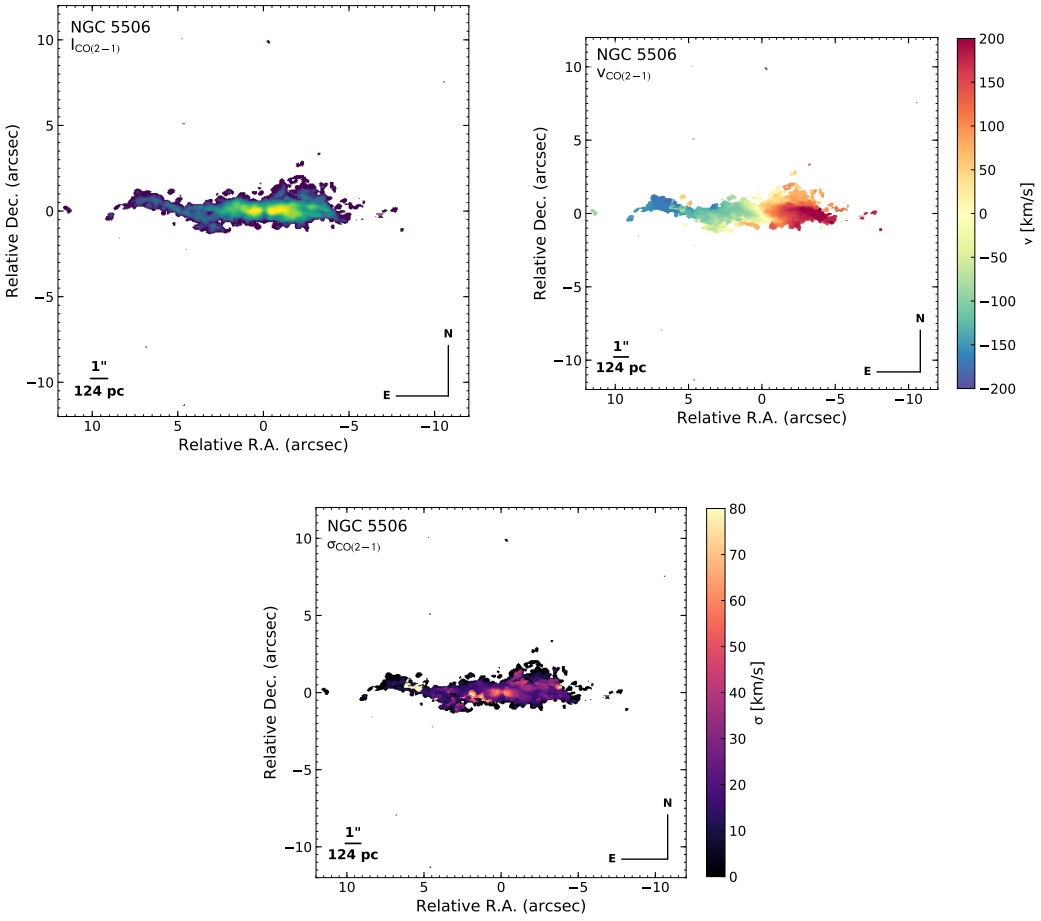

FIGURE B.19 – Moment 0 (left), Moment 1 (center), and Moment 2 (right) maps of the $CO(2-1)$ emission line for the galaxy NGC 5506. The Moment 0 map shows the integrated intensity, the Moment 1 map shows the velocity field, and the Moment 2 map displays the velocity dispersion.

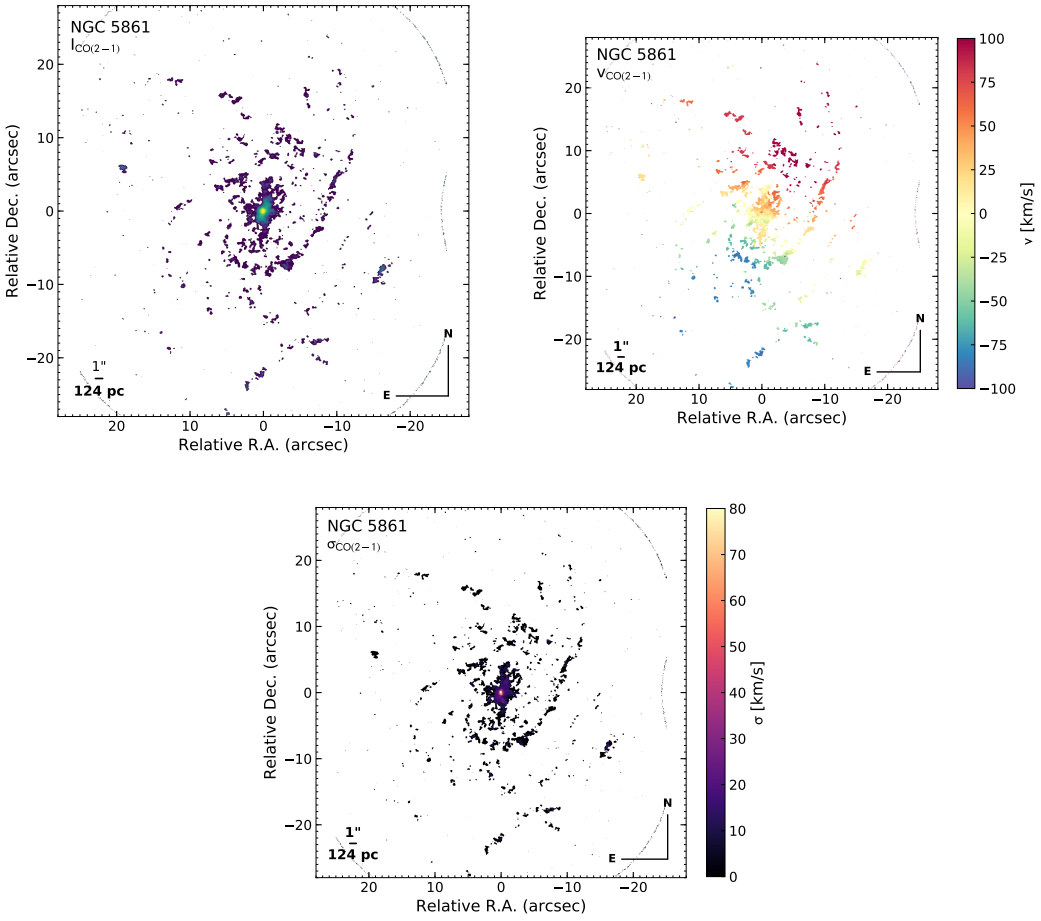

FIGURE B.20 – Moment 0 (left), Moment 1 (center), and Moment 2 (right) maps of the $CO(2-1)$ emission line for the galaxy NGC 5861. The Moment 0 map shows the integrated intensity, the Moment 1 map shows the velocity field, and the Moment 2 map displays the velocity dispersion.

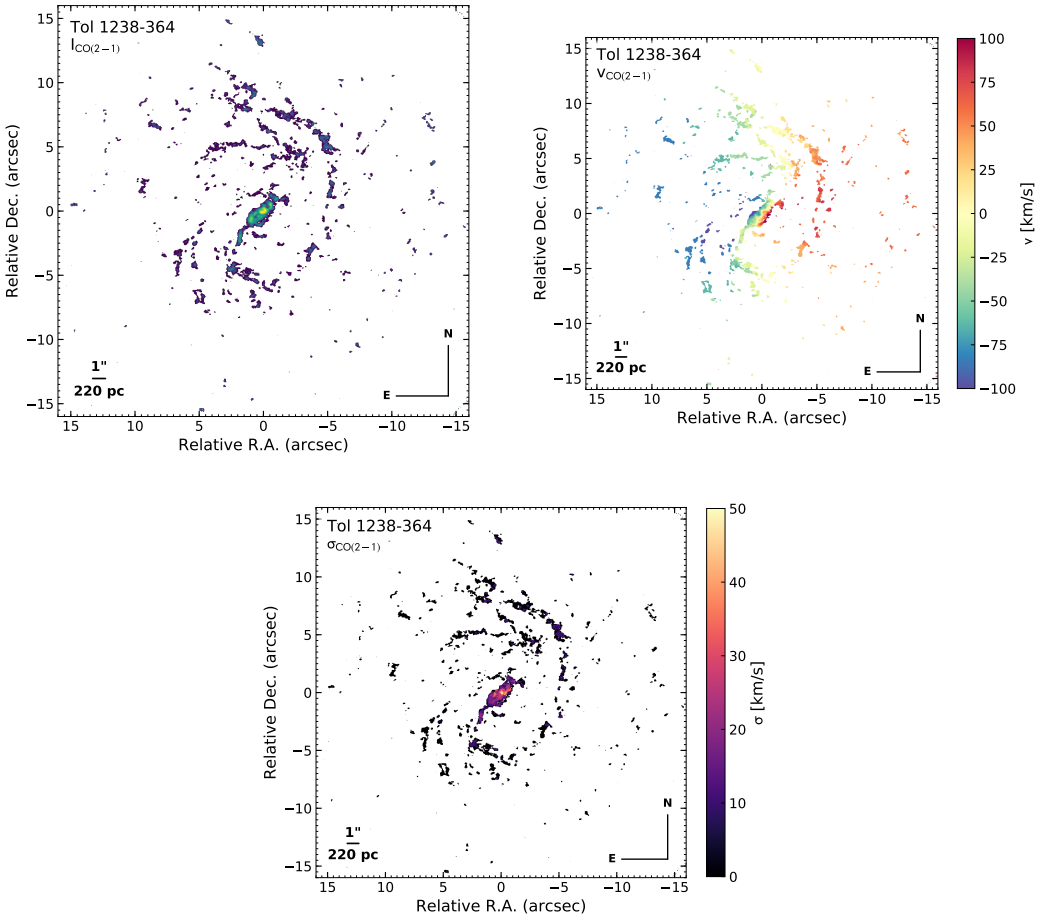

FIGURE B.21 – Moment 0 (left), Moment 1 (center), and Moment 2 (right) maps of the $CO(2-1)$ emission line for the galaxy TOL 1238. The Moment 0 map shows the integrated intensity, the Moment 1 map shows the velocity field, and the Moment 2 map displays the velocity dispersion.

Appendix C - TWIST sample Results
3D-Barolo Results (Maps)

3d-Barolo plots for TWIST sample

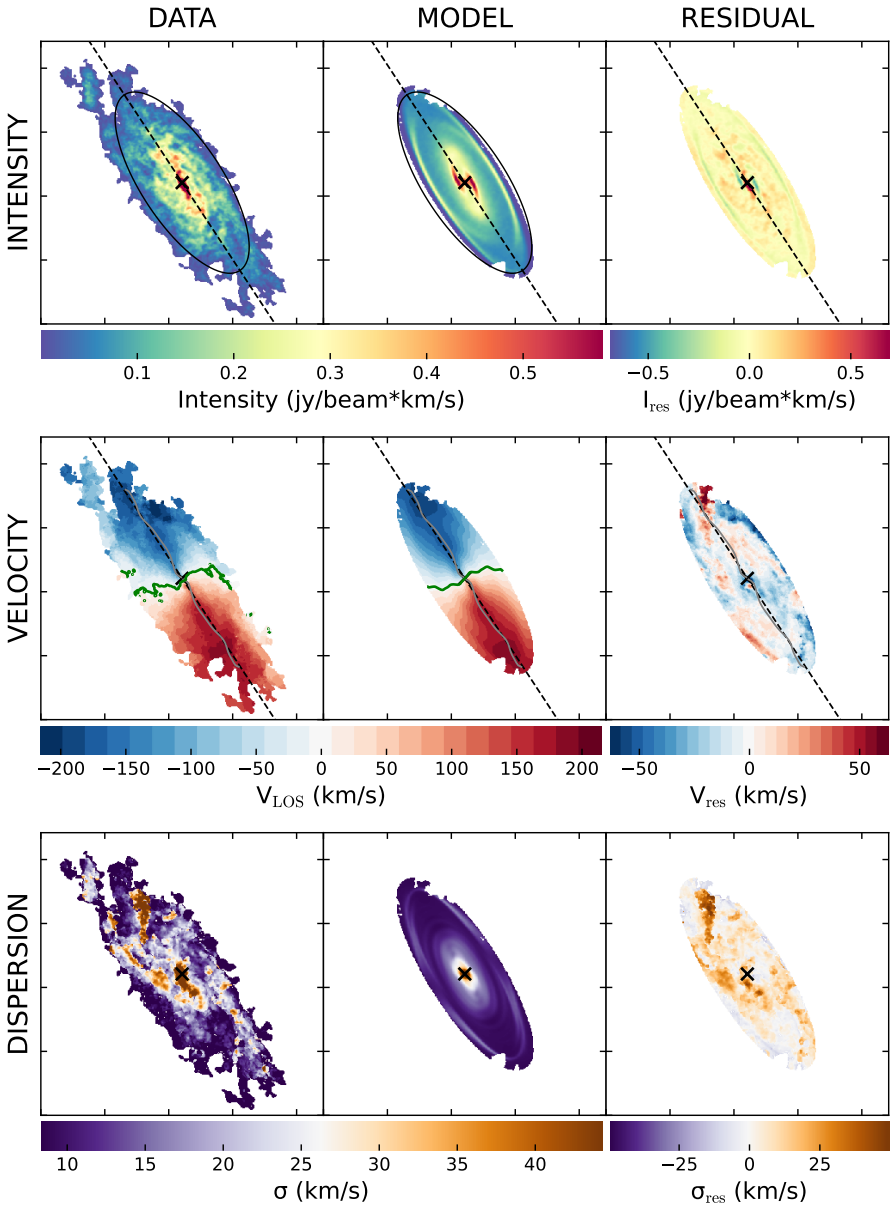

FIGURE C.1 – Intensity, velocity, and dispersion maps for IC 5169 using 3D-Barolo with azimuthal normalization. Each panel contains a grid of 3x3 images showing the data, model, and residuals for intensity (top row), velocity (middle row), and velocity dispersion (bottom row).

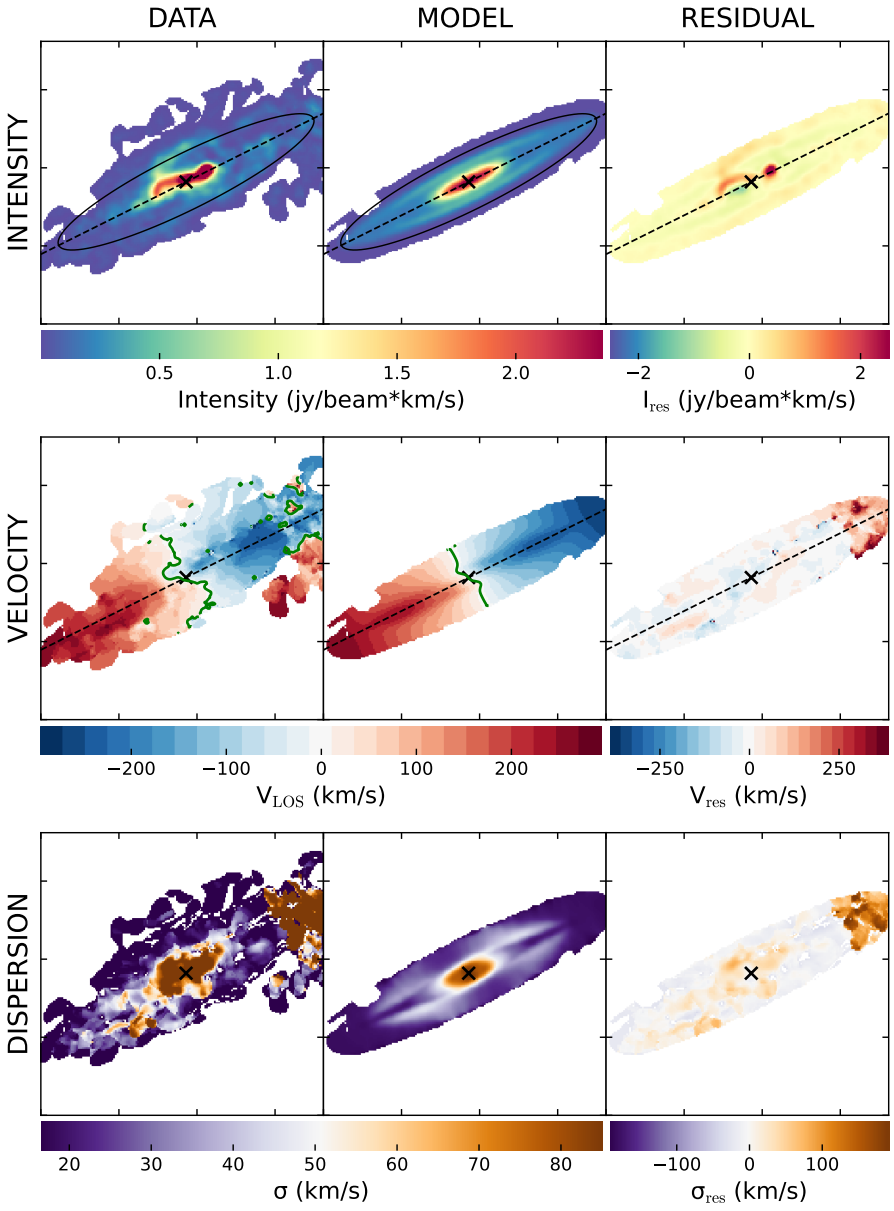

FIGURE C.2 – Intensity, velocity, and dispersion maps for IC 5063 using 3D-Barolo with azimuthal normalization. Each panel contains a grid of 3x3 images showing the data, model, and residuals for intensity (top row), velocity (middle row), and velocity dispersion (bottom row).

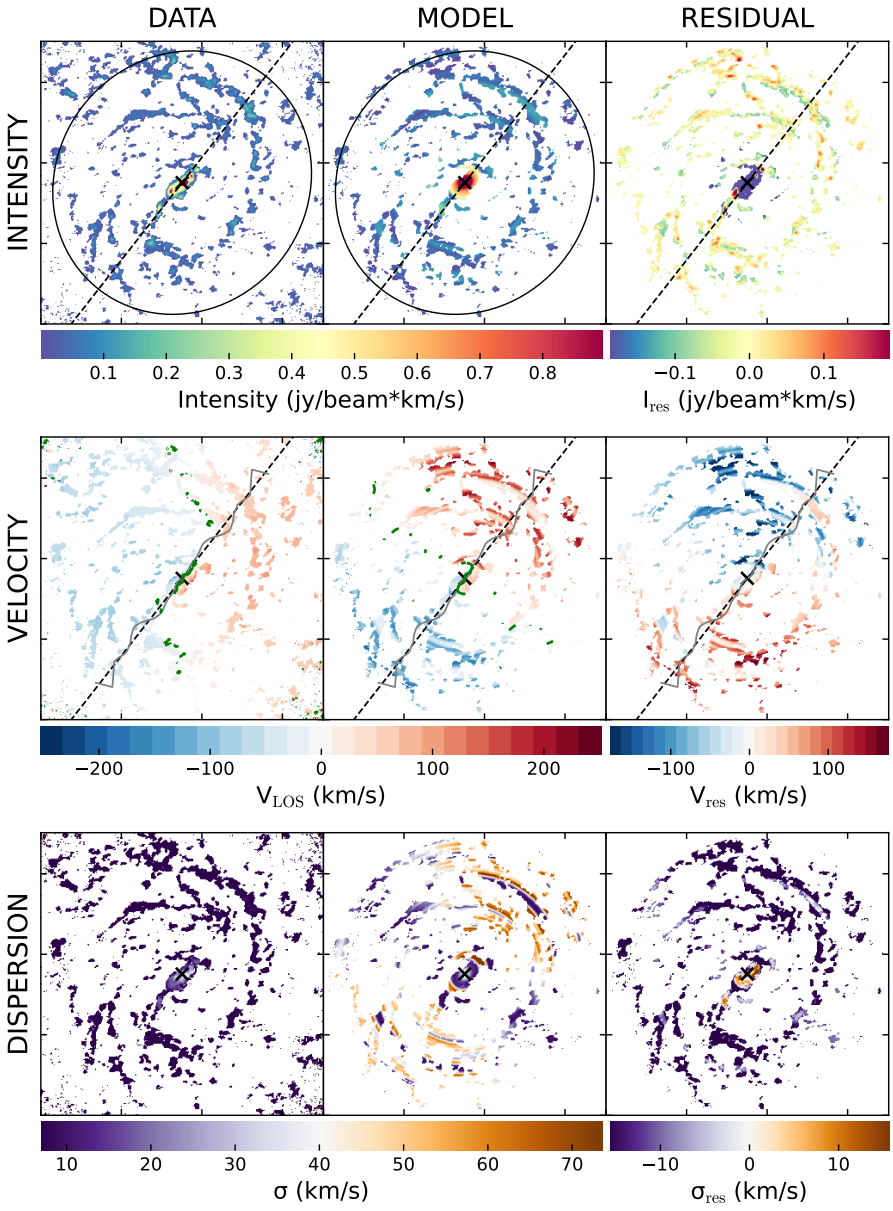

FIGURE C.3 – Intensity, velocity, and dispersion maps for IC 3639 using 3D-Barolo with azimuthal normalization. Each panel contains a grid of 3x3 images showing the data, model, and residuals for intensity (top row), velocity (middle row), and velocity dispersion (bottom row).

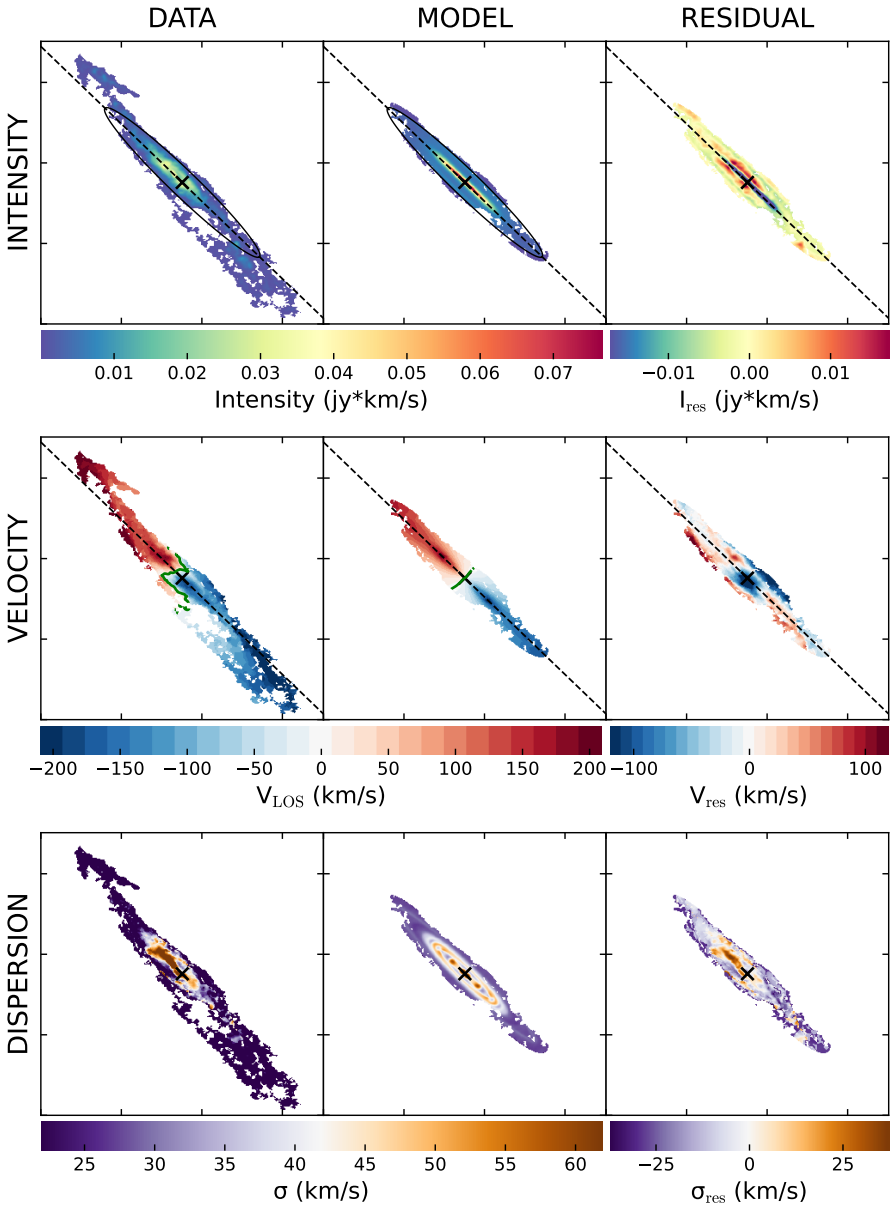

FIGURE C.4 – Intensity, velocity, and dispersion maps for Mrk 1333 using 3D-Barolo with azimuthal normalization. Each panel contains a grid of 3x3 images showing the data, model, and residuals for intensity (top row), velocity (middle row), and velocity dispersion (bottom row).

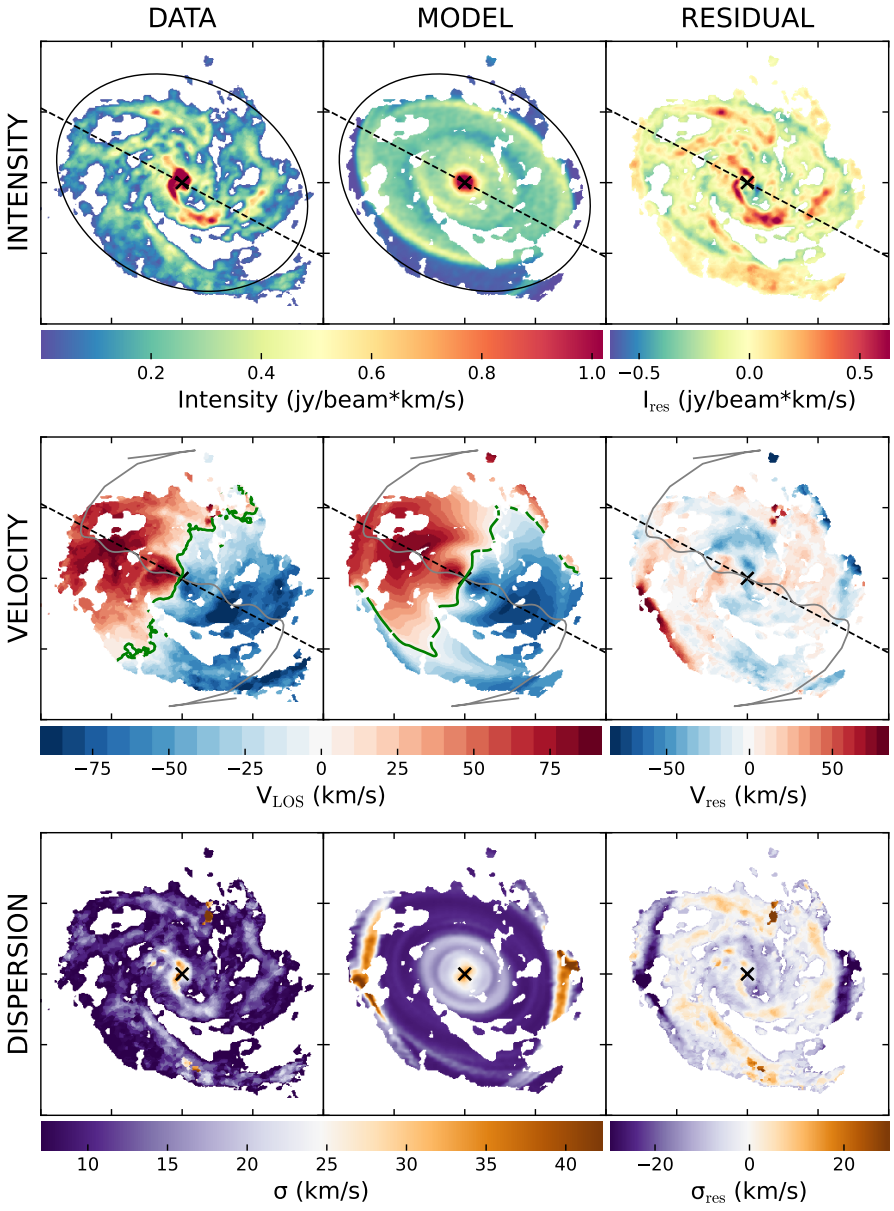

FIGURE C.5 – Intensity, velocity, and dispersion maps for MCG-5-11-06 using 3D-Barolo with azimuthal normalization. Each panel contains a grid of 3x3 images showing the data, model, and residuals for intensity (top row), velocity (middle row), and velocity dispersion (bottom row).

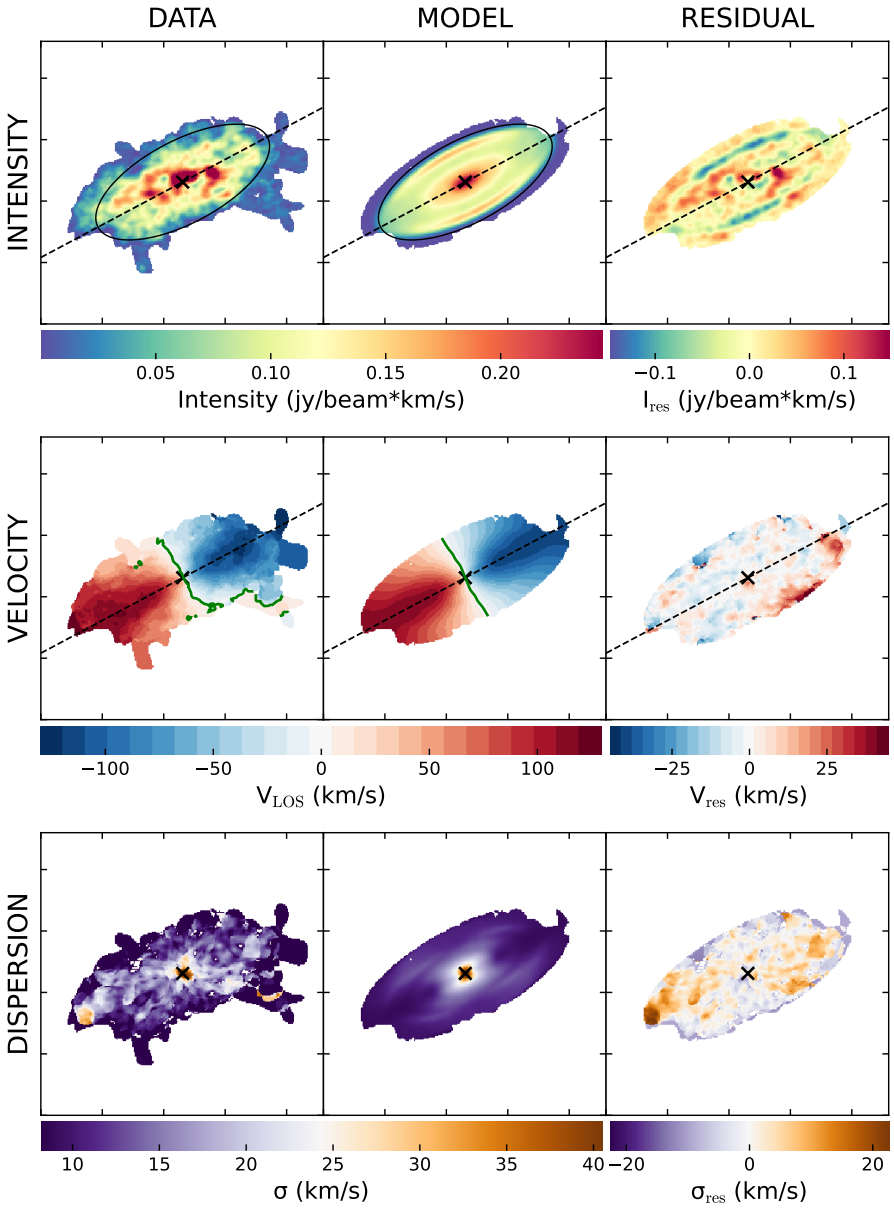

FIGURE C.6 – Intensity, velocity, and dispersion maps for MCG-6-30-15 using 3D-Barolo with azimuthal normalization. Each panel contains a grid of 3x3 images showing the data, model, and residuals for intensity (top row), velocity (middle row), and velocity dispersion (bottom row).

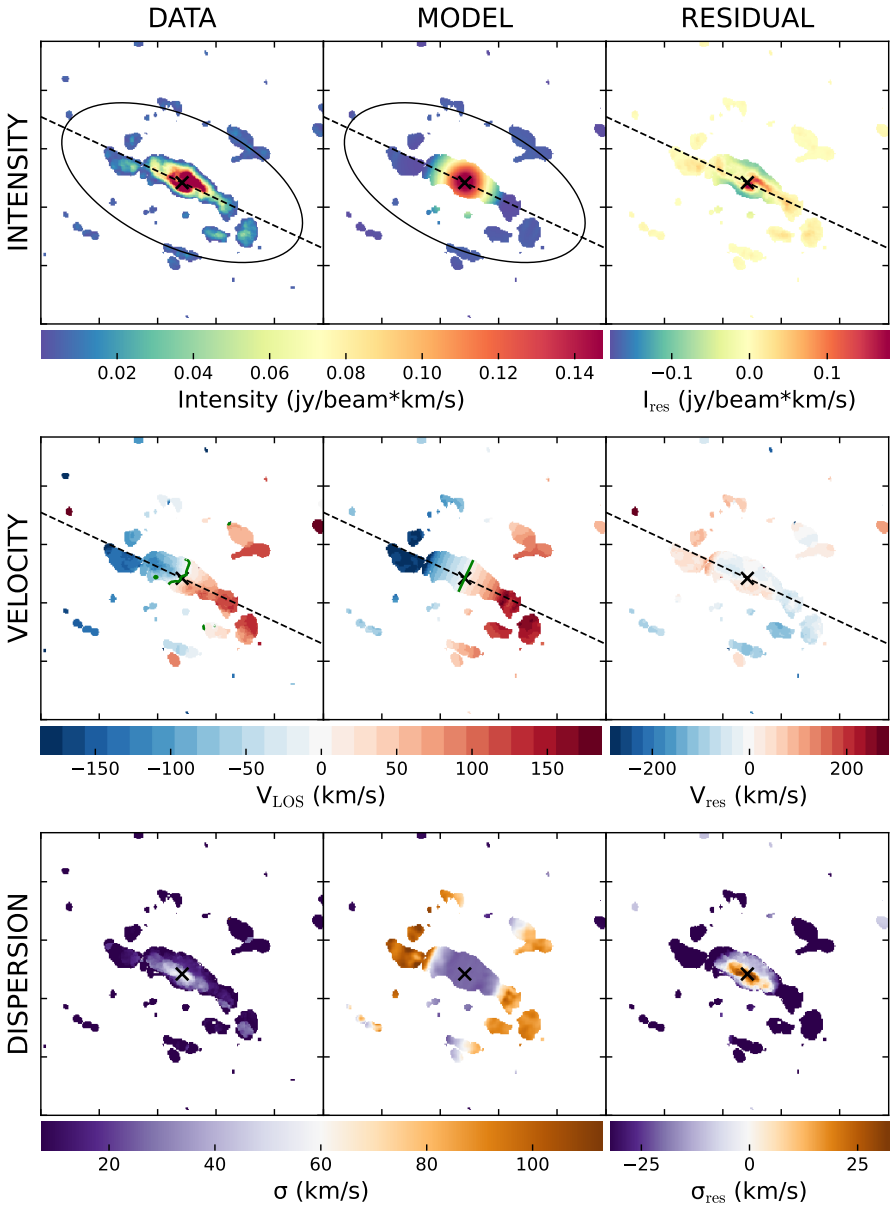

FIGURE C.7 – Intensity, velocity, and dispersion maps for NGC 424 using 3D-Barolo with azimuthal normalization. Each panel contains a grid of 3x3 images showing the data, model, and residuals for intensity (top row), velocity (middle row), and velocity dispersion (bottom row).

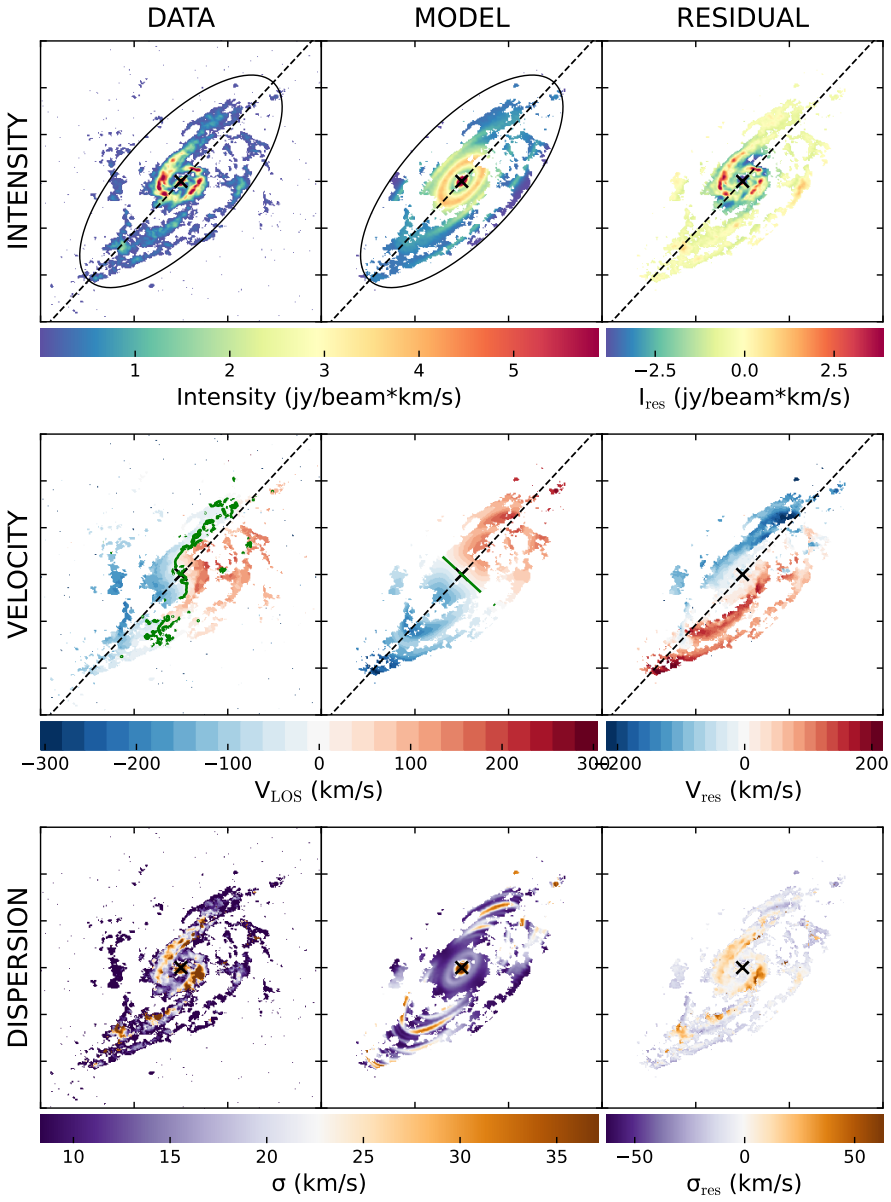

FIGURE C.8 – Intensity, velocity, and dispersion maps for NGC 613 using 3D-BAROLO with azimuthal normalization. Each panel contains a grid of 3x3 images showing the data, model, and residuals for intensity (top row), velocity (middle row), and velocity dispersion (bottom row).

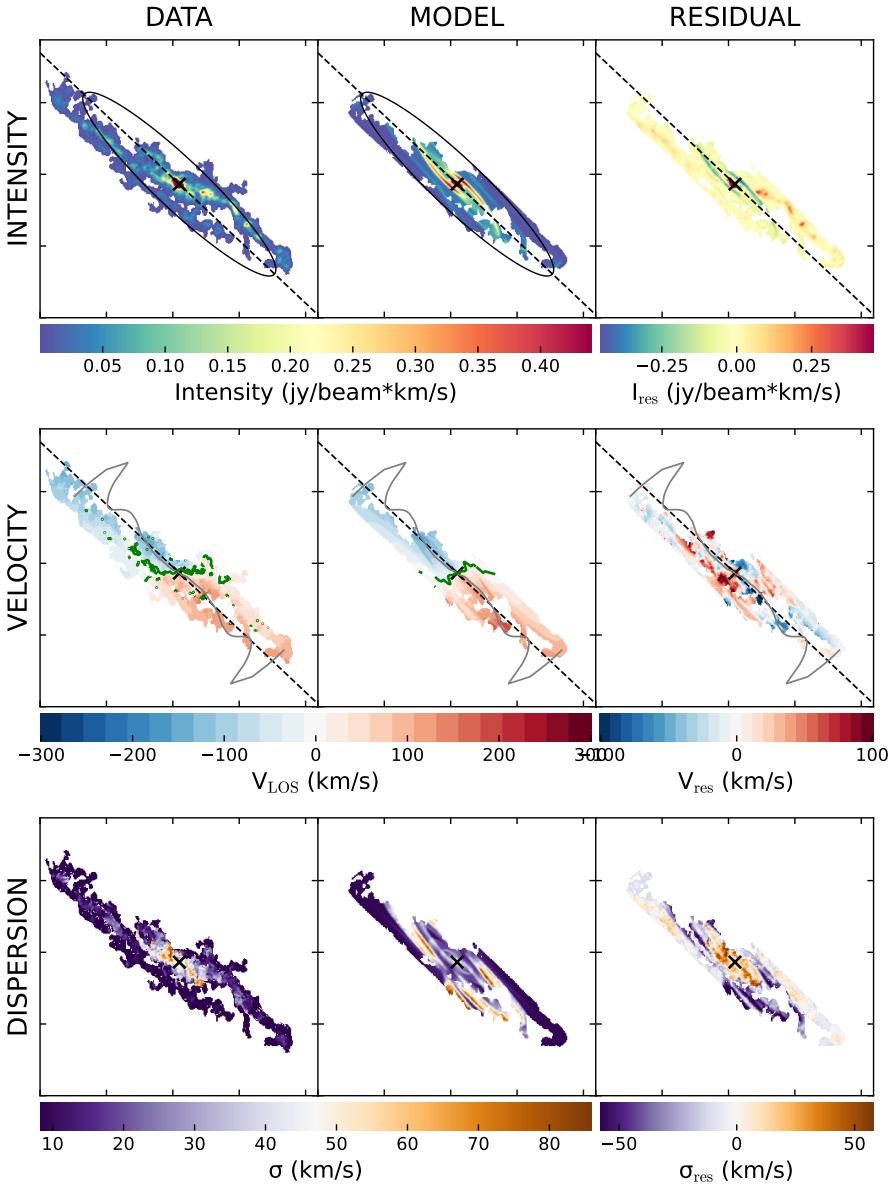

FIGURE C.9 – Intensity, velocity, and dispersion maps for NGC 1125 using 3D-Barolo with azimuthal normalization. Each panel contains a grid of 3x3 images showing the data, model, and residuals for intensity (top row), velocity (middle row), and velocity dispersion (bottom row).

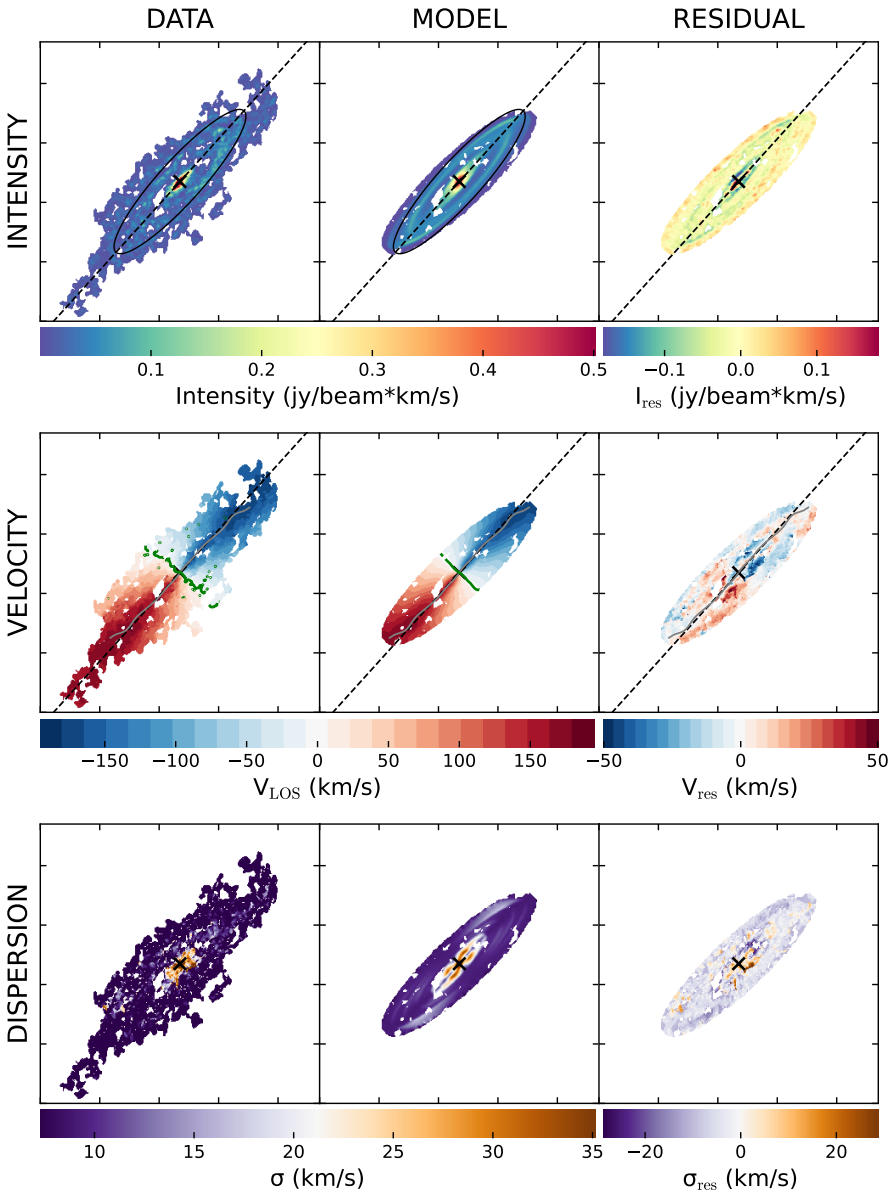

FIGURE C.10 – Intensity, velocity, and dispersion maps for NGC 1320 using 3D-Barolo with azimuthal normalization. Each panel contains a grid of 3x3 images showing the data, model, and residuals for intensity (top row), velocity (middle row), and velocity dispersion (bottom row).

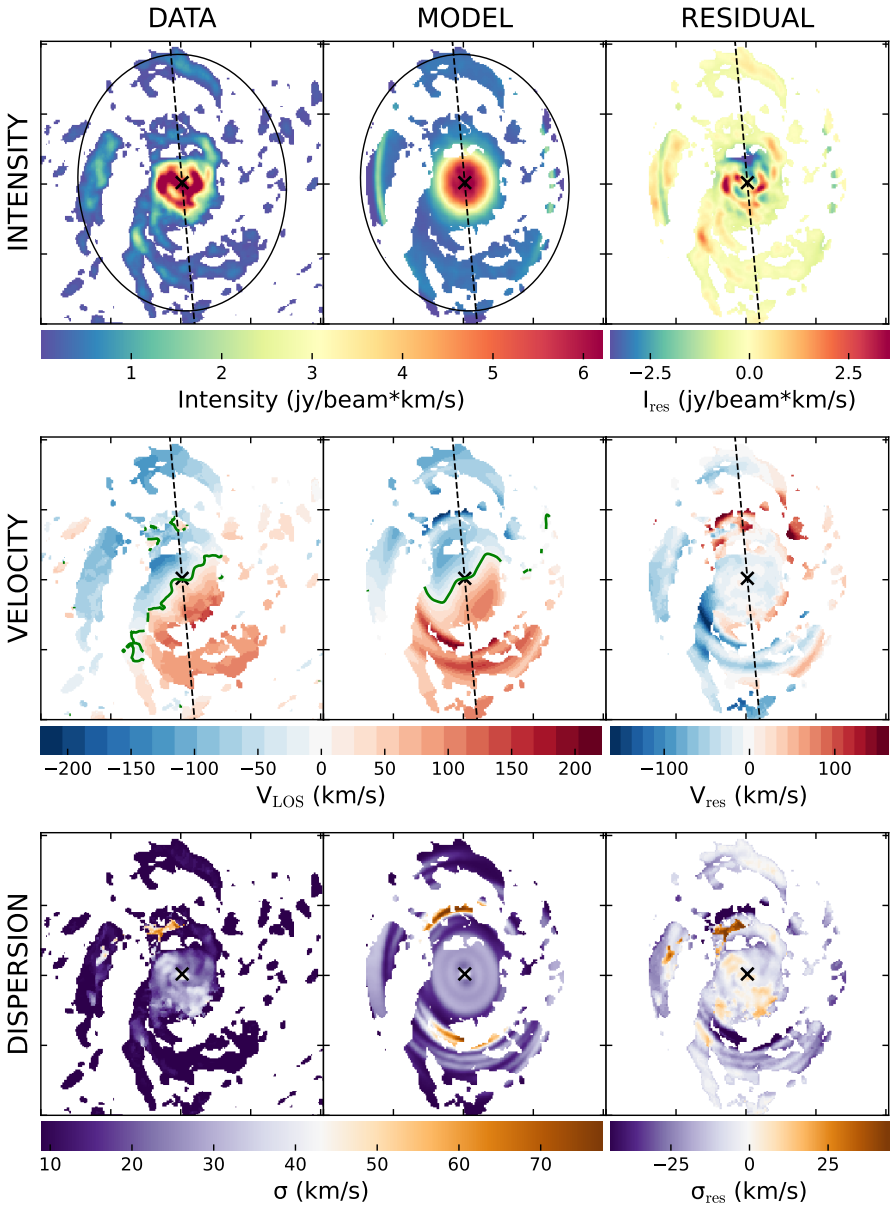

FIGURE C.11 – Intensity, velocity, and dispersion maps for NGC 1566 using 3D-Barolo with azimuthal normalization. Each panel contains a grid of 3x3 images showing the data, model, and residuals for intensity (top row), velocity (middle row), and velocity dispersion (bottom row).

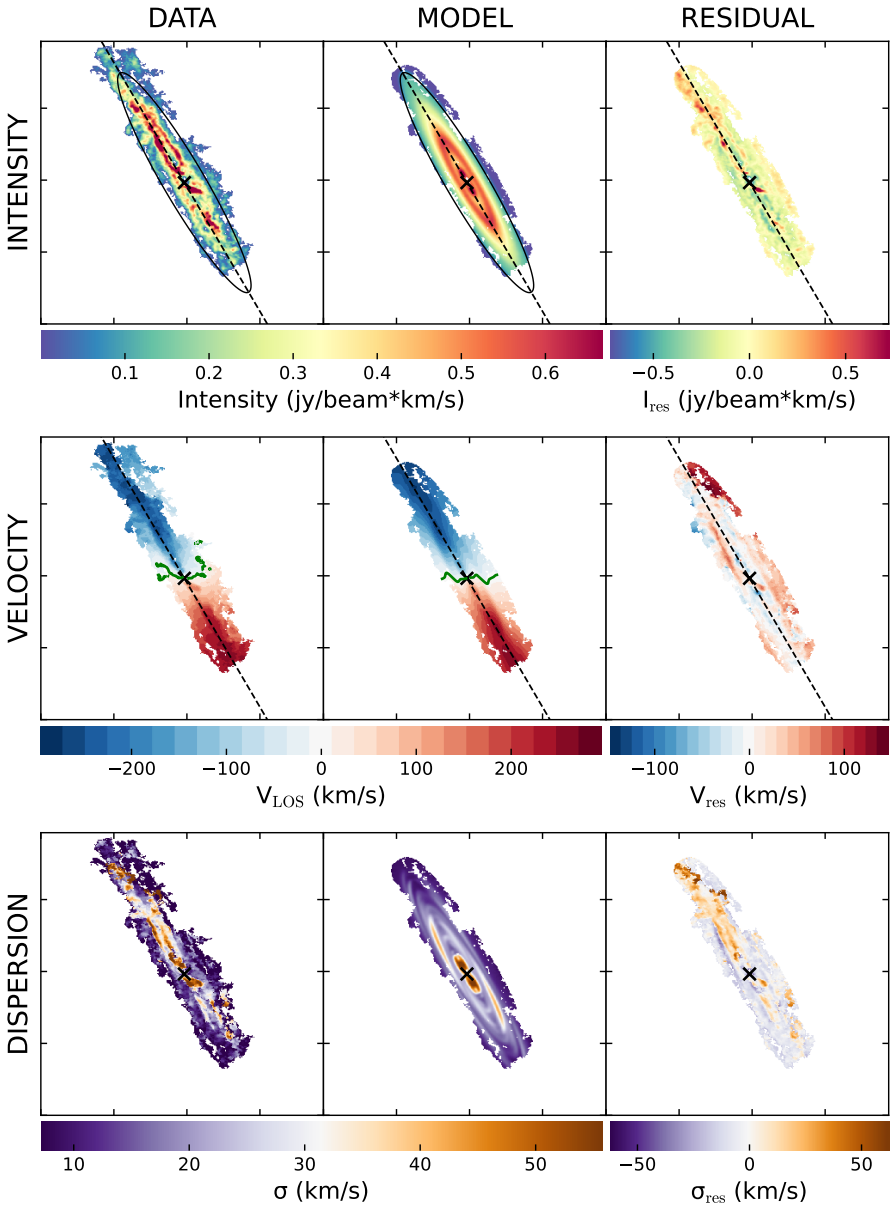

FIGURE C.12 – Intensity, velocity, and dispersion maps for NGC 2992 using 3D-Barolo with azimuthal normalization. Each panel contains a grid of 3x3 images showing the data, model, and residuals for intensity (top row), velocity (middle row), and velocity dispersion (bottom row).

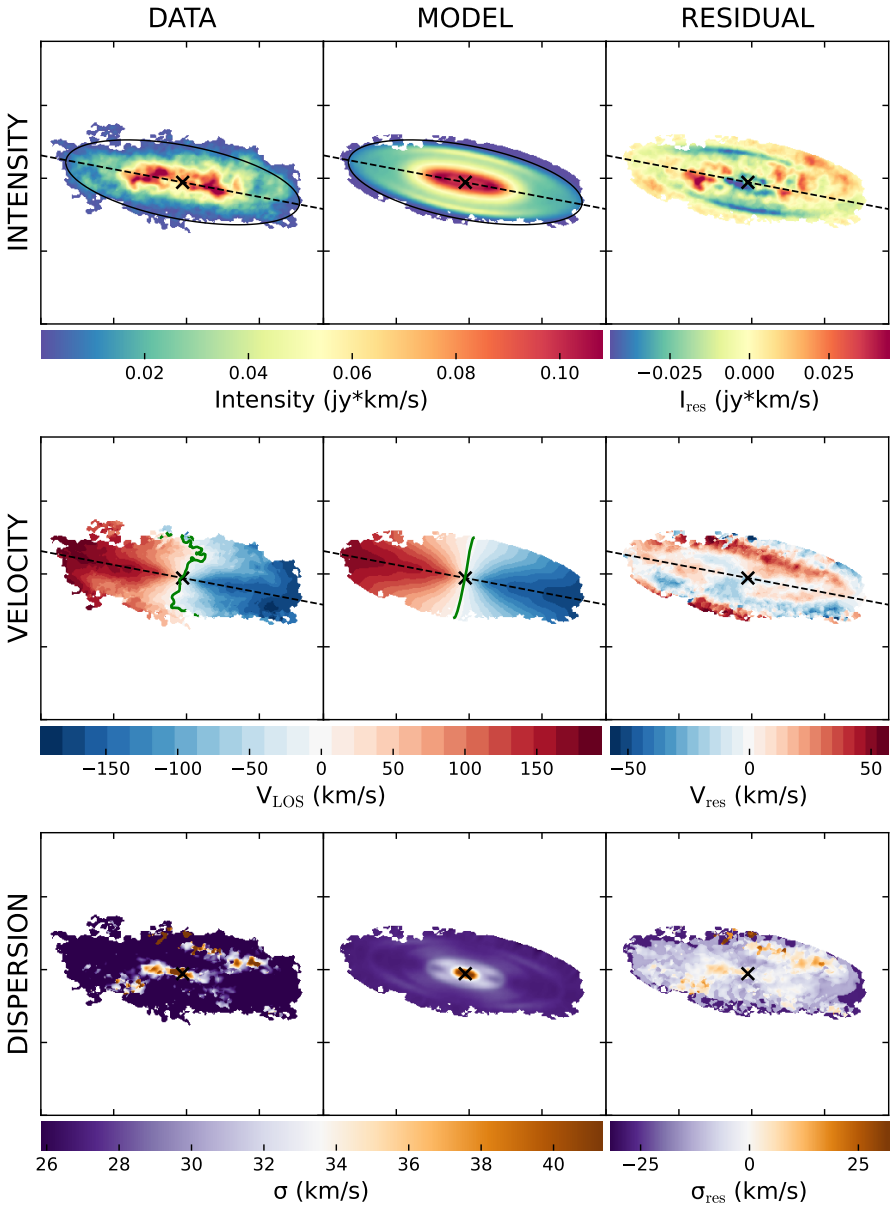

FIGURE C.13 – Intensity, velocity, and dispersion maps for NGC 4845 using 3D-Barolo with azimuthal normalization. Each panel contains a grid of 3x3 images showing the data, model, and residuals for intensity (top row), velocity (middle row), and velocity dispersion (bottom row).

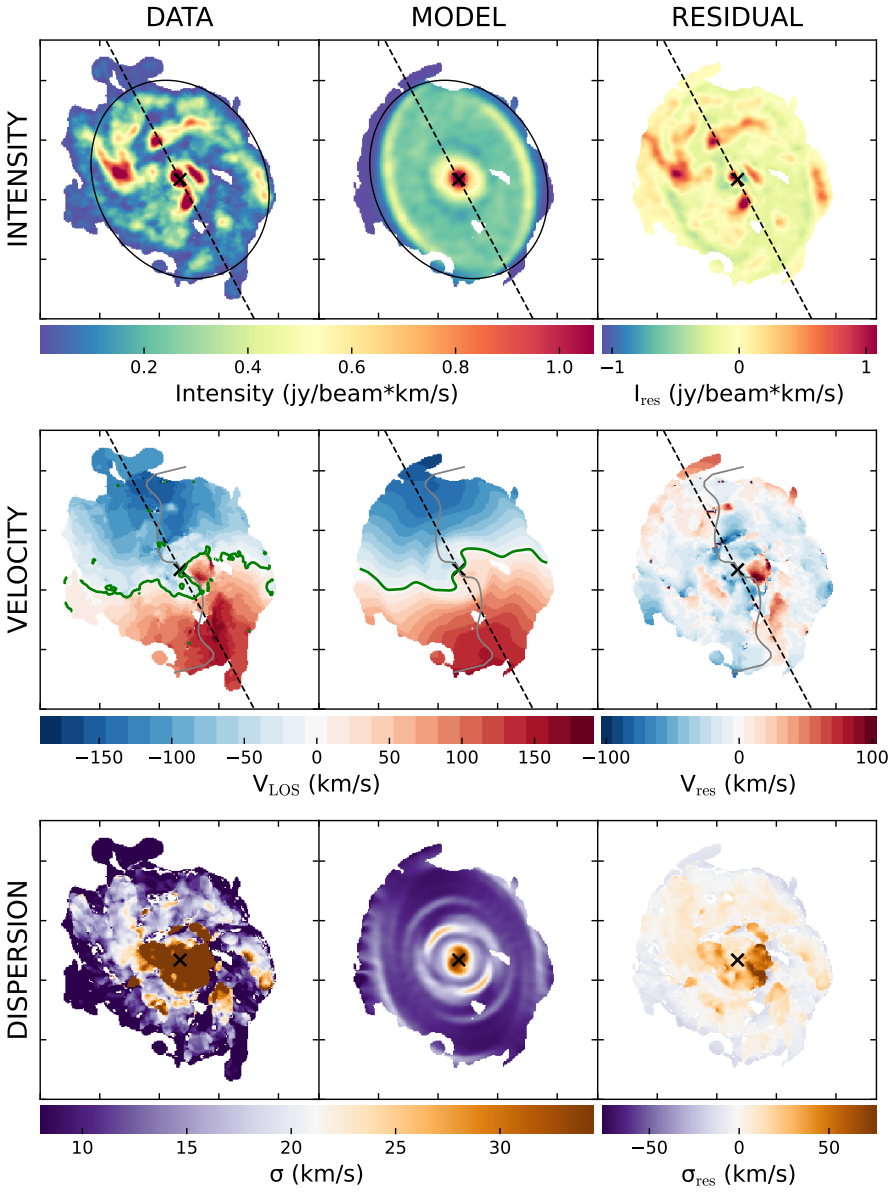

FIGURE C.14 – Intensity, velocity, and dispersion maps for NGC 4941 using 3D-Barolo with azimuthal normalization. Each panel contains a grid of 3x3 images showing the data, model, and residuals for intensity (top row), velocity (middle row), and velocity dispersion (bottom row).

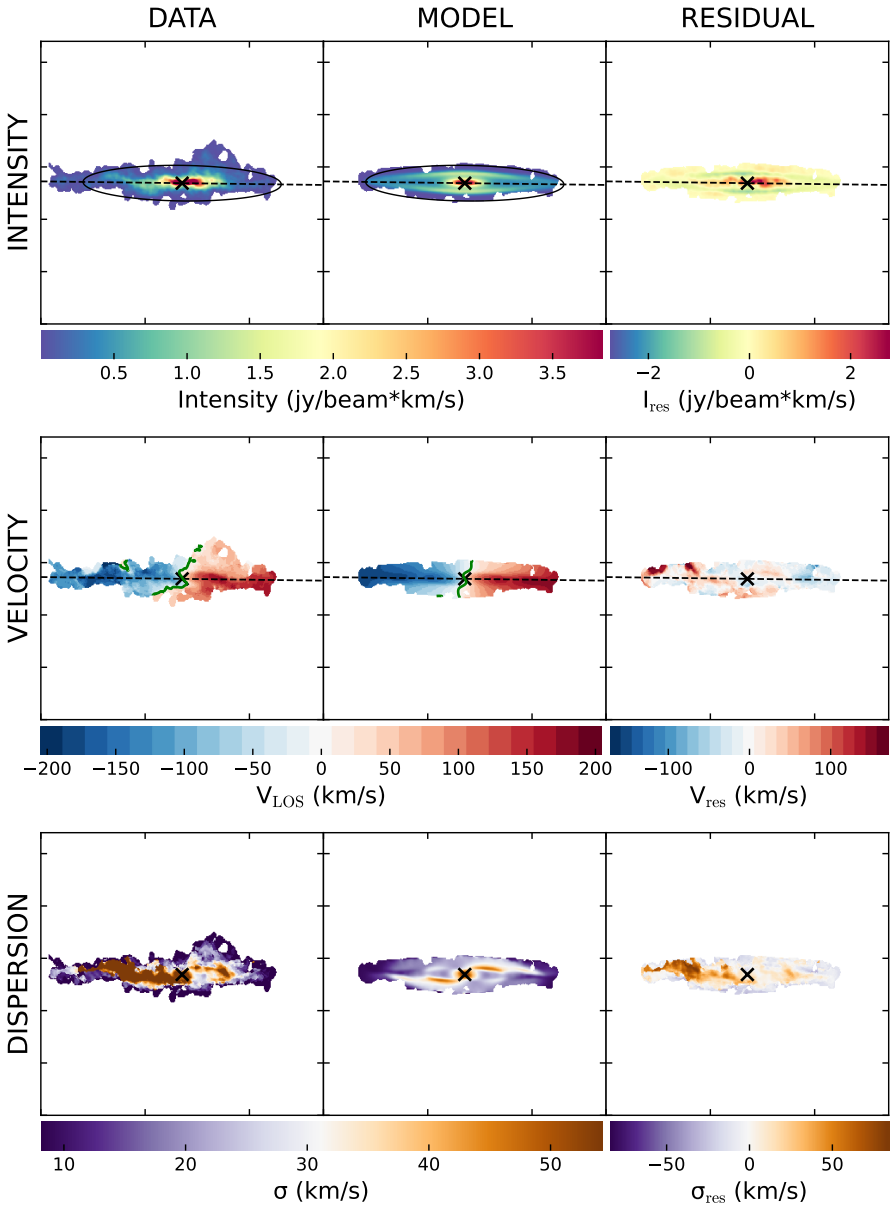

FIGURE C.15 – Intensity, velocity, and dispersion maps for NGC 5506 using 3D-BAROLO with azimuthal normalization. Each panel contains a grid of 3x3 images showing the data, model, and residuals for intensity (top row), velocity (middle row), and velocity dispersion (bottom row).

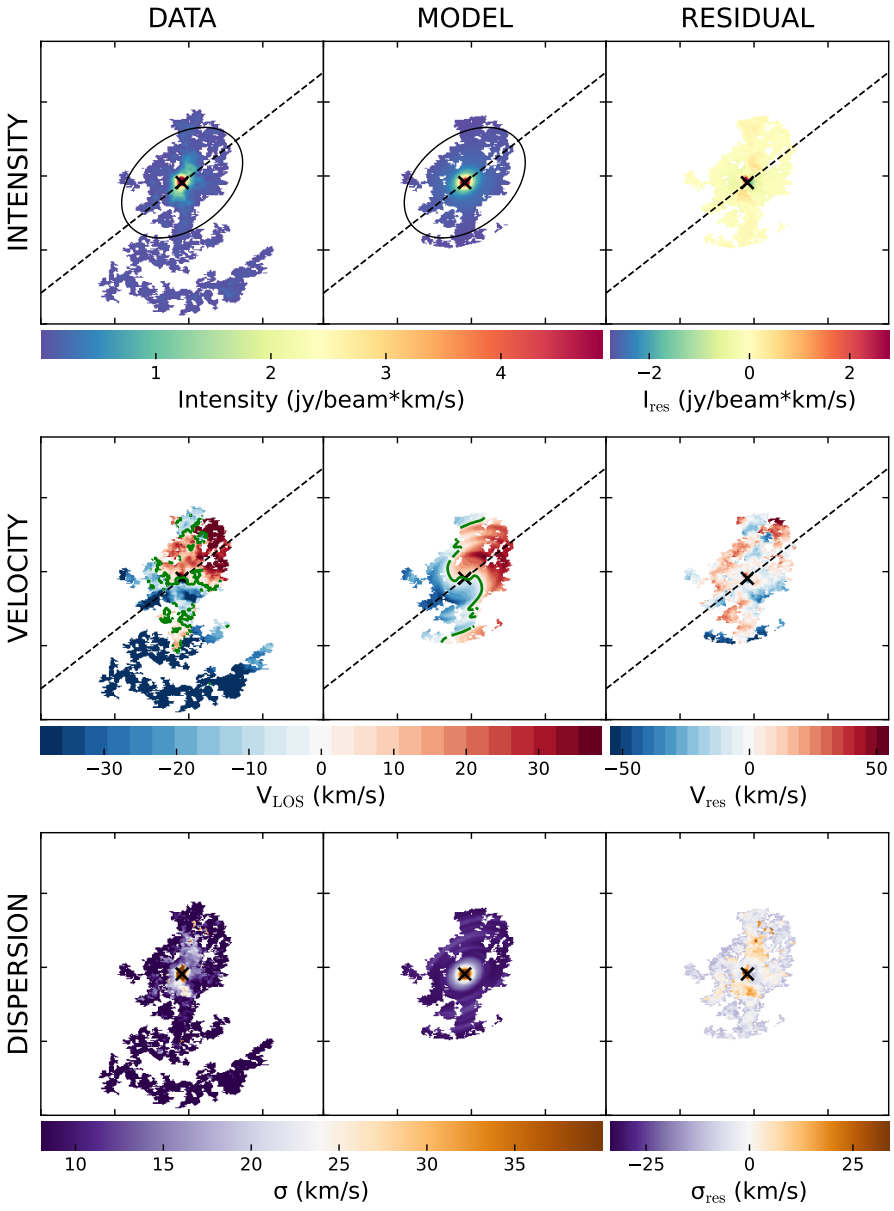

FIGURE C.16 – Intensity, velocity, and dispersion maps for NGC 5861 using 3D-Barolo with azimuthal normalization. Each panel contains a grid of 3x3 images showing the data, model, and residuals for intensity (top row), velocity (middle row), and velocity dispersion (bottom row).

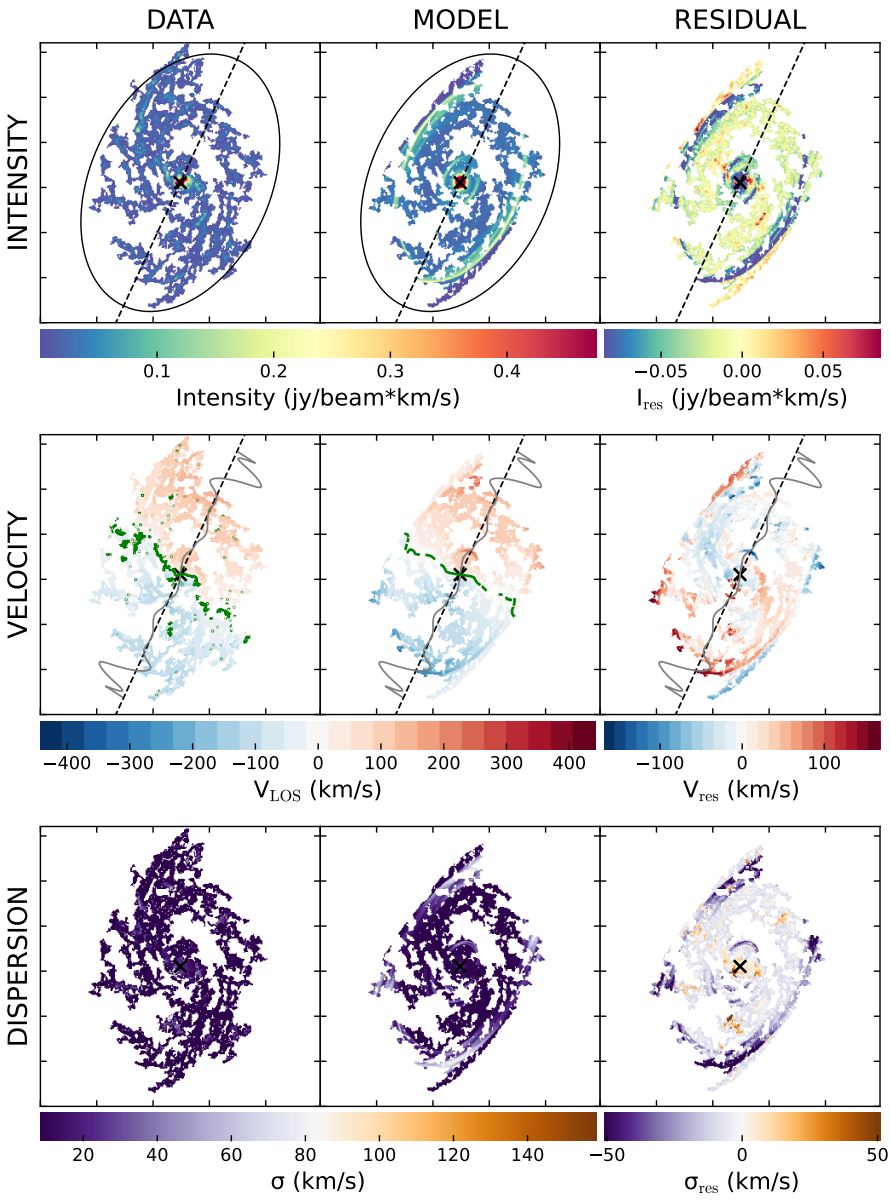

FIGURE C.17 – Intensity, velocity, and dispersion maps for NGC 6890 using 3D-BAROLO with azimuthal normalization. Each panel contains a grid of 3x3 images showing the data, model, and residuals for intensity (top row), velocity (middle row), and velocity dispersion (bottom row).

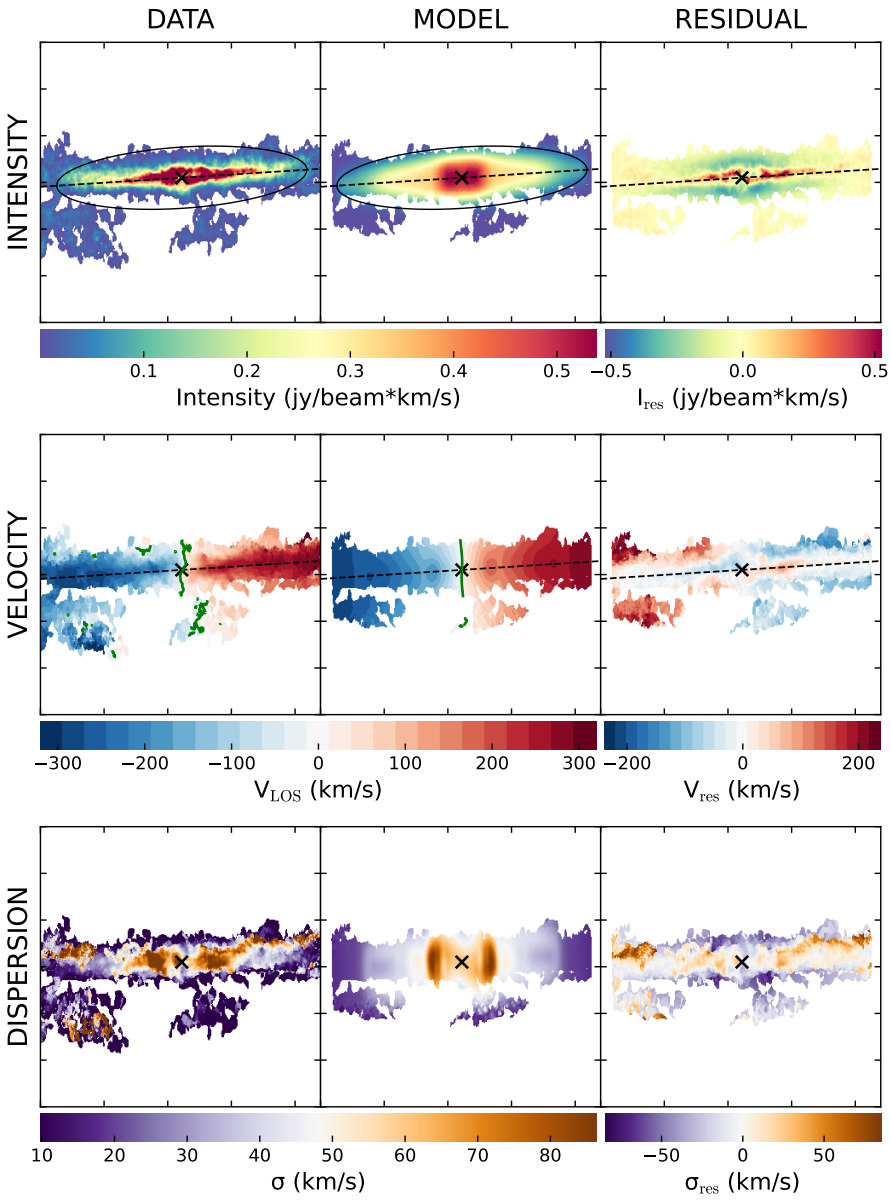

FIGURE C.18 – Intensity, velocity, and dispersion maps for NGC 7172 using 3D-BAROLO with azimuthal normalization. Each panel contains a grid of 3x3 images showing the data, model, and residuals for intensity (top row), velocity (middle row), and velocity dispersion (bottom row).

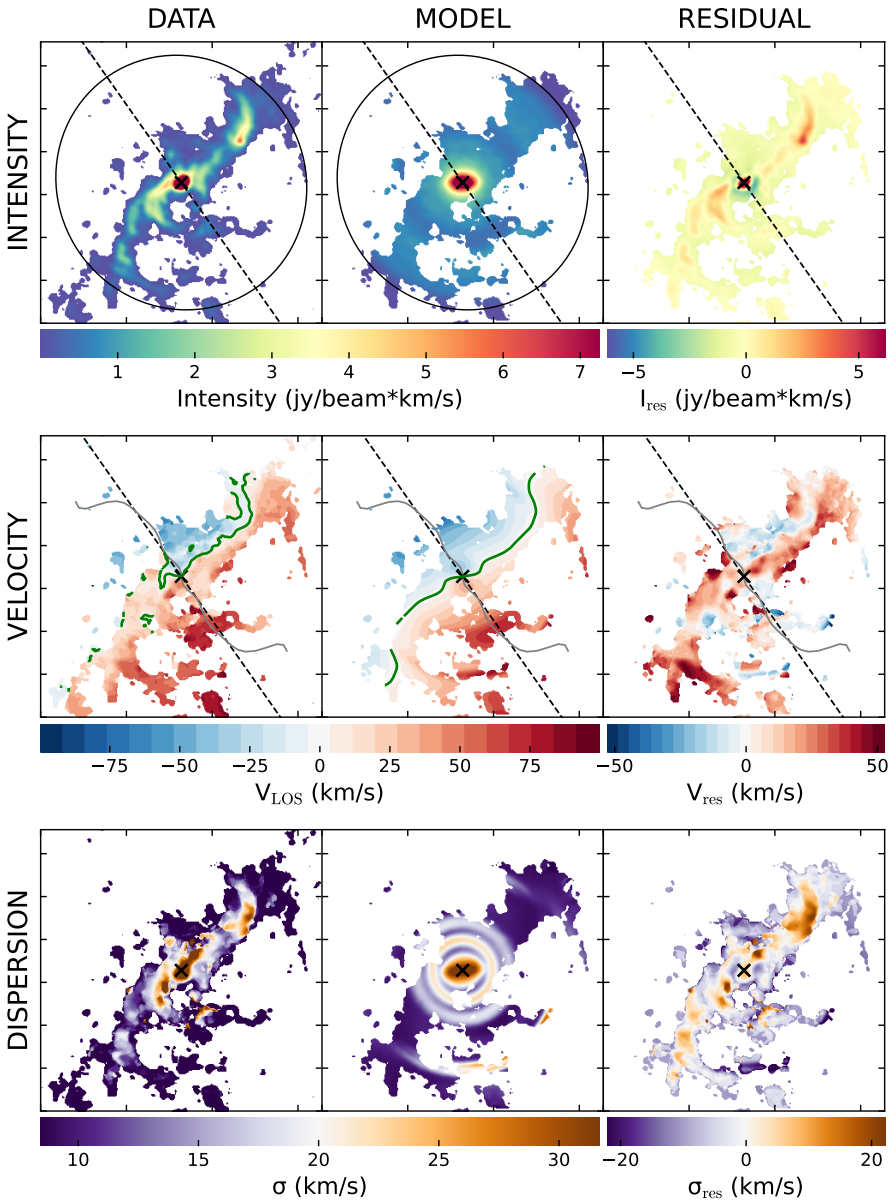

FIGURE C.19 – Intensity, velocity, and dispersion maps for NGC 7496 using 3D-BAROLO with azimuthal normalization. Each panel contains a grid of 3x3 images showing the data, model, and residuals for intensity (top row), velocity (middle row), and velocity dispersion (bottom row).

Appendix D - TWIST sample Results - PV diagrams

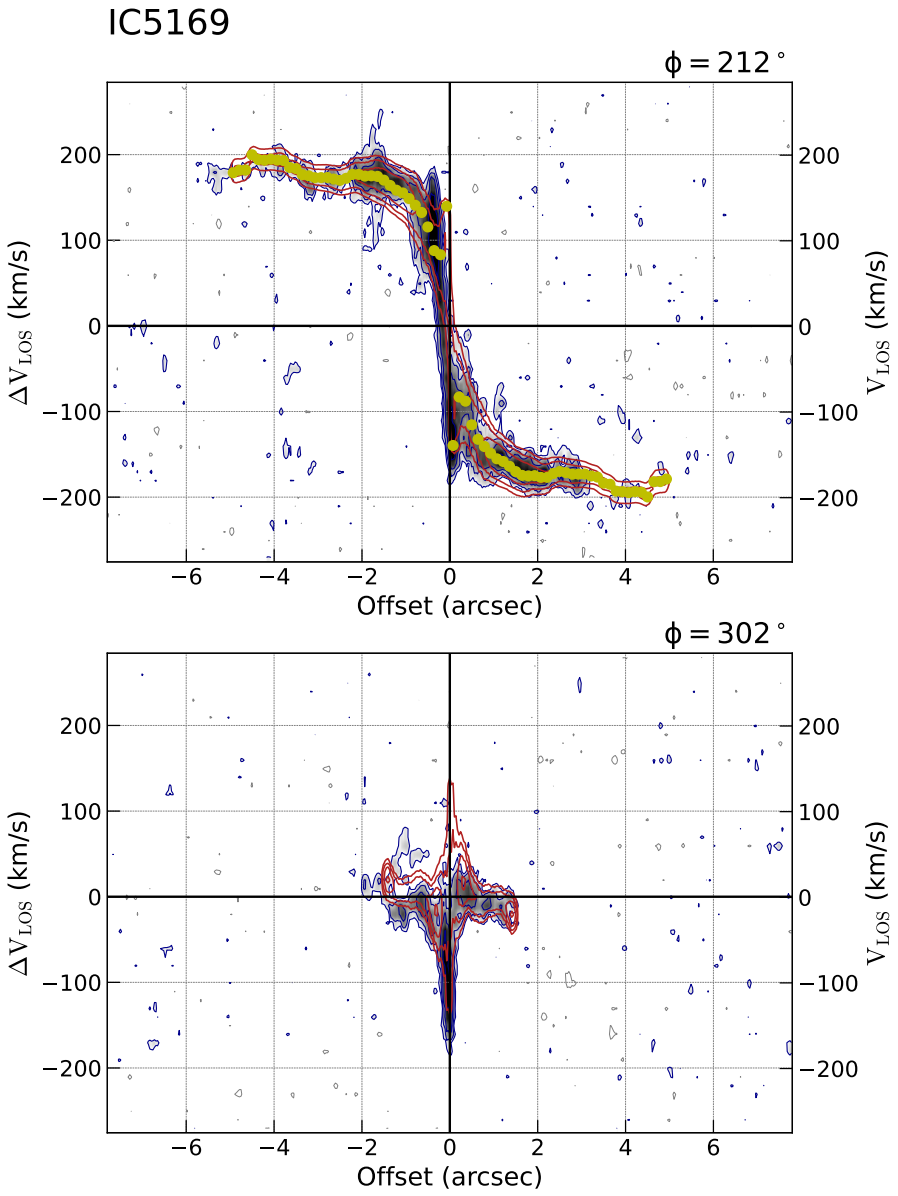

FIGURE D.1 – Position-Velocity (p-v) diagram for IC 5169 using 3D-Barolo with azimuthal normalization.

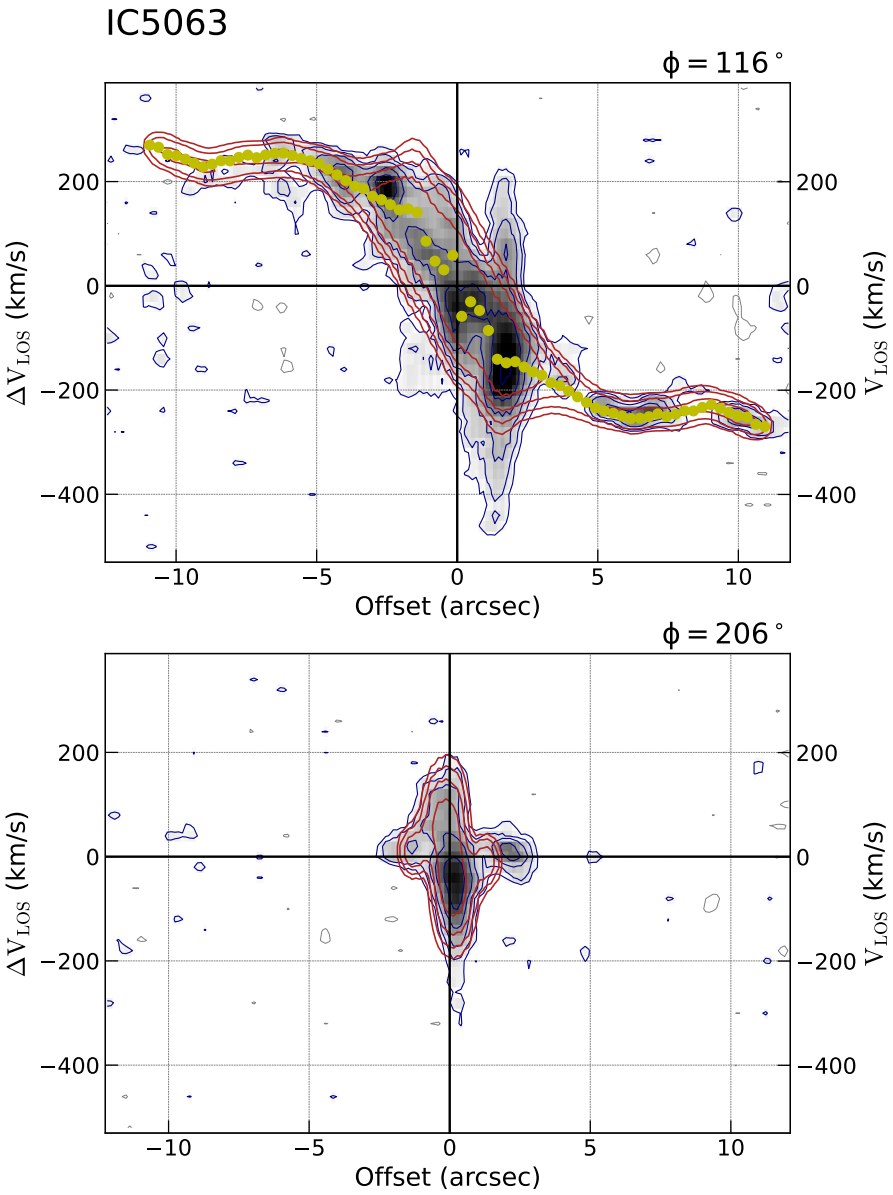

FIGURE D.2 – Position-Velocity (p-v) diagram for IC 5063 using 3D-Barolo with azimuthal normalization.

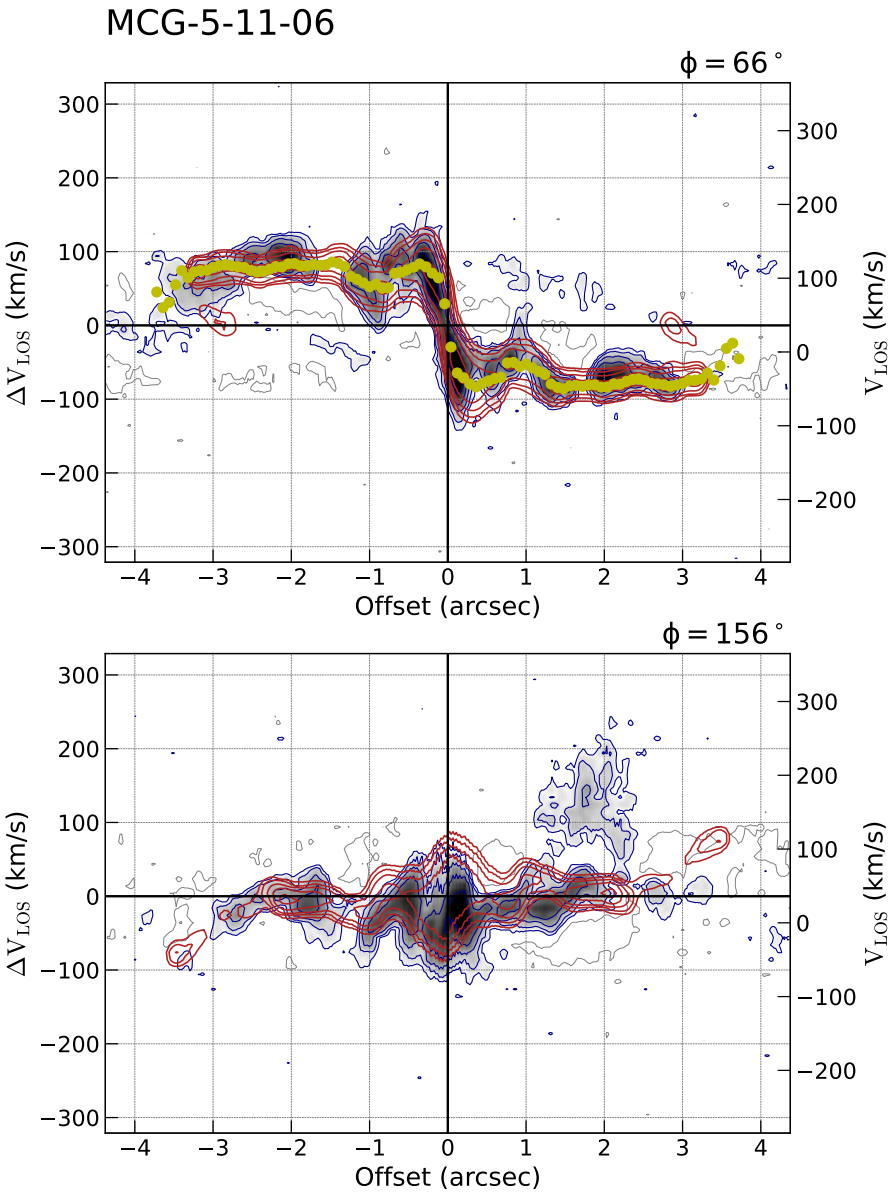

FIGURE D.3 – Position-Velocity (p-v) diagram for MCG-5-11-06 using 3D-Barolo with azimuthal normalization.

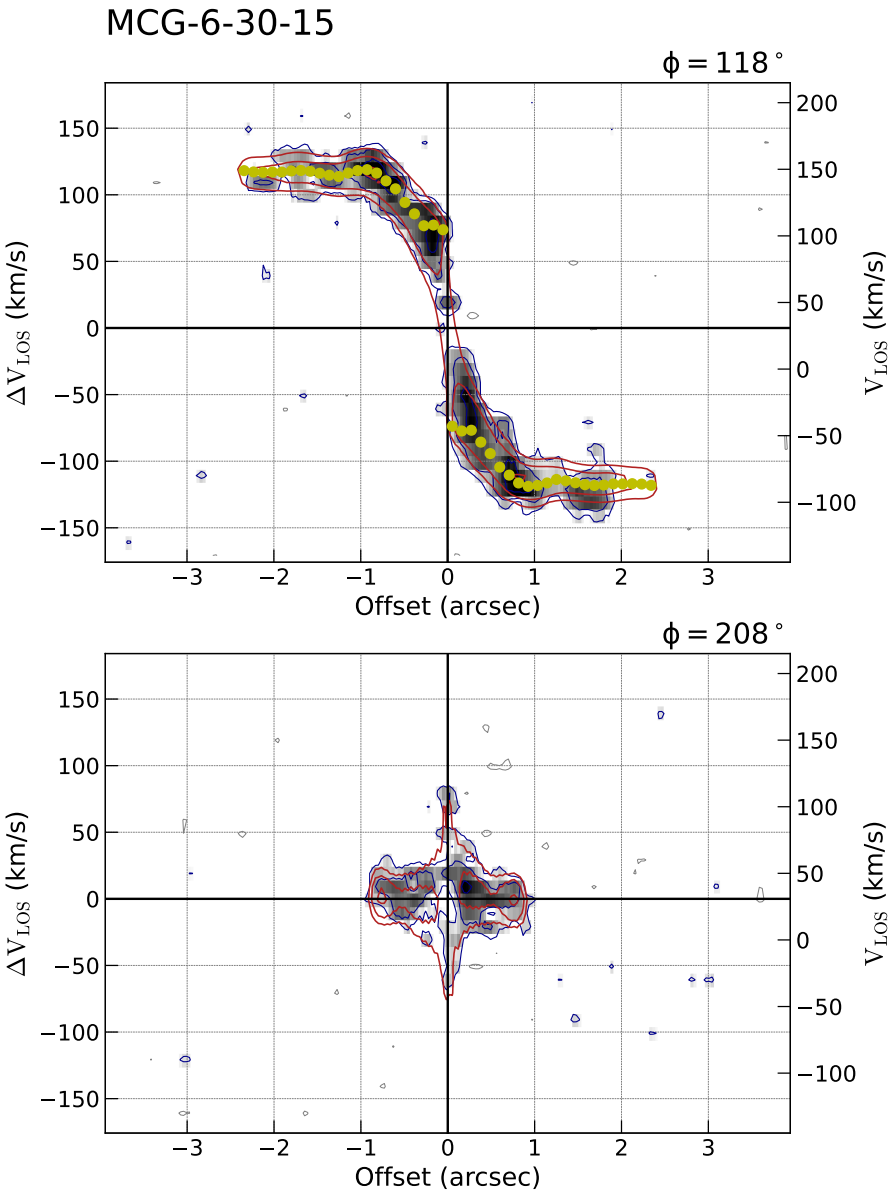

FIGURE D.4 – Position-Velocity (p-v) diagram for MCG-6-30-15 using 3D-Barolo with azimuthal normalization.

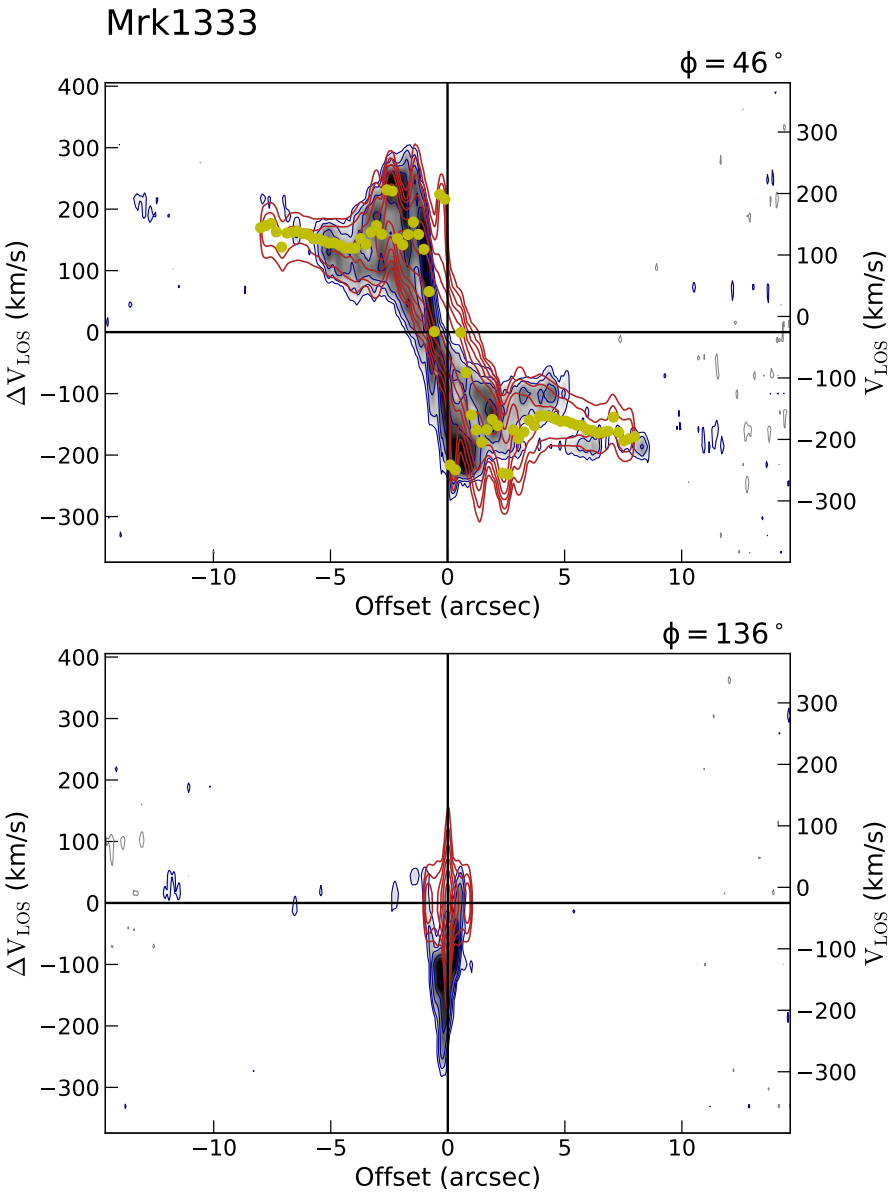

FIGURE D.5 – Position-Velocity (p-v) diagram for Mrk 1333 using 3D-Barolo with azimuthal normalization.

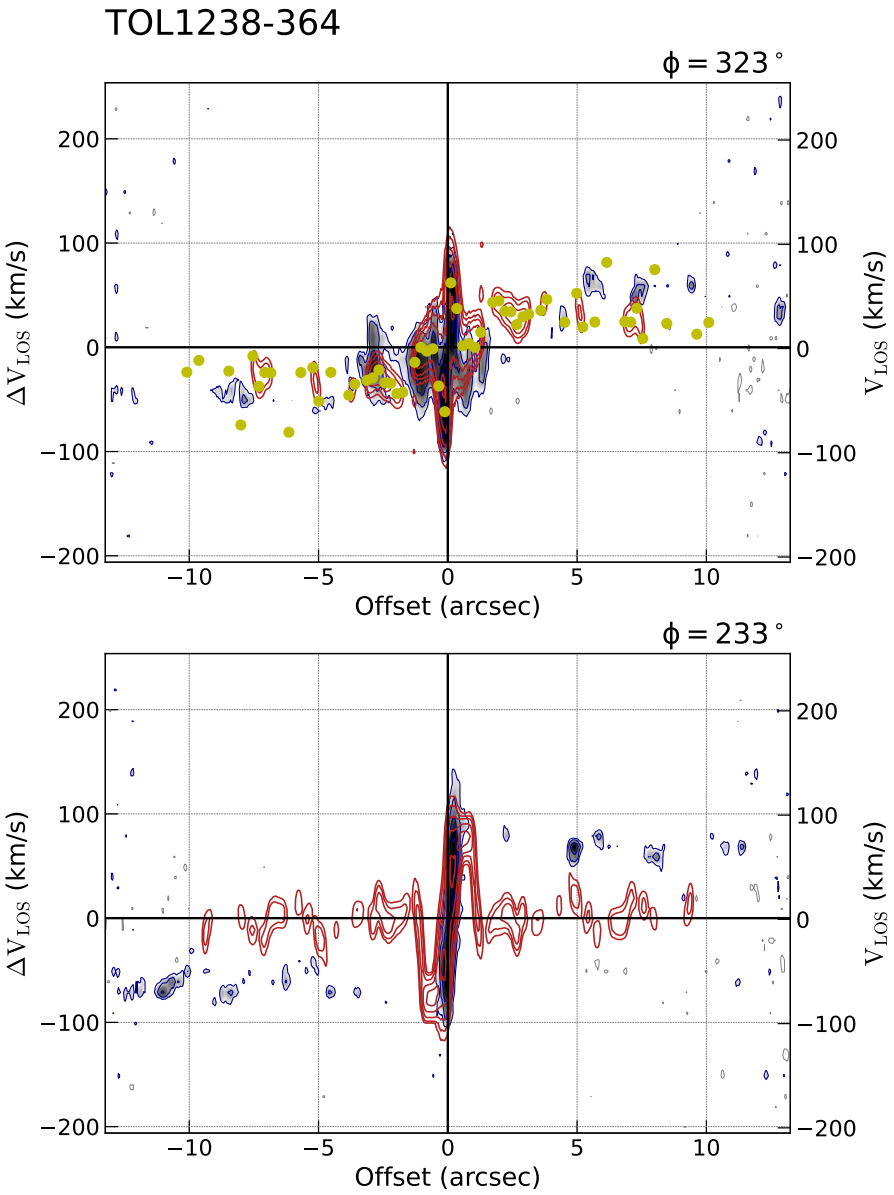

FIGURE D.6 – Position-Velocity (p-v) diagram for IC3639 using 3D-Barolo with azimuthal normalization.

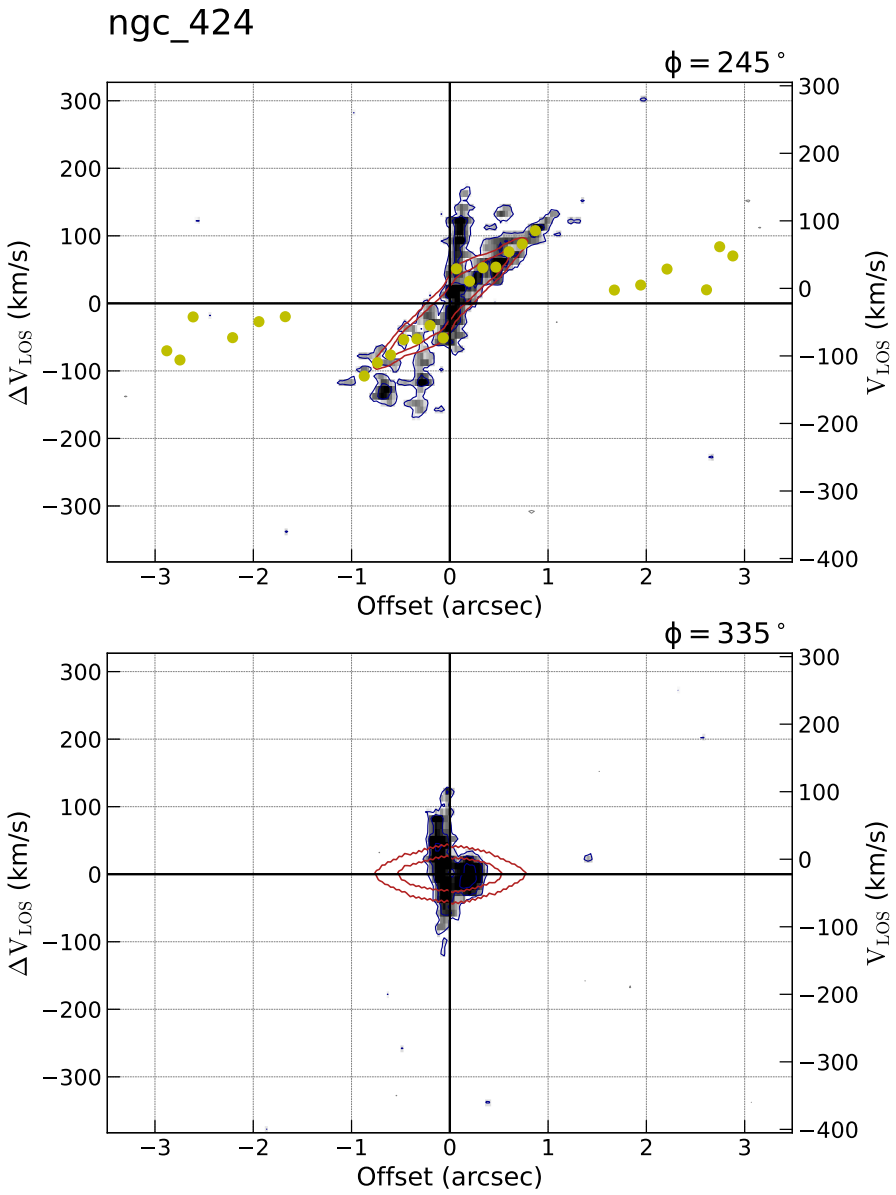

FIGURE D.7 – Position-Velocity (p-v) diagram for NGC 424 using 3D-Barolo with azimuthal normalization.

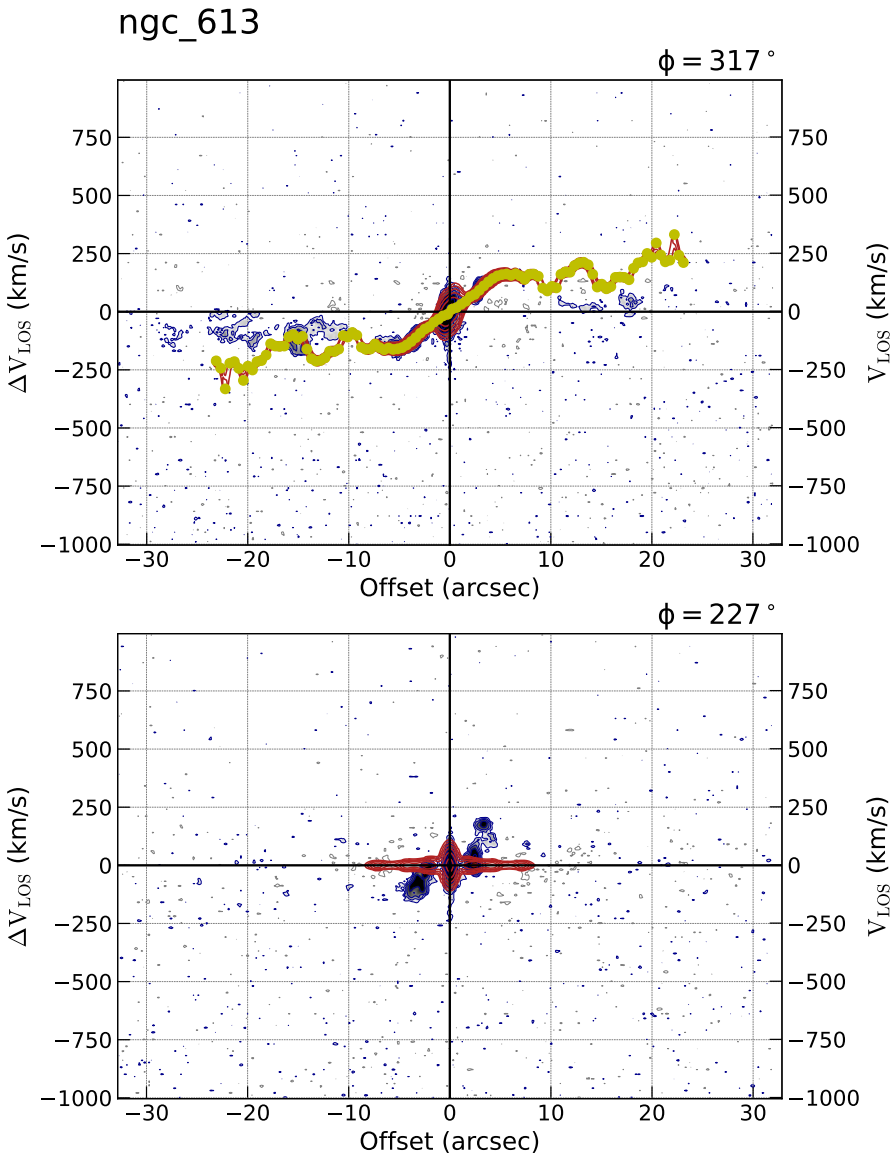

FIGURE D.8 – Position-Velocity (p-v) diagram for NGC 613 using 3D-Barolo with azimuthal normalization.

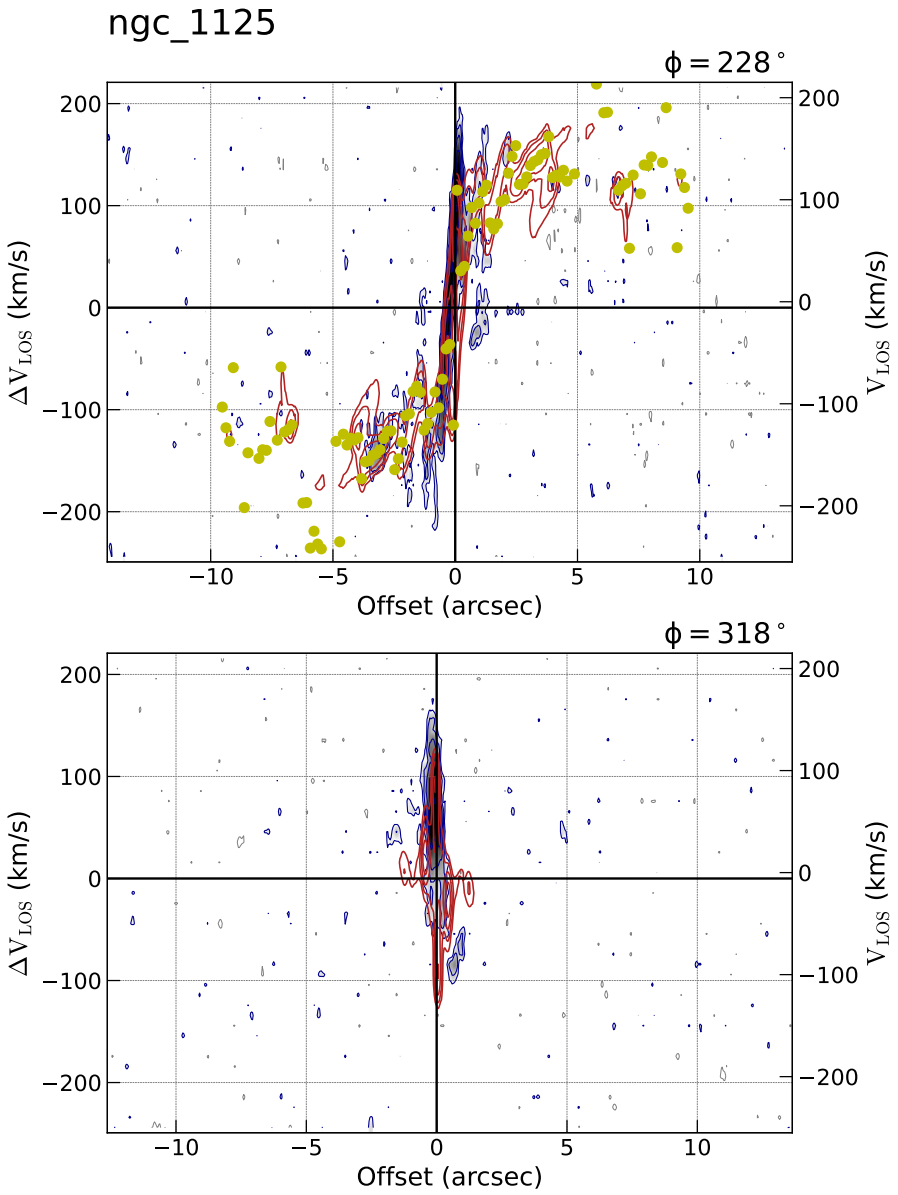

FIGURE D.9 – Position-Velocity (p-v) diagram for NGC 1125 using 3D-Barolo with azimuthal normalization.

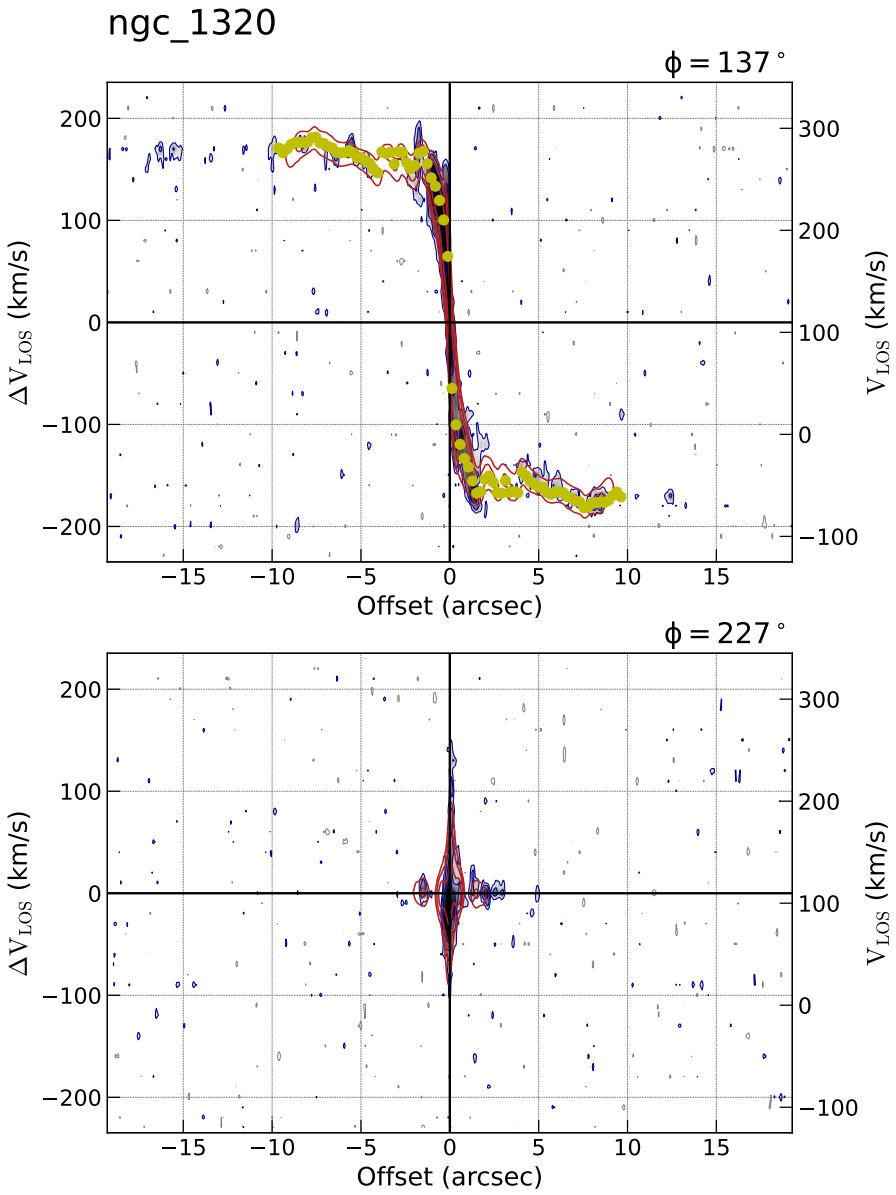

FIGURE D.10 – Position-Velocity (p-v) diagram for NGC 1320 using 3D-Barolo with azimuthal normalization.

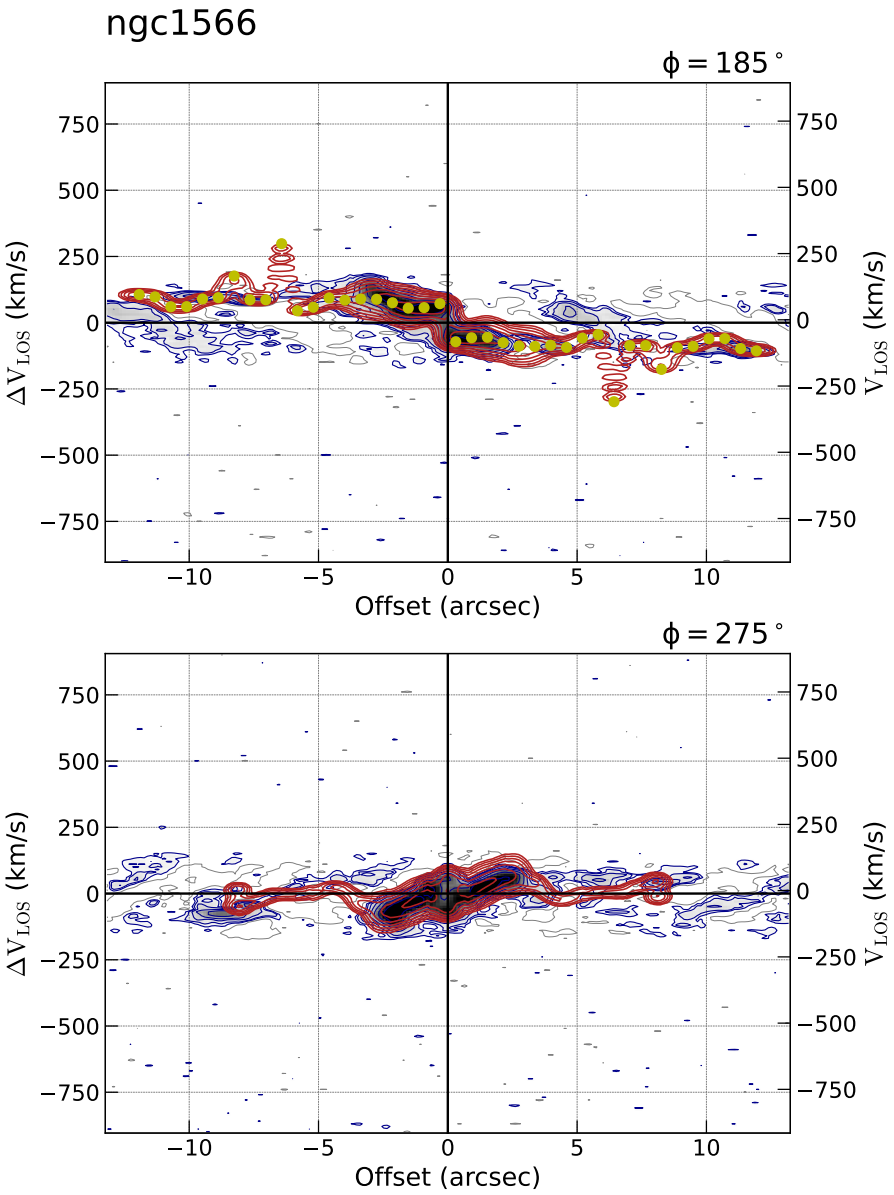

FIGURE D.11 – Position-Velocity (p-v) diagram for NGC 1566 using 3D-Barolo with azimuthal normalization.

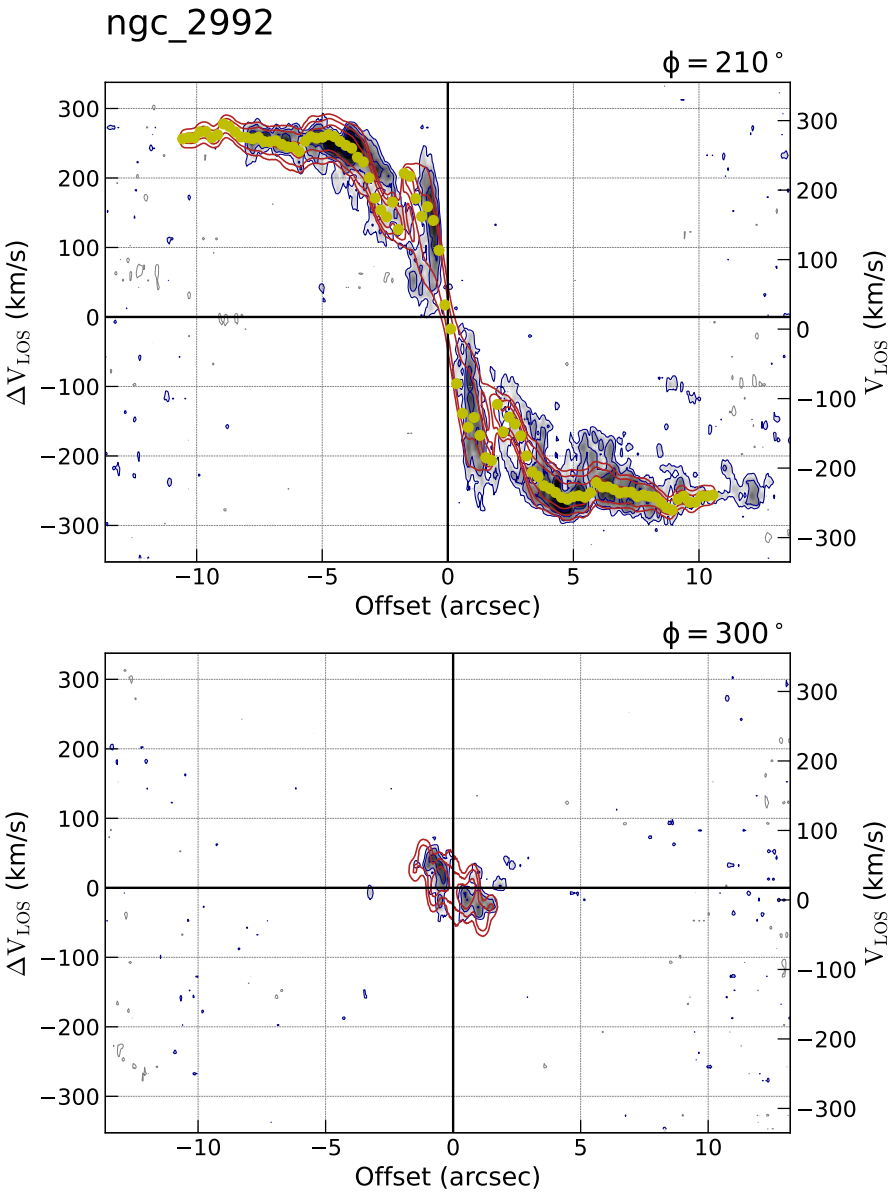

FIGURE D.12 – Position-Velocity (p-v) diagram for NGC 2992 using 3D-Barolo with azimuthal normalization.

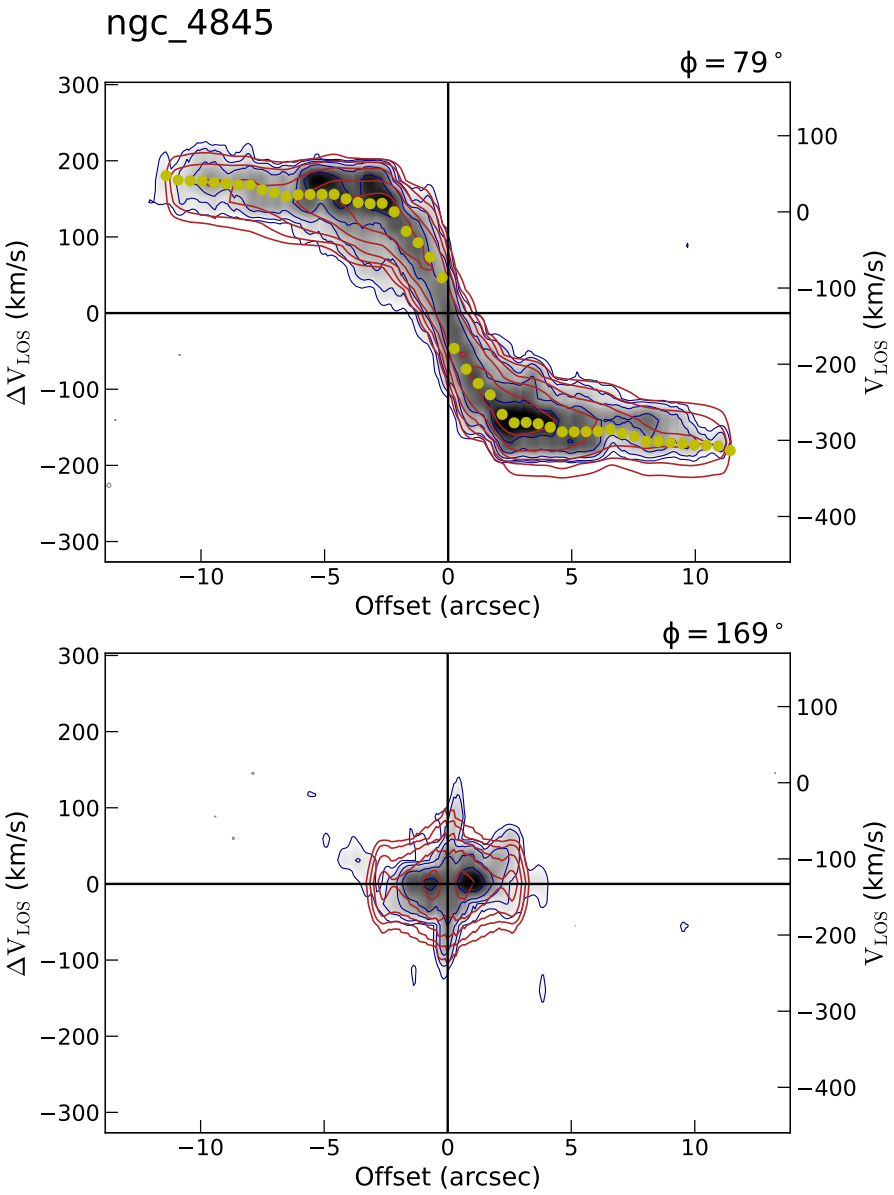

FIGURE D.13 – Position-Velocity (p-v) diagram for NGC 4845 using 3D-Barolo with azimuthal normalization.

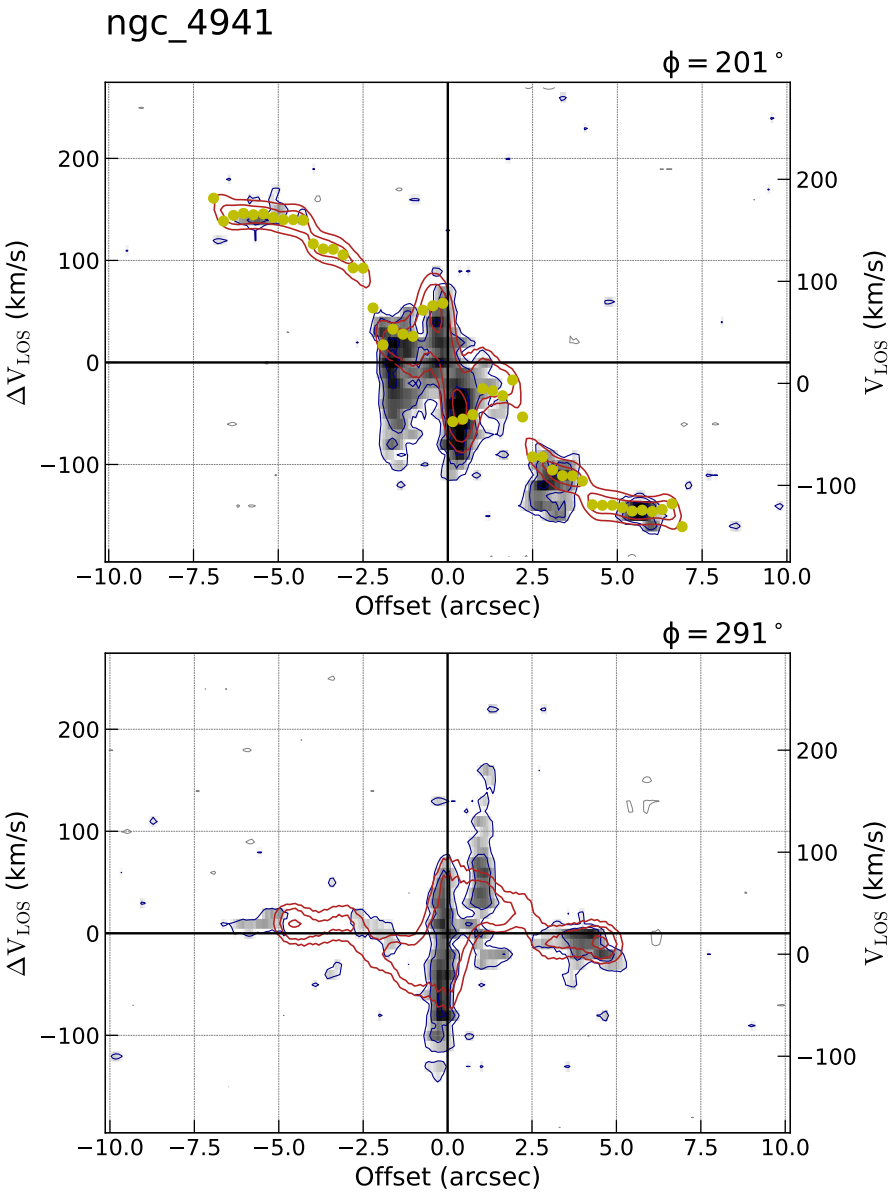

FIGURE D.14 – Position-Velocity (p-v) diagram for NGC 4941 using 3D-Barolo with azimuthal normalization.

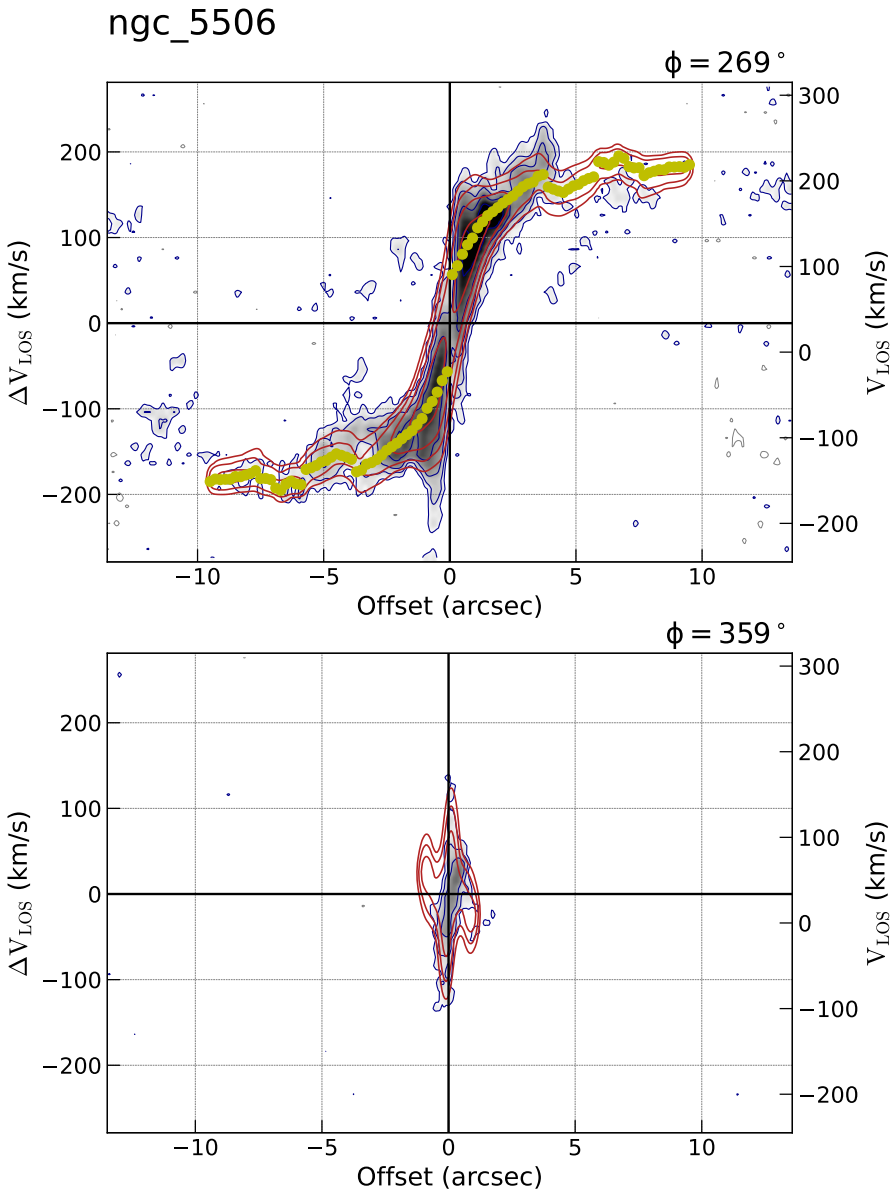

FIGURE D.15 – Position-Velocity (p-v) diagram for NGC 5506 using 3D-Barolo with azimuthal normalization.

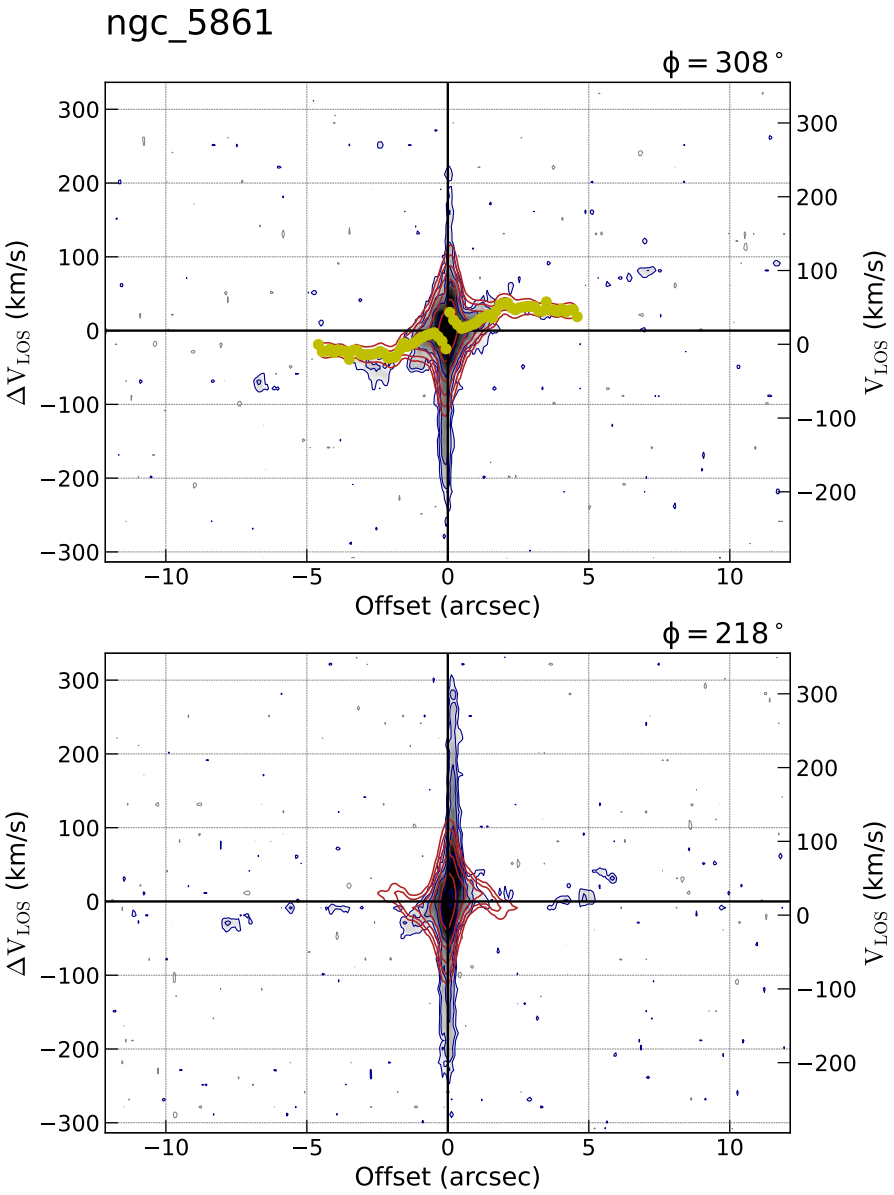

FIGURE D.16 – Position-Velocity (p-v) diagram for NGC 5861 using 3D-Barolo with azimuthal normalization.

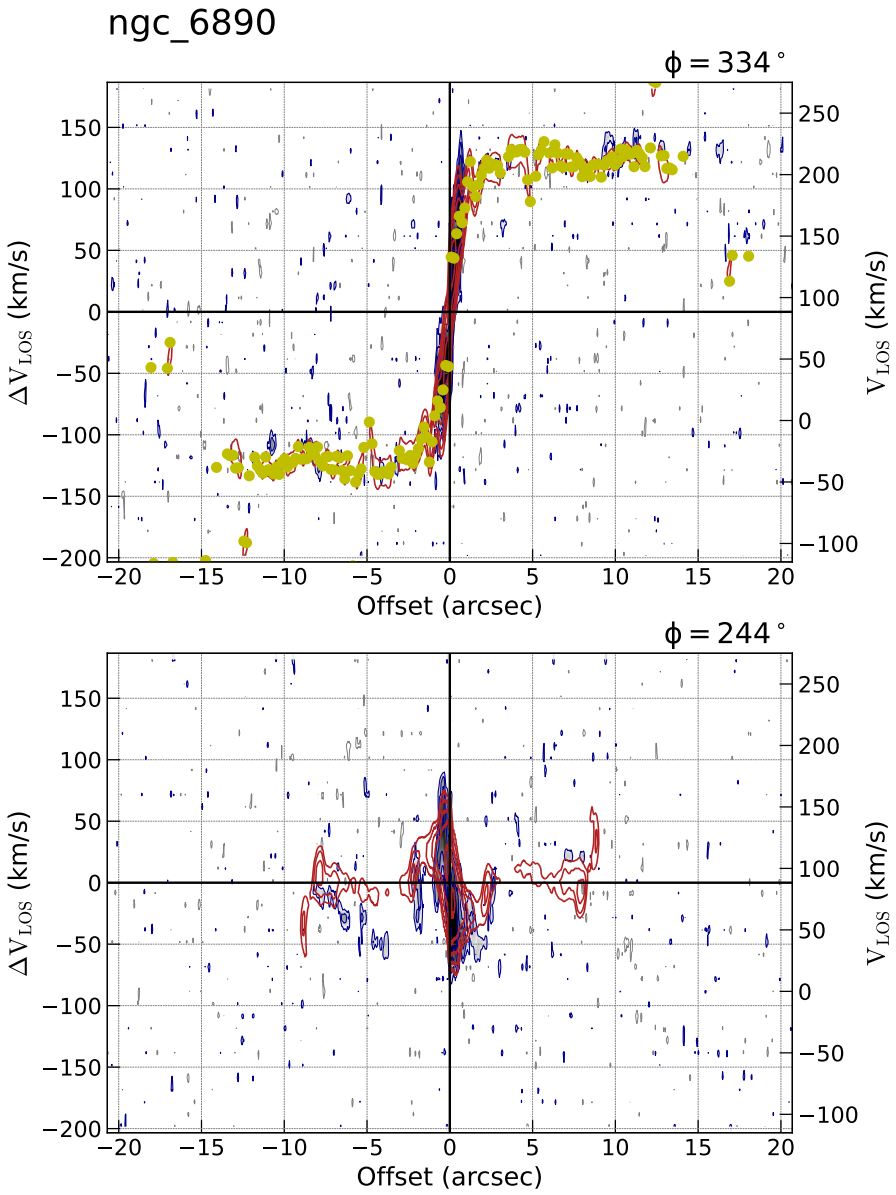

FIGURE D.17 – Position-Velocity (p-v) diagram for NGC 6890 using 3D-Barolo with azimuthal normalization.

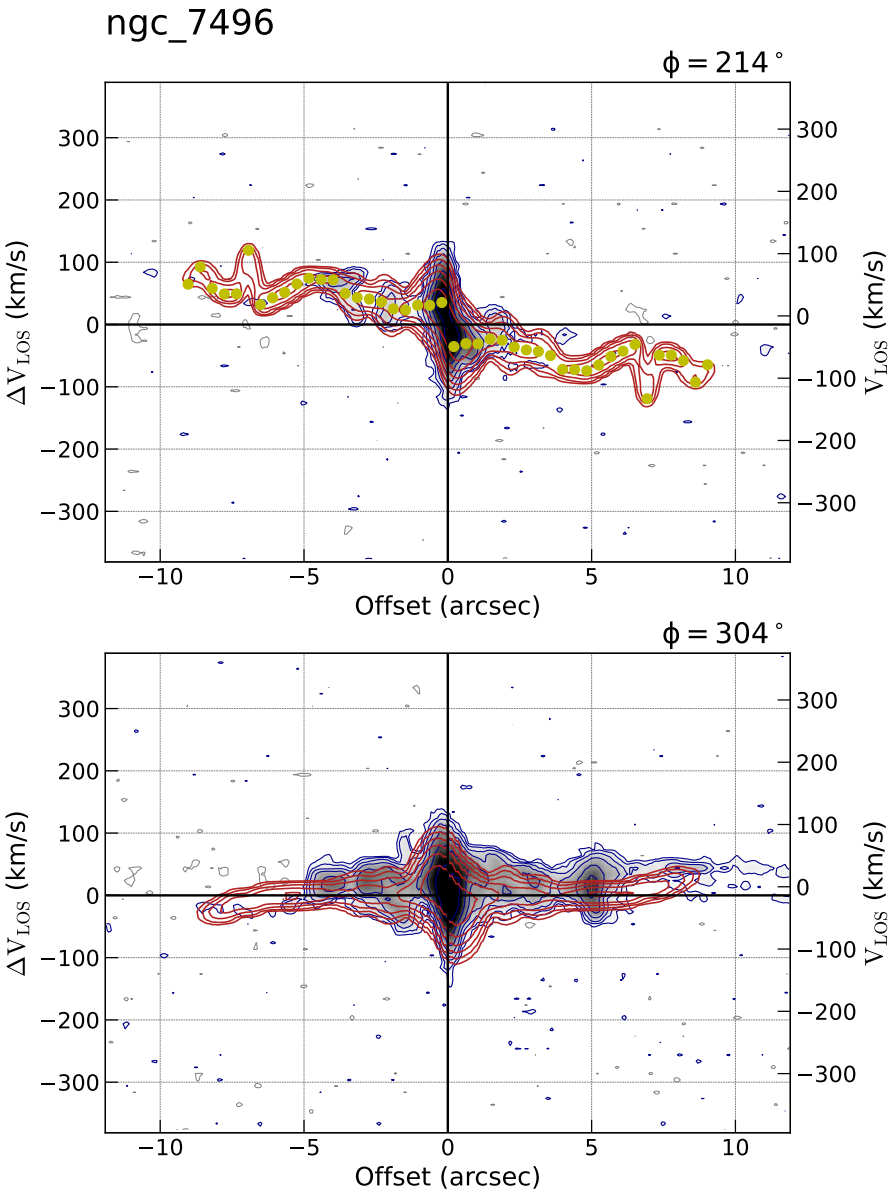

FIGURE D.18 – Position-Velocity (p-v) diagram for NGC 7496 using 3D-Barolo with azimuthal normalization.

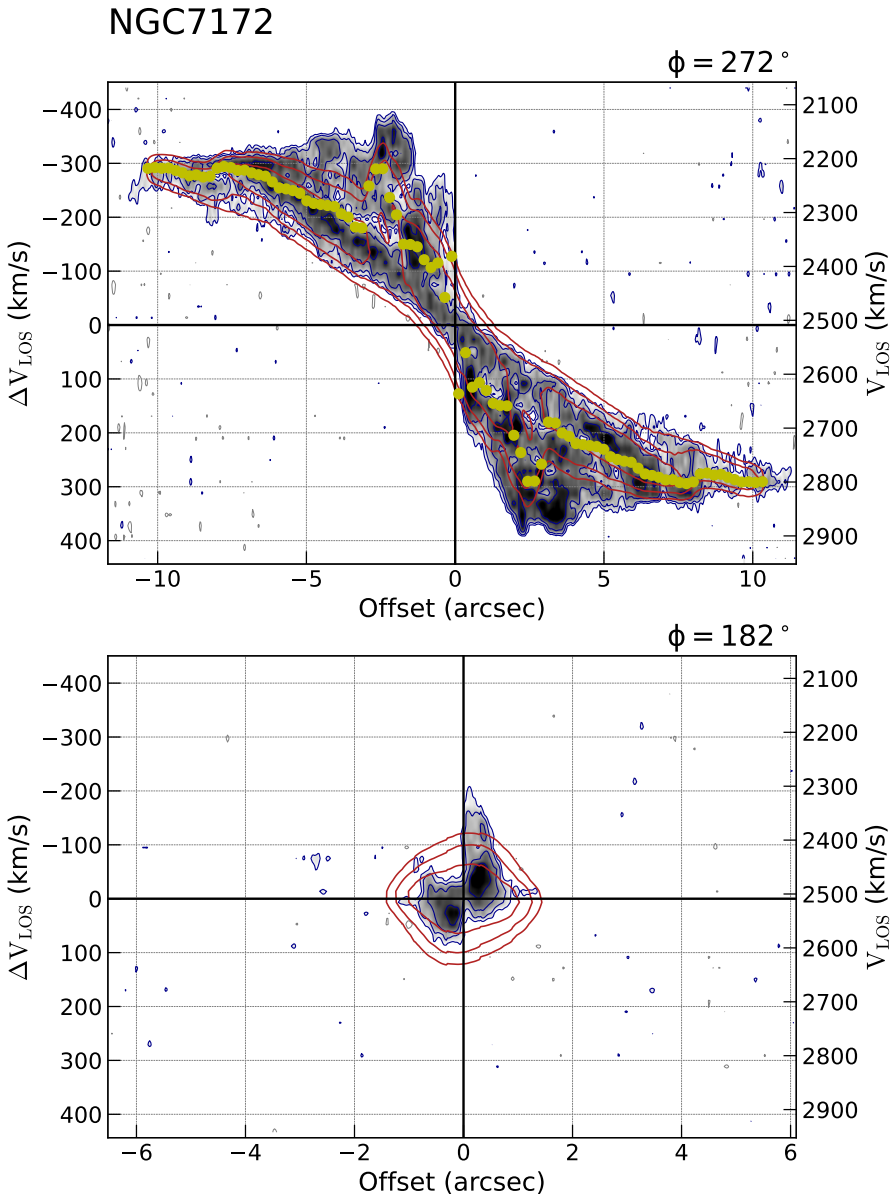

FIGURE D.19 – Position-Velocity (p-v) diagram for NGC 7172 using 3D-BAROLO with azimuthal normalization.

Appendix E - TWIST Fit Parameter results

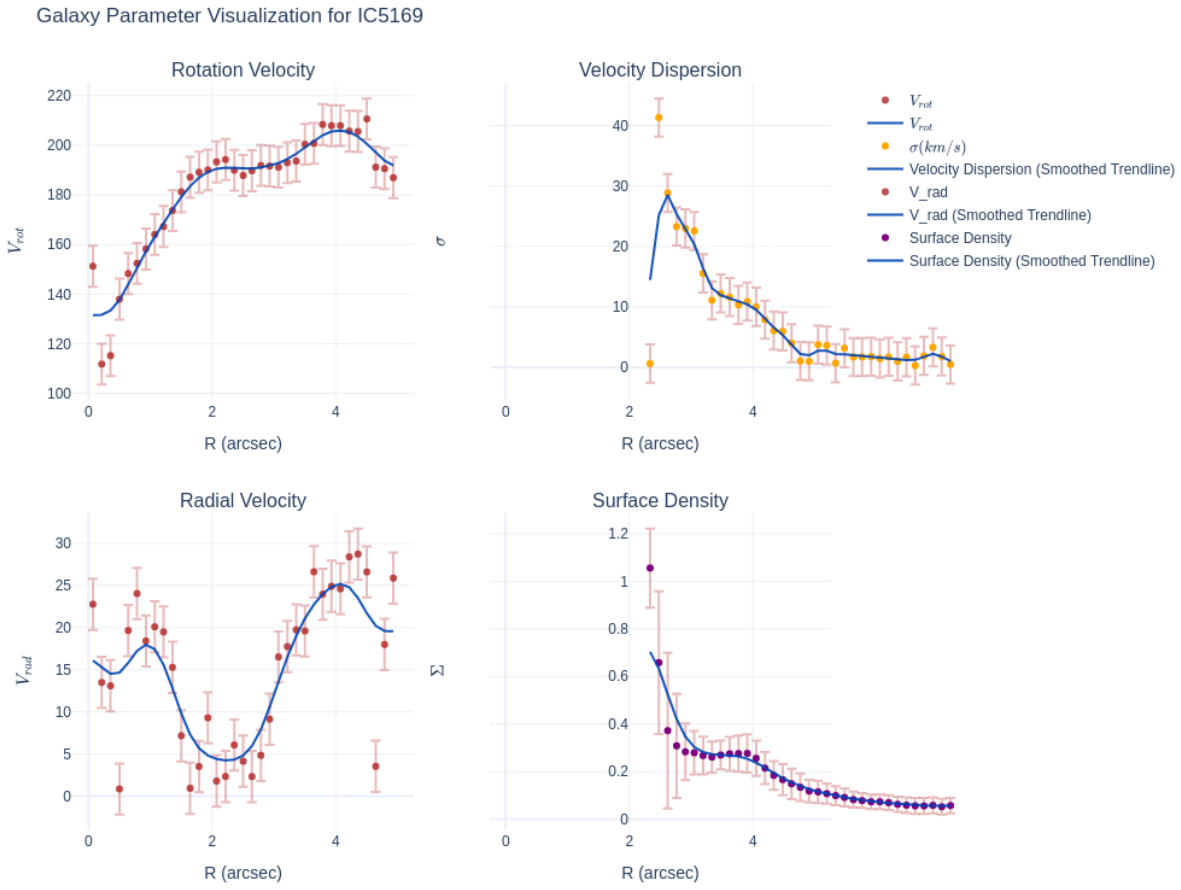

FIGURE E.1 – Best-fit parameters for the galaxy IC5169. From top left to bottom right, the subplots show Rotation Velocity with trendline and error bars as a function of radius, Velocity Dispersion with error bars as a function of radius, Radial Velocity with trendline as a function of radius, and Surface Density as a function of radius for the galaxy.

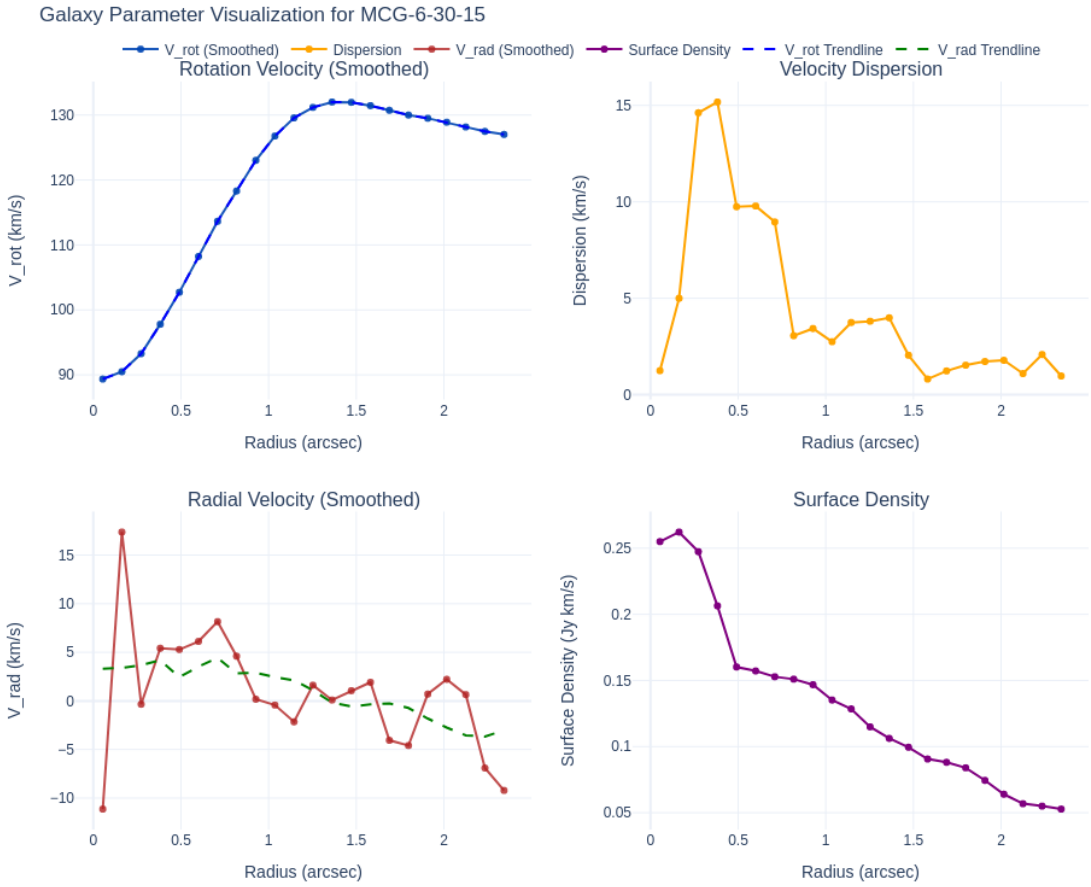

FIGURE E.2 – Best-fit parameters for the galaxy MCG-6-30-15. From top left to bottom right, the subplots show Rotation Velocity with trendline and error bars as a function of radius, Velocity Dispersion with error bars as a function of radius, Radial Velocity with trendline as a function of radius, and Surface Density as a function of radius for the galaxy.

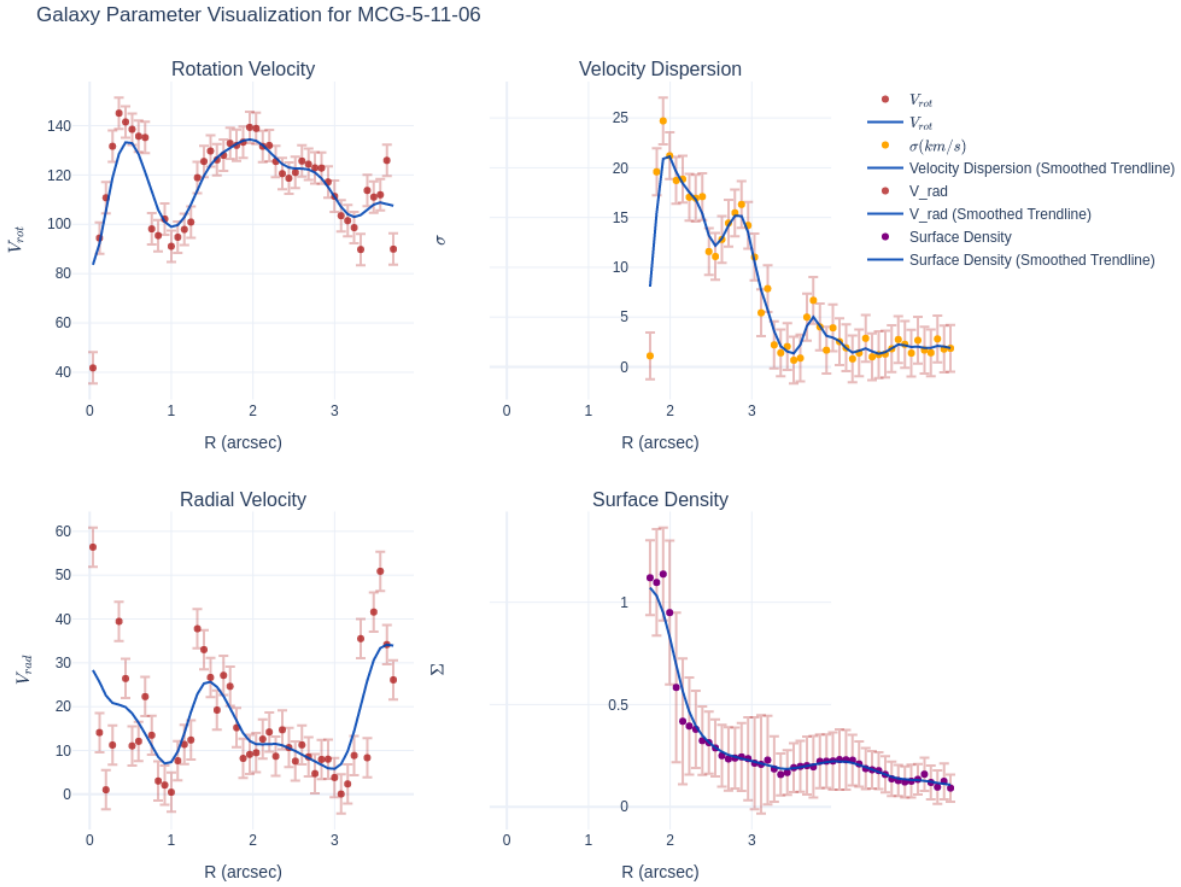

FIGURE E.3 – Best-fit parameters for the galaxy MCG-5-11-06. From top left to bottom right, the subplots show Rotation Velocity with trendline and error bars as a function of radius, Velocity Dispersion with error bars as a function of radius, Radial Velocity with trendline as a function of radius, and Surface Density as a function of radius for the galaxy.

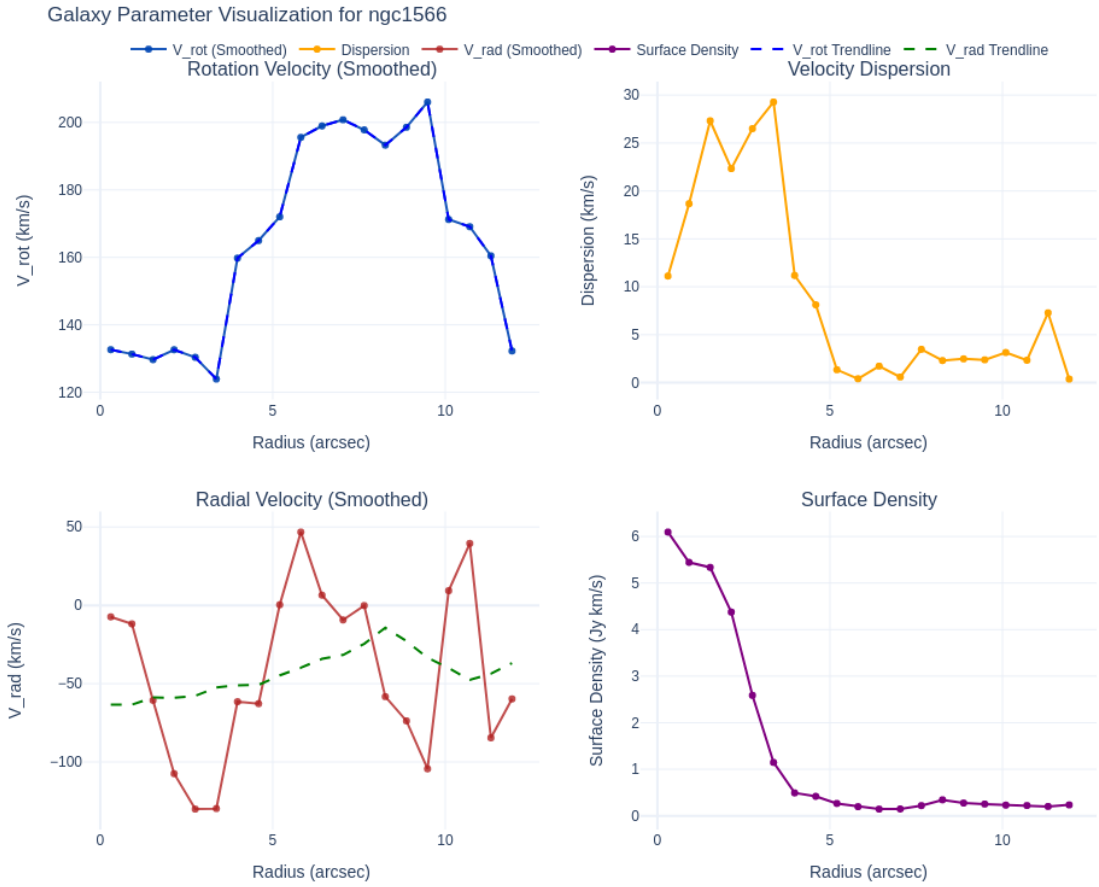

FIGURE E.4 – Best-fit parameters for the galaxy ngc1566. From top left to bottom right, the subplots show Rotation Velocity with trendline and error bars as a function of radius, Velocity Dispersion with error bars as a function of radius, Radial Velocity with trendline as a function of radius, and Surface Density as a function of radius for the galaxy.

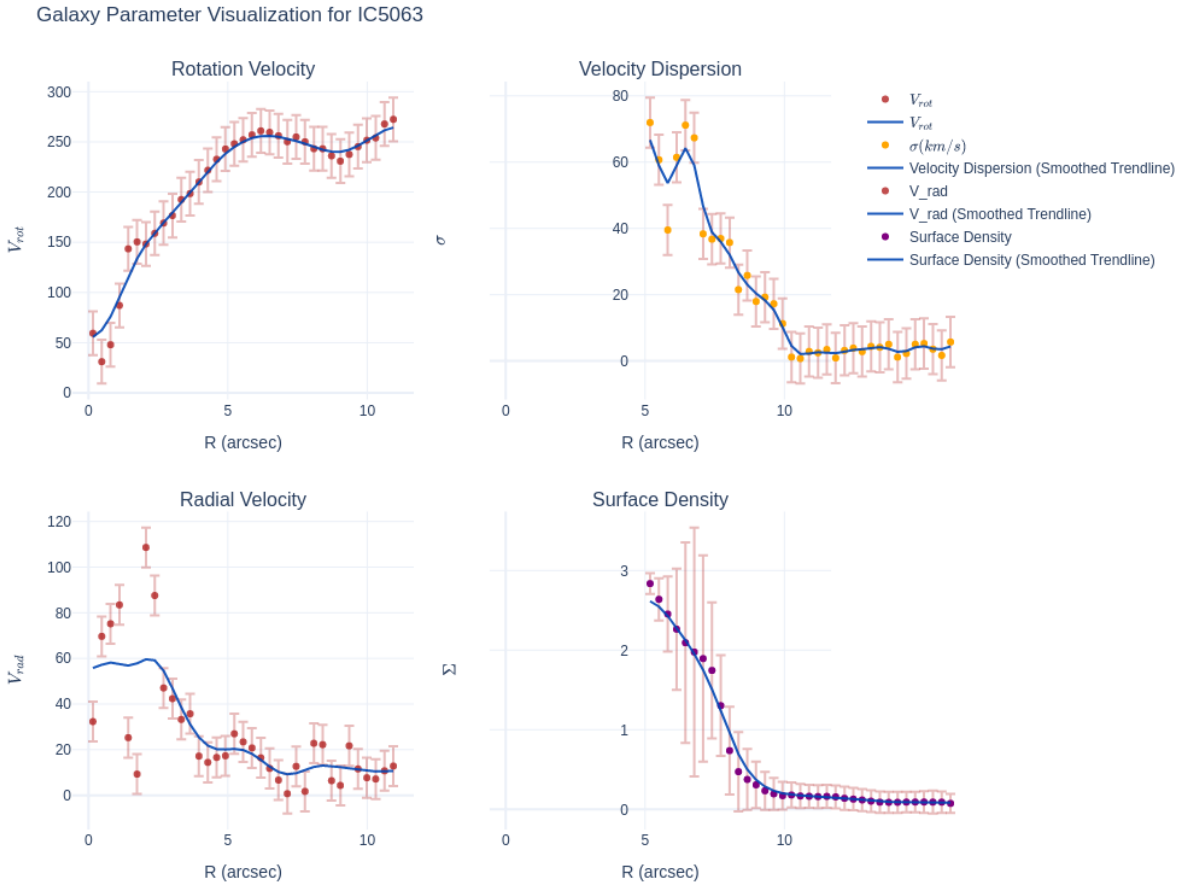

FIGURE E.5 – Best-fit parameters for the galaxy IC5063. From top left to bottom right, the subplots show Rotation Velocity with trendline and error bars as a function of radius, Velocity Dispersion with error bars as a function of radius, Radial Velocity with trendline as a function of radius, and Surface Density as a function of radius for the galaxy.

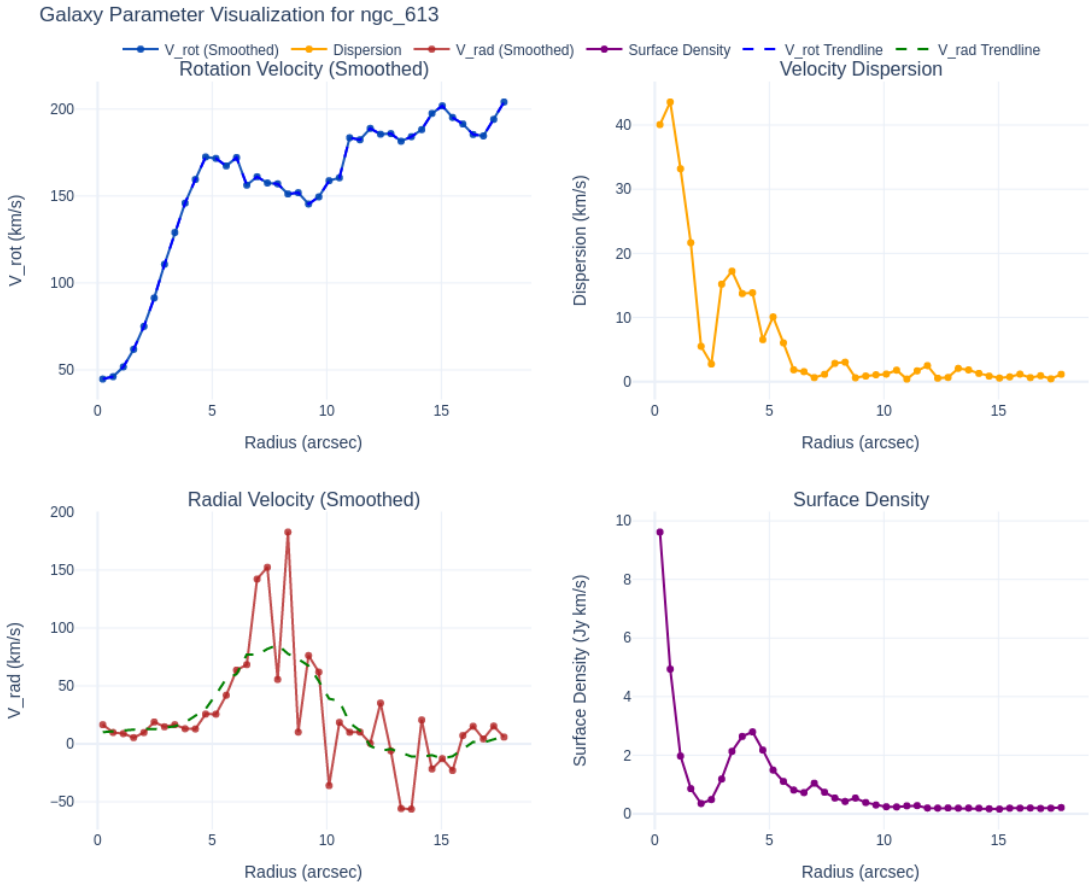

FIGURE E.6 – Best-fit parameters for the galaxy ngc613. From top left to bottom right, the subplots show Rotation Velocity with trendline and error bars as a function of radius, Velocity Dispersion with error bars as a function of radius, Radial Velocity with trendline as a function of radius, and Surface Density as a function of radius for the galaxy.

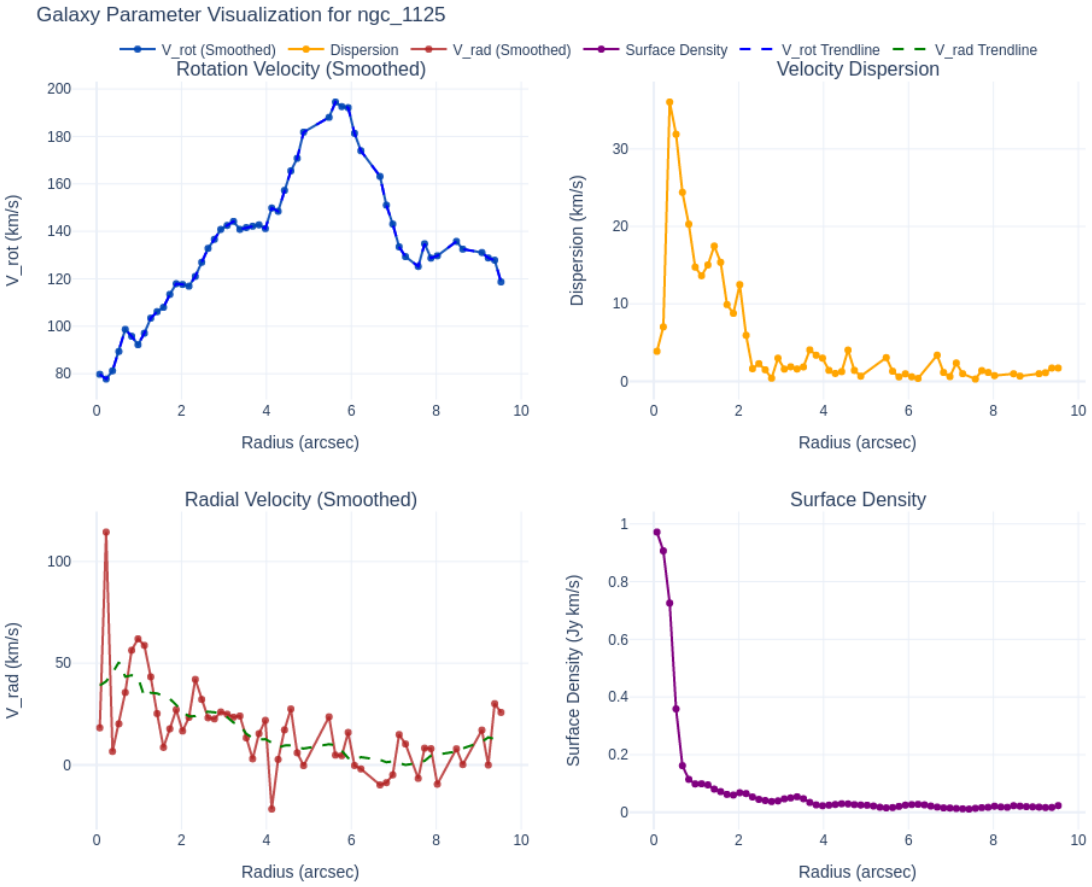

FIGURE E.7 – Best-fit parameters for the galaxy ngc1125. From top left to bottom right, the subplots show Rotation Velocity with trendline and error bars as a function of radius, Velocity Dispersion with error bars as a function of radius, Radial Velocity with trendline as a function of radius, and Surface Density as a function of radius for the galaxy.

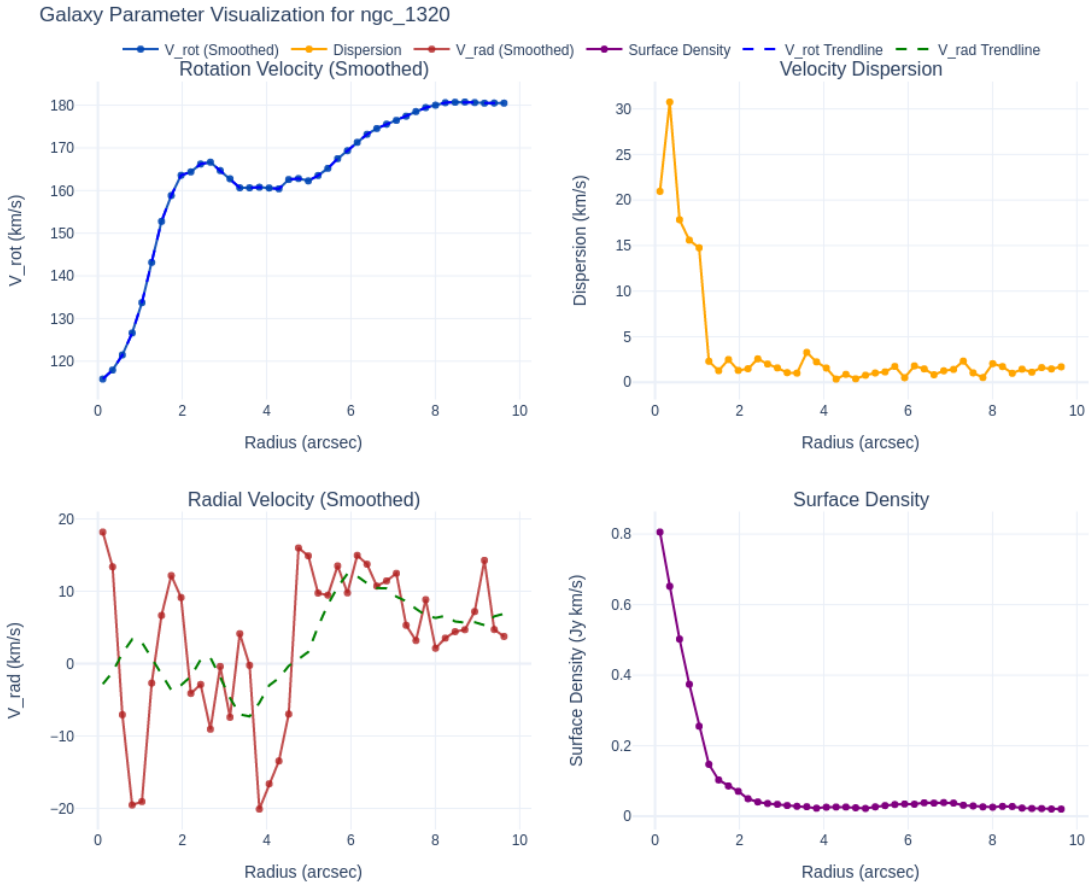

FIGURE E.8 – Best-fit parameters for the galaxy ngc1320. From top left to bottom right, the subplots show Rotation Velocity with trendline and error bars as a function of radius, Velocity Dispersion with error bars as a function of radius, Radial Velocity with trendline as a function of radius, and Surface Density as a function of radius for the galaxy.

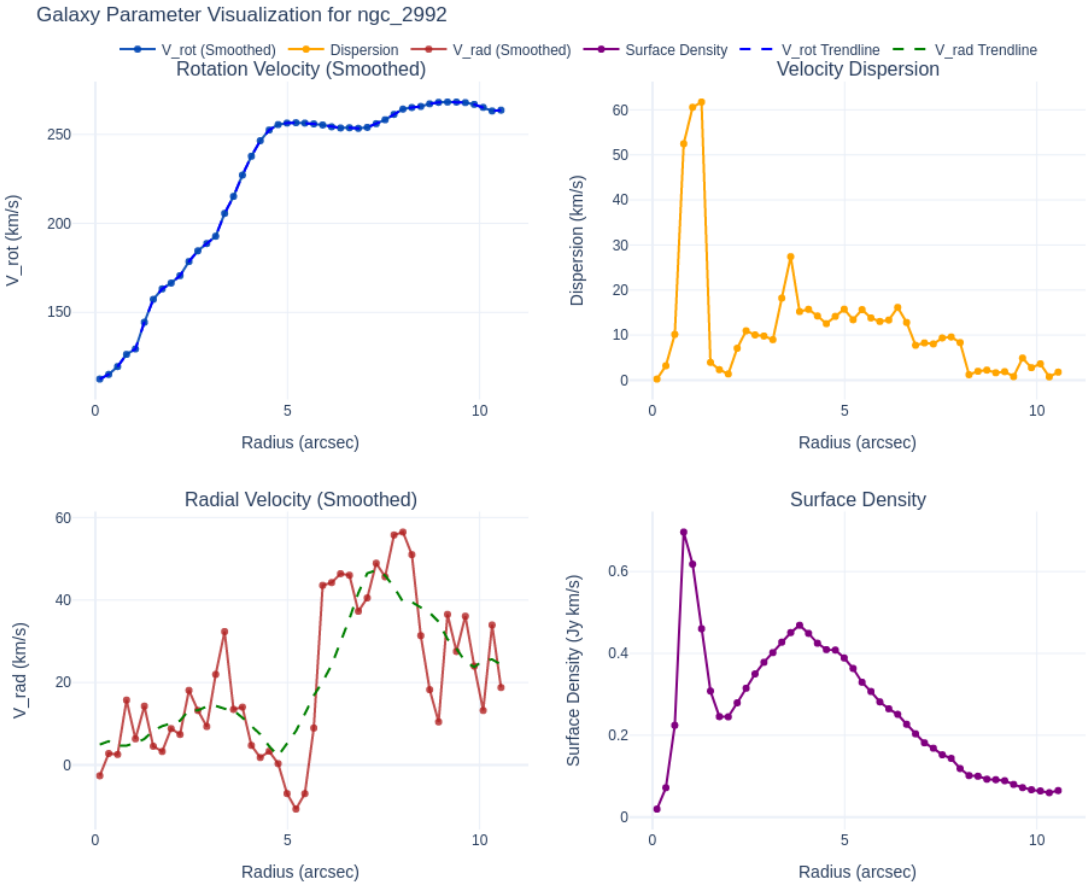

FIGURE E.9 – Best-fit parameters for the galaxy ngc2992. From top left to bottom right, the subplots show Rotation Velocity with trendline and error bars as a function of radius, Velocity Dispersion with error bars as a function of radius, Radial Velocity with trendline as a function of radius, and Surface Density as a function of radius for the galaxy.

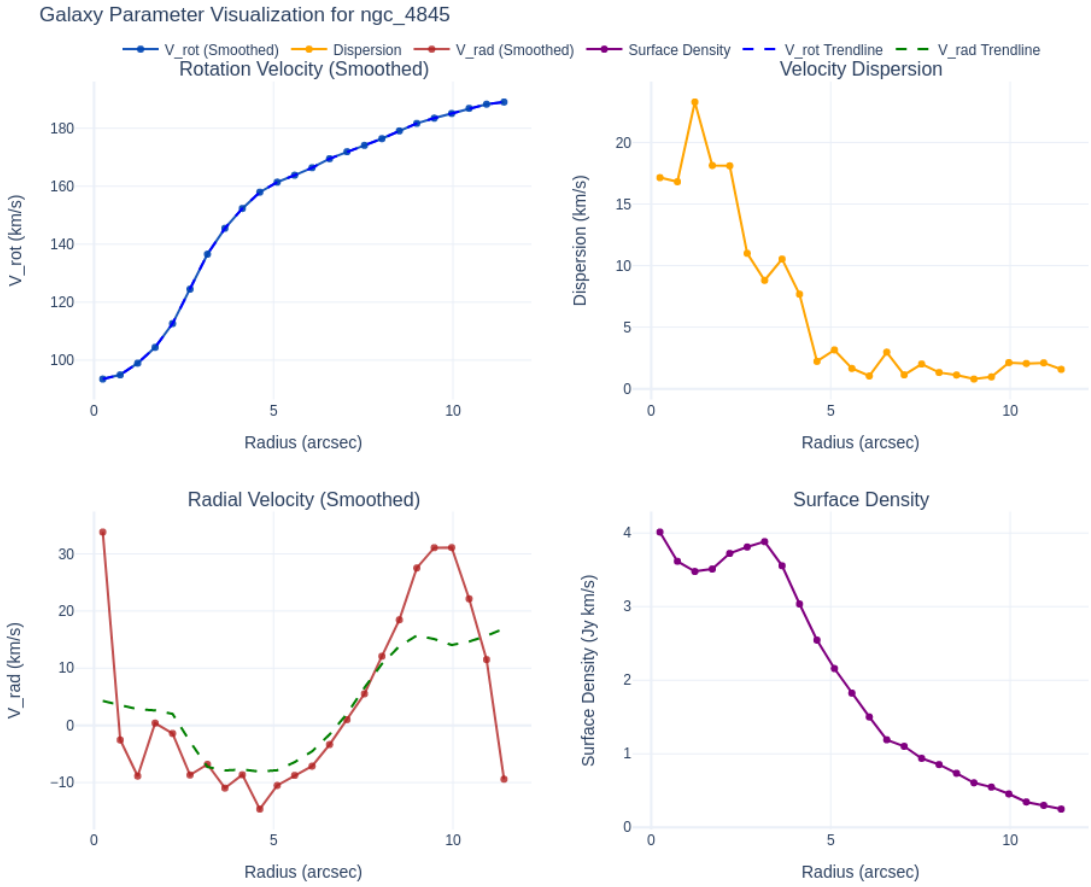

FIGURE E.10 – Best-fit parameters for the galaxy ngc4845. From top left to bottom right, the subplots show Rotation Velocity with trendline and error bars as a function of radius, Velocity Dispersion with error bars as a function of radius, Radial Velocity with trendline as a function of radius, and Surface Density as a function of radius for the galaxy.

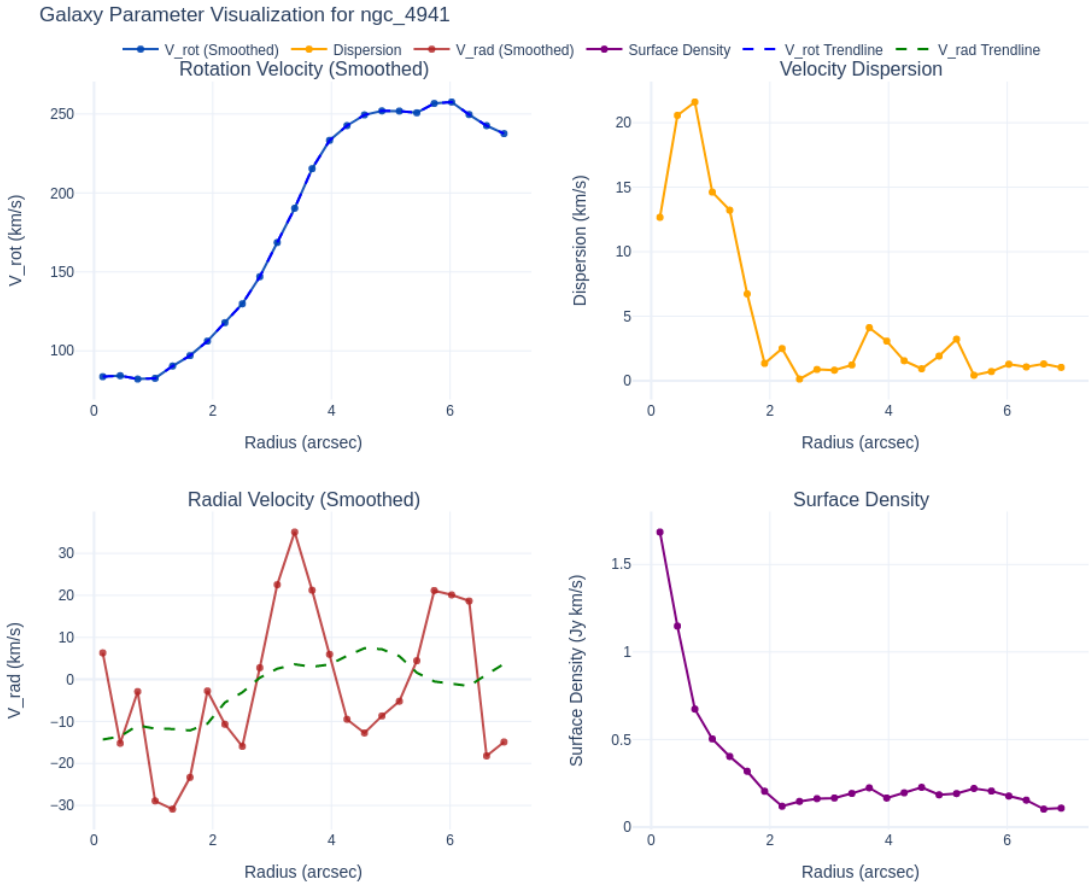

FIGURE E.11 – Best-fit parameters for the galaxy ngc4941. From top left to bottom right, the subplots show Rotation Velocity with trendline and error bars as a function of radius, Velocity Dispersion with error bars as a function of radius, Radial Velocity with trendline as a function of radius, and Surface Density as a function of radius for the galaxy.

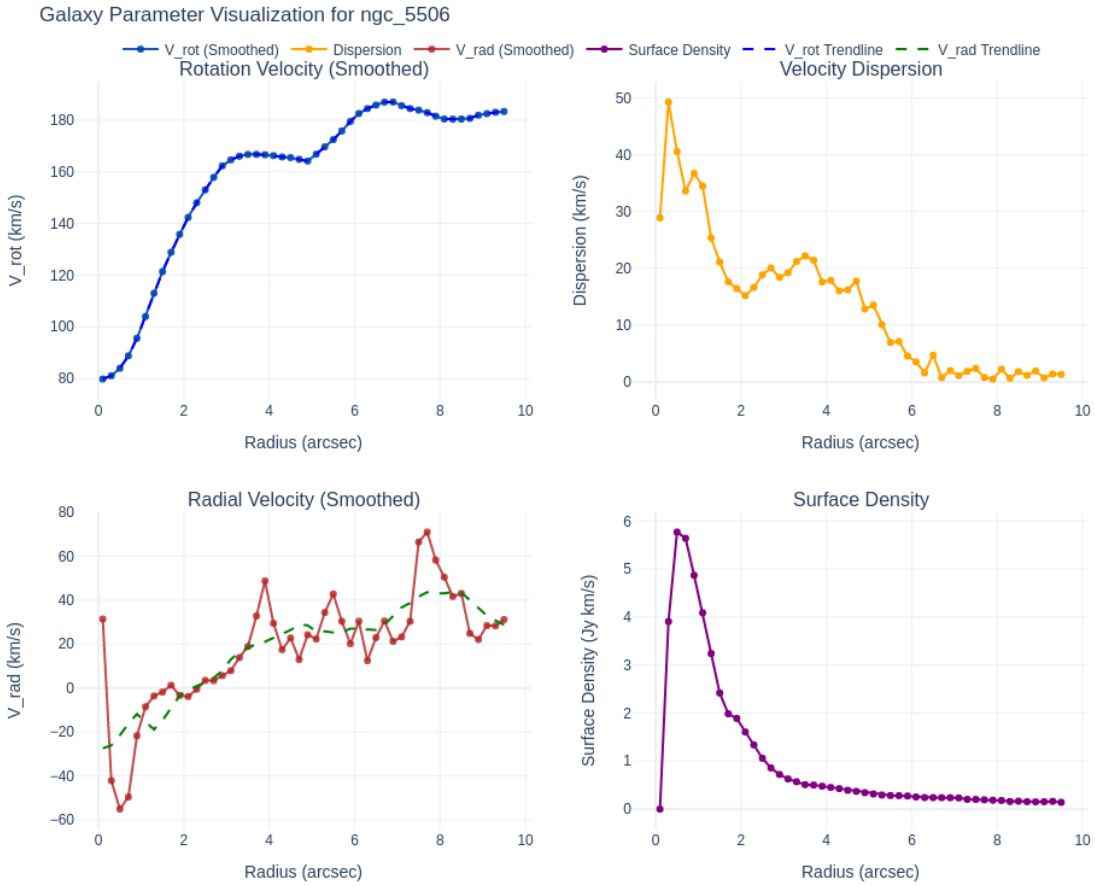

FIGURE E.12 – Best-fit parameters for the galaxy ngc5506. From top left to bottom right, the subplots show Rotation Velocity with trendline and error bars as a function of radius, Velocity Dispersion with error bars as a function of radius, Radial Velocity with trendline as a function of radius, and Surface Density as a function of radius for the galaxy.

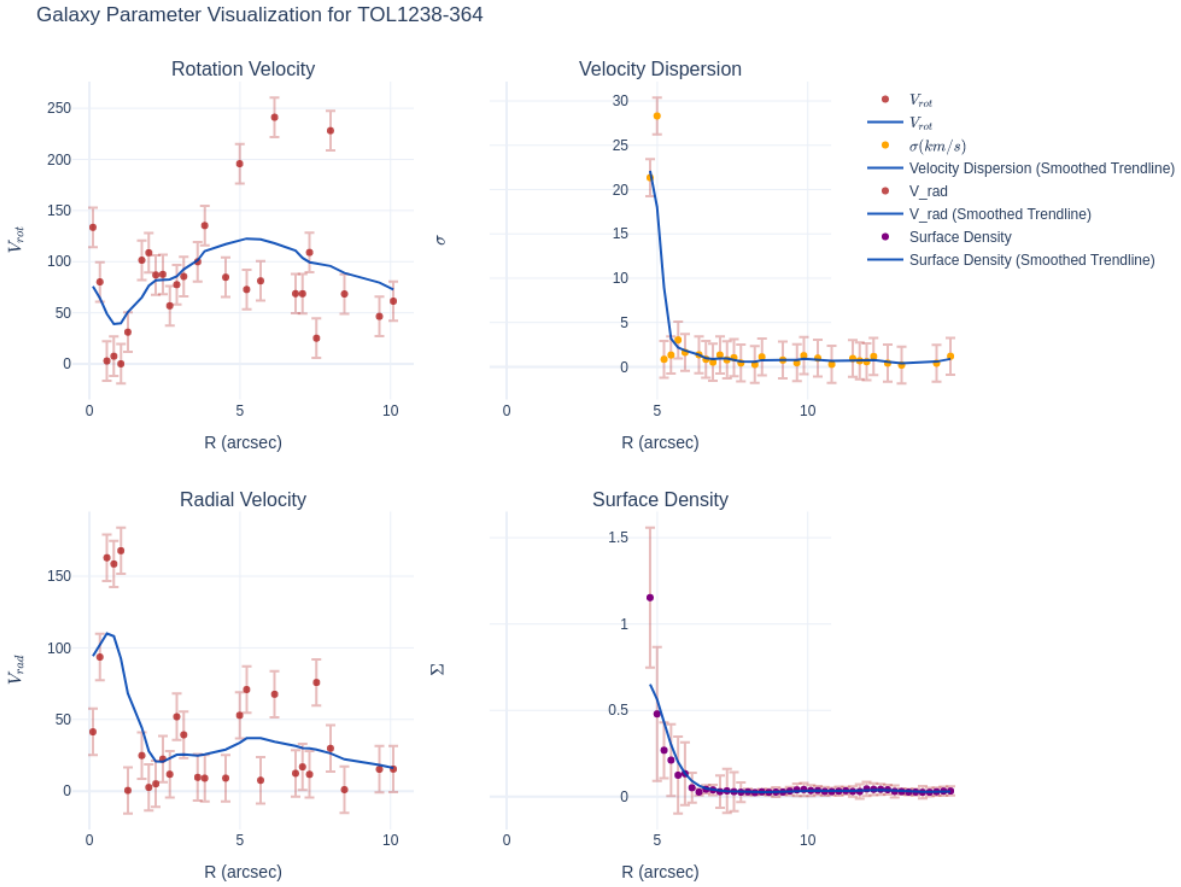

FIGURE E.13 – Best-fit parameters for the galaxy IC3639. From top left to bottom right, the subplots show Rotation Velocity with trendline and error bars as a function of radius, Velocity Dispersion with error bars as a function of radius, Radial Velocity with trendline as a function of radius, and Surface Density as a function of radius for the galaxy.

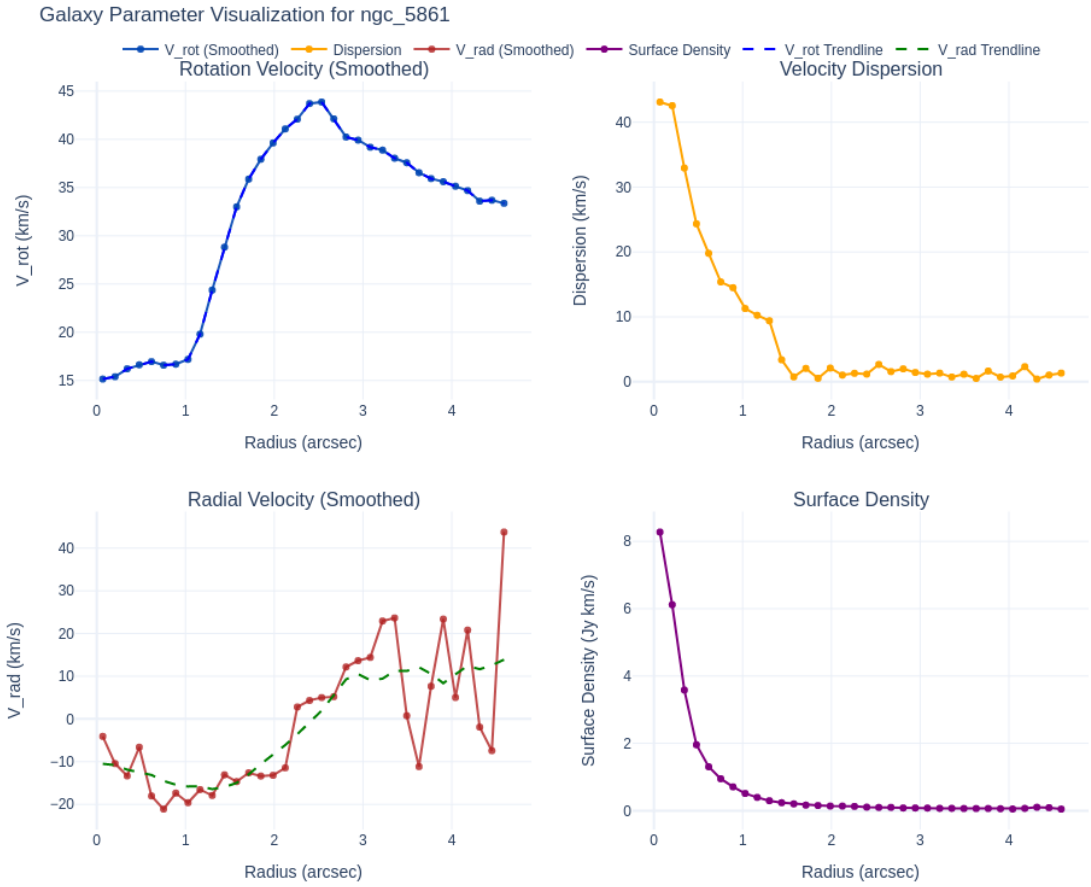

FIGURE E.14 – Best-fit parameters for the galaxy ngc5861. From top left to bottom right, the subplots show Rotation Velocity with trendline and error bars as a function of radius, Velocity Dispersion with error bars as a function of radius, Radial Velocity with trendline as a function of radius, and Surface Density as a function of radius for the galaxy.

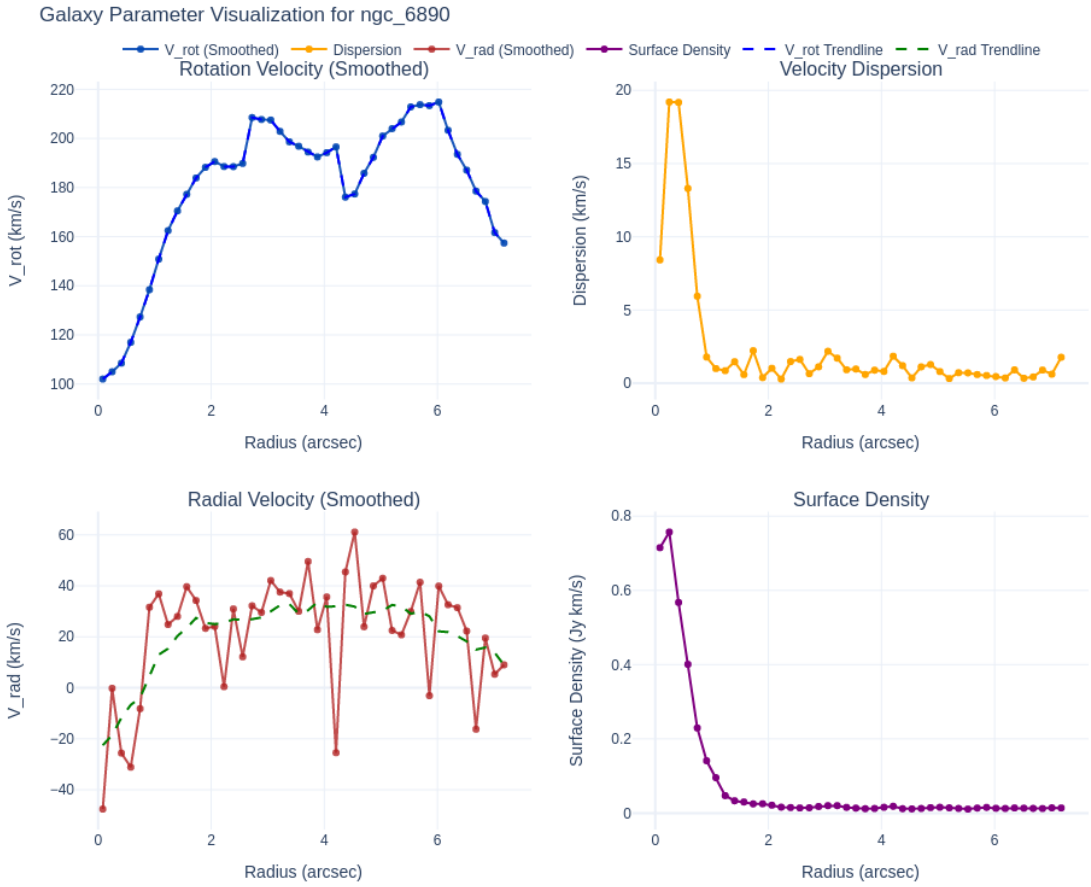

FIGURE E.15 – Best-fit parameters for the galaxy ngc6890. From top left to bottom right, the subplots show Rotation Velocity with trendline and error bars as a function of radius, Velocity Dispersion with error bars as a function of radius, Radial Velocity with trendline as a function of radius, and Surface Density as a function of radius for the galaxy.

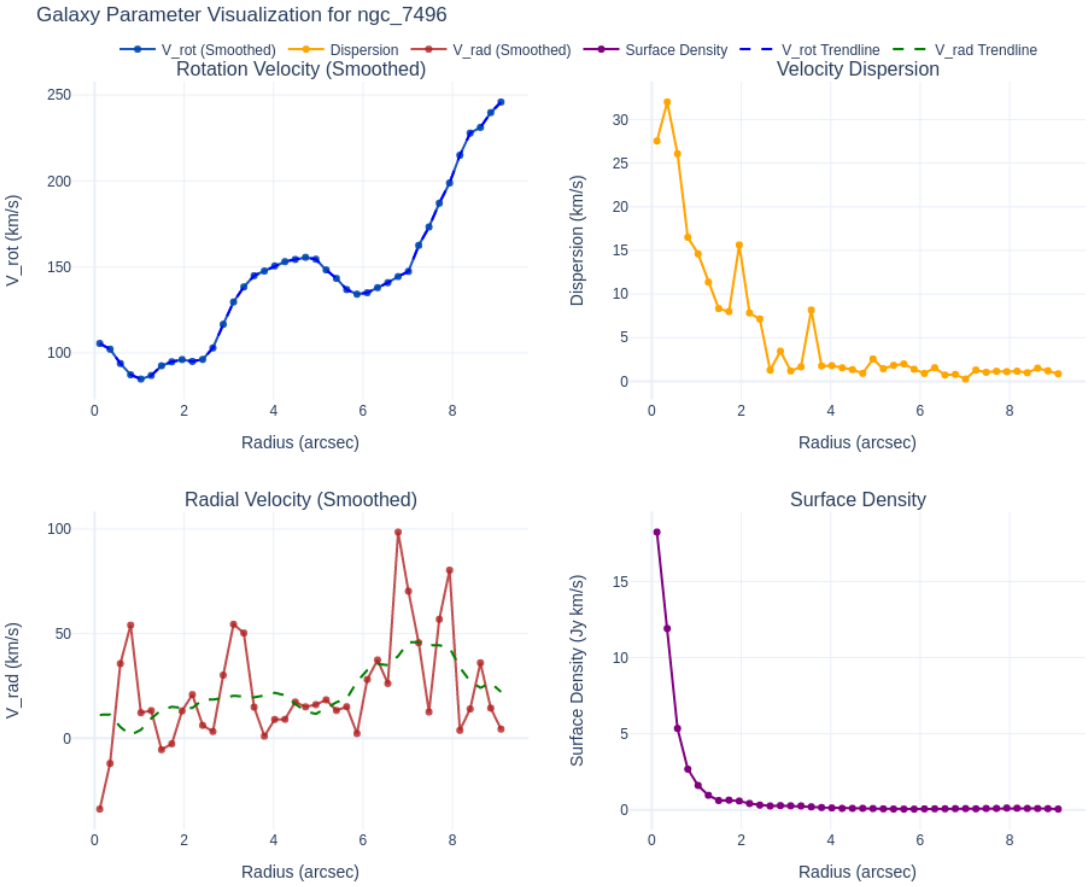

FIGURE E.16 – Best-fit parameters for the galaxy ngc6890. From top left to bottom right, the subplots show Rotation Velocity with trendline and error bars as a function of radius, Velocity Dispersion with error bars as a function of radius, Radial Velocity with trendline as a function of radius, and Surface Density as a function of radius for the galaxy.

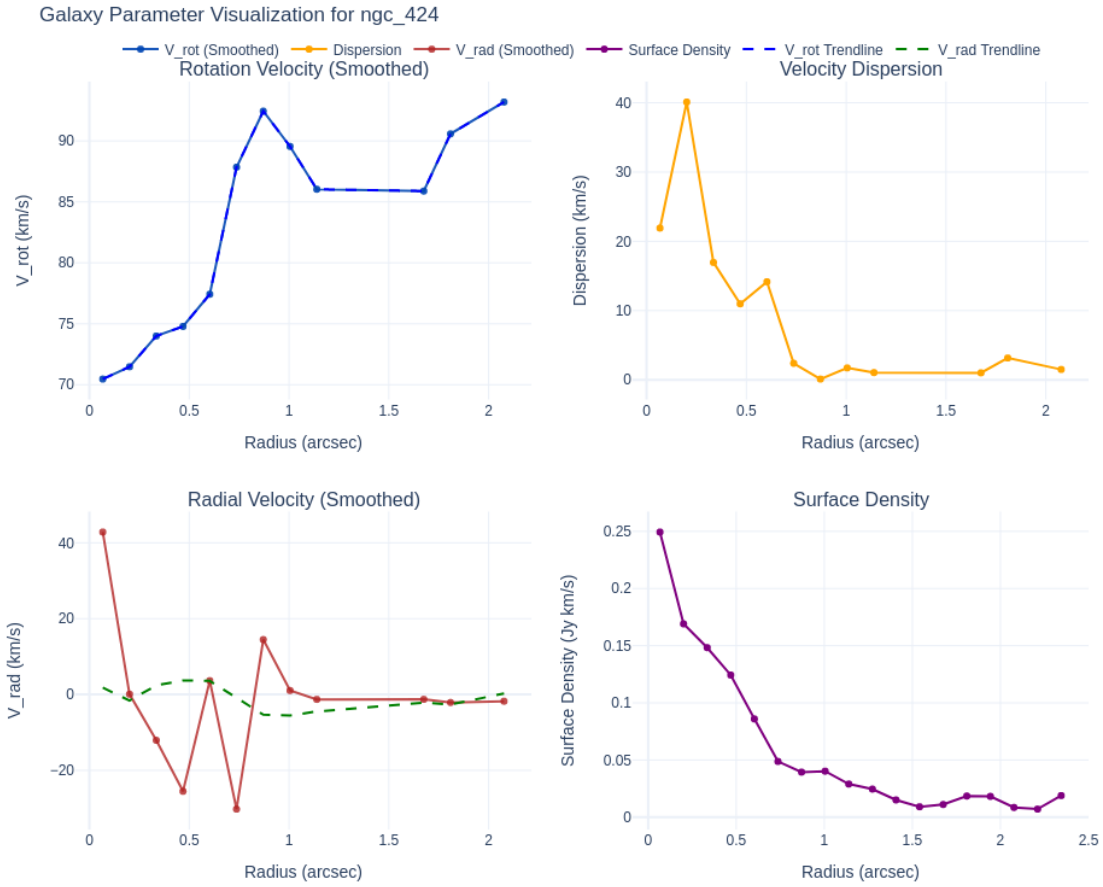

FIGURE E.17 – Best-fit parameters for the galaxy ngc424. From top left to bottom right, the subplots show Rotation Velocity with trendline and error bars as a function of radius, Velocity Dispersion with error bars as a function of radius, Radial Velocity with trendline as a function of radius, and Surface Density as a function of radius for the galaxy.

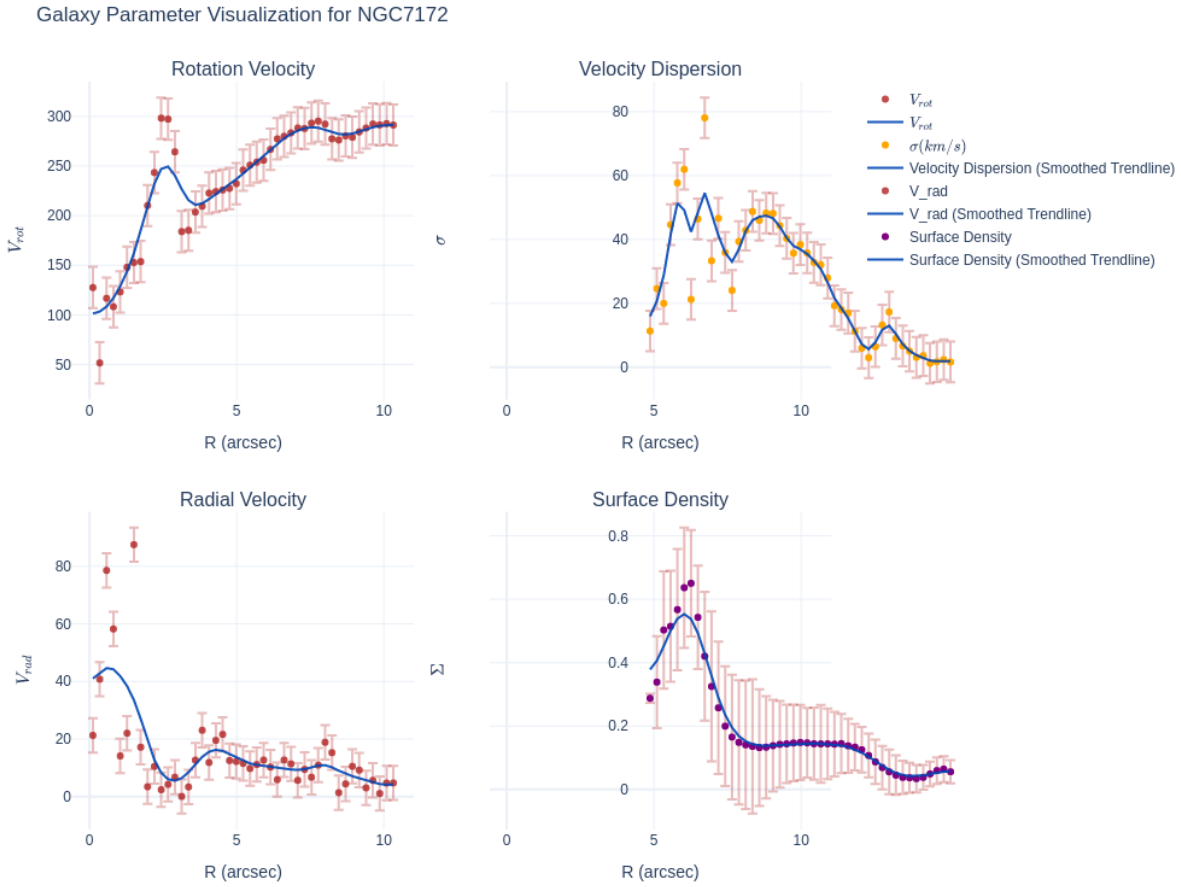

FIGURE E.18 – Best-fit parameters for the galaxy NGC7172. From top left to bottom right, the subplots show Rotation Velocity with trendline and error bars as a function of radius, Velocity Dispersion with error bars as a function of radius, Radial Velocity with trendline as a function of radius, and Surface Density as a function of radius for the galaxy.

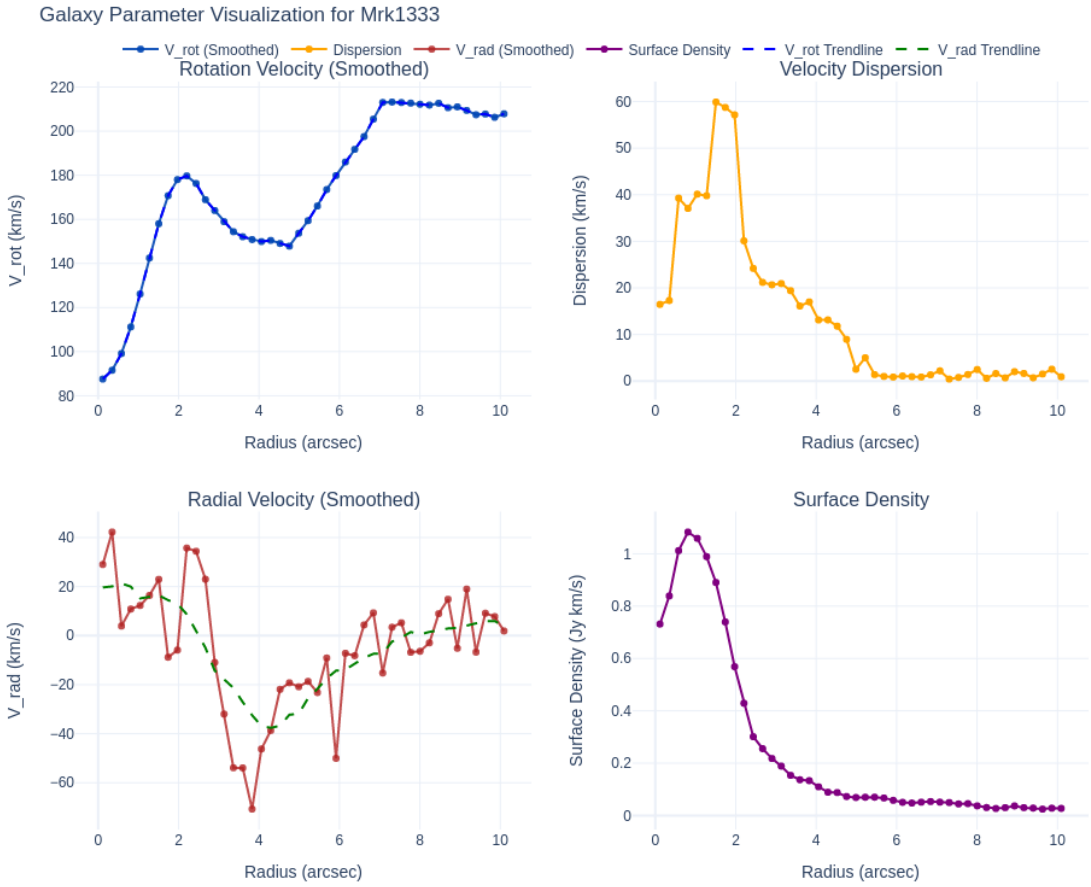

FIGURE E.19 – Best-fit parameters for the galaxy Mrk1333. From top left to bottom right, the subplots show Rotation Velocity with trendline and error bars as a function of radius, Velocity Dispersion with error bars as a function of radius, Radial Velocity with trendline as a function of radius, and Surface Density as a function of radius for the galaxy.

Appendix F - TWIST sample Result - Line Profile Emission

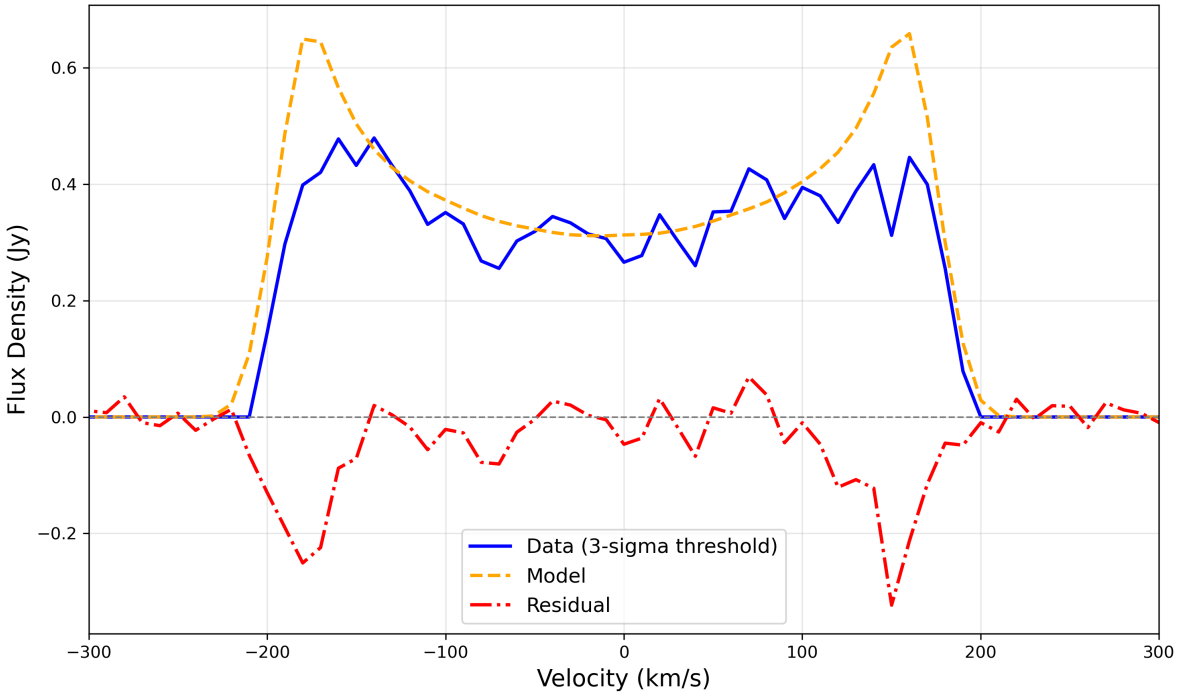

FIGURE F.1 – Line emission profile of the IC 5169 derived from ALMA CO(2-1) observations (Project ID: 2017.1.00236.S), showing flux density as a function of velocity. The solid blue line represents the observed data (above the 3-sigma threshold), the orange dashed line corresponds to the 3D-BAROLO modeling result, and the red dash-dot line indicates the residual flux, obtained by subtracting the model from the observed data cube. This profile highlights the kinematic structure and distribution of molecular gas.

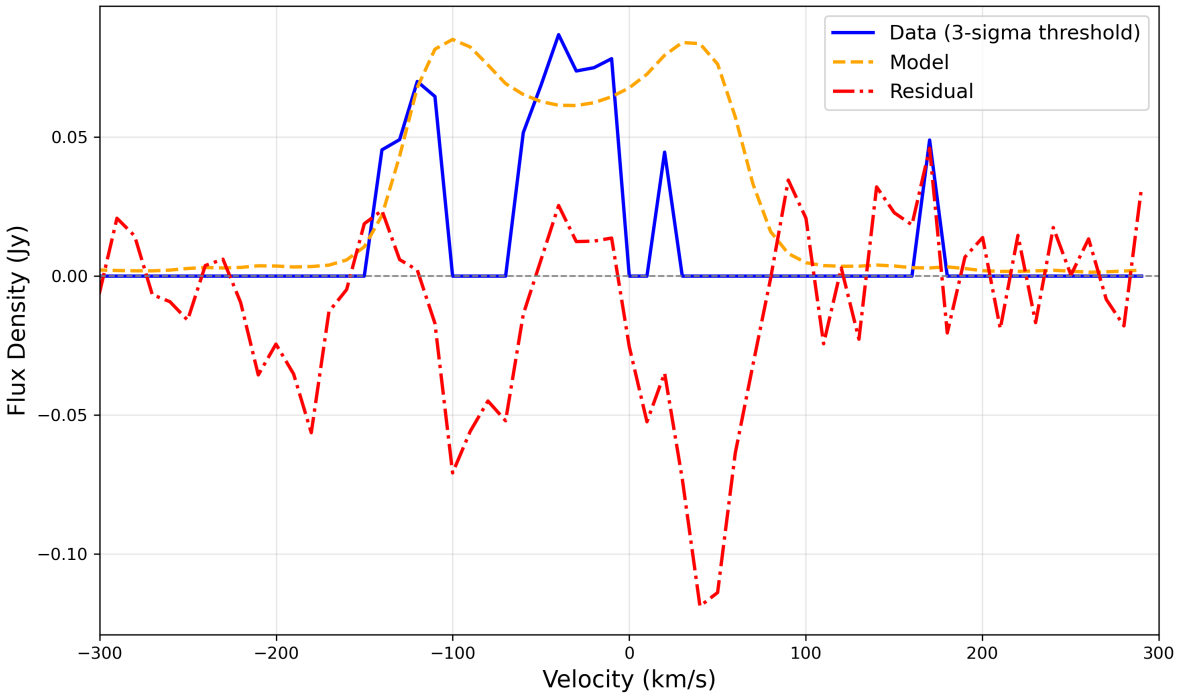

FIGURE F.2 – Line emission profile of the NGC 424 derived from ALMA CO(2-1) observations (Project ID: 2017.1.00236.S), showing flux density as a function of velocity. The solid blue line represents the observed data (above the 3-sigma threshold), the orange dashed line corresponds to the 3D-BAROLO modeling result, and the red dash-dot line indicates the residual flux, obtained by subtracting the model from the observed data cube. This profile highlights the kinematic structure and distribution of molecular gas.

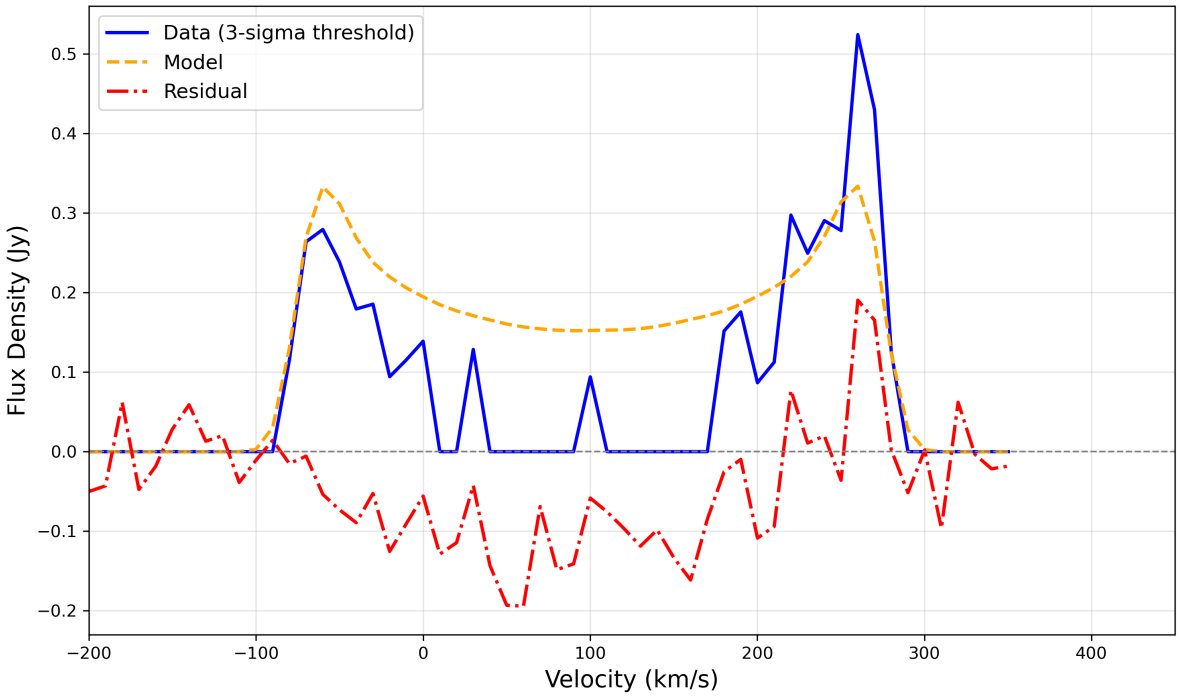

FIGURE F.3 – Line emission profile of the ngc 1320 derived from ALMA CO(2-1) observations (Project ID: 2017.1.00236.S), showing flux density as a function of velocity. The solid blue line represents the observed data (above the 3-sigma threshold), the orange dashed line corresponds to the 3D-BAROLO modeling result, and the red dash-dot line indicates the residual flux, obtained by subtracting the model from the observed data cube. This profile highlights the kinematic structure and distribution of molecular gas.

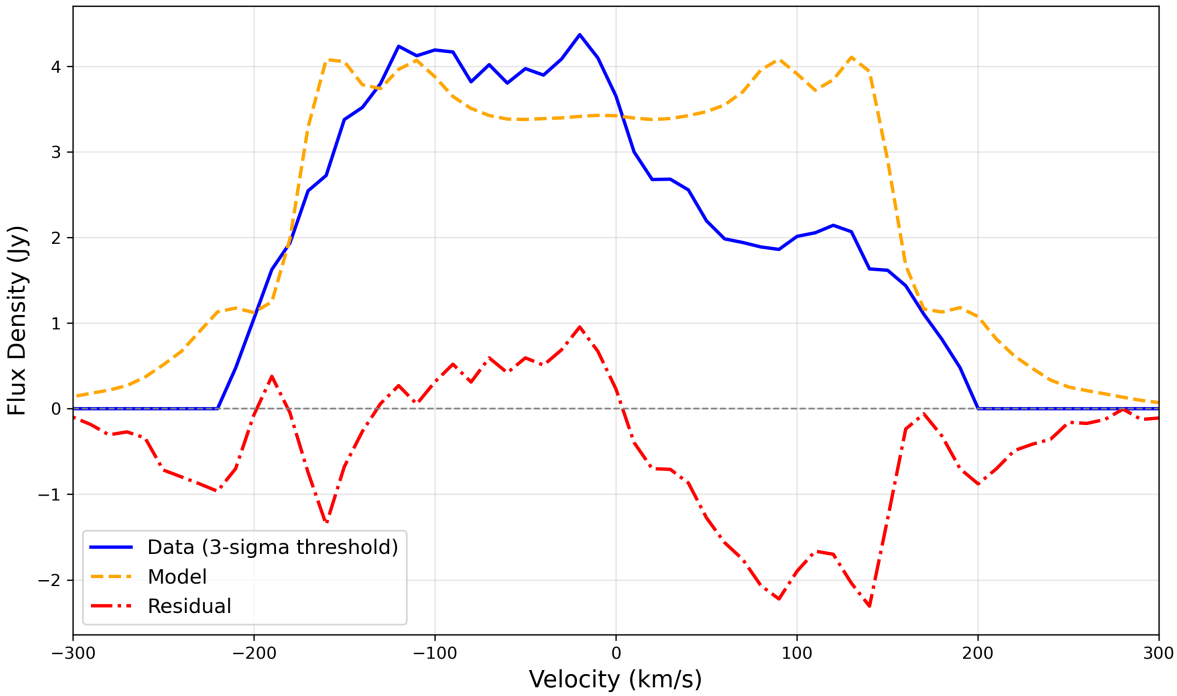

FIGURE F.4 – Line emission profile of the ngc 613 derived from ALMA CO(2-1) observations (Project ID: 2017.1.00236.S), showing flux density as a function of velocity. The solid blue line represents the observed data (above the 3-sigma threshold), the orange dashed line corresponds to the 3D-BAROLO modeling result, and the red dash-dot line indicates the residual flux, obtained by subtracting the model from the observed data cube. This profile highlights the kinematic structure and distribution of molecular gas.

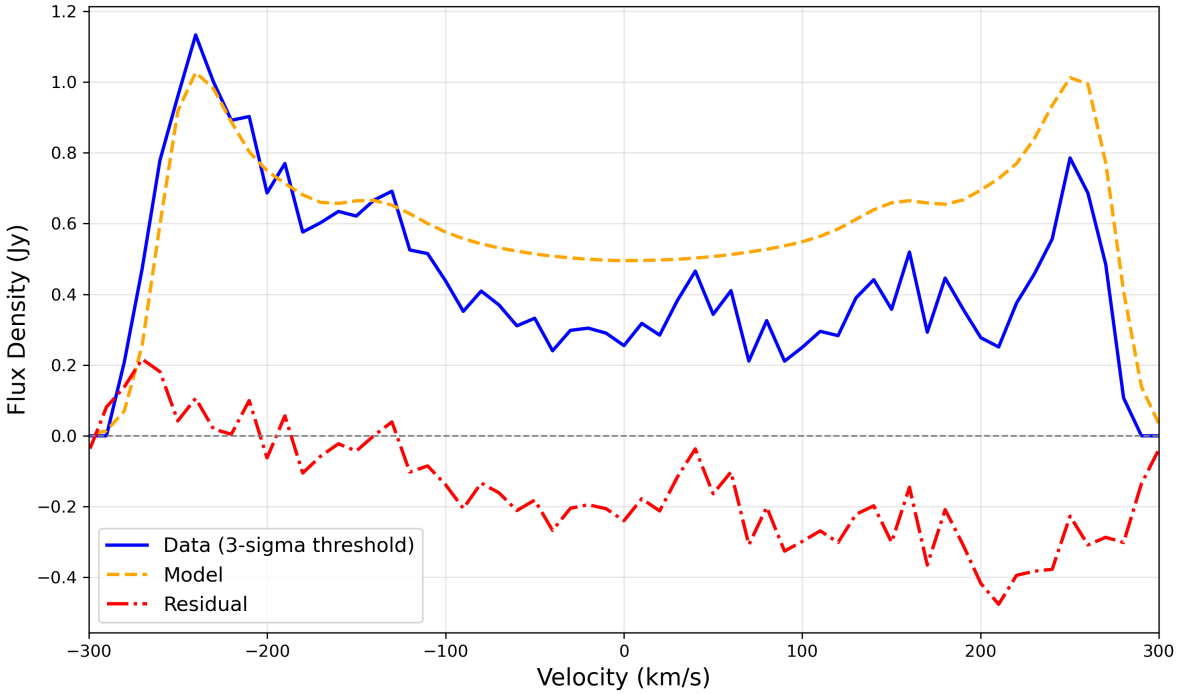

FIGURE F.5 – Line emission profile of the ngc 2992 derived from ALMA CO(2-1) observations (Project ID: 2017.1.00236.S), showing flux density as a function of velocity. The solid blue line represents the observed data (above the 3-sigma threshold), the orange dashed line corresponds to the 3D-BAROLO modeling result, and the red dash-dot line indicates the residual flux, obtained by subtracting the model from the observed data cube. This profile highlights the kinematic structure and distribution of molecular gas.

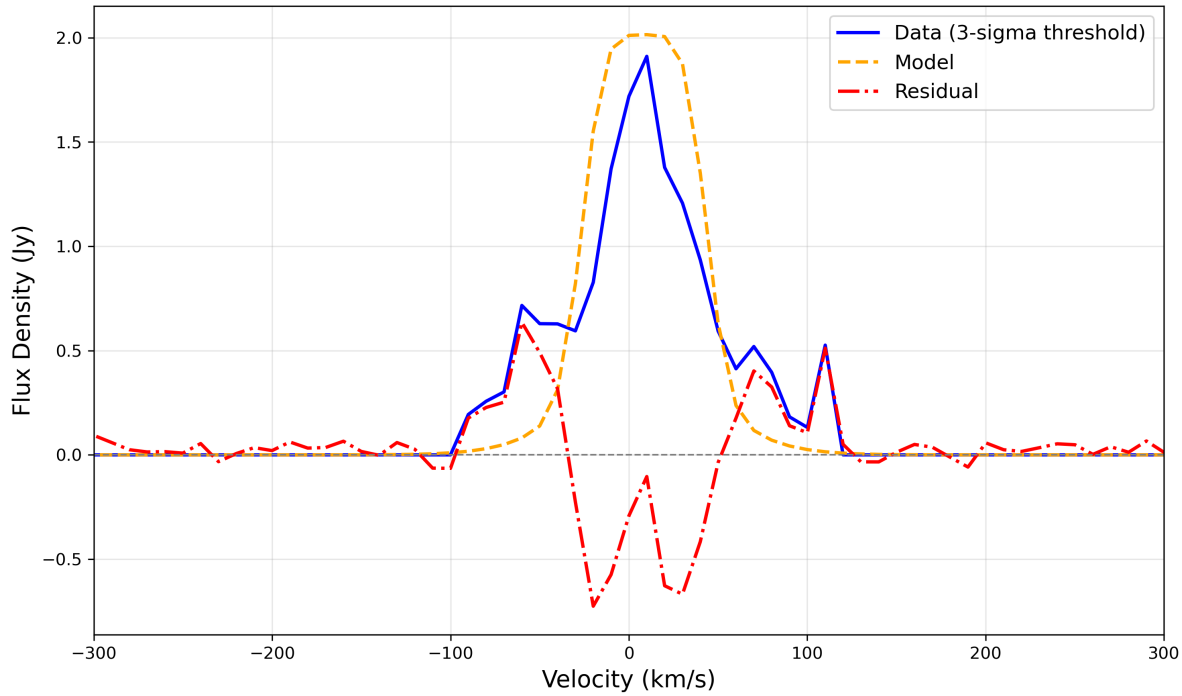

FIGURE F.6 – Line emission profile of the ngc 5861 derived from ALMA CO(2-1) observations (Project ID: 2017.1.00236.S), showing flux density as a function of velocity. The solid blue line represents the observed data (above the 3-sigma threshold), the orange dashed line corresponds to the 3D-BAROLO modeling result, and the red dash-dot line indicates the residual flux, obtained by subtracting the model from the observed data cube. This profile highlights the kinematic structure and distribution of molecular gas.

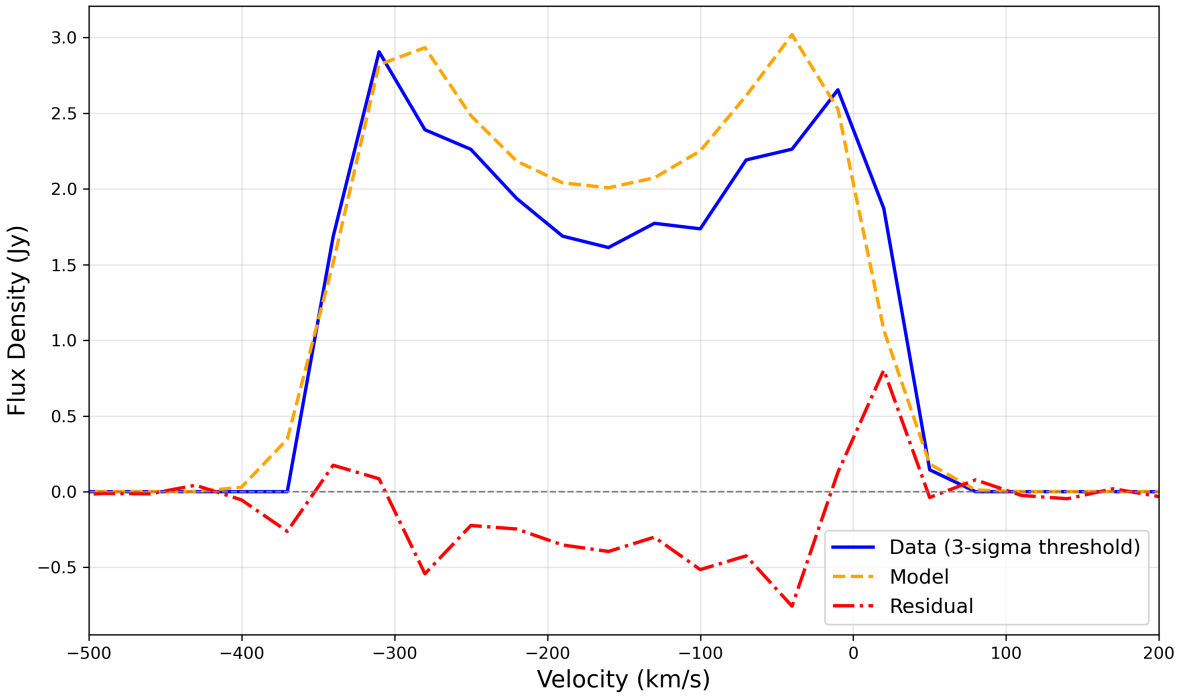

FIGURE F.7 – Line emission profile of the ngc 4845 derived from ALMA CO(2-1) observations (Project ID: 2017.1.00236.S), showing flux density as a function of velocity. The solid blue line represents the observed data (above the 3-sigma threshold), the orange dashed line corresponds to the 3D-BAROLO modeling result, and the red dash-dot line indicates the residual flux, obtained by subtracting the model from the observed data cube. This profile highlights the kinematic structure and distribution of molecular gas.

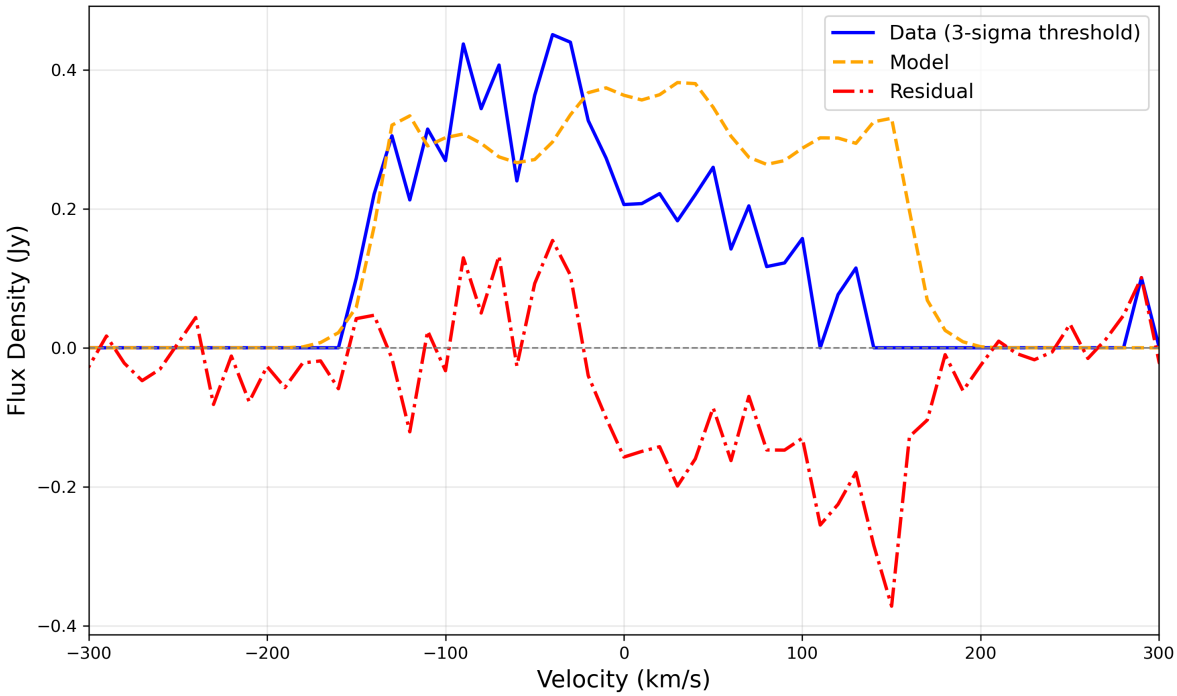

FIGURE F.8 – Line emission profile of the ngc 4941 derived from ALMA CO(2-1) observations (Project ID: 2017.1.00236.S), showing flux density as a function of velocity. The solid blue line represents the observed data (above the 3-sigma threshold), the orange dashed line corresponds to the 3D-BAROLO modeling result, and the red dash-dot line indicates the residual flux, obtained by subtracting the model from the observed data cube. This profile highlights the kinematic structure and distribution of molecular gas.

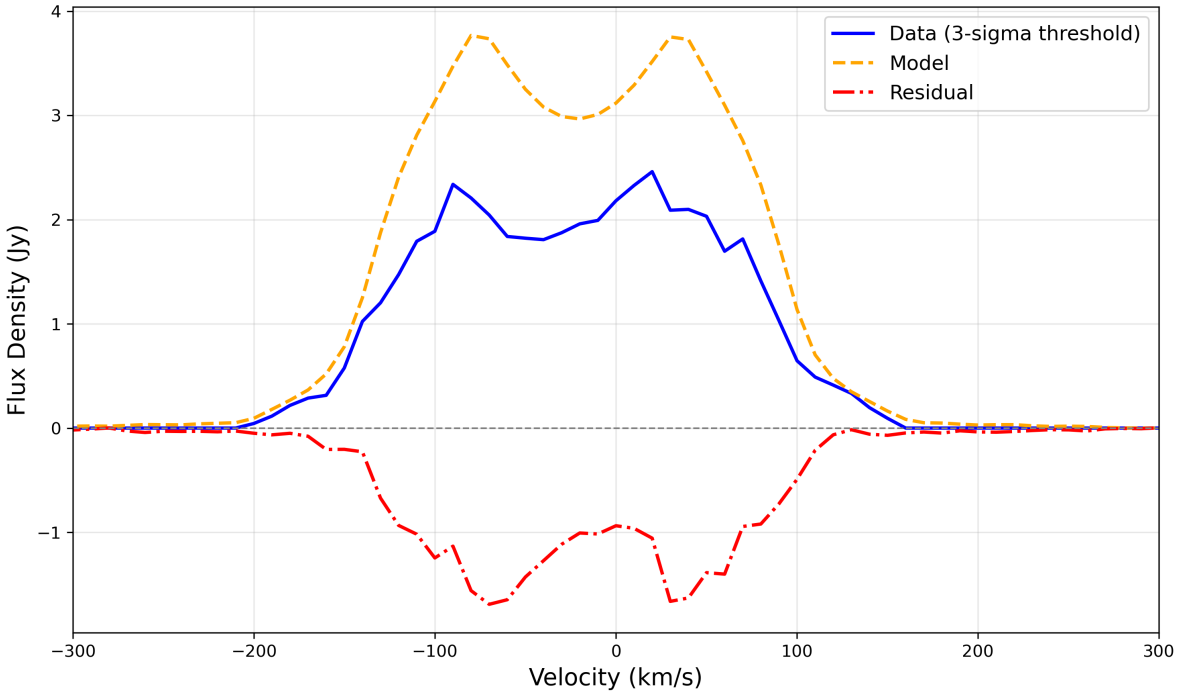

FIGURE F.9 – Line emission profile of the ngc 1566 derived from ALMA CO(2-1) observations (Project ID: 2017.1.00236.S), showing flux density as a function of velocity. The solid blue line represents the observed data (above the 3-sigma threshold), the orange dashed line corresponds to the 3D-BAROLO modeling result, and the red dash-dot line indicates the residual flux, obtained by subtracting the model from the observed data cube. This profile highlights the kinematic structure and distribution of molecular gas.

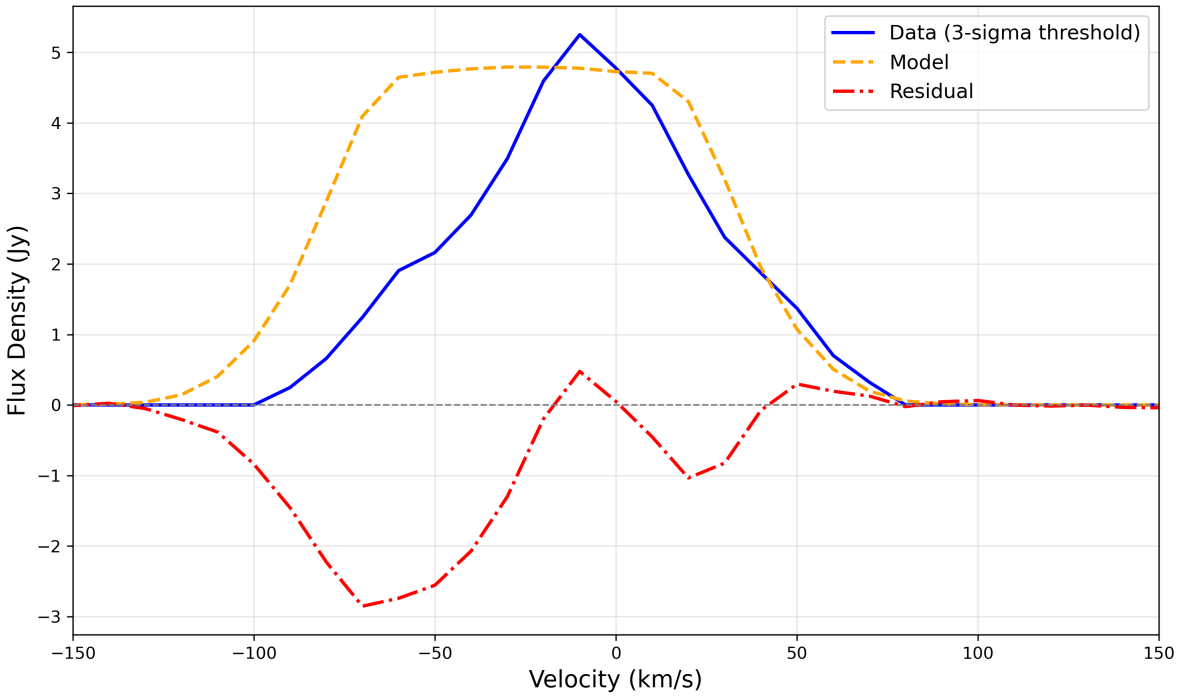

FIGURE F.10 – Line emission profile of the ngc 7496 derived from ALMA CO(2-1) observations (Project ID: 2017.1.00236.S), showing flux density as a function of velocity. The solid blue line represents the observed data (above the 3-sigma threshold), the orange dashed line corresponds to the 3D-BAROLO modeling result, and the red dash-dot line indicates the residual flux, obtained by subtracting the model from the observed data cube. This profile highlights the kinematic structure and distribution of molecular gas.

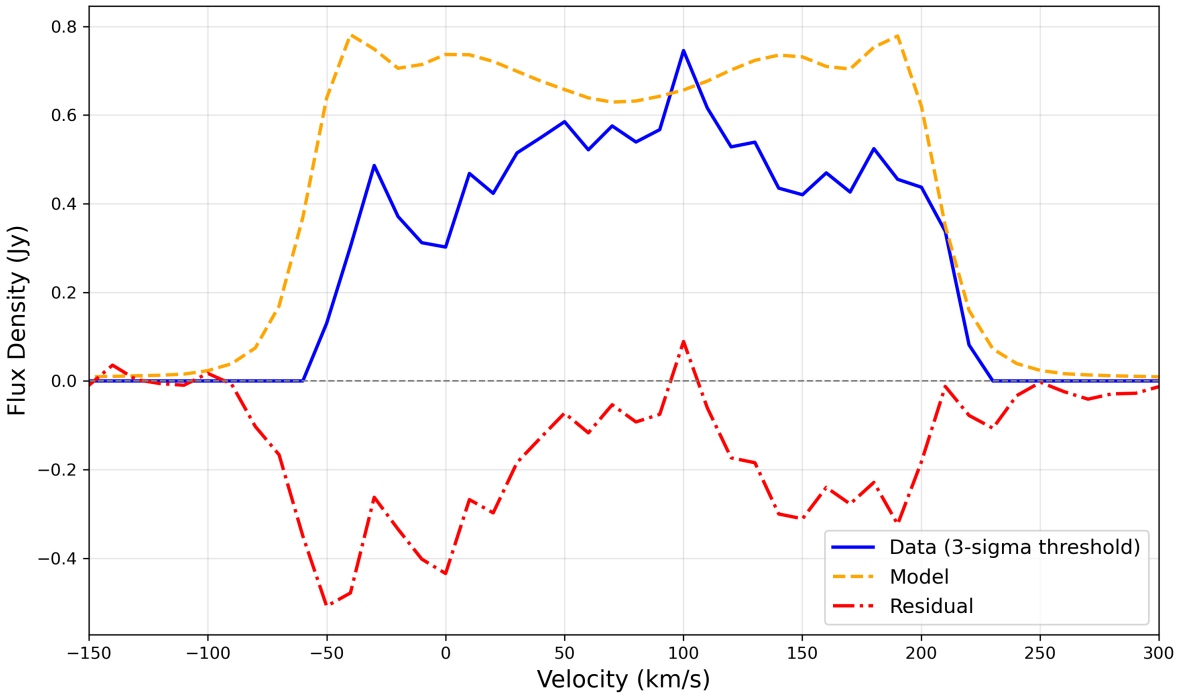

FIGURE F.11 – Line emission profile of the ngc 6890 derived from ALMA CO(2-1) observations (Project ID: 2017.1.00236.S), showing flux density as a function of velocity. The solid blue line represents the observed data (above the 3-sigma threshold), the orange dashed line corresponds to the 3D-BAROLO modeling result, and the red dash-dot line indicates the residual flux, obtained by subtracting the model from the observed data cube. This profile highlights the kinematic structure and distribution of molecular gas.

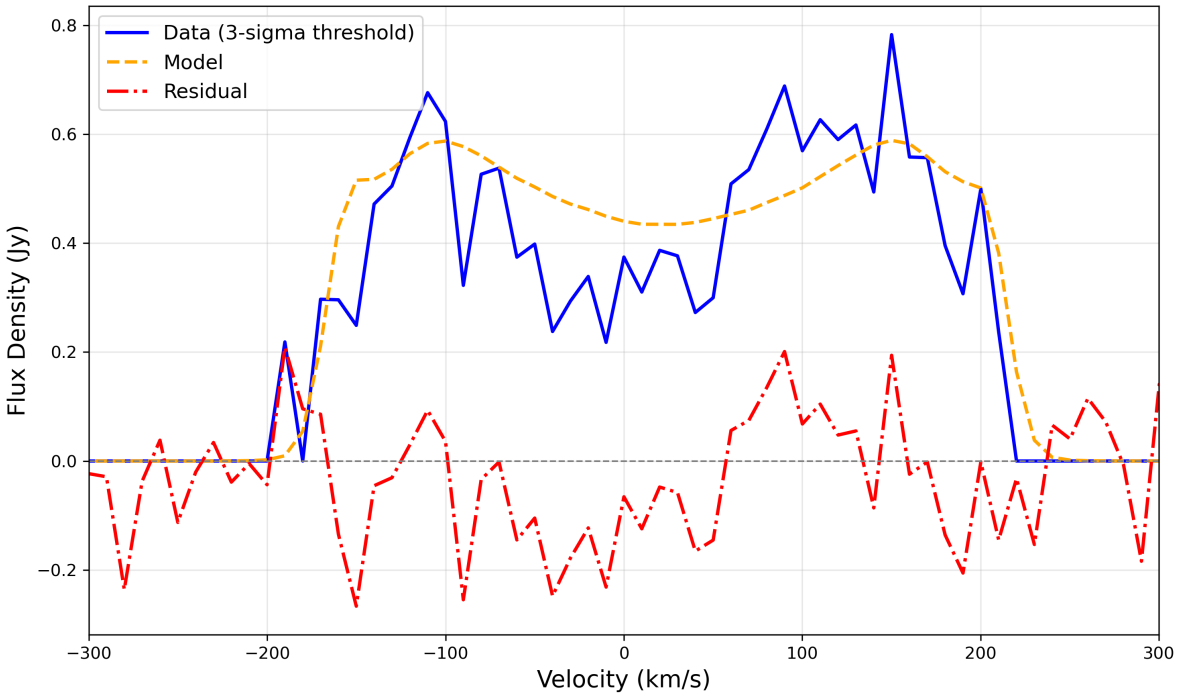

FIGURE F.12 – Line emission profile of the ngc 5506 derived from ALMA CO(2-1) observations (Project ID: 2017.1.00236.S), showing flux density as a function of velocity. The solid blue line represents the observed data (above the 3-sigma threshold), the orange dashed line corresponds to the 3D-BAROLO modeling result, and the red dash-dot line indicates the residual flux, obtained by subtracting the model from the observed data cube. This profile highlights the kinematic structure and distribution of molecular gas.

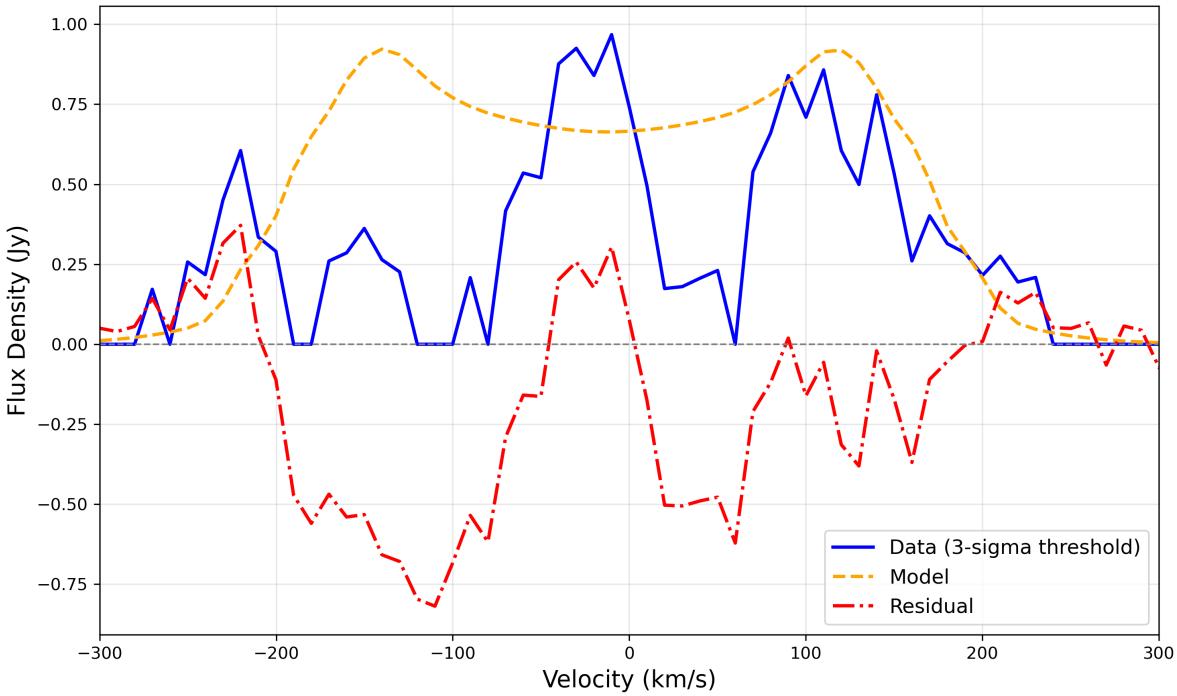

FIGURE F.13 – Line emission profile of the Mrk1333 derived from ALMA CO(2-1) observations (Project ID: 2017.1.00236.S), showing flux density as a function of velocity. The solid blue line represents the observed data (above the 3-sigma threshold), the orange dashed line corresponds to the 3D-BAROLO modeling result, and the red dash-dot line indicates the residual flux, obtained by subtracting the model from the observed data cube. This profile highlights the kinematic structure and distribution of molecular gas.

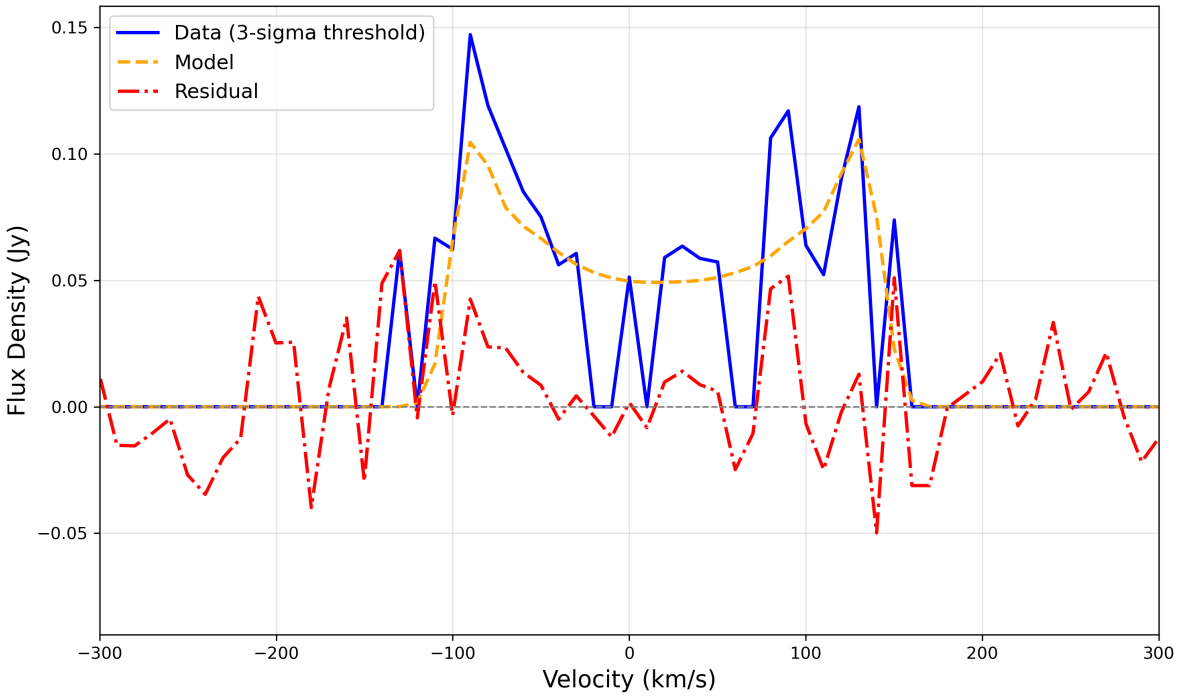

FIGURE F.14 – Line emission profile of the MCG-6-30-15 derived from ALMA CO(2-1) observations (Project ID: 2017.1.00236.S), showing flux density as a function of velocity. The solid blue line represents the observed data (above the 3-sigma threshold), the orange dashed line corresponds to the 3D-BAROLO modeling result, and the red dash-dot line indicates the residual flux, obtained by subtracting the model from the observed data cube. This profile highlights the kinematic structure and distribution of molecular gas.

Appendix G - TWIST Exploratory Data Analysis

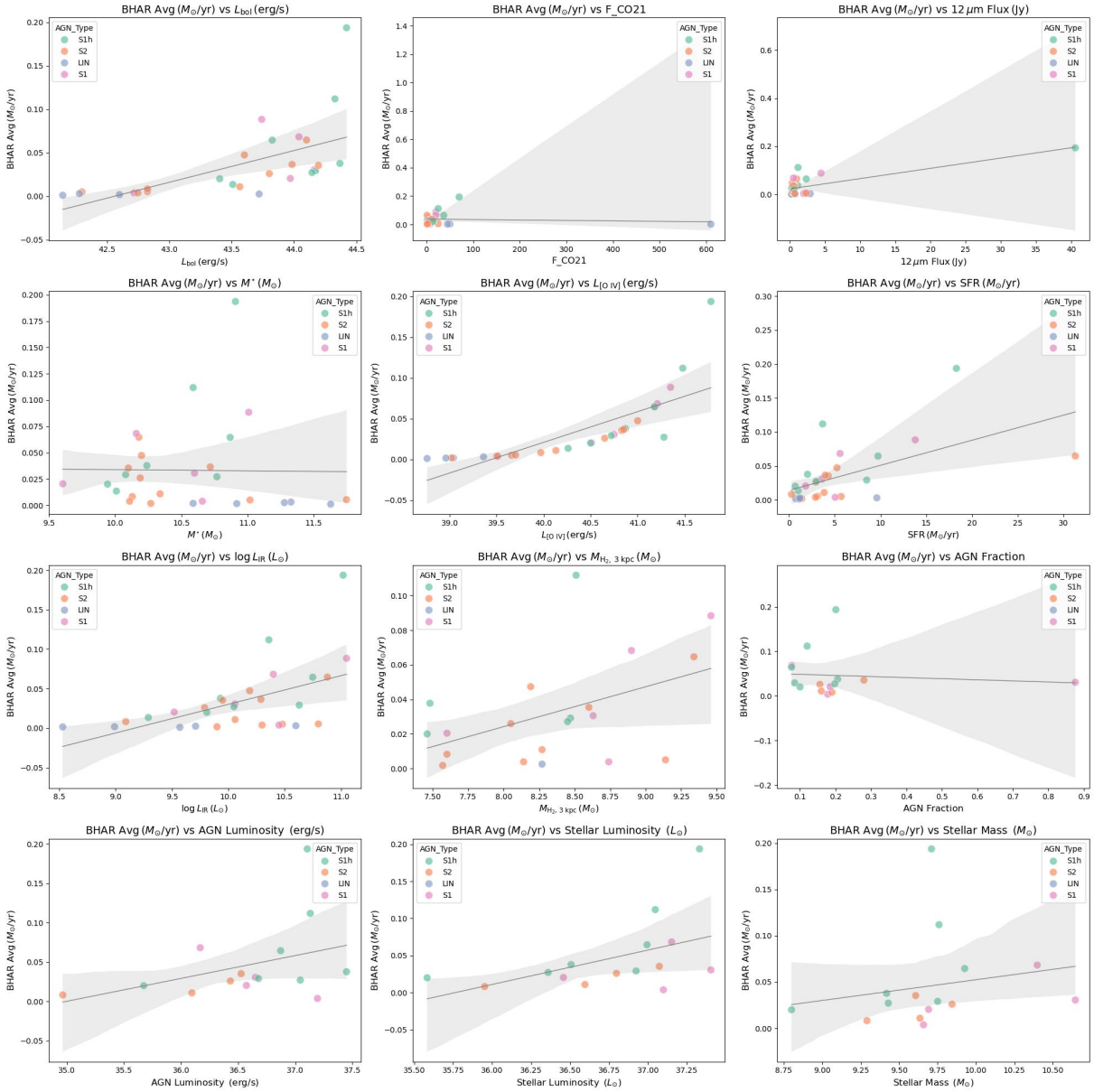

FIGURE G.1 – Scatter plot of exploratory data analysis for scatter BHAR avg part 1

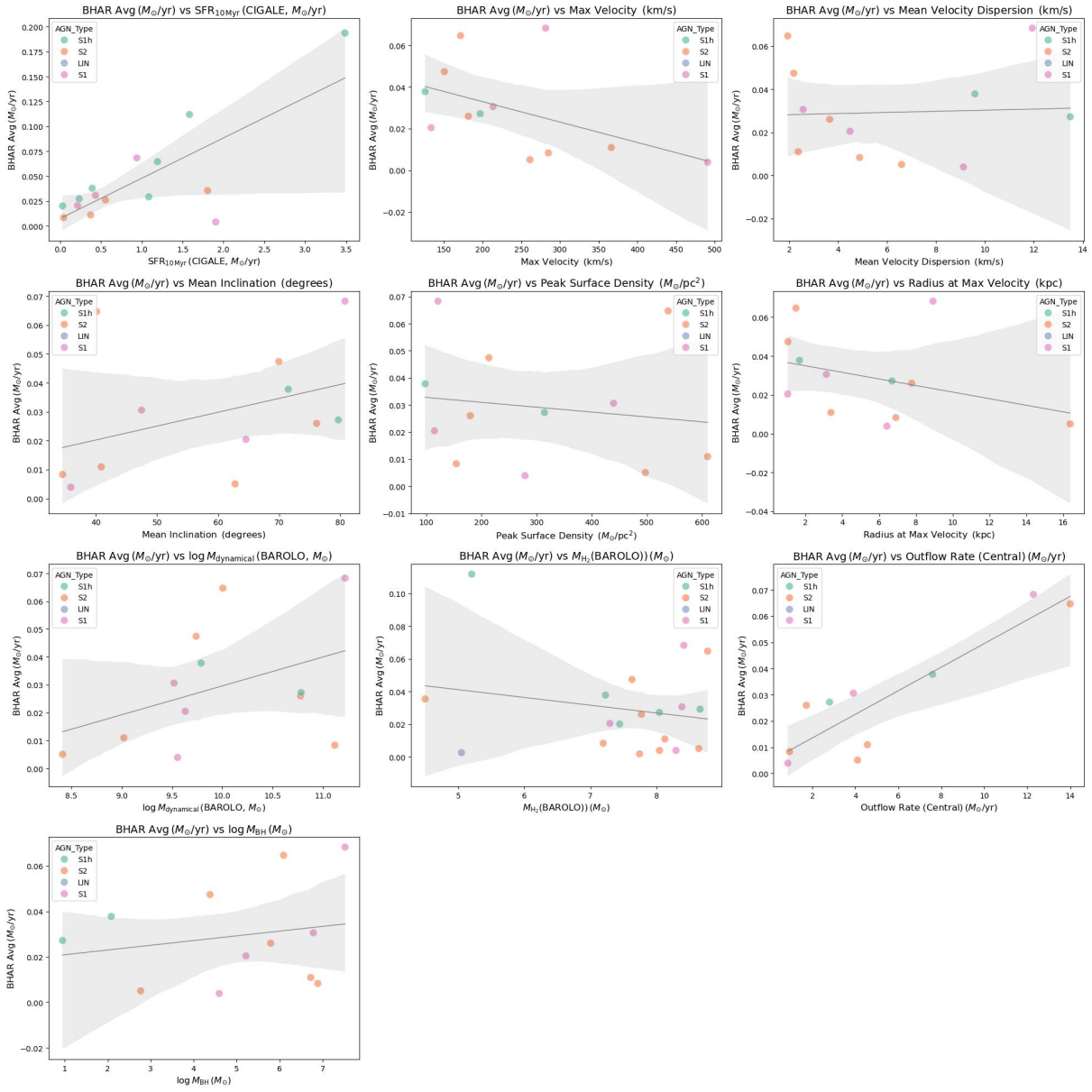

FIGURE G.2 – Scatter plot of exploratory data analysis for scatter BHAR avg part 2

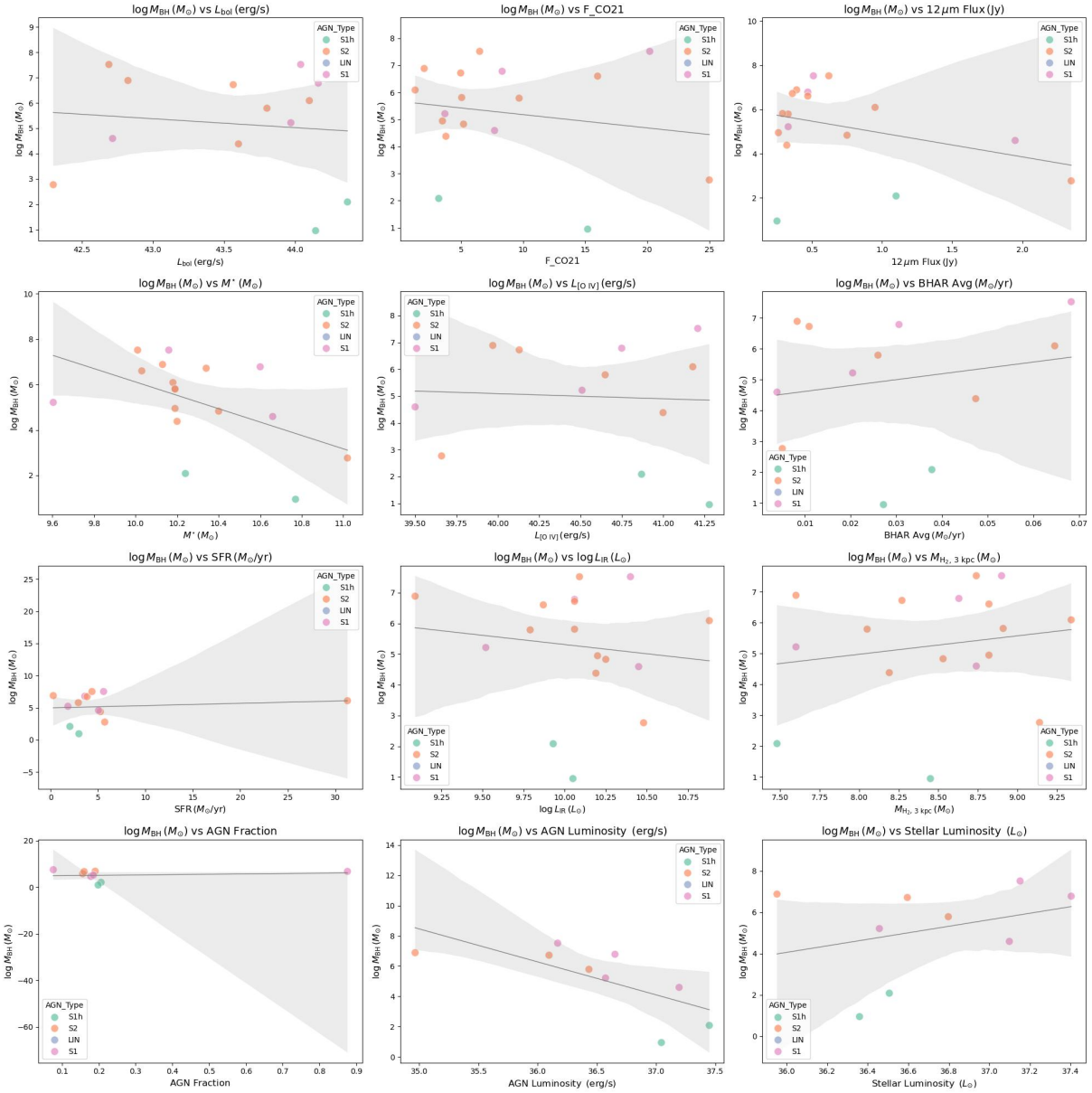

FIGURE G.3 – Scatter plot of exploratory data analysis for scatter BH mass log part 1

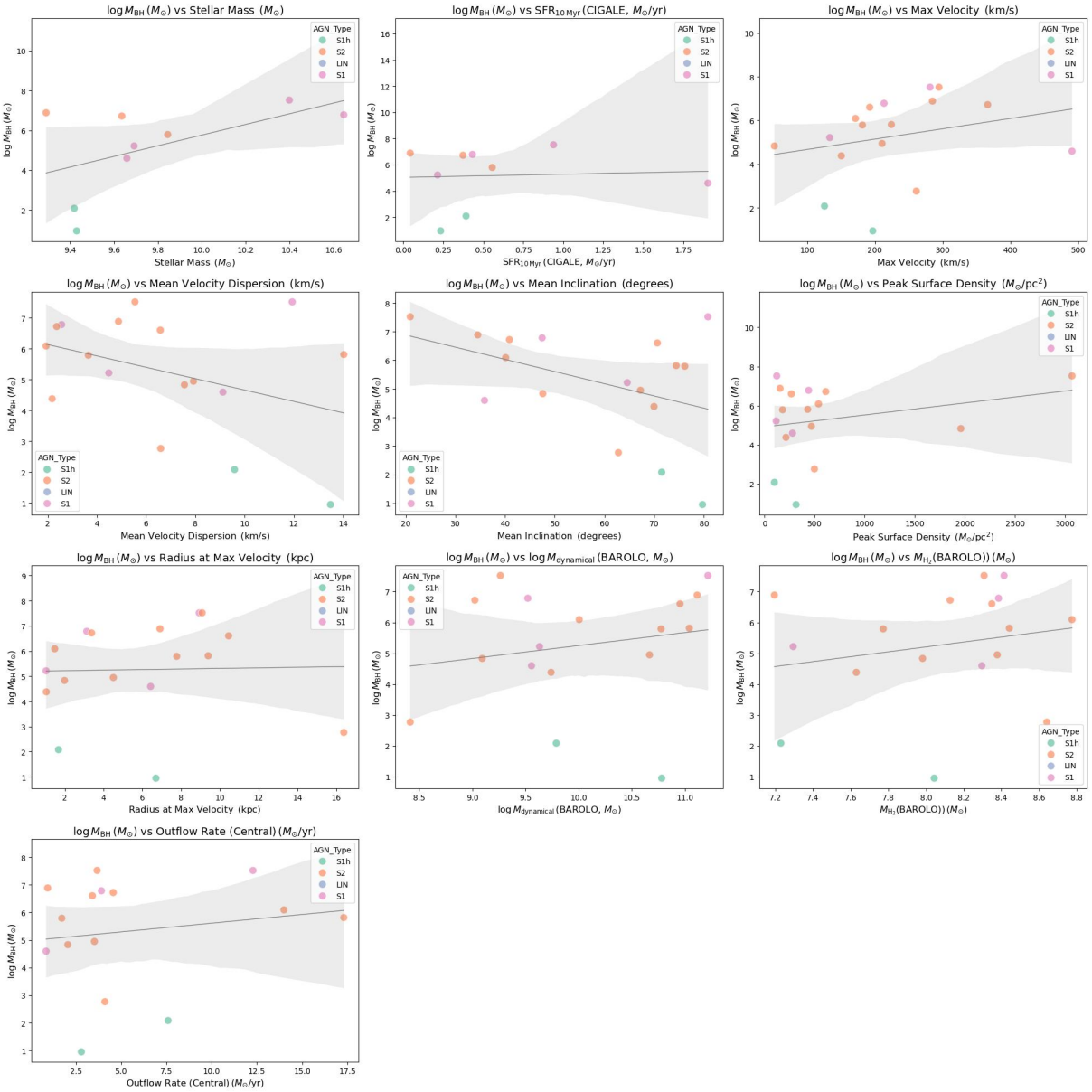

FIGURE G.4 – Scatter plot of exploratory data analysis for scatter BH mass log part 2

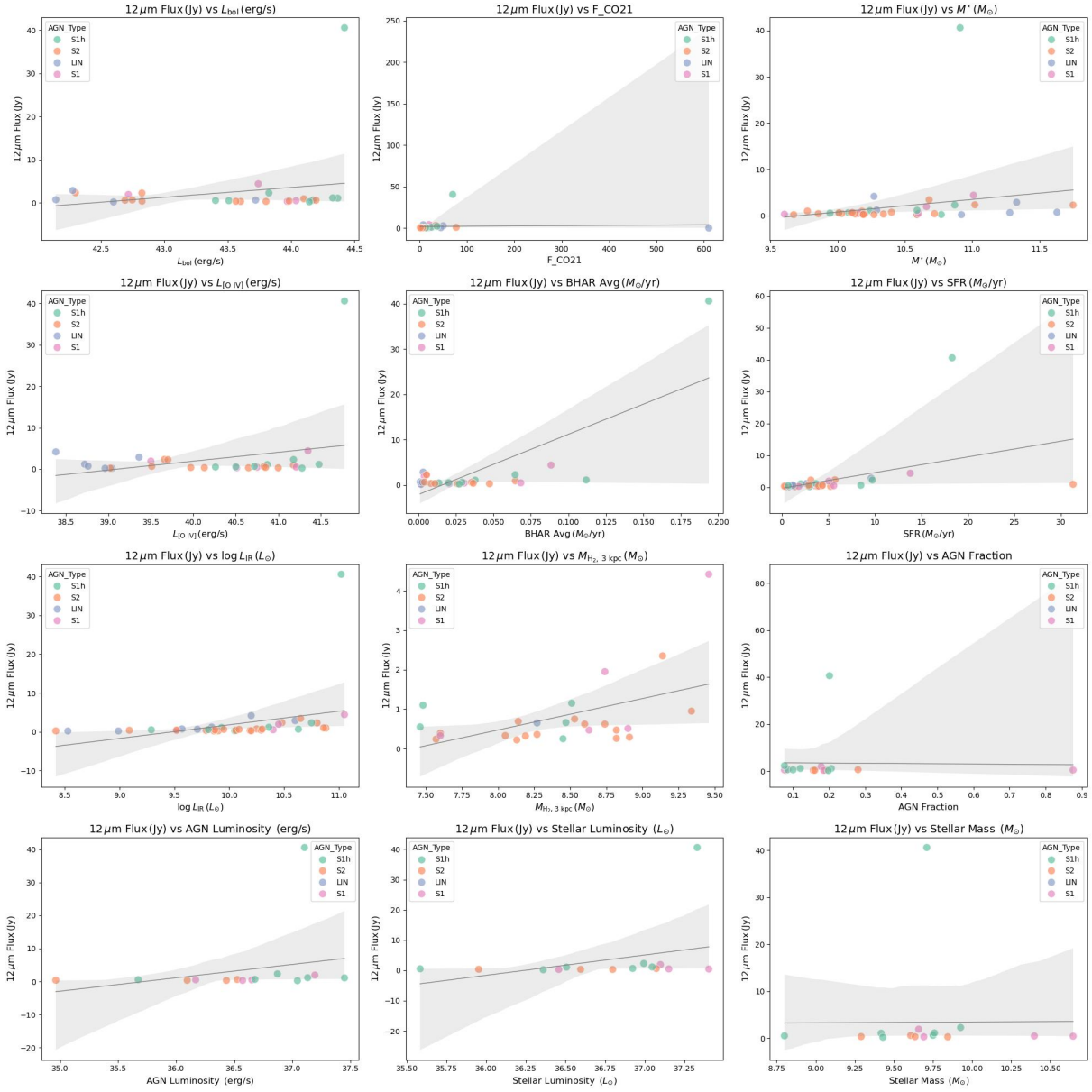

FIGURE G.5 – Scatter plot of exploratory data analysis for scatter F 12 part 1

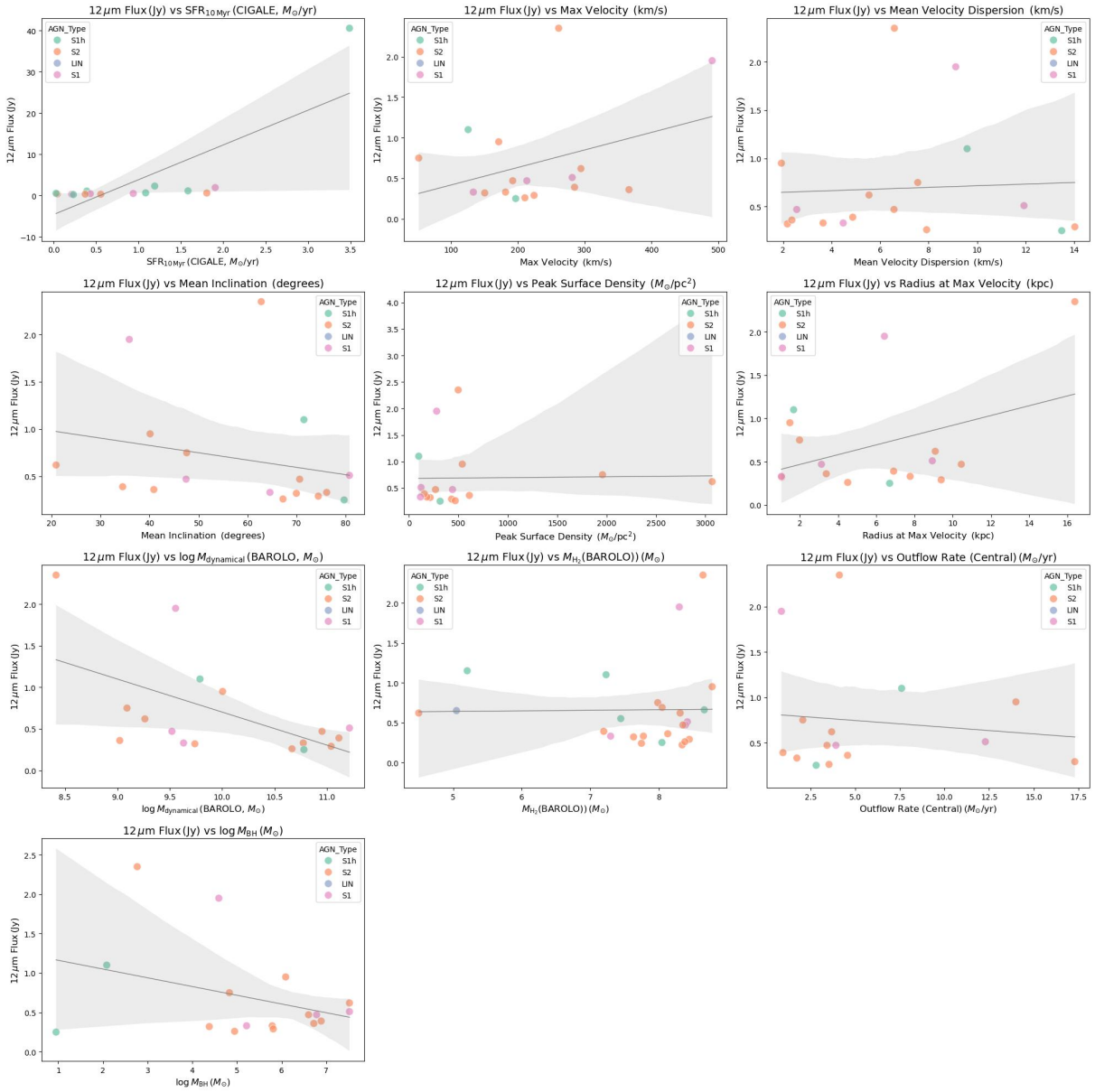

FIGURE G.6 – Scatter plot of exploratory data analysis for scatter F 12 part 2

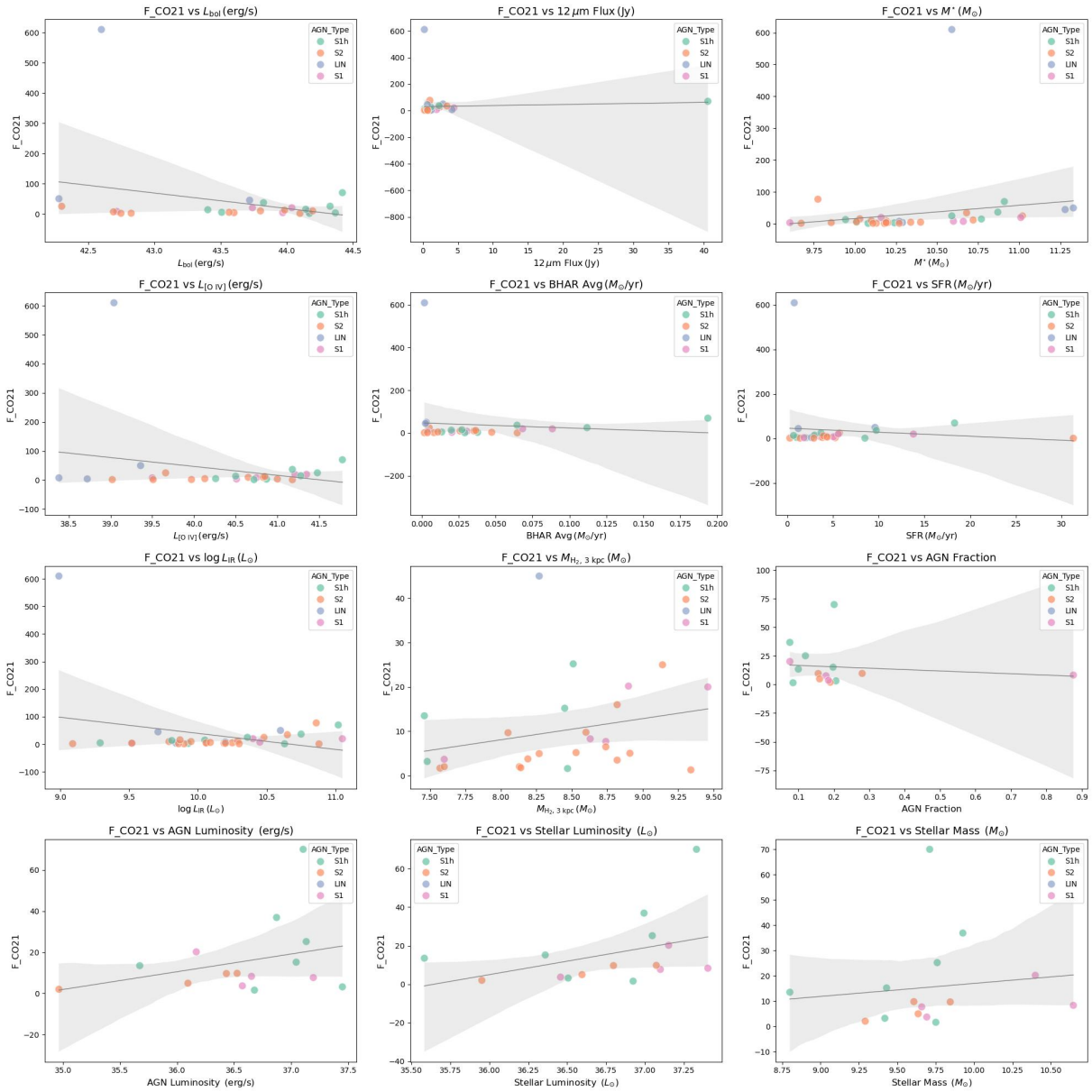

FIGURE G.7 – Scatter plot of exploratory data analysis for scatter F CO21 part 1

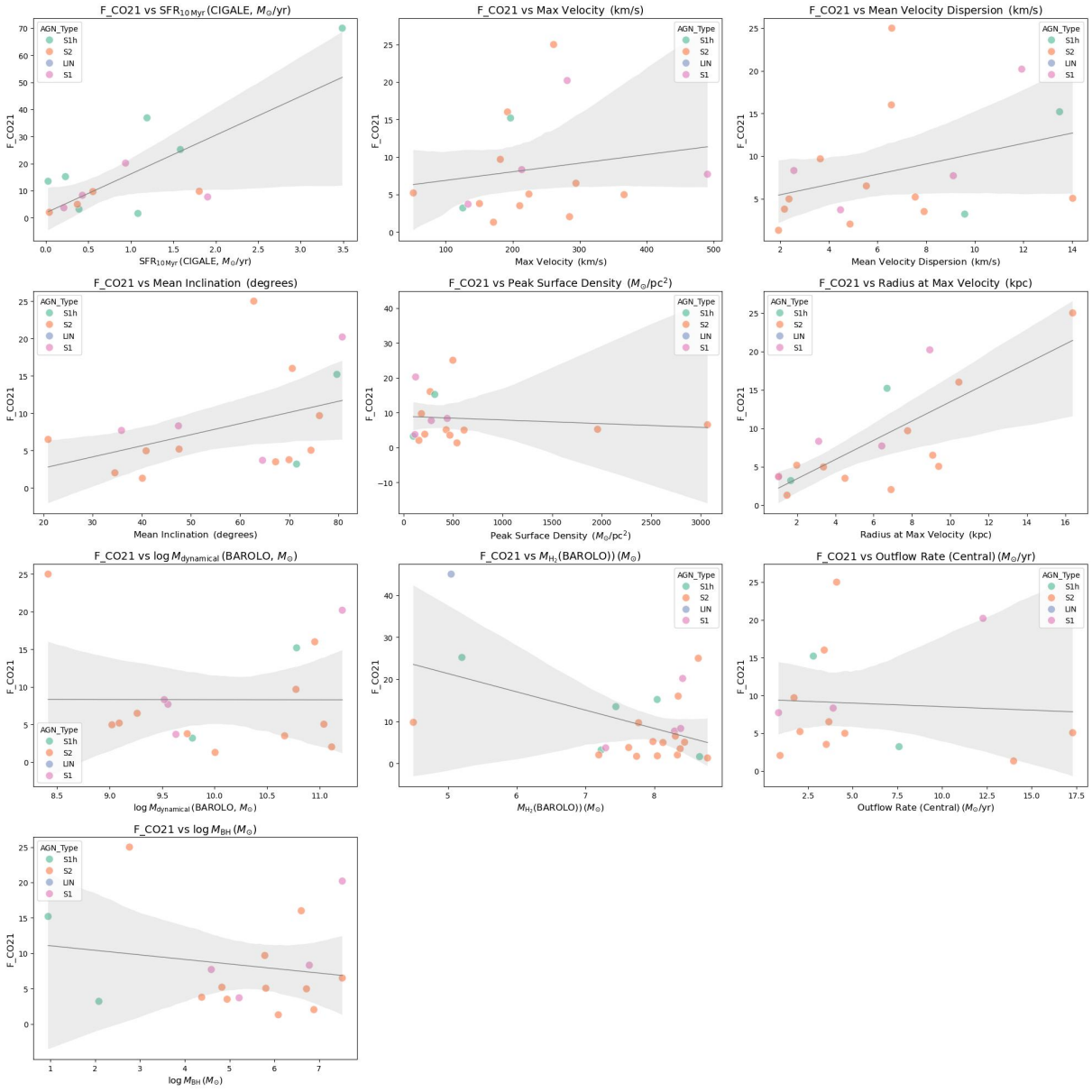

FIGURE G.8 – Scatter plot of exploratory data analysis for scatter F CO21 part 2

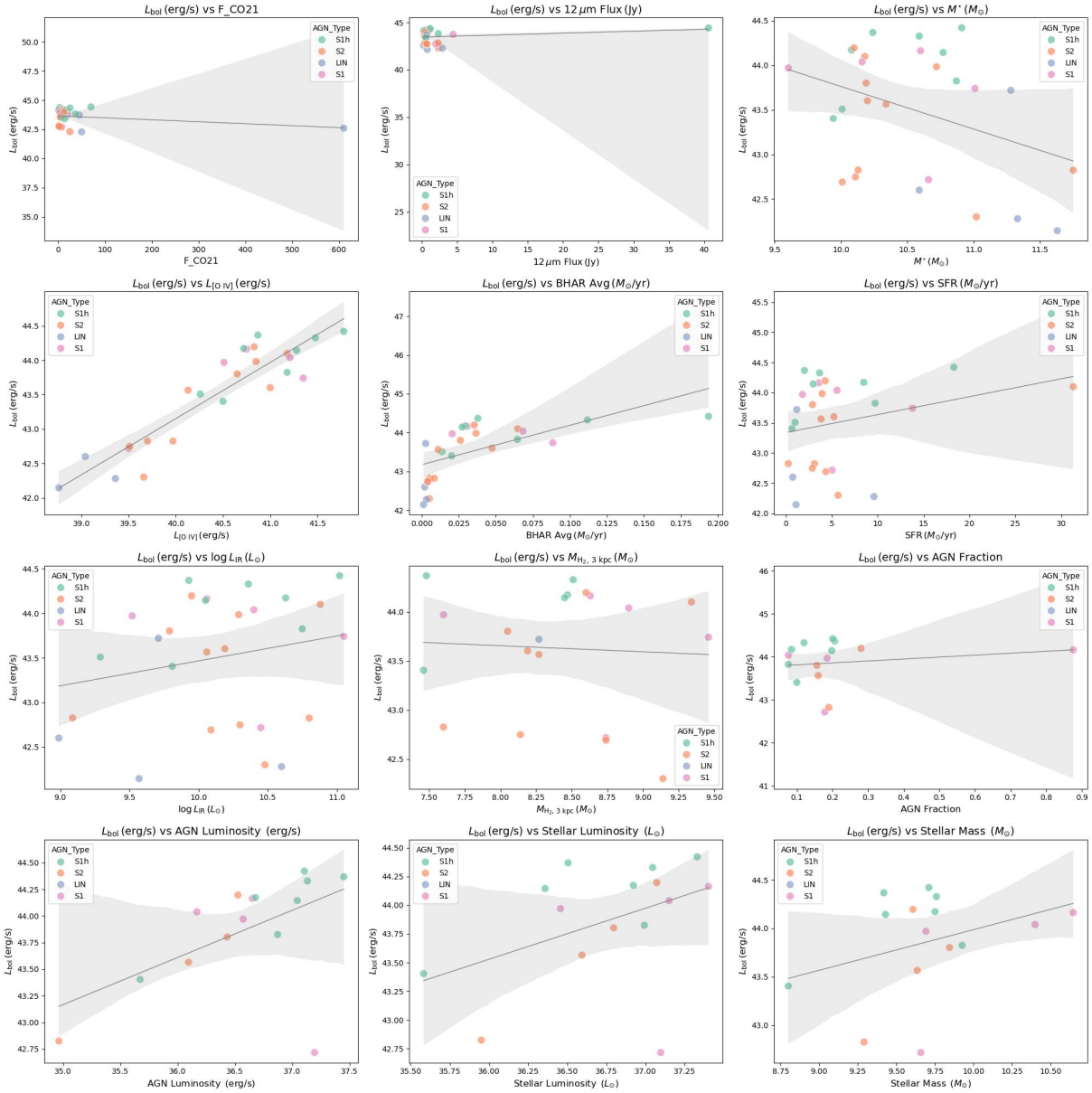

FIGURE G.9 – Scatter plot of exploratory data analysis for scatter L bol part 1

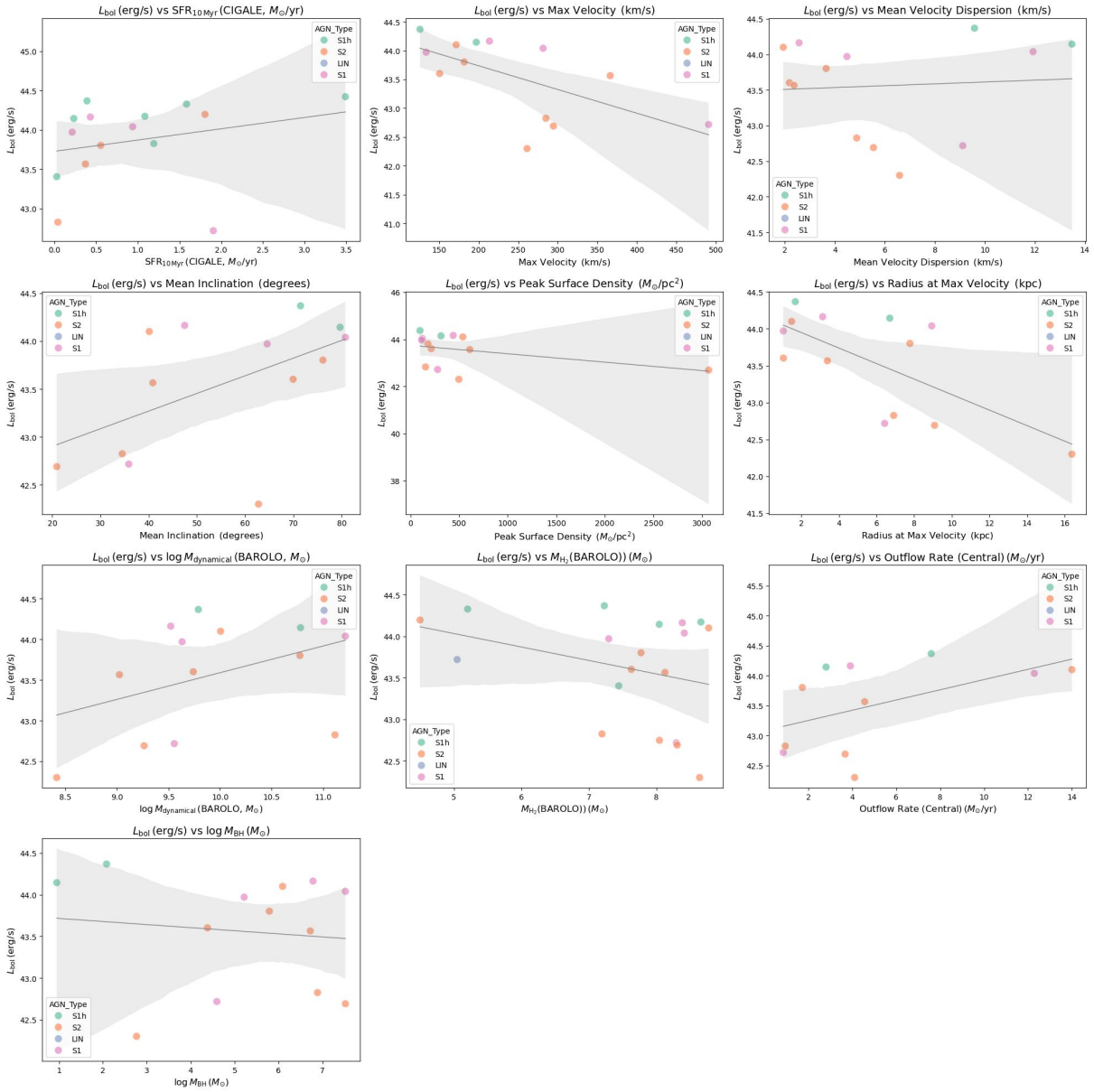

FIGURE G.10 – Scatter plot of exploratory data analysis for scatter L bol part 2

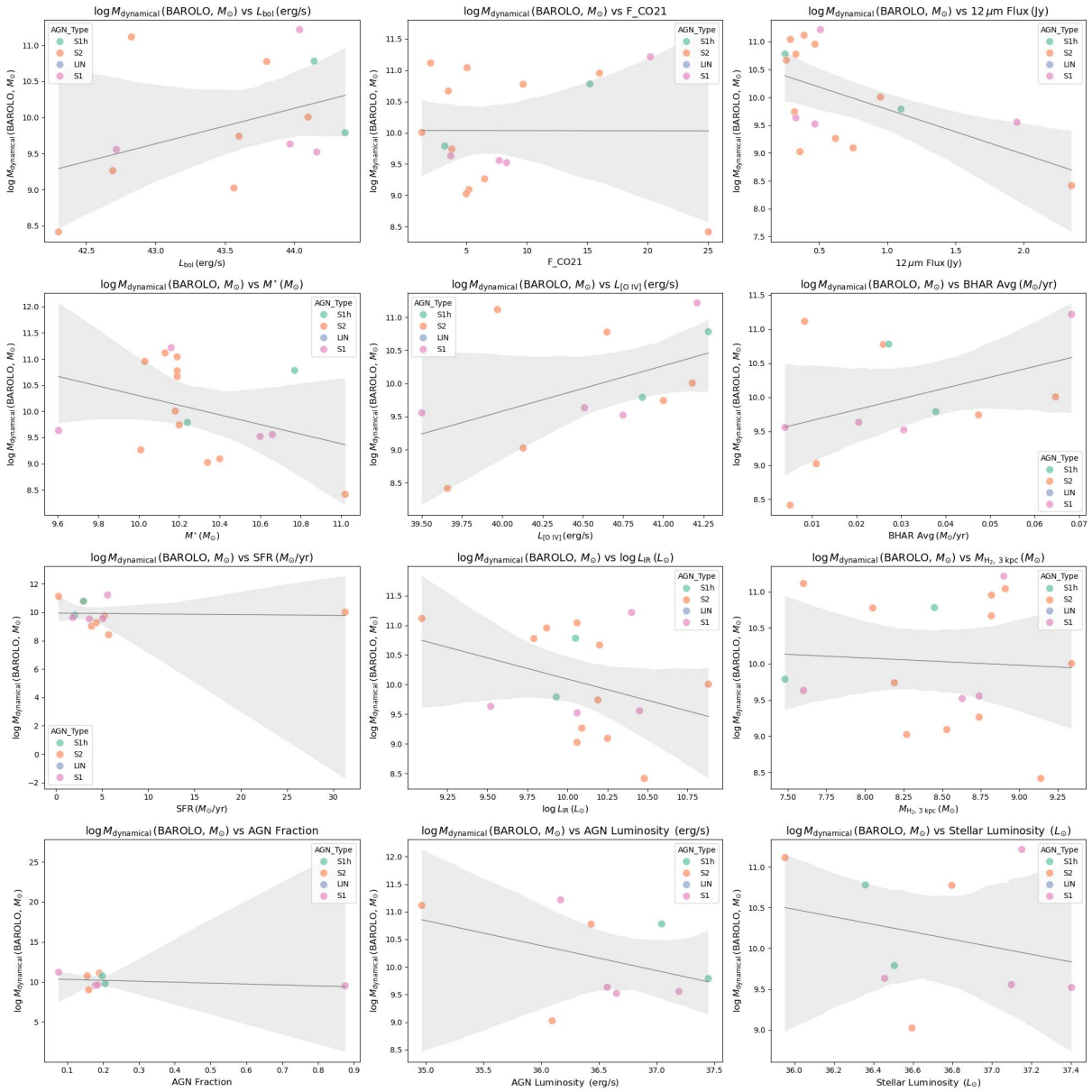

FIGURE G.11 – Scatter plot of exploratory data analysis for scatter Log Dynamical Mass BAROLO part 1

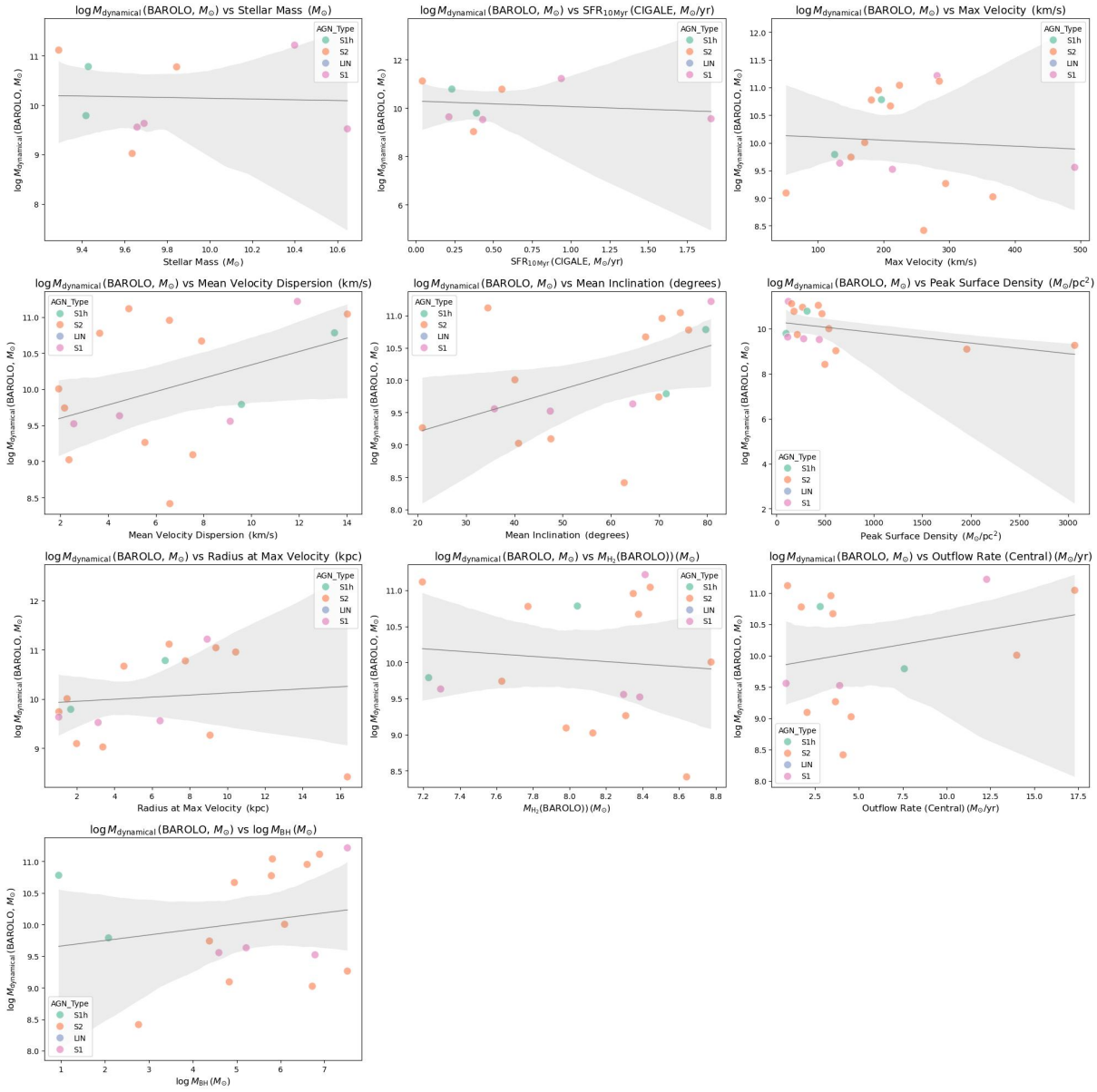

FIGURE G.12 – Scatter plot of exploratory data analysis for scatter Log Dynamical Mass BAROLO part 2

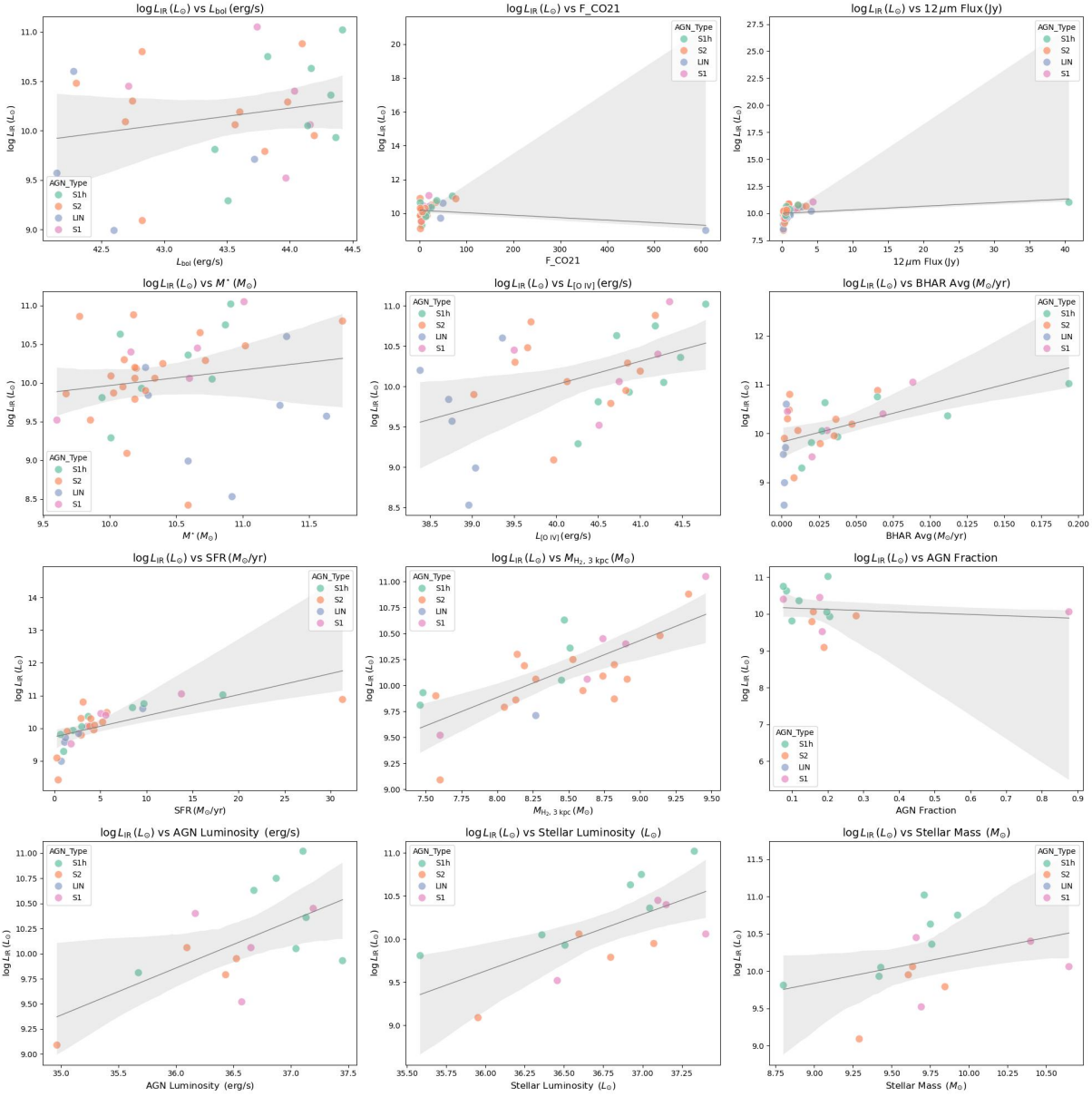

FIGURE G.13 – Scatter plot of exploratory data analysis for scatter Log L IR part 1

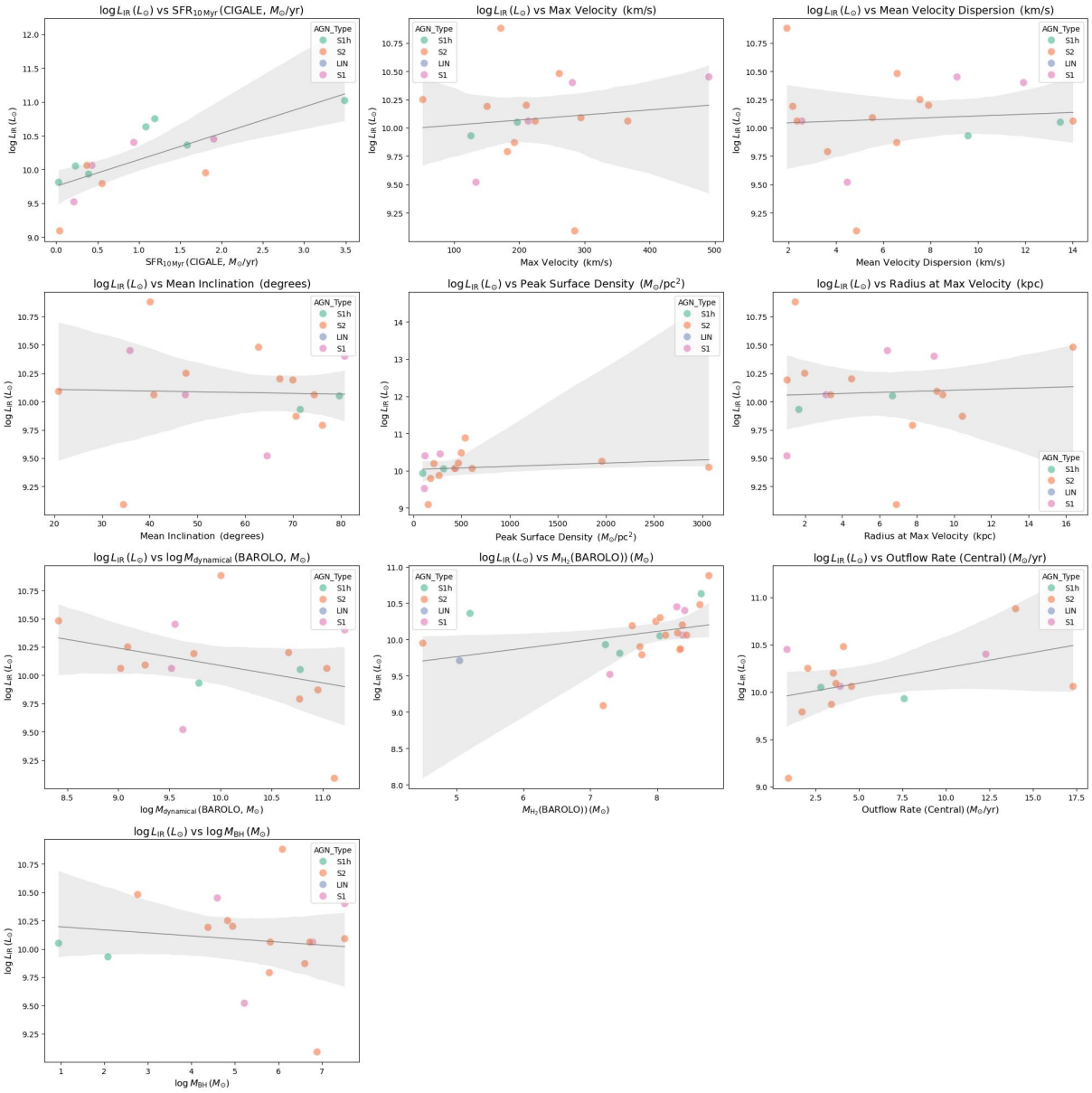

FIGURE G.14 – Scatter plot of exploratory data analysis for scatter Log L IR part 2

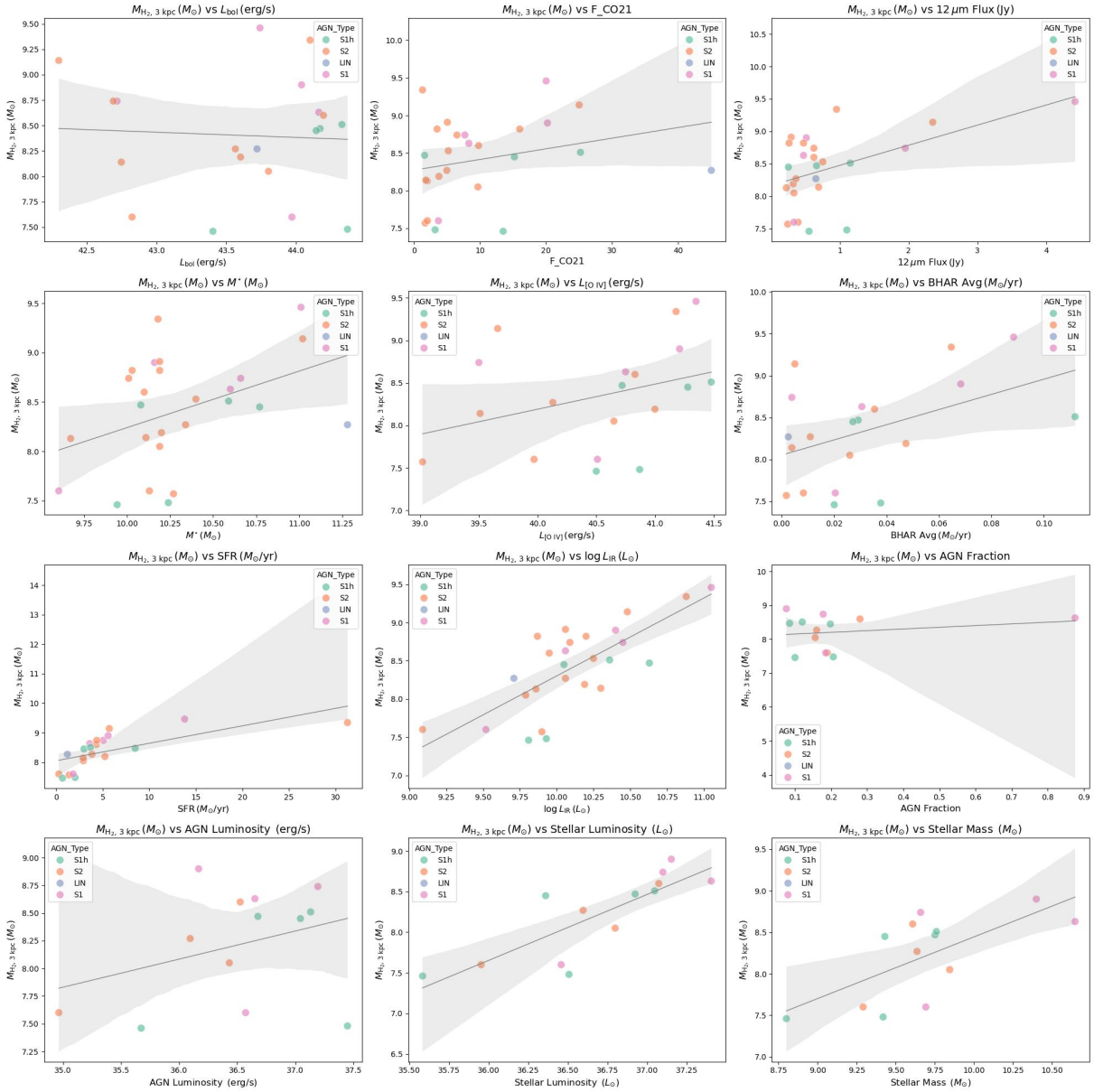

FIGURE G.15 – Scatter plot of exploratory data analysis for scatter Log MH2 3kpc part 1

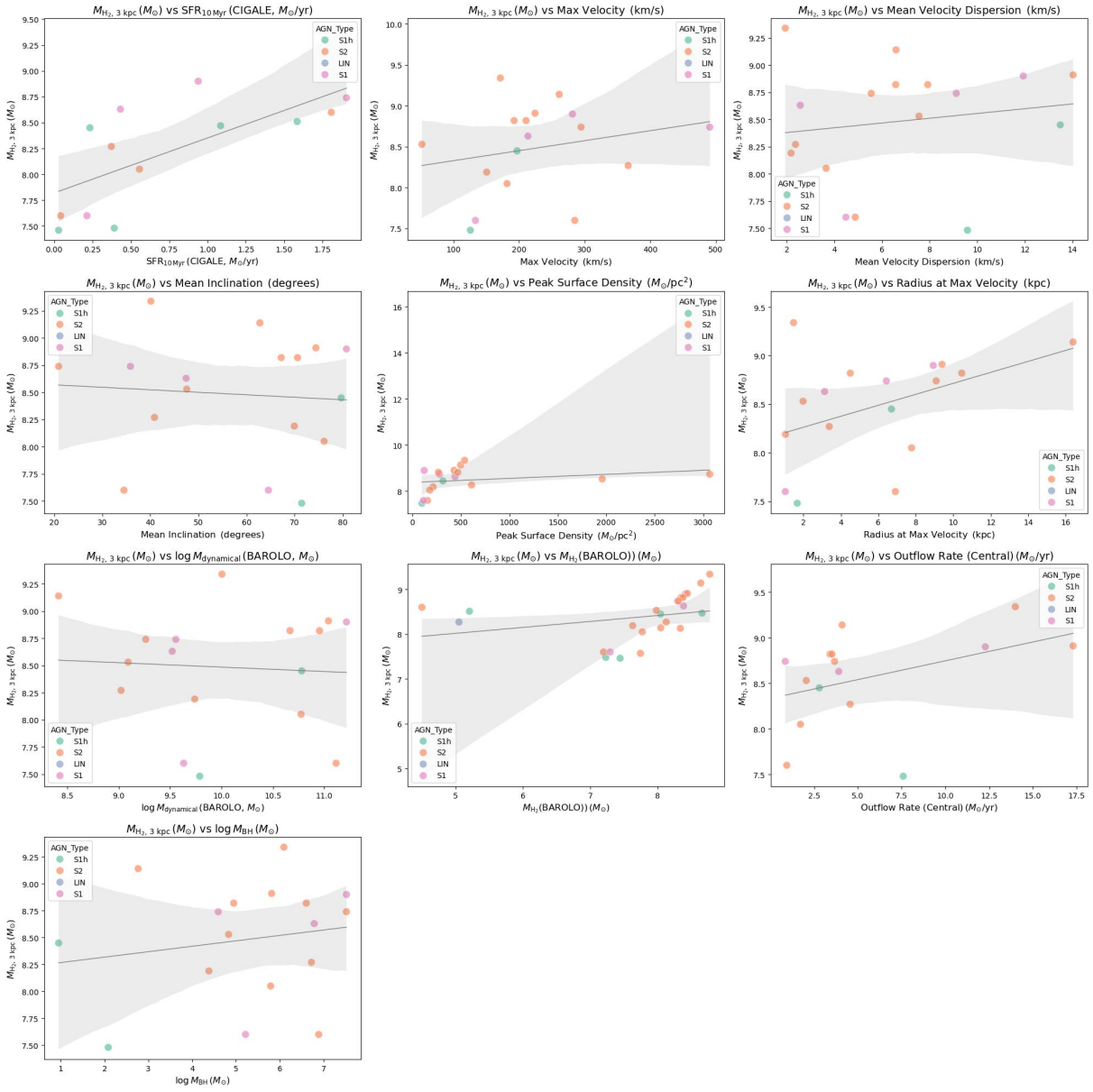

FIGURE G.16 – Scatter plot of exploratory data analysis for scatter Log MH2 3kpc part 2

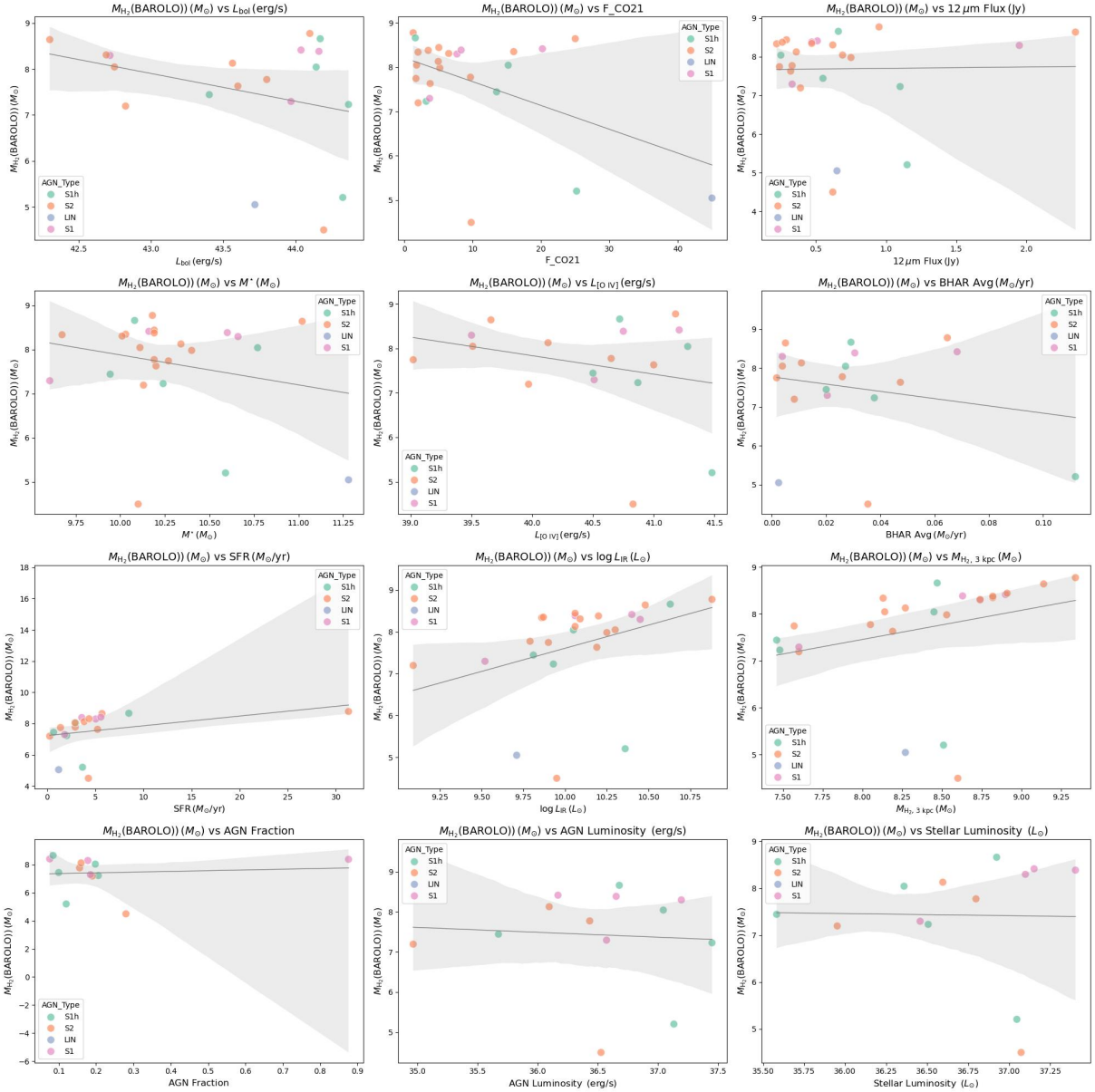

FIGURE G.17 – Scatter plot of exploratory data analysis for scatter M H2 Barolo avg part 1

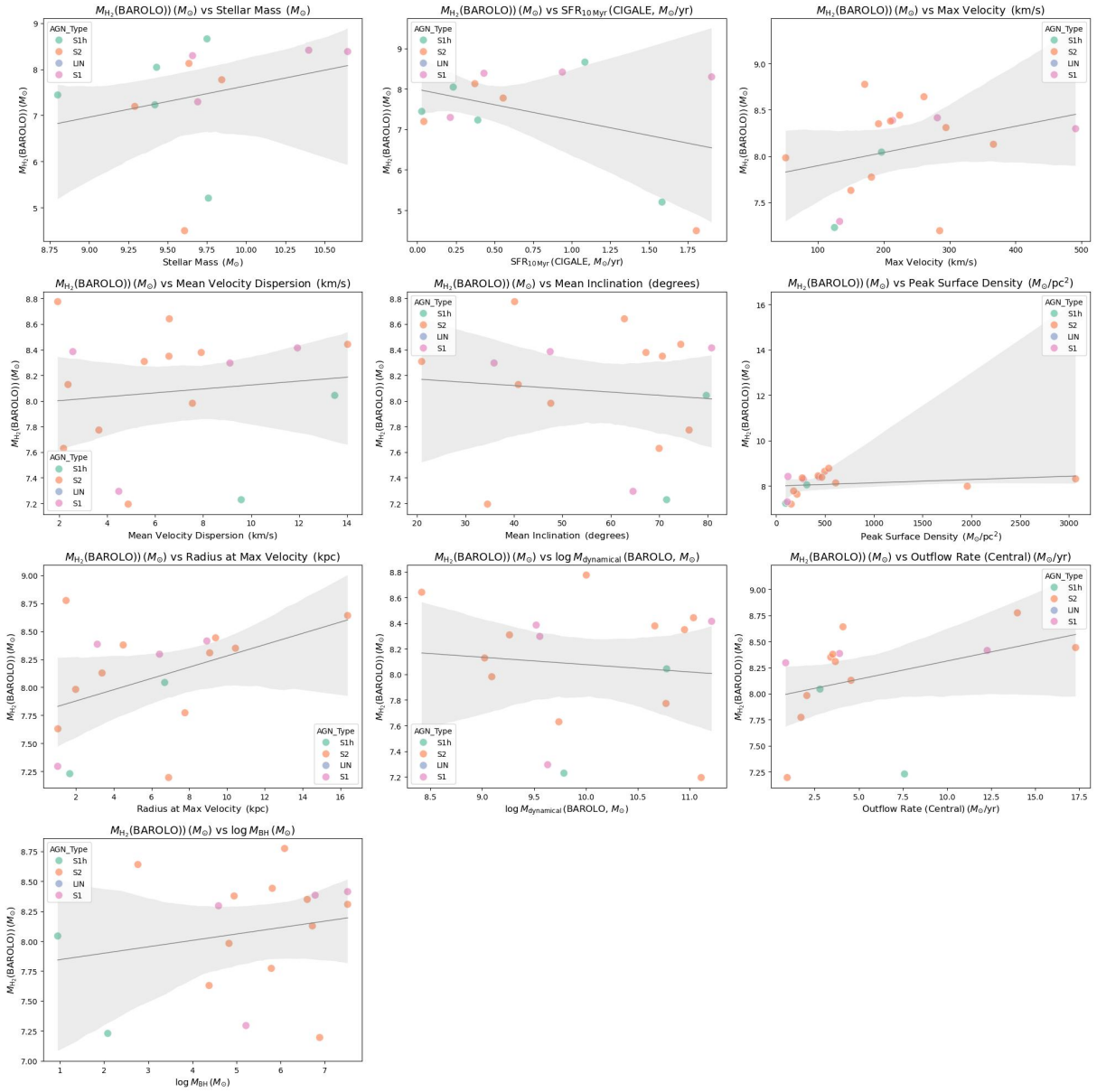

FIGURE G.18 – Scatter plot of exploratory data analysis for scatter M H2 Barolo avg part 2

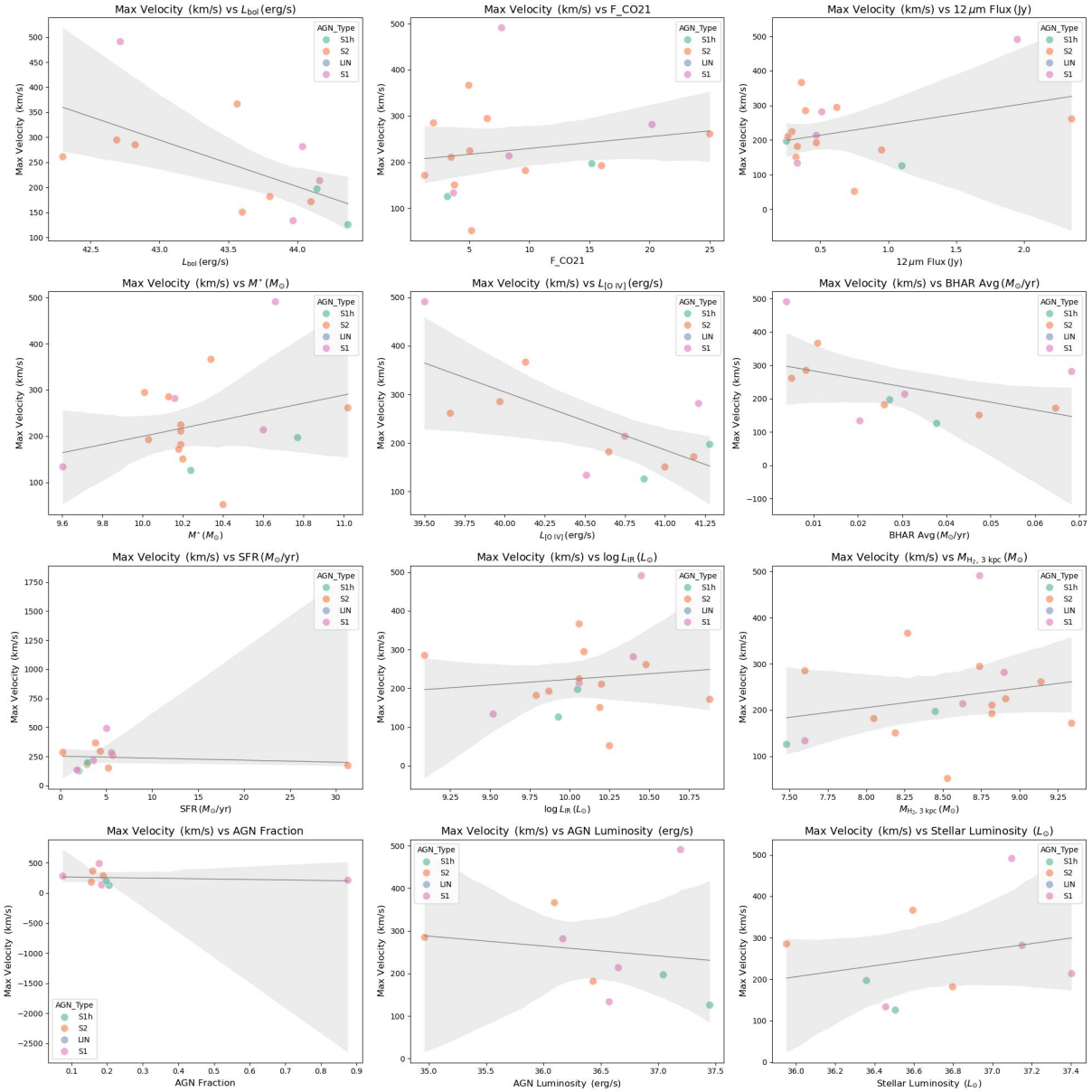

FIGURE G.19 – Scatter plot of exploratory data analysis for scatter Max Velocity BAROLO part 1

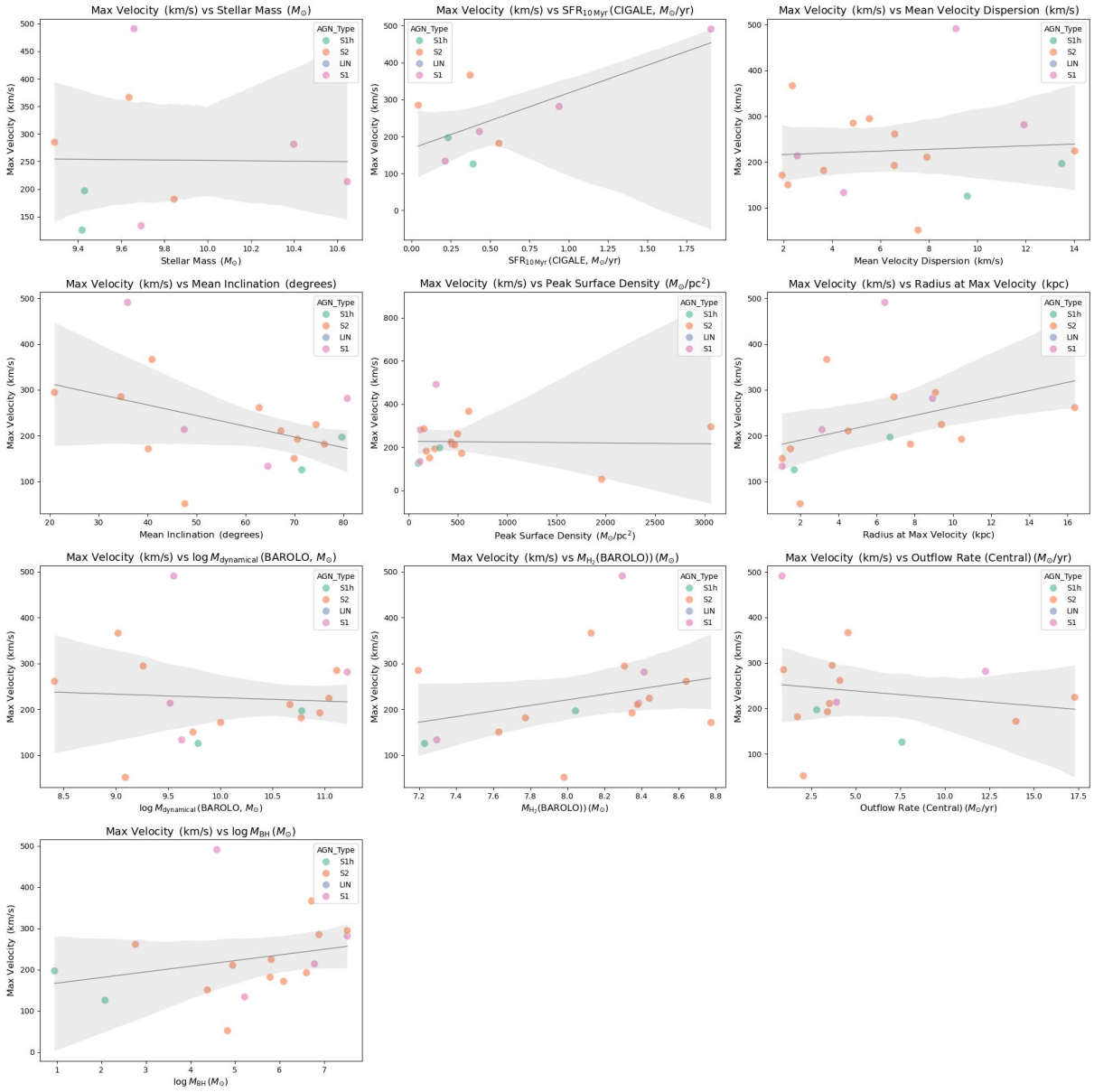

FIGURE G.20 – Scatter plot of exploratory data analysis for scatter Max Velocity BAROLO part 2

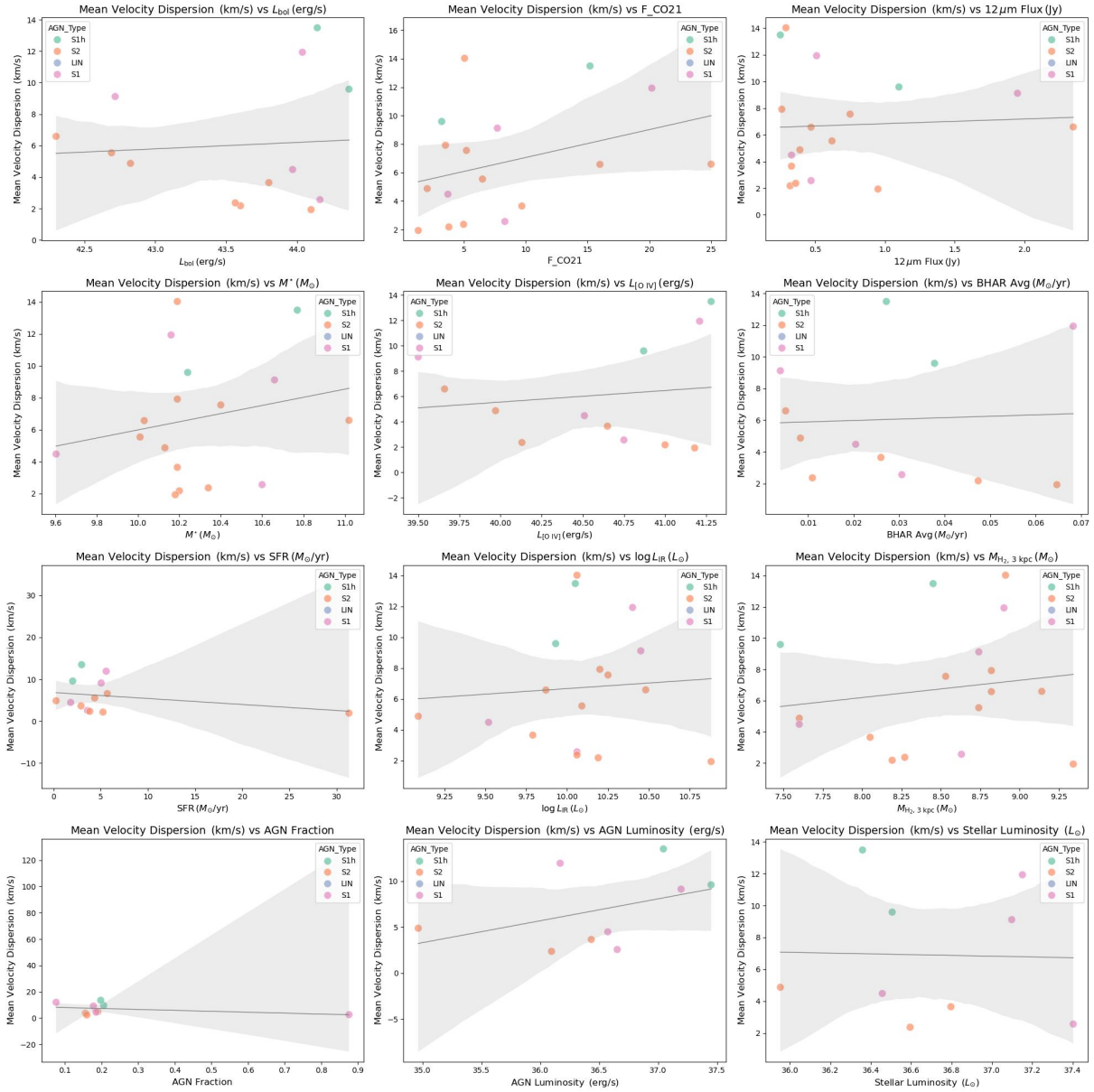

FIGURE G.21 – Scatter plot of exploratory data analysis for scatter Mean Dispersion BAROLO part 1

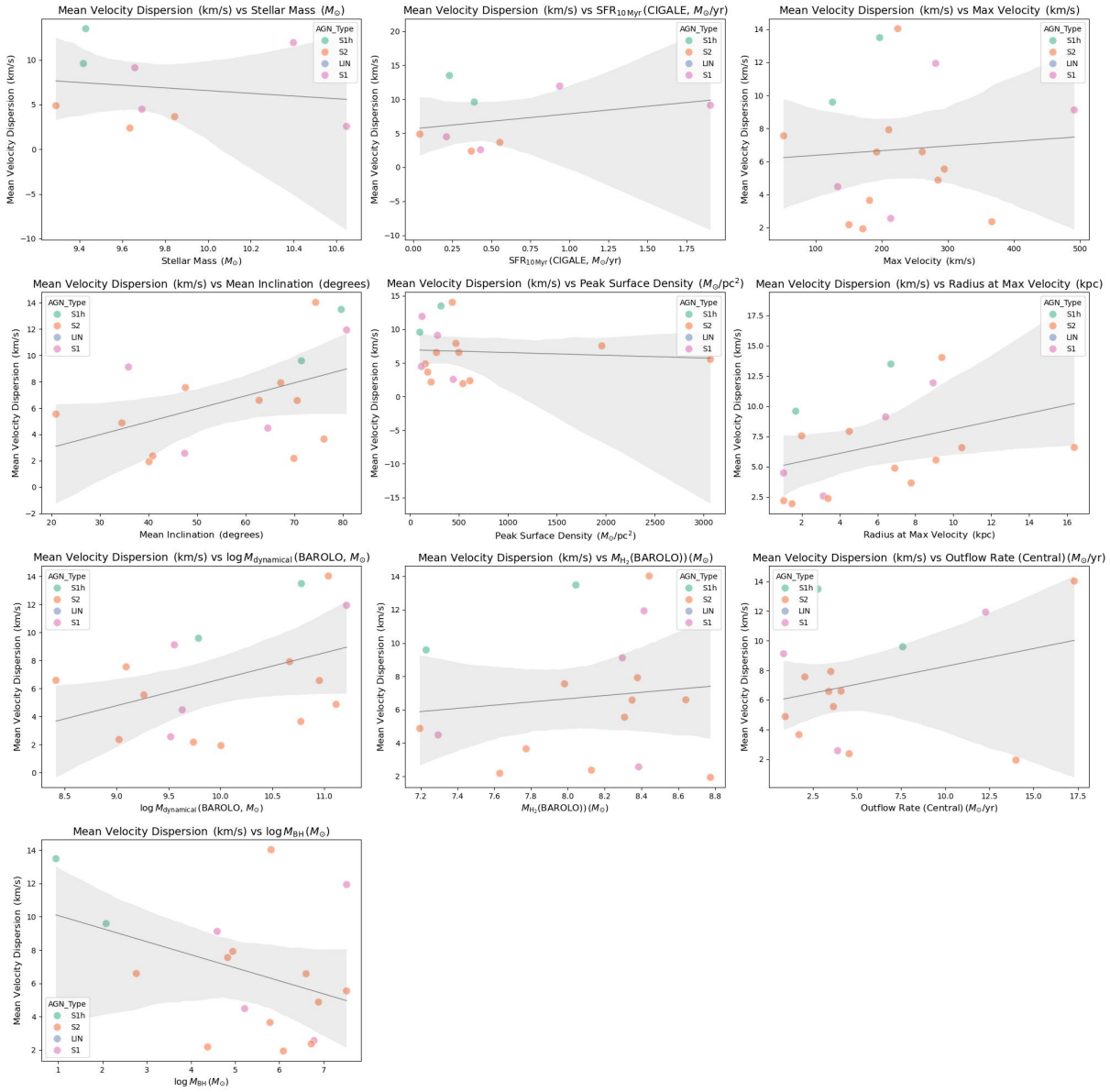

FIGURE G.22 – Scatter plot of exploratory data analysis for scatter Mean Dispersion BAROLO part 2

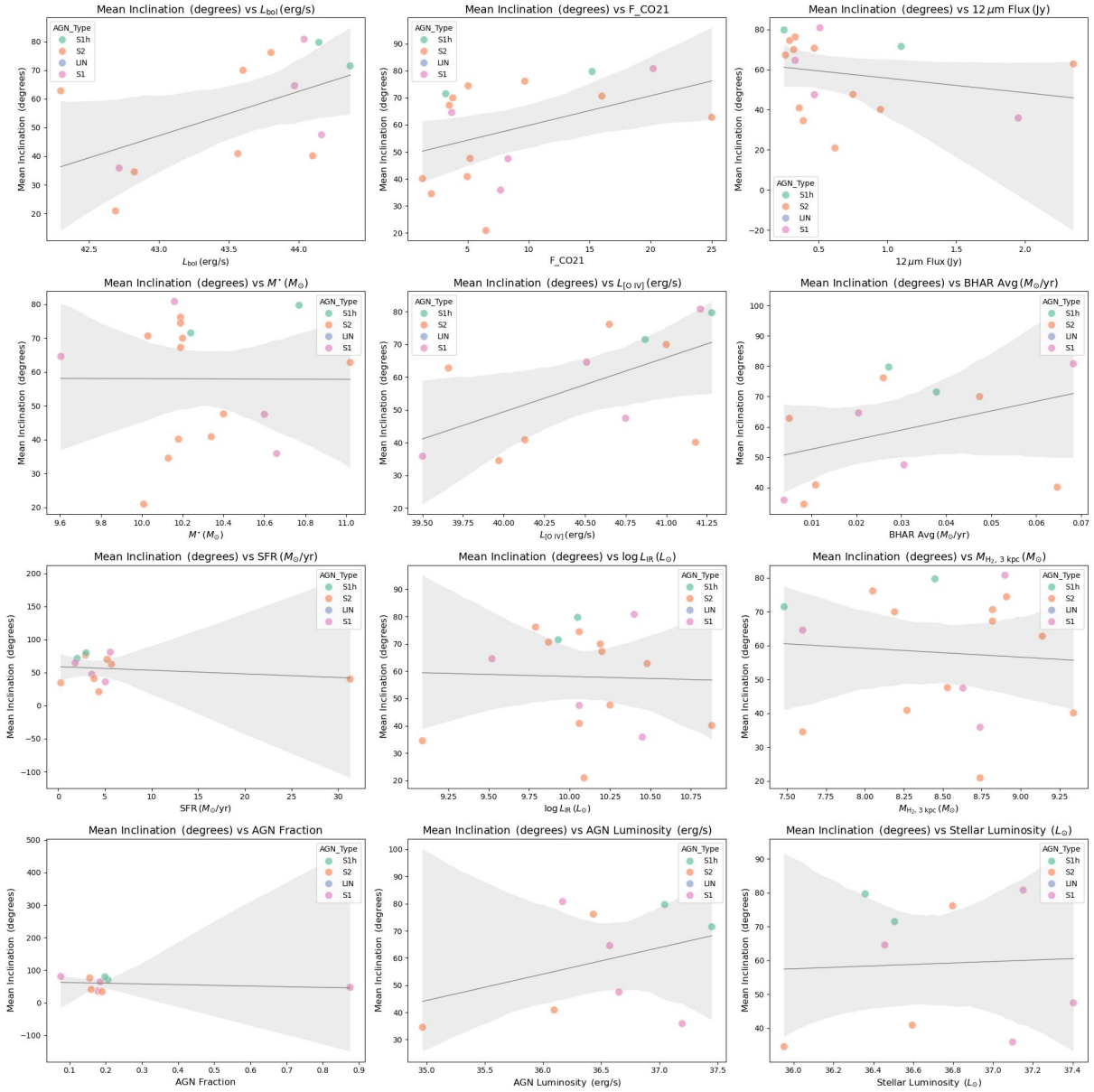

FIGURE G.23 – Scatter plot of exploratory data analysis for scatter Mean Inclination BAROLO part 1

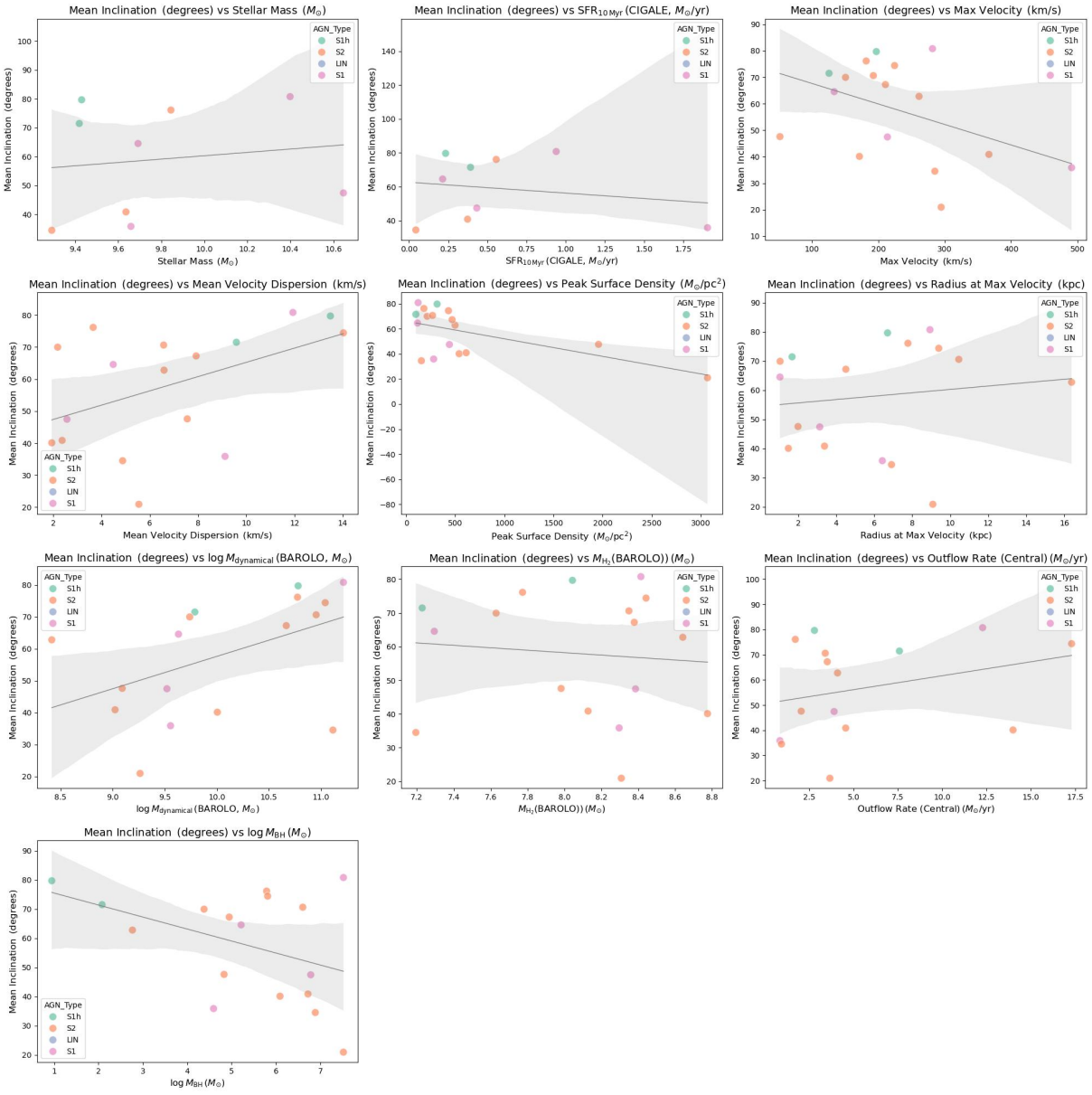

FIGURE G.24 – Scatter plot of exploratory data analysis for scatter Mean Inclination BAROLO part 2

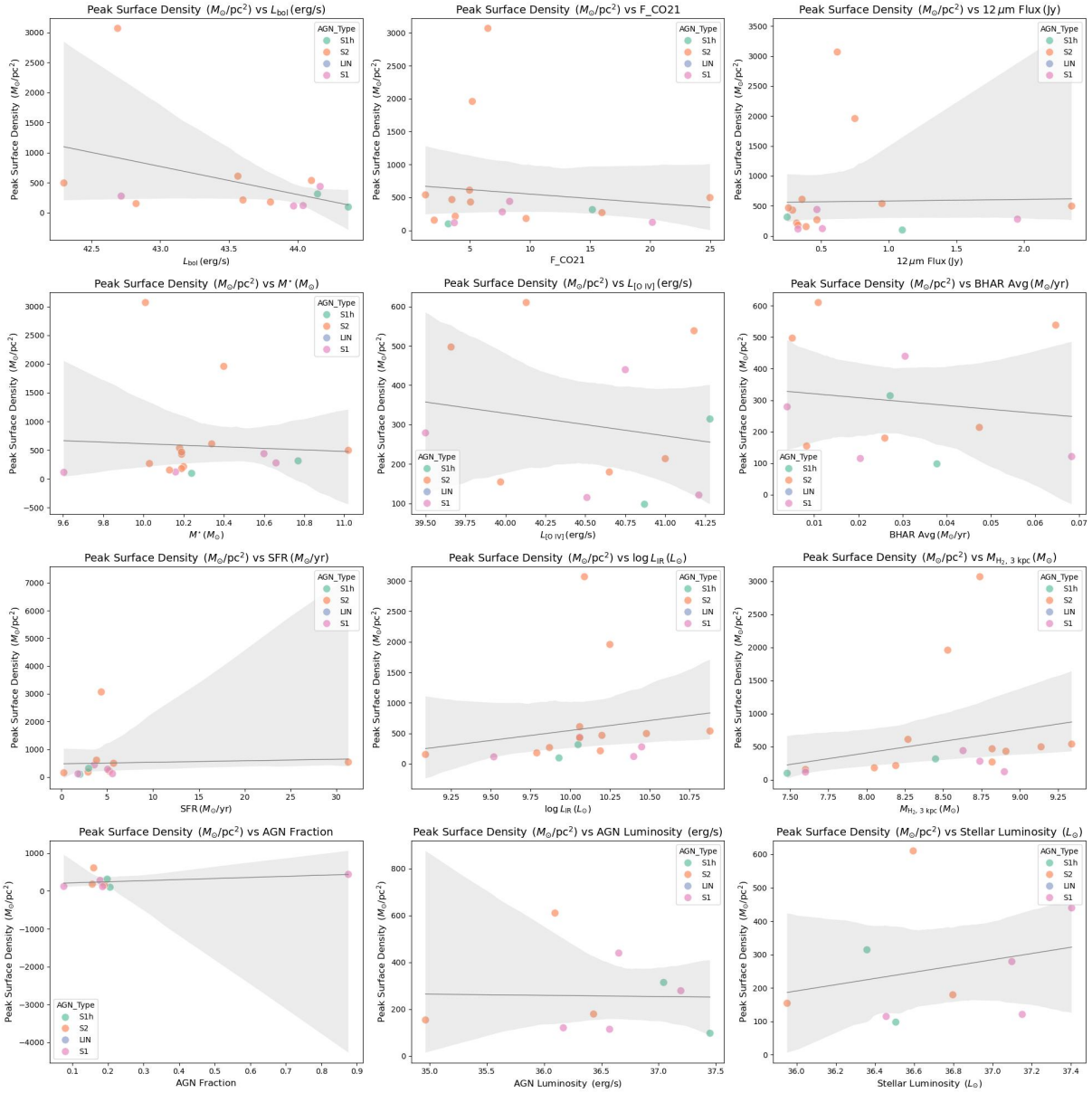

FIGURE G.25 – Scatter plot of exploratory data analysis for scatter Peak Surface Density BAROLO part 1

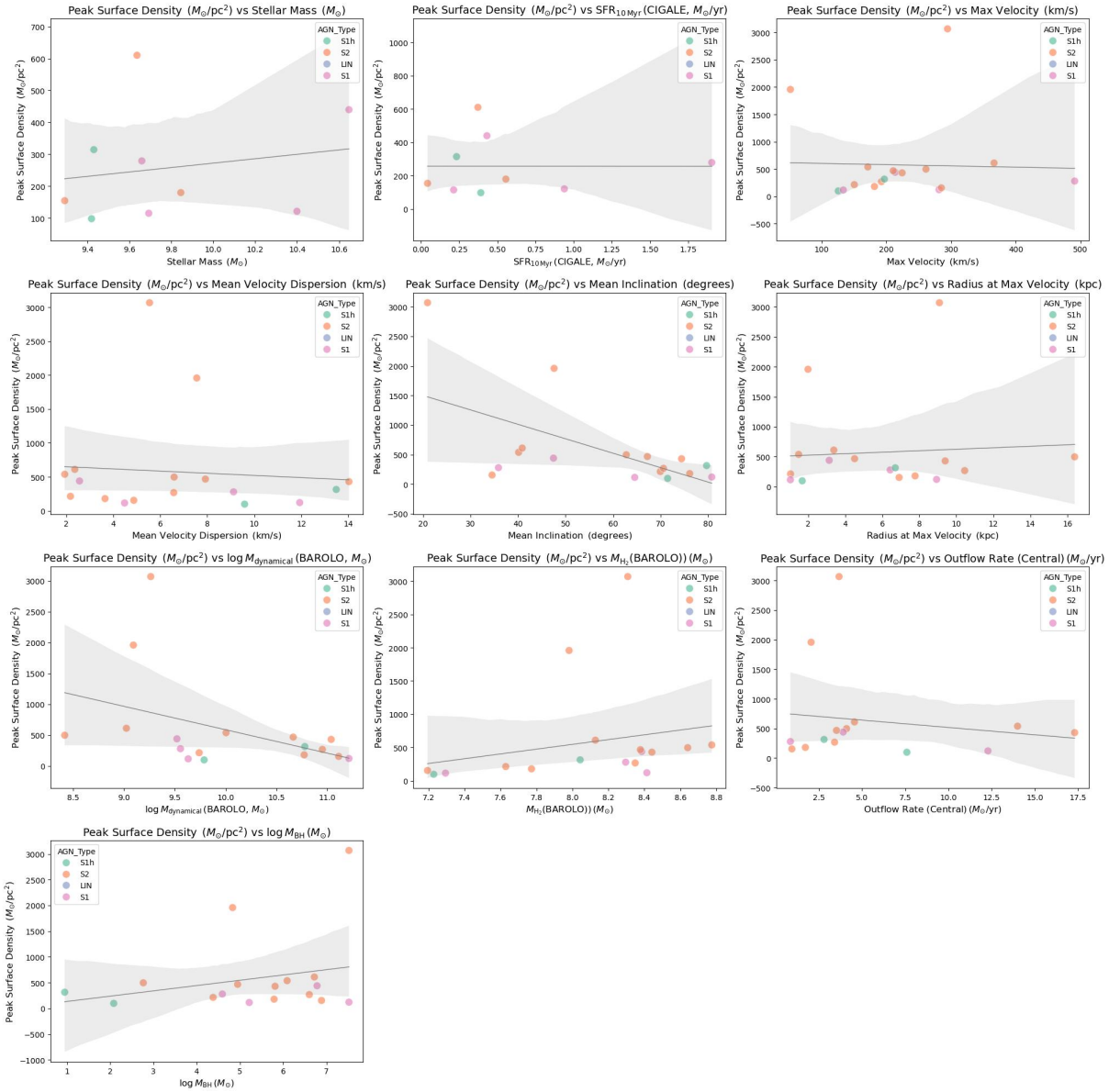

FIGURE G.26 – Scatter plot of exploratory data analysis for scatter Peak Surface Density BAROLO part 2

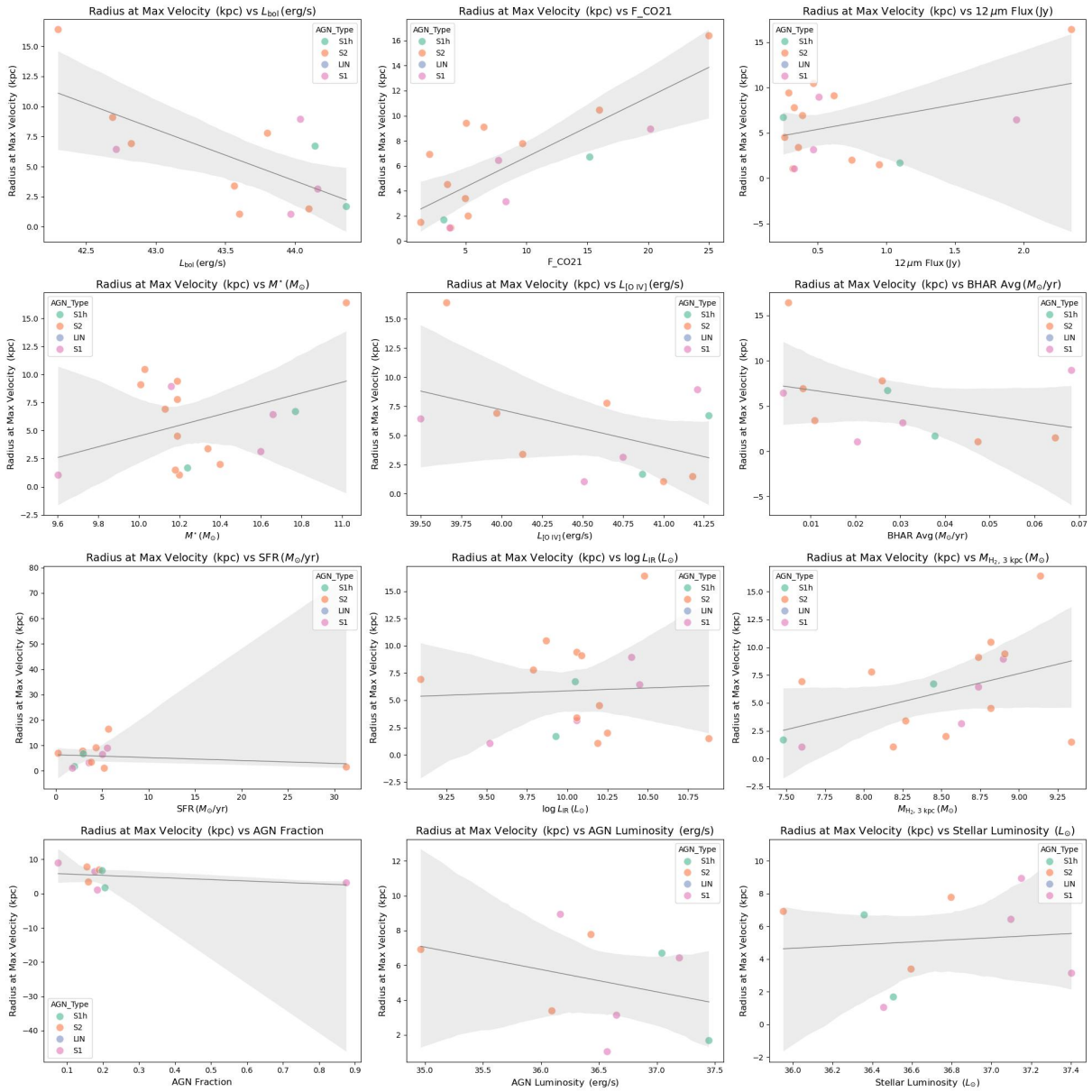

FIGURE G.27 – Scatter plot of exploratory data analysis for scatter Radius Max Velocity BAROLO part 1

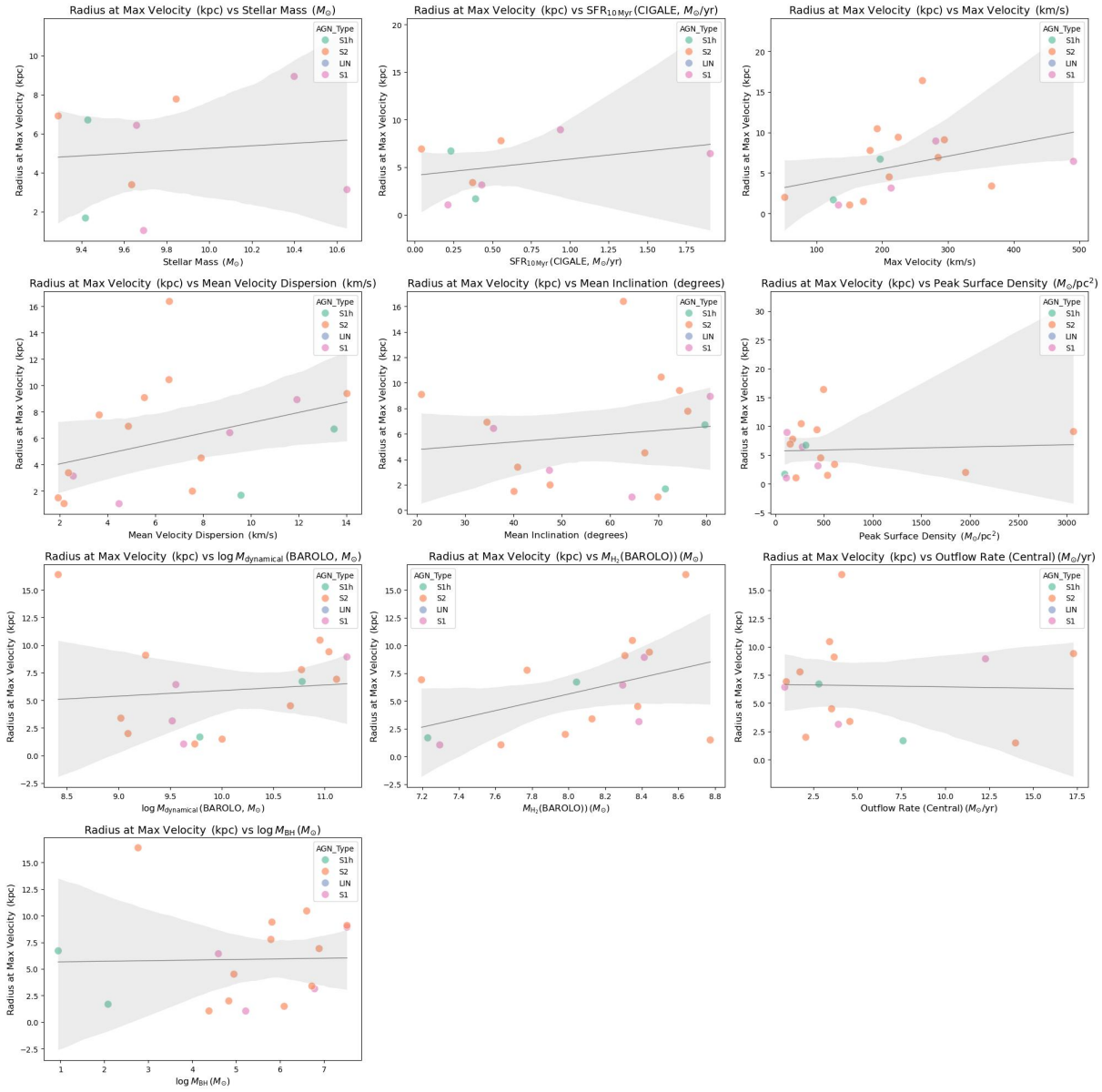

FIGURE G.28 – Scatter plot of exploratory data analysis for scatter Radius Max Velocity BAROLO part 2

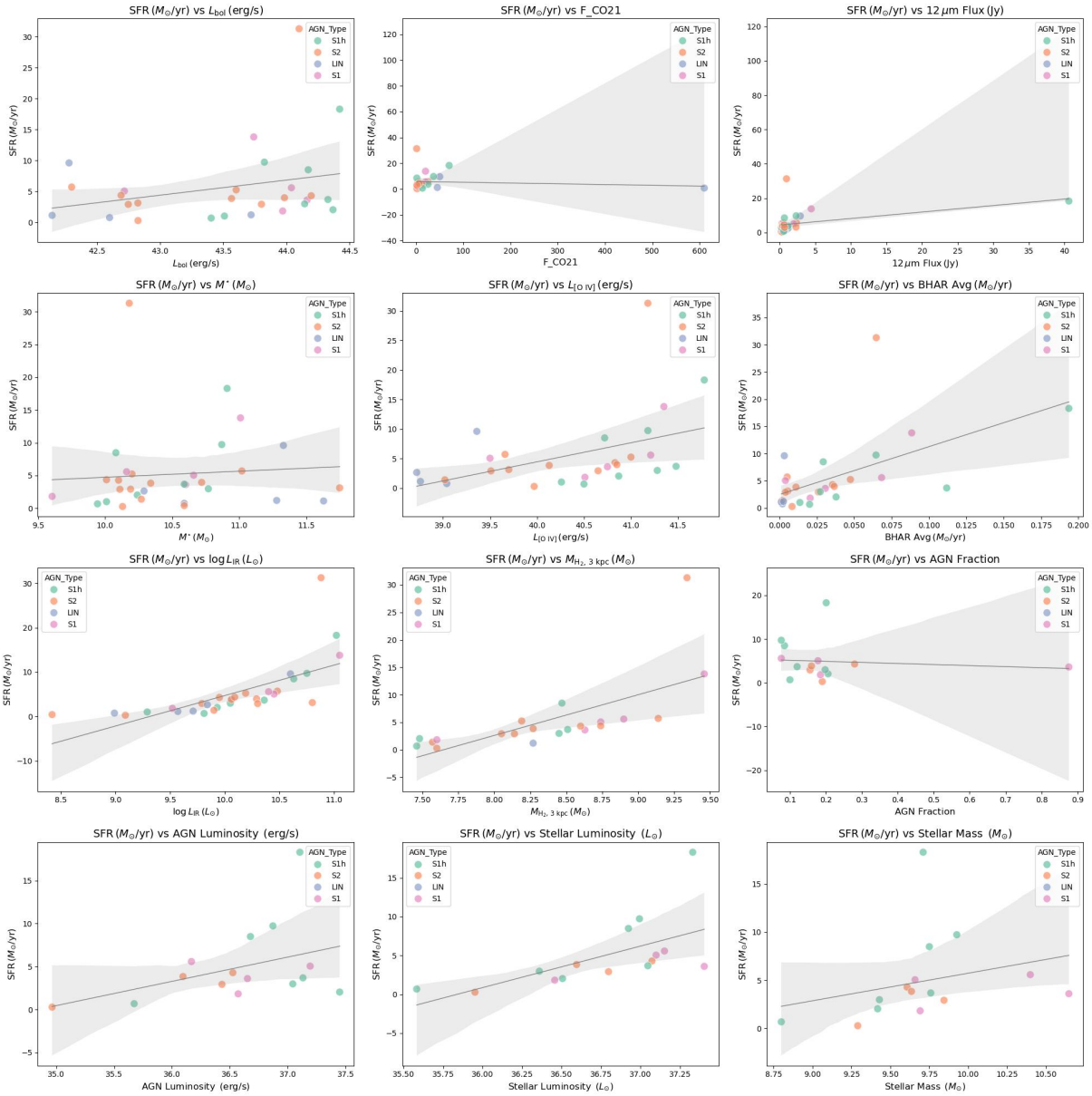

FIGURE G.29 – Scatter plot of exploratory data analysis for scatter SFR part 1

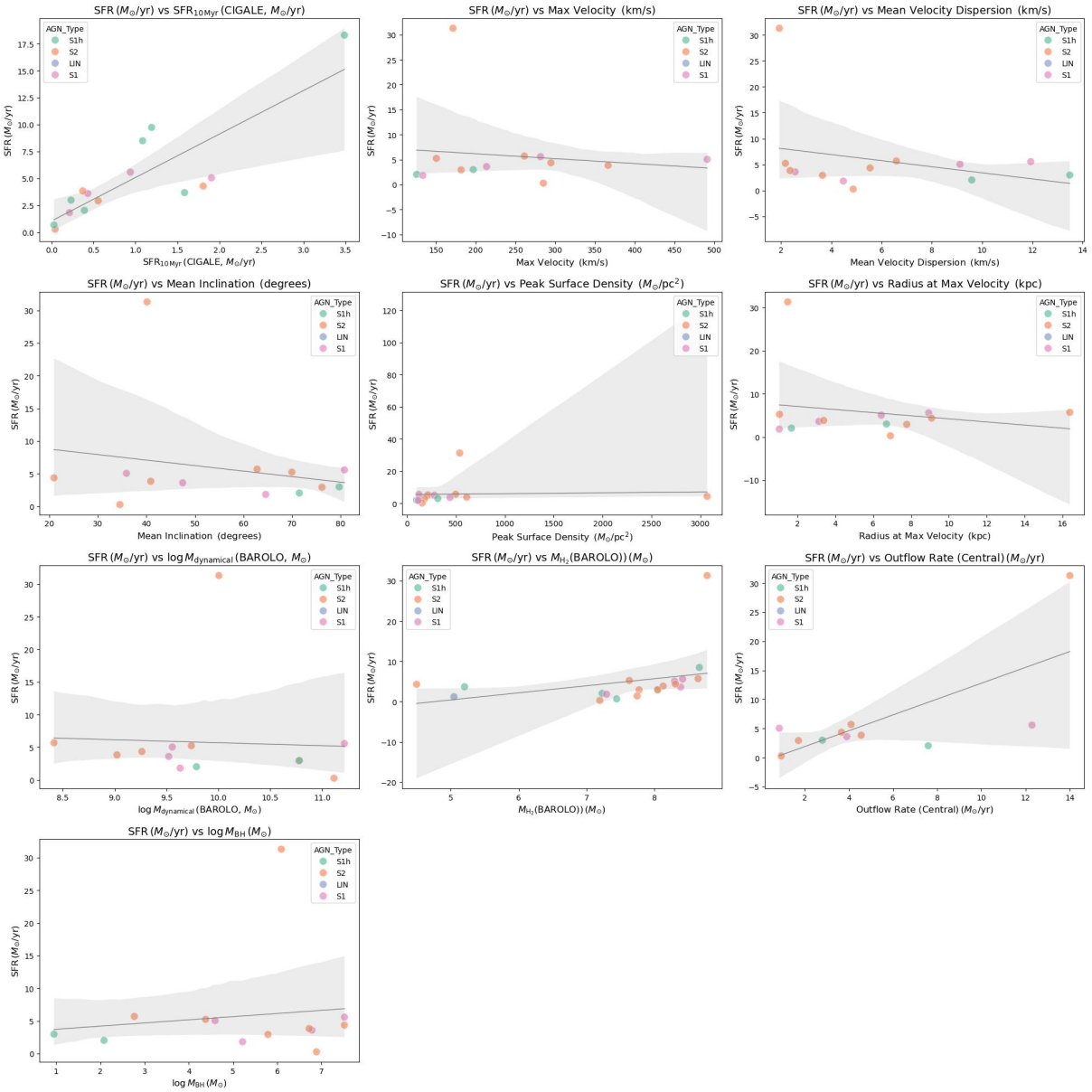

FIGURE G.30 – Scatter plot of exploratory data analysis for scatter SFR part 2

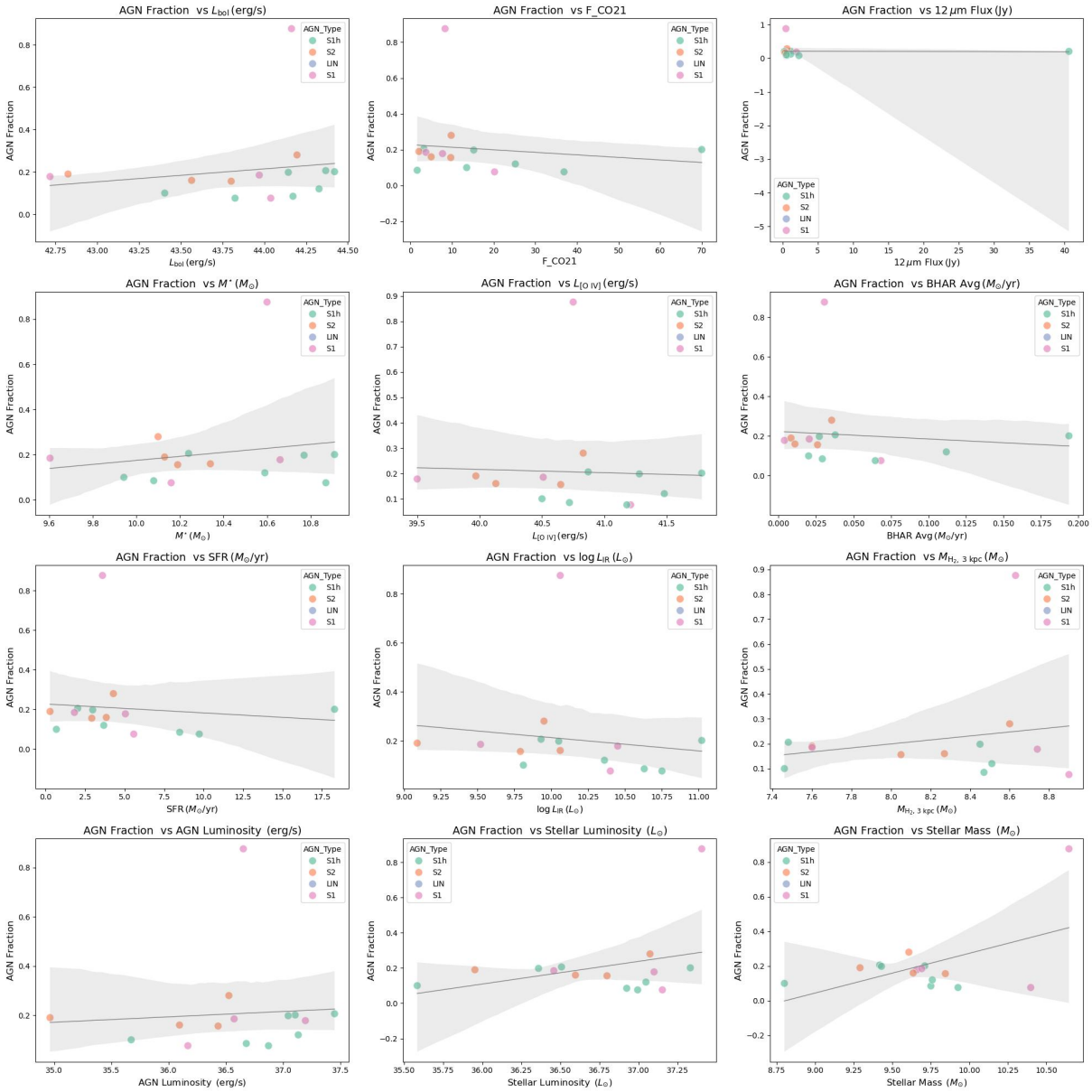

FIGURE G.31 – Scatter plot of exploratory data analysis for scatter agn.fracAGN CIGALE part 1

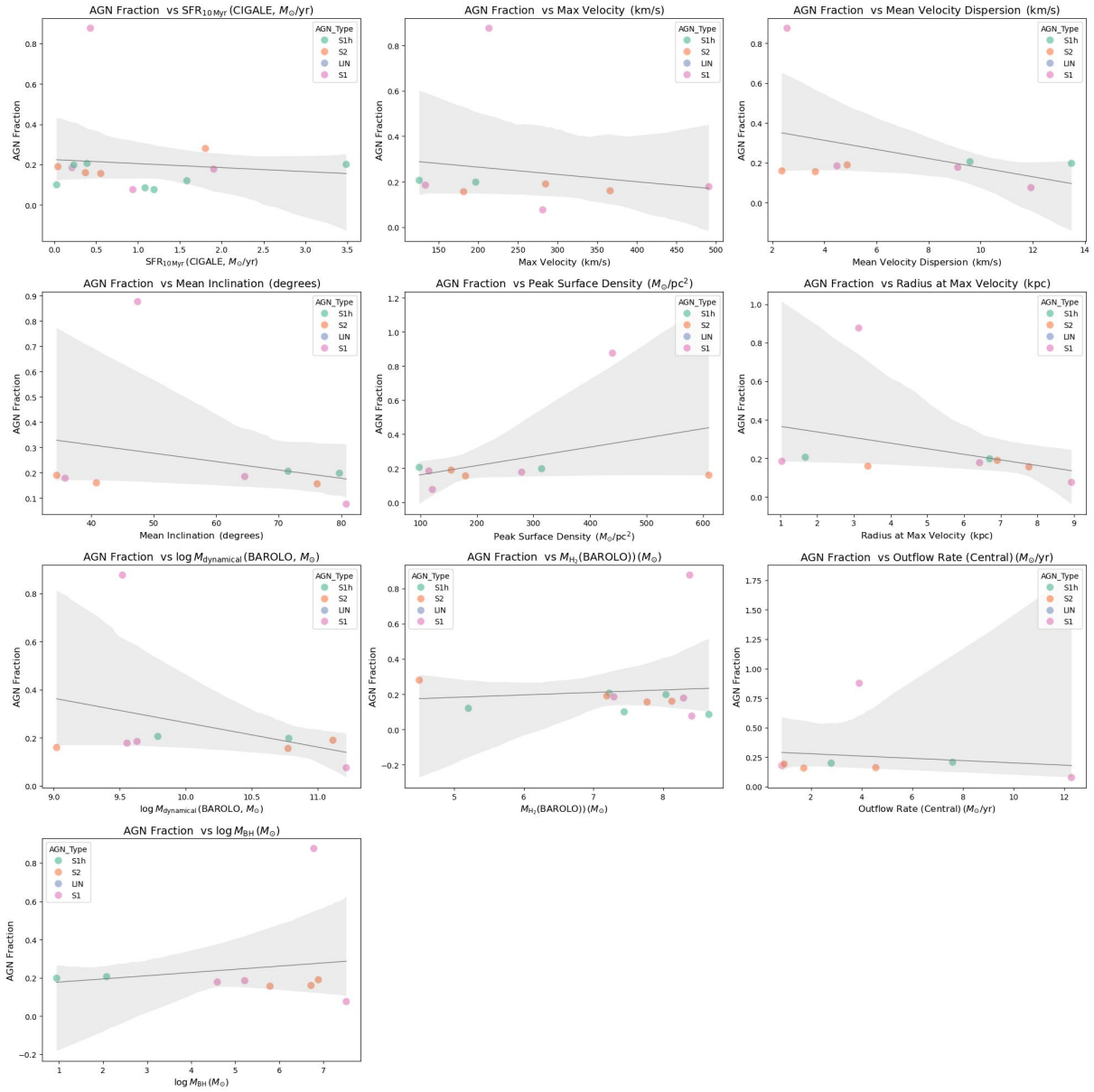

FIGURE G.32 – Scatter plot of exploratory data analysis for scatter agn.fracAGN CIGALE part 2

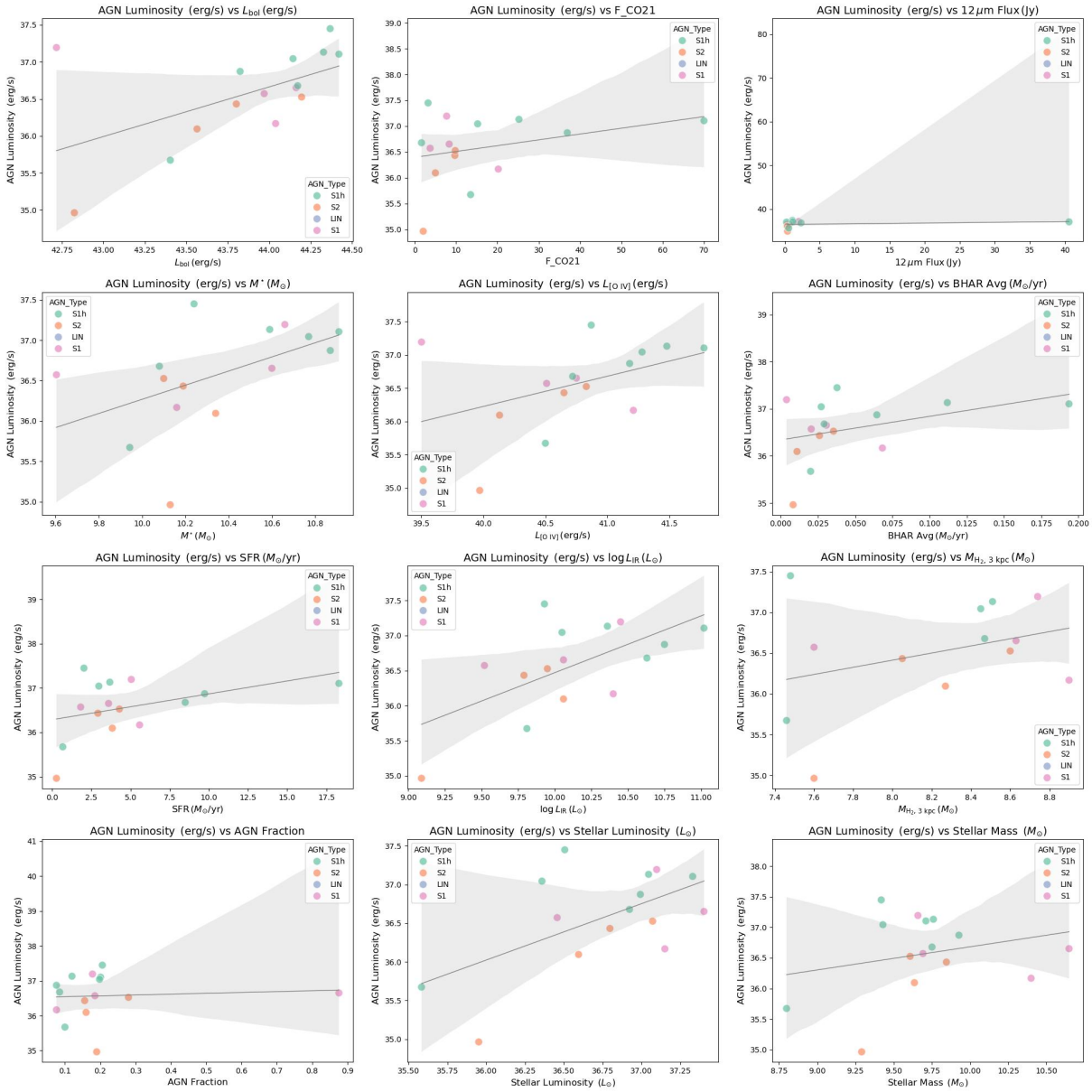

FIGURE G.33 – Scatter plot of exploratory data analysis for scatter agn.luminosity CIGALE part 1

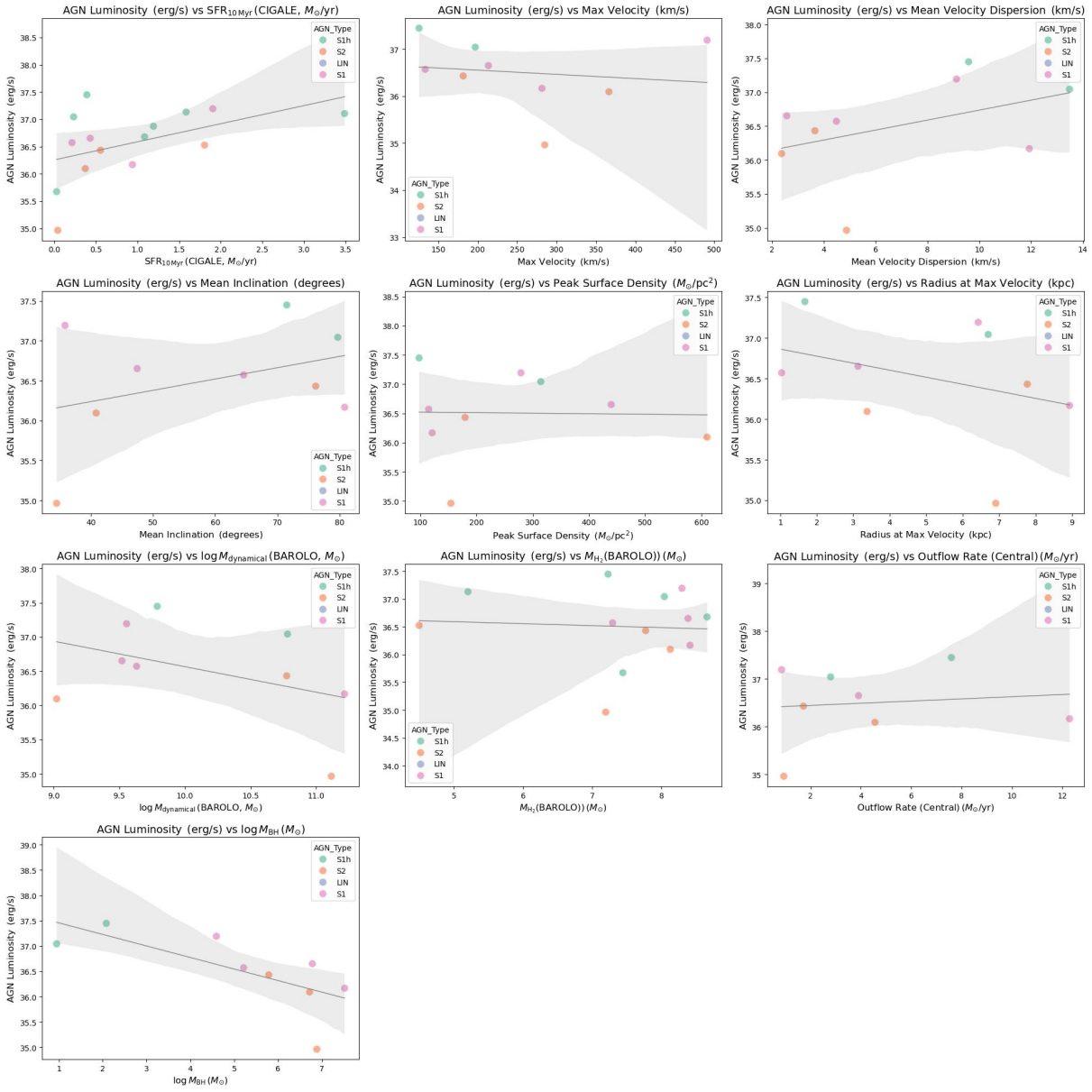

FIGURE G.34 – Scatter plot of exploratory data analysis for scatter agn.luminosity CIGALE part 2

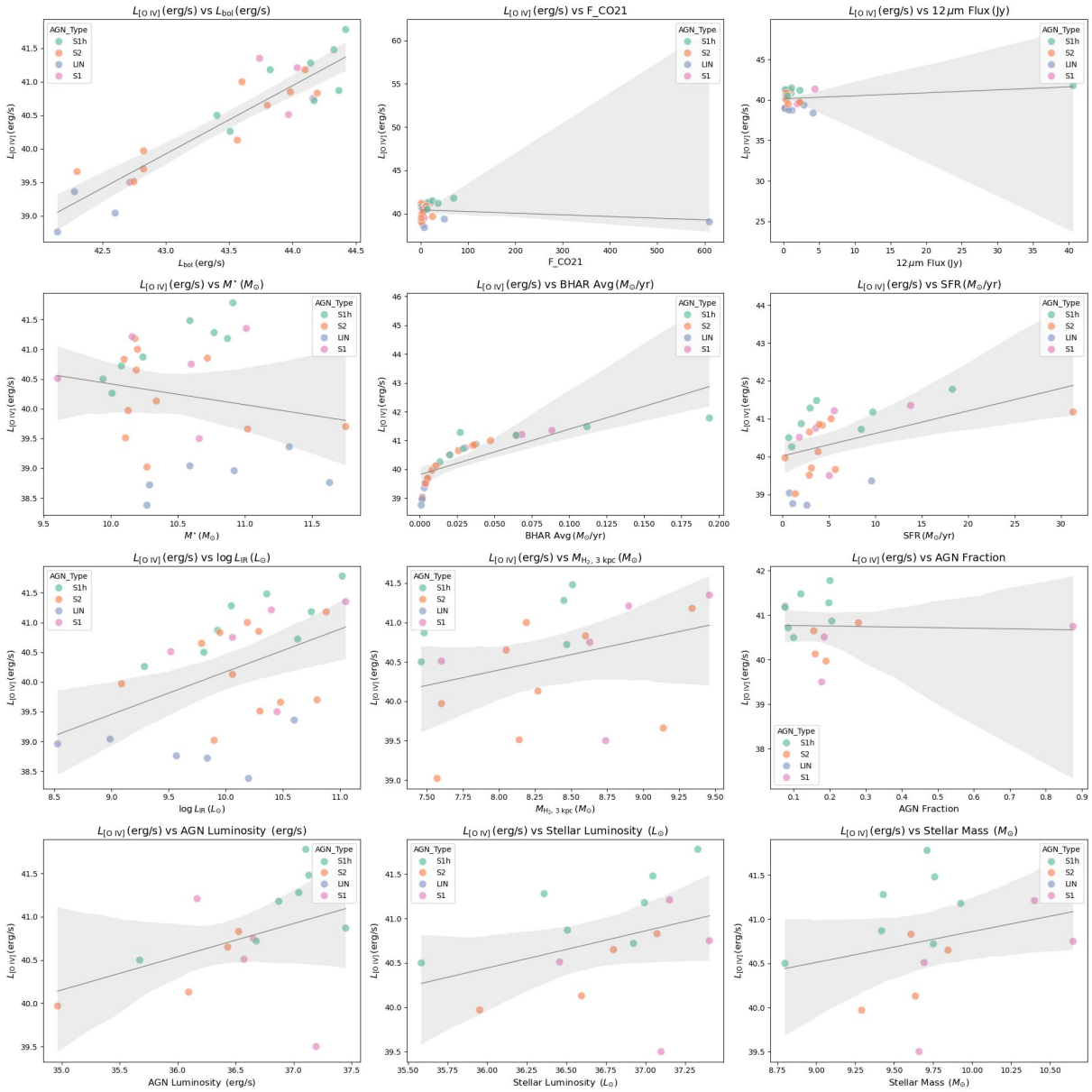

FIGURE G.35 – Scatter plot of exploratory data analysis for scatter log L OIV part 1

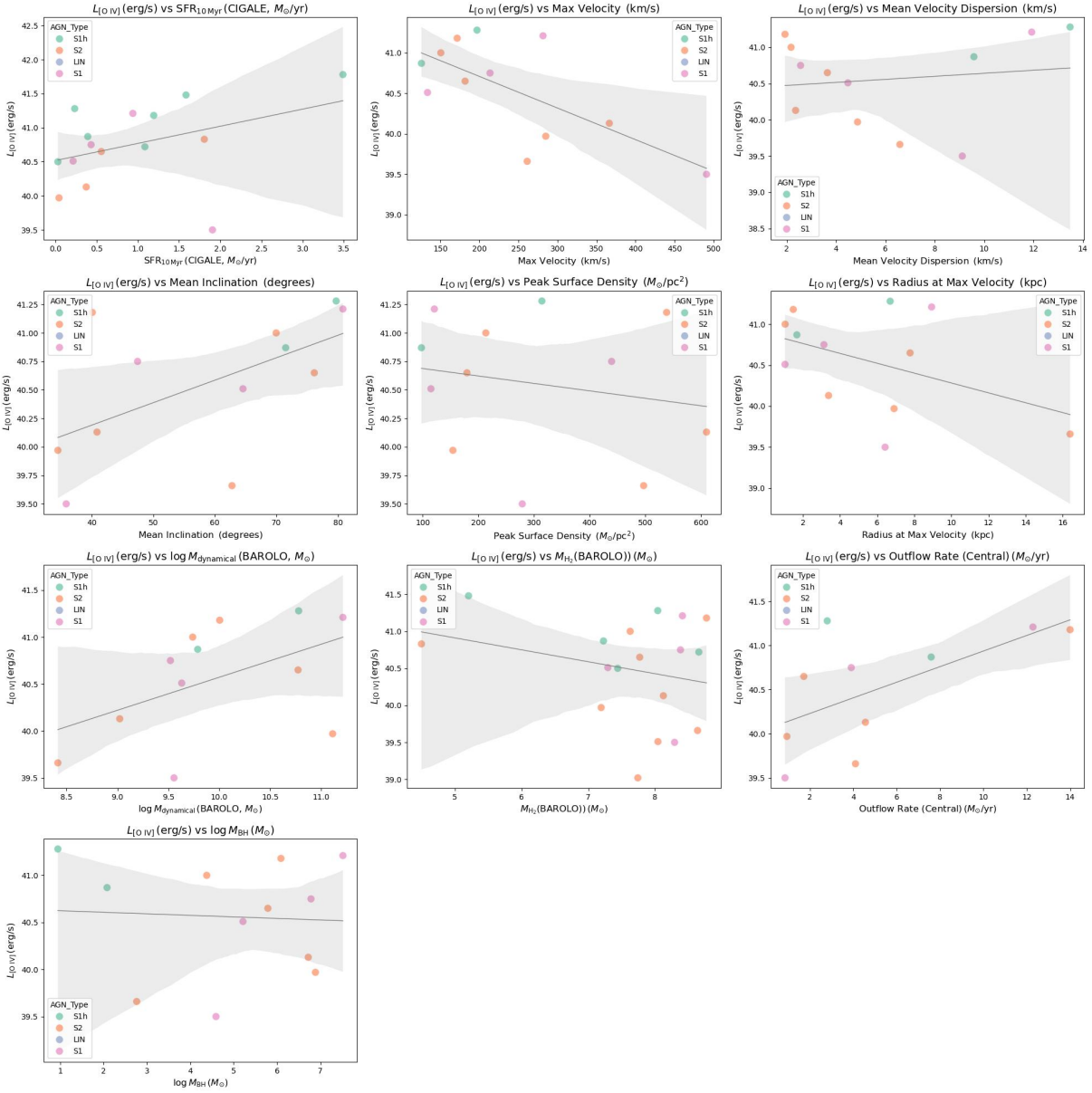

FIGURE G.36 – Scatter plot of exploratory data analysis for scatter log L OIV part 2

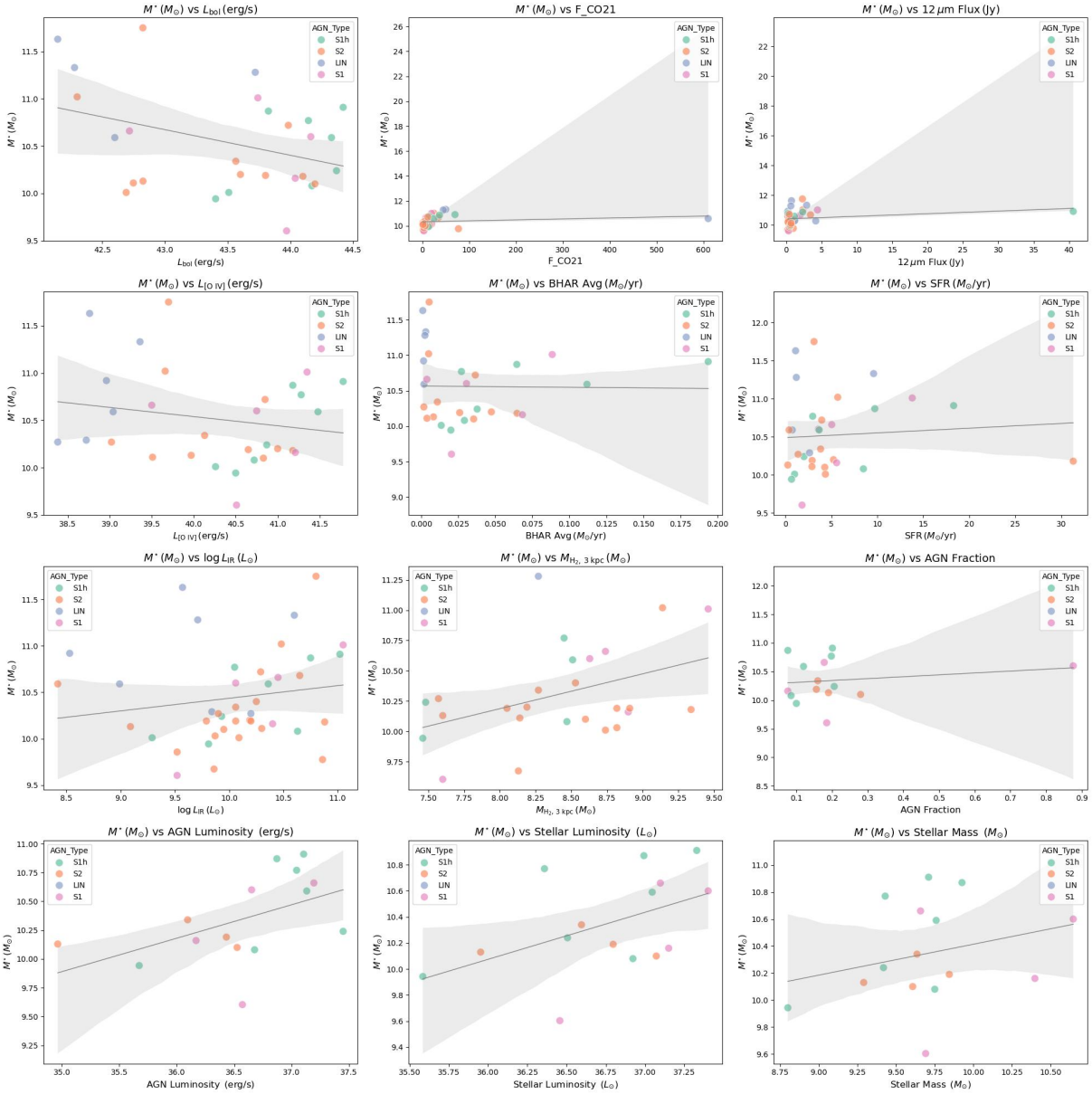

FIGURE G.37 – Scatter plot of exploratory data analysis for scatter log M star part 1

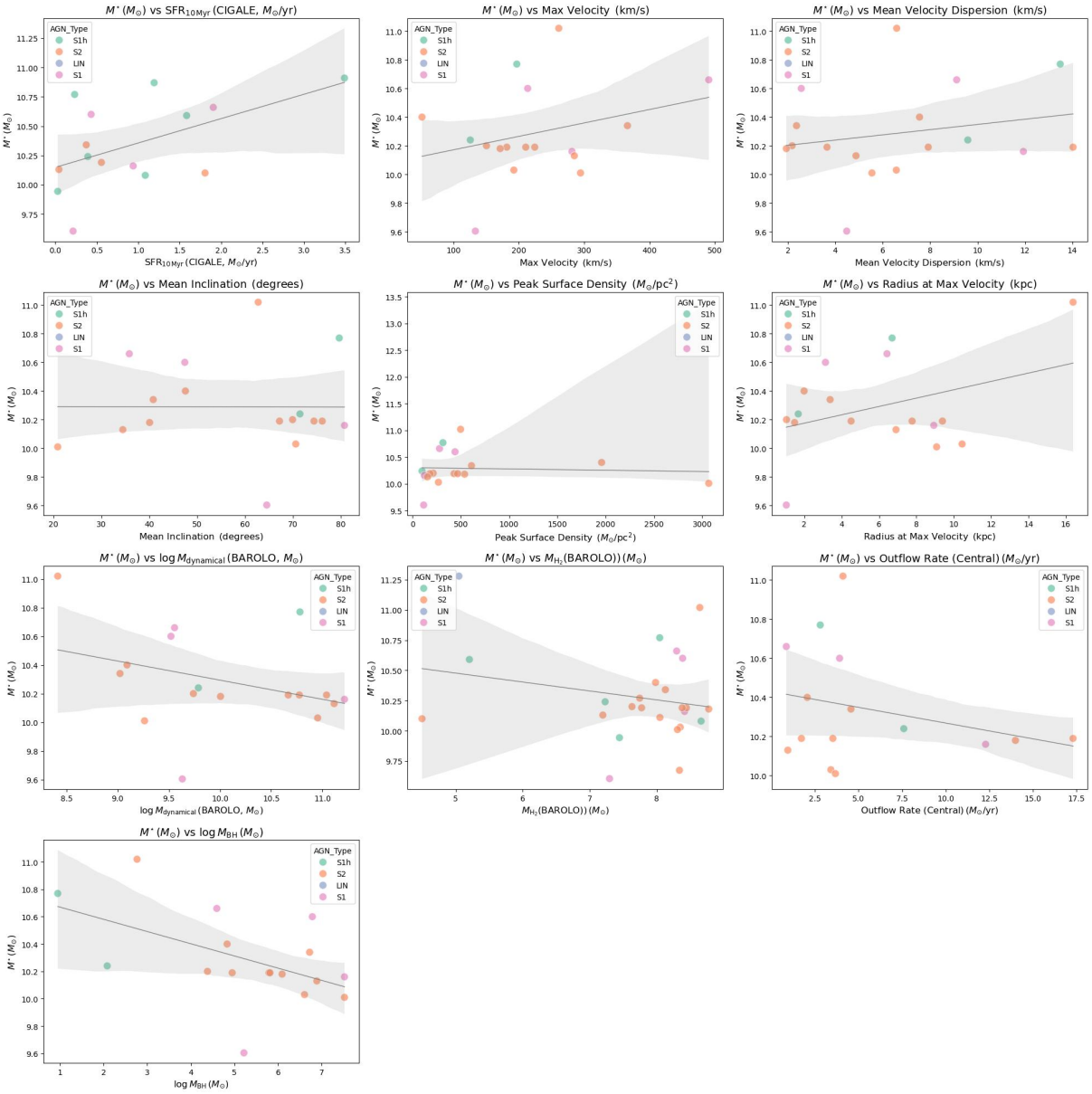

FIGURE G.38 – Scatter plot of exploratory data analysis for scatter log M star part 2

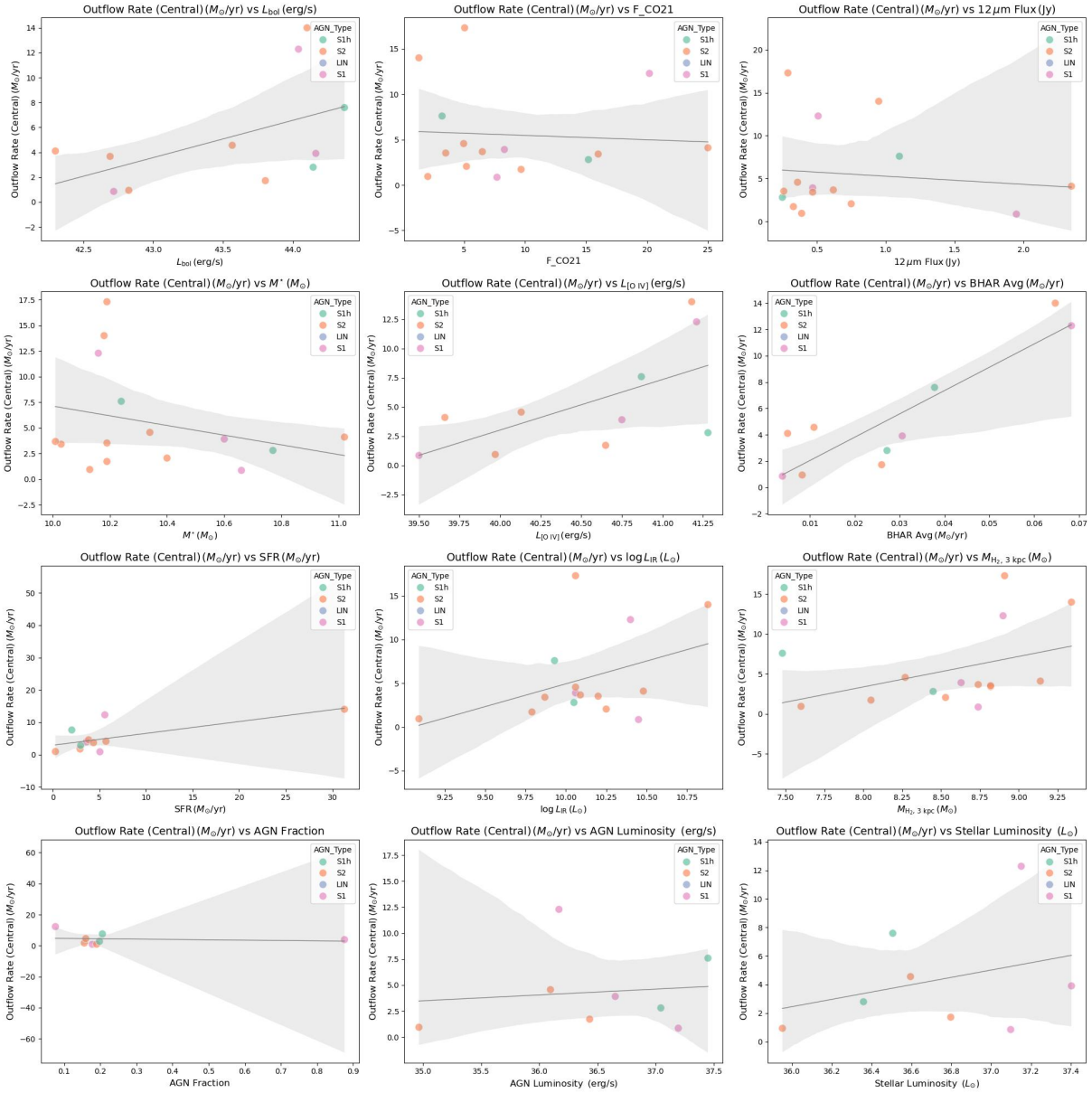

FIGURE G.39 – Scatter plot of exploratory data analysis for scatter outflow rate central part 1

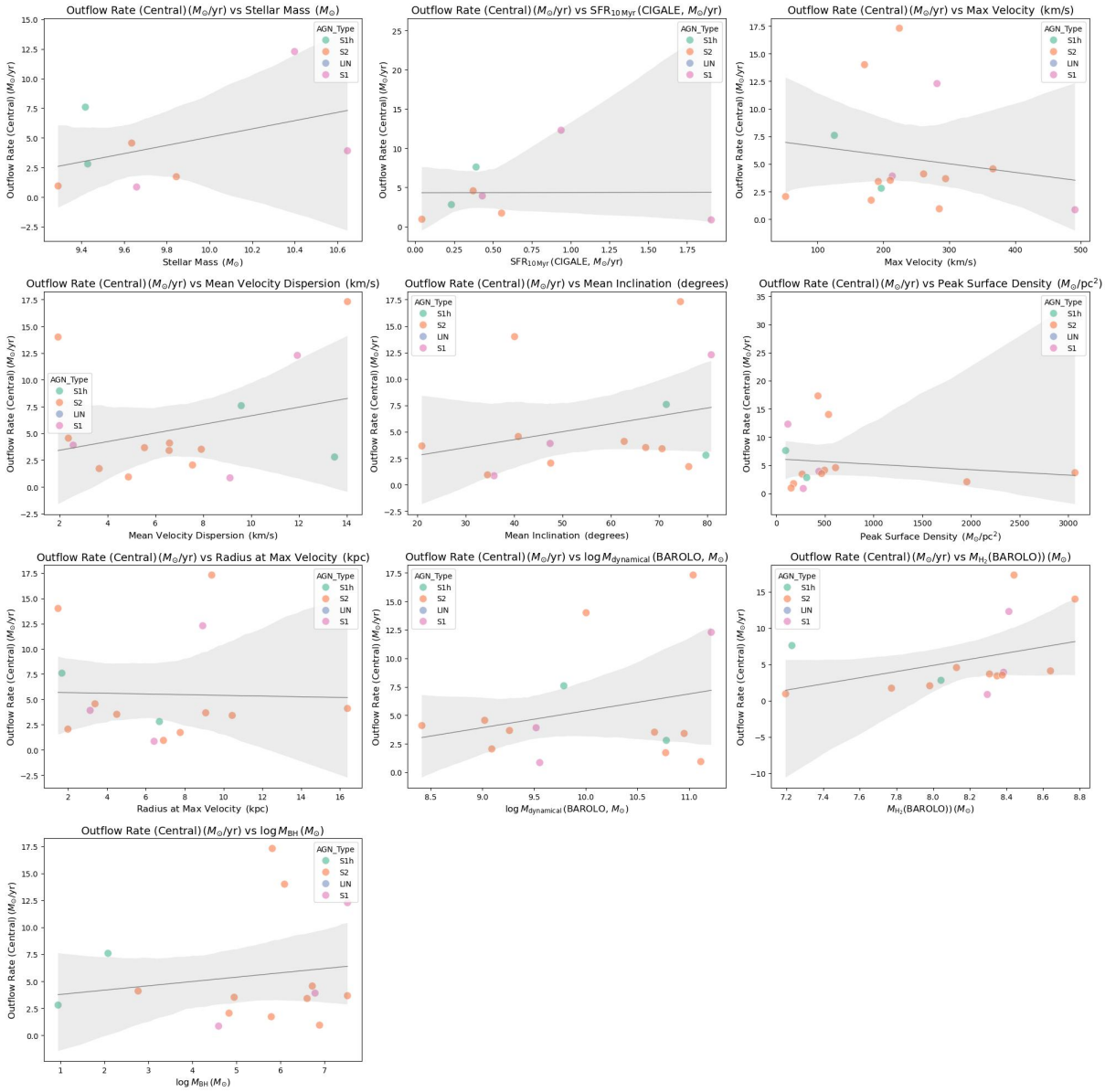

FIGURE G.40 – Scatter plot of exploratory data analysis for scatter outflow rate central part 2

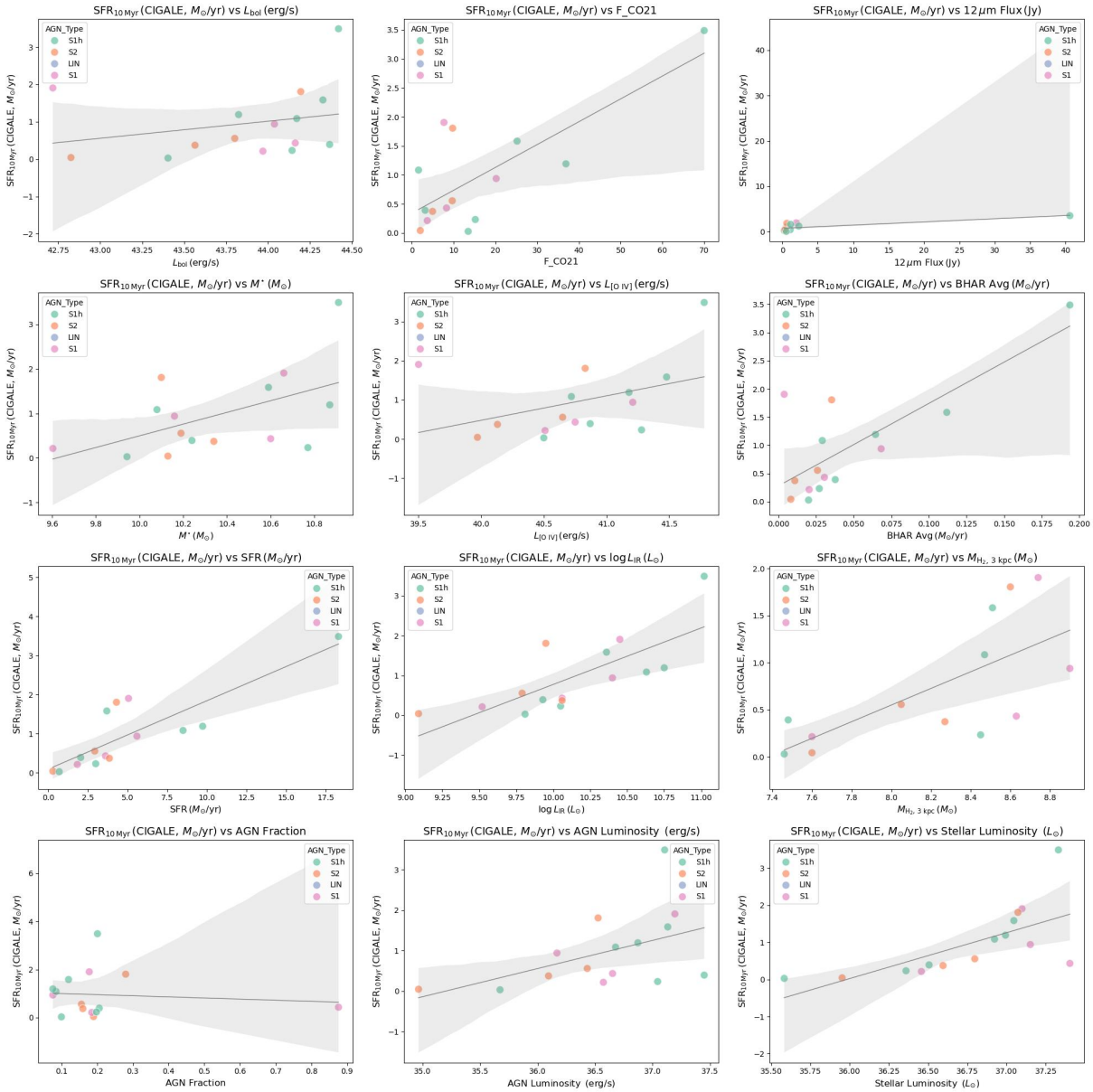

FIGURE G.41 – Scatter plot of exploratory data analysis for scatter sfh.sfr10Myrs CIGALE part 1

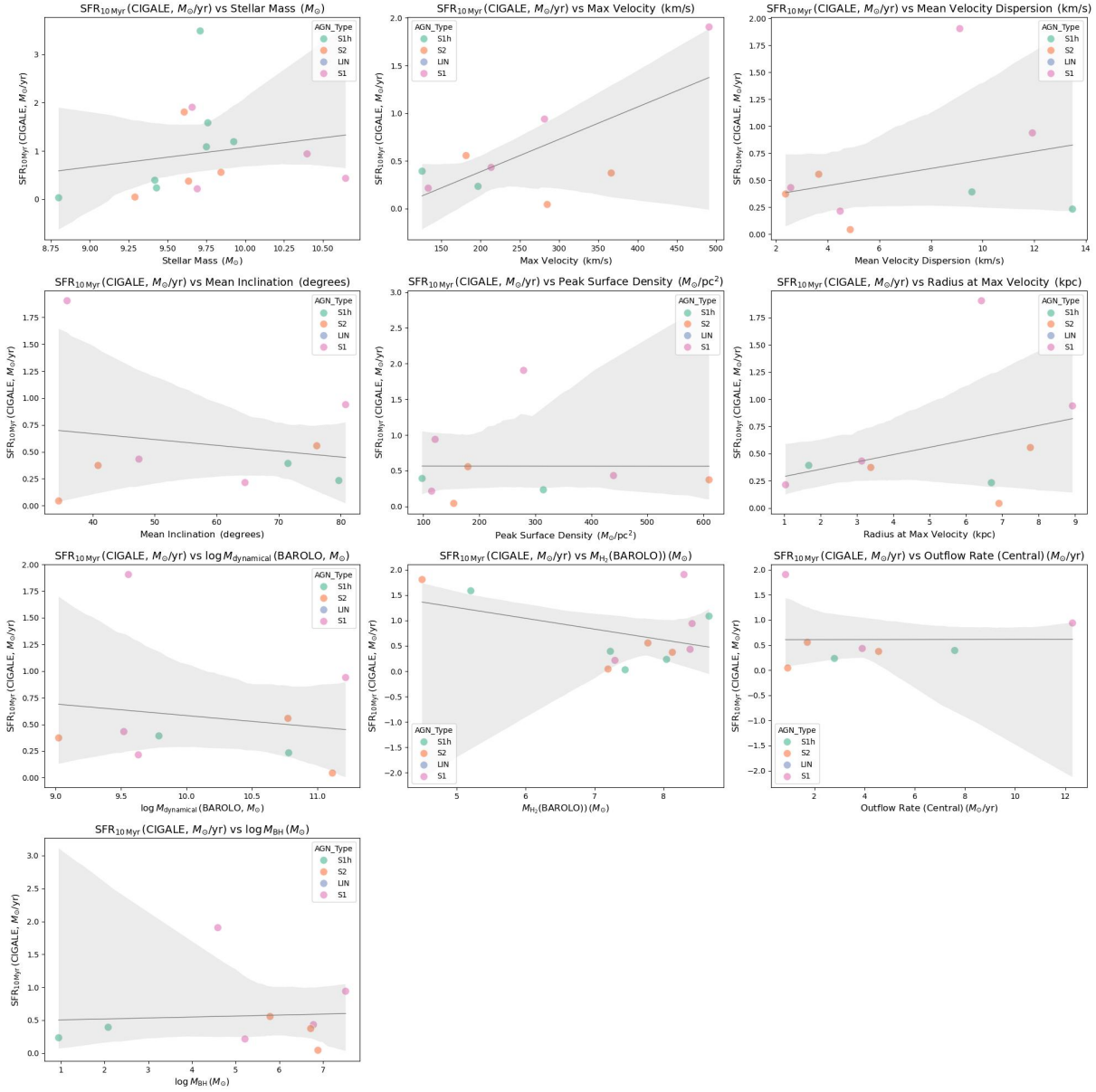

FIGURE G.42 – Scatter plot of exploratory data analysis for scatter sfh.sfr10Myrs CIGALE part 2

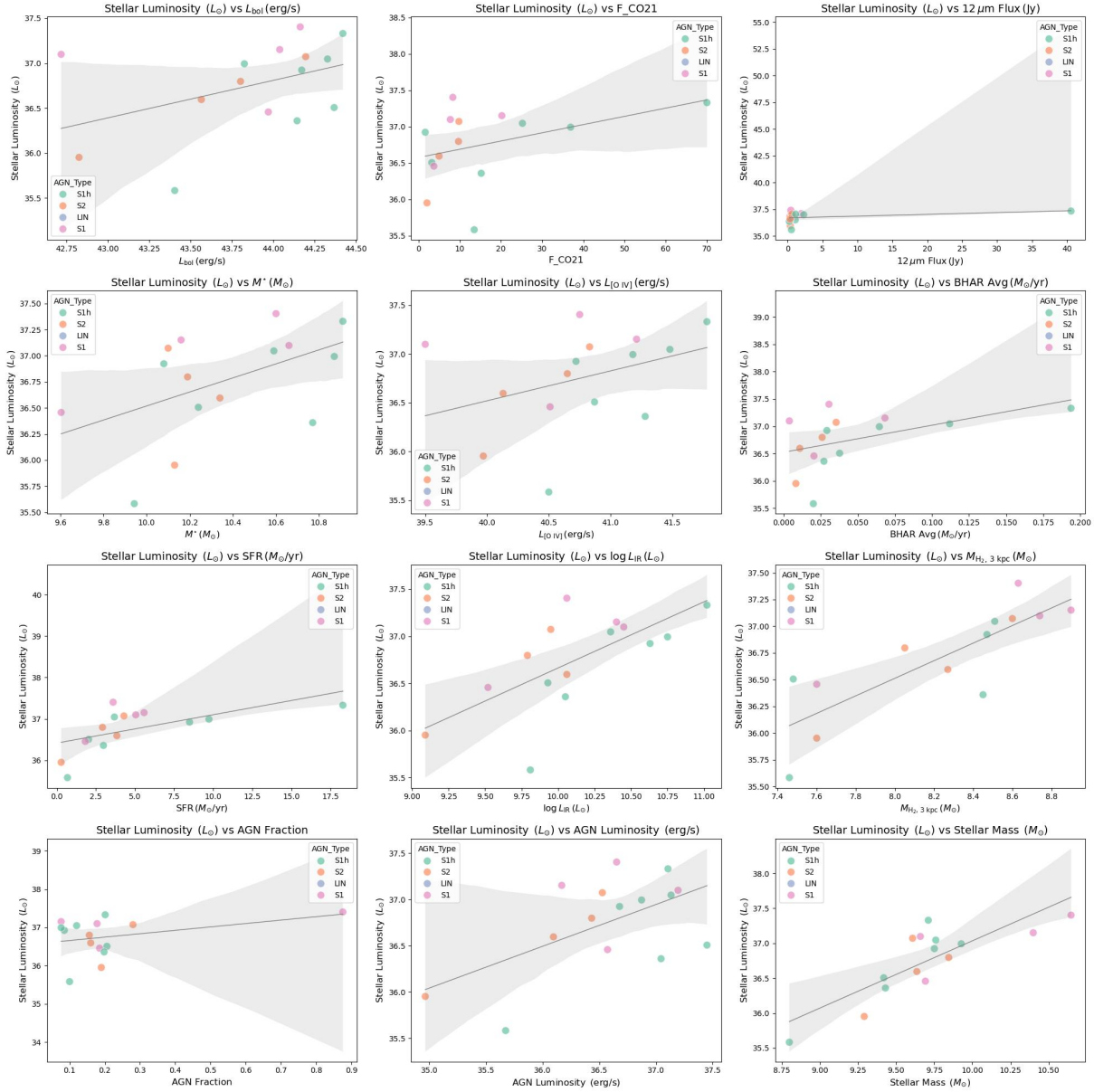

FIGURE G.43 – Scatter plot of exploratory data analysis for scatter stellar.lum CIGALE part 1

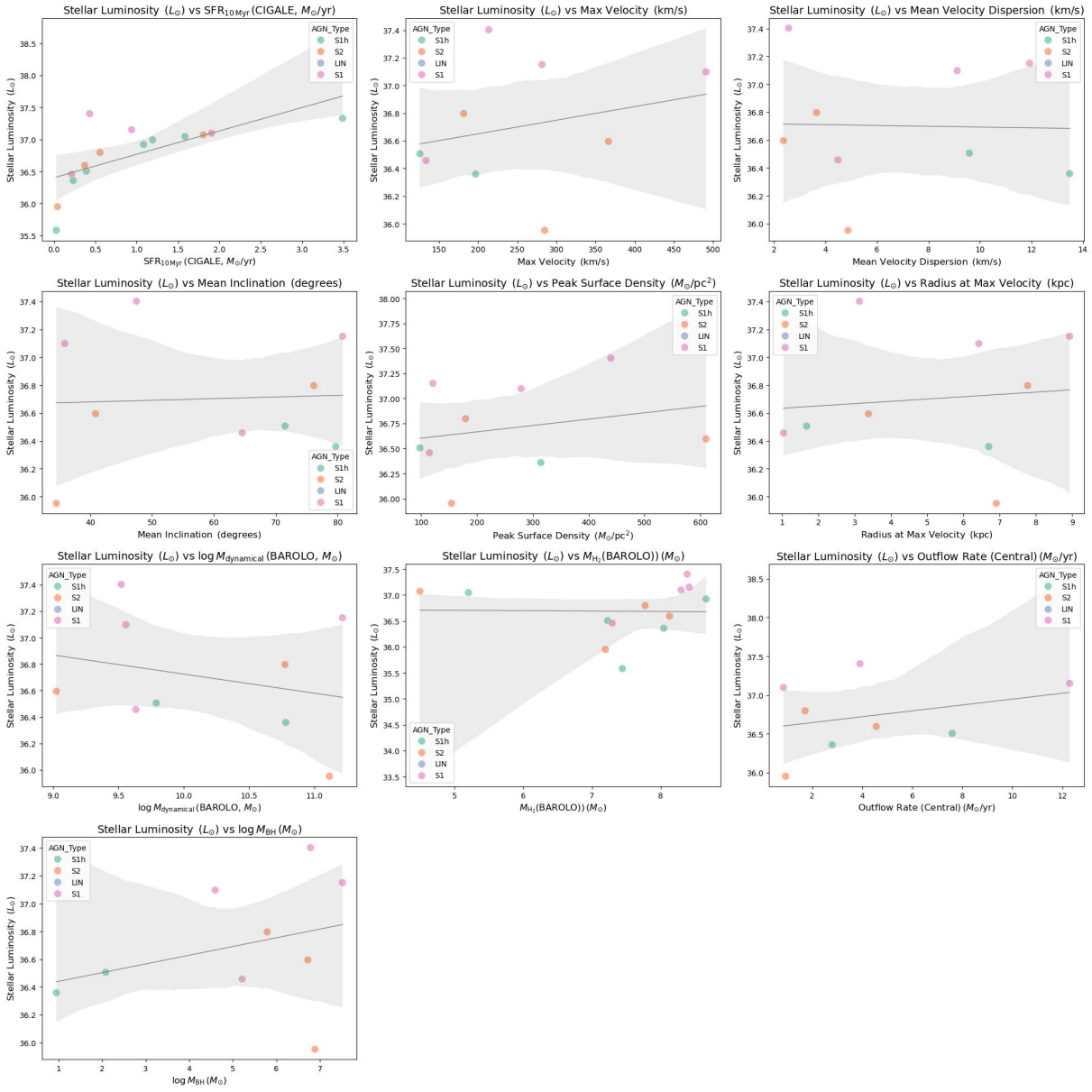

FIGURE G.44 – Scatter plot of exploratory data analysis for scatter stellar.lum CIGALE part 2

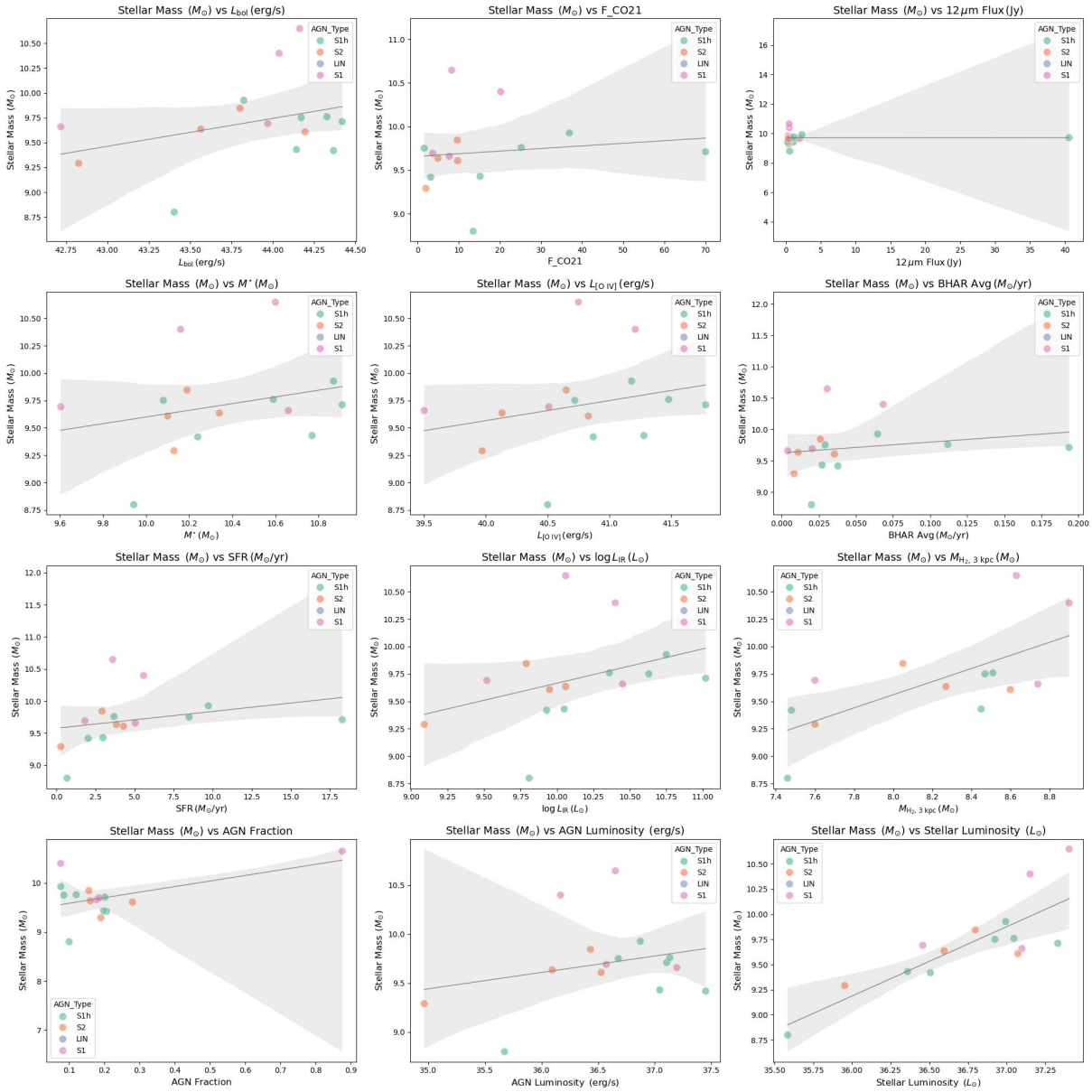

FIGURE G.45 – Scatter plot of exploratory data analysis for scatter stellar.m star CIGALE part 1

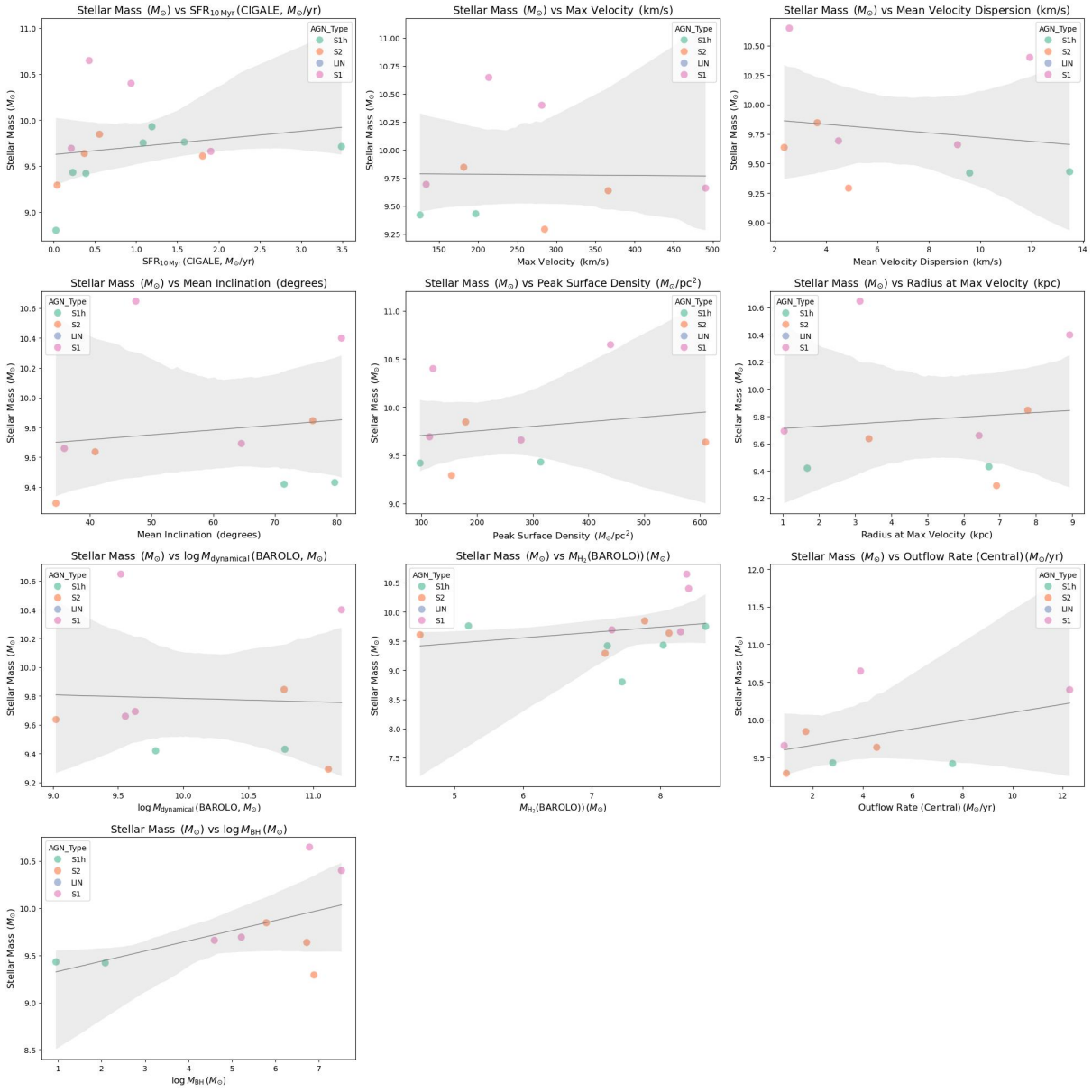

FIGURE G.46 – Scatter plot of exploratory data analysis for scatter stellar.m star CIGALE part 2

Appendix H - SED

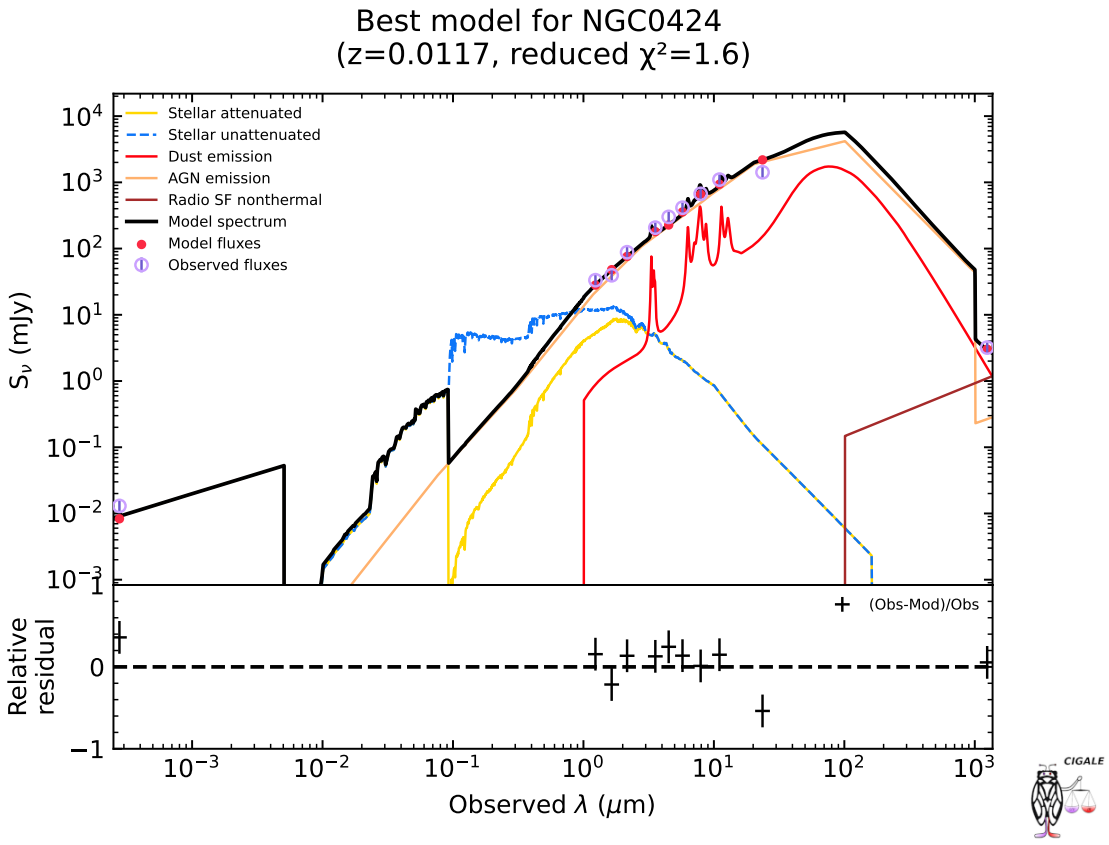

FIGURE H.1 – SED for NGC 424 using CIGALE

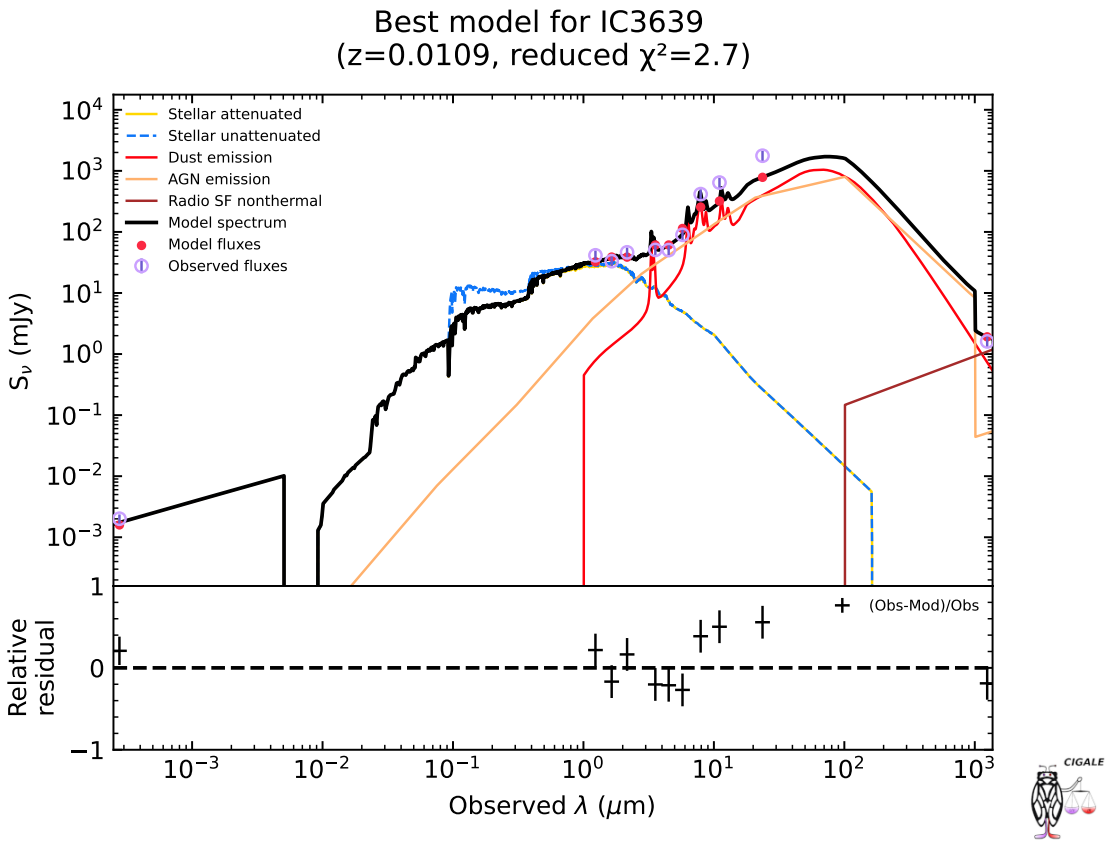

FIGURE H.2 – SED for IC3639 using CIGALE

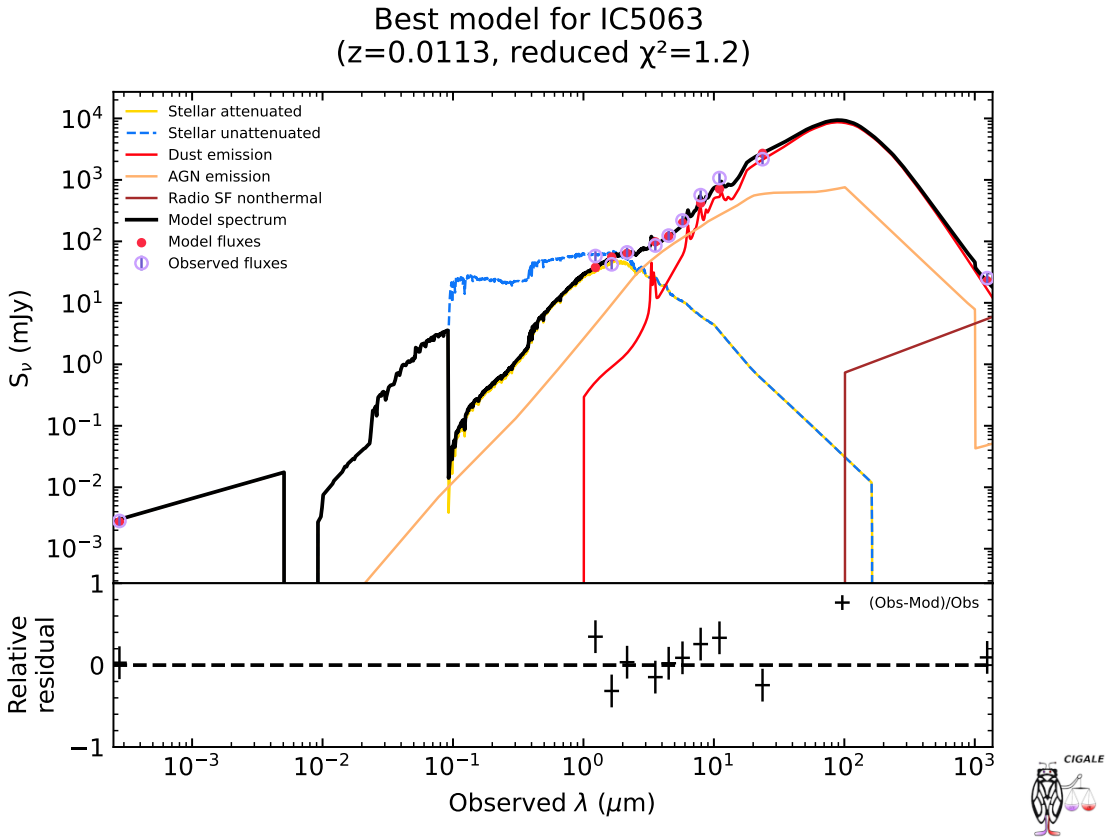

FIGURE H.3 – SED for IC5063 using CIGALE

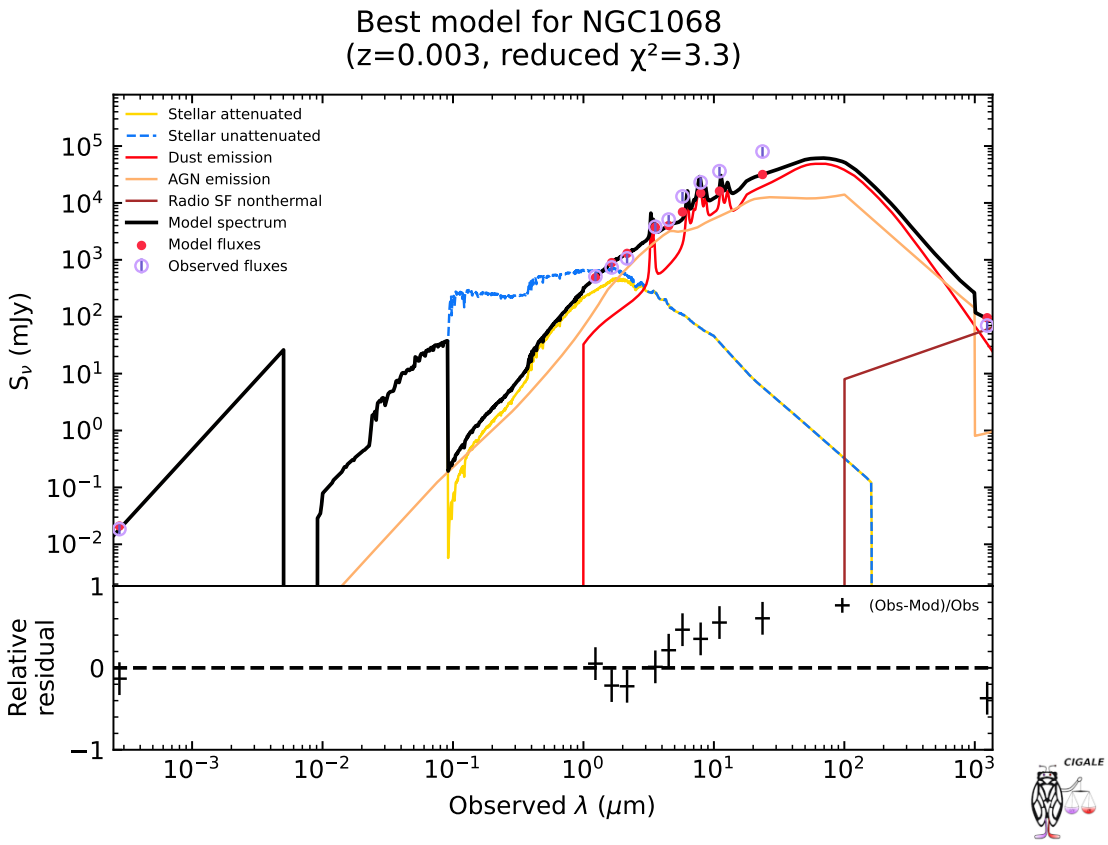

FIGURE H.4 – SED for NGC 1068 using CIGALE

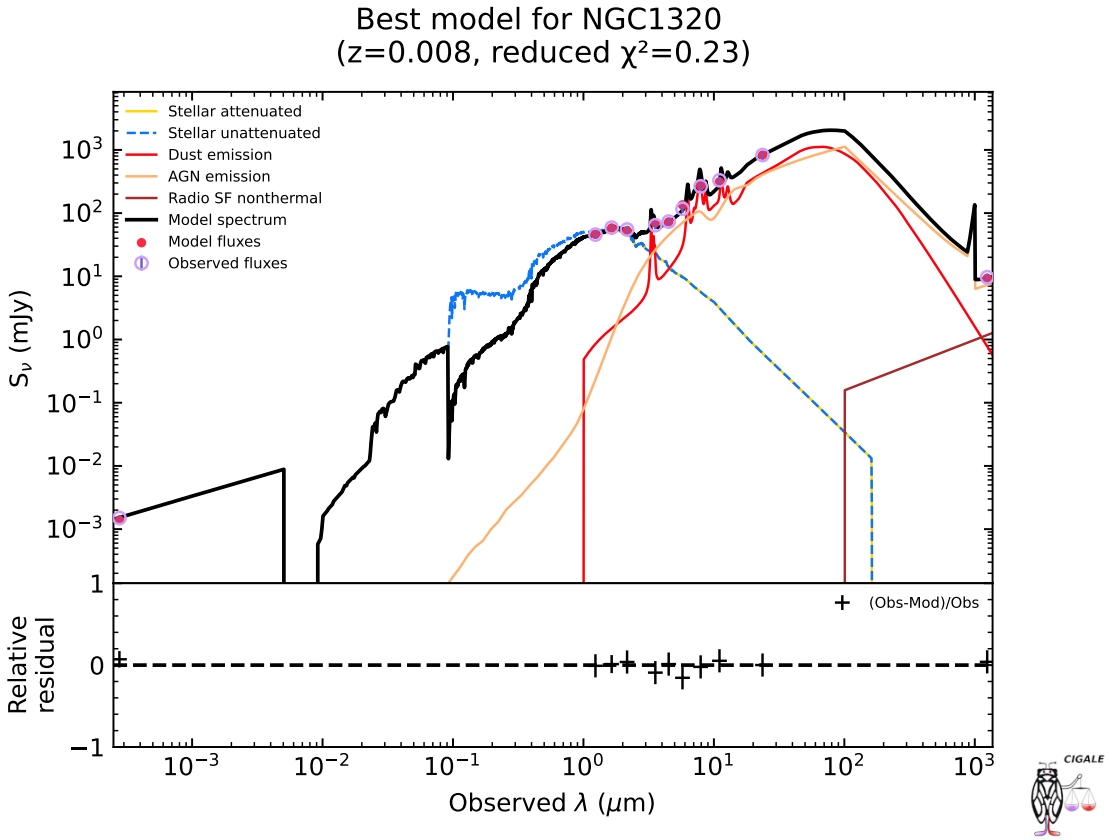

FIGURE H.5 – SED for NGC 1320 using CIGALE

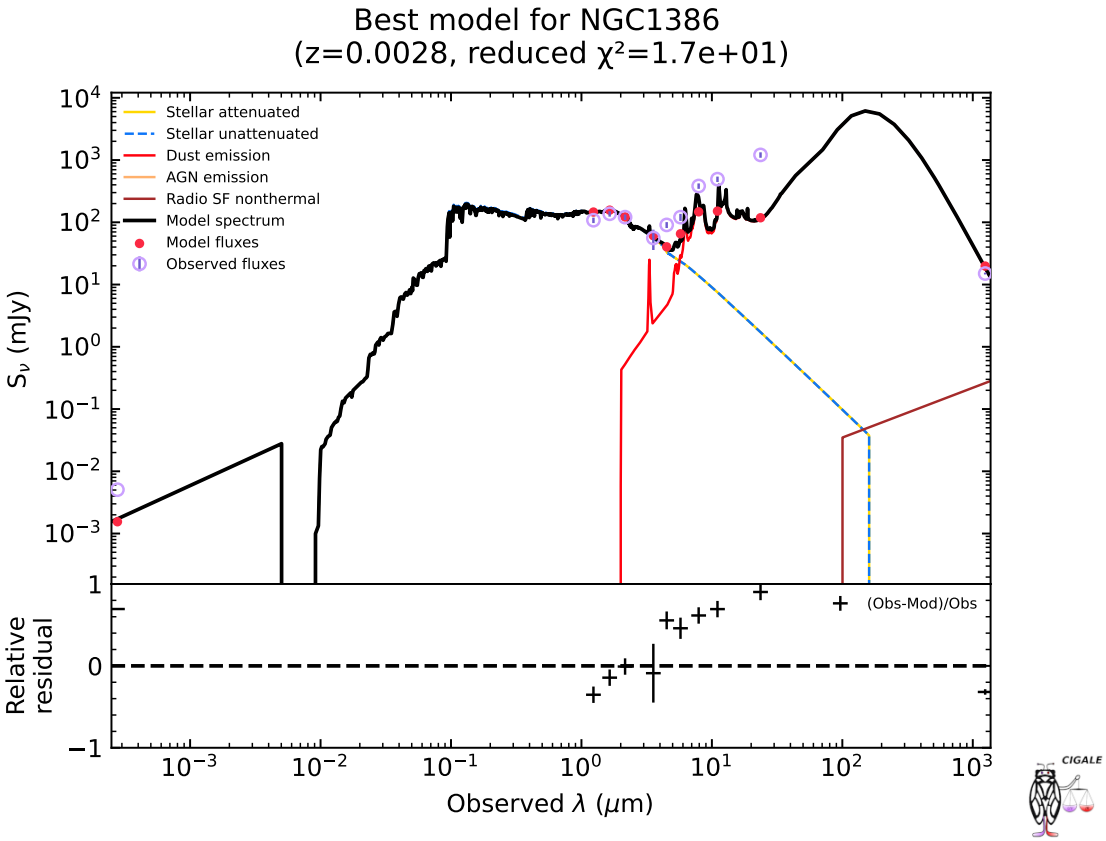

FIGURE H.6 – SED for NGC 1386 using CIGALE

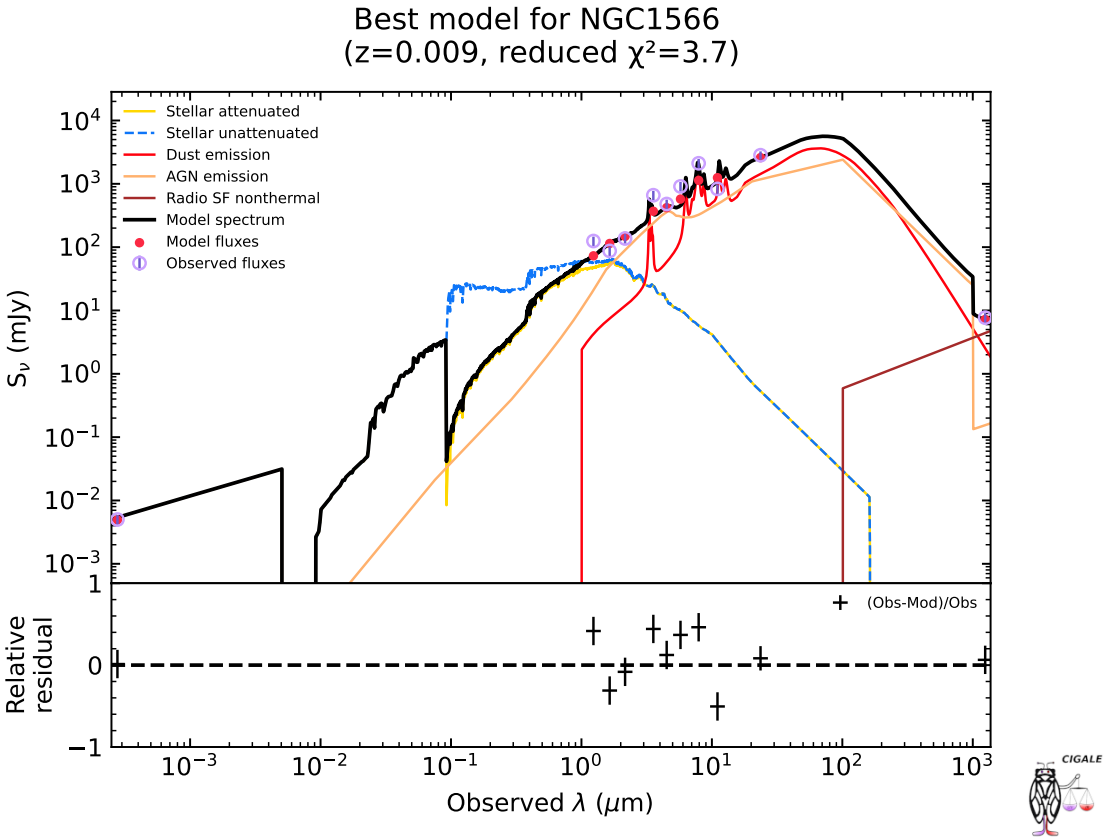

FIGURE H.7 – SED for NGC 1566 using CIGALE

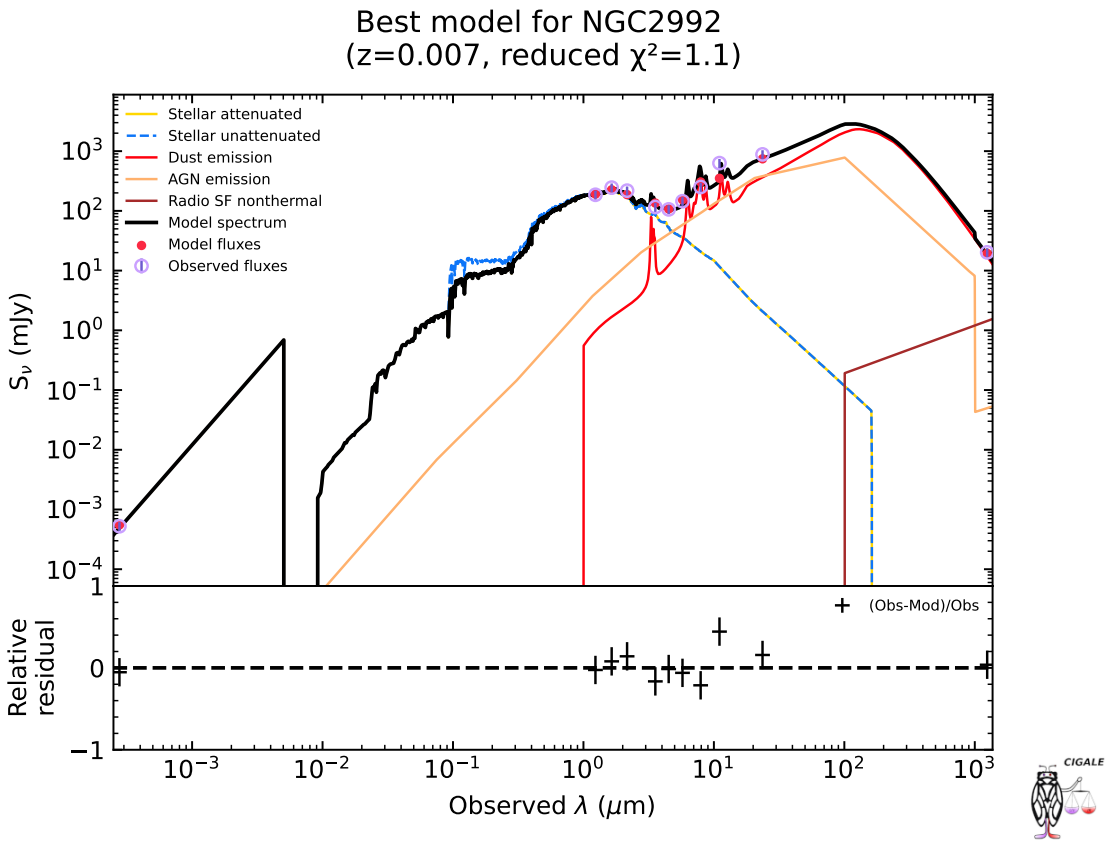

FIGURE H.8 – SED for NGC 2992 using CIGALE

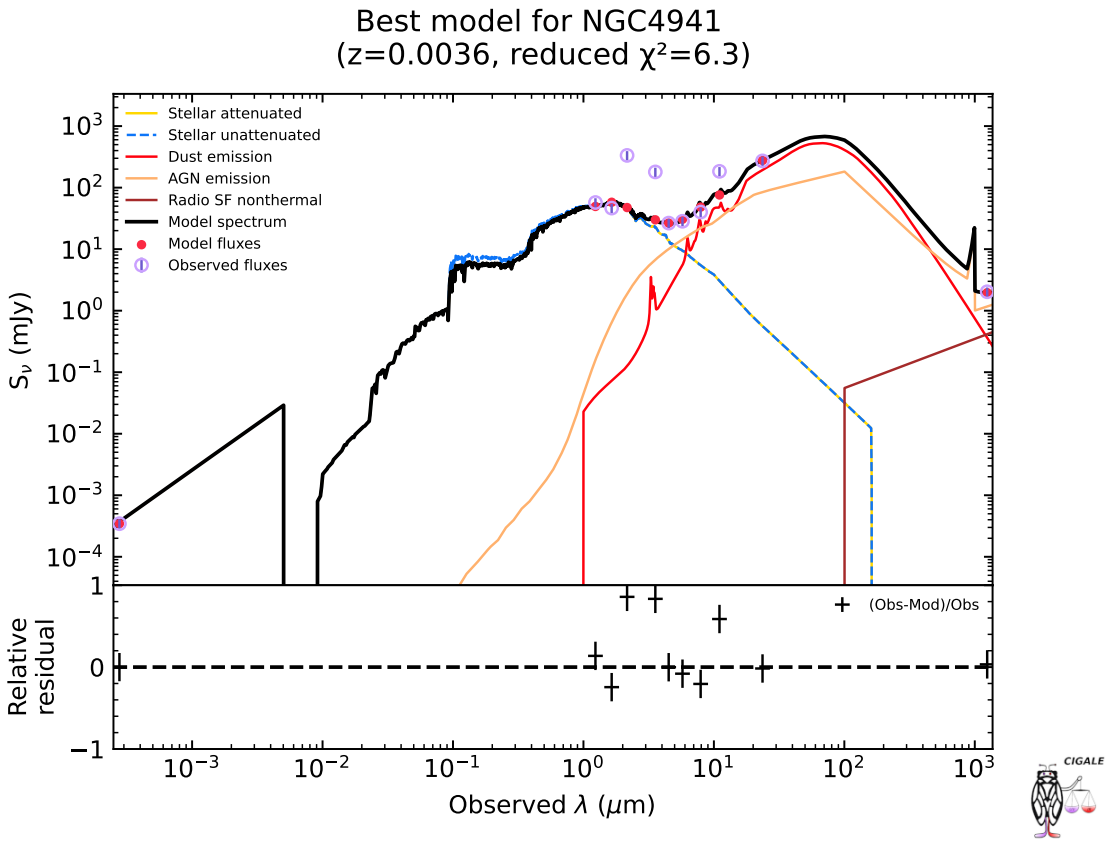

FIGURE H.9 – SED for NGC 4941 using CIGALE

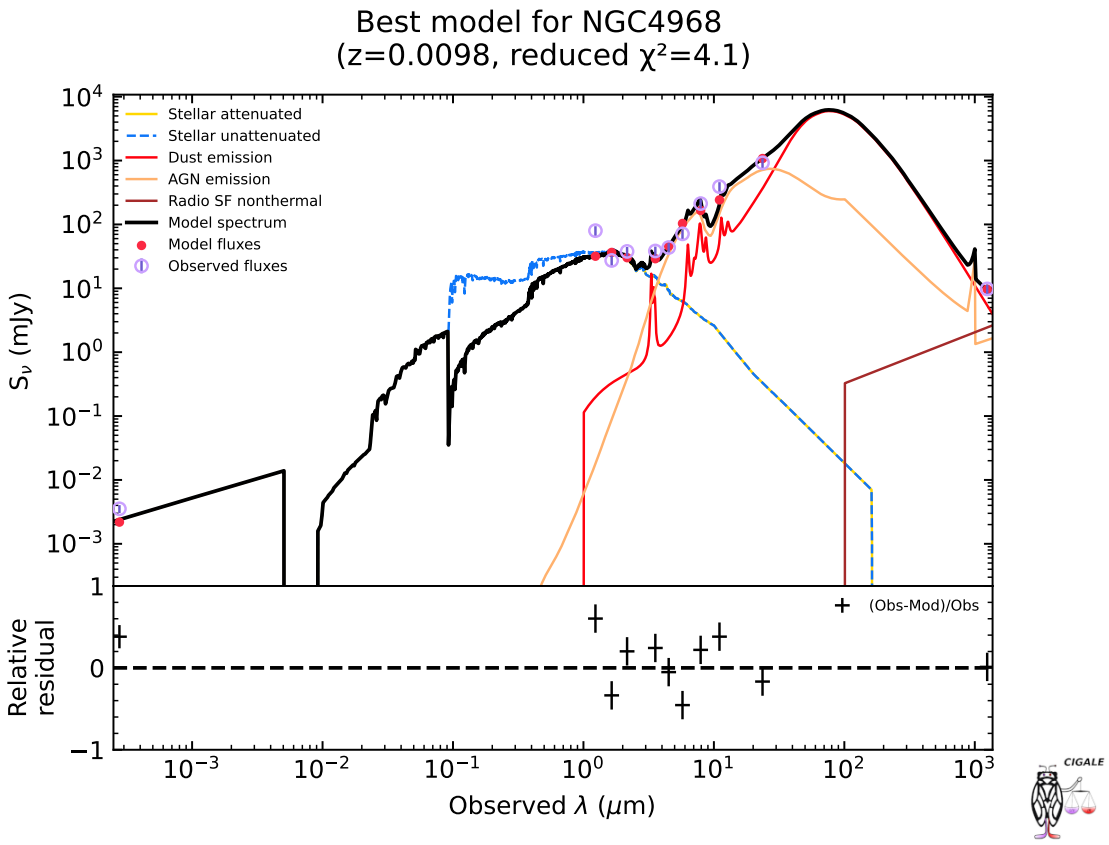

FIGURE H.10 – SED for NGC 4968 using CIGALE

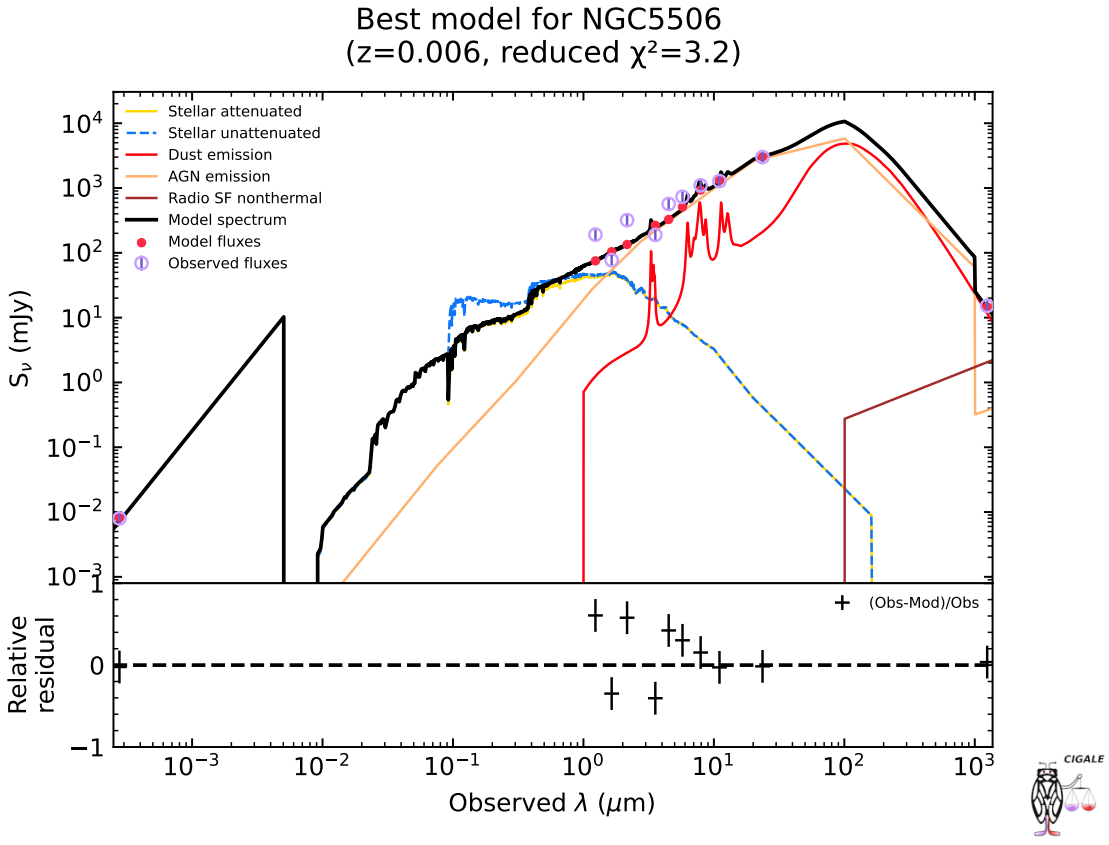

FIGURE H.11 – SED for NGC 5506 using CIGALE

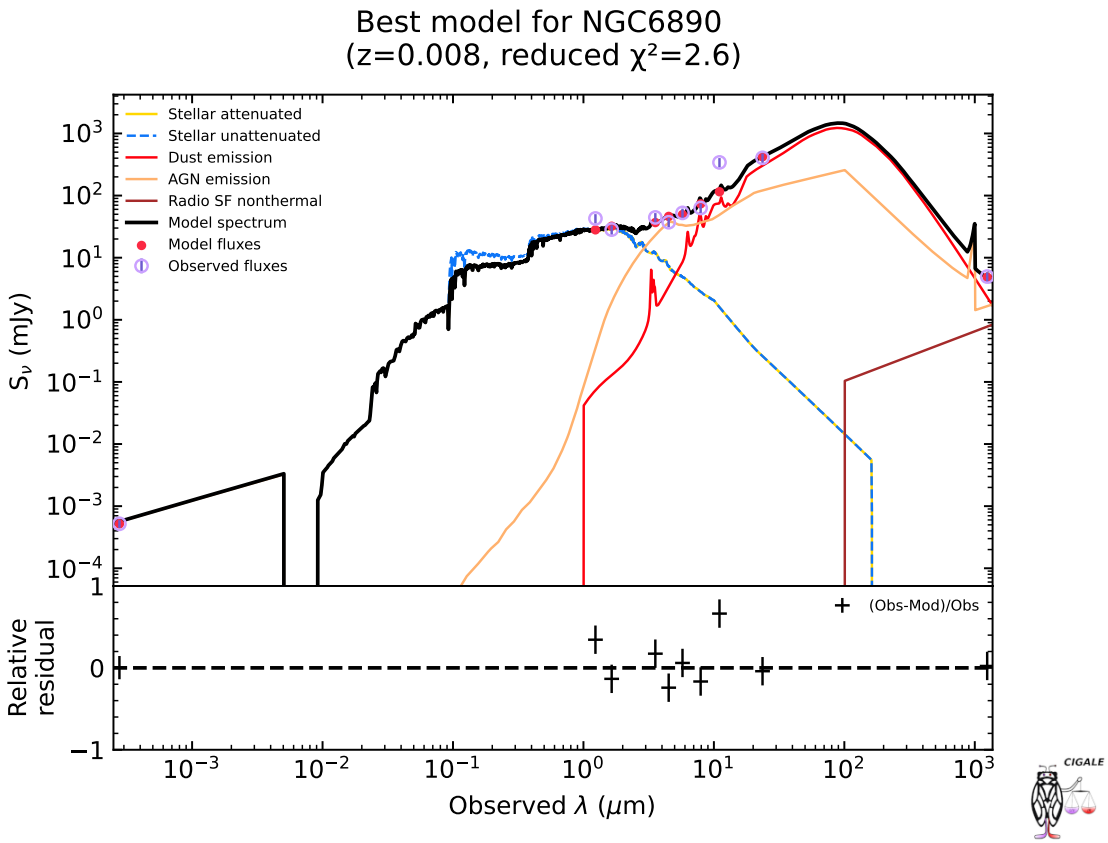

FIGURE H.12 – SED for NGC 6890 using CIGALE

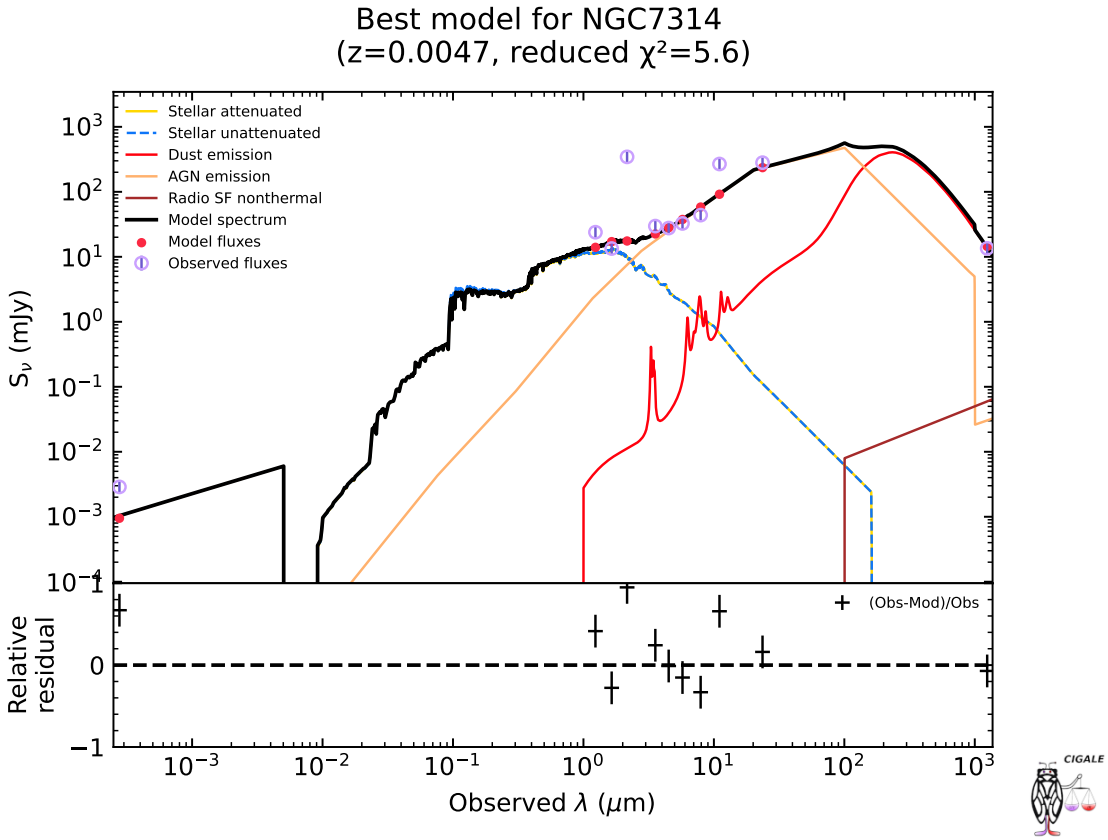

FIGURE H.13 – SED for NGC 7314 using CIGALE

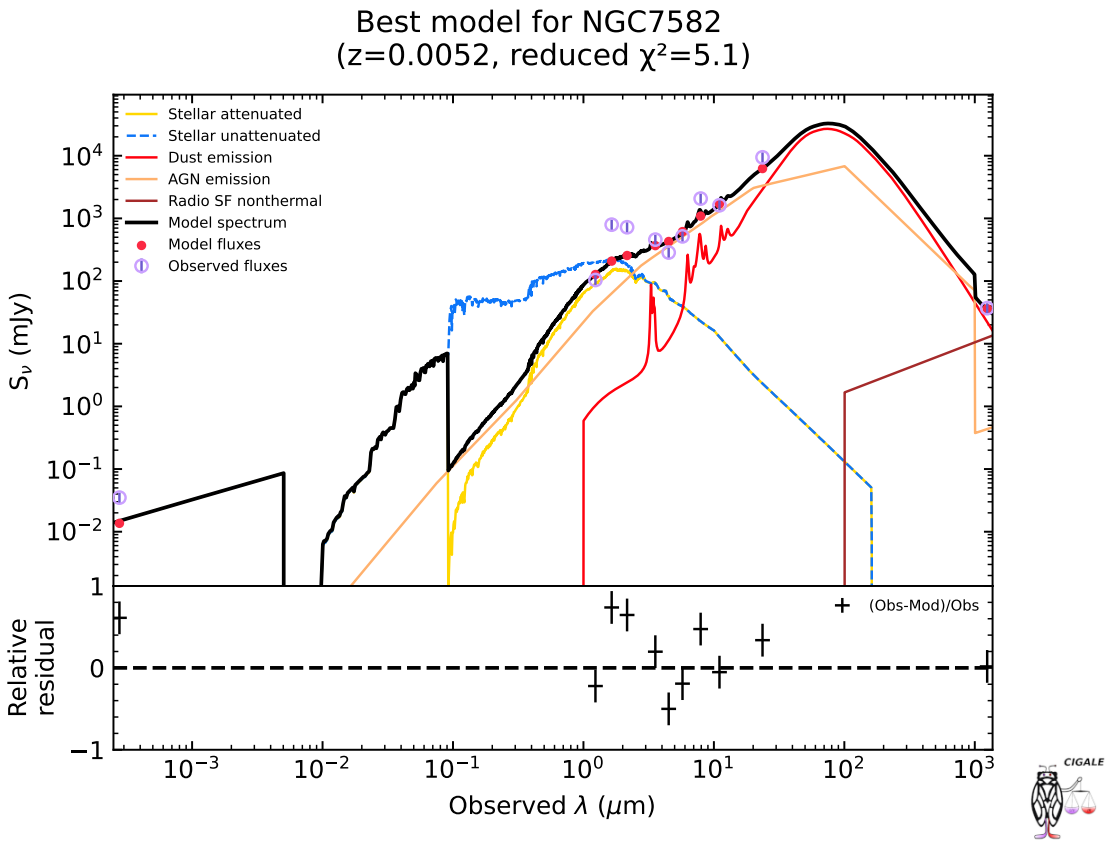

FIGURE H.14 – SED for NGC 7582 using CIGALE

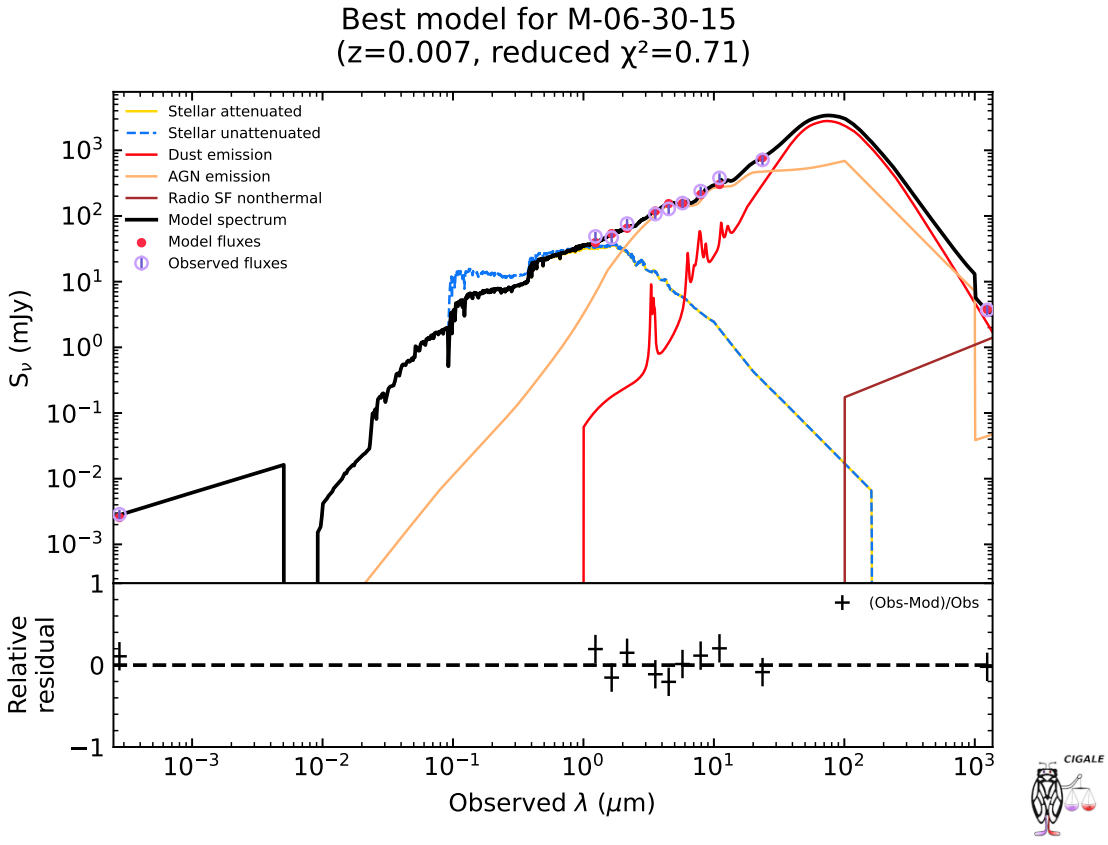

FIGURE H.15 – SED for M-06-30-15 using CIGALE

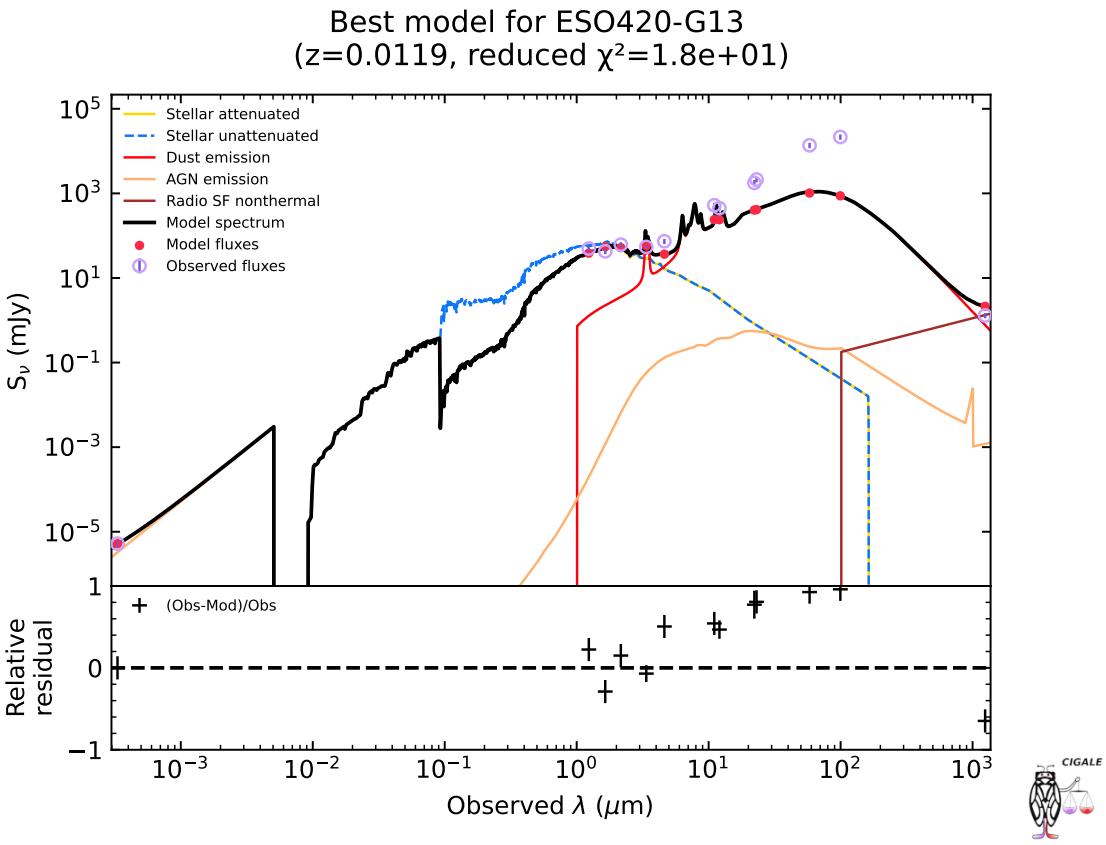

FIGURE H.16 – SED for M-05-11-06 using CIGALE

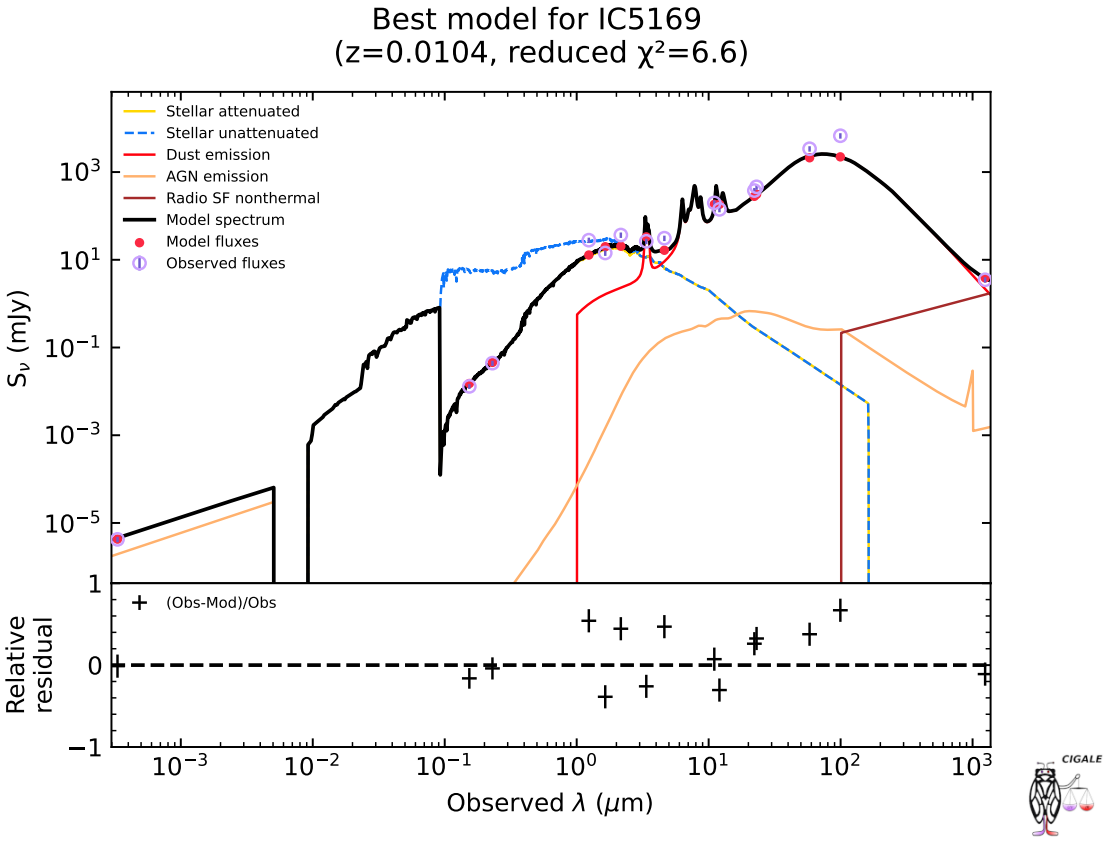

FIGURE H.17 – SED for IC5169 using CIGALE

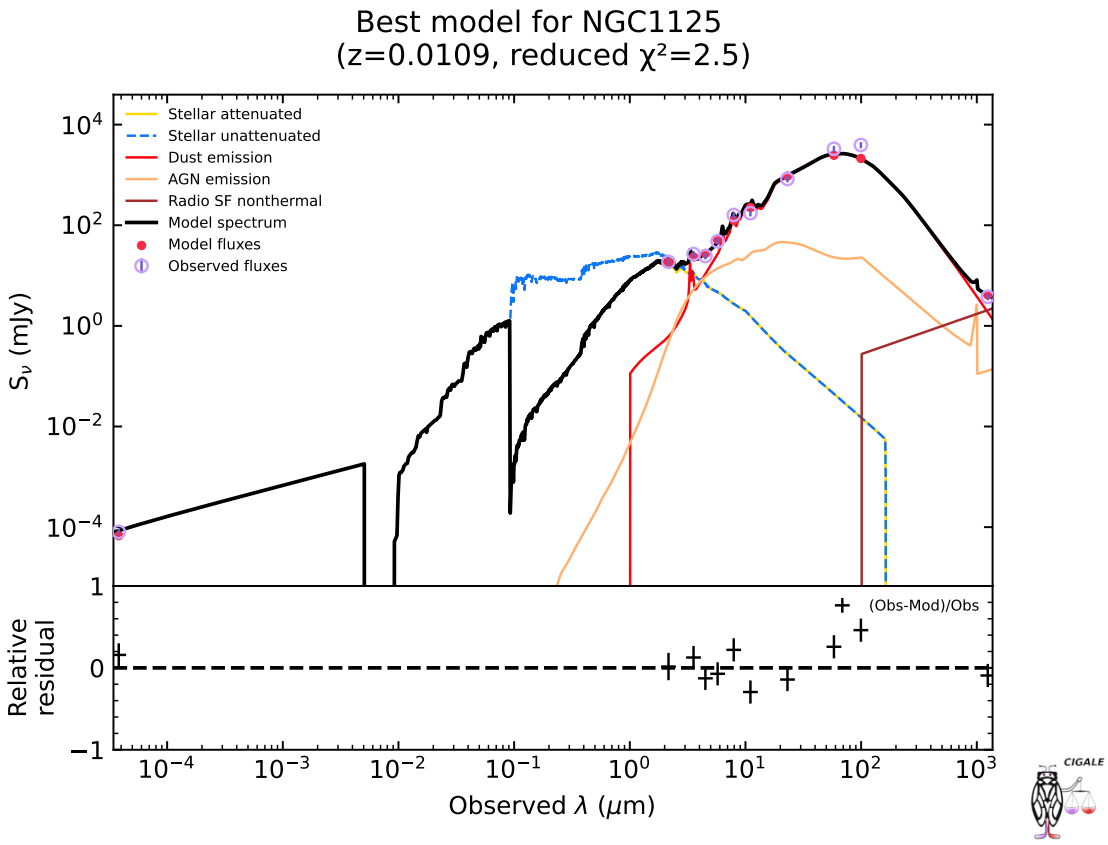

FIGURE H.18 – SED for NGC1125 using CIGALE

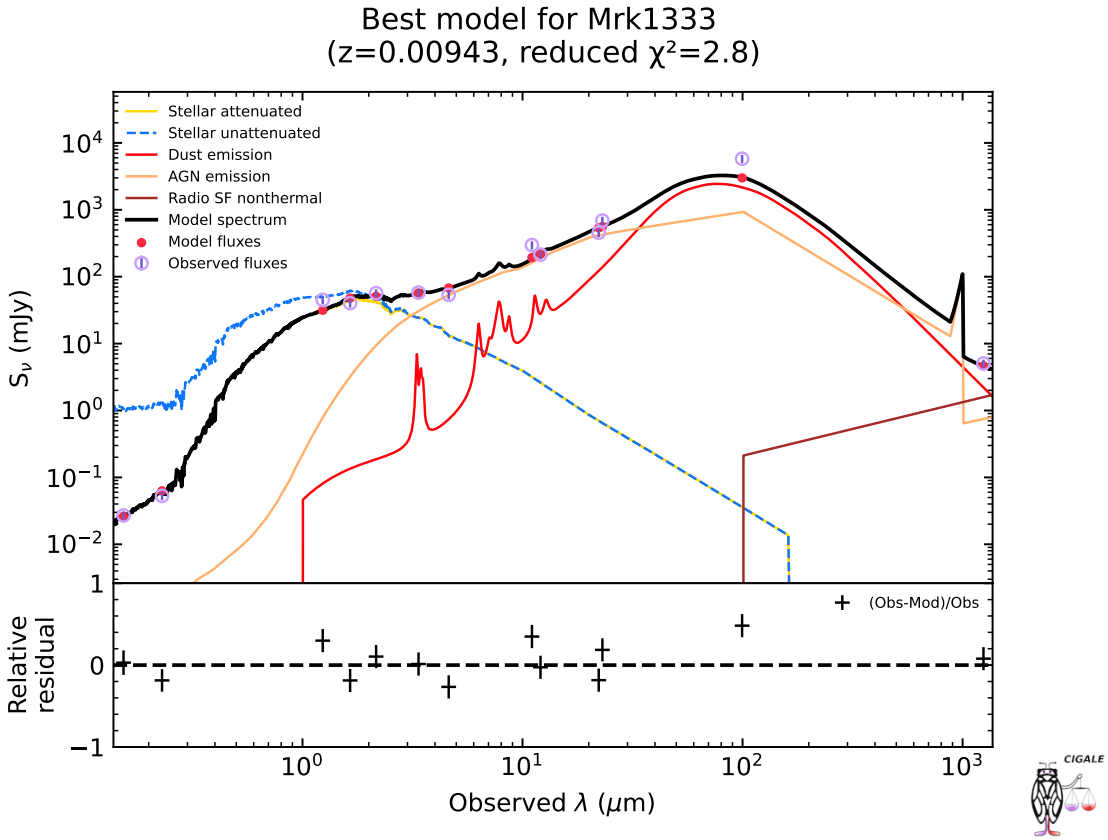

FIGURE H.19 – SED for MRK1333 using CIGALE

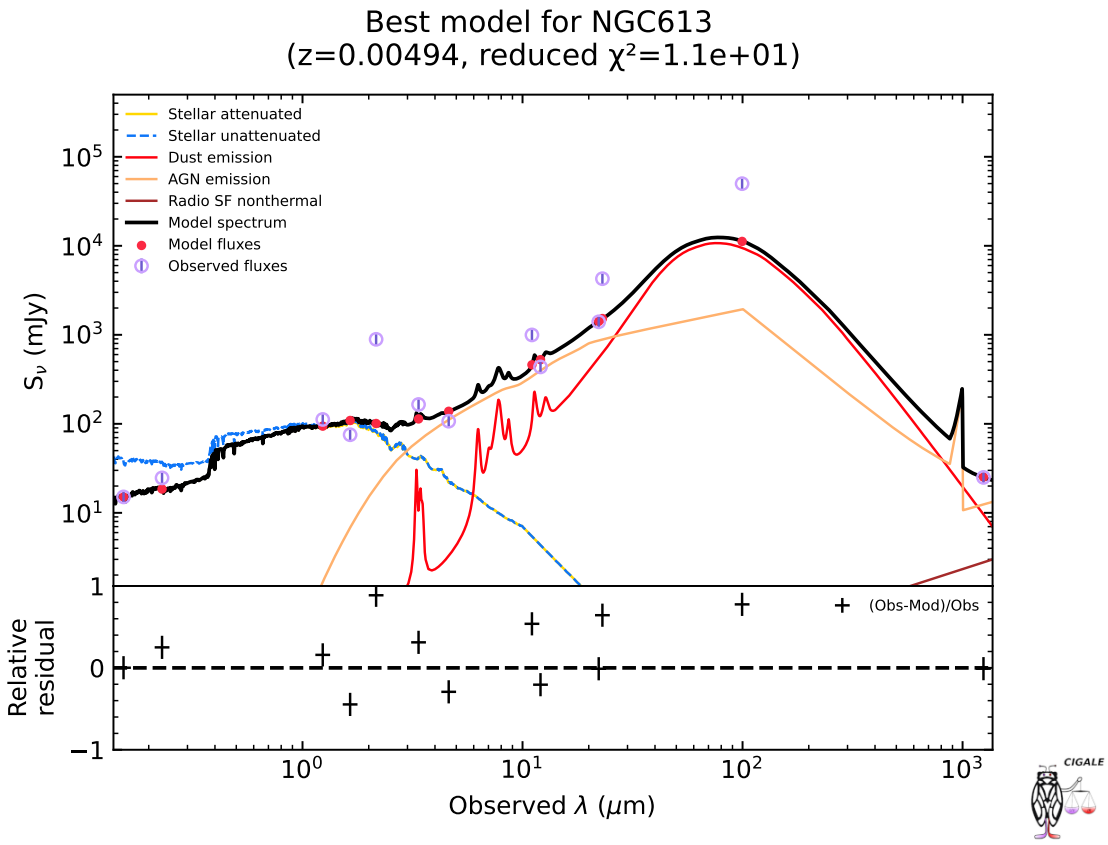

FIGURE H.20 – SED for NGC613 using CIGALE

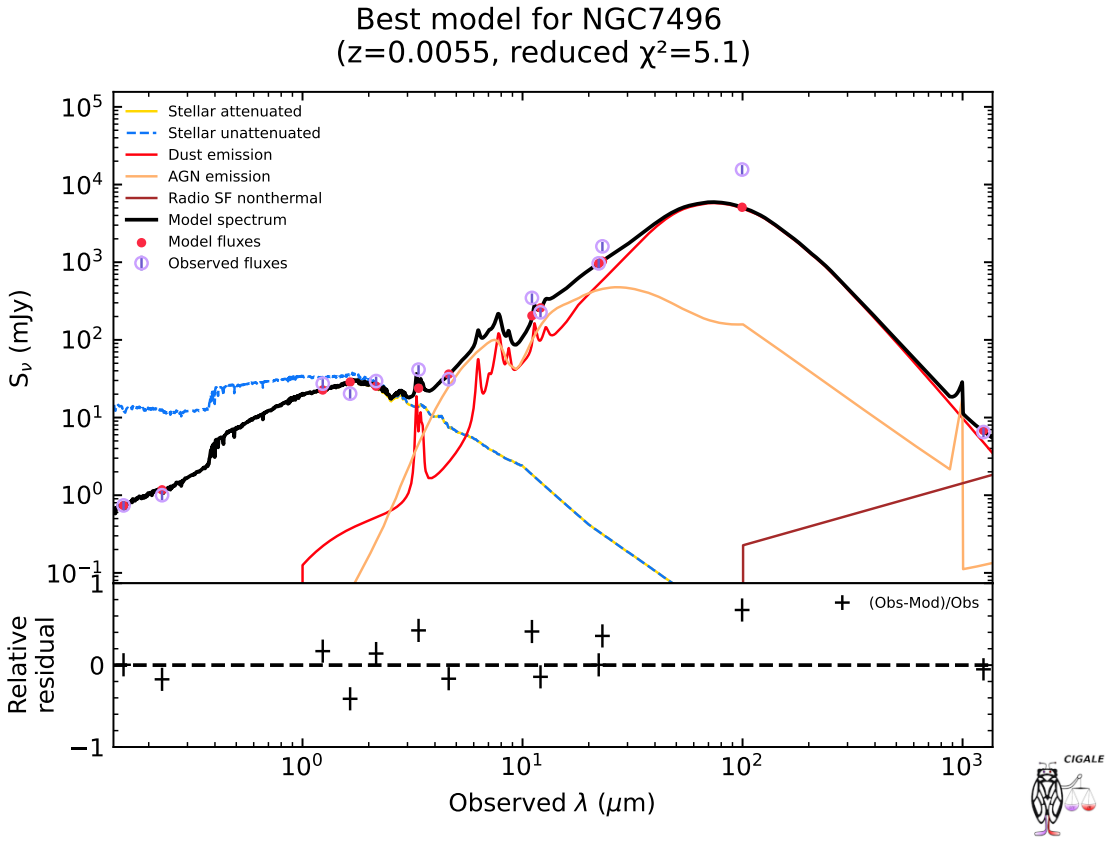

FIGURE H.21 – SED for NGC7496 using CIGALE

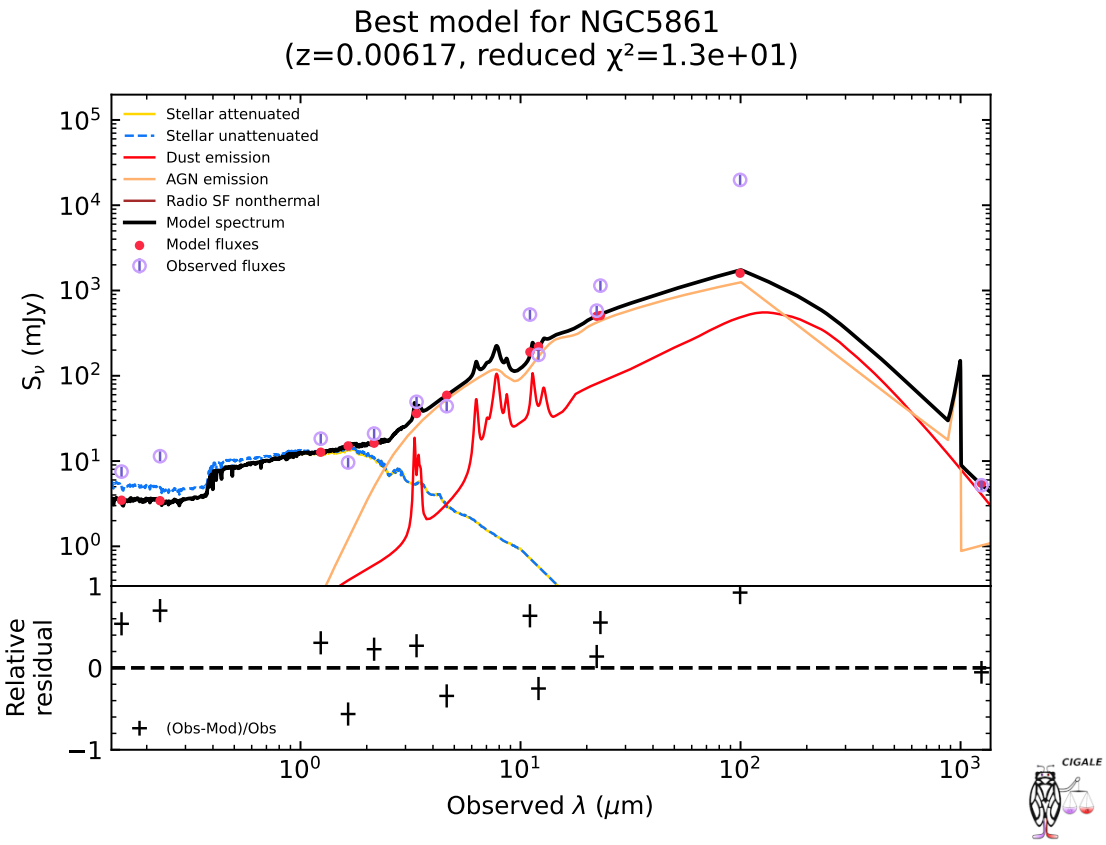

FIGURE H.22 – SED for NGC5861 using CIGALE

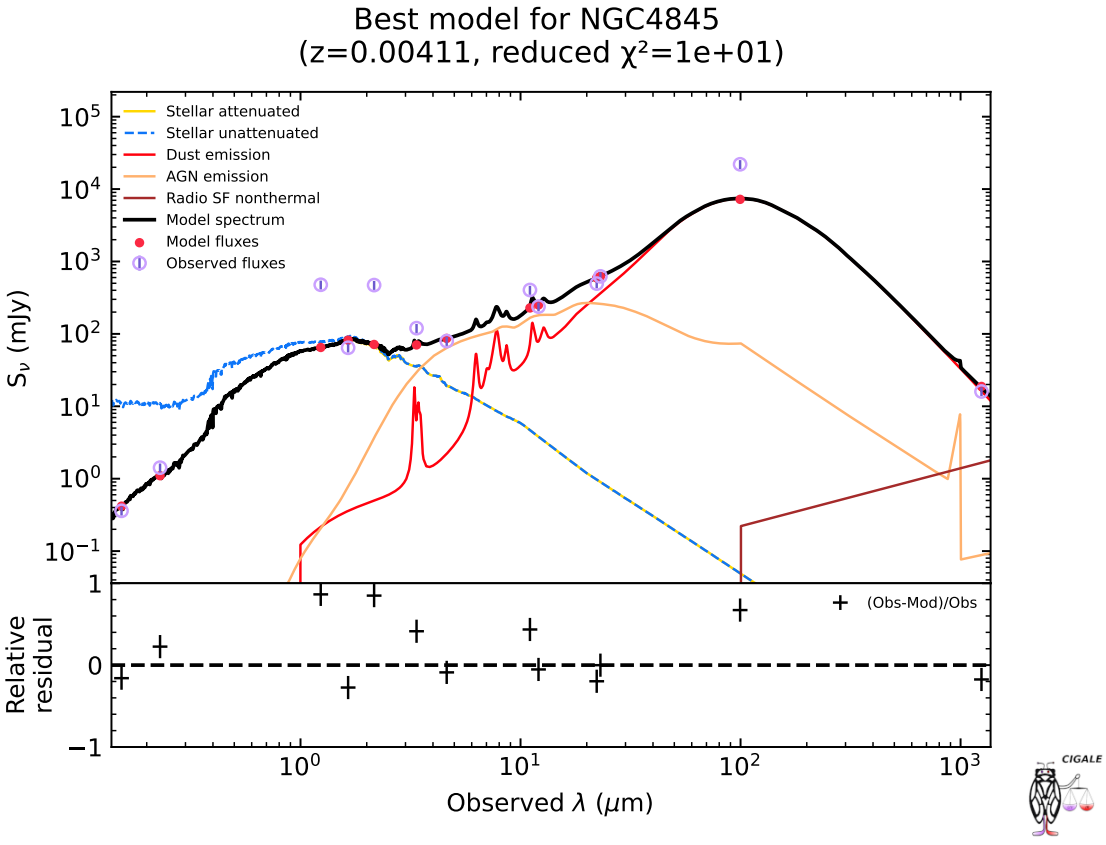

FIGURE H.23 – SED for NGC4845 using CIGALE

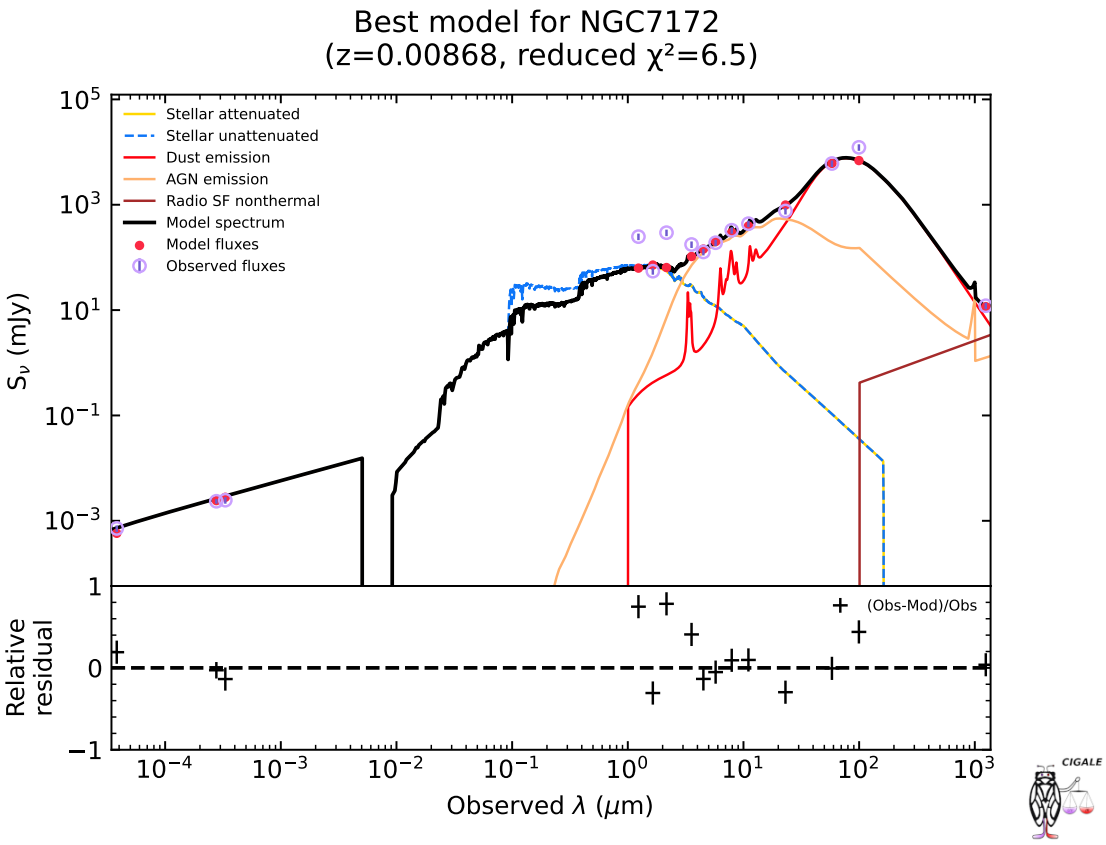

FIGURE H.24 – SED for NGC7172 using CIGALE

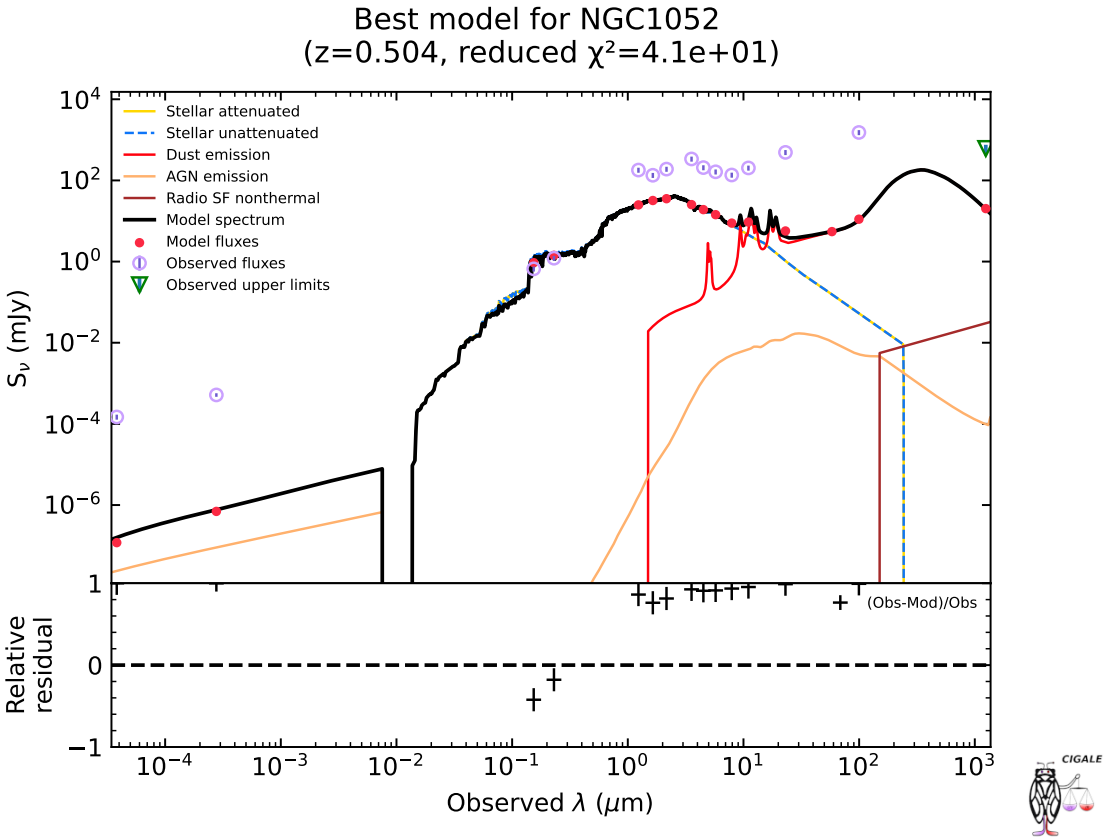

FIGURE H.25 – SED for NGC1052 using CIGALE

FOLHA DE REGISTRO DO DOCUMENTO

1. CLASSIFICAÇÃO/TIPO	2. DATA	3. REGISTRO N°	4. N° DE PÁGINAS
TD	26 de março de 2025	DCTA/ITA/TD-005/2025	301

5. TÍTULO E SUBTÍTULO:

Multiwavelength studies of AGN feeding & feedback mechanisms in the nearby universe.

6. AUTOR(ES):

Khashayar Kianfar

7. INSTITUIÇÃO(ÕES)/ÓRGÃO(S) INTERNO(S)/DIVISÃO(ÕES):

Instituto Tecnológico de Aeronáutica – ITA

8. PALAVRAS-CHAVE SUGERIDAS PELO AUTOR:

Núcleos Ativos de Galáxias (AGN), Dinâmica do Gás Molecular, Formação Estelar, Evolução de Galáxias, Observações ALMA CO(2-1), Amostra TWIST, Modelagem 3D-Barolo, Galáxia Seyfert 1 (NGC 4593), Entradas e Saídas de Gás, Distribuição Espectral de Energia (SED), CIGALE, Meio Interestelar (ISM)

9.PALAVRAS-CHAVE RESULTANTES DE INDEXAÇÃO:

Galáxias; Dinâmica dos gases; Formação de estrelas; Evolução estelar; Teoria molecular; Astrofísica; Astronomia; Física.

10. APRESENTAÇÃO: **(X) Nacional** **( ) Internacional**

ITA, São José dos Campos. Curso de Doutorado. Programa de Pós-Graduação em Física. Área de Fisica Nuclear. Orientador: Prof. Dr. Franciole da Cunha Marinho; coorientadora: Dra. Paola Andreani. Defesa em 24/02/2025. Publicada em 2025.

11. RESUMO:

This thesis investigates the role of AGN in influencing the molecular gas dynamics and star formation within their host galaxies, focusing on the TWIST sample of nearby AGN host galaxies. Using high-resolution CO(2-1) data from the ALMA and multi-wavelength observations, we analyze the interaction between AGNs and the interstellar medium (ISM), examining how AGN activity drives gas inflows and outflows that shape galaxy evolution. Our study begins with a detailed analysis of NGC 4593, a Seyfert 1 galaxy with a prominent bar and active nucleus. We used ALMA CO(2-1) observations alongside 3D-Barolo and discFit kinematic modeling to assess gas distribution and dynamics. The modeling reveals a complex structure, including a central molecular zone (CMZ)-like ring with strong rotational motion and significant non-circular features aligned with the bar potential. We detect a molecular outflow along the galaxy's minor axis, extending approximately 220 pc from the nucleus and comprising about 10% of the galaxy's total CO(2-1) flux. The estimated total molecular gas mass is $1 - 5 \times 108$ M⊙,, and the supermassive black hole (SMBH) mass is calculated to be log (MBH /M⊙) = 6.89 ± 0.04. Spectral energy distribution (SED) modeling with CIGALE reveals an AGN fraction of 0.88 and a moderate star formation rate of 0.42 M⊙ yr^{-1} . Building on this framework, we applied the same methodology to 20 additional galaxies within the TWIST sample. For each galaxy, we derived the kinematics and morphology of the molecular gas using 3D-Barolo and performed spectral energy distribution fitting with CIGALE to determine star formation rates, AGN luminosities, AGN fractions, stellar masses, molecular gas masses, and black hole masses. Our analysis identified clear signatures of either gas inflows or outflows in several galaxies, enabling us to calculate outflow mass rates for roughly 20 of the 41 galaxies studied.

12. GRAU DE SIGILO:

(X) OSTENSIVO	( ) RESERVADO	( ) SECRETO